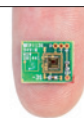


# THIS WEEK

## EDITORIALS

**MADDOX PRIZE** The first award-winners who stood up for science **p.160**

**WORLD VIEW** What the new leadership in China means for research **p.161**



**EAR PLUG** Tiny chip generates electricity from audio power **p.162**

## Ignition switch

*The US National Ignition Facility has so far failed to generate fusion energy, but repurposing it as a tool to study nuclear weapons and basic science could be its saving grace.*

On a breezy day in 2009, action star Arnold Schwarzenegger, then governor of California, took to the stage to dedicate the National Ignition Facility (NIF), the world's most powerful laser. "I can see already my friends in Hollywood being very upset that their stuff that they show on the big screen is obsolete," the governor quipped in front of the recently completed facility, which uses lasers to squeeze fusion energy from a tiny pellet of hydrogen fuel. "Fusion energy may be exactly what will power future generations on the globe," he added.

Fast-forward three years and the script is somewhat different: the lofty hopes of Schwarzenegger and other politicians who attended the ceremony that day seem less realistic. At the end of September, officials at Lawrence Livermore National Laboratory (LLNL) in Livermore, California, where the NIF is based, announced that the facility would miss a crucial milestone to produce ignition — releasing as much energy from fusion as is supplied by the lasers. After an intense, six-year effort, the facility remains a factor of ten away from that goal. In the coming weeks, LLNL scientists are expected to lay out an alternative, much longer, path to ignition, while senior officials refocus the laser's work (see page 170). For now, thanks in large part to the NIF's role in nuclear-weapons science, politicians will allow the research programme to trundle on at a cost of US\$280 million per year. But the great unfulfilled promise of the NIF should serve as a cautionary lesson for scientists who promote Hollywood solutions from their research.

The NIF is a jaw-dropping piece of technology. It trains 192 separate laser beams on to a capsule of hydrogen fuel a few millimetres long. The power from the lasers compresses the fuel until it fuses, creating energy from the mass of the hydrogen isotopes. The NIF's goal is to produce break-even energy from this fusion — no mean feat, considering that the input energy can be up to 1.8 megajoules.

In 2005, the LLNL and the US National Nuclear Security Administration, which oversees the lab, laid out a plan to reach the break-even point. The National Ignition Campaign, which kicked off the following year, aimed to bring the fledgling facility up to full power, kit it out with diagnostics and perform a series of tests on its hydrogen fuel. Tellingly, the original plan does not commit the lab to reach ignition, but instead called for "a credible ignition experimental campaign".

But during the past six years, expectations around the NIF have grown well beyond that credible campaign. In many ways, the lab itself is to blame for the unrealism. Lab officials gave tours to prominent politicians and journalists in which they promised a lot more than just ignition. The NIF, they claimed, was the first step on the road to potentially unlimited fusion energy. In support of their dream, LLNL scientists developed a prototype for an electricity-producing reactor that they hoped would gain financing once ignition was achieved.

But problems were mounting even as the lab eagerly promised clean, cheap electricity. Outside reviewers noted that the hydrogen fuel was not being compressed properly. The computer codes used to predict the facility's performance were themselves operating badly. Privately,

most people familiar with the programme had known for more than a year that the NIF could not reach ignition in the time allowed. Yet the LLNL stubbornly insisted that it might yet meet its goal. Enthusiasm gave way to saving face, as the leadership struggled to hold the line and keep up the appearance that all was going well.

Fortunately, this is not the end of the NIF. In addition to carrying the far-off promise of clean energy, the facility also mimics the physics of nuclear weapons. Scientists at the lab will now use it to address

**"The line between optimism and overselling is a thin one that can too easily be crossed."**

questions about the ageing US nuclear stockpile. The lasers can provide physicists with an invaluable tool to study how materials behave at enormous temperatures and pressures — similar, say, to those in Earth's interior. Despite the bluster of some at the lab, politicians have always recognized the value of this work, and they are willing to continue funding it for now.

The size and cost of the NIF make it an easy target for criticism, but those working there are hardly alone in their hubris. From stem cells to materials science, researchers around the globe make daily headlines with bold claims about what can be done in their fields. Politicians and the public, eager for solutions to the world's many problems, embrace their words. The process is often healthy: scientists insert caveats, and citizens are given a vague sense that things may not work out. But striking the balance between enthusiasm and conservatism can be difficult. The NIF reminds us that the line between optimism and overselling is a thin one that can too easily be crossed.

Pride comes before a fall. Now the NIF has to find its feet all over again. ■

## Science aid

*Donors and African governments must invest in advanced science and maths education.*

Of the eight United Nations Millennium Development Goals — the flagship international-development targets that world leaders set themselves for 2015 — none addresses how to improve education beyond the primary level.

Increasing literacy, eliminating hunger and reducing child mortality are all laudable goals and they have rightly been the focus of global development policies, especially in Africa. But the failure to consider secondary education, and beyond, as a development issue is an oversight. And it is a blind spot shared by Western donors,

non-governmental aid organizations and African governments alike.

Without support for post-primary mathematics and science education, Africa will remain dependent on foreign experts to craft policy, meet the needs of industry, perform research, combat disease and run the economy. Africa needs African experts, for the local knowledge they bring — particularly in fields such as epidemiology — but also because true independence will be achieved only when such skills can be found domestically.

In a report to a 2009 UN conference in Addis Ababa on strengthening sciences in Africa, Aderemi Kuku, a US-based Nigerian mathematician and founder of the Mathematicians of the African Diaspora network, said that the continent has no critical mass in a single field of mathematics. He warned: “When the present generation of University teachers and researchers in Mathematics and Physics, disappear from the scene due to retirement etc., the situation will be near disaster unless urgent steps are taken.”

As we report on page 176, Neil Turok, a South African cosmologist and head of the Perimeter Institute for Theoretical Physics in Waterloo, Canada, has led efforts to combat this trend. Turok pioneered the construction of the African Institute for Mathematical Sciences (AIMS), a hothouse of post-secondary mathematics teaching and research in Muizenberg, South Africa. The model has now been adopted in Ghana and Senegal, too. Turok hopes for a total of 15 institutes across the continent. He laments what he calls a science faculty “generation gap” and is critical of the way that international

donors tend to emphasize basic education.

“Nobody’s been interested,” he told *Nature*. “The West for many years has been happy to deal with Africa on a charity basis, but investing in skills in people was not a priority. This was a major error.”

Bravo to AIMS for responding to the crisis of maths and science education on the continent, but, as Turok and his colleagues will be the first to say, the efforts remain modest given the scale of what is needed.

**“Science needs Africa as much as Africa needs science.”**

International donors and African governments must learn from the example. They should consider how to add post-secondary maths and science education to their development plans. It need not be expensive and it need not drain significant resources from other projects. In the space of ten years, AIMS has built a network of successful mathematics institutes for a few tens of millions of dollars.

And think of the payback. Science needs Africa as much as Africa needs science. What a waste of human talent not to have Africa participate as a scientific peer, for a world content to wait for Africa’s entry into science. What advances has humanity missed out on by having the continent so cut off from the mainstream of scientific debate and discovery?

The late evolutionary biologist Stephen Jay Gould once said: “I am, somehow, less interested in the weight and convolutions of Einstein’s brain than in the near certainty that people of equal talent have lived and died in cotton fields and sweatshops.” Africa has that talent. Some of it may be discovered at AIMS. But much of it will not be. ■

## John Maddox prize

*Two strong-minded individuals are the first winners of an award for standing up for science.*

The British psychiatrist Simon Wessely and the Chinese science writer Shi-min Fang are the two inaugural winners of the John Maddox Prize. Sponsored by *Nature* and the Kohn Foundation, and stimulated and organized by the UK-based charity Sense About Science, the prize commemorates a former Editor of *Nature*, John Maddox. John was distinguished for his championing of robust science. The prize rewards individuals who have promoted sound science and evidence on a matter of public interest, with an emphasis on those who have faced difficulty or opposition in doing so. In this inaugural year, the judges (see [go.nature.com/9rvd1t](http://go.nature.com/9rvd1t)) were able to make two awards, each of £2,000 (US\$3,200).

China’s rush to modernize and the communist government’s celebration of science and technology have firmly embraced scientists and scientific achievements, sometimes uncritically. And into that permissive milieu has walked a plethora of opportunists ready to take advantage of the situation with padded CVs, fraudulent and plagiarized articles, bogus medicines and medical procedures carried out without clinical evidence.

In 2000, Shi-min Fang started to expose these escapades in his New Threads website. As an outsider, trained as a biochemist but turned science writer and commentator, he has done much of what the scientific community aims, but often fails, to do — root out the fakers.

For example, Fang called into question DNA supplements that were widely advertised as a means to rejuvenate the tired, the pregnant and the old. Eventually, the government issued warnings about the supplements. Fang seemed to especially relish smacking down powerful or popular scientists. He even challenged official support of traditional Chinese medicine. But his targets fought back, in one case with particular hostility. In the summer of 2010, thugs hired by a urologist attacked Fang with a hammer and, according to Fang, tried to kill him. Fang had previously challenged not only the efficacy of a surgical

procedure developed by the urologist, but also his CV.

Fang imposes transparency on an opaque system. He has opened a forum for criticism and debate in a community that is otherwise devoid of it.

Simon Wessely is a psychiatrist at the Institute of Psychiatry, King’s College London, who has specialized in two areas above all — the mental health of military personnel and veterans, and chronic fatigue syndrome. He and his colleagues demonstrated substantial overlap in symptoms between chronic fatigue syndrome and clinical depression. He carried out a massive and ambitious study to test the link between common viral infections and later fatigue, and found that there is no simple causal association. He subsequently developed a treatment approach using cognitive-behavioural therapy techniques, which in many cases brought about substantial improvement and in some was life transforming. This treatment was tested in large clinical trials and can now be found in the guidelines of the United Kingdom’s National Institute for Health and Clinical Excellence.

“All along the way,” says the individual who nominated him for the prize, “Wessely has had to suffer continued abuse and obstruction from a powerful minority of people who, under the guise of self-help organizations, have sought to promote an extreme and narrow version of the disorder. This version repudiates any psychological or psychiatric element to the extent that psychiatry is viewed as a contemptible discipline, which, by association, denigrates psychiatric patients. Hostile letters, e-mails and even death threats have been directed at Professor Wessely over two decades. Mischievous complaints have been made against him and his clinical team, and bogus questions raised in the Houses of Parliament. He has suffered a vigorous Internet assault and coordinated attempts have been made to turn him into a hate figure. He has been compared to Josef Mengele — particularly hurtful since Simon is the son of Holocaust survivors. Simon has, perhaps naively, tried to deal with most of these by seeking dialogue and trying to educate and reassure, rather than by responding in kind.”

Wessely is the first to acknowledge that others working in this field have received similar or even worse abuse. Nevertheless, the prize recognizes the very public stand that Wessely has taken over these issues. *Nature* congratulates Simon Wessely and Shi-min Fang on their awards. ■

➔ **NATURE.COM**  
To comment online,  
click on Editorials at:  
[go.nature.com/xhbnq](http://go.nature.com/xhbnq)



W. H. KUANG



## China's new leaders must keep science in focus

*By bringing in people with more varied backgrounds, China's leadership change could benefit science, argues Peng Gong.*

**T**his is a big month for the world's superpowers. The United States elects its next president this week, and the following week brings the first change in China's leadership for ten years.

Since 1989, the political bureau (politburo) of the Communist Party of China has been dominated by officials trained in engineering. This time, appointees with backgrounds in economics and administration are expected to constitute more than half of the standing committee, the most powerful section of the politburo. The scientific community inside and outside the country is wondering how this shift will affect the future of scientific research in China.

I believe that China will continue to prioritize the development of science and technology over the next ten years. The country is half-way through a 15-year science and technology programme to transform it into an 'innovation-oriented society'. Internal desire and external pressure to deliver this are strong.

In 1978, the influential reformist Deng Xiaoping began economic reforms that saw China open its door to the world. He viewed science and technology as "the primary productive forces" of his strategy to transform a poor agricultural country into an affluent nation; a strategy that has been faithfully followed over the past three decades.

Meanwhile, the influx of large-scale foreign investment has attracted high-level management and technology talents from all over the world. However, many Chinese students educated abroad do not return after they graduate. To combat this, and to draw fresh talent to the country, China launched the 'Thousand Talents' programme in 2008 to entice the best researchers in science, technology, engineering and management. By the summer of 2012, the programme had attracted more than 2,000 such high-end professionals to China. Furthermore, the number of acquisitions of foreign companies by Chinese enterprises is increasing. It is to be expected that, as experience in the global market accumulates in the science and technology sectors, improvements will be seen at home.

Pressure to increase core competitiveness will also drive continued investment in science. China may have the second largest economy in the world, but that does not mean it is competitive. Recent reports suggest that profits from China's expected 2012 export of 1 billion mobile phones will be, on average, less than US\$0.5 per phone.

Ubiquitous technology such as the remote control, personal computers, HTML (the markup language used to make Web pages) and the Global Positioning System (GPS), and specialized tools such as genetic sequencing

and zero-emission fuel cells, are considered to be among the top 50 inventions of the past 50 years. None came out of China.

How can China's new leaders address these research issues? Three elements determine the fate of all organizations: people, resources and management.

With regard to people, China's talent pool is increasing, but there is still a shortage of scientists who are creative and original thinkers. In the next ten years, more foreign scientists must be recruited and China must enhance its own capacity to train original minds. To retain scientists from overseas, specially allocated research support should be provided for at least their first five years in China.

In terms of resources, research and development (R&D) investment in China has grown more than tenfold in ten years, from around US\$12 billion in 2001 to about \$135 billion in 2011. Invest-

ment in basic science and applied research increased more than sixfold; but the percentage of investment for public research organizations and universities dropped from 38% to 24%, indicating more input from the private and non-governmental sectors. The new leadership should increase investment in these institutions, particularly the major research universities.

The biggest challenge in ensuring the healthy development of scientific research is management. Better management would improve academic culture, scientific ethics, resource sharing and communication and cooperation. China must pay talented individuals in accordance with

international standards. Personnel and project review should encourage scientific adventure and tolerate failure. Dogmatic budgetary regulations on research projects must be revised to allow flexible requests of personnel, operational and material costs, and to give more freedom to principal investigators. These changes, even with the current level of R&D investment, have the potential to advance scientific research by making more effective use of funds.

The Chinese science system looks like it was designed by an engineer. Project conception time is included in grant accounting, there are mid-term and annual reviews with external audits to check on progress, including counts of the number of published papers. Science should not be managed as an engineering project. With more top administrators from economics, science, social science and management backgrounds, I hope that the new regime will change this for the better. ■

**Peng Gong** is in the Center for Earth System Science at Tsinghua University, China, and the Department of Environmental Science, Policy and Management, University of California, Berkeley, USA. e-mail: penggong@tsinghua.edu.cn

**THERE IS STILL A  
SHORTAGE OF  
SCIENTISTS  
WHO ARE CREATIVE  
AND ORIGINAL  
THINKERS.**

➔ **NATURE.COM**  
Discuss this article  
online at:  
[go.nature.com/7s3srz](http://go.nature.com/7s3srz)

# RESEARCH HIGHLIGHTS

Selections from the  
scientific literature

## EVOLUTION

### Thank Grandma for longevity

Grandmothers have driven the evolution of longer lifespans, extending them by around 25 years in a theoretical population of apes, according to a mathematical model that tests the 'grandmother hypothesis'.

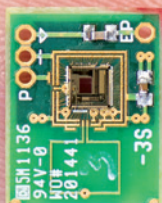
According to this theory, women evolved lifespans that extend well past the menopause because older women can boost their daughters' fertility — by taking care of grandchildren. Kristen Hawkes at the University of Utah in Salt Lake City and her colleagues modelled a population of apes, and found that their lifespans evolved from an ape-like range of around 35 years to a human one of roughly 60 years when older females contributed to infant care. Grandmothers enabled mothers to have their next baby sooner without reducing their previous offspring's chances of survival. *Proc. R. Soc. B* <http://dx.doi.org/10.1098/rspb.2012.1751> (2012)

## BIOELECTRONICS

### Power from the ear

Researchers in Massachusetts have found a way to extract power from the ear.

Konstantina Stankovic of the Massachusetts Ear



and Eye Infirmary in Boston, Anantha Chandrakasan at the Massachusetts Institute of Technology in Cambridge and their colleagues developed a chip (pictured) that can exploit the inner ear's electrical potential, which is generated to convert sound into neural impulses. The team inserted electrodes from the chip through a natural opening into the inner ear of an anaesthetized guinea pig. The chip extracted around 1 nanowatt of power for up to five hours — enough to power a small radio transmitter.

The system could eventually be used to harvest power for

devices that diagnose and treat hearing loss in humans, the authors suggest.

*Nature Biotechnol.* <http://dx.doi.org/10.1038/nbt.2394> (2012)

## MICROBIOLOGY

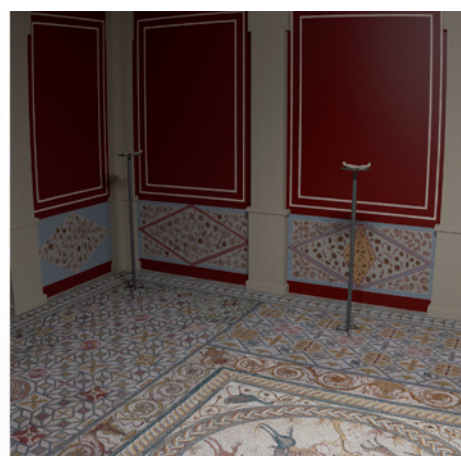
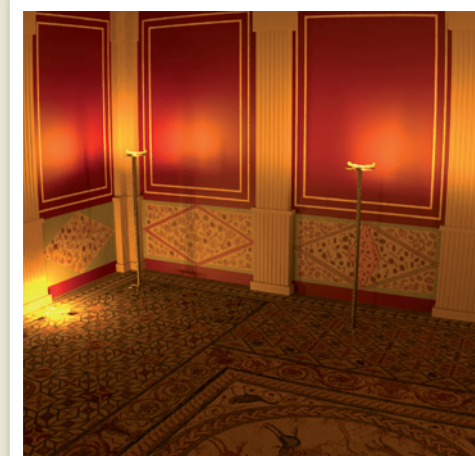
### Typhoid fever in a mouse

A mouse model of typhoid fever could help scientists to develop vaccines against a disease that infects some 20 million people and kills more than 220,000 worldwide each year.

Mice are normally immune to the bacterium

*Salmonella typhi*, which causes typhoid fever in humans. However, a team led by Sankar Ghosh at Columbia University in New York has shown that mice that lack an immune-system receptor called TLR11 — which recognizes a bacterial protein called flagellin — become susceptible to *S. typhi* and develop a deadly systemic infection akin to typhoid.

When mice that lack TLR11 were vaccinated with killed *S. typhi* or with serum from previously infected mice, they proved resistant to subsequent typhoid infection. *Cell* 151, 590–602 (2012)



## ARCHAEOLOGY

### A new light on the past

An ancient Roman home can be seen through the eyes of its long-dead owners, thanks to imaging technology that makes digital reconstructions of cultural relics appear more realistic.

Archaeological excavations of the 'House of the Fountains' — built in the first century AD in the Roman town of Conimbriga in Portugal — revealed fountain-filled gardens, wall frescoes and elaborate mosaic tile floors. To get a sense of what the house might have looked like when illuminated by candlelight, Alexandrino Gonçalves of the Polytechnic Institute of

Leiria, Portugal, and his team made digital reconstructions of a room using high-dynamic-range imaging technology, which captures light intensity levels with a sensitivity similar to that of the human eye. Volunteers favoured candlelit images (pictured left) over those illuminated with electric light (right), describing the former as "warm" and "comforting". Eye-tracking experiments suggested that volunteers focused more on the frescoes and mosaics when viewing them under candlelight than under electric lighting. *J. Archaeol. Sci.* 40, 116–128 (2013)

A. GONÇALVES

P.P. MERCIER

## GEOSCIENCE

## The rapid melt of Greenland

The melting that occurred across 98.6% of the Greenland ice sheet this summer was so rare that the most recent equivalent melt was in 1889.

Ordinarily, melting occurs over about half of the surface area of Greenland's ice during summertime. Son Nghiem of NASA's Jet Propulsion Laboratory in Pasadena, California, and his colleagues detected this year's extreme melt using three satellite sensors that differ in their resolution, spatial coverage and their ability to detect thawing ice. In combination, the sensors' data revealed the extent of the melt — a result verified by temperature data from weather stations and on-the-ground observations.

The melting event coincided with an unusually warm ridge of air hovering over the ice sheet, the authors say.

*Geophys. Res. Lett.* <http://dx.doi.org/10.1029/2012GL053611> (2012)

## PALAEOLOGY

## First flying fish fossil found

A series of remarkably well preserved fossils found in Xingyi, China, have allowed researchers to describe the earliest fish known to take to the air.

*Potianichthys xingyiensis* (pictured) is not an ancestor of modern flying fish. However, it is the oldest animal yet

found belonging to a group of fish — the Thoracopteridae — that evolved their gliding skills separately between 200 million and 250 million years ago, according to a report by Ke-Qin Gao at Peking University in Beijing and his colleagues. The animal, measuring just 15 centimetres long, had a pair of large pectoral fins that probably functioned as its main wings, and pelvic fins that were used as secondary wings. A large and asymmetric tail probably provided thrust to launch the animal into the air.

This is the first Thoracopteride found in Asia and expands the known range of these early flying fish from the west to the east side of the prehistoric Palaeotethys Ocean. *Proc. R. Soc. B* <http://dx.doi.org/10.1098/rspb.2012.2261> (2012)

For a longer story on this research, see [go.nature.com/url8m5](http://go.nature.com/url8m5)

## STEM CELLS

## Immune response spurs cell switch

Controlling cellular immune responses could help researchers to turn adult cells into embryonic-like stem cells without having to insert any genetic material.

The most efficient way to reprogram adult cells is to genetically alter them, but this can cause problems in cell therapy. John Cooke at Stanford University in California and his colleagues found that the viruses that are normally used to deliver reprogramming genes into cells alter the cells in another, unanticipated way. The inflammatory response to the virus induces changes that open up the structure of chromatin — the tightly packaged DNA and protein that makes up chromosomes.

Using virus-free reprogramming techniques and a synthetic molecule to activate an inflammatory pathway in adult cells, the researchers obtained 25 reprogrammed cell colonies per experiment. No such

## COMMUNITY CHOICE

The most viewed papers in science

## NEUROSCIENCE

## Two ways to forget

**HIGHLY READ**  
on [www.cell.com](http://www.cell.com)  
in October

People call on two different brain mechanisms to suppress unwanted memories.

Roland Benoit and Michael Anderson at the University of Cambridge, UK, asked 36 volunteers to commit a list of words to memory, along with a partner word for each to serve as a reminder. The duo then imaged the volunteers' brains using functional magnetic resonance imaging as the subjects employed different strategies to suppress those memories. When prompted by a reminder word, half tried to suppress the memory of the partnered word, whereas the other half attempted to recall a substitute word.

Both strategies suppressed the memory, but the volunteers engaged distinct neural pathways in the brain for each. The findings may boost understanding of conditions in which the regulation of memory is disturbed, such as post-traumatic stress disorder, the authors say.

*Neuron* 76, 450–460 (2012)

colonies were generated if the immune pathway was inhibited. Controlling inflammatory pathways could make it easier not only to produce genetically unaltered, reprogrammed stem cells, but also to direct cell fate in other ways.

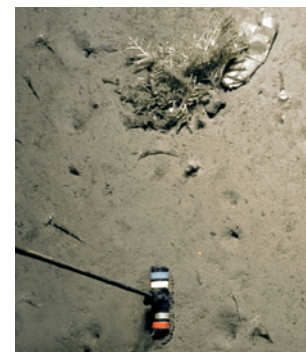
*Cell* 151, 547–558 (2012)

## ENVIRONMENTAL SCIENCE

## Litter bugs leave Arctic legacy

Litter on the Arctic Ocean floor has increased drastically since 2002, with plastic waste making up the majority of the debris.

Melanie Bergmann and Michael Klages of the Alfred Wegener Institute for Polar and Marine Research in Bremerhaven, Germany, analysed photographs of the ocean floor captured 2,500 metres below the surface. In 2002, the researchers identified 7 pieces of litter in a survey area of 1,926 square metres. In 2011, they reported 11 pieces in a smaller area — representing a doubling of litter density. Two-thirds of the rubbish was colonized by



ALFRED WEGENER INST. POLAR AND MARINE RES.

invertebrate species, including sponges and sea anemones (cardboard and paper packaging with a sponge, pictured).

The increase may be due to shrinking sea ice, which is opening up the ocean to greater human activity and to plastic transported north by the Atlantic current, the authors suggest. With plastic production unlikely to cease, more and more of it may accumulate in the Arctic.

*Mar. Pollut. Bull.* <http://dx.doi.org/10.1016/j.marpolbul.2012.09.018> (2012)

**NATURE.COM**

For the latest research published by Nature visit:

[www.nature.com/latestresearch](http://www.nature.com/latestresearch)



R. SOC.



# SEVEN DAYS

The news in brief

## POLICY

### Antarctic reserves

Negotiations on creating three huge marine reserves in Antarctic waters have broken down, dealing a major blow to conservation plans. Meeting in Hobart, Australia, the 25 members of the Commission for the Conservation of Antarctic Marine Living Resources failed to agree unanimously on any of the reserves, which would have established fishing bans and set aside regions as reference areas for scientists studying the impact of climate change on fragile polar ecosystems (see *Nature* **490**, 324; 2012). The reserves will be discussed again in July. See [go.nature.com/xxzjbd](http://go.nature.com/xxzjbd) for more.

### Mekong megadam

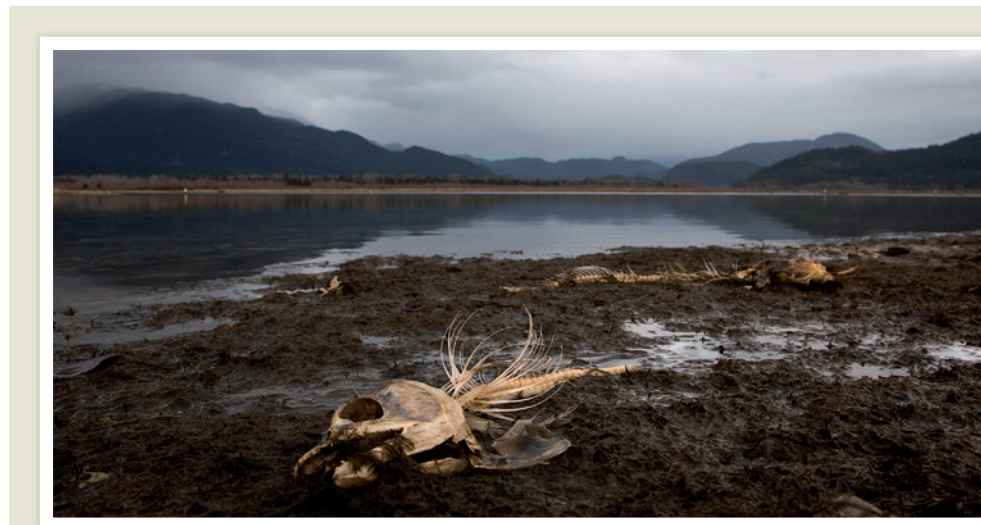
Work to build a massive dam on the lower Mekong river in Laos is to formally begin on 7 November, deputy minister of energy and mines Viraphonh Viravong said on 5 November. Environmentalists fear that the US\$3.5-billion Xayaburi dam will reduce fish stocks and biodiversity.

### China genetic rules

China's government has published a draft regulation to improve the protection of donors in human genetic research. It proposes to license organizations that store and collect "human genetic resources" (materials such as organs, cells and DNA), update requirements on informed consent and prohibit the sale or export of genetic materials. The draft, published on 31 October, is open to feedback for a month.

### UK merger dropped

A contentious plan to merge two major British research centres has been shelved



A. CLARK/REUTERS

## Sockeye salmon threats assessed

Canada's Department of Fisheries and Oceans should focus on protecting wild fish, and a separate department should be charged with promoting the fish-farming industry to avoid confusion over the department's role, according to a report on sockeye salmon (*Oncorhynchus nerka*) populations released on 31 October. The Cohen Commission, led by a Supreme Court

judge, was asked by the federal government in 2009 to investigate the collapse in the numbers of salmon returning to British Columbia's Fraser River over past decades. The commission found no single cause for the decline, but blames the government for reducing protection of the salmon's habitats. See [go.nature.com/sles5b](http://go.nature.com/sles5b) for more.

following criticism from politicians and scientists. The Natural Environment Research Council had suggested merging two centres that it runs — the British Antarctic Survey in Cambridge and the National Oceanography Centre in Southampton — to save money, but announced on 2 November that it would scrap the idea. Job cuts are still in the offing, however. See [go.nature.com/prcepr](http://go.nature.com/prcepr) for more.

### Climate services

The World Meteorological Organization in Geneva, Switzerland, has agreed to implement a 'Global Framework for Climate Services', which will provide and manage information about how Earth's changing climate affects everything from crop production to

disaster planning. The international framework, agreed at a meeting in Geneva on 31 October, will initially focus on water, health, food security and disaster risk reduction. Some scientists have been concerned by the proliferation of climate-service providers who may be overselling the abilities of climate models to guide policy-makers and local people. See [go.nature.com/rbxxnq](http://go.nature.com/rbxxnq) for more.

## PEOPLE

### Sound science wins

Shi-min Fang, a freelance science journalist based in Beijing, and Simon Wessely, a psychiatrist at King's College London, are the joint winners of the inaugural John Maddox Prize, for individuals who

have promoted sound science and evidence on a matter of public interest. The £2,000 (US\$3,200) prize, announced on 6 November, is awarded by *Nature* and Sense About Science, a London-based science-advocacy group, and is supported by the Kohn Foundation. See page 160 and [go.nature.com/owyfbg](http://go.nature.com/owyfbg) for more.

## RESEARCH

### Food emissions

The global food system, from fertilizer manufacture to food storage and packaging, is responsible for up to one-third of all anthropogenic greenhouse-gas emissions, according to analyses published on 31 October. The work was done by the Consultative Group on International

Agricultural Research (CGIAR), a partnership of 15 research centres around the world. Reducing agriculture's carbon footprint is central to limiting climate change, the CGIAR said. See [go.nature.com/wxng5](http://go.nature.com/wxng5) for more.

## No Mars methane

Scientists controlling NASA's Curiosity rover on Mars said on 2 November that they had not detected methane on the red planet. Methane could be a sign of bacterial life, although trace amounts might also be produced by cometary impacts or geological reaction. The gas has been detected by various Mars observers in the past decade, but the Curiosity finding does not support those claims. See page 174 for more.

## Retractions stigma

A retraction results in fewer citations and less funding for other studies in the same field, according to an analysis of the PubMed biomedical citation database by the US National Bureau of Economic Research in Cambridge, Massachusetts (see [go.nature.com/nf88fw](http://go.nature.com/nf88fw)). On average, retractions resulted in a 5.7% decrease in the citation rate of related papers compared with control papers, and caused a drop of 50–73% in research funding from the US National Institutes of Health for related studies. See [go.nature.com/vxlk3p](http://go.nature.com/vxlk3p) for more.



## Moon shot

Chang'e 3, China's third lunar mission, will land on Sinus Iridum — the 'Bay of Rainbows' — China's National Space Administration said on 29 October. Whereas China's two earlier missions were orbiters, Chang'e 3, scheduled to launch next year, includes plans for a robotic lander and rover (prototype pictured).

## Storm aftermath

Universities and research institutes along the US east coast were battered by Hurricane Sandy last week, with New York University one of the worst hit (see page 169). The storm has added urgency to long-term calls by engineers and scientists for measures to help adapt to climate change (see page 167).

## Data demand

The *British Medical Journal* will not publish clinical trials of drugs or devices

from January 2013 unless they are accompanied by a commitment to make anonymized patient data available on request. Fiona Godlee, the journal's editor-in-chief, announced the move in an editorial on 29 October (F. Godlee *Br. Med. J.* 345, e7304; 2012).

## BUSINESS

## Anthrax fight

Advisers to the US Food and Drug Administration (FDA) have recommended approving a monoclonal antibody developed to treat anthrax. On 2 November, an FDA committee voted in favour of raxibacumab, which would be the first large biological drug against the anthrax bacterium (it is currently treated with small-molecule antibiotics). The FDA is expected to decide by 15 December. The drug was developed by biotechnology company Human Genome Sciences, which was bought by London-based pharmaceutical firm GlaxoSmithKline earlier this year. The US government helped to fund raxibacumab's development and has already begun to stockpile it.

## Sclerosis success

A drug designed to reverse the nerve damage caused by multiple sclerosis has shown success in two late-stage clinical trials. Disability levels

## COMING UP

### 12 NOVEMBER

The Paris-based International Energy Agency launches its 2012 *World Energy Outlook* report in London, with special analyses on the economic potential for energy efficiency, and the water–energy nexus. [www.worldenergyoutlook.org](http://www.worldenergyoutlook.org)

### 15–18 NOVEMBER

Discussions of Thomas Kuhn's 50-year-old classic publication, *The Structure of Scientific Revolutions*, feature at a combined meeting of the US History of Science Society and the Philosophy of Science Association in San Diego, California. [www.hssonline.org/Meeting](http://www.hssonline.org/Meeting)

improved in patients taking the monoclonal antibody alemtuzumab (which is made by Genzyme in Cambridge, Massachusetts), but not in those on standard interferon beta-1a therapy. The trial results were published on 1 November in *The Lancet*. See [go.nature.com/phawy5](http://go.nature.com/phawy5) for more.

## Gene therapy boost

Glybera, a treatment for a rare genetic disease that leaves patients unable to break down fats, has become the first gene therapy to be approved by the European Commission. The European Medicines Agency backed Glybera in July (see *Nature* <http://doi.org/10.1038/nature11037>; 2012) but the treatment required the commission's approval before it could be sold in the European Union. News of the 25 October approval emerged last week. See [go.nature.com/seu9y7](http://go.nature.com/seu9y7) for more.

➔ [NATURE.COM](http://NATURE.COM)

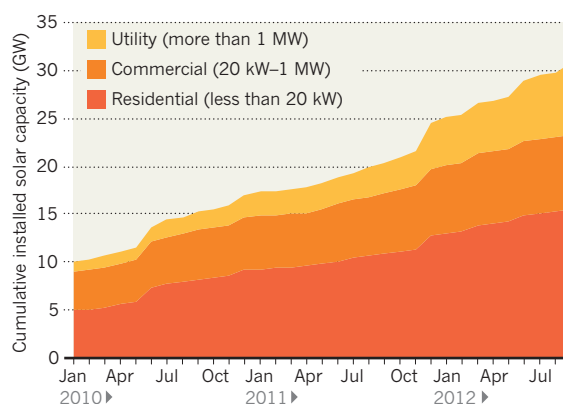
For daily news updates see:  
[www.nature.com/news](http://www.nature.com/news)

## TREND WATCH

German enthusiasm for solar power is undimmed despite subsidies being cut by more than one-third since last December. The country has installed more than 30 gigawatts (GW) of capacity, almost twice that of the world's second-largest solar installer, Italy. That is a sizeable share of Germany's average electricity use of 80 GW. But residential power bills are an estimated 20% higher than they would be without renewables, says Jenny Chase of analysts Bloomberg New Energy Finance.

## GERMANY'S SOLAR SURGE

Almost 1 gigawatt (GW) of solar capacity was installed in September this year, pushing the country's total beyond 30 GW.





# NEWS IN FOCUS

**ENERGY** Giant laser shifts focus from energy to weapons research **p.170**

**GENOMICS** A wikipedia for disease genes begins to take shape **p.171**

**PLANETARY SCIENCE** Doubts cast on hidden Martian biosphere **p.174**



**DEVELOPMENT** A training ground for African Einsteins **p.176**

B. MATTHEWS/AP



Flooded streets under Manhattan Bridge in Brooklyn illustrate New York's growing vulnerability to destructive storm surges.

## CLIMATE CHANGE

# Hurricane sweeps US into climate-adaptation debate

*Manhattan flooding bolsters argument for a massive engineering project to protect New York.*

BY JEFF TOLLEFSON

**A**s Hurricane Sandy drove a 4.2-metre-high wall of salt water into the heart of New York city and the surrounding coast late on the evening of 29 October, scientists and engineers ticked through a nightmare checklist of predicted storm-surge effects that they had been drafting for more than a decade. Catastrophic flooding in low-lying areas?

Check. Submerged tunnels and subway lines in lower Manhattan? Check. Damaged electricity substations and widespread power outages? Check.

"All of our predictions came true," says Malcolm Bowman, who specializes in storm-surge modelling at Stony Brook University in New York. Bowman has argued for building storm-surge barriers around New York for more than a decade. Sandy's arrival, Bowman

says, stands as sad proof that current policies are woefully inadequate.

In a single night, the massive storm dealt a crippling blow to one of the world's foremost economic and industrial hubs, destroying thousands of homes and leaving millions of people without electricity or reliable access to food, water and petrol. A week later, outlying neighbourhoods were still in crisis. Like Hurricane Katrina in 2005, Sandy quickly came ►



► to embody the nebulous threat of global warming while reviving discussions about how best to prepare New York and other coastal areas for a future of rising sea levels and a more volatile climate. And a topic largely ignored by both major political parties throughout a long and combative presidential campaign suddenly took centre stage just days before the election.

Sobered by climate scientists' predictions that a warming atmosphere and rising sea levels are likely to bring large storms to the US east coast with increasing frequency, political leaders in the region raised the alarm about the long-term threat. On 31 October, New York governor Andrew Cuomo called for "fundamental rethinking of our built environment". A day later, New York city mayor Michael Bloomberg cited the storm as he offered a surprise endorsement of President Barack Obama over Republican challenger Mitt Romney. Bloomberg, who had previously expressed disappointment in both candidates, now praised Obama's efforts to lower carbon emissions with tighter regulations on coal plants and higher fuel-economy standards for vehicles. He also praised Romney's role in developing a regional cap-and-trade scheme as governor of Massachusetts, but then blasted him for reversing course on climate during his presidential run. "I want our president to place scientific evidence and risk management above electoral politics," Bloomberg wrote.

Sandy was fuelled by surface waters that were roughly 3°C above average along the east coast. Only a fraction of that — roughly 0.6°C — can reasonably be attributed to global warming. But even though scientists are loath to attribute any given weather event to global warming, hurricanes are demonstrably increasing in power "and have been for the past 20 years", says Kerry Emanuel, a hurricane expert at the Massachusetts Institute of Technology (MIT) in Cambridge.

Sandy was unusual not only in its power but also in its course. Tropical cyclones that move so far north at this time of year are often swept out to sea. But a high-pressure system south of Greenland forced it inland, where it merged with a traditional winter storm system moving in from the west.

Two studies published in February and March this year<sup>1,2</sup> suggest that warming due to increasing ice loss in the Arctic Ocean could be altering regional air circulation, causing a more meandering jet stream. The net effect, researchers say, is an increase in the likelihood

of severe winter storms and other extreme weather events across the United States, Europe and northern China. Although the idea remains controversial, some scientists wonder whether the same phenomenon could lead to an increase in hurricanes such as Sandy and Irene, which last year roared up the coast from North Carolina to New York and came perilously close to flooding the city as Sandy did. "These are very early days, but I happen to think it's a very promising line of research," says Emanuel, who was not involved in the studies.

A study of tidal-gauge records dating back to 1923 and published last month<sup>3</sup> found that the likelihood of large surge events roughly doubles during warm years compared with cold years. New York is at particular risk, according to a study published in February<sup>4</sup> by Emanuel and other scientists at MIT and Princeton University in New Jersey. By 2100, more intense storms

The system envisaged by Bowman and others would include an 8-kilometre-wide barrier approximately 6 metres high that could be opened and closed at the entrance to New York's harbour, and a second barrier at the entrance to Long Island Sound (see 'Surge stoppers'). He puts the cost at around US\$15 billion, about the same amount that Congress allocated to the US Army Corps of Engineers in 2005 to build a storm-surge barrier system around New Orleans. Estimates put the damage caused by Sandy at between \$30 billion and \$50 billion.

Some scientists worry that a single focus on sea barriers could be counterproductive. By disrupting river outflow and increasing sedimentation, such barriers could alter ecosystems. And by diverting storm surges, they might exacerbate flooding in areas that are not protected, such as Jamaica Bay in southern Brooklyn.

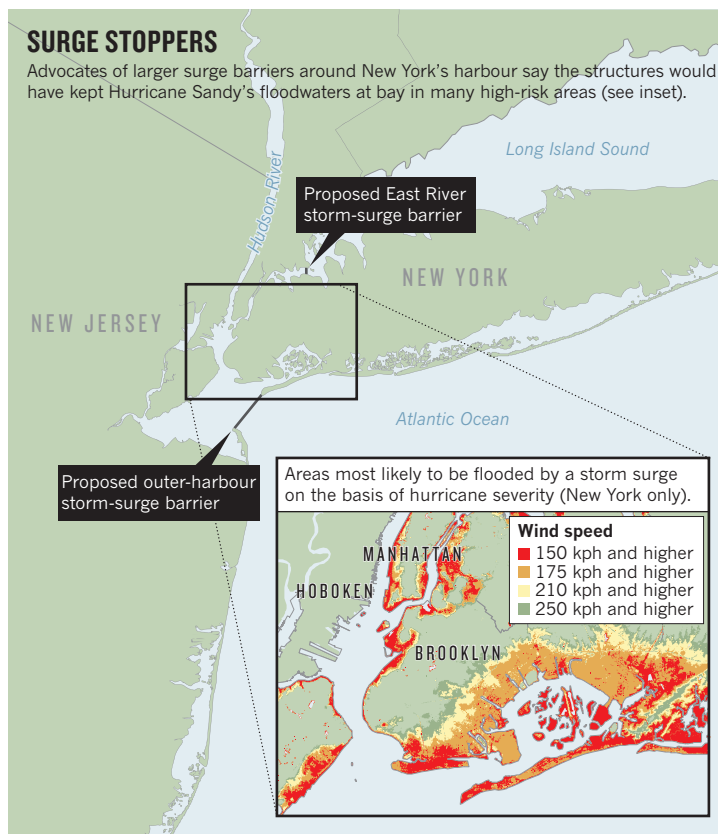
Moreover, sea barriers do not protect against severe rain storms that generate inland flooding.

"Sandy clearly shows that we have to do the barrier studies now," says Cynthia Rosenzweig, co-chair of the New York climate panel and a senior scientist at NASA's Goddard Institute for Space Studies in New York. "But I think we need to consider an integrated and holistic set of solutions, and not put all of our eggs in the barriers."

New York has already begun to implement a broad plan drawn up in 2007 to make the city more resilient to the expected effects of climate change by moving electrical equipment out of basements and adopting new urban sea-shore designs that can withstand occasional flooding. It remains unclear how much these efforts might have helped to lessen the impact of last week's storm. But as the city and the region restore basic services in the coming days and weeks, Rosenzweig says, scientists and government officials must ensure that any rebuilding

is done with the long view of global warming in mind.

"Although we may not see a storm of this magnitude for some time," Rosenzweig adds, "the adaptation process in the city must continue moving forward." ■



and a potential sea-level rise of one metre could combine to cause flooding in the city every 3–20 years on a scale now seen once a century.

The storm has added new urgency to discussions of adaptation in forums including the New York City Panel on Climate Change, which Bloomberg set up in 2008. Bowman and others have advocated a system of sea barriers or dykes, similar to those constructed in London, the Netherlands and more recently in St Petersburg, Russia. "If we had implemented a regional barrier system, there would have been no significant damage" within New York's harbour, he says.

1. Liu, J., Curry, J. A., Wang, H., Song, M. & Horton, R. M. *Proc. Natl Acad. Sci. USA* **109**, 4074–4079 (2012).
2. Francis, J. A. & Vavrus, S. J. *Geophys. Res. Lett.* **39**, L06801 (2012).
3. Grinsted, A., Moore, J. C. & Jevrejeva, S. *Proc. Natl Acad. Sci. USA* <http://dx.doi.org/10.1073/pnas.1209542109> (2012).
4. Lin, N., Emanuel, K., Oppenheimer, M. & Vanmarcke, E. *Nature Clim. Change* **2**, 462–467 (2012).



Patients were evacuated from New York's Langone Medical Center when backup power failed.

#### HURRICANE SANDY

# Researchers battle storm's wrath

*New York University lost crucial mouse colonies, but students and staff helped to save equipment and patients.*

BY BRENDAN BORRELL

For Benjamin Bartelle, the first sign that Hurricane Sandy was no ordinary storm came when each of the lab's windows popped open, scattering papers across the floor. It was about 7.30 p.m. on 29 October, and Bartelle was on the fifth floor of the Skirball Institute of Biomolecular Medicine, part of the New York University (NYU) Langone Medical Center in Manhattan. Outside, in exposed parts of the city, winds were gusting at up to 160 kilometres per hour as the storm made landfall.

Bartelle, a recent PhD finishing his last experiments in protein engineering, braced the windows shut with 20-litre water bottles. Soon after, an alarm sounded at the fish facility down the hall, and Jesus Torres-Vasquez, who studies blood-vessel formation in zebrafish, came up to check. That's when the building went dark. Sixteen blocks to the south, a record storm surge had caused the East River to break its banks, flooding a substation and triggering a blackout across the downtown area. But the Langone Medical Center, also located alongside the river, was threatened in a more direct way.

As Hurricane Sandy battered the US eastern seaboard that night, the many universities, labs and research stations in its path would feel the

effects of power outages, damaging winds and flooding. None was hit as badly as the Langone.

The medical centre was within the evacuation zone that had been declared the day before, but hospitals and nursing homes were exempt because of the risks of moving patients. The 705-bed Tisch Hospital and three connected research buildings at the Langone are equipped with backup generators and meet all safety standards, according to the NYU. Sandbags were stacked around the buildings in preparation, and maintenance workers were on call. Staff at underground mouse facilities would be working through the night to monitor tens of thousands of mice used in research projects from cancer to neurobiology.

At the Skirball, the backup power kicked in after a few minutes, but something was still amiss. Neurobiologist Wenbiao Gan and his lab staff took the lift down to the basement to find it more than ankle deep in water. They waded in to retrieve lasers and other equipment. When Bartelle saw them return with wet trouser legs, he looked out of the window. The other medical centre buildings were dark, including the Joan and Joel Smilow Research Center, a 13-storey glass and brick edifice that is also part of the Langone centre, and nearest to the river. If the Skirball was getting wet, the Smilow centre was in even bigger trouble; its basement, housing

about 10,000 mice and rats, is almost 10 metres below water level. The flood waters had surged into that building so forcefully that animal-care workers had to evacuate. The mutant and transgenic mice housed in quarantine there were left to their fates.

Bartelle headed for a residence hall but was soon dragged into a different drama, when a member of the hospital staff came in shouting: "We have to evacuate the patients from Tisch Hospital! We need all the hands we can get!" By 9 p.m., hundreds of medical and graduate students had assembled in the hospital lobby. Under the direction of the New York City Fire Department, they scaled 16 flights of stairs and brought 215 patients down on plastic sleds. On the ground floor, the patients — some of them in a coma, others recovering from surgery — were transferred to gurneys and ambulances and on to other hospitals. The students were still working 12 hours later.

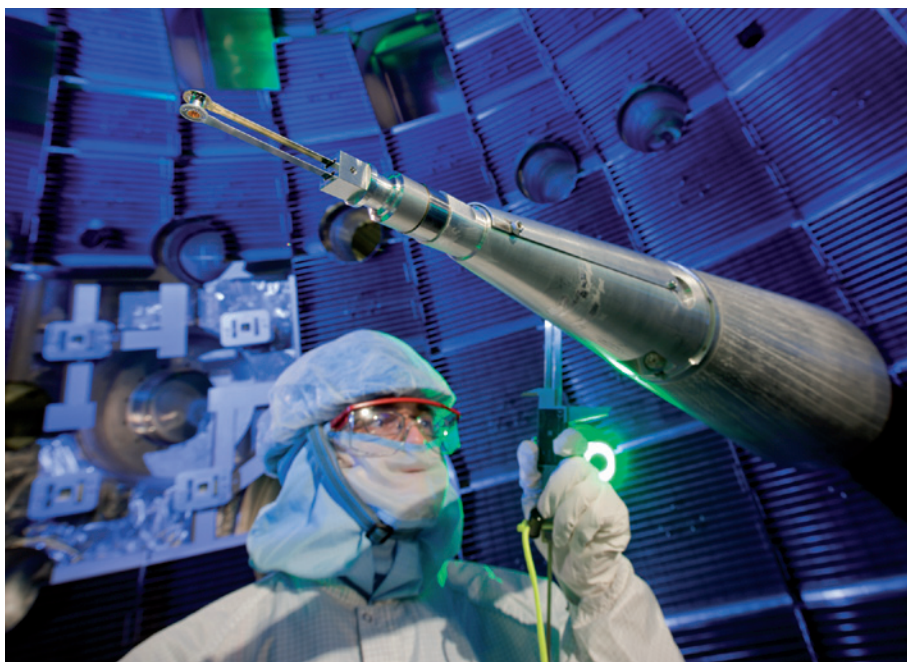
By then, it was clear that much of the Langone had flooded, with freezer outages and water damage affecting the labs of 30–50 principal investigators. Worst affected was the Smilow, where severe flooding in the basement disabled the pumps feeding fuel to backup generators on the roof. A leak also spilled diesel inside the animal facility, and all the mice there drowned or died from inhaling diesel fumes. Neurobiologist Gordon Fishell lost about 2,500 mice representing 40 genetic variants, which he had developed for studies of forebrain development over more than a decade.

As NYU officials tally the damage, they will inevitably have to address the issue of whether the disaster could have been avoided or minimized. "Putting animals (or electrical control equipment) in a basement within a stone's throw from a tidal river is not a wise idea," immunologist Alan Frey wrote in an e-mail to *Nature* after losing all of his mice, which were housed at the Smilow. At the Texas Medical Center in Houston in 2001, Tropical Storm Allison destroyed millions of dollars of equipment and killed thousands of lab animals ranging from mice to monkeys. In the aftermath, engineers constructed flood gates and moved animal facilities and crucial components of the power system out of the basement.

The Smilow, which opened in 2006, can withstand a storm surge of about 3.7 metres — 20% higher than that expected from a once-per-century flood, according to the NYU. Now that Sandy has overtopped those defences, officials say that they will be assessing what they can do differently in the future.

Bartelle, whose work was spared by the disaster, says that he won't forget the efforts made that night to get patients out of harm's way — especially by students and researchers at the Smilow who knew they were facing disastrous losses to their work. "Why does the tragedy happen to the person right next to you? They don't deserve it any more than you do," he says. "It's going to be difficult moving forward for everybody." ■





The NIF's lasers blast a tiny pellet containing isotopes of hydrogen to trigger fusion reactions.

#### FUSION RESEARCH

# Laser lab shifts focus to warheads

*US ignition facility will devote less time to energy research.*

BY GEOFF BRUMFIEL

**A**fter an unsuccessful campaign to demonstrate the principles of a futuristic fusion power plant, the world's most powerful laser facility is set to change course and emphasize its nuclear weapons research.

For the past six years, scientists and engineers at the US National Ignition Facility (NIF) have been working flat out to focus 192 laser beams on a gold-lined 'hohlraum' capsule, just a few millimetres long, containing a pellet of hydrogen isotopes. As 500 terawatts of laser power hits the capsule, it generates X-rays that blast into the pellet, causing the atoms of deuterium and tritium inside to fuse. The fusion converts a tiny amount of their mass into a burst of energy (see 'The NIF's fusion strategy').

The goal of the National Ignition Campaign (NIC) is reflected in its name: 'ignition', in which the fusion reaction generates as much energy as the lasers supply. Success, NIF officials say, could pave the way to developing a power plant that would implode nearly 1,000 pellets a minute (see *Nature* **483**, 133–134; 2012). But unexpected technical problems left the NIF well short of its goal when the

campaign finally ended in September.

Now federal officials and the US Congress are preparing to set a new direction for the US\$3.5-billion facility at the Lawrence Livermore National Laboratory in California. A series of reports commissioned by the government, Congress and the University of California, which administers the lab, are all due later this month. They are expected to outline plans to cut its time for ignition research from 80% to 50% and to give the National Nuclear Security Administration (NNSA), which is responsible for maintaining the US nuclear arsenal, a more central role in determining the NIF's priorities. The NNSA is planning to emphasize experiments that mimic conditions inside nuclear weapons, generating data to validate the computer codes used to check that the nation's warheads remain viable — essential work, given the voluntary moratorium on underground testing that began in 1992.

Nobody has given up on ignition, declares Donald Cook, deputy administrator for defence programmes at the NNSA. But a new programme for generating net energy will take a slower, more methodical approach. "We're now going to get right into the science of

what issues are preventing ignition and work through them," he says. "But we believe that's going to take a fair amount of work."

Significant progress has already been made towards ignition, according to physicist Robert Byer at Stanford University in California, who is leading the University of California's review of the NIF. "The laser itself has been quite remarkable," he says. One shot can deliver 1.85 megajoules of energy, roughly what the lab originally promised. The instruments used to study the pellet are also performing well, he says.

Yet on the basis of data obtained from the imploding pellets, researchers think that they are still far from reaching the conditions necessary for ignition. One problem seems to be that too much of the laser light is scattering back out of the capsule. Another is that the pellet is being squeezed asymmetrically, which lowers the pressure at its centre. The asymmetry also causes the isotopes to mix unevenly, lowering the temperature in the pellet. "Nature pushes back: that's my shorthand version of what's going on," Byer says.

Nature isn't the only one pushing back — the NIF's funders in Congress also want answers. "We're disappointed," says one congressional staff member, who spoke to *Nature* only on condition of anonymity. Critics say that the lab's enthusiastic promotion of the idea that laser fusion could generate electrical power led many in Congress to believe that they were funding an energy project, when in fact laser fusion is decades from producing electricity. "The lab overemphasized and oversold the energy aspect of the NIF, at the expense of the very important and successful work it was doing in stockpile stewardship and basic science," says a senior scientist familiar with the NIF programme.

The NIF's current director Ed Moses bristles at accusations that ignition was overemphasized. "I don't think it was oversold or undersold. It just was," Moses insists that "remarkable progress" has been made in the past 16 months, since the NIF began working with hydrogen-pellet targets. "The goal was to do the initial exploration of the ignition conditions and see where we were, which is what we've done."

But there is likely to be less time for ignition experiments in the coming year, says Cook. Livermore will still control the programme's day-to-day operation, but the NNSA's headquarters in Washington DC will set priorities as the facility expands its stockpile stewardship work. Already, the NIF has been able to address crucial questions about how energy passes from the fission stage of a nuclear weapon to its much more powerful fusion stage. Future research will assess the 'boost phase' of the weapon — during which a small quantity of deuterium and tritium at the centre of the first stage is used to boost the initial fission phase of the explosion.

The shift in priorities worries Riccardo Betti,

LAWRENCE LIVERMORE NATL LAB.

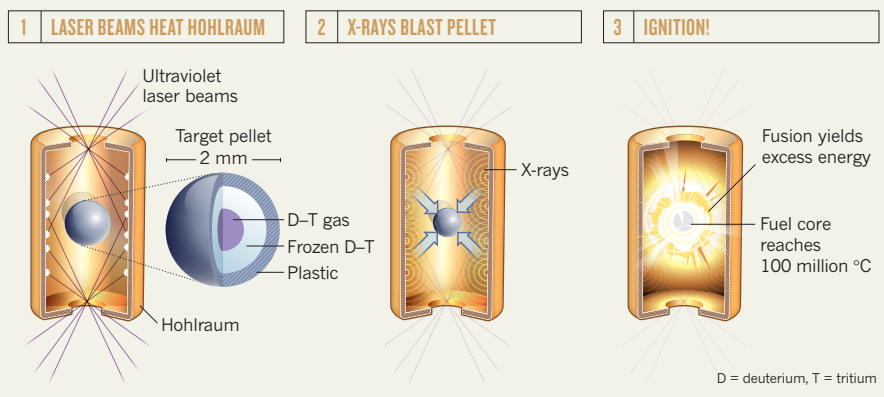


a laser fusion researcher at the University of Rochester in New York. “They have to make sure that the ignition effort doesn’t become subcritical,” he warns.

Keeping momentum in the ignition campaign may be crucial, because many in Congress still believe in the energy-research mission being pushed by the lab. Lawmakers have mandated that a new plan for reaching ignition be delivered to them by the end of the month. Politicians are ready to accept that it may take longer than originally stated, but they need to see evidence that it is on course, the congressional staff member says: “It can’t just be an open-ended: ‘Just give us money, we promise we will do good science.’” And if the NIF fails to reach its ignition goal in a few more years? “Then we’ll have to evaluate whether it’s worth continuing to fund the facility.” ■ [SEE EDITORIAL P.159](#)

## THE NIF’S FUSION STRATEGY

As the NIF’s laser beams hit the gold hohlraum capsule (1), they generate X-rays that blast the outer layer of the pellet (2), compressing the hydrogen isotopes until they fuse (3).



## GENETICS

# One-stop shop for disease genes

*NIH database integrates data from clinical genetic testing labs and literature.*

BY MONYA BAKER

When Heidi Rehm surveys a patient’s genes and finds a variant she’s never seen before, she improvises. First Rehm, who directs a clinical genetics testing laboratory at Partners HealthCare in Cambridge, Massachusetts, checks through as many as ten databases to learn whether that variant has ever been associated with disease. Then she may ask colleagues at other clinical sequencing laboratories whether they have seen it. But the launch this week of a database known as ClinVar will make her job much easier — and allow her to ask more sophisticated questions.

Developed by the US National Institutes of Health (NIH) National Center for Biotechnology Information (NCBI) in Bethesda, Maryland, ClinVar integrates dozens of existing databases. It also provides, for the first time, a central place in which clinical testing laboratories can deposit their data, because most currently keep their data within the laboratory. By aggregating such information, ClinVar’s creators hope to accelerate clinicians’ understanding of the effects of variants as well as reveal whether different laboratories are interpreting the same variant in different ways.

“There is a growing recognition that a clinical lab may see a mutation once or never, so it’s better if all those data could be pooled,” explains James Ostell, chief of the information engineering branch at the NCBI and a member of the ClinVar team. Such information could not only help laboratories to improve quality, it could also prompt research on new variants.

“For everybody in the field, I think there will be a sigh of relief that this is finally happening,” says Stephen Kingsmore, who is using whole-genome sequencing to pin down genetic causes of rare diseases in newborns at the Children’s Mercy Center for Pediatric Genome Medicine in Kansas City, Missouri. He predicts that his team will turn to ClinVar every time it finds a mysterious variant in a patient sample.

ClinVar was built with computational analyses in mind. It uses standard nomenclature to describe disease, is designed to allow researchers to incorporate the data into their own software and supports searches for long lists of variants. “It provides a forum that is computer

**“I think there will be a sigh of relief that this is finally happening.”**

readable for people to develop tools to find connections between genetics and disease,” Ostell says. Already containing data on 30,000 variants, ClinVar is expected to grow quickly because of a shift in sequencing technologies and practices. Whereas researchers typically used to screen DNA samples only for the presence or absence of known mutations, it is now becoming more common to sequence a relevant gene in its entirety, revealing a plethora of never-before-seen mutations that may or may not be harmful. ClinVar has the capacity to hold detailed information about variants and disease links — although it will not hold the full-genome data that could potentially identify a patient.

ClinVar’s success will hinge on the quantity

and quality of the data deposited there. If the submission processes are too onerous, then laboratories won’t participate, says David Dimmock, who is leading a whole genome-sequencing project at the Medical College of Wisconsin in Milwaukee. But even if the data in ClinVar swell, he and others worry that new users of the database will not be sufficiently sceptical of its contents. Existing databases often classify a variant as pathogenic when in fact it is not, and ClinVar might compound the problem by aggregating such mistakes, he says.

Another concern is that ClinVar could undermine well-regarded specialist labs that evaluate variants for particular diseases. “There is no revenue stream to pay an expert to review the data because you can get the data for free in ClinVar,” says Dimmock. “This could paradoxically be a way in which the interpretation of variants ceases.”

Rehm, who is co-leading an effort to help clinical labs to submit data to ClinVar, says that she once shared that concern. What changed her mind was the fact that so many of the variants that her lab and others identify are unique. She has collected data from more than 5,000 patients, she says, yet two-thirds of the potentially clinically relevant variants she sees have never turned up in her lab before, and she often has to tell patients that their variants cannot be interpreted. The only remedy, she says, is for labs to share genetic information from a much broader patient population.

Kingsmore agrees. “Patients are going to be getting the best thinking of the community as opposed to an individual lab.” ■



More high-energy photons will be extracted from Fermi Gamma-ray Space Telescope observations.

## ASTROPHYSICS

# Space telescope to get software fix

*Upgrade could help  $\gamma$ -ray observatory to detect dark matter.*

BY RON COWEN

Since its launch in 2008, NASA's Fermi Gamma-ray Space Telescope has trained its detectors on the most violent regions in the cosmos, recording some of the highest-energy photons known —  $\gamma$ -rays billions of times more energetic than visible light. But to astronomers' chagrin, the most revealing photons have sometimes slipped through.

Long-standing but little-publicized software problems, and insufficient memory in one of the detectors, have clouded the vision of the world's leading  $\gamma$ -ray telescope to the highest-energy  $\gamma$ -rays. The flaws do not seriously threaten the satellite's observations at low energies. But they have hampered studies at energies greater than 10 billion electronvolts (GeV), which could yield clues to dark matter and the powerful stellar explosions known as  $\gamma$ -ray bursts, says particle physicist Bill Atwood at the University of California, Santa Cruz, a member of the Fermi team who helped to design the craft's instruments.

Now the team is closing the net. A workaround for the memory deficiency was uploaded

to the spacecraft two weeks ago, and new software is being tested, the team reported last week at the Fourth International Fermi Symposium in Monterey, California. Expected to be in routine use by the end of 2013, the software, called Pass 8, will boost the amount of usable data at energies greater than 10 GeV by some 60%. The result, says Atwood, "will be a complete renaissance in the science this instrument will do".

Physicists working at particle accelerators typically revise their software within months of seeing what their data looks like. But four years after launch, Fermi researchers are only now replacing the main algorithm used to analyse the  $\gamma$ -ray data. The team had to convince itself that the labour-intensive software overhaul was needed, given how well the mission was performing, says Fermi researcher Elliott Bloom of the SLAC National Accelerator Laboratory in Menlo Park, California.

When  $\gamma$ -rays strike Fermi, they first encounter a tracker consisting of silicon-strip detectors interleaved with tungsten foil. The foil converts the photons into pairs of electrons and positrons that are recorded in the silicon strips. But the

original software was not adept at handling the complex showers of charged particles created by the highest-energy  $\gamma$ -rays. It also had trouble identifying  $\gamma$ -rays that slip through the tracker and slam into Fermi's calorimeter, which measures photon energies. The algorithm could not always distinguish between  $\gamma$ -rays and spurious strikes of other particles such as cosmic rays.

Because these previously ignored signals are hidden in the raw data transmitted to Earth, researchers can apply Pass 8 to data from Fermi's four years of operation to resurrect some of the missing photons. But because of the memory flaw, the data are incomplete. Two years before launch, tests revealed that the tracker's detectors collected much more information than could be stored in memory — "a woefully stupid error," says Atwood. But by then, a hardware fix could have delayed the mission or even threatened it with cancellation. Memory overload was originally prevented by truncating the data collected by each silicon strip. In the new strategy, the data from all the strips are collected and then truncated en masse, which is a more efficient use of the limited memory.

Tests of the software fixes are yielding tantalizing results. At the symposium, Melissa Pesce-Rollins at the National Institute for Nuclear Physics in Pisa, Italy, reported that she and her colleagues had used Pass 8 to reanalyse ten  $\gamma$ -ray bursts detected by Fermi. They found four new photons with energies greater than 10 GeV, including one, from a burst 3.7 billion parsecs (12.2 billion light years) from Earth, at 27.5 GeV — the highest-energy photon ever observed at this distance. These photons, passing through a haze of background light, can offer information about the stars that existed when the Universe was still evolving; the fact that the photons got through at all is a hint that the first stars were not as massive or as numerous as is typically assumed. "Physicists are always striving for perfection and that is essentially what Pass 8 is all about," says Pesce-Rollins.

Other researchers say that the fixes will put Fermi closer to detecting clues to dark-matter particles, which can annihilate each other and produce high-energy  $\gamma$ -rays. At the symposium, Christoph Weniger of the Max Planck Institute for Physics in Munich reported hints of an annihilation signal from the Galactic Centre, where theorists speculate that dark matter might lurk. Pass 8 could transform that tentative result into a bona fide discovery. ■



**MORE  
ONLINE**

### TOP STORY



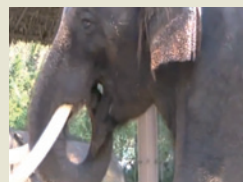
Blind mole rats may hold key to cancer  
[go.nature.com/nuzx6](http://go.nature.com/nuzx6)

### MORE NEWS

- Astronomers set up telescope timeshare [go.nature.com/h1si5w](http://go.nature.com/h1si5w)
- Health sector opens purse for US election [go.nature.com/gp6omw](http://go.nature.com/gp6omw)
- General anaesthetic disrupts brain communication [go.nature.com/o3akzn](http://go.nature.com/o3akzn)

### FROM THE BLOG

Asian elephant says 'hello' in Korean  
[go.nature.com/gdcsvz](http://go.nature.com/gdcsvz)





## RESEARCH POLICY

# Irish science adviser office axed

*Researchers worried that they have lost a voice for investment in science.*

BY DECLAN BUTLER

Researchers in Ireland, one of the European economies hit hardest by the recession, fear that they have lost a strong defender of science. When Ireland embraced austerity after the financial crisis struck in 2008, the country's chief science adviser (CSA) helped to persuade the government to spare science, and urged it not to neglect longer-term investments in research capacity. Now, however, the government has abolished the CSA's office and transferred its responsibilities to the head of Science Foundation Ireland (SFI), the country's largest research-funding agency.

The last CSA, Patrick Cunningham, an internationally renowned animal geneticist at Trinity College Dublin, ended his term in August. On 26 October, the government announced that the CSA's role would be taken over by Mark Ferguson, director general of SFI, and that the CSA's office — with just two support staff seconded from elsewhere — would be axed as part of sweeping public-service reforms. The move has alarmed researchers, who are sceptical that Ferguson can devote adequate time to the role, given his demanding post at SFI. And they question whether the head of a national research-funding agency, charged with implementing government policy, can be seen to provide truly independent advice. "Many of us are mesmerized by this. It's bewildering and illogical," says Peter Gallagher, an astrophysicist at Trinity College. "It's a complete conflict of interest."

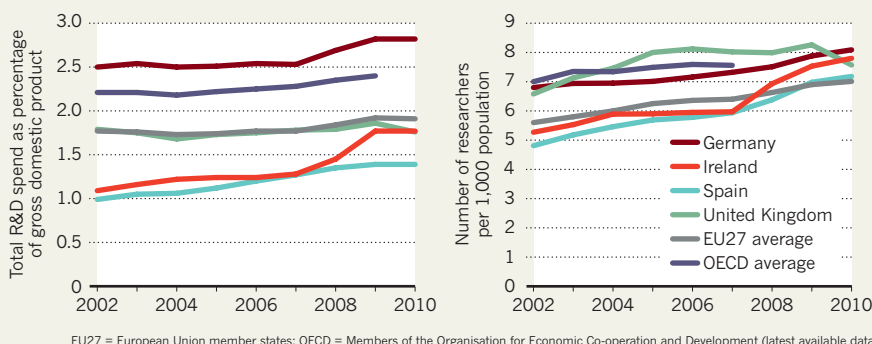
There is "self-evidently" a potential for conflicts of interest, agrees Cunningham, not least because SFI is one of many competing interests in the Irish research and funding space. "I have great respect for Mark's credentials, capacity and personality, and I'm sure he will act with the greatest integrity," he says. "It's more a problem of outside perception. That's a real challenge to somebody who has to be seen to act as an independent adviser."

Ferguson, who has led SFI since January, acknowledges the potential for conflicts of interest. Ideally, the roles of the CSA and head of SFI should be separate, he says, but under the current economic conditions he found the government's plan to be "perfectly reasonable". He adds that any conflict would be mitigated by his intention to act mainly as an arms-length facilitator in generating opinions and advice. As to finding the time, he says that he will "just have to work harder".

Researchers say that science in Ireland needs more of the kind of analysis and advice

## A CELTIC TIGER IN THE LAB

Ireland's research spending and researcher employment rose in the mid to late 2000s, buoyed by public and private investment, but has since declined.



that Cunningham provided. R&D funding from all sources rose significantly in the mid to late 2000s (see 'A Celtic tiger in the lab'), and although government research spending declined in 2010 and 2011 to pre-2007 levels, it has so far escaped the savage cuts that have hit other sectors of public spending in Ireland. But with Irish public finances under intense pressure, bigger cuts in science spending may be inevitable in the coming years. "There's a very big job ahead to defend the science budget," says David McConnell, a geneticist at Trinity College. "The financial pressures on Ireland are ferocious."

In March, the government also announced that it would refocus public research spending on just 14 areas with the greatest potential for creating jobs and wealth. Ferguson has prominently supported the move, and says that it will bring more "balance" to the

foundation's portfolio, which he believes has been too skewed towards blue-skies research at the expense of targeted research.

Many Irish researchers accept that at a time of economic crisis the government has to prioritize research spending to some extent. "We have to show that researchers are collectively as concerned as anyone else about the huge crisis that we face nationally," says McConnell, arguing that it is up to researchers to put forward good proposals within the priority headings. But some worry for the future of fields that don't fit these pigeonholes. "This is a death knell for many of us in frontier or basic research, such as pure mathematics, evolutionary biology, astrophysics or particle physics," laments Gallagher. Many also argue that the government is focusing too much on illusory short-term pay-offs from research. Long-term investments, such as building research infrastructure and training the best scientists, are crucial to attract the international high-tech investments that remain Ireland's main driver of growth, says Cunningham. Similar investments in education and research underpinned the country's economic boom from the mid-1990s until 2007.

Researchers say that the research-prioritization exercise is itself one example of why an independent CSA is preferable, arguing that the head of SFI can hardly be asked to assess a policy that his agency is promoting. McConnell wonders why the government didn't instead draw upon the pool of recently retired leading Irish researchers, many of whom, he says, would have been "honoured" to do the job with a minimum of remuneration and support. As another scientist comments: "Closing the office entirely sends negative signals to our international colleagues, who will ask the question: 'Just how serious is Ireland about its science?'" ■



Dual role for funding-agency head Mark Ferguson.

SOURCE: OECD; FORFAS





If there is methane on Mars it has so far eluded detection by the Curiosity rover.

## PLANETARY SCIENCE

# Hopes linger for Mars methane

*But negative signal from the Curiosity rover raises questions about planned European mission.*

BY ERIC HAND

Last week's preliminary verdict from the Mars rover Curiosity on whether the planet's atmosphere contains methane ended weeks of anticipation. But the verdict — a qualified no — seems unlikely to end years of controversy.

Sporadic claims of Martian methane in the past decade have met with scepticism — and not just because the measurements are difficult to make. Methane at levels of tens of parts per billion could be a sign that microbes are at work on the planet, lending urgency to proposals to hunt for a subterranean Martian biosphere. The European Space Agency (ESA) has already taken steps in this direction, and is planning an orbiter that would map methane sources as a precursor to sending a rover to look for Martian

life. Yet some scientists believe that this is premature, even quixotic, and could distract from the current agenda of NASA's rover, which is to look for signs that the planet was habitable at some time in its warmer and wetter past.

The Curiosity team couldn't quite lay the methane question to rest. In a 2 November announcement of the rover's first atmospheric results, the team said that, with 95% certainty, Martian methane does not exceed 5 parts per billion (p.p.b.), a level that could more readily be explained by non-biological geochemical reactions or by comet impacts delivering pulses of the gas from space. And the true value could be zero. "Bottom line is that we have no detection of methane so far," says Chris Webster,

a Mars scientist at the Jet Propulsion Laboratory in Pasadena, California, and principal investigator for the Tunable Laser Spectrometer (TLS), the rover instrument with a crucial role in looking for the gas.

Yet the upper limit offers wriggle room for scientists who have been trying to shore up their previous detections. The team performed only four tests with the TLS, which shines a laser into a small chamber filled with Martian air to look for methane's absorption spectrum. And some residual air from Earth trapped in the instrument had forced the team to change the planned experimental protocol, resulting in a surprisingly wide standard error.

Michael Mumma, of the Goddard Space Flight Center in Greenbelt, Maryland, says that the Curiosity results are consistent with his own observations using Earth-based telescopes. His team reported evidence of a plume of gas on Mars in 2003 with methane levels as high as 45 p.p.b. (M. J. Mumma *et al. Science* **323**, 1041–1045; 2009). Mumma's latest ground-based observations, from 2009–10, have found no methane, and have an upper limit of 6 p.p.b., similar to Curiosity's. One possibility, he says, is that Mars generates isolated bursts of methane, which then disperse.

Curiosity's result also doesn't faze researchers planning the ESA's Trace Gas Orbiter, which is due to launch in 2016. "I'm not worried right now," says Olivier Witasse, the mission's project scientist at the European Space Research and Technology Centre in Noordwijk, the Netherlands. "I think it's not the end of the story."

The ESA mission would add another chapter. In one mode, the orbiter will map the global distribution of gases, using light reflected from the Martian surface. But it will also stare at the rim of the planet, using the Sun as a backlight to map methane concentration as a function of altitude. Manish Patel at the Open University in Milton Keynes, UK, a member of one of the instrument teams, says that the orbiter should be able to detect concentrations as low as 14 parts per trillion — well below the 100 parts per trillion limit that the Curiosity team thinks it can achieve.

Patel hopes that such precision won't be needed, and that the next lot of Curiosity measurements will reveal methane at higher levels. That could bolster support from European politicians and keep the mission on track, he says.

Although Witasse also hopes for a positive methane result, he says that the ESA mission will still have value even if methane is absent. By looking at isotopic ratios of noble gases, the orbiter could help chart how the Martian atmosphere has steadily eroded over time. The craft could also map the seasonal movements of carbon dioxide and water vapour. And it could detect faint traces of sulphur compounds that might point to residual subterranean volcanic activity. "Even if there is no methane I will not be worried," he says. "There are other gases that are interesting." ■

➔ **NATURE.COM**

For more on the Mars rover Curiosity see: [go.nature.com/ihnt1b](http://go.nature.com/ihnt1b)

Students at AIMS in South Africa use time on the beach to reflect on and discuss ideas.



# Africa's counting house

The African Institute for Mathematical Sciences was set up to breed a new generation of numerical talent. Now it is spreading across the continent.

BY LEIGH PHILLIPS

Alex Bamunoba is not quite sure how many siblings he has. "My father was polygamous, so we ended up being very many," he says. "Something close to 30 brothers and sisters, with different step-mums." But when it comes to the branch of pure mathematics known as number theory, Bamunoba is on solid ground. He won a place in a PhD programme at Stellenbosch University in South Africa, and he hopes to teach mathematics in his home country, Uganda, or elsewhere in Africa.

The bridge that took Bamunoba from a Ugandan village to Stellenbosch is the African Institute for Mathematical Sciences (AIMS). The aim of AIMS, which was started in 2002 by cosmologist Neil Turok, is to recruit the brightest students from across Africa and match them up with a faculty of top-tier

mathematicians, computer scientists and physicists from around the world for a one-year postgraduate diploma in maths. Turok argues that a generation of mathematically trained graduates will empower Africa by strengthening the continent's research base and by focusing on fields that are key to industry and policy, ranging from mathematical modelling to computing, censuses and financial management. "There is nothing more cost-effective for development than mathematics," says Turok, who is head of Canada's Perimeter Institute for Theoretical Physics in Waterloo.

Ten years on, AIMS, based in Muizenberg, South Africa, has graduated 407 students, of whom 315 are still in Africa (see 'Where the graduates go'). Around

40% have gone on to do PhDs, one-quarter are working in academia as postdocs, researchers or teachers, and nearly 7% are in industry. Turok's team is proud to have produced statisticians for the Zambian Energy Regulation Board, systems engineers for Namibian IT consulting firms, epidemiology researchers in South Africa and lecturers at multiple African universities who in turn educate hundreds of students each year.

"What AIMS is doing is so important," says Kwame Akyeampong, a senior policy analyst and mathematician with the United Nations Educational, Scientific and Cultural Organization (UNESCO) in Paris, who specializes in education evaluation. "Africa is deluding itself if it thinks it can produce a South Korea or a China without advanced maths and science training."

**NATURE.COM**  
For more on science in Africa, see [www.nature.com/africa](http://www.nature.com/africa)

AIMS-SOUTH AFRICA



Now Turok and his team are expanding. In the past 14 months, they have opened institutes in Senegal and Ghana. Next year, they plan to open a fourth in Ethiopia. Turok's long-term vision is a network of 15 such schools throughout Africa. "Our future goal is to have a major impact on Africa's development," says Turok. "This will require training large numbers — many thousands — of students, so they form a highly skilled community."

And to build that community, says Turok, AIMS is pioneering a new style of education. "We're reinventing the university," he says, "and if you want to do this, the best place to come is Africa."

## EARLY INSPIRATION

Turok was born in Johannesburg, to prominent anti-apartheid militants. His parents were imprisoned for their activism, and his father is still an ANC member of parliament. Neil Turok left the country to pursue studies in theoretical physics in the United Kingdom and the United States. But he remained strongly connected to — and increasingly frustrated by — his home continent. "About a trillion dollars has been spent on aid to Africa over the past decade, with no obvious results," he says.

Part of the problem, according to Turok, is a lack of mathematical expertise in African governments. "They bring in consultants from Europe or buy off-the-shelf software that may not be appropriate. Major policy decisions are being made off the back of this with such poor understanding." Yet African education systems are in no position to fill the gap. "Universities over the past 30–40 years have suffered from chronic underinvestment, privatization, isolation and a terrible loss of morale," he says. "The teaching of mathematics and sciences has really been in crisis."

After Turok came up with the idea for AIMS, he convinced the South African theoretical physicist Fritz Hahne to become the school's first director. In 2002, using a 1-million-rand (US\$100,000) donation from the Turok family, the pair bought and transformed a rundown art deco hotel a street away from the beach in a small town 21 kilometres from Cape Town. In August 2003, with funding from international donors and the South African government, the institute opened its doors to the first 30 students. Today, the annual cohort stands at 50.

A visitor to the institute today steps off the scruffy yellow cars of Cape Town's metropolitan railway and smells the sharp tang of the Atlantic ocean. The beach and its crashing waves have long made this village, with its vegan café-cum-bookshop and marijuana-fragraned jazz hangout, a magnet for surfers and freethinkers. The peach-coloured institute, filled with utopian mathematicians, seems right at home.

The programme is divided into three parts. An introductory phase ensures that everyone

has a common grounding in problem-solving and computing, and a good grasp of English. This is followed by intensive three-week courses in topics such as biomedical signal processing, quantum computing and natural-systems modelling, taught by instructors who fly in from around the world. All this is rounded out with a seven-week research project that can form the basis of doctoral work should a student decide to continue to a PhD. Students are tested in oral examinations rather than in written ones, in an effort to test their knowledge of ideas rather than their skill at passing a test.

The three-week courses have been key to the institute's success, says Turok. In the past year, course teachers have included 15 South African and 18 international academics, including mathematicians Laurent Lafforgue and Maxim Kontsevich, both winners of the Fields Medal (the International Medal for Outstanding Discoveries in Mathematics) and based at the Institute of Advanced Scientific Studies near Paris. The village's long, surfer-friendly beach is one attraction for instructors, jokes Barry Green, the school's director since 2010 and former head of Stellenbosch University's Department of Mathematical Sciences. "But more seriously,

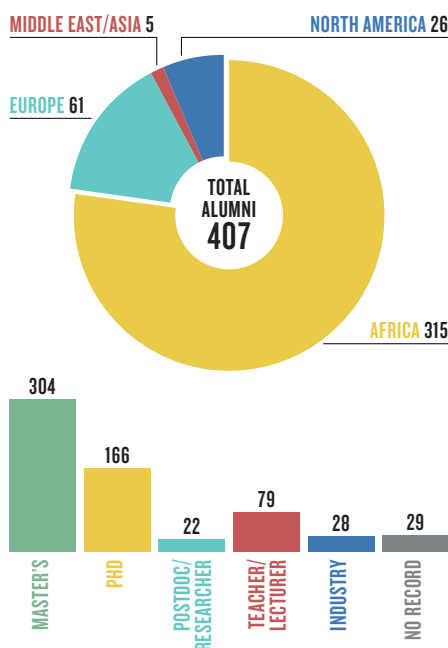
before. I was thinking: 'Where the hell am I?'" The level of interaction is intense, says Aguilar. Students work all hours and go for long walks on the beach to thrash out ideas. Instructors and students live on site and eat together in the cafeteria, where the lively discussion continues. "The schedule says we should be working with them for two hours a day, but really, it's more like five." And after three weeks, he says, "they were writing their own programmes, doing loops, doing integrals, derivations. I thought: 'This is just fantastic.'"

The institute's fees also set it apart. There are none: travel, accommodation, food and a stipend are all covered by AIMS, at a cost of roughly \$10,000 per student per year. Turok says that this is essential in a continent where some students wouldn't be able to afford even the plane ticket to Cape Town. AIMS South Africa now costs 18 million rand a year to run, with an extra 1.5 million rand for an enrichment programme for elementary and secondary school teachers and pupils and 5 million rand for the attached research centre. The South African government currently funds the school's infrastructure and research groups to the tune of 13 million rand, and tuition costs are paid for by donors.

Above all, the institute's success hinges on finding and recruiting good students, which it does through a network of trusted contacts in academia that keep an eye out for mathematical talent. Tina Ambinintsoa Malalanirainy Rakotoson, a tiny woman from Madagascar who writes down her name for a reporter to make sure it's not misspelt, wanted to come because her home country doesn't offer high-level training in the aspects of mathematics that fascinate her. She beams when she talks about the school and the thrill of being with students from across the continent. "Everybody speaks science. It's very exciting. It's not really like this back home," she says. "It's like a library with people instead of books."

## WHERE THE GRADUATES GO

Most of the alumni from the African Institute for Mathematical Sciences have stayed in Africa and in academia.



it's because we're flexible. With courses three weeks long, it's easy for people to get away."

Juan Rodríguez Aguilar, a computer scientist at Spain's Artificial Intelligence Research Institute in Bellaterra, last year taught a short course on the programming language Python and, seduced by the experience, is back again this year. "It was so shocking when I first went to the lab," he says. "It slowly became clear that some people had never seen a computer

## INCLUSIVE APPROACH

But is AIMS helping Africa? The school's administration is certainly proud that most of its alumni have remained in the continent. "When students want to build their career, it's normal that they may want to go elsewhere," says Green. "But we want to have a significant number that stay." Students are instilled with the school's mission to help Africa, and its leaders often talk of its 'pan-African spirit' — a term from the days of anti-colonial and anti-Apartheid struggle denoting the unity of the continent.

Turok and his colleagues are also making tangible efforts to keep students there. In 2008, AIMS opened a research centre across the road from the main building, funded by the South African government to the tune of 5 million rand per year. There, current and former AIMS students mix with academics, postdocs and PhD students from elsewhere. "We realized we had created such a unique community.

Such highly motivated students,” Turok says. “Why were we sending them away? Here, they would be much more encouraged to do path-breaking research.”

The research centre hosts four research groups, which explore cosmology and astrophysics, mathematical biology, computational algebra and mathematical finance. “We picked ideas that were not very mainstream in Africa, but very modern, that could then be spun off to universities after ten years,” says Bruce Bassett, the ebullient head of the cosmology research group. With Africa’s sky-high incidence of HIV, malaria and tuberculosis, it was obvious to focus on mathematical biology, which can help to tackle such diseases through systems biology, for example, or epidemiological modelling.

The cosmology group, the largest at AIMS, is girding itself for rapid growth alongside the two giant astronomy facilities planned for South Africa: the Square Kilometre Array (SKA), a €1.5-billion (US\$1.9-billion) effort to build the world’s largest radio telescope (see *Nature* **485**, 555–556; 2012) in South Africa and Australia; and South Africa’s MeerKAT, a giant radio telescope in its own right and the technology demonstrator for SKA. The group hopes to develop methods for handling the overwhelming amounts of data that these instruments will generate as they survey the sky.

The focus on cosmology and astrophysics, Turok admits, has prompted observers to ask: “What’s that got to do with Africa’s needs?”

“But that’s missing the point,” he says. “It’s not about bringing Africa up to some mediocre level, or worse, about mere survival. It’s about demonstrating that Africa can produce world-leading scientists.”

### IN SEARCH OF EXCELLENCE

Charles Leadbeater, a London-based expert who has advised companies and governments on education innovation, compares AIMS to the Indian Institutes of Technology, a network of regional public engineering schools developed in the 1960s, and their successors, the Indian Institutes of Information Technology, which, he says, have been real drivers of the country’s development. He also praises AIMS’s intensive teaching structure. “There are really few places at any level that quite have that dynamic, highly creative, lateral community feel. It’s like going to Pixar or Google,” he says.

But Akyeampong says that higher education alone can’t drive Africa’s development. “What’s really lacking is excellence in maths education at the base” for children in their first few years of schooling, he says. “Until that is resolved, you are never going to get the critical mass of mathematically literate that will have the serious impact on development that the AIMS people are hoping for,” he says.

AIMS has had its rough patches. The South African government has long demanded more return on its investment, and pushes AIMS to take in more domestic students. AIMS



Neil Turok (centre) is trying to inspire young Africans to pursue careers in mathematical sciences.

**“There is nothing more cost-effective for development than mathematics.”**

responded by adding a second intake in January — after South Africa’s summer — to fit with the country’s educational timetable and open it up to students.

And the expansion of AIMS to other countries has caused growing pains. Funders were sceptical, and a partnership to start an AIMS centre with the African University of Science and Technology (AUST), a private university set up by the World Bank in 2007 in Abuja, Nigeria, foundered. One reason, says Turok, is that the AUST charges US\$20,000 a year, but AIMS insisted that all costs be covered. “They also don’t emphasize the importance of having women students the way we do,” says Turok. “We have a minimum placement of 30% women students. They have two to three women out of a hundred students. From our point of view, this is unacceptable.” After the first flush of success with the South African campus and initial efforts to expand, “we seemed to be in danger of losing momentum”, says Jan Groenewald, an IT specialist at AIMS.

But in 2008, Groenewald says, things started to go their way. An AIMS alumna Esra Khaleel from Darfur in Sudan came up with the idea of an ‘African Einstein’. Turok adopted that branding, and the proposed network of institutes became known as the ‘Next Einstein Initiative’. “It turned out to be a hit with students and funders,” Groenewald says. “Then things started to move really fast.” In 2010, Google awarded AIMS US\$3 million to the project, and last year, the

Canadian government committed Can\$20 million (US\$20 million) over five years. The initiative now encompasses an office in Cape Town with more than ten full-time staff, as well as the new centres in Ghana and Senegal. As the centres proliferate, the plan is to open neighbouring research groups with their own mathematical specializations. The Senegal institute in M’bour, 80 kilometres south of Dakar, will be specializing in mathematics associated with solar energy and erosion — two natural topics in a country threatened by a steadily advancing Saharan desert.

Hahne, who continues to teach at the school, says gruffly that he is not fond of the branding. “I’m not looking for the next Einstein,” he says. “I’m looking for the solid development of science in Africa.” But Turok, who says that the Perimeter Institute has now modelled its one-year master’s programme on AIMS, is clear that there is substance beneath the slogan. “Africa is the greatest untapped pool of scientific talent anywhere, and no one realizes this,” he says.

Rakotoson does. Although some of her friends back home also like maths, they enter finance “to make money”, she says. “They don’t love mathematics. I love it!”

“Do you want to know why?” she asks, leaning forward, as if divulging a secret. “It’s because it’s like a game. When you know all the rules, you’ll always win.” ■ SEE EDITORIAL P.159

**Leigh Phillips** is an International Development Research Centre fellow at Nature.





Mount Cayesh and other peaks in Peru's Cordillera Blanca hold the densest concentration of glaciers in the tropics, but the ice is rapidly retreating.

# GOODBYE GLACIERS

*Researchers are racing to determine how shrinking glaciers in the Andes will affect the water supply of millions of people.*

BY BARBARA FRASER

**F**rom the shade of an adobe house overlooking Peru's Santa River, Jimmy Melgarejo squints at the dual peaks of Mount Huascarán looming against a cloudless sky. "The snow keeps getting farther away," says Melgarejo, a farmer worried about his livelihood. "It's moving up, little by little. When the snow disappears, there will be no water."

Throughout the Andes, millions of people voice the same concern as they watch climate change eat away at the mountain chain's icy mantle. But although everyone fears a water shortage, they do not know how quickly it will come or how severe it will be.

An interdisciplinary team of scientists is now trying to provide some answers through a US\$1-million project funded by the US National Science Foundation. The crew, which pulls together hydrologists, geochemists, geographers and historians, mainly from the United States and Canada, is tracking the fate of glacial meltwater as it runs from

**NATURE.COM**

For a slideshow  
and podcast on the  
research project see:  
[go.nature.com/tqnxav](http://go.nature.com/tqnxav)

B. FRASER

the mountains down to the ocean. Their goal is to develop models to forecast water flow and its effects on residents downstream. The rapid changes in the Andes “warrant a new kind of interdisciplinary, integrated study”, says geographer Bryan Mark of Ohio State University in Columbus, who is one of the principal investigators of the project. “We’re trying to cross traditional boundaries, so we’re not studying water separately from people.”

Peru has the largest mass of tropical glaciers in the world, and most are in the Cordillera Blanca, or White Mountains (see ‘Going with the flow’). The snow-capped range towering over the Santa River, which winds 347 kilometres to the desert coast, is “the most densely glaciated mountain range in the tropics”, says Mathias Vuille, a climate scientist at the State University of New York in Albany. With so much melting ice, and hundreds of thousands of people dependent on the glaciers, the Santa River valley — also known as the Callejón de Huaylas — has become a prime place to assess the changes caused by global warming.

As the most comprehensive study so far to examine melting glaciers and their impacts, the project will arm policy-makers with crucial information about how to adapt to climate change in the region, says Mark. The project could also contribute to models for other watersheds in the Andes and for ones as far away as the Himalayas.

The results so far present a mixed forecast. Despite the fears of Melgarejo and other residents, the river will not dry up completely during the dry season. But increasing demands on river water for drinking, irrigation and electricity generation will lead to conflicts over the dwindling — and increasingly expensive — resource. And there is not much time to plan for the changes. “This is a reality now,” says Michel Baraer, a project member and hydrologist at the University of Quebec, Canada. “We don’t have 50 years to adapt.”

## THE HEAT IS ON

On a crisp morning in July, Mark, Baraer and some colleagues with the project climb a lupin-fringed path to Lake Cuchillacocha, which sits at 4,600 metres above sea level, just below a glacier on Mount Pucaranra. There, they work in shifts through the day and frigid night, taking infrared images every half hour of the glacier and surrounding rock. Other instruments on and around the glacier’s tongue record solar radiation, wind speed and direction, temperature and humidity.

The researchers are studying how quickly the ice, rock and lake warm up during the day and cool at night. By correlating these detailed data with measurements of ice thickness and extent made remotely by satellite and planes, the team hopes to develop models for forecasting how quickly glaciers will retreat across the Cordillera Blanca and what the impacts will be.

Earlier studies have shown that glaciers in the mountain range have shrunk by 20–30% since 1970 (ref. 1), and the rate seems to be accelerating. Researchers at the French Research Institute for Development (IRD) in Marseilles have found that the glaciated area in the tropical Andes is now decreasing by 3% a year (ref. 1).

Because the amount of precipitation has not changed much over the past few decades, researchers blame rising temperatures for the glacial retreat; the region has warmed an average of about 0.1 °C per decade since the 1970s, said Antoine Rabatel, a glaciologist at France’s University of Grenoble and a member of the IRD study, at a conference at Santiago Antúnez de Mayolo National University in Huaraz in early July.

According to Rabatel, glaciers above 5,400 metres — such as those on Huascarán, Peru’s highest peak — will shrink but survive because temperatures there will remain relatively cool. But those at lower elevations are doomed to disappear. In the past few decades, those glaciers have lost twice as much mass as ones at higher elevations<sup>1</sup>.

That is bad news for residents because the glaciers serve as a buffer, locking up precipitation during the rainy season and releasing water slowly during the dry season, between June and September, when almost no rain falls.

“You can think of glaciers as hydrological Prozac — they smooth out the highs and lows,” says Jeffrey McKenzie, a hydrogeologist at McGill

## GOING WITH THE FLOW

Researchers are studying how the retreat of glaciers in the Cordillera Blanca is affecting people along the Santa River and its tributaries.



University in Montreal, Canada. Without the glaciers, downstream water users will have to adapt to greater variability between the wet and dry seasons.

From Lake Cuchillacocha, the Quilcayhuanca River tumbles down a broad, glacially carved valley. At a site about 7 kilometres downstream, McKenzie dips a probe into the river and measures a pH of 3.4. The lake is even worse, with a pH of 2.8. McKenzie, who is studying the interaction between surface water and groundwater, explains that many lakes and rivers in the Cordillera Blanca are naturally acidic because glaciers grind over rocks rich in sulphate, which gets dissolved into the meltwater.

McKenzie also collects samples to identify the water’s geochemical ‘fingerprint’ — its concentrations of stable isotopes of oxygen and hydrogen as well as several types of dissolved ions, which meltwater picks up as it flows through rocks near the leading edge of the glacier. Those data have allowed McKenzie and his colleagues to calculate that glaciers contribute about 30% of the water in the Santa River during the dry season<sup>2</sup>; the rest comes from wet-season precipitation that slowly flows through groundwater and eventually reaches the river.

The finding suggests that after the glaciers melt away, substantial amounts of water from rain and snow will still flow through the Santa River during the dry season. Yet with the population and agriculture expanding in the region, losing even 30% of the river flow during that season could still cause severe distress, particularly during a drought, says Baraer. And residents may not have much time to prepare because Baraer calculates that the Santa River valley has already passed a critical point known as ‘peak water’.

When glaciers first begin to recede, the rivers downstream initially swell with the added meltwater until the glacial supply starts to ebb. After that peak water point, the amount of discharge drops off sharply. Baraer and his colleagues studied discharge records for nine tributaries of the Santa River, with data going back to the 1950s. The records suggest that seven of the nine catchments passed the peak water point between the 1960s and the 1980s (ref. 2).



Georg Kaser, co-chair of the Climate and Cryospheric Research Center at the University of Innsbruck in Austria, cautions that without data from all catchments, it is difficult to know whether peak water has passed for the entire Santa River watershed. The ice caps on the higher mountains in the centre of the Cordillera Blanca remain largely intact, he notes. Nonetheless, the results should prompt Peruvians, especially policy-makers, to finally deal with the threat of declining water supplies, says Kaser. “We have been telling them for more than 20 years that this peak flow will come soon, but we just spoke into the wind,” he says.

Peru currently has no comprehensive plan for addressing future water shortages in the Santa River catchment, according to Gabriel Quijandria, vice-minister for strategic development of natural resources in the environment ministry. “There needs to be a substantial improvement in the way water is used,” he says.

Construction of small reservoirs that could be tapped in the dry season could be “part of the answer, but not all of it”, Quijandria says. Some researchers, however, question the feasibility of building artificial reservoirs within the steep topography of the Cordillera Blanca, where earthquakes are a constant threat.

For McKenzie, peak water is only part of the story. To forecast discharge rates more accurately, he is studying how the glacial meltwater and precipitation eventually reach the Santa River. The valley floor below Lake Cuchillacocha is a boggy wetland that acts as a sponge, storing meltwater and water from precipitation and releasing it gradually into the river. McKenzie has found that it takes groundwater an average of 18 months to work its way through the wetland and into the river.

This year, McKenzie spent two weeks drilling narrow bore holes up to 6 metres deep in the Quilcayhuanca Valley and another one farther north. Material from the holes provided clues about the composition of the soil, and in some of the holes McKenzie installed piezometers — devices that use pressure to gauge water levels. By next year, he expects to have data that will help to answer questions about the direction, levels and fluctuations of groundwater movement. From there, the researchers intend to model how the flow of groundwater into the river system will change as the meltwater decreases. They are also concerned about the threat of human activities in the upper valleys; livestock grazing and extraction of peat for potting soil could dry out the wetlands and diminish their capacity to store water, warn the researchers.

## EXTREME FLOODS

Although residents of the Santa River valley fret over forecasts of declining flows, they also worry about the opposite problem: too much water. The lakes at the feet of glaciers are often contained by unstable natural dams that give way in outburst floods, caused, for example, by a large chunk of ice dropping into the water. And the glaciers can steepen as they melt, making them more prone to avalanches. Outburst floods and avalanches have killed more than 25,000 people in the Callejón de Huaylas since the 1940s, says Mark Carey, an environmental historian at the University of Oregon in Eugene who is one of the leaders of the glacier project. The largest city in the Santa River valley, Huaraz, and many smaller towns are built on the deposits of former floods and landslides, he says. An outburst flood could kill tens of thousands of people, he estimates.

The National Water Authority in Peru currently monitors more than 35 lakes, according to Jesús Gómez of the agency’s glaciology unit. He says that the agency has prepared for the risk by lowering water levels when they reach a dangerous point, but an unusually large ice fall could still cause a flood, and the unit’s \$300,000 annual budget is not sufficient to install automated systems that could warn of an advancing flood.

The shrinking glaciers could also amplify other hazards, notably water pollution. Downstream from Huaraz, Mark gingerly steps past a stream of raw sewage pouring into the Santa River from the tiny community of Mancos. Nearby, Alfonso Fernández, a Chilean doctoral candidate studying with Mark, lays out

an array of small plastic bottles on a rock and uses a syringe to sample the water. Back in the lab, a team will analyse them for isotopic signatures to pinpoint the source of the water and will measure concentrations of pollutants such as heavy metals.

Sewage is not the only problem. Some tributaries of the Santa River contain naturally high levels of heavy metals, whereas others leach arsenic, cadmium and lead from tailings at old mine sites. The water quality in the river will probably fall as decreasing discharge concentrates the pollution, says Mark.

That could intensify competition for clean water, says Adán Pajuelo, president of a local irrigation committee, as he deftly cuts carnations in a field in Cruz de Mayo, a farming community near glacier-fed Lake Parón. In 2008, local farmers

accused Duke Energy, a US power company, of overdrawing water from Lake Parón for its hydroelectric dam downstream. The farmers padlocked the lake’s sluice gates, which limited the amount of water the company could draw from the lake.

The stand-off lasted nearly two years, until national government officials brokered a truce. Tensions have subsided, but Pajuelo worries that a drought year combined with impacts from a gold mine slated to be built near the lake could leave the farmers with only a small flow of polluted water to irrigate their crops.

Competition gets even stiffer downstream, where the river plunges through a narrow canyon past the hydroelectric plant towards the Pacific Ocean. In the coastal desert, asparagus, artichokes, fruit trees and sugar cane — mostly bound for export markets — sprout from land that was barren just over a decade ago. The Chavimochic irrigation project, which diverts water from the Santa River to irrigate 75,000 hectares of land, will cover more than twice that area when it is complete.

“Export agriculture is transforming the region,” says Jeffrey Bury, a geographer at the University of California, Santa Cruz, who is a principal investigator on the Santa River project. If the peak water scenario holds true, he says, “that will put inevitable tension on what the water is supposed to be used for and who is supposed to get it”.

All the issues affecting the Santa River come together at its mouth on the Peruvian coast. In the dry days of July, the once mighty river has shrivelled into a narrow stream trickling among cobbles and rubbish. If demands for water continue to grow, says Carey, then within a few years, it is possible that in the dry months no water from the Cordillera Blanca will reach the sea. ■



A researcher launches a doppler device to measure stream discharge.

B. FRASER

Barbara Fraser is a freelance writer in Lima, Peru.

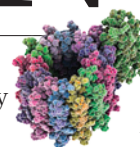
1. Rabatel, A. et al. *Cryosphere Discuss.* **6**, 2477–2536 (2012).
2. Baraer, M. et al. *J. Glaciol.* **58**, 134–150 (2012).

# COMMENT

**HISTORY** Centenary of the equation that launched crystallography **p.186**

**CONSERVATION** Suburbanites' conflicted relationship with wild animals **p.188**

**BIOLOGY** How life turns random energy into useful work **p.191**



**OBITUARY** Keith Campbell, creator of Dolly the sheep, remembered **p.193**

JOEL WEINSTOCK LAB



The whipworm *Trichuris suis* is currently in trials for treating Crohn's disease and ulcerative colitis.

## The worm returns

Joel V. Weinstock explains why several clinical trials are deliberately infecting people with helminths to treat autoimmune diseases.

For as long as modern humans have existed, they have carried parasitic worms. That is around 200,000 years. Like many bacteria, some roundworms and flatworms (helminths) reside harmlessly in the gut. Others can cause problems.

Before antibiotics and improvements in sanitation, gastrointestinal infections — mostly with bacteria — killed perhaps one in five children and many adults. Now, thanks to clean food and water and hygienic sanitation, it is rare for a child in the Western world to die from such infections. These advances in hygiene have also 'dewormed' much of the developed world.

Meanwhile, the twentieth century saw

a rapid increase in an entirely new set of diseases, such as inflammatory bowel disease (the focus of my research). These once-rare diseases, caused by autoimmunity, have become relatively common in less than a century. Why?

This question was plaguing me as I sat in a plane on the runway of Chicago's O'Hare airport for five hours one day during the mid-1990s. I was on my way to a grant-review session for the Crohn's and Colitis Foundation of America when lightning struck the control tower, forcing us

to wait until the airport could get up and running again.

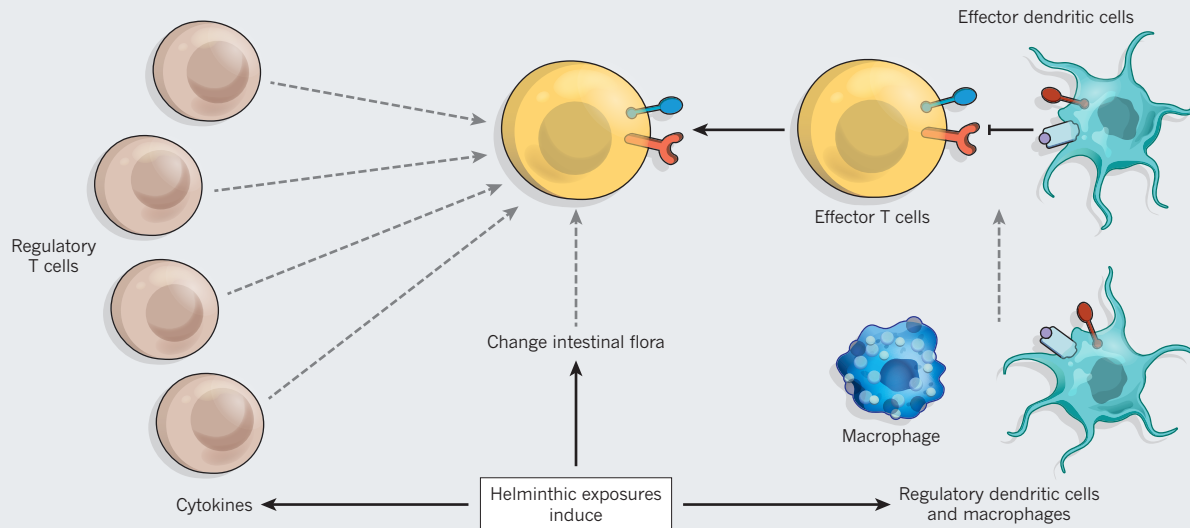
I was writing a review article at the time, on inflammatory bowel disease, and editing a book about parasites. That day, I was focusing on a chapter about how the 'evil' properties of intestinal parasites are often overblown. Considering the vast number of people who have carried them throughout history, the occurrence of associated disease is surprisingly infrequent. I was reminded of a classic teaching in parasitology, that a 'good' parasite imparts some advantage to its host — because if the host dies, so does the worm. Clearly, after thousands of years of co-evolution, the human immune system ►

► **NATURE.COM**  
Treating multiple sclerosis using helminths:  
<http://doi.org/jnq>



## PATH OF A PARASITE

Infection with helminths prevents effector T cells from triggering autoimmune reactions through three mechanisms: increasing the activity of regulatory T cells and stimulating cytokine release that dampens effector T cells (left); turning on macrophages and regulatory dendritic cells that prevent effector dendritic cells from activating T cells (right); and changing intestinal flora to boost 'probiotic' bacteria.



► has evolved to handle the presence of most parasitic worms, which have, in turn, developed adaptations that enable them to live for years in a human host.

Was it possible that improved hygiene, by ridding our bodies of parasitic worms and beneficial bacteria alike, made way for the newer problem of immune-mediated diseases? And could reintroducing parasitic worms protect people against those diseases?

That brainstorm in the middle of a lightning storm has turned into an active area of research. Several ongoing clinical trials, in which patients with inflammatory bowel disease or multiple sclerosis are colonized with an intestinal worm, have produced early evidence that the treatment may be safe and effective.

This counterintuitive hypothesis has captured the imagination of the popular press, and drawn the opprobrium of sceptics. The World Health Organization estimates<sup>1</sup> that nearly 50 million children under the age of five were treated for parasitic worms in 2006. Some of these parasites can damage the liver, bladder or eyes. How could such an infection actually improve health?

### TOO CLEAN

Helminths, being parasitic, evolved independently of the 'worms' people often think of, such as earthworms. Some take up residence in the gut after the host swallows their eggs in contaminated water or food. Even gardening in contaminated soil or playing in the mud can cause an infection. Others, such as hookworm, burrow into the body through the skin and ride the

blood to the lungs. Humans then cough up and swallow the larvae, which grow into adult worms in the gastrointestinal tract. Other helminths have even more complex life cycles.

Today, most helminths are found in developing countries in which poor sanitation contaminates water and soil. In Europe and the United States such infections are rare, but as recently as the 1930s and 1940s, up to 70% of children in some rural parts of the southern United States carried helminths<sup>2</sup>.

At the time of my insight on the O'Hare tarmac, I had been researching intestinal parasites for many years. Different species of worm cause a variety of effects. Some, such as *Schistosoma*, can impair the liver or bladder. Biliary flukes and some species of schistosome can predispose people to biliary and bladder cancer, respectively. Heavy acute infections with some helminths can cause diarrhoea and nausea. Hookworm can cause iron-deficiency anaemia in heavily infected, susceptible hosts.

Despite the potential dangers of some helminths, when I proposed the connection between the decrease in parasitic infections and the rise of autoimmunity, I had some historical facts on my side. In the United States and Europe, Crohn's disease first emerged in affluent populations living in hygienic conditions in the more northerly latitudes, where colder temperatures are less hospitable to soil-borne helminths<sup>3</sup>.

*"The first patient eagerly consumed the 2,500 nearly microscopic eggs."*

One of the last US groups to present with Crohn's disease was African Americans<sup>4</sup>, who are, on average, poorer than their white counterparts. Similarly, in Europe, autoimmune diseases are more common in the richer Western Europe than in Eastern Europe.

Today, Native American reservations, which have relatively high rates of infection with parasitic worms, also have lower rates of inflammatory bowel disease. Latinos born and raised in South America rarely develop this gut disorder. If their children are born in the United States, where conditions are often more sanitary, they have a much higher risk of the disease.

### TESTING A THEORY

When I returned to my laboratory (then at the University of Iowa in Iowa City), I told my colleagues about my theory. Some of them were intrigued and wanted to start experiments. Others thought I was joking.

We had access to parasitic worms — already a focus of our research — and to mouse models of inflammatory bowel disease. Sure enough, when we gave the mice enteric worms such as *Heligmosomoides bakeri* or *Trichuris muris* by feeding tube<sup>5</sup>, or schistosome eggs by injection<sup>6</sup>, the animals were protected from autoimmune disease.

To test the therapy in humans, we selected *Trichuris suis*, a whipworm that typically infects pigs but can survive for a few months in people. Evidence suggested that this was a safe choice — if swallowed, the worm remains in the gut and does not pass into the bloodstream, and pig farmers are commonly exposed to it without

medical reports of associated illness.

We began with a dose of 2,500 eggs — one investigator in an earlier study had given themselves a similar dose to prove that this organism could colonize the human intestine, and reported no clinical symptoms<sup>7</sup>. We infected pigs with *T. suis* eggs, then isolated adult worms from the infected animals and cultured them *in vitro*. The worms survived long enough to produce eggs that could be harvested and cleaned for clinical use.

Our institutional review committee gave us permission to try a dose in one patient. It was not hard to find a volunteer; many patients with inflammatory disease do not do well on conventional therapy and readily seek alternative approaches. The first patient in the study had untreatable Crohn's disease, and he eagerly consumed the 2,500 nearly microscopic eggs, which we gave to him in a popular sports drink. We held our breaths.

After six weeks — the time it takes for *T. suis* eggs to mature into adult worms — he reported no adverse events and showed improvement in disease symptoms that lasted for several months. In another trial, three more patients with Crohn's and another three with ulcerative colitis all reported substantial improvements (or complete remission), with no side effects.

Eventually, we administered live eggs every two weeks for 24 weeks to 29 patients with Crohn's disease. By week 24, nearly 80% of them reported a decrease in symptoms, and 72% were in remission — more than one would expect from a placebo effect. None reported side effects<sup>8</sup>. In another trial of 54 patients with ulcerative colitis, about half of whom were given placebo, 43% of helminth-treated patients improved after 12 weeks, compared with only 17% of those given a placebo<sup>9</sup>.

Several pharmaceutical companies have since taken

on the task of developing *T. suis* eggs as a drug. Both the US Food and Drug Administration and the European Medicines Agency have formally approved the manufacturing process and allowed further testing.

At present, a multi-centre trial in Europe conducted by drug firm Dr Falk Pharma, based in Freiburg, Germany, is enrolling nearly 300 patients with Crohn's disease; an interim analysis of the data suggests the treatment is safe. Coronado Biosciences, a firm based in Burlington, Massachusetts, and for which I am a consultant, is running a similar multi-centre, double-blind trial for Crohn's disease. There are trials under way in multiple sclerosis and autism, and others set to begin in ulcerative colitis, psoriasis, type 1 diabetes and other immune-mediated diseases.

Some investigators worry that helminths could weaken patients' immune systems and leave them more vulnerable to some types of infectious disease, even under careful medical supervision. But as long as society maintains its current modern hygienic standards, I consider this risk to be negligible. Given the lack of side effects from helminth therapy, morbidity from immune-mediated diseases and the toxicities of modern therapies for them almost certainly exceed the risk from helminthic exposure.

## HOW IT WORKS

Worms seem to have three major effects on the immune system (see 'Path of a parasite'). First, they seem to cause changes that activate regulatory T cells such as T<sub>reg</sub>. These cells dampen immune responses and curb autoimmunity — by, for example, ramping up the production of regulatory molecules such as interleukin-10 and transforming growth factor- $\beta$ .

Second, helminths seem to act on other cells — regulatory dendritic cells and macrophages. These prevent the switching on of dangerous effector T cells, which normally leads to inflammation and disease.

Both of these effects seem to protect from autoimmunity in a redundant fashion. My colleagues and I have found that when we block regulatory T cells or regulatory dendritic cells in helminth-infected mice, the animals are still protected from developing colitis<sup>10</sup> — either type of cell is sufficient in its own right to protect the mice. This redundancy may be one of the reasons why helminths are so effective in controlling these immune-mediated diseases.

Third, worms seem to alter the bacterial composition of intestinal flora. Research in mice suggests that helminths promote the growth of gut microorganisms typically considered to be 'probiotic', which help to maintain intestinal health.

The more we learn about the changes that helminths induce, the more we will understand about how autoimmunity develops and be able to devise more therapies — consisting of either helminths or agents that mimic their actions in the gut.

**"Worms seem to have three major effects on the immune system."**

For me, the project has generated the gamut of emotions for nearly 20 years now. The scientific and medical com-

munity initially received the hypothesis with a mixture of fascination and vocal scepticism. Thankfully, this research eventually obtained funding from the US National Institutes of Health and support from organizations such as the Crohn's and Colitis Foundation of America. Most of my colleagues took a neutral stance, waiting for more data. Today, studying the effects of alterations to intestinal flora and fauna on health and disease is one of the hottest areas in medical research, and investigations of the impact of helminths are increasing.

The public-hygiene measures and vaccine programmes to eliminate enteric and other types of infections have vastly improved quality of life during the past 100 years, with many more lives saved than taken. The goal now is to reintroduce organisms into people in a controlled and predictable way, to prevent immune-mediated disease without increasing the risk of serious infection. ■

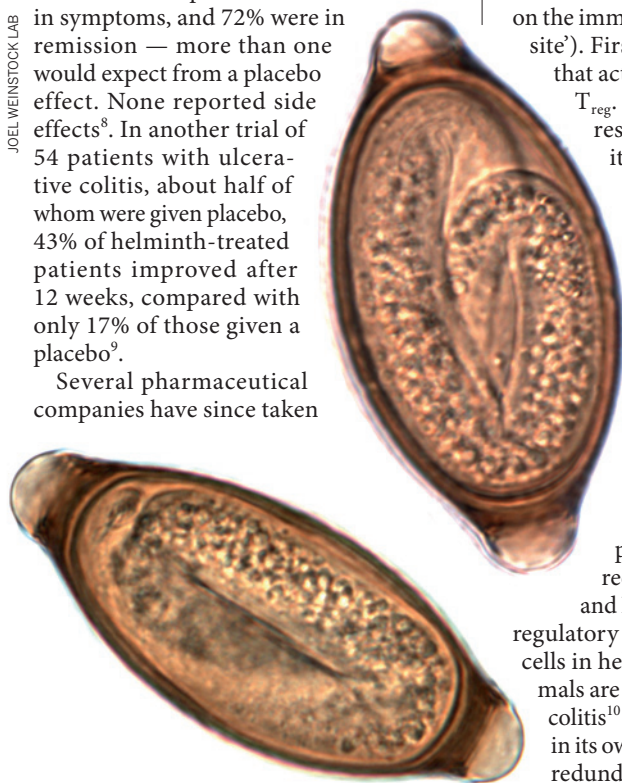
Joel V. Weinstock is a professor at Tufts University and is chief of the Division of Gastroenterology and Hepatology at Tufts Medical Center, Boston, Massachusetts 02111, USA.

e-mail: jweinstock2@tuftsmedicalcenter.org

- Partners for Parasite Control. *Action Against Worms 8* (World Health Organization, 2007).
- Weinstock, J. V., Summers, R. & Elliott, D. E. *Gut* **53**, 7–9 (2004).
- Shivananda, S. *et al.* *Gut* **39**, 690–697 (1996).
- Sonnenberg, A., McCarty, D. J. & Jacobsen, S. J. *Gastroenterology* **100**, 143–149 (1991).
- Elliott, D. E., Urban, J. F. Jr, Argo, C. K. & Weinstock, J. V. *FASEB J.* **14**, 1848–1855 (2000).
- Elliott, D. E. *et al.* *Am. J. Physiol.* **284**, G385–G391 (2003).
- Beer, R. J. *Res. Vet. Sci.* **20**, 47–54 (1976).
- Summers, R. W., Elliott, D. E., Urban, J. F. Jr, Thompson, R. & Weinstock, J. V. *Gut* **54**, 87–90 (2005).
- Summers, R. W., Elliott, D. E., Urban, J. F. Jr, Thompson, R. A. & Weinstock, J. V. *Gastroenterology* **128**, 825–832 (2005).
- Blum, A. M. *et al.* *J. Immunol.* **189**, 2512–2520 (2012).

Competing financial interests declared; see [tinyurl.com/blhtgo](http://tinyurl.com/blhtgo) for details.

JOEL WEINSTOCK LAB



Several pharmaceutical firms are developing eggs of the pig parasite *Trichuris suis* as a drug.





Lawrence Bragg remains the youngest ever winner of a Nobel prize, aged just 25.

# The birth of X-ray crystallography

A century ago this week, physicist Lawrence Bragg announced an equation that revolutionized fields from mineralogy to biology, writes **John Meurig Thomas**.

In the summer of 1912, a 22-year-old graduate student went on holiday with his parents to Britain's Yorkshire coast. There, his father, the physicist William H. Bragg, received a letter describing a dramatic lecture given by the German theoretical physicist Max Laue.

Laue's lecture reported the first observation by his colleagues Walter Friedrich and Paul Knipping<sup>1</sup> of the diffraction of X-rays by a crystal — the mineral zinc sulphide (ZnS). This proved that X-rays were waves, settling a controversy that had lasted the 17 years since their discovery. Bragg and his son Lawrence worked feverishly on X-ray diffraction all that summer at the University

of Leeds, UK, where William was professor of physics.

On returning to the University of Cambridge at the end of the holiday, Lawrence had a revolutionary idea. Laue's results, he reasoned, could be interpreted simply as arising from the reflection of X-rays by planes of atoms in the crystal. He realized that X-ray observations, of the kind initiated by Laue, provide evidence from which the arrangement of atoms in the crystal could be inferred.

To explain the patterns they saw (pictured), Laue and his colleagues had assumed that their X-ray source was polychromatic — comprising six or seven distinct

wavelengths — and that the structure of ZnS was a three-dimensional array of tiny cubes, with the zinc and sulphur atoms occupying each alternate corner.

Lawrence examined the X-ray photographs and noted that some of the diffraction spots were elliptical and that some had different intensities. In a paper read by his supervisor, J. J. Thomson, to the Cambridge Philosophical Society on 11 November 1912, Lawrence made two important proposals<sup>2</sup> to account for these features.

First, he suggested that Laue's results arose from the reflection of a continuous range of X-ray wavelengths by planes of atoms within the crystal. This interpretation yielded Bragg's law of X-ray diffraction:  $n\lambda = 2d\sin\theta$ , where  $\theta$  is the angle of incidence of X-rays of wavelength  $\lambda$ ,  $d$  is the separation of the reflecting planes and  $n$  is an integer. Second, he proposed that Laue's diffraction pattern from ZnS was characteristic of atoms located not only at the corners of the three-dimensional array of cubes, but also at the centre of the faces of each cube — a face-centred lattice.

So far, some two dozen Nobel prizes have been awarded for work related to X-ray crystallography, the technique Bragg set in train with his paper and used for his pioneering work on the structures of minerals, metals, their oxides and alloys. His colleagues were the first to use X-ray crystallography to determine the structures of a protein and an enzyme, and to formulate the model for the DNA double helix<sup>3</sup>. In my view, the technique is still the single most powerful analytical tool for scientists in physics, biology, medicine, materials and Earth sciences, as well as for many breeds of engineer.

## VISIONARIES

In the audience in Cambridge in November 1912 was the physicist C. T. R. Wilson, whose work using cloud chambers to track cosmic rays earned him the Nobel prize in 1927. Wilson suggested that X-rays should also reflect from the external faces of crystals, provided the surfaces were sufficiently smooth. So Lawrence tested whether X-rays that reflected from the cleavage face of mica — known for its supposed flatness at the atomic scale — could be photographed. In December 1912, *Nature* published his paper on 'The Specular Reflection of X-rays'<sup>4</sup>.

William Bragg quickly demonstrated that his X-ray spectrometer could detect diffracted monochromatic X-rays — not on photographic plate, but with a gas ionization detector. The power of Bragg's law, together with William's spectrometer for recording the intensities of reflected X-rays of fixed wavelength, was spectacularly demonstrated in two 1913 papers. Lawrence published one on the structures of crystals of sodium chloride, potassium chloride,

potassium bromide and potassium iodide<sup>5</sup>, and another with his father<sup>6</sup> on diamond.

The Braggs' approach provided a reliable way to determine the internal architecture of all crystalline solids, and thus to explain their properties. Once the structure of diamond was discovered — with its infinite array of carbon atoms bonded strongly to others in three dimensions — its hardness could be understood. Likewise, when X-ray crystallography revealed the structure of graphite in the 1930s, its softness made sense. Diamond and graphite have the same composition, but their structures make them mechanically, chemically and electronically very different.

Not until after the First World War did shock and exhilaration greet the publication of these papers, when their content filtered through to the textbooks. Shock, because Bragg had incontrovertibly established, contrary to what all chemists thought at the time, that there was no molecule of sodium chloride inside rock salt — simply an extended alternation of sodium and chloride ions. A particularly intemperate attack was mounted by Henry Armstrong, former president of the Chemical Society of London. Writing in *Nature* in 1927, he described the “chess-board pattern” of atoms in sodium chloride as “repugnant to common sense” and “absurd to the *n*...th degree”<sup>7</sup>. Others were exhilarated because the structure of diamond confirmed the tetrahedral coordination of carbon as envisaged by J. H. van't Hoff and others 40 years earlier.

For the next several decades, the Braggs' equation and spectrometer became the cornerstones of X-ray crystallography, largely supplanting Laue's polychromatic X-ray diffraction procedure. (Some experimentalists used both methods — notably, Linus Pauling in his determination of the structures of haematite and corundum in 1925.)

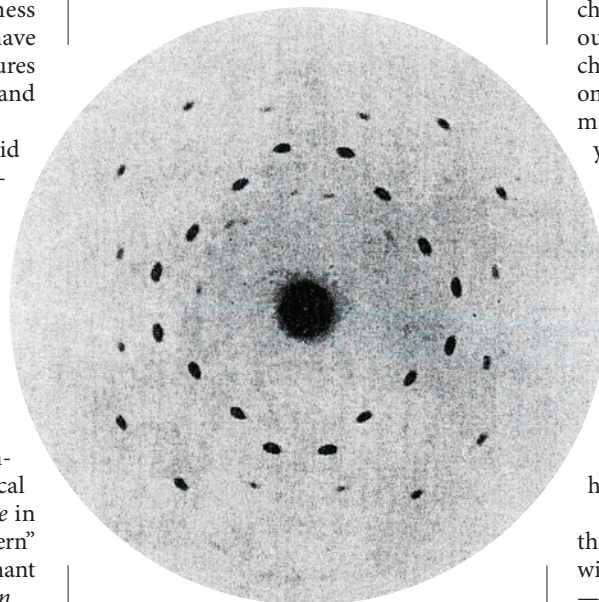
## NOBEL HAUL

At 25, Lawrence Bragg is still the youngest ever recipient of the Nobel prize, which he shared with his father in 1915 “for their services in the analysis of crystal structure by means of X-rays”. He kept working at a prodigious pace for some 50 more years<sup>8</sup>. Laue was awarded the Nobel prize in 1914 for the discovery of X-ray diffraction by crystals but, unlike Lawrence, he largely ceased to work on its consequences, turning to relativity and other pastures in theoretical physics.

In 1919, Lawrence succeeded Ernest Rutherford as chair of physics at the University of Manchester, UK. Using techniques that flowed from his 1912 and 1913 papers, he accounted for the chemical and physical properties of silicates, the dominant members of the mineral kingdom, which traditional chemistry had not

explained in satisfactory atomic terms. He explained, for example, why mica and talc are so soft, but beryl is tough.

He showed that many minerals, especially silicates, are dominated by essentially space-filling, negatively charged oxygen atoms. He found that other, smaller (cationic) atoms are lodged in the interstices, and discovered a constant tetrahedral coordination of four oxygen atoms, whatever the ratio of silicon



Max Laue's photo of X-ray diffraction from ZnS revealed spots of varying shape and intensity.

to oxygen. At Manchester he also solved the structures of  $\gamma$ -brass, magnetic alloys and many others fundamental to the development of the modern theory of metals.

In 1938, Bragg again replaced Rutherford, this time as Cavendish professor at the University of Cambridge. Here, after the Second World War, he encouraged his protégés Max Perutz and John Kendrew in their fiendishly difficult X-ray crystallographic determination of the proteins haemoglobin and myoglobin. Later, he gave free reign to Francis Crick and James Watson's X-ray work on DNA.

## SEEING IS BELIEVING

In 1953, Bragg became director of, and Fulleren professor at, the Royal Institution of Great Britain (RI) in London, where he appointed David Phillips, Tony North and others to investigate biological structures, with Perutz and Kendrew as honorary readers. A special automated, linear X-ray diffractometer built at the RI enabled Kendrew, Phillips and others to produce the first structure of a protein — myoglobin. It also helped Phillips and Louise Johnson to establish the structure and mode of action of lysozyme, the first enzyme to yield to Bragg's X-ray technique. While at the RI, Bragg had

the satisfaction of hearing, in 1962, of the award of Nobel prizes to his acolytes Perutz, Kendrew, Crick and Watson.

The Braggs' method of structure determination is still at the heart of modern X-ray crystallography. It is now almost completely automated by sophisticated, ultra-sensitive X-ray detectors and associated algorithms for data analysis of hundreds of thousands of diffraction intensities.

Meanwhile, the advent of accessible synchrotron radiation sources and rapid read-out detectors is especially well suited to charting structural changes that take place on sub-picosecond timescales in biological macromolecules such as the photoactive yellow protein PYP<sup>9</sup>. A striking example is the work of an international team of researchers<sup>10</sup>, almost exactly a century after the pioneering papers by Bragg and Laue. The team aimed femtosecond synchrotron pulses at a stream of droplets containing biologically significant macromolecules such as photosystem I, which is central to photosynthesis. The X-ray pulses are short enough to avert radiation damage, but sufficiently intense to produce high-quality diffraction data.

The seminal work begun in Yorkshire that summer of 1912 still resonates worldwide. Just this week, Venki Ramakrishnan — who shared the Nobel Prize in Chemistry in 2009 for unravelling the structure of the ribosome, which catalyses protein synthesis — was scheduled to lecture the Cambridge Philosophical Society. His theme? “Seeing is believing: how a century after its discovery, Bragg's law allows us to peer into molecules that read the information in our genes.” ■

**John Meurig Thomas** was Lawrence Bragg's successor-but-one as director and Fulleren professor at the Royal Institution. He is now in the Department of Materials Science and Metallurgy, University of Cambridge, Cambridge CB2 3QZ, UK. e-mail: jmt2@cam.ac.uk

1. Friedrich, W., Knipping, P. & Laue, M. In *Sitzungsberichte der Math. Phys. Klasse (Kgl.) Bayerische Akademie der Wissenschaften* 303–322 (1912).
2. Bragg, W. L. *Proc. Camb. Phil. Soc.* **17**, 43–57 (1913).
3. Bragg, W. L. in *Fifty Years of X-ray Diffraction* (ed. Ewald, P. P.) 531–539 (International Union of Crystallography, 1962).
4. Bragg, W. L. *Nature* **90**, 410 (1912).
5. Bragg, W. L. *Proc. R. Soc. Lond. A* **89**, 248–277 (1913).
6. Bragg, W. H. & Bragg, W. L. *Proc. R. Soc. Lond. A* **89**, 277–291 (1913).
7. Armstrong, H. E. *Nature* **120**, 478–479 (1927).
8. Thomas, J. M. & Phillips, D. C. (eds) *Selections and Reflections: The Legacy of Sir Lawrence Bragg* (Science Reviews, 1990).
9. Rubinstenn, G. et al. *Nature Struct. Biol.* **5**, 568–570 (1998).
10. Spence, J. C. H., Weierstall, U. & Chapman, H. N. *Rep. Prog. Phys.* **75**, 102601 (2012).





T. RETTIG/WORCESTER TELEGRAM &amp; GAZETTE/AP

A bear raids a vegetable patch in Rutland, Massachusetts.

## CONSERVATION

# Backyard jungles

Stuart Pimm explores today's collision between bears, beavers and US suburbanites.

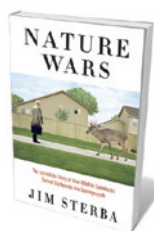
It's a spring Monday morning and the departmental office puts a phone call through. I can already guess it's someone calling to ask for "an ornithologist". I know the caller will be irate and expecting me to solve his problem. Yes, I have the answer; no, he's not going to like it. So, I listen to the tirade about how woodpeckers drum on his home at 5 a.m. at the weekend. Will I remove them? No. Can he shoot them? No. What can my distressed caller do?

With insight that makes him think I'm a modern-day Sherlock Holmes, I tell him he lives in a cedar-clad home (such homes resonate to woodpecker drumming better than trees). It is surrounded by forest (that's where woodpeckers live). He probably also has Canada geese on his lawn and white-tailed deer eating his vegetable garden, I confidently suggest.

Jim Sterba's *Nature Wars* is about the extraordinarily inconsistent attitudes to the natural world harboured by Americans today. We love nature, hate nature;

want it near us, but not too close; want it to be not, well, too natural. As Sterba writes: "This book tells the story of how we turned a wildlife comeback miracle into a mess." The book covers the relatively familiar tale of how we tamed and cleared the wilderness, and details how the forest returned and how, after the Second World War, we moved into it.

The singular fact is that for more than a decade, most Americans have lived in suburbia, and those east of the Mississippi in suburban forests. As Sterba puts it, "we are essentially forest dwellers". Drive the 3,000 kilometres north from Florida to New



**Nature Wars: The Incredible Story of How Wildlife Comebacks Turned Backyards into Battlegrounds**  
JIM STERBA  
Crown: 2012. 368 pp.  
\$26, £17.99

England along Interstate 95 and it is forest almost all the way. By contrast, on the drive north on the M1 from London, England's green and pleasant land is still mostly cropland and pasture — as is much of western Europe.

The fact that the eastern United States was radically deforested more than a century ago is obvious. The trees are still too small to be "old growth" and they get larger each year. Heading north in the direction of Sterba's weekend home, and well inside New York City, forests have reclaimed fields still delineated by stone walls. The low point of US forest cover occurred in about 1870. By then, young men were moving west, where they and their families were to almost completely and permanently convert the prairie ecosystems into rich croplands. In the depleted forests that they abandoned, wildlife had taken a beating.

Some forest species, such as the passenger pigeon and the ivory-billed woodpecker, dwindled to extinction. Others

became merely rare, but recovered as the forest returned. Some did very well indeed. Bears, deer and turkeys had close calls. Beavers — “North America’s first commodity animal” — which were hunted for their fur, disappeared across much of the country. It is ironic, as Sterba notes, that their comeback has reminded us of their immense destructiveness.

By far the best part of this book is its catalogue of our responses to such species. Yes, my phone caller wants his nice forest home, but he doesn’t feel he signed up for the deer, coyotes and black bears that come with it. Deer carry ticks that spread Lyme disease. Yet he might post cheques to an animal-rights group campaigning to stop official annual deer culls, even as his gun-toting neighbour burns to join the cull.

Meanwhile, trendy restaurants serve venison — nearly all of it imported from New Zealand, Sterba tells us. The blood and guts involved in killing a deer and cutting it up for the freezer is just too much for many. And whereas taking out young females would be the most effective way to control deer populations, many hunters think that killing males is the only sporting thing to do.

It isn’t all one way, of course. Pet cats wreak havoc on millions of small birds — many lured in by bird feeders. The stores that sell the feeders and the food to go in them thrive: bird feeders have even altered the wintering ranges of several species.

My most unwelcome advice to my phone caller? I love woodpeckers; I think beavers are extraordinary animals, the quintessential ecosystem engineers; and I eat the venison my graduate students shoot. Bears demand respect, but are not quite as terrifying as the lions that sniff around

**“We love nature, hate nature; want it near us, but not to close; want it to be, well, not too natural.”**

my tent in Africa when I’m doing fieldwork. So, I advise my caller to lie back and enjoy his home, woodpeckers and all. He hangs up in fury.

As Sterba so ably explains, the great majority of Americans are now disconnected from nature and live mostly indoors. Viewing “a goldfinch on the bird feeder outside the living room window” is perfection. The outside, itself, is altogether too messy, too threatening and too noisy at 5 a.m. on a spring morning. ■

**Stuart Pimm** is professor of conservation at the Nicholas School of the Environment, Duke University, Durham, North Carolina 27708, USA, and author of *The World According to Pimm: A Scientist Audits the Earth*.  
e-mail: [stuartpimm@me.com](mailto:stuartpimm@me.com)

## Books in brief



### Regenesi: How Synthetic Biology Will Reinvent Nature and Ourselves

George M. Church and Ed Regis BASIC BOOKS 304 pp. \$28 (2012)

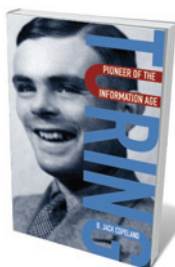
The life sciences emerge as the new high-tech in this paean to synthetic biology. Geneticist George Church and science writer Ed Regis show how reprogramming “genetic software” radically skews outputs, from microbes that create plastic by metabolizing maize (corn) sugar to potentially reverse engineering Neanderthals from a human stem cell. Each step in the genome’s evolution serves as a springboard for expositions of how synthetic biology will revolutionize renewable energy, multivirus resistance and more.



### Near-Earth Objects: Finding Them Before They Find Us

Donald K. Yeomans PRINCETON UNIVERSITY PRESS 192 pp. \$24.95 (2012)

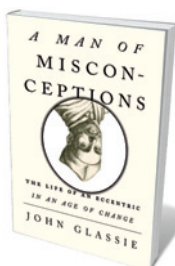
As Earth creeps on its course around the Sun, it is exposed to a relentless barrage of asteroids and comets. Donald Yeomans, who manages NASA’s Near-Earth Object Program Office, offers an introduction to the science of these lethal monsters, one of which may have seen off the dinosaurs 65 million years ago and created the Chicxulub crater. Yeomans shows how the threats are balanced by potential boons, such as the theoretical delivery of the building blocks of life on Earth. Can these reeling masses even become interplanetary pitstops on the road to Mars?



### Turing: Pioneer of the Information Age

B. Jack Copeland OXFORD UNIVERSITY PRESS 320 pp. £14.99 (2012)

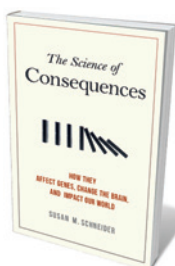
A tangle of speculation surrounds Alan Turing’s last two years. Jack Copeland takes it on with aplomb in this expertly integrated life and work, based on years of discussion with Turing’s colleagues and friends. A well-drawn portrait of the man — moody, humorous, seriously *sportif* and brimming with momentous ideas — this is also a catalogue of his fundamental achievements in computing and artificial intelligence. Crucially, Copeland’s fresh take on the lead-up to Turing’s death, from the hormone therapy he endured to his final hours, is based on a sober assessment of compelling evidence.



### A Man of Misconceptions: The Life of an Eccentric in an Age of Change

John Glassie RIVERHEAD 352 pp. \$26.95 (2012)

He thought Earth hollow, influenced Leibniz’s ideas on the binary system, predicted germ theory — Baroque Jesuit Athanasius Kircher was doubly endowed with avid curiosity and variable judgement. In an era in which science teetered at the edge of the rational, Kircher’s investigation of optics, Egyptian hieroglyphs, magnetism and more led to flashes of brilliance in swathes of murk. And, as John Glassie demonstrates, some of the findings inspired or seeped into the work of later pioneers, from Mesmer to Champollion.



### The Science of Consequences: How They Affect Genes, Change the Brain, and Impact Our World

Susan M. Schneider PROMETHEUS 352 pp. £18.99 (2012)

Biopsychologist Susan Schneider, a protégé of twentieth-century behaviourist B. F. Skinner, reveals the effects of actions’ consequences on evolution, the genome and the brain. Learning from consequences, she argues, helps to reconfigure the brain across species. And, she avers, such insights can inform real-life applications, from the treatment of depression to solving global issues such as overfishing.





Josef Kristofolletti's massive mural of the ATLAS particle detector adorns a building at CERN.

## PARTICLE PHYSICS

# Going massive

Jonathan Butterworth enjoys the latest chronicle of the hunt for the 'most wanted' particle.

**T**he discovery of a Higgs boson, announced on 4 July, was both a long time coming and unexpectedly quick. A long time, considering that the first theoretical papers suggesting how hidden symmetries might have a role in the origin of mass were published in 1964. Quick, because most of us working on the experimental search did not expect to get the answer until the end of this year.

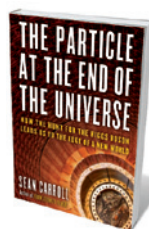
So it is not surprising that Caltech physicist Sean Carroll's *The Particle at the End of the Universe* should emerge soon after the big discovery at CERN, Europe's high-energy physics facility near Geneva in Switzerland. The particle-physics coup is a massive (no pun intended) step forward in our understanding of the underlying physical laws of the Universe, and Carroll seizes the chance to give a wide-ranging discussion of particle physics, how the experiments are carried out and the significance of the discovery itself.

The result is much heavier on the science than, say, Ian Sample's *Massive: The Hunt for the God Particle* (Virgin, 2010), which focuses more on the history and context of the search for the Higgs. Both are excellent, and complementary.

Most of Carroll's book could have been — and probably was — written months or even

years ago. Like the Large Hadron Collider (LHC) with which the discovery was made, it was a risk-free investment of time. Had a Higgs not shown up, the theoretical edifice that had clicked into place since the publication of the key papers (by, depending on your taste in assignment of credit, Yoichiro Nambu, Philip Anderson, Robert Brout, François Englert, Peter Higgs, Carl Hagen, Gerald Guralnik, Tom Kibble and Gerard t'Hooft, among many others) would have been revealed as a facade. The experimental answer was always going to be definitive, and the moment would have been right to produce this book either way.

Carroll has an unintimidating style, but as befits a first-rate particle cosmologist, he presents the real information with little blurring and without a blizzard of maths. He starts with the latest news — the 4 July seminars and the accompanying



**The Particle at the End of the Universe: How the Hunt for the Higgs Boson Leads Us to the Edge of a New World**

SEAN CARROLL  
Dutton: 2012. 352 pp.  
\$27.95, £16.99

excitement — then gives an accurate primer on the standard model of particle physics. He enumerates the forces and particles, and discusses the role of quantum fields and symmetries, as well as the accelerators and detectors that provide the evidence to keep the crazy concepts rooted in reality. Towards the end of the book, Carroll touches on the discovery's impact.

I could have done without the *Winnie the Pooh*-style subtitles to each chapter, such as "In which we suggest that everything in the universe is made out of fields". But this is a minor flaw and, elsewhere, he discusses the issues and events with passion and clarity.

An example is the moment, nine days after the LHC was switched on in 2008, when one-eighth of it suffered a catastrophic leak of liquid helium. Or, as Carroll accurately puts it, "it exploded". The disappointment, the challenges of explaining the event to the public and of dealing with the alleged risks of turning on the machine — 'Black holes will eat you!' — are beautifully done.

Carroll gives a sense of the intensity (and the international nature) of the effort of building and running the LHC. I was not surprised by his report that 1 in 16 of the passengers passing through Geneva airport are in some way associated with CERN. I have frequently been one of them. And that is just the tip of an iceberg of teleconferences, e-mails, night shifts and a general shortage of sleep.

The book finishes with a compelling discussion of the new discovery as a possible gateway to understanding the many open issues in particle physics and cosmology. Why is there more matter than antimatter? What are dark energy and dark matter? And are supersymmetry and strings anything more than nice ideas? As a fundamentally novel kind of object and evidence of a new quantum field permeating the Universe, a Higgs boson (whether exactly the standard model Higgs boson or not) may well be the key to more doors in these directions.

Carroll is an experienced advocate for engagement between the scientific community and the general public who, as taxpayers, fund much of the process of discovery. He also acknowledges the distinct possibility that the Higgs boson may never lead directly to applications, while covering the value of new knowledge for its own sake and the benefits of the spin-off technologies developed in the search. On this long journey — which is far from over yet — Carroll is an eloquent and able guide. ■

**Jonathan Butterworth** is a physics professor at University College London, and a member of the High Energy Physics group on the ATLAS experiment at CERN's Large Hadron Collider in Geneva, Switzerland.  
e-mail: j.butterworth@ucl.ac.uk



## BIOPHYSICS

# DNA dynamos

A look at how life's mechanics are deciphered at the molecular level fascinates **Mark Haw**.

For all its triumphs, physics has yet to answer the most personal question about our Universe: what is it that makes us? Peter Hoffmann's *Life's Ratchet* surveys how the field is squaring up to this challenge.

Everything is made of atoms. So why can I think, write, even develop new models of my own existence, while the chair I'm sitting on cannot? Somehow, in living things, matter makes molecular mechanisms with the ability to harvest the energy to organize, maintain and propagate themselves. That opens up a world of potent complexity that leads to cells, plants, animals and humans. One example of this mastery over energy is the molecular 'ratchet' of Hoffman's title.

This is a physicochemical mechanism by

which molecules such as proteins convert otherwise inaccessible, random fluctuations in chemical energy into useful work, enabling molecules to move, construct, deconstruct and generally carry out the nanometre-scale activities that keep us alive. Exactly why the molecules in biological entities can do this and the stuff in the chemistry laboratory's test tubes cannot is the theme of the book, more or less successfully introducing a popular audience to the latest science on how life works.

*Life's Ratchet* starts, like my own book *Middle World* (Macmillan, 2007), with a somewhat revolutionary premise. This is that life is a dynamic process, a thing of moving parts, not a question of frozen chemical formulae, DNA sequences or abstract genetic information. Proteins involved in DNA replication, for example, must move along the DNA molecule to 'unzip' its two helical strands.

Why science has struggled to solve how life works is due, in part, to a historical penchant in biology to study life's static structure. Since Francis Crick and James Watson's discovery of the double helix almost 60 years ago, many a career has rested on the expert measurement and interpretation of the sequence and spatial arrangement of amino acids in this or that protein. Such information is vital, of course — X-ray diffraction patterns tell us all about the sculptural complexity of life. But they shed little light on how molecules move to achieve the tasks necessary for living.

It has taken the development of techniques such as single-molecule optical tweezing and fast, high-resolution nuclear magnetic resonance to probe the moving parts of life. Such measurements, as Hoffman describes, are part of the exciting quest to take biology beyond

**A subunit of the enzyme ATP synthase, which provides chemical energy to cells.**

nineteenth-century theories of equilibrium thermodynamics and into a molecular world shaped by the interplay of randomness and physical interactions.

The continual harvest and conversion of energy by molecules, on their own or in concert, is necessary for all life processes — to transport signals and biomolecular cargo (such as nutrients across cell membranes), to chemically synthesize and to chemically destroy. Equilibrium thermodynamics safely ignores energy fluctuations. But experiments done during the past ten years or so show with startling directness that such fluctuations are required for, say, a motor protein to transport its chemical cargo within a cell.

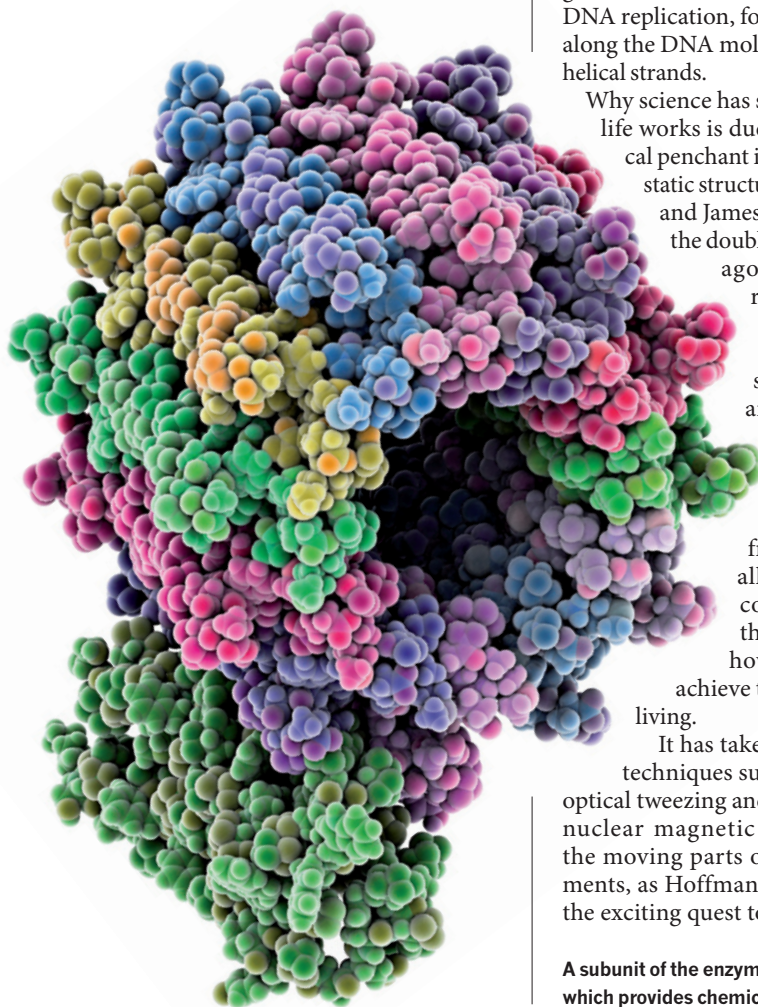
*Life's Ratchet* engagingly tells the story of how science has begun to realize the potential for matter to spontaneously construct complex processes, such as those inherent to living systems. The book is a good mix of history and the latest concepts, straightforwardly explained. A few too many personal anecdotes add little to the story — the sign, maybe, of an editor trying a bit too hard to follow the 'standard model' of popular science.

But the book's important message is that there is a revolution brewing. This revolution will not tell us what matter is made of. Instead, as described in *Life's Ratchet*, it will tell us how matter and energy combine to make me and you. ■

**Mark Haw** is in the Department of Chemical and Process Engineering, University of Strathclyde, Glasgow, UK. He is the author of *Middle World: The Restless Heart of Matter and Life*.  
e-mail: mark.haw@strath.ac.uk



**Life's Ratchet: How Molecular Machines Extract Order from Chaos**  
PETER M. HOFFMANN  
Basic Books: 2012.  
288 pp. \$27.99,  
£18.99



LAGUNA DESIGN/SPL

## CORRECTION

A review of 'Ghosts in the Machine' (J. Glausiusz *Nature* **488**, 279; 2012) reiterated incorrect information provided by the exhibition that Alan Turing underwent orgone therapy to 'cure' his homosexuality; he was in fact treated with hormones. Furthermore, Einstein did not actually pronounce the orgone energy accumulator "a dud" (for details, see his letter of 7 February 1941 in W. Reich *The Einstein Affair* Orgone Institute Press; 1953).



# Correspondence

## L'Aquila: governance flaws exposed

The decision of an Italian court to hold several scientists accountable for deaths caused by the L'Aquila earthquake (*Nature* **490**, 446; 2012) is indicative of flaws in the sensitive, but indispensable, relationship between science and politics.

Implicating a scientific advisory committee in the death of so many people in L'Aquila reflects troubling tendencies in modern Western governance: Italy seems to have made scientists co-responsible for governing the country. The court's decision might also deflect attention away from the failures of the democratic institutions responsible for dealing with the aftermath of the earthquake.

Such defects can be corrected only through recognizing the democratic accountability of government as well as the science it enlists for policy-making.

**Erik Aarden\*** *Harvard Kennedy School Cambridge, Massachusetts, USA.*

*erik\_aarden@hks.harvard.edu*

*\*On behalf of 4 co-authors (see [go.nature.com/axfa3u](http://go.nature.com/axfa3u) for full list).*

## L'Aquila: science is not a crystal ball

The manslaughter convictions of seismologists in Italy offer a timely reminder of science's core functions to both scientists and non-scientists (*Nature* **490**, 446; 2012).

Over time, combining existing scientific data and new methods has allowed scientists to predict possible outcomes and associated probabilities. But the accurate prediction of certain events is, and will continue to be, challenging — particularly in economics, climate research, disease pandemics and natural disasters. Science can predict the probabilities of events occurring under a given set of circumstances, but not the events that will occur.

The public may not fully

appreciate probabilities and risk assessment, but scientists must work to change this. Researchers need to be able to present information about uncertainty, prediction and probabilities in simple terms, and to convey information to the public and to government that is accurate, consistent and clear.

**Peter L. F. Fast** *University of Quebec, Rimouski, Quebec, Canada.*

*peter.fast@gmail.com*

## Rigid guidelines may restrict research

Our research centre is already planning to adopt the excellent guidelines suggested by Story Landis and colleagues to improve reporting standards in preclinical research (S. C. Landis *et al.* *Nature* **490**, 187–191; 2012). However, I am concerned about the wholesale adoption of recommendations that could, paradoxically, have a restrictive effect on the early stages of basic research.

Curiosity and observation are critical to science, and although blinding is good experimental practice in most research scenarios, it should follow an exploratory period. In several of the behavioural studies conducted in our lab over many years, we have done the experiment at least twice — once unblinded and then blinded — followed by a check that we get the same results. Usually we do, but not always. Sometimes we deliberately include a procedure that causes performance to fall to chance (see, for example, D. Tse *et al.* *Science* **316**, 76–82; 2007). If it does not, there might be uncontrolled variables.

Researchers thrive on noticing something subtle and pursuing it, but this is most effective when they do not have one hand tied behind their backs. Stringent guidelines should then follow.

**Richard Morris** *Centre for Cognitive and Neural Systems, University of Edinburgh, UK.*  
*r.g.m.morris@ed.ac.uk*

## Call for a European integrity standard

The global market for diplomas and academic rankings has had the unintended consequence of stimulating misconduct, from data manipulation and plagiarism, to sheer fraud. If incentives for integrity prove too hard to create, then at least some of the reasons for cheating must be obliterated through an acknowledgement of the problem in Europe-wide policy initiatives.

At the Second World Conference on the Right to Education this week in Brussels, we shall propose that the next ministerial communiqué of the Bologna Process in 2015 includes a clear reference to integrity as a principle. The Bologna Process is an agreement between European countries that ensures comparability in the standards and quality of higher-education qualifications.

Furthermore, the revised version of the European Standards and Guidelines for Quality Assurance, to be adopted by the 47 Bologna Process ministers in 2015, should include a standard that is linked to academic integrity (with substantive indicators), which could be added to all national and institutional quality-assurance systems.

We believe that an organization such as the Council of Europe has enforcement capabilities that can create momentum for peer pressure and encourage integrity. A standard-setting text, such as a recommendation by the Council of Ministers, or even a convention on this topic, would be timely given the deepening lack of public trust in higher-education credentials.

We do not expect that a few new international rules alone can change much. But we aim to create ways for institutions to become entrepreneurs of integrity in their own countries, as some models already exist (A. Mungiu-Pippidi and A. E. Dusu *Int. J. Educ. Dev.* **31**, 532–546; 2011).

**Alina Mungiu-Pippidi** *Hertie School of Governance, Berlin, Germany.*

*pippidi@hertie-school.org*

**Ligia Deca** *University of Luxembourg, Luxembourg.*

## Europe on the rise in Science and Nature

I analysed the geographic distribution of authors of papers in *Nature* and *Science* during 1996–2010 (data from Thomson Reuters' Science Citation Index; 2012) and found that both journals are publishing an increasing number of contributions from Europe. In *Nature* these now predominate alongside papers from the United States; in *Science*, European publications have successfully eroded the monolithic US dominance of the mid-to-late 1990s.

Within Europe, the preponderance of publications from the United Kingdom in *Nature* during the 1990s has given way since 2000 to papers from Germany, France, Switzerland, the Netherlands, Italy, Spain, Sweden and others (in that order). Spain has markedly increased its presence in both journals: comparing two 5-year periods (2001–05 and 2006–10), publications from Spain increased from 156 to 226 in *Nature* and from 80 to 203 in *Science*.

The UNESCO Science Report 2010 found that the publication gap between developed and developing countries is also closing, largely thanks to the proliferation of digital information and communication technologies. The proportion of papers from developed countries fell from 84.3% in 2002 to 75.3% in 2008; those from developing countries showed an increase from 20.9% to 32% over the same period.

**Julio González-Alvarez** *Jaume I University, Castellón de la Plana, Spain.*  
*gonzalez@psb.uji.es*

# Keith H. Campbell

## (1954–2012)

Creator of Dolly, the first mammal cloned from an adult body cell.

Keith Campbell was the inspiration behind Dolly the sheep, the first mammal to be cloned from an adult body cell. He died on 5 October at the age of 58. A few days later, the Nobel committee recognized the importance of the field by awarding the 2012 medicine prize to John Gurdon and Shinya Yamanaka for their achievements in reprogramming cells.

In 1995, Campbell — then at the Roslin Institute near Edinburgh, UK — conceived of a method to generate a pair of cloned lambs, Morag and Megan, from a cell taken from a sheep embryo. In his opinion, these were “the first animals produced from differentiated cells because these cells had differentiated in culture”. It took Dolly, however, to convince the scientific community that differentiated mammalian body cells — which had already become specialized for a particular function — could be reprogrammed to produce an entire organism.

In the mid-1990s, the consensus among cell biologists was that clones could not be produced from cells that had become specialized. Decades earlier, Gurdon, a British developmental biologist, had managed to produce adult frogs by transferring the nuclei of tadpole cells into eggs stripped of their own nuclei. But reprogramming differentiated mammalian embryonic cells or adult body cells was thought unlikely to work.

Campbell's breakthrough was realizing that he could reprogram the nuclear information in a donor cell if he coordinated the cell cycles of the donor embryo cell and the recipient egg. By depriving the cells in his laboratory cultures of nutrient-rich serum, he forced them to enter a quiescent state. When cell division was reactivated, the cell cycles were aligned. By transferring the nucleus of an embryo cell into an egg cell from which the chromatin had been removed, and then activating that nuclear material, he created Morag and Megan.

Wanting to track down exactly when the developmental potential of embryonic cells was lost, Campbell and Ian Wilmut, the Roslin Institute's group leader, asked their colleague James McWhir for some adult cells. McWhir gave them some sheep mammary-gland cells that happened to be in the freezer. The Edinburgh-based biotechnology

company PPL Therapeutics, which was collaborating with the Roslin Institute, was using the sheep cells for experiments on drug development.

I always wonder who was most surprised when, after being transferred into a ewe, one of the embryos derived from the nucleus of



a mammary-gland cell developed into an apparently normal lamb: the ewe, the farm hands or the research team? Wilmut certainly was surprised. I think Campbell was optimistic that even adult cells could be reprogrammed.

Campbell was born in 1954 in Birmingham, UK, and grew up there and in the Scottish city of Perth. He graduated from Queen Elizabeth College, London, in 1978 with a bachelor's degree in microbiology. After various jobs, including a locum position as chief medical laboratory technologist in South Yemen, he started a PhD in 1980 at the University of Sussex, UK. It was at Queen Elizabeth College and as a postgraduate student studying frog-egg maturation that Campbell developed his interest in the control of cell division and in the factors that direct the behaviour of cell nuclei. After postdoctoral positions at the universities of Edinburgh and Dundee, Campbell joined the Roslin Institute in 1991.

Campbell left the institute in 1997

to become head of embryology at PPL Therapeutics, where he led work on cloning pigs. In 1999, he became professor of animal development at the University of Nottingham, UK, where he continued to work on nuclear reprogramming and cloning techniques. (PPL Therapeutics was sold when it ran into financial problems in 2003, largely because of the difficulty of using animal cloning to develop pharmaceutical products.)

Despite the tremendous media stir prompted by Dolly's birth, animal cloning has never really come of age as a commercially useful biotechnology. This is mainly because, in most species, epigenetic marks (experience-dependent molecular alterations that alter how genes behave, but not their sequence), carried over in the introduced chromatin, cause embryonic losses and post-natal abnormalities. Yet somatic cell cloning has proved a very useful tool in mouse developmental and cell biology, and has made significant contributions to stem-cell biology. In 2008, Campbell and Wilmut were jointly awarded half of the prestigious Shaw Prize in Life Science and Medicine, with Yamanaka winning the other half.

Keith was acutely aware that the cloning method he had pioneered drew strong opposition from some, including conservative religious groups and members of the Green Party. He defended his work, saying that it was important for the progress of biology and possibly medicine, but he was strongly opposed to human reproductive cloning.

A great companion and argumentative in a delightful way, Keith was a strong supporter of his colleagues and a proud father of his daughters Claire and Lauren. It was perfectly in keeping with his wry humour that he named Dolly the sheep after the singer Dolly Parton, and told *The New York Times* in 1997 that sex “will always be the preferred way of having children”. Cloning, he said, is “far too expensive and a lot less fun than the original method”. ■

**Alan Trounson** is at the California Institute for Regenerative Medicine, San Francisco, California 94107, USA. He became a close friend of Keith Campbell after meeting him in 1993.

e-mail: [atrounson@cirm.ca.gov](mailto:atrounson@cirm.ca.gov)



# THE CANDIDATE POOL

*A treatment for the future.*

BY BRIAN HURREL & JEFF SAMSON

“OK people, let’s make this quick,” Frank Poole snapped. He gazed around the table at the assortment of harried-looking men and women. “Jenkinson will be arriving in 20 minutes, and I want this wrapped up before he does.” He brushed a hand through a thick shock of silver hair, shot his cuffs and jabbed a finger at the man to his right. “Holderman, what have you got?”

The young man cleared his throat with preppy politeness and held up a stack of notes. “Think of it as *Primary Colors* meets *Sid and Nancy*. Sex, drugs, love children, murder-suicide. Absolutely scandalous.”

Poole shook his head. “No good.” He continued clockwise around the table, snapped his fingers at a lithe, hatchet-faced blonde. “Paladino. Talk to me.”

“*Soylent Green* meets *The Sum of All Fears*,” she said. “Twenty per cent unemployment, food riots, an increasingly anarchic southern border, and a nuclear terror strike on Washington for good measure.”

“Absolutely not,” said Poole. “Who’s next? Stormont?”

“Massive environmental chaos caused by deregulation and corruption,” said Stormont. “We’re talking entire ecosystems destroyed. Total societal breakdown. Bandits, fortified towns, cannibals. Think *The Day After Tomorrow* meets *The Road Warrior*.”

Poole leaned back in his chair, his stare fixed on the gaunt young man with horn-rimmed glasses and a five o’clock shadow at 7 a.m.. He swivelled, rapping his fingers on the table. “Hmm ... that’s a tough one ... I mean, who doesn’t love *The Road Warrior*?” Poole shot forward, bracing himself with his hands on the edge of the table. “No.”

He pointed at the man directly across from him. “Bumstead. Wow me.”

“Progressivism gone wild,” said the smallish man sporting a third-degree tan and a shimmering suit he couldn’t afford. “Ultra-nanny state with soaring deficits, unfunded liabilities and industry-crippling legislation. Individual liberty a distant memory — the Constitution and Bill of Rights dismantled and replaced with the Articles of Fairness and the ...” he paused, smirking. “Feel Good Doctrine.”

Poole stared at the man. “Is that a joke?”

“I’m afraid not, sir,” he continued. “Think *Atlas Shrugged* meets 1984, only decidedly less optimistic.”



Poole slammed a fist on the table. “Enough with the dystopias! This can’t be all you’ve got for me!” He glowered at the old but wiry-looking man at Bumstead’s left. “Nalesnik, give me something ... anything!”

Nalesnik threw his bony hands up dramatically. “Imagine *The Undiscovered Country* — but not in space — and *The Parallax View*, combined. An assassination during an inaugural speech, a military coup, a —”

“Christ!” Poole exploded. “Didn’t I just say no more dystopias? We’re running out of time, people.”

He gestured to a 30-something who would have been quite attractive without her oversized sweater, shapeless hair helmet and thick-rimmed reading glasses. “Wellington, I’m going to assume you don’t have a top hat full of rabbits on your person.”

The woman clasped her hands, straightened her back and sighed loudly. Her voice was halting. “*It’s A Wonderful Life* meets *The American President* ... with shades of *Leave it to Beaver* and *Pleasantville*.”

Poole’s eyebrows shot towards his hairline. “Go on,” he said, his voice uncharacteristically bright.

“A complete societal shift. Crime, employment, divorce, patriotism, trust in government ... even table manners — all at levels not seen since the 1950s. In short, a resurgent America. A world leader again.”

“I’m liking it,” Poole said, rubbing his hands together. “Who’s your lead?”

“Barbara Gundermunsen.”

“Gundermunsen? From Fargo?” Poole shook his head. “I don’t buy it. Her record

and disposition aside, her name alone is more than most people can swallow. It’s four syllables, for chrissake.”

“Eisenhower has four syllables,” interjected Bumstead.

Poole glared at the man in the sleek suit. “Why do you think everyone called him Ike?” he snapped. “And Gundermunsen doesn’t shorten well.”

“No,” said Wellington, her hair flopping from side to side as she shook her head. “But that’s irrelevant. In time they’ll call her the Iron Maiden.” She started to push her papers across the table, but paused, her face seeming to flush and harden. She breathed in deeply, exhaled, then slid her treatment towards Poole’s twitching fingers. “It’s all there.”

The woman shifted uncomfortably in her seat as Poole skimmed the pages with a widening smile. She cleared her throat in exaggerated fashion. “Not to rain on the inaugural parade, but Chairman Jenkinson would be furious if he knew what was going on here. He’s as straight as they come.”

“Then it’s a good thing he never will, isn’t it?” Poole said without looking up.

“But sir,” she said, “this isn’t just highly unethical. It’s illegal. If the Fair Election Commission or the House Committee on Temporal Integ —”

“My dear,” said Poole, locking eyes with her, “if you think for a minute that the other parties aren’t testing the waters of every possible time stream, then you’re too naive to be in this business.”

“I just don’t care for it, sir,” she said.

“Sometimes you have to do the wrong thing to do the right thing. Capiche?”

“Yes sir.”

“Right. Now that we’ve taken care of our moral qualms, let’s tell Senator Gundermunsen that she is now the official Technocratic candidate for the 2036 presidential race.”

The people around the table rose, gathered up their documents and scattered. Poole leaned back in his chair and flipped to the next page of the treatment. “Wellington,” he shouted, stopping her hurried exit.

“Yes?” she asked, turning to face him.

“You’re sure about this? Meek and mild Barbara Gundermunsen?” he asked, dubiously.

“The Iron Maiden ... sir,” she intoned.

Poole looked back at the treatment and smiled broadly. “I think we have a winner.” ■

**Brian Hurrel and Jeff Samson** live in New Jersey with their families. They thank their wives for tolerating their collaborations.

➔ NATURE.COM

Follow Futures:

@NatureFutures

go.nature.com/mtoodm

## Mice and men show the way

Disorders caused by single genes, such as fragile X syndrome, share symptoms with the genetically complex autism spectrum disorders. It emerges that effective drugs for the former may lead to therapies for the latter.

EVDOKIA ANAGNOSTOU

The translation of findings from genomics and animal studies into therapies for neurodevelopmental disorders, such as autism, is still in its infancy. One promising approach is to align animal studies with clinical trials, as Henderson *et al.*<sup>1</sup> and Berry-Kravis *et al.*<sup>2</sup> report in *Science Translational Medicine*. Their data suggest that the drug arbaclofen (STX209) reverses symptoms related to fragile X syndrome in a mouse model of the disorder. It also promotes social engagement in patients with fragile X syndrome who show marked social impairment.

Fragile X syndrome is the most common inherited cause of autism spectrum disorders<sup>3</sup>. It is characterized by various behavioural and physiological abnormalities, including social withdrawal, anxiety, intellectual disability, aggression and epilepsy. It results from silenced transcription of the *FMR1* gene and subsequent loss of its product FMRP, an RNA-binding protein that inhibits protein synthesis.

To understand the functional implications of FMRP loss, *FMR1* has been knocked out in various organisms, including mice and flies<sup>4</sup>. The result is increased protein synthesis in neuronal projections called dendrites, and a higher density of dendritic spines — dynamic structures that mediate synaptic communication between neurons. Such changes are also seen in some humans with fragile X syndrome.

Specifically, it seems that activation of the glutamate receptor mGluR5 in the neuronal membrane leads to increased protein synthesis in the synapse, and FMRP acts as a brake on this process. In fragile X syndrome, synaptic protein synthesis proceeds uncontrollably<sup>5</sup>. Deficiencies in neurotransmission mediated by the inhibitory molecule GABA have also been observed in brain regions of *Fmr1*-knockout mice that are associated with neurodevelopmental disorders in humans — for example, the amygdala, striatum and somatosensory cortex<sup>6</sup>. Arbaclofen is a GABA-receptor agonist, and so it may enhance GABA-mediated inhibitory neurotransmission directly or as a negative modulator of the mGluR5 pathway<sup>7</sup>.

Henderson *et al.* find that treatment of *Fmr1*-knockout mice with arbaclofen restores

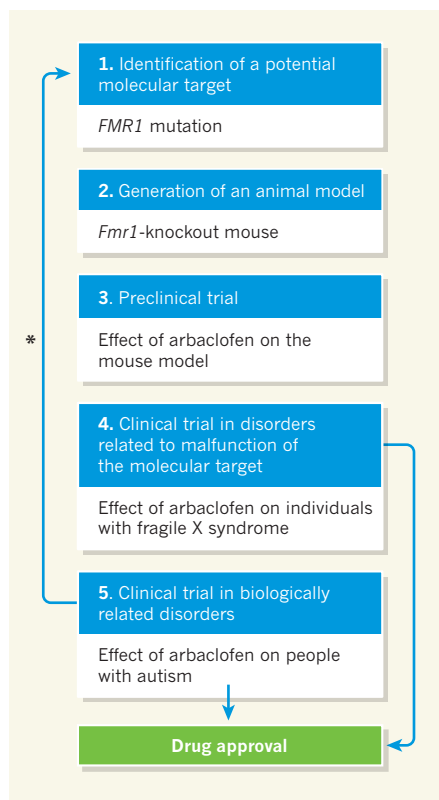


**Figure 1 | From lab to clinic.** The pathway shown in blue represents one feasible approach to finding treatments for related single-gene and genetically complex disorders. A specific example (shown in white) tests the efficacy of the drug arbaclofen in animals or humans with mutations in *FMR1*. This gene is mutated in individuals with the autism-related disorder fragile X syndrome. Two papers<sup>1,2</sup> describe studies that correspond to steps 3 and 4, aimed at finding drugs to treat fragile X syndrome and thus also autism spectrum disorders. Studying treatment response patterns (asterisk) may inform the understanding of the biology of the disease.

protein synthesis to normal levels and reverses dendritic-spine abnormalities that are observed in both affected mice and humans.

Similarly, as part of a phase II clinical trial, Berry-Kravis *et al.* gave either arbaclofen or a placebo drug to 63 patients with fragile X syndrome (age 6–39 years). Four weeks later, the treatments were switched, so that all subjects received the drug or the placebo at different

times during the trial. The drug was quite well tolerated, but had no effect on the patients' irritability and aggression, the authors' main outcome measure. However, when the results of 27 patients who had high levels of social impairment — a core aspect of the disorder that is traditionally thought to be resistant to medical intervention — were subjected to a post-hoc analysis, significant improvement was observed on the basis of several measures of social engagement.

This paper shows that findings in animal models of fragile X syndrome can be successfully translated into effects on humans and are thus of therapeutic relevance. Nonetheless, it has several limitations. First, the age range of the subjects is wide, as it included children, adolescents and adults. Given that fragile X syndrome is a developmental disorder, the effects of medication may vary according to the developmental stage. On the other hand, it may be a reasonable first step to look at a wide age range when studying a relatively rare disorder.

Second, the number of individuals investigated as part of the post-hoc analysis is too small to draw any conclusions with confidence. It is reassuring that the observation was replicated across different measures of social engagement and social impairment, but larger trials designed to measure the effect of arbaclofen will be necessary to confirm it.

Third, because the study was designed to investigate arbaclofen's effects on irritability, the drug was given to patients for only a short time. Measuring the effects on social engagement definitively will require longer studies. Regardless of these shortcomings, however, the significance of Berry-Kravis and colleagues' work should not be underestimated.

Although several large drug trials have been carried out in patients with autism spectrum disorders in the past two decades<sup>8</sup>, most were not based on the previous identification, through basic research, of molecular targets for intervention. Instead, the assumption was that if symptoms are shared between various disorders, then the neurobiology associated with them must be shared too. Consequently, researchers borrowed medications used to treat disorders that had similar signs and symptoms to autism. This approach has had some



success (for instance, in treating irritability and aggression with atypical antipsychotics, and hyperactivity and attention deficit with stimulants); but it has not produced an agent that may be useful for treating the core symptoms — repetitive behaviours and deficits in social function and communication.

The present studies signal that, with the progress made in genomics and molecular neuroscience, autism research may be ready for translational approaches (Fig. 1). For example, rare causative mutations are being identified at fairly high rates, and knowledge of the functional consequences of such mutations may lead to an understanding of the common biological processes affected in related disorders. Studies in animals therefore seem crucial if we are to understand the neurobiological effects of such rare mutations.

Nonetheless, researchers have mixed feelings about the value of animal models of neurodevelopmental and neuropsychiatric disorders for drug discovery, given the previous lack of success. I think that modelling a human mutation or its equivalent in animals is a feasible approach for investigating the effect of pharmacological manipulations on the underlying biological deficits, irrespective of cross-species differences in the behavioural profiles associated with such mutations. As is evident from the present papers, at least under certain circumstances, this approach may lead to successes in the treatment of otherwise recalcitrant behaviours.

The most exciting implication of this work, however, is that by understanding the biological effects of a compound, its therapeutic effects can be extended beyond a specific single-gene disorder to heterogeneous syndromes with overlapping deficits at a biological level. In other words, although a mutation may be responsible for a few cases of, say, autism (in this case, only about 1–5% of individuals with autism spectrum disorders have fragile X syndrome), it is likely that there is a larger proportion of individuals with autism and/or intellectual disability who are 'fragile-X-like'. As such, treatments developed for fragile X syndrome may be effective for large numbers of such individuals.

But caution should be exercised when using this approach, because deviation in either direction from an optimal level of synaptic protein synthesis may lead to behavioural and cognitive problems. Evidence for this is emerging from other neurodevelopmental disorders, including tuberous sclerosis, Rett syndrome, neurofibromatosis and Phelan–McDermid syndrome<sup>9–11</sup>. For example, both fragile X syndrome and tuberous sclerosis are caused by single-gene mutations that ultimately affect synaptic protein synthesis, and both are associated with autism-like features and cognitive difficulties. Nonetheless, knockout in mice of *Tsc2*, one of two genes that are mutated in tuberous sclerosis, leads to diminished

synaptic protein synthesis<sup>12</sup>, in contrast to the enhanced protein synthesis seen when *Fmr1* is knocked out.

Attempts to extend the lessons learnt from single-gene disorders to more complex syndromes may therefore be tougher than expected. Consequently, information on behaviour, cognition and diagnosis alone may not be sufficient to guide the choice of treatment. In other words, to identify medications for individuals with autism, intellectual disability and related disorders, it will be essential to determine whether an individual is, for example, fragile-X-like or 'TSC-like' by using biomarkers that could be used in the clinic. The two papers are proof of principle that aligning mouse studies and human clinical trials holds promise. They also indicate that understanding single-gene-associated disease mechanisms that potentially represent final common pathways of several biological processes offers exciting opportunities for experimental therapeutics in neurodevelopmental and neuropsychiatric disorders. ■

## IMAGING

## The fog clears

**A technique has been developed to image a fluorescent object hiding behind a light-scattering screen without the need for a detector behind the screen. The approach could find applications in imaging biological tissue. [SEE LETTER P.232](#)**

DEMETRI PSALTIS  
& IOANNIS N. PAPADOPOULOS

A golfer faced with the problem of hitting a ball out of the woods after an errant shot sometimes makes a brave choice: she aims straight for the trees, swinging the club as hard as possible in the hope that the ball will bounce off the trees and miraculously emerge from the woods. On page 232 of this issue, Bertolotti *et al.*<sup>1</sup> describe a technique for imaging objects through light-scattering media, such as fog and human tissue, that overcomes a challenge that is in some ways similar to this one.

Consider light from a torch passing through a human hand. Information about the shapes of the bones, or even the cells, that make up the hand is thought to be encrypted in this transmitted light (Fig. 1), but a simple device such as a lens cannot be used to image the hand's interior. Numerous attempts have been made to retrieve the shapes of objects that hide behind or are within media that transmit and scatter light. Some of the photons that travel through a light-scattering medium do so without interacting with any of the medium's constituent matter. Such 'ballistic' photons exit the medium a little earlier than their

**Evdokia Anagnostou is at the Bloorview Research Institute, Department of Pediatrics, University of Toronto, Toronto, Ontario M4G 1R8, Canada.**

**e-mail: eanagnostou@hollandbloorview.ca**

- Henderson, C. *et al. Sci. Transl. Med.* **4**, 152ra128 (2012).
- Berry-Kravis, E. M. *et al. Sci. Transl. Med.* **4**, 152ra127 (2012).
- Hagerman, R. J. *J. Dev. Behav. Pediatr.* **27**, 63–74 (2006).
- D'Hulst, C. & Kooy, R. F. *J. Med. Genet.* **46**, 577–584 (2009).
- Dölen, G. & Bear, M. F. *J. Physiol. (Lond.)* **586**, 1503–1508 (2008).
- Paluszkiwicz, S. M., Martin, B. S. & Huntsman, M. M. *Dev. Neurosci.* **33**, 349–364 (2011).
- Isaacson, J. S. & Hille, B. *Neuron* **18**, 143–152 (1997).
- Anagnostou, E. & Hansen, R. *Curr. Opin. Pediatr.* **23**, 621–627 (2011).
- Ehninger, D., De Vries, P. J. & Silva, A. J. *J. Intellect. Disabil. Res.* **53**, 838–851 (2009).
- Acosta, M. T., Gioia, G. A. & Silva, A. J. *Curr. Neurol. Neurosci. Rep.* **6**, 136–143 (2006).
- Tropea, D. *et al. Proc. Natl Acad. Sci. USA* **106**, 2029–2034 (2009).
- Auerbach, B. D., Osterweil, E. K. & Bear, M. F. *Nature* **480**, 63–68 (2011).

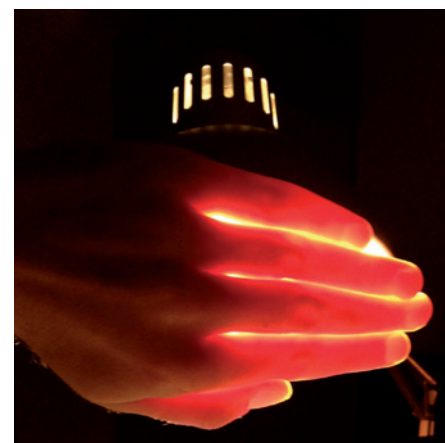


**Figure 1 | Seeing through.** A light source placed behind a human hand emits photons that travel through the hand. Information about the hand's interior, such as its bones or cells, is encoded in the light's field but cannot be directly retrieved because it is scrambled by the scattering properties of human tissue. Bertolotti *et al.*<sup>1</sup> propose a method for retrieving such information.

non-ballistic counterparts, which bounce off the matter as they pass through the scattering medium. If the ballistic photons alone are captured in a detector, the blurring effects of scattering can be avoided<sup>2</sup>. However, for

D.P. & I.N.P.

strongly scattering media such as a human hand, ballistic light can propagate only short distances (about 1 millimetre in human tissue) without scattering. Therefore, image quality rapidly degrades as we attempt to see deeper into the tissue<sup>3,4</sup>.

Another approach for seeing through a scattering medium is to use a technique called phase conjugation. In this method, the paths of all the photons are reversed and, as the photons travel backwards, the scattering that occurred over the course of their forward paths is undone<sup>5–7</sup>. We can understand how this works by returning to the golf analogy. To hit the ball out of the woods, the player would need to have memorized the exact direction in which the ball was travelling when it hit the ground. If she could then hit the ball in precisely the same direction but backwards, the ball would retrace its path and exit the woods. Unfortunately, the ball would end up at the location from which the errant shot was made, and not near the hole as the player would wish. Phase conjugation has a similar problem. A double pass through the same scattering medium gives a well-focused image of the object. However, this image forms right next to the object hiding behind the scattering medium, and thus in a position in which it cannot be observed.

In their study, Bertolotti and colleagues demonstrate that it is possible to form an image of an object hiding behind a scattering screen without the need to put a detector or a light beacon behind the screen. The authors placed a 50-micrometre-wide, two-dimensional fluorescent object at a distance of 6 mm behind a scattering screen, and shone laser light onto the screen. The light transmitted through the screen resulted in a random light pattern (speckle pattern), on the other side of the screen, that illuminated the fluorescent object. The researchers then measured the fluorescence that was generated by the object and transmitted back through the screen.

But how could they use these fluorescence measurements to form an image of the object, given that the speckle pattern illuminating the object was randomly generated by the scattering screen? The authors used fluorescence measurements of the object not only to form the image, but also as a beacon to probe the scattering medium<sup>8,9</sup> so as to be able to undo its blurring effect on the image. First, they made multiple measurements by adjusting the angle of illumination slightly, thereby changing the unknown speckle pattern in a predictable way. Second, they repeated their experiment many times to obtain statistical averages of the properties of the scattering screen. These measurements supplied them with the information they needed to form the image.

This technique is capable of imaging objects some distance away (6 mm in the current study) from a thin scatterer (about 3–5 µm thick for ground glass). For example, it could

be used to image two-dimensional fluorescent objects in blood or other liquids surrounded by a thin scattering layer. The approach will probably be extended to three-dimensional objects and possibly to non-fluorescent objects. However, major innovation would be required to expand the technique to permit imaging of objects behind or inside thick scattering media. For now, Bertolotti and colleagues' demonstration that it is possible to see clearly a fluorescent object behind a scattering screen, beyond the ballistic spatial limit, will almost certainly intensify the search for ways to use light to see through human tissue.

What does this story suggest for our golfer who wishes to hit the ball out of the woods and direct it towards the hole? She might have to hit many balls in various directions, the equivalent of adjusting the illumination angle in the authors' experiment. She might also have to engage many friends to stand around the golf course and shout back when a ball hits them, just as fluorescent molecules send light back when photons hit them. Even after hitting all these mulligans (second-chance shots in golf), she would not know how to strike the ball in the direction of the hole. However, if

she hit enough of her friends during this unusual game, she would know where her friends were standing (the image of the object). But she would still not know how to hit a single shot through the trees and towards the hole — the analogue of ballistic passage through the scattering medium. ■

**Demetri Psaltis and Ioannis N. Papadopoulos**  
are at the Optics Laboratory, School of Engineering, École Polytechnique Fédérale de Lausanne, 1015 Lausanne, Switzerland.  
e-mail: demetri.psaltis@epfl.ch

1. Bertolotti, J. *et al.* *Nature* **491**, 232–234 (2012).
2. Wang, L., Ho, P., Liu, C., Zhang, G. & Alfano, R. *Science* **253**, 769–771 (1991).
3. Alex, A. *et al.* *J. Biomed. Opt.* **15**, 026025 (2010).
4. Helmchen, F. & Denk, W. *Nature Methods* **2**, 932–940 (2005).
5. Leith, E. N. & Upatnieks, J. *J. Opt. Soc. Am.* **56**, 523 (1966).
6. Kogelnik, H. & Pennington, K. S. *J. Opt. Soc. Am.* **58**, 273–274 (1968).
7. Agarwal, G. S., Friberg, A. T. & Wolf, E. *J. Opt. Soc. Am.* **73**, 529–537 (1983).
8. Vellekoop, I. M. & Mosk, A. P. *Opt. Lett.* **32**, 2309–2311 (2007).
9. Hsieh, C. L., Pu, Y., Grange, R., Laporte, G. & Psaltis, D. *Opt. Express* **18**, 20723–20731 (2010).

## BIOCHEMISTRY

# A glimpse of molecular competition

**Single-molecule studies reveal how the DNA-repair protein RecA overcomes competition from another protein to bind to single-stranded DNA, and how other mediator proteins assist in this process. [SEE LETTER P.274](#)**

SUSAN T. LOVETT

Chromosomes consist of two interwound DNA strands millions of base pairs in length. These long molecules inevitably suffer breakage, which can be induced by ionizing radiation, biochemicals or natural DNA processing within cells. Double-strand breaks in DNA are not normally lethal to a cell, and can be accurately repaired by a process known as homologous recombination<sup>1,2</sup>, during which a broken DNA fragment searches for and pairs with an intact strand from another DNA molecule that carries an identical (homologous) sequence. The search process is remarkable in two respects: the homologous partner can be found even among the many millions of non-homologous segments, and the crucial base sequence can be recognized even when it is largely buried within a DNA double helix.

In all domains of life, this extraordinary search and pairing process is made possible by a class of structurally related proteins of

which the RecA protein from the bacterium *Escherichia coli* is the most-studied member. To initiate the recombination process, a filament composed of many RecA molecules must form on single-stranded DNA (ssDNA). But in doing so, the protein has to compete for binding with another resident protein, the ssDNA-binding protein (SSB)<sup>3</sup>. On page 274 of this issue, Bell *et al.*<sup>4</sup> present single-molecule images of fluorescent RecA as it binds to ssDNA and extends to form a filament\*. Although there have been other single-molecule studies<sup>5–12</sup> of RecA and of the analogous protein Rad51 from humans, this is the first study to visualize RecA binding to its natural substrate: extensively SSB-coated ssDNA. It is also the first to examine the effects of recombination 'mediators', proteins that potentiate recombination *in vivo* by aiding RecA-filament formation<sup>13,14</sup>, particularly on SSB-coated DNA.

\*This article and the paper under discussion<sup>4</sup> were published online on 24 October 2012.



The process of RecA-filament formation is complex. The RecA filament has a dynamic structure, which means that molecules continually join and leave it. This is much like the filaments formed from the proteins tubulin and actin, which make up the 'skeleton' within cells. But the situation for RecA is more complicated than that for tubulin and actin because RecA filaments must form on a molecular scaffold, ssDNA, and compete with SSB for access to this scaffold. RecA binding to ssDNA occurs in two kinetically distinct phases: nucleation, which is the initial binding to ssDNA; and extension, in which additional RecA molecules are recruited to generate a polymeric structure, and which can occur at different rates at either end of the resulting filament.

Bell and colleagues' real-time observation of single RecA molecules binding to SSB-coated ssDNA allowed the nucleation step to be distinguished from the extension step. The authors report that, in the presence of ATP — a nucleotide cofactor for RecA — or its analogues, nucleating clusters of RecA formed randomly and slowly (over a time course of minutes to hours) on SSB-coated ssDNA. The nature of the dependence of nucleation on RecA concentration indicates that a RecA dimer is the nucleating species (Fig. 1). This makes sense, because a RecA dimer is the smallest RecA oligomer that has a functional ATP-binding site, which is constructed at the interface of two adjacent RecA molecules<sup>15</sup>.

The latest study also clarifies the role of nucleotide cofactors in RecA nucleation. Bell *et al.* observed that nucleation was considerably faster when ATP was replaced with the nucleotides ATPγS or deoxy-ATP (dATP). The cofactors are hydrolysed (converted from a triphosphate to a diphosphate form) by RecA, but the rates at which the various nucleotides are hydrolysed differ widely. The authors found that a lower propensity for hydrolysis fails to correlate with a nucleotide's ability to promote RecA nucleation. These results support the idea that nucleotide binding induces RecA to adopt a conformation that has a high affinity for ssDNA, and that the nucleotides differ in their ability to induce this conformational transition: ATPγS is better than dATP, which is better than ATP.

The authors observed that, after initial RecA nucleation on SSB-coated ssDNA, RecA filaments grew at a rate comparable to those measured in studies of the protein in bulk<sup>16,17</sup>, and with a linear dependence on RecA concentration. These findings are consistent with a growth mechanism in which monomeric RecA molecules are added to the end of the growing filament.

By performing nucleation using RecA molecules that had been tagged with a red fluorescent label, and then performing extension using RecA bearing a green fluorescent label, Bell *et al.* showed that the RecA filament

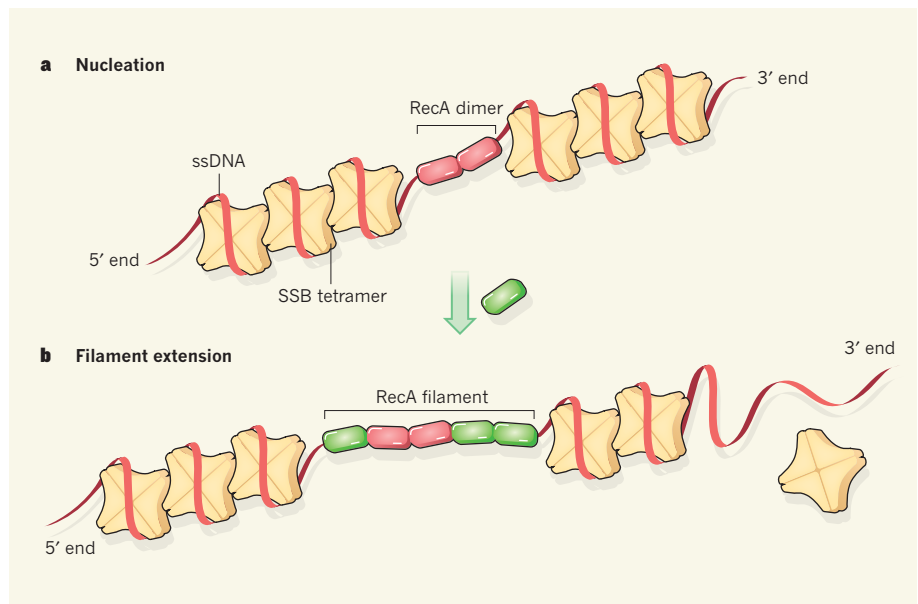


**Figure 1 | Nucleation and extension of RecA filaments.** The DNA-repair enzyme RecA binds to single-stranded DNA (ssDNA), but must compete for binding with ssDNA-binding proteins (SSBs). **a**, Tetrameric SSBs wrap ssDNA around themselves, whereas RecA initially binds (nucleates) as a dimer on SSB-free regions of ssDNA. **b**, SSB can slide along ssDNA or dissociate from it, generating new sections of SSB-free DNA. Bell *et al.*<sup>4</sup> report that further monomers of RecA (green) add to these sections at both ends of the RecA dimer, extending the dimer to form a RecA filament. Net growth of the filament occurs in the 5'-to-3' direction.

extends at both ends — that is, in both the 5'-to-3' direction of the ssDNA and the 3'-to-5' direction (Fig. 1). However, extension in the 5'-to-3' direction was about 50% faster than that in the opposite direction. This preference has also been found previously in an electron-microscope analysis of RecA filaments<sup>18</sup> and a study of RecA-mediated DNA-strand exchange<sup>16</sup>. These studies initially led to the notion that RecA filaments extend only in the 5'-to-3' direction. Bell and colleagues' single-molecule experiments, along with those of others<sup>5,12</sup>, clearly show that this is incorrect: net growth is 5' to 3', but growth occurs in both directions. And the authors found that, unlike RecA-filament nucleation, RecA-filament extension is broadly insensitive to the nucleotide cofactor used.

When the authors performed experiments at physiological pH, they found that filament nucleation and extension on SSB-coated ssDNA was extremely inefficient. This might reflect the situation *in vivo*, in which mediator proteins are needed to initiate recombination<sup>13,14</sup>. The requirement for mediators may help to avoid inappropriate RecA assembly on ssDNA that is transiently exposed during DNA replication, thereby restricting RecA to bona fide recombination substrates.

But perhaps the most noteworthy breakthrough of Bell and colleagues' work was the direct observation of RecA-filament formation stimulated by the mediator proteins RecF and RecOR. It had previously been proposed<sup>13,14</sup> that the recombination mediator proteins RecF, RecO and RecR specifically allow RecA

to overcome competition with SSB for binding to ssDNA, and it is therefore imperative to view mediator effects in the context of SSB-coated ssDNA. Bell and co-workers' study provides the first demonstration of the effects of mediators on single molecules, and offers the opportunity to distinguish between such effects on RecA-filament nucleation and extension. The authors found that RecF stimulates RecA-filament formation on SSB-bound ssDNA through nucleation, whereas RecOR stimulates both nucleation and filament extension.

Compared with previous single-molecule studies<sup>11,12</sup> of RecA binding to ssDNA, Bell *et al.* draw different conclusions about the oligomers involved in RecA nucleation and extension and the influence of nucleotide cofactors. It remains to be seen whether these differences are due to the presence of competing SSB or result from other features of the experimental system.

In Bell and colleagues' experiments, RecA presumably binds to ssDNA that is transiently exposed as SSB releases it or slides away (Fig. 1). RecA and SSB have distinctly different binding modes: each RecA monomer binds three nucleotides of ssDNA that are in a stretched conformation, whereas tetramers of SSB bind and wrap 65 nucleotides of ssDNA around their surface. RecA does not bind to SSB directly and must therefore replace SSB on ssDNA using a passive mechanism. By contrast, the mediator protein RecO does interact directly with SSB and may actively aid its removal<sup>19</sup>. But the exact mechanism by which RecO and other mediator proteins enhance

nucleation or filament extension remains unclear. Future single-molecule imaging studies are therefore needed to identify the mechanisms by which RecA and Rad51 filaments are modulated by different proteins. This is not just of intellectual interest — the human breast cancer type 2 susceptibility protein BRCA2 belongs to the same class of recombination mediator protein as RecFOR, and so an understanding of RecA/Rad51-filament modulation might aid our understanding of cancers that involve BRCA2 mutations. ■

**Susan T. Lovett** is in the Department of Biology, Brandeis University, Waltham, Massachusetts 02454-9110, USA.  
e-mail: lovett@brandeis.edu

## ASTRONOMY

# Meet our closest neighbour

The discovery of a possible extrasolar planet that has the same mass as Earth and orbits  $\alpha$  Centauri B, a member of the closest star system to the Sun, is both a technical achievement and cause for excitement. [SEE ARTICLE P.207](#)

ARTIE P. HATZES

One big goal of astronomers studying exoplanets — planets that orbit stars other than the Sun — is the detection of an Earth-mass planet in the habitable zone of a Sun-like star. The habitable zone is usually defined as the range of distances from the parent star at which water, if present, would be liquid. On page 207 of this issue, Dumusque *et al.*<sup>1</sup> report the discovery of a candidate exoplanet that brings this goal one step closer\*.

Finding exoplanets is nothing new — several hundred have already been discovered. What makes the planet identified by Dumusque and colleagues special and exciting is its mass and location: it has approximately the same mass as Earth, and it orbits  $\alpha$  Centauri B, a member of the closest star system to the Sun. Because of its proximity, it would be a good target for further investigations. For example, reflected starlight or radiated light from the planet would enable us to study its atmosphere, if present, or possibly its surface composition. So far, such studies have been possible only for much larger planets<sup>2,3</sup>. In addition, the authors' spectral analysis of the system is a demonstration that weak planetary signals can be extracted from a star's spectrum.

If it is confirmed, the new candidate planet

- Persky, N. S. & Lovett, S. T. *Crit. Rev. Biochem. Mol. Biol.* **43**, 347–370 (2008).
- Maher, R. L., Branagan, A. M. & Morrical, S. W. *J. Cell. Biochem.* **112**, 2672–2682 (2011).
- Shereda, R. D., Kozlov, A. G., Lohman, T. M., Cox, M. M. & Keck, J. L. *Crit. Rev. Biochem. Mol. Biol.* **43**, 289–318 (2008).
- Bell, J. C., Plank, J. L., Dombrowski, C. C. & Kowalczykowski, S. C. *Nature* **491**, 274–278 (2012).
- Galletto, R., Amitani, I., Baskin, R. J. & Kowalczykowski, S. C. *Nature* **443**, 875–878 (2006).
- Handa, N., Amitani, I., Gumlaw, N., Sandler, S. J. & Kowalczykowski, S. C. *J. Biol. Chem.* **284**, 18664–18673 (2009).
- Hilario, J., Amitani, I., Baskin, R. J. & Kowalczykowski, S. C. *Proc. Natl Acad. Sci. USA* **106**, 361–368 (2009).
- Modesti, M. *et al. Structure* **15**, 599–609 (2007).
- Shivashankar, G. V., Feingold, M., Krichevsky, O. & Libchaber, A. *Proc. Natl Acad. Sci. USA* **96**, 7916–7921 (1999).
- van der Heijden, T. *et al. Nucleic Acids Res.* **35**, 5646–5657 (2007).
- van Loenhout, M. T., van der Heijden, T., Kanaar, R., Wyman, C. & Dekker, C. *Nucleic Acids Res.* **37**, 4089–4099 (2009).
- Joo, C. *et al. Cell* **126**, 515–517 (2006).
- Morimatsu, K. & Kowalczykowski, S. C. *Mol. Cell* **11**, 1337–1347 (2003).
- Urmez, K., Chi, N. W. & Kolodner, R. D. *Proc. Natl Acad. Sci. USA* **90**, 3875–3879 (1993).
- Chen, Z., Yang, H. & Pavletich, N. P. *Nature* **453**, 489–494 (2008).
- Kowalczykowski, S. C. *Annu. Rev. Biophys.* **20**, 539–575 (1991).
- Thresher, R. J., Christiansen, G. & Griffith, J. D. *J. Mol. Biol.* **201**, 101–113 (1988).
- Register, J. C. III & Griffith, J. J. *Biol. Chem.* **260**, 12308–12312 (1985).
- Urmez, K. & Kolodner, R. D. *J. Biol. Chem.* **269**, 30005–30013 (1994).

comparison, the Doppler wobble caused by 51 Peg b is 50 m s<sup>-1</sup>, or about 100-fold bigger. Doppler measurements this fine require very stable instruments. The authors used the HARPS spectrograph mounted on the European Southern Observatory's 3.6-m telescope located in La Silla, Chile — the most stable spectrograph in the world for this type of measurement.

The second and much more daunting challenge was the extraction of the planet's signal from the 'noise' caused by the variability of the star. Like our Sun,  $\alpha$  Centauri B has spots (regions that are darker and cooler than the rest of the star's surface), which are caused by magnetic activity. These spots can create signals in the data that look similar to that caused by the planet, making it hard to distinguish between planetary and stellar signals. The data show that the stellar-activity signal was three times larger than that due to the planet. The researchers used 23 parameters related to the star's rotation period to model the variation in stellar

activity, and then filtered it out from the data, unveiling the planet's signal. The fact that so many parameters had to be used emphasizes the complexity of the stellar signal.

So is this Earth-mass planet real? Only time will tell. As the American astronomer Carl Sagan once said, "Extraordinary claims require extraordinary evidence". Although a planet-like signal is present in the data, the discovery does not quite provide the "extraordinary evidence". It is a weak signal in the presence of a larger, more complicated signal. In my opinion, the matter is still open to debate. Other analytical tools, using alternative ways of filtering out the stellar variability, might arrive at different conclusions on the basis of the same data. However, if we want to find a real Earth

would qualify as the nearest exoplanet to our Solar System. The planet is too close to its host star, and therefore too hot, to be habitable — its orbital period, or 'year', is only 3.236 days. However, as previous research has shown, multi-planet systems are common<sup>4</sup>: where there is one planet there may be more. So it is conceivable that  $\alpha$  Centauri B has more companions, maybe even in the habitable zone. But this is speculation, and detecting further planets would be even more difficult than finding this one.

To understand the significance of this finding, some context is needed. Since the discovery<sup>5</sup> in 1995 of the giant exoplanet 51 Peg b, the first planet to be found orbiting a Sun-like star, the detectable mass of exoplanets has decreased from the mass of Jupiter to the mass of Earth. An Earth-mass exoplanet is 150 times smaller than 51 Peg b. Planet hunters have been able to find ever smaller planets owing to a combination of improved instruments and better analysis methods. Dumusque *et al.* detected the new candidate planet using the 'Doppler wobble', which is the effect caused by the planet's gravitational pull on the motion of its host star<sup>6</sup>. If confirmed, this would be the lowest-mass planet discovered using the Doppler-wobble method.

In their search for the exoplanet, Dumusque and colleagues faced two main challenges. The first was detecting such a small Doppler wobble, a mere 0.51 metres per second. In

**"The authors' spectral analysis of the system is a demonstration that weak planetary signals can be extracted from a star's spectrum."**

\*This article and the paper under discussion<sup>1</sup> were published online on 17 October 2012.



twin around a Sun-like star, we have to devise robust methods for filtering out the star's variability. By providing researchers with a valuable data set for testing their analytical tools, the present study is a step in that direction.

In the coming months, astronomers will certainly be scrutinizing these measurements. Only if other analyses come to the

same conclusion can we be sure that this planet exists. Better yet, independent measurements should be made with other facilities and instruments to confirm this candidate planet. ■

**Artie P. Hatzes** is at the Thuringian State Observatory, Tautenburg 07778, Germany. e-mail: artie@tls-tautenburg.de

1. Dumusque, X. *et al.* *Nature* **491**, 207–211 (2012).
2. Snellen, I. A. G., de Mooij, E. J. W. & Albrecht, S. *Nature* **459**, 543–545 (2009).
3. Knutson, H. A. *et al.* *Astrophys. J.* **754**, 22 (2012).
4. Latham, D. W. *et al.* *Astrophys. J.* **732**, L24 (2011).
5. Mayor, M. & Queloz, D. *Nature* **378**, 355–359 (1995).
6. Campbell, B., Walker, G. A. H. & Yang, S. *Astrophys. J.* **331**, 902–921 (1988).

## MICROBIOLOGY

# Bacterial power cords

**Geochemical reactions in upper layers of marine sediments are coupled to those in deeper zones. It turns out that centimetre-long bacterial filaments acting as electrical cables are the metabolic link between the layers. SEE ARTICLE P.218**

GEMMA REGUERA

A few years ago, any suggestion that microbes could function as power cables to transmit electric currents across centimetre distances would have been met with scepticism. Yet this is exactly what Pfeffer *et al.*<sup>1</sup> report on page 218 of this issue. The authors provide compelling evidence linking the presence of long filaments of a previously unknown group of bacteria to the electric currents that couple spatially separated geochemical reactions in marine sediments\*.

In the oceans, atmospheric oxygen diffuses from the water into the upper layers of the underlying sediment. Here, it is rapidly consumed by microorganisms, which use the oxygen as the terminal acceptor of electrons that are generated during the metabolism of organic matter to gain energy for growth. As a result, oxygen concentrations drop sharply in the uppermost layer of the sediment (the oxic zone), leaving the deeper layers oxygen-free (anoxic). Microbes in the anoxic layers therefore rely on other electron-accepting molecules such as sulphate ( $\text{SO}_4^{2-}$ ) to fulfil their energy needs (Fig. 1). The transfer of electrons to sulphate, however, generates hydrogen sulphide ( $\text{H}_2\text{S}$ ), a gas that is toxic to oxygen-consuming organisms. Yet hydrogen sulphide levels can be controlled by microbes that convert it into sulphate or into other oxidized sulphur compounds.

Although the oxic and sulphide layers are typically separated by millimetres to centimetres of sediment, reductions in oxygen availability in the upper layer rapidly lead to the accumulation of hydrogen sulphide and the expansion of the sulphide region<sup>2</sup>. As soon as oxygen is available again, hydrogen sulphide

consumption resumes and the sulphide layer recedes. The responses are so fast as to exclude mechanisms based on the diffusion of molecules, and they can be explained only by the action of electric currents.

Such electric currents might be mediated by bacterial conductive appendages (microbial nanowires)<sup>3–5</sup>, electron-shuttling solid phases (such as humic substances generated during the decomposition of organic matter)<sup>6</sup> and/or conductive minerals<sup>7</sup>. However, evidence so far suggests that these mediators enable the flow of electrons only across nanometre to micrometre distances, whereas the oxic and sulphide sediment layers are typically separated by millimetre to centimetre distances.

Now Pfeffer *et al.* report that sulphidic marine sediments are densely colonized by long, multicellular bacterial filaments — some reaching lengths (up to 1.5 centimetres) that correspond well to the spatial separation of the oxic and sulphide layers. The authors provide experimental evidence that the filaments are required for the electrical coupling between sediment layers. For example, when they cut the filaments or used filters to prevent their passage, oxygen consumption in the upper region was reduced and the sulphide layer expanded.

The filamentous microbes belong to the family Desulfobulbaceae, a morphologically diverse group of bacteria with members previously shown<sup>8</sup> to both generate and consume hydrogen sulphide; these reactions are localized to the space (periplasm) contained between the cytoplasmic (or inner) membrane and the outer membrane. Interestingly, the outer membrane of the filamentous microbes is structured as ridges, which define tubular channels of periplasm running along the cells, and continue as junctions between neighbouring cells. Furthermore, although the outer membrane of the ridges and junctions acts as an insulator, their internal content is highly charged. These unique structural and electrical

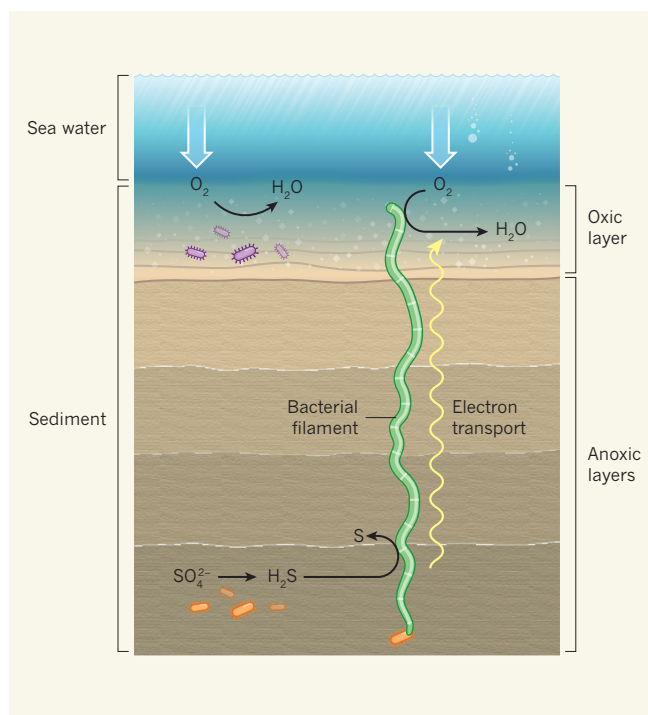


**Figure 1 | Electrifying microbial filaments.** Microorganisms (purple) in the upper layers of marine sediments use oxygen ( $\text{O}_2$ ) that diffuses from sea water as an acceptor of electrons, which they produce in energy-generating metabolic reactions. As a result, other microbes (orange) in deeper, anoxic layers (where oxygen is scarce or absent) have to use other electron acceptors such as sulphate ( $\text{SO}_4^{2-}$ ) for growth. Transfer of electrons to oxygen results in the formation of water, whereas electron transfer to sulphate produces hydrogen sulphide ( $\text{H}_2\text{S}$ ), which is poisonous to many organisms. Pfeffer *et al.*<sup>1</sup> provide evidence that long bacterial filaments could transport electrons generated when hydrogen sulphide is converted into sulphur (S) at the bottom of the sediments and use them to consume oxygen in the upper layers.

\*This article and the paper under discussion<sup>1</sup> were published online on 24 October 2012.

properties hint at a potential mechanism for electron transfer involving the periplasmic conduits.

The authors propose a plausible model in which cells at one end of the filament oxidize hydrogen sulphide to supply electrons to the oxygen-consuming cells located at the opposite end (Fig. 1). However, the idea that the microbial filaments behave as living, centimetre-long power cords, presumably transporting electrons through continuous tubular channels, defies our understanding of biological electron transfer. Nevertheless, it is known that the periplasm of some bacteria that use metals as electron acceptors houses abundant metal-containing proteins, mostly of the cytochrome class, that allow electrons to flow from the inner to the outer membrane<sup>9</sup>. Cytochromes and microbial nanowires can transmit electric currents across micrometre-thick films formed by these bacteria. Therefore, similar mechanisms — but contained within tubular periplasmic ridges — might mediate long-range electron transfer in the *Desulfobulbaceae* filaments.

Pfeffer and colleagues' report raises questions about the ecological role of these bacteria as well. If widespread, the bacterial cables could constitute the main mechanism for the transport of electric currents in marine sulphidic sediments. However, it is unclear whether they act alone or in concert with other microbes. When the authors cut the filaments or prevented their permeation through the sediments with filters, they might have also disrupted other microbial electrical networks. Hence, to assess the exact contribution of the filaments to the electric currents of the sediments, it will be crucial to confirm that electrons can travel along the filaments and to measure the transport rates. Furthermore, the ability to consume the toxic hydrogen sulphide, if demonstrated, might allow the bacteria to outcompete other microbes, and promote metabolic interactions with others.

Finally, it should be noted that the bacterial cables might not simply provide a mechanism to cope with toxic hydrogen sulphide in sediments. Rather, they could enable a more widespread biological process for energy transfer and the coupling of spatially separated biogeochemical reactions. As noted in an earlier report<sup>2</sup>, hydrogen sulphide consumption in some subsurface sediments is not high enough to sustain the levels of oxygen consumption measured in the sediment's top layer. Thus, other biogeochemical reactions could be electrically coupled to the reduction of oxygen in sediments as well.

Pfeffer and colleagues' report adds to the growing body of evidence highlighting the crucial role that microbial electron transfer has in global geochemical processes and in the functioning of ecosystems. These are indeed exciting times for microbiologists, and the present work reminds us — one

more time — just how much more awaits discovery. ■

**Gemma Reguera** is in the Department of Microbiology and Molecular Genetics, Michigan State University, East Lansing, Michigan 48824, USA.  
e-mail: reguera@msu.edu

1. Pfeffer, C. *et al.* *Nature* **491**, 218–221 (2012).
2. Nielsen, L. P., Risgaard-Petersen, N., Fossing, H., Christensen, P. B. & Sayama, M. *Nature*

**463**, 1071–1074 (2010).

3. El-Naggar, M. Y. *et al.* *Proc. Natl Acad. Sci. USA* **107**, 18127–18131 (2010).
4. Gorby, Y. A. *et al.* *Proc. Natl Acad. Sci. USA* **103**, 11358–11363 (2006).
5. Reguera, G. *et al.* *Nature* **435**, 1098–1101 (2005).
6. Roden, E. E. *et al.* *Nature Geosci.* **3**, 417–421 (2010).
7. Kato, S., Hashimoto, K. & Watanabe, K. *Proc. Natl Acad. Sci. USA* **109**, 10042–10046 (2012).
8. Fuseler, K., Krekeler, D., Sydow, U. & Cypionka, H. *FEMS Microbiol. Lett.* **144**, 129–134 (1996).
9. Shi, L., Squier, T. C., Zachara, J. M. & Fredrickson, J. K. *Mol. Microbiol.* **65**, 12–20 (2007).

## APPLIED PHYSICS

# Brighter images with no added noise

**A special type of optical amplifier based on a vapour of rubidium has been demonstrated that makes faint images brighter without adding noise. This concept could find use in biological imaging and image processing.**

STÉPHANE CLEMMEN & ALEXANDER GAETA

Anyone who has adjusted the sensitivity settings of a camera in weak light will have noticed that increasing the electronic gain of the camera's light sensor yields images of poor quality. This observation reveals a general property of amplification of signals: it is accompanied by noise. However, there are special conditions in which such noise can be circumvented. Writing in *Physical Review Letters*, Corzo *et al.*<sup>1</sup> describe how they have achieved this in the amplification of faint images.

In the quest to improve the accuracy of measurement and observation of a system, certain fundamental bounds exist that limit the precision with which a physical quantity can be determined. Specifically, according to Heisenberg's uncertainty principle, it is not possible to attain perfect precision in simultaneously determining a system's observable quantity and its conjugate variable; two variables,  $X$  and  $Y$ , are conjugate variables if they are related to one another through a mathematical operation known as a Fourier transform. Examples of pairs of conjugate variables include time and frequency, and position and momentum. The case in which the uncertainties  $\Delta X$  and  $\Delta Y$  in  $X$  and  $Y$ , respectively, are equal and minimal is known as the standard quantum limit for  $X$  and  $Y$ , and a system in such a state of minimum uncertainty is said to be in a coherent state. However, because the uncertainties are not necessarily equal, measurements can be performed that have a precision beyond the standard quantum limit. Such precision can be achieved using 'squeezed' states<sup>2</sup>, in which one of the two

conjugate variables has a smaller (squeezed) uncertainty than that associated with coherent states.

For light, the conjugate variables  $X$  and  $Y$  are typically taken to be the quadratures that define the light's time-varying electromagnetic field:  $E(t) = X\cos(2\pi\nu t) + Y\sin(2\pi\nu t)$ , where  $t$  denotes time and  $\nu$  is frequency. Figure 1 shows a comparison between the electromagnetic field in a coherent state, typically that of a laser beam, and one in a squeezed state<sup>2,3</sup>. Squeezing can be produced by a nonlinear optical process called four-wave mixing, in which two photons at frequencies  $\nu_1$  and  $\nu_2$  are annihilated and two new photons at frequencies  $\nu_3$  and  $\nu_4$  are created while satisfying conservation of energy, and therefore frequency:  $\nu_1 + \nu_2 = \nu_3 + \nu_4$ . For this process to occur efficiently, another rule, known as phase matching, must apply. This states that the sum of the momenta of the interacting photons at these frequencies is conserved (that is, the sum of the propagation constants  $k_1 + k_2 = k_3 + k_4$ ). The result of this interaction is that the uncertainties in the quadratures of the generated photon field become unequal, such that one is less than (squeezed) that of a coherent state and the other is greater.

The interaction that produces squeezing represents a special type of linear amplifier. The most common form of amplifier produces phase-insensitive amplification (PIA), in which both quadratures of the field are amplified equally. But phase-sensitive amplification (PSA), in which one quadrature is amplified while the other is de-amplified, can also be realized. In PIA, the quotient between the signal-to-noise ratio of the input field and that of the output, amplified field — the noise figure



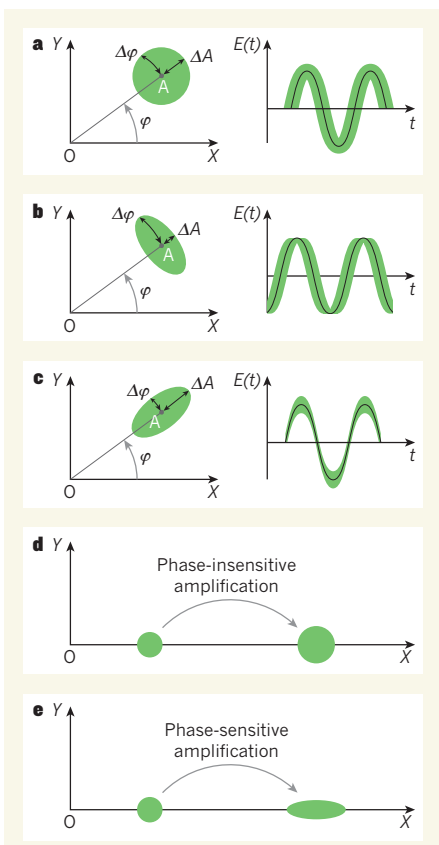


**Figure 1 | Coherent and squeezed states.**

**a**, Conceptual representation of a coherent state of light.  $X$  and  $Y$  represent the quadratures of the light's electromagnetic field at frequency  $\nu$ :  $E(t) = X\cos(2\pi\nu t) + Y\sin(2\pi\nu t)$ , where  $t$  is time. The distance  $OA$  is the field's amplitude  $A$ , and the angle  $\phi$  is the phase (where the field's peaks and dips lie). The size of the disk represents the uncertainties in the amplitude and phase,  $\Delta A$  and  $\Delta\phi$ , which are equal in value. The field's temporal evolution is shown on the right. **b**, A squeezed state, in which  $\Delta A$  is smaller and  $\Delta\phi$  larger than their coherent-state equivalents. **c**, A phase-squeezed state, in which  $\Delta\phi$  is smaller and  $\Delta A$  larger than their coherent-state analogues. **d**, In a type of field amplification known as phase-insensitive amplification, the total uncertainty (area of the disk) is amplified. **e**, In phase-sensitive amplification, the total uncertainty remains constant. Corzo *et al.*<sup>1</sup> have applied this form of amplification to faint images.

— approaches 2 for large values of the gain. By contrast, the noise figure for the PSA can be unity, independently of the value of the gain<sup>4</sup>.

The first demonstrations<sup>5,6</sup> of noiseless amplification (that is, with no degradation of the signal-to-noise ratio of the input signal) by means of PSA were followed by a proposal to apply it to the light fields associated with faint images<sup>7</sup>, which was subsequently demonstrated experimentally<sup>8</sup>. In their study, Corzo *et al.* attained PSA noiseless amplification, based on four-wave mixing, of faint images in a set-up<sup>9</sup> that had been used to demonstrate quantum entanglement between spatially extended light fields. Previous noiseless

amplification of images<sup>8,10</sup> has been achieved using certain crystals that display a non-linear optical response when light propagates through them. The authors' image amplifier is based on an atomic vapour of rubidium that exhibits a highly nonlinear optical response owing to the 'near-resonant' nature of the interaction between the rubidium vapour and the light fields. As a result, 'pump' light beams at frequencies  $\nu_1$  and  $\nu_2$  do not need to be tightly focused in the amplifying medium, thereby relaxing the requirement of phase matching and allowing a larger number of image pixels to be amplified.

In Corzo and colleagues' experiment, the four-wave mixing process involves two pump fields whose frequencies ( $\nu_1$  and  $\nu_2$ ) are nearly the same as the frequencies associated with two atomic transitions in a vapour of rubidium,  $\nu_{ge}$  and  $\nu_{ie}$ . The signal to be amplified is at a frequency  $\nu_s$ , such that  $\nu_1 + \nu_2 = 2\nu_s$ . Unlike many four-wave-mixing experiments, spontaneous emission noise is negligible as long as  $\nu_1$ ,  $\nu_2$  and  $\nu_s$  are sufficiently detuned from  $\nu_{ge}$  and  $\nu_{ie}$ . The authors show that, for a gain of 3.9, the noise figure remains nearly equal to unity for this PSA approach to amplifying faint images, and is well below the predicted value for an ideal (with no added noise) PIA method. What's more, they demonstrate that this amplifier can provide gain for more than 2,000 pixels, allowing the amplification of fairly complex image patterns.

The authors' PSA technique could be used in several applications, for example when a detector (camera) is either insufficiently sensitive to light or too noisy. A future path for this research would be to create amplifiers that operate in the mid- and far-infrared, or X-ray, wavelength regimes. In the X-ray regime, a PSA could reduce the exposure of biological tissues to harmful radiation. However, most of these applications would require transposing the wavelength of operation of the current demonstration to these other wavelengths. In principle, this is possible using different sets of atomic transitions and/or systems. For applications in which there is no control over the light source (such as in astronomical imaging), another issue is the frequency bandwidth of the nonlinear medium. For interactions in rubidium vapour, the frequency bandwidth over which the nonlinear interaction occurs efficiently is very narrow and must be close to the atomic-transition frequencies. This provides additional motivation to develop nonlinear materials that can operate over broad bandwidths and have a large nonlinear response. ■

**Stéphane Clemmen and Alexander Gaeta** are in the School of Applied and Engineering Physics, Cornell University, Ithaca, New York 14853, USA.  
e-mails: sc764@cornell.edu;  
a.gaeta@cornell.edu



## 50 Years Ago

This year's Nobel Prize for Chemistry has been awarded jointly to Dr. M. F. Perutz ... and Dr. J. C. Kendrew. This most welcome announcement follows quickly on that concerning the award of the Nobel Prize for Medicine to another member of the staff of the same Laboratory, Dr. F. H. C. Crick (jointly with Dr. M. H. F. Wilkins and Prof. W. Watson; see *Nature* of October 27, 1962, p.319) ... The award was made for their work on the structures of globular proteins.  
**From *Nature* 10 November 1962**

## 100 Years Ago

Attention has been directed to the relationship of tuberculosis and milk, and to the problem of a pure milk supply and the methods whereby this may be ensured ... Now Bullock, from a very carefully survey of the literature of the subject, comes to the conclusion that pulmonary tuberculosis is produced almost always, if not exclusively, by tubercle bacilli of the *human* type. More than two-thirds of human tuberculosis is, therefore, certainly not due to the *bovine* bacillus or to milk infection. Bullock further remarks that the *bovine* tubercle bacillus plays a relatively unimportant rôle in the production of tuberculosis in man! ... The fact is, we have no data indicating the infectivity by feeding of ordinary mixed milk ... Assuming that a danger of tuberculous infection from milk exists, how can it be prevented? Pasteurisation has had a great deal said in its favour, and efficient pasteurisation does destroy the tubercle bacillus. But pasteurisation, as commonly carried out, is uncertain in its action, and there are various other objections to this process.  
**From *Nature* 7 November 1912**

1. Corzo, N. V., Marino, A. M., Jones, K. M. & Lett, P. D. *Phys. Rev. Lett.* **109**, 043602 (2012).
2. Walls, D. F. *Nature* **306**, 141–146 (1983).
3. Slusher, R. E., Hollberg, L. W., Yurke, B., Mertz, J. C. & Valley, J. F. *Phys. Rev. Lett.* **55**, 2409–2412 (1985).
4. Caves, C. M. *Phys. Rev. D* **26**, 1817–1939 (1982).
5. Levenson, J. A., Abram, I., Rivera, T. & Grangier, P. *J. Opt. Soc. Am. B* **10**, 2233–2238 (1993).
6. Ou, Z. Y., Pereira, S. F. & Kimble, H. J. *Phys. Rev. Lett.* **70**, 3239–3242 (1993).
7. Kolobov, M. I. & Lugiato, L. A. *Phys. Rev. A* **52**, 4930–4940 (1995).
8. Choi, S.-K., Vasilyev, M. & Kumar, P. *Phys. Rev. Lett.* **83**, 1938–1941 (1999).
9. Boyer, V., Marino, A. M., Pooser, R. C. & Lett, P. D. *Science* **321**, 544–547 (2008).
10. Lopez, L., Treps, N., Chalopin, B., Fabre, C. & Maître, A. *Phys. Rev. Lett.* **100**, 013604 (2008).

## STRUCTURAL BIOLOGY

# A toolbox for protein design

Some of the principles underlying how amino-acid sequences determine the three-dimensional structures of proteins have been defined. This has enabled a successful approach to designing protein folds from scratch. [SEE ARTICLE P.222](#)

BIRTE HÖCKER

Proteins are the molecular machines of the cell. In order to function, they have to fold into a defined three-dimensional (tertiary) conformation known as the native structure, which is encoded by the amino-acid sequence of the protein chain. It would be immensely useful to be able to predict native structures from amino-acid sequences, but our understanding of how such sequences determine the three-dimensional arrangements of proteins is limited. On page 222 of this issue, Koga *et al.*<sup>1</sup> describe a set of rules that relate secondary protein-structure patterns —  $\alpha$ -helices and  $\beta$ -sheets — to tertiary features. They also show how these principles can be used to design amino-acid sequences that fold into predefined topologies.

The folded state of a protein is stabilized by many different non-covalent interactions. These interactions form as the protein folds into its native conformation, which, under physiological conditions, corresponds to

the thermodynamically most stable, lowest-energy conformation. When a protein's energy landscape — a map of every possible protein conformation and the associated energy levels, plotted as a two- or three-dimensional representation — is considered, the folding path can be envisaged as a funnel in which the formation of local stabilizing interactions contributes to a decrease in the protein's overall energy and so leads to the native protein conformation<sup>2</sup>.

However, if non-covalent interactions form that are energetically favourable but do not exist in the native conformation, this will lead to an accumulation of non-native states. Proteins therefore have to select the biologically relevant native structure over the large number of possible non-native conformations. If non-native states can be 'discouraged' from forming, this will improve the folding path of the protein chain, because it does not get trapped in energy minima associated with non-native states.

Naturally evolved proteins have 'smooth'

folding funnels that lack non-native-state energy minima, and so Koga *et al.* set out to find the principles that help these proteins to differentiate between native and non-native conformations. They focused on local structural patterns that strongly favour the formation of single tertiary motifs — compact tertiary structures that consist of a few adjacent secondary structures.

By combining computer simulations with an analysis of test sets of naturally occurring protein sequences, the authors established three fundamental rules that describe the relationships between local interactions and tertiary-motif formation in the  $\beta\beta$ - 'hairpin' structure and the  $\alpha\beta$ - and  $\beta\alpha$ -motifs. They found that the orientation of the secondary structural elements with respect to each other primarily depends on the number of amino acids in the peptide loop that connects them, as well as on the direction in which the amino-acid side chains of the  $\beta$ -strands are pointing. Notably, the positioning of the secondary elements is independent of the specific amino-acid residues in the loop's sequence.

On the basis of this set of fundamental rules, Koga *et al.* identified a second, emergent set of rules describing the lengths of secondary structural elements, and of the peptide loops connecting them, needed for three larger tertiary motifs:  $\beta\beta\alpha$ ,  $\alpha\beta\beta$  and  $\beta\alpha\beta$ . Together with the widely used Ramachandran plots<sup>3</sup> (which allow the possible conformations of amino-acid residues in proteins to be determined), these rules make up a toolbox of fundamental principles for designing tertiary structures.

Koga and colleagues went on to implement these principles, with remarkable results. They designed five different folds with similar topologies, and which consisted of several  $\alpha$ -helices,  $\beta$ -strands and minimal connecting loops. For each topology, the authors calculated the thermodynamic stability of possible sequences and conformations to find the ones that had the lowest energies. To refine these sequences, they incorporated large,

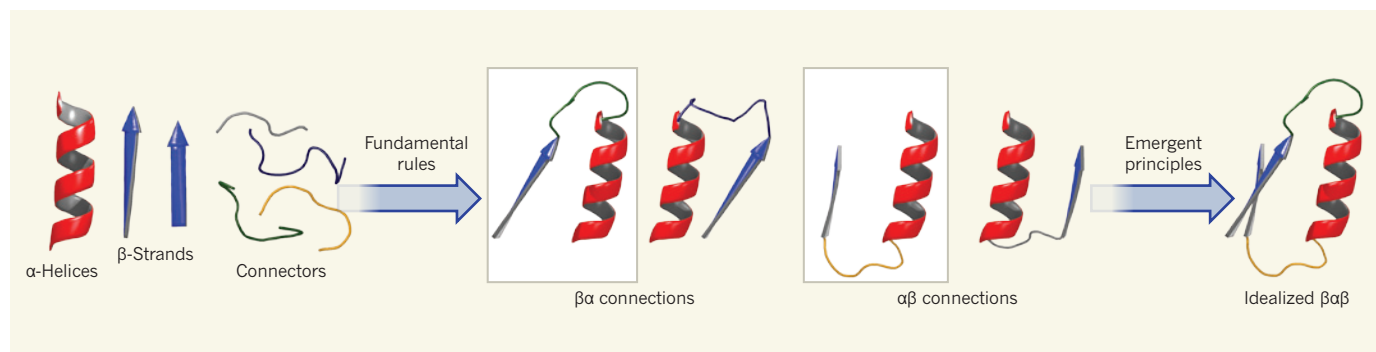


**Figure 1 | Protein assembly demystified.** Proteins are constructed from secondary structures known as  $\alpha$ -helices and  $\beta$ -strands, connected by protein loops. Koga *et al.*<sup>1</sup> have defined fundamental rules that describe how local interactions in secondary structures relate to the assembly of simple tertiary motifs (compact, three-dimensional structures that consist of a few adjacent

secondary structures, such as the  $\beta\alpha$ - and  $\alpha\beta$ -motifs shown). In this example, different connecting loops direct the  $\alpha$ -helix to pack against different sides of the  $\beta$ -strand. These rules, in turn, form the basis of emergent principles governing the design of 'ideal', more complex motifs, such as the  $\beta\alpha\beta$ -structure shown, which is constructed from the  $\beta\alpha$ - and  $\alpha\beta$ -motifs shown in grey boxes.



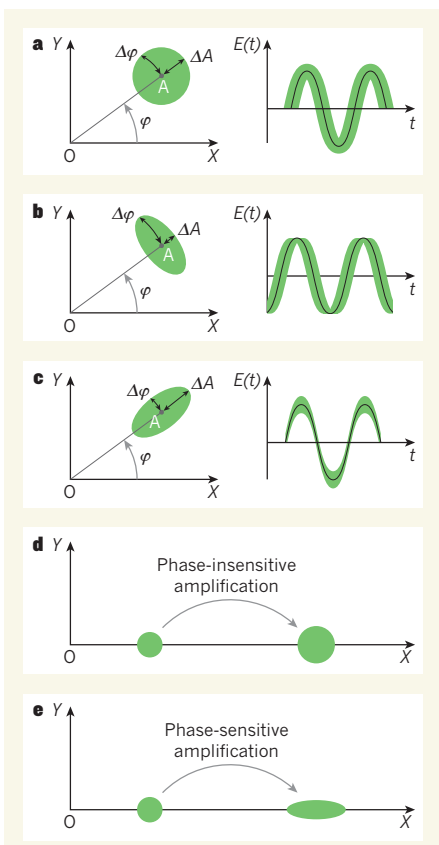


**Figure 1 | Coherent and squeezed states.** **a**, Conceptual representation of a coherent state of light.  $X$  and  $Y$  represent the quadratures of the light's electromagnetic field at frequency  $\nu$ :  $E(t) = X\cos(2\pi\nu t) + Y\sin(2\pi\nu t)$ , where  $t$  is time. The distance  $OA$  is the field's amplitude  $A$ , and the angle  $\varphi$  is the phase (where the field's peaks and dips lie). The size of the disk represents the uncertainties in the amplitude and phase,  $\Delta A$  and  $\Delta\varphi$ , which are equal in value. The field's temporal evolution is shown on the right. **b**, A squeezed state, in which  $\Delta A$  is smaller and  $\Delta\varphi$  larger than their coherent-state equivalents. **c**, A phase-squeezed state, in which  $\Delta\varphi$  is smaller and  $\Delta A$  larger than their coherent-state analogues. **d**, In a type of field amplification known as phase-insensitive amplification, the total uncertainty (area of the disk) is amplified. **e**, In phase-sensitive amplification, the total uncertainty remains constant. Corzo *et al.*<sup>1</sup> have applied this form of amplification to faint images.

— approaches 2 for large values of the gain. By contrast, the noise figure for the PSA can be unity, independently of the value of the gain<sup>4</sup>.

The first demonstrations<sup>5,6</sup> of noiseless amplification (that is, with no degradation of the signal-to-noise ratio of the input signal) by means of PSA were followed by a proposal to apply it to the light fields associated with faint images<sup>7</sup>, which was subsequently demonstrated experimentally<sup>8</sup>. In their study, Corzo *et al.* attained PSA noiseless amplification, based on four-wave mixing, of faint images in a set-up<sup>9</sup> that had been used to demonstrate quantum entanglement between spatially extended light fields. Previous noiseless

amplification of images<sup>8,10</sup> has been achieved using certain crystals that display a non-linear optical response when light propagates through them. The authors' image amplifier is based on an atomic vapour of rubidium that exhibits a highly nonlinear optical response owing to the 'near-resonant' nature of the interaction between the rubidium vapour and the light fields. As a result, 'pump' light beams at frequencies  $\nu_1$  and  $\nu_2$  do not need to be tightly focused in the amplifying medium, thereby relaxing the requirement of phase matching and allowing a larger number of image pixels to be amplified.

In Corzo and colleagues' experiment, the four-wave mixing process involves two pump fields whose frequencies ( $\nu_1$  and  $\nu_2$ ) are nearly the same as the frequencies associated with two atomic transitions in a vapour of rubidium,  $\nu_{ge}$  and  $\nu_{ie}$ . The signal to be amplified is at a frequency  $\nu_s$ , such that  $\nu_1 + \nu_2 = 2\nu_s$ . Unlike many four-wave-mixing experiments, spontaneous emission noise is negligible as long as  $\nu_1$ ,  $\nu_2$  and  $\nu_s$  are sufficiently detuned from  $\nu_{ge}$  and  $\nu_{ie}$ . The authors show that, for a gain of 3.9, the noise figure remains nearly equal to unity for this PSA approach to amplifying faint images, and is well below the predicted value for an ideal (with no added noise) PIA method. What's more, they demonstrate that this amplifier can provide gain for more than 2,000 pixels, allowing the amplification of fairly complex image patterns.

The authors' PSA technique could be used in several applications, for example when a detector (camera) is either insufficiently sensitive to light or too noisy. A future path for this research would be to create amplifiers that operate in the mid- and far-infrared, or X-ray, wavelength regimes. In the X-ray regime, a PSA could reduce the exposure of biological tissues to harmful radiation. However, most of these applications would require transposing the wavelength of operation of the current demonstration to these other wavelengths. In principle, this is possible using different sets of atomic transitions and/or systems. For applications in which there is no control over the light source (such as in astronomical imaging), another issue is the frequency bandwidth of the nonlinear medium. For interactions in rubidium vapour, the frequency bandwidth over which the nonlinear interaction occurs efficiently is very narrow and must be close to the atomic-transition frequencies. This provides additional motivation to develop nonlinear materials that can operate over broad bandwidths and have a large nonlinear response. ■

**Stéphane Clemmen and Alexander Gaeta** are in the School of Applied and Engineering Physics, Cornell University, Ithaca, New York 14853, USA.  
e-mails: sc764@cornell.edu;  
a.gaeta@cornell.edu



## 50 Years Ago

This year's Nobel Prize for Chemistry has been awarded jointly to Dr. M. F. Perutz ... and Dr. J. C. Kendrew. This most welcome announcement follows quickly on that concerning the award of the Nobel Prize for Medicine to another member of the staff of the same Laboratory, Dr. F. H. C. Crick (jointly with Dr. M. H. F. Wilkins and Prof. W. Watson; see *Nature* of October 27, 1962, p.319) ... The award was made for their work on the structures of globular proteins.  
**From *Nature* 10 November 1962**

## 100 Years Ago

Attention has been directed to the relationship of tuberculosis and milk, and to the problem of a pure milk supply and the methods whereby this may be ensured ... Now Bullock, from a very carefully survey of the literature of the subject, comes to the conclusion that pulmonary tuberculosis is produced almost always, if not exclusively, by tubercle bacilli of the *human* type. More than two-thirds of human tuberculosis is, therefore, certainly not due to the *bovine* bacillus or to milk infection. Bullock further remarks that the *bovine* tubercle bacillus plays a relatively unimportant rôle in the production of tuberculosis in man! ... The fact is, we have no data indicating the infectivity by feeding of ordinary mixed milk ... Assuming that a danger of tuberculous infection from milk exists, how can it be prevented? Pasteurisation has had a great deal said in its favour, and efficient pasteurisation does destroy the tubercle bacillus. But pasteurisation, as commonly carried out, is uncertain in its action, and there are various other objections to this process.  
**From *Nature* 7 November 1912**

hydrophobic amino-acid residues in core regions of the folds to generate a strong driving force for folding, and used negative design — the incorporation of sequences that destabilize the formation of unwanted structures — at the edges of  $\beta$ -strands and protein surfaces to disfavour oligomerization.

The authors went on to synthesize the DNA that encodes several of their designed peptide sequences, to see if the peptides can be expressed in cells, and, if so, whether they fold into the predicted tertiary structures. They found that many of the peptide sequences could be expressed, and that the peptides displayed spectroscopic features typical of proteins formed from mixed  $\alpha$ - and  $\beta$ -subunits. Of these sequences, many were highly stable even when exposed to heat. Some were monomeric and were amenable to analysis by nuclear magnetic resonance spectroscopy, allowing Koga *et al.* to determine the structure in solution of a designed sequence for each of the five fold types. The experimentally determined structures agreed well with the computational design models. The success rate of the authors' design strategy, defined as the percentage of experimentally tested proteins for each fold that exhibited a full set of desirable characteristics (see Table 1 of the paper<sup>1</sup>), was extraordinarily high, at 8–40%.

Researchers from the same laboratory as Koga *et al.* had previously reported<sup>4</sup> the impressive preparation of Top7 — a 93-residue  $\alpha/\beta$ -protein designed to adopt a tertiary structure not found in nature, and which incidentally satisfies the newly established design principles<sup>1</sup>. But the success of Koga and colleagues' protocol, and its incorporation of negative design, is a big step forward compared with that earlier work. With lengths of 80–100 amino acids, the authors' protein structures are comparable in size to small protein domains that act as building blocks of larger, more complex proteins. The design of custom protein scaffolds that perform new functions is now conceivable, as is the assembly of bigger designed domains and quaternary complexes.

Like machines, proteins can be assembled from smaller parts — such as secondary structural elements and single tertiary motifs — if those parts are connected by the right joints to form the 'chassis' for a specific function (Fig. 1). New enzymatic functions, such as the ability to catalyse a simple proton-transfer reaction<sup>5,6</sup>, have already been introduced into existing protein scaffolds in this way. Nevertheless, it is still tricky to design proteins that catalyse more complex reactions<sup>7</sup>, or which bind to specific ligand molecules<sup>8</sup>. The use of customized protein scaffolds might offer advantages for such efforts, but 'ideal' structures containing minimal peptide loops, such as those found in Koga and colleagues' sequences, will not, in many cases, provide enough space for catalytic (or ligand-binding)

sites. Such sites in naturally occurring proteins are often surrounded by longer loops.

So the next challenge for *de novo* enzyme design is to find ways of mitigating the potentially destabilizing effect of non-ideal loops, to allow the introduction of catalytic (and often charged) residues. A look at natural proteins illustrates how compromises can be struck. For example, the common TIM-barrel fold consists of eight  $\alpha$ -helices and eight  $\beta$ -strands alternating along the peptide backbone, and always harbours its catalytic residues in long loops found on one side of the barrel; the opposite side has short loops, and helps to stabilize the fold<sup>9</sup>. So perhaps a partial implementation of Koga and colleagues' fundamental rules — one that allows longer loops and/or naturally observed motifs to be copied in some places — will lead to further improvements in enzyme design. Other applications of the rules, such as

predicting protein structures, might be just as interesting. ■

**Birte Höcker** is at the Max Planck Institute for Developmental Biology, 72076 Tübingen, Germany.

e-mail: birte.hoecker@tuebingen.mpg.de

1. Koga, N. *et al.* *Nature* **491**, 222–227 (2012).
2. Leopold, P. E., Montal, M. & Onuchic, J. N. *Proc. Natl Acad. Sci. USA* **89**, 8721–8725 (1992).
3. Ramachandran, G. N., Ramakrishnan, C. & Sasisekharan, V. *J. Mol. Biol.* **7**, 95–99 (1963).
4. Kuhlman, B. *et al.* *Science* **302**, 1364–1368 (2003).
5. Röthlisberger, D. *et al.* *Nature* **453**, 190–195 (2008).
6. Korendovych, I. V. *et al.* *Proc. Natl Acad. Sci. USA* **108**, 6823–6827 (2011).
7. Baker, D. *Protein Sci.* **19**, 1817–1819 (2010).
8. Schreier, B., Stumpp, C., Wiesner, S. & Höcker, B. *Proc. Natl Acad. Sci. USA* **106**, 18491–18496 (2009).
9. Sterner, R. & Höcker, B. *Chem. Rev.* **105**, 4038–4055 (2005).

#### ASTROPHYSICS

## Cosmic explosions in the young Universe

**The discovery of two superluminous supernovae at large distances from Earth pushes the frontier of supernova studies to just 1.5 billion years after the Big Bang, and suggests that they may be common in the young Universe. SEE LETTER P.228**

STEPHEN J. SMARTT

**A**stronomers thrive in unexplored territory — whether that is the depths of dust clouds in our Galaxy, the immediate surroundings of a black hole or the farthest reaches of the Universe. For several decades, they have used the largest telescopes on Earth and in space to find the most distant sources of light in the Universe. The more distant the object, the longer its light has taken to travel to Earth, and the further back in time we can look. The most distant galaxies tell us how the Universe looked just 500 million years after the Big Bang<sup>1,2</sup>. Of course, the more luminous an object, the easier it is to detect at large distances. The discovery of new types of luminous stellar explosion, which only a few years ago were unknown, has opened a new window on the distant Universe. On page 228 of this issue, Cooke *et al.*<sup>3</sup> present the discovery of two distant stellar explosions, both of which seem to be superluminous supernovae\*.

Supernovae are stellar explosions that, until recently, were thought to come in two distinct varieties: type Ia supernovae and core-collapse supernovae. Type Ia supernovae originate from white-dwarf stars in two-star systems

that reach a critical mass by gaining mass from the companion star. Core-collapse supernovae derive from massive stars that fuse increasingly heavier elements in their cores, starting from hydrogen and helium and going all the way up to iron. This iron core eventually becomes too massive to support itself against gravity, collapsing and releasing about  $10^{46}$  joules of energy. The release of this energy, mostly in the form of neutrinos, drives a shock wave that causes the visible supernova when it hits the surface of the star. The resulting supernova radiates energy for several months, at a rate 1 billion times that of the Sun.

The search for type Ia supernovae in the distant Universe is well documented, and their use as standard candles to discover the existence of 'dark energy' resulted in last year's Nobel Prize in Physics. This discovery was made possible by finding these type Ia supernovae at large distances, corresponding to a redshift of about 0.7 — a time when the Universe was 7 billion years old, half its present age. The most recent surveys for type Ia supernovae, conducted with the Hubble Space Telescope, have detected<sup>4</sup> them out to redshift 1.55, whereas high-redshift core-collapse supernovae have been found<sup>5</sup> associated with  $\gamma$ -ray bursts at around redshift 1.

Cooke *et al.* have used data from the

\*This article and the paper under discussion<sup>3</sup> were published online on 31 October 2012.



Canada-France-Hawaii Telescope (CFHT) Legacy Survey in a new way to find, at high redshift, much more luminous supernovae than type Ia and core-collapse supernovae. In the past few years, surveys of the nearby Universe covering a wide field of view discovered a hitherto unknown group of supernovae that has been labelled<sup>6–8</sup> as “superluminous” and “ultraluminous” (Fig. 1). These are typically 10 times more luminous than type Ia supernovae and 100 times more luminous than normal core-collapse supernovae. A flurry of activity by astronomers getting to grips with these unusual events has resulted in their categorization into at least three distinct groups on the basis of their observed characteristics<sup>9</sup>. These results led Cooke *et al.* to apply a clever technique<sup>10</sup> to search for the most distant events. The authors added up all the available images from the CFHT Legacy Survey, which were taken at monthly intervals, to perform a search of a large volume of the high-redshift Universe. They found two transient events that look similar to some of the lower-redshift, superluminous supernovae.

One theory for the origin of superluminous supernovae, known as the pair-instability hypothesis, is that the progenitors were very massive stars, about 100–300 solar masses. In the 1960s, theorists predicted that if such massive stars could retain much of their initial mass, then their cores could get big enough and hot enough to create electron–positron pairs<sup>11</sup> (the positron is the electron’s antiparticle). This process can reduce the internal pressure of the stars such that their cores contract and reach temperatures greater than  $10^9$  °C — some 250 times hotter than the Sun’s core. This core contraction could result in 60 solar masses of carbon and oxygen instantly undergoing a massive thermonuclear explosion and fusing to make heavier elements all the way up to the iron group. This explosion produces unstable, radioactive nickel-56, which can decay to stable iron-56, releasing  $\gamma$ -rays that heat the supernova to superluminous intensities.

Models predict that 4–10 solar masses of nickel-56 could be produced. This process is similar to what goes on in a type Ia supernova, but in that case only 0.7 solar masses of nickel-56 are generated from a tiny white-dwarf star. Cooke *et al.* propose that the two superluminous supernovae that they have found are pair-instability supernovae.

Given their redshifts of 2.05 and 3.9, the new supernovae exploded 3 billion and 1.5 billion years after the Big Bang, respectively. The redshift-3.9 event is the most distant supernova discovered to date, although  $\gamma$ -ray bursts that might be associated with supernovae have been found at higher redshifts<sup>2,5</sup>. These new supernovae are undoubtedly intriguing transient events. Spectra of their host galaxies, obtained using the Keck telescope in Hawaii,

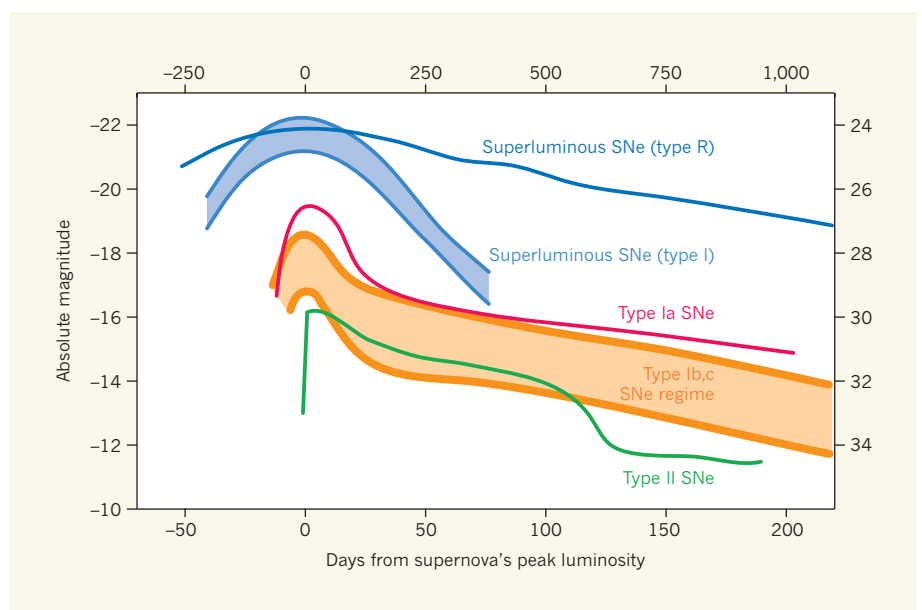


**Figure 1 | Superluminous supernovae and cosmological time dilation.** The graph plots luminosity against time for two types of superluminous supernova (R and I; see ref. 9) and for the traditional types (supernovae (SNe) type Ia and the core-collapse subtypes Ib, Ic and II). Magnitude is a logarithmic measure of an object’s luminosity, with one unit of magnitude corresponding to a factor of 2.5 in luminosity. The intrinsic (absolute) magnitude is shown on the left and the observed magnitude for a supernova at redshift ( $z$ ) 4 is shown on the right. Time is shown in days from the supernova’s peak luminosity, with time at the supernova’s location at the bottom and time as observed on Earth for a redshift-4 supernova at the top. Cooke *et al.*<sup>3</sup> have discovered two superluminous supernovae, at redshifts 2.05 and 3.9, by adding together images from the CFHT Legacy Survey in monthly blocks. This approach does not result in loss of time resolution when looking back at high redshifts. Cosmological time dilation means that observers see the Universe evolve more slowly, by a factor of  $1 + z$ , than they would if they were at the object’s location. The authors obtained an effective time sampling of the real variation in luminosity five times shorter than is actually observed for the redshift-3.9 supernova.

allowed the unambiguous measurement of the redshifts. However, there are no spectra of the supernovae themselves, which would be crucial for confirming their physical nature. In addition, there is only one well-documented case of a pair-instability supernova candidate, called SN2007bi, in the local Universe with which to compare the new systems<sup>12,13</sup>. Papers and posters presented at supernova-related conferences in the past year indicate that wide-field surveys shallower than that undertaken by Cooke *et al.* have found a few more examples — but they are rare<sup>9</sup>. The physical nature of SN2007bi has also been subject to debate, with some authors doubting its pair-instability nature and suggesting a normal core-collapse mechanism in a very massive star<sup>13</sup> or a supernova enhanced by a magnetic neutron star<sup>14</sup>.

For many years, astronomers have dreamed of finding the first supernovae in the Universe at redshifts beyond 10, and theory has predicted that very massive stars and pair-instability supernovae could be prevalent at such redshifts. In one leap, Cooke *et al.* have expanded our horizons to show that it is now possible to find supernovae out to redshift 4. Uncertainty remains over the nature of these superluminous explosions both at high and low redshifts. Yet the work of Cooke *et al.* shows that superluminous supernovae, of

some type, existed in the young Universe, and that their frequency might be much higher than we see locally. The next challenge is to find them as they reach peak luminosity, obtain their spectra to understand exactly what they are, and use them as probes of the high-redshift Universe<sup>15</sup>. ■

**Stephen J. Smartt** is at the *Astrophysics Research Centre, School of Mathematics and Physics, Queen’s University Belfast, Belfast BT7 1NN, UK.*  
e-mail: s.smartt@qub.ac.uk

1. Zheng, W. *et al. Nature* **489**, 406–408 (2012).
2. Tanvir, N. R. *et al. Nature* **461**, 1254–1257 (2009).
3. Cooke, J. *et al. Nature* **491**, 228–231 (2012).
4. Rodney, S. A. *et al. Astrophys. J.* **746**, 5 (2012).
5. Hjorth, J. & Bloom, J. S. in *Gamma-Ray Bursts* (eds Kouveliotou, C., Wijers, R. A. M. J. & Woosley, S. E.) Ch. 9 (Cambridge Univ. Press, 2011).
6. Quimby, R. M. *et al. Nature* **474**, 487–489 (2011).
7. Pastorello, A. *et al. Astrophys. J. Lett.* **724**, L16 (2010).
8. Chomiuk, L. *et al. Astrophys. J.* **743**, 114 (2011).
9. Gal-Yam, A. *Science* **337**, 927–932 (2012).
10. Cooke, J. *et al. Nature* **460**, 237–239 (2009).
11. Rakavy, G. & Shaviv, G. *Astrophys. J.* **148**, 803 (1967).
12. Gal-Yam, A. *et al. Nature* **462**, 624–627 (2009).
13. Young, D. R. *et al. Astron. Astrophys.* **512**, A70 (2010).
14. Dessart, L. *et al. Mon. Not. R. Astron. Soc. Lett.* **426**, L76–L80 (2012).
15. Berger, E. *et al. Astrophys. J. Lett.* **755**, L29 (2012).

# An Earth-mass planet orbiting $\alpha$ Centauri B

Xavier Dumusque<sup>1,2</sup>, Francesco Pepe<sup>1</sup>, Christophe Lovis<sup>1</sup>, Damien Ségransan<sup>1</sup>, Johannes Sahlmann<sup>1</sup>, Willy Benz<sup>3</sup>, François Bouchy<sup>1,4</sup>, Michel Mayor<sup>1</sup>, Didier Queloz<sup>1</sup>, Nuno Santos<sup>2,5</sup> & Stéphane Udry<sup>1</sup>

**Exoplanets down to the size of Earth have been found, but not in the habitable zone—that is, at a distance from the parent star at which water, if present, would be liquid. There are planets in the habitable zone of stars cooler than our Sun, but for reasons such as tidal locking and strong stellar activity, they are unlikely to harbour water-carbon life as we know it. The detection of a habitable Earth-mass planet orbiting a star similar to our Sun is extremely difficult, because such a signal is overwhelmed by stellar perturbations. Here we report the detection of an Earth-mass planet orbiting our neighbour star  $\alpha$  Centauri B, a member of the closest stellar system to the Sun. The planet has an orbital period of 3.236 days and is about 0.04 astronomical units from the star (one astronomical unit is the Earth-Sun distance).**

Since the discovery of the first exoplanet orbiting a solar-type star in 1995<sup>1</sup>, the number of known planets has not stopped growing: at present, there are more than 750 confirmed planets<sup>2</sup> with minimum mass estimates, and over 2,300 transiting planet candidates detected with the Kepler satellite that are awaiting confirmation. Two main detection techniques have led to this impressive number of discoveries: the radial-velocity technique, which measures the change in the velocity of the central star due to the gravitational pull of an orbiting planet; and the transit method, which measures the small reduction in flux when a planet passes in front of its host star. These two techniques are complementary; the former gives the minimum mass of a planet (minimum because the orbital inclination of the planet is unknown), whereas the latter gives a planet's radius.

One of the major challenges in the search for exoplanets is the detection of an Earth twin, that is, an Earth-mass planet orbiting in the star's habitable zone. In this regard,  $\alpha$  Centauri B is one of the most interesting targets. At a distance of 1.3 parsecs, it is a member of the closest stellar system to the Sun, composed of itself,  $\alpha$  Centauri A and Proxima Centauri. It also exhibits low stellar activity, similar to the solar activity level, usually associated with a small perturbing contribution of intrinsic stellar activity to the measured radial velocities.  $\alpha$  Centauri B is cooler than the Sun (effective temperature<sup>3–6</sup>  $5,214 \pm 33$  K, spectral type K1V), and has a smaller mass than our parent star<sup>7</sup> ( $0.934 \pm 0.006$  solar masses). These two conditions ease the detection of a potentially habitable planet using radial velocities; the relative coolness implies a habitable zone closer to the star, and the smaller mass leads to a stronger radial-velocity variation for a similar-mass planet. In addition, theoretical studies show that the formation of an Earth twin is possible around  $\alpha$  Centauri B<sup>8,9</sup>. Finally, the brightness of the star (visual magnitude 1.33) would allow for an efficient characterization of the atmosphere of potentially orbiting planets.

An Earth twin induces a typical radial-velocity variation of a few tenths of a metre per second on a star like  $\alpha$  Centauri B. Such detections, technically possible with the most stable high-resolution spectrographs, are however challenging due to the presence of intrinsic stellar signals inducing a radial-velocity 'jitter' at the level of a few metres per second, even for quiet stars.

We report here the discovery of a planetary companion around  $\alpha$  Centauri B, unveiled by a radial-velocity signal with a semi-amplitude  $K$  of  $0.51 \text{ m s}^{-1}$ , a period  $P$  of 3.236 d, and a semi-major axis  $a$  of

0.04 astronomical units (AU). This planet, with a minimum mass similar to that of Earth, is both the lightest orbiting a solar-type star and the closest to the Solar System found to date. Being much closer to its parent star than Earth is to the Sun, it is not an Earth twin. However, the small amplitude of the signal shows that the radial-velocity technique is capable of reaching the precision needed to detect habitable super-Earth planets around stars similar to our Sun, or even habitable Earths around cooler stars (that is, M-dwarfs). In addition, statistical studies of exoplanets suggest that low-mass planets are preferentially formed in multi-planetary systems<sup>10–12</sup>. There is therefore a high probability that other planets orbit  $\alpha$  Centauri B, perhaps in its habitable zone.

## High-precision radial velocities

High-precision measurements were obtained for  $\alpha$  Centauri B between February 2008 and July 2011 using the HARPS spectrograph (Supplementary Information section 1, and Supplementary Data). HARPS is a high-resolution ( $R = 110,000$ ) cross-dispersed echelle spectrograph installed on the 3.6-m telescope at La Silla Observatory (ESO, Chile). This instrument has demonstrated a long-term precision of  $0.8 \text{ m s}^{-1}$ , thereby becoming the most powerful machine with which to hunt for exoplanets using the radial-velocity technique<sup>12,13,14</sup>.  $\alpha$  Centauri B was observed with HARPS following an intensive observational strategy, optimized to sample high- and medium-frequency intrinsic stellar signals<sup>15</sup>, which makes it possible to model and consequently remove their perturbing contributions. The star was observed every possible night three times, with exposure times of ten minutes, and with measurements optimally separated by two hours<sup>14</sup>.

The raw radial velocities of  $\alpha$  Centauri B (Fig. 1a) exhibit several contributing signals that we could identify. Their origin is associated with instrumental noise, stellar oscillation modes, granulation at the surface of the star, rotational activity, long-term activity induced by a magnetic cycle, the orbital motion of the binary composed of  $\alpha$  Centauri A and B, light contamination from  $\alpha$  Centauri A, and imprecise stellar coordinates.

In the following, we will consider each of these contributions separately, modelling and removing them one by one, from the largest to the smallest amplitude. The model parameters estimated for each contribution will then be used as initial conditions for a global fit that

<sup>1</sup>Observatoire de Genève, Université de Genève, 51 chemin des Maillettes, CH-1290 Sauverny, Switzerland. <sup>2</sup>Centro de Astrofísica da Universidade do Porto, Rua das Estrelas, P-4150-762 Porto, Portugal.

<sup>3</sup>Physikalisches Institut Universität Bern, Sidlerstrasse 5, CH-3012 Bern, Switzerland. <sup>4</sup>Institut d'Astrophysique de Paris, UMR7095 CNRS, Université Pierre & Marie Curie, 98bis Boulevard Arago, F-75014 Paris, France. <sup>5</sup>Departamento de Física e Astronomia, Faculdade de Ciências, Universidade do Porto, Rua do Campo Alegre s/n, P-4169-007 Porto, Portugal.



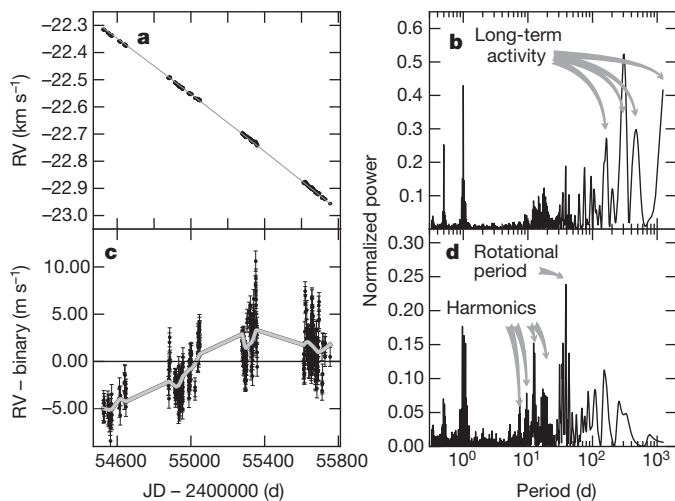


**Figure 1 | Radial velocities of  $\alpha$  Centauri B and fitting the long-timescale stellar signals.** **a**, Raw radial velocities (RV) and the fit of the binary's signature ( $\alpha$  Centauri B orbiting  $\alpha$  Centauri A). In the residuals (**c**), signals at long period are visible. These signals, highlighted by grey arrows ('long-term activity') in periodogram **b**, correspond to the effect of the magnetic cycle. The grey curve in **c** shows the variation of the low-frequency part of the activity index scaled to the radial-velocity variation. When these low-frequency perturbations are removed, signals induced by rotational activity, pointed out by grey arrows in periodogram **d**, can be seen at the rotation period of the star and its harmonics. JD, Julian date. Error bars in **c**,  $1\sigma$ .

will remove all the identified radial-velocity signals. In the residuals, we will be able to search for small-amplitude planetary signals.

### Perturbing signals for planet searches

$\alpha$  Centauri B is a quiet star among the targets monitored in searches for low-mass planets. However, the very high precision of HARPS allows us to discern in the measurements different perturbing signals at the metre-per-second level. Compared to the radial-velocity signal induced by terrestrial planets, a few to a few tens of centimetres per second, these perturbing signals are non-negligible and must be modelled and mitigated before searching for small-mass planets.

**Instrumental noise.** Guiding noise and other possible instrumental noise are not considered in the data error bars. Their global effect is estimated to be  $0.7 \text{ m s}^{-1}$ , given the typical dispersion obtained for the most stable stars of the HARPS high-precision programme<sup>14</sup>.

**Stellar oscillation modes.**  $\alpha$  Centauri B exhibits high-frequency oscillation modes<sup>16,17</sup>, with typical periods of less than five minutes. An exposure time of ten minutes thus averages out efficiently, to a level of a few centimetres per second, the signal due to oscillation modes.

**Granulation.**  $\alpha$  Centauri B is a solar-type star and has therefore an outer convection zone responsible for a granulation pattern on its surface. Depending on temperature, granulation cells have positive or negative radial velocities, resulting in a non-zero global radial-velocity signal when their individual contributions are integrated over the disk of the star, weighted by the luminosity of the cells. The granulation effect introduces radial-velocity variations on timescales ranging from 15 min to several hours<sup>18,19</sup>. For  $\alpha$  Centauri B, models of granulation<sup>20</sup> suggest an r.m.s. radial velocity of  $0.6 \text{ m s}^{-1}$ .

**Rotational activity signal.** Owing to stellar rotation and the Doppler effect, one side of the star has a positive radial velocity compared to the average, while the other side has a negative one. However, if a spot (darker or brighter than the mean stellar surface) is present on one side of the star, the velocity balance will be broken and a residual radial velocity will be measured. With stellar rotation, a spot will move from one side of the stellar disk to the other, introducing periodic signals at the stellar rotational period and the corresponding harmonics<sup>21</sup>. The lifetime of spots on the stellar surface is typically a few rotational

periods<sup>22</sup>, so after several rotations, the configuration of spots will be different, thus changing the phase and amplitude of the signal.

The radial velocities of  $\alpha$  Centauri B show a clear signal at 38.7 d (Figs 1d and 2b), which corresponds to the rotational period of the star<sup>23</sup>. An efficient way to model rotational activity effects is to select radial-velocity measurements over time intervals of a few rotational periods, and fit sine waves at the rotational period and the corresponding harmonics<sup>21</sup> (Supplementary Information section 2). The best fit for the rotational activity signal for each observational season can be seen in Fig. 3.

**Long-term activity signal.** During a solar-like magnetic cycle, the number of spots on the stellar surface (dark spots, plage faculae) varies from zero to several hundreds. Inside these spots, a strong magnetic field is present, which freezes the convection<sup>24–28</sup>. For the Sun, as for other stars similar to  $\alpha$  Centauri B in spectral type<sup>29</sup>, convection induces a blueshift of the stellar spectra<sup>30–32</sup>. Therefore, no convection means no convective blueshift inside these regions, and so the spectrum of the integrated stellar surface will appear redshifted. Because a redshift means a measured positive radial velocity, a positive correlation between the magnetic cycle variation and the long-term radial-velocity variation is then expected.

$\alpha$  Centauri B shows signs of weak but detectable chromospheric activity, evidenced by the re-emission in the centre of the Ca II H and K lines (the  $\log(R'_{\text{HK}})$  activity index).  $\alpha$  Centauri B exhibits a magnetic cycle with a minimum amplitude of  $A_{R'_{\text{HK}}} \approx 0.11 \text{ dex}$  (Fig. 2a). To correct the radial-velocity effect due to the magnetic cycle (see Fig. 1b and c), we assume a linear correlation between the  $\log(R'_{\text{HK}})$  activity index and the activity-related radial-velocity variation<sup>33</sup> (that is, both variations have the same shape; Supplementary Information section 3).

**Orbital motion.** The orbital period of the binary composed of  $\alpha$  Centauri A and B is  $P_{\text{AB}} = 79.91 \text{ yr}$  (ref. 7). The HARPS observations of  $\alpha$  Centauri B cover an interval of only four years. The orbit of the system over such an interval can then adequately be approximated by a second order polynomial (see Fig. 1a).

**Light contamination.** Owing to the close separation on the sky between  $\alpha$  Centauri A and B, the spectra of B can be contaminated by light coming from A when the observing conditions are poor. The resulting effect on the radial-velocity measurements was estimated

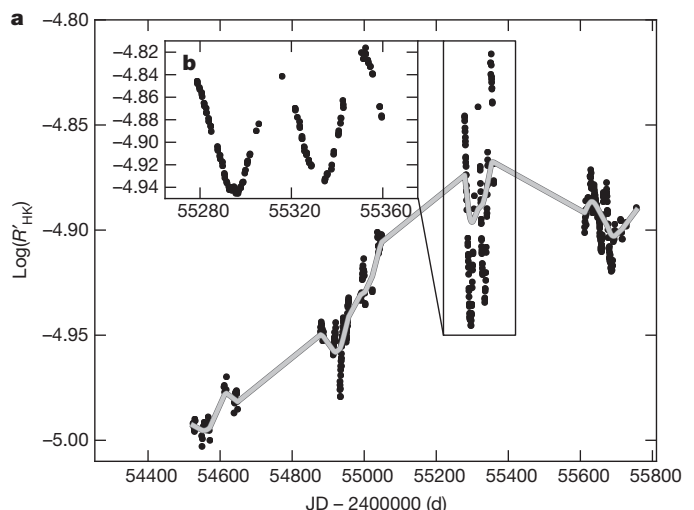


**Figure 2 | Magnetic cycle of  $\alpha$  Centauri B.** **a**, The grey curve represents a low pass filter applied to the activity index measurements (data points). **b**, The observations done in 2010 are zoomed in to show the variation induced by rotational activity, which highlights the HARPS precision in determining activity indexes. Error bars ( $1\sigma$ ) are smaller than the data points (that is, smaller than 0.015 dex).

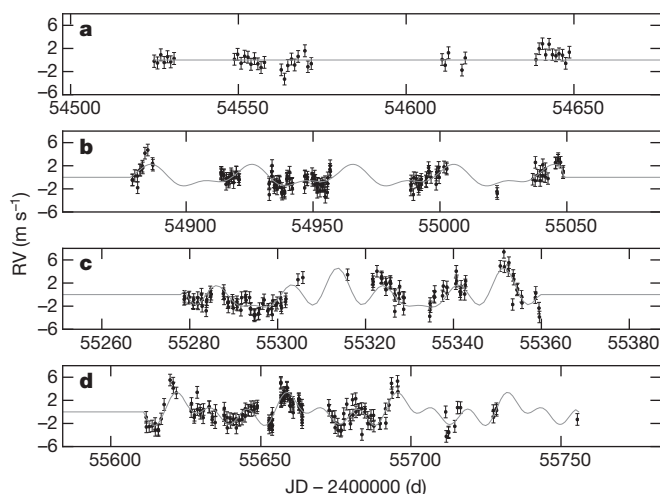


**Figure 3 | Fit of the rotational activity.** **a–d**, Radial velocities (RV) of  $\alpha$  Centauri B after correction of the binary's signature (of  $\alpha$  Centauri A), magnetic-cycle and coordinates effects, for the years 2008 (**a**), 2009 (**b**), 2010 (**c**) and 2011 (**d**), are shown as black dots with  $1\sigma$  error bars. The grey curve represents for each plot the fit of the rotational activity signal, adjusting sinusoids at the stellar rotational period and the corresponding harmonics. The rotational period estimated from the stellar activity model decreases from the second season of observation to the last, with estimated periods (in days) of 39.76 (**b**), 37.80 (**c**) and 36.71 (**d**) (Supplementary Information section 6). This can be explained if the star exhibits differential rotation. Indeed, it has been shown for the Sun that spots appear at a latitude of  $+30^\circ$  or  $-30^\circ$  at the start of a magnetic cycle (like in 2008) and then migrate towards the equator during the cycle. Owing to differential rotation, observed for the Sun, the rotational period estimated by activity modelling should decrease from the start to the end of a magnetic cycle. A similar effect is seen here for  $\alpha$  Centauri B. We therefore believe that differential rotational has been detected here for this slow rotator<sup>41</sup> (X.D. *et al.*, manuscript in preparation).

and problematic observations discarded (Supplementary Information section 4).

**Imprecise stellar coordinates.** When estimating stellar radial velocities with regard to the barycentre of the Solar System, we need to remove the component of the velocity of the Earth in the direction of the star. Imprecise coordinates will then result in an imprecise correction and therefore in a residual signal in the radial velocities. This effect was first pointed out when searching for planets around pulsars, when the times of arrival were varying periodically in time owing to imprecise pulsar coordinates<sup>34</sup>. Owing to the circular orbit of the Earth around the Sun, this signal will be a sinusoid with a one-year period.  $\alpha$  Centauri A and B are gravitationally bound, resulting in a binary orbital motion, which has to be corrected to obtain precise coordinates for  $\alpha$  Centauri B (Supplementary Information section 5).

## Removing the various signals

The approaches used to remove or mitigate the effects of the various signals potentially masking the existence of a low-mass planet have been described in the preceding paragraphs. For contamination coming from  $\alpha$  Centauri A, we removed observations with a too-high level of contamination. For instrumental noise and granulation that cannot be easily modelled, the estimated radial-velocity contribution from each source is quadratically added as white noise to the raw error bars. For the other effects, parametric models have been proposed. A global fit to the data, including the binary signal, the long-term activity signal and the rotational activity effect, involves 23 free parameters (Supplementary Information section 6).

## A planet with a minimum mass that of the Earth

The generalized Lomb-Scargle periodogram<sup>35</sup> of the radial-velocity residuals shows two peaks at 3.236 and 0.762 d, with a false alarm

probability (FAP) lower than a conservative 1% limit (Fig. 4a). These two periods are aliases of one another. A careful analysis of the structure in frequency of the periodogram suggests that the peak at 3.236 d is the true signal (Supplementary Information section 7).

The global model makes use of parameters associated with different timescales. One could thus worry whether the signal at 3.236 d could have been introduced during the process of eliminating the stellar signals. We performed Monte Carlo simulations to determine if this could be the case, and concluded that the signal is real and not an artefact of the fitting process (Supplementary Information section 8).

The peak at 3.236 d in the radial-velocity residuals is significant with a FAP of 0.02%. Using a Markov chain Monte Carlo algorithm coupled to a genetic algorithm to characterize the Keplerian solution, we obtained a signal with a well-constrained period and amplitude. The eccentricity is poorly constrained but is compatible with zero within a  $1.4\sigma$  uncertainty (Supplementary Information section 9). To fit this planetary signal simultaneously with the other contributions to the radial velocities, we added a sinusoidal signal representing the circular planet orbit to the global fit (Supplementary Information section 6). The observed dispersion of the residuals around the final solution is  $1.20 \text{ m s}^{-1}$  and the reduced  $\chi^2$  value is 1.51 (with 26 parameters for 459 radial-velocity points). The semi-amplitude of the planetary signal is  $K = 0.51 \pm 0.04 \text{ m s}^{-1}$ , which corresponds to a planet with a minimum mass of  $1.13 \pm 0.09$  Earth masses considering a stellar mass of 0.934 solar masses and with an orbital period of  $P = 3.2357 \pm 0.0008 \text{ d}$ . The orbital and planet parameters are given in Table 1. In the residuals of the global fit, a signal with an FAP of 0.3% is present; however, it could have multiple origins (Supplementary Information section 6).

In Fig. 5, we show the radial-velocity measurements corrected for stellar and binary effects, folded in phase with the 3.236-d period, superimposed on the derived solution for the planetary signal. In

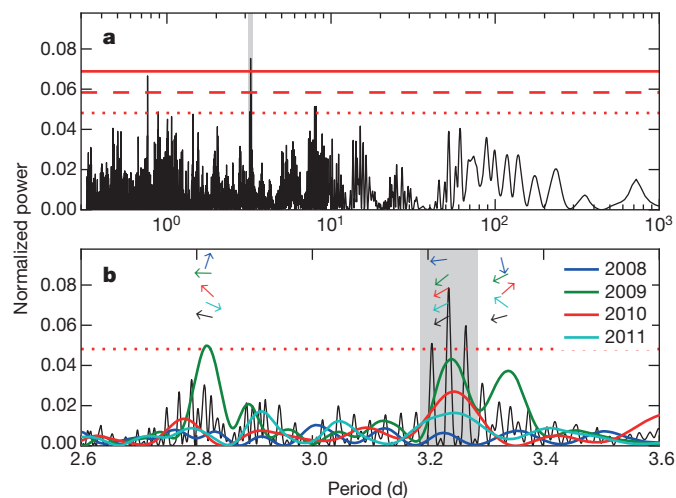


**Figure 4 | Periodograms of the radial-velocity residuals after removing the non-planetary signals.** **a**, The periodogram of the velocities after correction for stellar, imprecise coordinates and binary effects, with continuous, dashed and dotted lines indicating the 0.1%, 1% and 10% FAP, respectively. The highest peak, at 3.236 d inside the shaded region, has an FAP of 0.02%. **b**, A small part of the periodogram around the planet signal is represented. The periodogram for all seasons is shown in black, and the yearly periodograms for each observational period (2008, 2009, 2010 and 2011) are shown in different colours. The amplitudes of the yearly periodograms are normalized so that the 10% FAP of each matches the 10% FAP of the periodogram for all seasons. The phase of the most important peaks is shown (arrows); the direction of the arrow gives the phase between  $0^\circ$  and  $360^\circ$ . For each year of observation, the peak at 3.236 d conserves the same phase, which is expected for a planetary signal. On the contrary, the peak at 2.8 d and its alias at 3.35 d do not keep the same phase and are therefore associated with noise (these peaks appear only in 2009 and their FAPs are higher than 10%).



**Table 1 | Orbital parameters of the planet orbiting  $\alpha$  Centauri B**

Parameter	Value
Orbital period (d)	$3.2357 \pm 0.0008$
Time of maximum velocity (BJD)	$2455280.17 \pm 0.17$
Eccentricity	0.0 (fixed)
Velocity semi-amplitude ( $\text{m s}^{-1}$ )	$0.51 \pm 0.04$
Minimum mass (Earth masses)	$1.13 \pm 0.09$
Number of data points	459
O – C residuals ( $\text{m s}^{-1}$ )	1.20
Reduced $\chi^2$ value	1.51

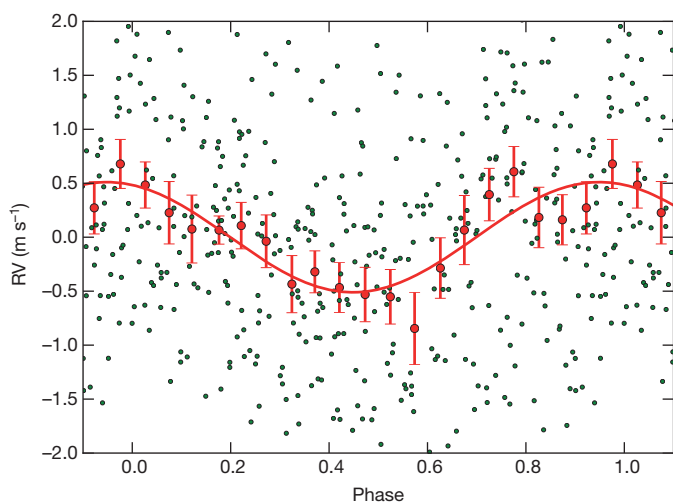
BJD, barycentric Julian date; O – C, observed minus calculated.

Fig. 4b we show that the 3.236-d signal conserves its phase for each observational year, which is expected for a planetary signal.

An important piece of information about the inner composition of an exoplanet is obtained when the planet is transiting its parent star, allowing its radius to be measured. Combined with the real mass estimate, the radius leads to the average density of the planet. In the present case, given a stellar radius<sup>36</sup> of 0.863 times the solar radius and assuming the radius of the planet is that of the Earth, the planet transit probability is estimated at 10%, with a transit depth of  $10^{-4}$ . The detection of a planet transit, only possible from space, would allow us to confirm the expected rocky nature of the detected planet around  $\alpha$  Centauri B.

The r.m.s. radial velocity induced by the stellar rotational activity amounts to  $1.5 \text{ m s}^{-1}$  on average. The detection of the tiny planetary signal, with a semi-amplitude  $K = 0.51 \text{ m s}^{-1}$ , thus demonstrates that stellar activity is not necessarily a definitive limitation to the detection of small-mass planets. Using an optimized observational strategy and the present knowledge about activity-induced radial-velocity effects, it is possible to model precisely and mitigate activity signals, and therefore improve considerably the planet detection limits.

With a separation from its parent star of only 0.04 AU, the planet is orbiting very close to  $\alpha$  Centauri B compared to the location of the habitable zone. However, the observed radial-velocity semi-amplitude is equivalent to that induced by a planet of minimum mass four times that of Earth in the habitable zone of the star ( $P = 200 \text{ d}$ ; ref. 37).

**Figure 5 | Phase-folded radial-velocity curve with a period of 3.2357 d.**

Green dots, radial velocities after correction of the stellar, binary and coordinates effects. Red dots, the same radial velocities binned in phase, with a bin size of 0.05. The error bar of a given bin is estimated using the weighted r.m.s. of the global fit residuals (including the planetary fit) that make this bin, divided by the square root of the number of measurements included in this bin. This estimation of the bin error bars assumes Gaussian noise, which is justified by the binning in phase, which regroups points that are uncorrelated in time. The r.m.s. around the planetary solution is  $1.20 \text{ m s}^{-1}$  for the raw points (green dots) and  $0.21 \text{ m s}^{-1}$  for the binned points (red dots). The red curve represents the global fit solution of the planet, with a semi-amplitude of  $0.51 \text{ m s}^{-1}$ .

The HARPS spectrograph therefore has the precision required to detect a new category of planets, namely habitable super-Earths. This sensitivity was expected from simulations of intrinsic stellar signals<sup>15</sup>, and actual observations of planetary systems<sup>14</sup>.

The optimized observational strategy used to monitor  $\alpha$  Centauri B is capable of reaching the precision needed to search for habitable super-Earths around solar-type stars using the radial-velocity technique. However, it requires an important investment in observation time, and thus only few targets can be observed over several years. Recent statistical analyses and theoretical models of planetary formation suggest that low-mass rocky planets and especially Earth twins should be common<sup>12,38–40</sup>. We are therefore confident that we are on the right path to the discovery of Earth analogues.

Received 3 August; accepted 13 September 2012.

Published online 17 October 2012.

- Mayor, M. & Queloz, D. A Jupiter-mass companion to a solar-type star. *Nature* **378**, 355–359 (1995).
- Schneider, J., Dedieu, C., Le Sidaner, P., Savalle, R. & Zolotukhin, I. Defining and cataloging exoplanets: the exoplanet.eu database. *Astron. Astrophys.* **532**, A79 (2011).
- Fuhrmann, K. et al. BESO échelle spectroscopy of solar-type stars at Cerro Armazones. *Mon. Not. R. Astron. Soc.* **411**, 2311–2318 (2011).
- Valenti, J. A. & Fischer, D. A. Spectroscopic properties of cool stars (SPOCS). I. 1040 F, G, and K dwarfs from Keck, Lick, and AAT planet search programs. *Astrophys. J. Suppl. Ser.* **159**, 141–166 (2005).
- Santos, N. C. et al. Spectroscopic metallicities for planet-host stars: extending the samples. *Astron. Astrophys.* **437**, 1127–1133 (2005).
- Neuforge-Verheecke, C. & Magain, P. Spectroscopic analysis of the Alpha Centauri system. *Astron. Astrophys.* **328**, 261–268 (1997).
- Pourbaix, D. et al. Constraining the difference in convective blueshift between the components of  $\alpha$  Centauri with precise radial velocities. *Astron. Astrophys.* **386**, 280–285 (2002).
- Xie, J.-W., Zhou, J.-L. & Ge, J. Planetesimal accretion in binary systems: could planets form around  $\alpha$  Centauri B? *Astrophys. J.* **708**, 1566–1578 (2010).
- Thébaud, P., Marzari, F. & Scholl, H. Planet formation in the habitable zone of  $\alpha$  Centauri B. *Mon. Not. R. Astron. Soc.* **393**, L21–L25 (2009).
- Lissauer, J. J., Ragozzine, D., Fabrycky, D. C., Steffen, J. H. & Ford, E. B. Architecture and dynamics of Kepler's candidate multiple transiting planet systems. *Astrophys. J. Suppl. Ser.* **197**, 8 (2011).
- Latham, D. W., Rowe, J. F., Quinn, S. N., Batalha, N. M. & Borucki, W. J. A first comparison of Kepler planet candidates in single and multiple systems. *Astrophys. J.* **732**, L24 (2011).
- Mayor, M. et al. The HARPS search for southern extra-solar planets. XXXIV. Occurrence, mass distribution and orbital properties of super-Earths and Neptune-mass planets. *Astron. Astrophys.* (submitted); preprint at <http://arxiv.org/abs/1109.2497> (2011).
- Lovis, C. et al. The HARPS search for southern extra-solar planets. XXVIII. Up to seven planets orbiting HD 10180: probing the architecture of low-mass planetary systems. *Astron. Astrophys.* **528**, A112 (2011).
- Pepe, F. et al. The HARPS search for Earth-like planets in the habitable zone. Very low mass planets around HD29794, HD8512 and HD192310. *Astron. Astrophys.* **534**, A58 (2011).
- Dumusque, X., Santos, N. C., Udry, S., Lovis, C. & Bonfils, X. Planetary detection limits taking into account stellar noise. II. Effect of stellar spot groups on radial-velocities. *Astron. Astrophys.* **527**, A82 (2011).
- Kjeldsen, H. et al. Solar-like oscillations in Alpha Centauri B. *Astrophys. J.* **635**, 1281–1290 (2005).
- Carrier, F. & Bourban, G. Solar-like oscillations in the K1 dwarf star alpha Cen B. *Astron. Astrophys.* **406**, L23–L26 (2003).
- Del Moro, D. Solar granulation properties derived from three different time series. *Astron. Astrophys.* **428**, 1007–1015 (2004).
- Title, A. M. et al. Statistical properties of solar granulation derived from the SOUP instrument on Spacelab 2. *Astrophys. J.* **336**, 475–494 (1989).
- Dumusque, X., Udry, S., Lovis, C., Santos, N. C. & Monteiro, M. J. Planetary detection limits taking into account stellar noise. I. Observational strategies to reduce stellar oscillation and granulation effects. *Astron. Astrophys.* **525**, A140 (2011).
- Boisse, I. et al. Disentangling between stellar activity and planetary signals. *Astron. Astrophys.* **528**, A4 (2011).
- Howard, R. & Murdin, P. in *Encyclopedia of Astronomy and Astrophysics* (ed. Murdin, P.) 3173–3177 (Institute of Physics Publishing, 2000).
- DeWaf, L. E., Datin, K. M. & Guinan, E. F. X-Ray, FUV, and UV observations of  $\alpha$  Centauri B: determination of long-term magnetic activity cycle and rotation period. *Astrophys. J.* **722**, 343–357 (2010).
- Meunier, N., Desort, M. & Lagrange, A.-M. Using the Sun to estimate Earth-like planets detection capabilities. II. Impact of plages. *Astron. Astrophys.* **512**, A39 (2010).
- Gray, D. F. *The Observation and Analysis of Stellar Photospheres* (Cambridge Univ. Press, 1992).
- Brandt, P. N. & Solanki, S. K. Solar line asymmetries and the magnetic filling factor. *Astron. Astrophys.* **231**, 221–234 (1990).

27. Livingston, W. C. Magnetic fields, convection and solar luminosity variability. *Nature* **297**, 208–209 (1982).
28. Dravins, D. in *Stellar Radial Velocities* (eds Philip, A. G. D. & Latham, D. W.) 311–320 (IAU Colloquium 88, IAU, 1985).
29. Gray, D. F. The third signature of stellar granulation. *Astrophys. J.* **697**, 1032–1043 (2009).
30. Dravins, D., Larsson, B. & Nordlund, A. Solar Fe II line asymmetries and wavelength shifts. *Astron. Astrophys.* **158**, 83–88 (1986).
31. Kaisig, M. & Durrant, C. J. The asymmetry of photospheric absorption lines. I — an analysis of mean solar line profiles. *Astron. Astrophys.* **116**, 332–340 (1982).
32. Beckers, J. M. & Nelson, G. D. Some comments on the limb shift of solar lines. II — The effect of granular motions. *Sol. Phys.* **58**, 243–261 (1978).
33. Lovis, C. *et al.* The HARPS search for southern extra-solar planets. XXXI. Magnetic activity cycles in solar-type stars: statistics and impact on precise radial velocities. *Astron. Astrophys.* (submitted); preprint at <http://arxiv.org/abs/1107.5325> (2011).
34. Wolszczan, A. & Kuchner, M. in *Exoplanets* (ed. Seager, S.) 175–190 (Univ. Arizona Press, 2010).
35. Zechmeister, M. & Kürster, M. The generalised Lomb-Scargle periodogram. A new formalism for the floating-mean and Keplerian periodograms. *Astron. Astrophys.* **496**, 577–584 (2009).
36. Kervella, P. *et al.* The diameters of  $\alpha$  Centauri A and B. A comparison of the asteroseismic and VINCI / VLT views. *Astron. Astrophys.* **404**, 1087–1097 (2003).
37. Selsis, F. *et al.* Habitable planets around the star Gliese 581? *Astron. Astrophys.* **476**, 1373–1387 (2007).
38. Bonfils, X. *et al.* The HARPS search for southern extra-solar planets. XXXI. The M-dwarf sample. *Astron. Astrophys.* (submitted) preprint at <http://arxiv.org/abs/1111.5019>.
39. Mordasini, C., Alibert, Y., Benz, W. & Naef, D. Extrasolar planet population synthesis. II. Statistical comparison with observations. *Astron. Astrophys.* **501**, 1161–1184 (2009).
40. Cassan, A. *et al.* One or more bound planets per Milky Way star from microlensing observations. *Nature* **481**, 167–169 (2012).
41. Barnes, J. R. *et al.* The dependence of differential rotation on temperature and rotation. *Mon. Not. R. Astron. Soc.* **357**, L1–L5 (2005).

**Supplementary Information** is available in the online version of the paper.

**Acknowledgements** The data presented here were obtained with the ESO 3.6-m telescope at La Silla Paranal Observatory, Chile. We thank the Swiss National Science Foundation (FNRS) for continuous support. We thank R. Mardeling for English revision. N.S. and X.D. acknowledge support by the European Research Council/European Community under FP7 through Starting Grant agreement number 239953, as well as from Fundacao para a Ciencia e a Tecnologia (FCT) through programme Ciencia 2007 funded by FCT/MCTES (Portugal) and POPH/FSE (EC), and in the form of grants PTDC/CTE-AST/098528/2008 and PTDC/CTE-AST/098604/2008.

**Author Contributions** F.P., C.L., W.B., F.B., M.M., D.Q., N.S. and S.U. obtained data under the ESO programme ‘Searching for Earth-analogs around nearby stars with HARPS’. The HARPS spectrograph was designed and built by F.P., C.L., W.B., F.B., M.M., D.Q. and S.U. C.L. and D.S. performed the reduction of the data. Data analysis was carried out by X.D., J.S., F.P., D.S. and C.L. All the work was supervised by S.U. All authors discussed the results and contributed to the manuscript.

**Author Information** Reprints and permissions information is available at [www.nature.com/reprints](http://www.nature.com/reprints). The authors declare no competing financial interests. Readers are welcome to comment on the online version of the paper. Correspondence and requests for materials should be addressed to X.D. ([xavier.dumusque@unige.ch](mailto:xavier.dumusque@unige.ch)) and F.P. ([francesco.pepe@unige.ch](mailto:francesco.pepe@unige.ch)).



# Input-specific control of reward and aversion in the ventral tegmental area

Stephan Lammel<sup>1\*</sup>, Byung Kook Lim<sup>1\*</sup>, Chen Ran<sup>1</sup>, Kee Wui Huang<sup>1</sup>, Michael J. Betley<sup>1</sup>, Kay M. Tye<sup>2</sup>, Karl Deisseroth<sup>3</sup> & Robert C. Malenka<sup>1</sup>

**Ventral tegmental area (VTA) dopamine neurons have important roles in adaptive and pathological brain functions related to reward and motivation. However, it is unknown whether subpopulations of VTA dopamine neurons participate in distinct circuits that encode different motivational signatures, and whether inputs to the VTA differentially modulate such circuits. Here we show that, because of differences in synaptic connectivity, activation of inputs to the VTA from the laterodorsal tegmentum and the lateral habenula elicit reward and aversion in mice, respectively. Laterodorsal tegmentum neurons preferentially synapse on dopamine neurons projecting to the nucleus accumbens lateral shell, whereas lateral habenula neurons synapse primarily on dopamine neurons projecting to the medial prefrontal cortex as well as on GABAergic ( $\gamma$ -aminobutyric-acid-containing) neurons in the rostromedial tegmental nucleus. These results establish that distinct VTA circuits generate reward and aversion, and thereby provide a new framework for understanding the circuit basis of adaptive and pathological motivated behaviours.**

The functional roles of VTA dopamine neurons have received great attention because they are the primary source of dopamine in target structures such as the medial prefrontal cortex (mPFC) and nucleus accumbens (NAc), which have important roles in a broad range of motivated behaviours and neuropsychiatric disorders<sup>1–3</sup>. Although dopamine neuron activity often correlates with a reward prediction error (that is, the difference between expected and actual rewards), these cells can also signal aversion, saliency, uncertainty and novelty<sup>2,3</sup>. They are heterogeneous in their anatomical location, targets to which they project, electrophysiological properties and several molecular features<sup>2,4–6</sup>. In addition, the VTA receives both excitatory and inhibitory input from distributed brain areas<sup>2,7,8</sup>. Thus different subpopulations of VTA dopamine and GABAergic neurons may subserve different functions<sup>1,2,4–7,9–15</sup>, but little is known about the afferent control of their activity and the circuits in which they are embedded.

Here we study the function and synaptic connectivity of two main inputs to the VTA from the laterodorsal tegmentum (LDT) and the lateral habenula (LHb). By achieving optogenetic control of LDT and LHb neurons/axons that project directly to the VTA and combining *in vivo* viral-mediated and anatomical-tracing methods with *ex vivo* electrophysiology during stimulation of specific VTA inputs, we define critical differences in the neural circuits responsible for this optogenetic control of reward and aversion.

## Inputs to the VTA from the LDT and LHb

To identify unambiguously the afferent inputs to the VTA, we used a rabies virus in which the glycoprotein is replaced by enhanced green fluorescent protein (RV-eGFP)<sup>16</sup>. Consistent with recent results<sup>17</sup>, injection of RV-eGFP into the VTA resulted in the expression of eGFP in diverse brain areas, with large clusters of eGFP-expressing cells in the PFC, NAc, lateral hypothalamus, LHb and LDT (Supplementary Fig. 1). We focused on inputs to the VTA from the LDT and LHb because both have roles in motivated behaviours by influencing VTA neuronal

activity and the consequent release of dopamine in target structures<sup>2,7,18</sup>. eGFP-positive LDT neurons expressed markers for both glutamatergic neurons (the glutamate transporter EAAC1 (also known as SLC1A1)) and cholinergic neurons (choline acetyltransferase; ChAT) (Supplementary Fig. 2)<sup>19,20</sup>. However, although 95% of LDT neurons projecting to the VTA expressed EAAC1, only ~7% expressed ChAT. LHb neurons are excited by the absence of an expected reward<sup>18</sup> and probably send direct inputs to GABAergic cells in the tail of the VTA, the rostromedial tegmental nucleus (RMTg)<sup>21,22</sup>, that inhibit VTA dopamine neurons<sup>23–26</sup>. eGFP-positive LHb neurons were immunopositive for EAAC1 but not for ChAT (Supplementary Fig. 2), indicating that LHb neurons projecting to the VTA are glutamatergic<sup>8</sup>.

To visualize fibres within the VTA from LDT and LHb we injected the anterograde tracer *Phaseolus vulgaris* leucoagglutinin (PHA-L). It was apparent that the density of LDT and LHb inputs differed between VTA subregions in which different subpopulations of dopamine neurons reside<sup>4,5</sup>. To test this conclusion, we simultaneously retrogradely labelled dopamine projection neurons and anterogradely labelled LDT or LHb fibres (Fig. 1a, h). Injection of PHA-L into the LDT and rabies virus expressing tdTomato (RV-tdTomato) into the NAc lateral shell (Fig. 1a, b) showed that RV-tdTomato cells were predominantly located in the lateral VTA (Fig. 1c), that in close proximity contained LDT terminals as well as tyrosine hydroxylase (TH)-immunopositive processes (Fig. 1d, e). More modest PHA-L labelling was observed in the medial VTA (Fig. 1f) and substantia nigra (Fig. 1g). By contrast, injection of PHA-L into the LHb and RV-tdTomato into the mPFC (Fig. 1h, i) showed RV-tdTomato cells mainly in the medial VTA (Fig. 1j) in close proximity to LHb terminals and TH-immunopositive processes (Fig. 1k, l). There was minimal PHA-L labelling of LHb inputs in the lateral VTA (Fig. 1m) or substantia nigra (Fig. 1n), but as expected<sup>21,22</sup> PHA-L terminals were present in the RMTg adjacent to GABAergic neurons (Supplementary Fig. 3). In additional experiments, we injected fluorescent retrobeads into the NAc lateral shell

<sup>1</sup>Nancy Pritzker Laboratory, Department of Psychiatry and Behavioral Sciences, Stanford University School of Medicine, 265 Campus Drive, Stanford, California 94305, USA. <sup>2</sup>Picower Institute for Learning and Memory, Department of Brain and Cognitive Sciences, Massachusetts Institute of Technology, Cambridge, Massachusetts 02139, USA. <sup>3</sup>Departments of Bioengineering and Psychiatry, Stanford University, Stanford, California 94305, USA.

\*These authors contributed equally to this work.

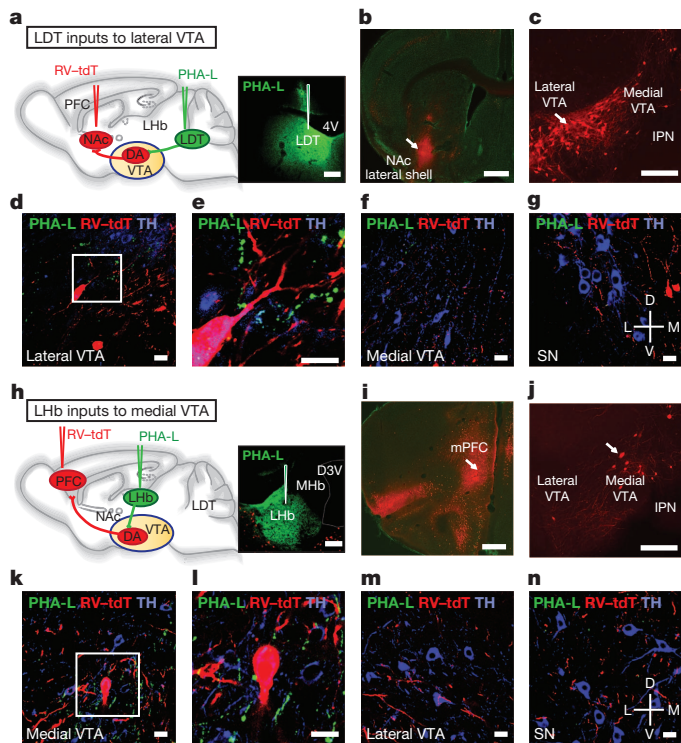


**Figure 1 | LDT and LHB preferentially project to distinct VTA subregions.** **a**, Injection sites for RV-tdTomato (RV-tdT) in the NAc and PHA-L in the LDT. Image shows PHA-L staining in LDT. **b**, RV-tdTomato in the NAc lateral shell. **c**, VTA neurons projecting to the NAc lateral shell are mainly located in the lateral VTA. **d**, **e**, PHA-L-labelled terminals (green) from the LDT are adjacent to cells projecting to the NAc lateral shell (red) as well as TH-immunopositive processes (blue), with white box in **d** depicting the area shown in **e**. **f**, **g**, Few PHA-L-labelled terminals were detected in the medial VTA (**f**) and in the substantia nigra (SN) (**g**). **h**, Injection sites for RV-tdTomato in mPFC and PHA-L in LHB. Image shows PHA-L staining in LHB. **i**, RV-tdTomato in the mPFC. **j**, VTA neurons projecting to the mPFC are mainly located in the medial VTA. **k**, **l**, PHA-L-labelled terminals (green) from the LHB are found adjacent to cells projecting to the mPFC (red) as well as TH-immunopositive processes (blue). White box in **k** depicts area shown in **l**. **m**, **n**, Few PHA-L-labelled terminals were detected in the lateral VTA (**m**) and the substantia nigra (**n**). 4V, fourth ventricle; D3V, dorsal third ventricle; DA, dopamine; IPN, interpeduncular nucleus; MHb, medial habenula. Scale bars, 200  $\mu$ m (**a**–**c**, **h**–**j**), 20  $\mu$ m (**d**–**g**, **k**–**n**).

or mPFC and labelled LDT or LHB inputs with PHA-L, respectively. A similar anatomical distribution of pre- and postsynaptic elements was observed (Supplementary Fig. 3).

### Input-specific control of reward and aversion

These anatomical results suggest that LDT and LHB inputs preferentially terminate in different VTA subregions adjacent to dopamine neuron subpopulations that project to different target structures (NAc lateral shell versus mPFC) and may subserve different behavioural functions<sup>5,6</sup>. To address functional differences in these inputs, we generated a rabies virus expressing the light-activated ion channel channelrhodopsin-2 (ChR2) fused to enhanced yellow fluorescent protein (eYFP; RV-ChR2) (Supplementary Fig. 4) and tested the consequences of the activation of the LDT-VTA and LHB-VTA pathways in a conditioned place preference (CPP) assay by injecting either RV-ChR2 or RV-eGFP into the VTA and implanting an optical fibre over LDT or LHB (Fig. 2a, b). Using a 3-day protocol (Fig. 2c), phasic stimulation of LDT neurons projecting to the VTA on day 2 caused a strong CPP on day 3 (Fig. 2d, f, g), whereas phasic stimulation of LHB neurons projecting to the VTA caused a strong conditioned place aversion (CPA) (Fig. 2e–g). Moreover, after completion of the day-3 testing procedure that involved no optical stimulation (defined as post-test 1),

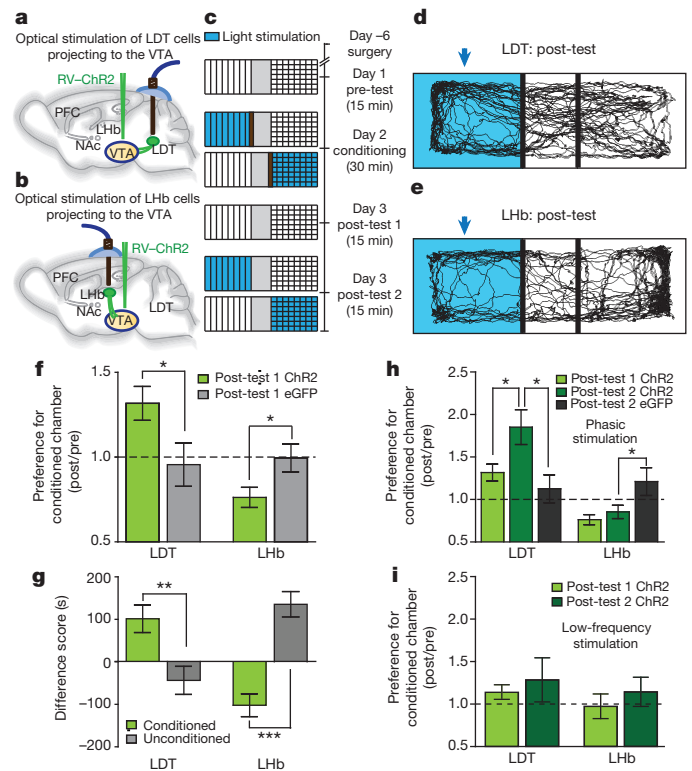


**Figure 2 | Stimulation of LDT and LHB inputs to the VTA elicits CPP and CPA.** **a**, **b**, RV-ChR2 injection into the VTA and optical stimulation of LDT (**a**) and LHB (**b**) projection neurons. **c**, Procedure to elicit and test CPP and CPA. **d**, **e**, Example day-3 mouse tracks, post-test 1. Arrow indicates the chamber in which LDT (**d**) or LHB (**e**) projection neurons were stimulated on day 2. **f**, Post-test 1/pre-test ratio of time spent in conditioned chamber was higher in LDT-ChR2 mice compared to LDT-eGFP mice (LDT-ChR2,  $1.32 \pm 0.1$ ,  $n = 8$ ; LDT-eGFP,  $0.96 \pm 0.13$ ,  $n = 7$ ) but lower in LHB-ChR2 mice (LHB-ChR2,  $0.76 \pm 0.06$ ,  $n = 9$ ; LHB-eGFP,  $0.99 \pm 0.08$ ,  $n = 11$ ). **g**, Differences between post-test 1 and pre-test in time mice spent in conditioned or unconditioned chambers (LDT-ChR2 mice, conditioned chamber,  $105.4 \pm 34.38$ ,  $n = 8$ ; unconditioned chamber,  $-51.1 \pm 26.76$ ,  $n = 8$ ) (LHB-ChR2 mice, conditioned chamber,  $-90.87 \pm 22.59$ ,  $n = 9$ ; unconditioned chamber,  $124.3 \pm 26.27$ ,  $n = 9$ ). **h**, Stimulation of LDT-ChR2 mice during post-test 2 enhanced preference for the conditioned chamber (LDT-ChR2 post-test 1,  $1.32 \pm 0.1$ ,  $n = 8$ ; post-test 2,  $1.85 \pm 0.2$ ,  $n = 8$ ; post-test 2 LDT-eGFP mice,  $1.13 \pm 0.16$ ,  $n = 7$ ). Stimulation of LHB-ChR2 mice during post-test 2 did not cause further aversion (LHB-ChR2 post-test 1,  $0.76 \pm 0.06$ ,  $n = 9$ ; post-test 2,  $0.85 \pm 0.08$ ,  $n = 9$ ), which was still present (LHB-eGFP post-test 2,  $1.22 \pm 0.16$ ,  $n = 11$ ). Post-test 1 results are the same as in **f**. **i**, Low-frequency stimulation of LDT-ChR2 and LHB-ChR2 cells did not elicit CPP or CPA (post-test 1, LDT-ChR2,  $1.13 \pm 0.09$ ,  $n = 6$ ; post-test 2, LDT-ChR2,  $1.28 \pm 0.26$ ,  $n = 6$ ; post-test 1, LHB-ChR2,  $0.97 \pm 0.14$ ,  $n = 7$ ; post-test 2, LHB-ChR2,  $1.14 \pm 0.17$ ,  $n = 6$ ). Error bars denote  $\pm$  s.e.m.  $*P < 0.05$ ,  $**P < 0.01$ ,  $***P < 0.001$ , Mann-Whitney U-test.

stimulating LDT neurons whenever animals were in the chamber in which they were conditioned on day 2 (defined as day 3, post-test 2) caused a further increase in CPP (Fig. 2h), whereas stimulating LHB neurons did not further enhance CPA (Fig. 2h) (See Supplementary Fig. 5 for non-normalized behavioural results).

Additional results indicate that the effects of stimulating LDT and LHB neurons projecting to the VTA were specific and due to driving activity in distinct populations of VTA neurons. First, animals that received intra-VTA injections of RV-eGFP showed no behavioural effects of phasic optical stimulation in LDT and LHB (Fig. 2f–h and Supplementary Fig. 5). Furthermore, low-frequency stimulation of ChR2 in the LDT and LHB had no effects in the CPP and CPA assays (Fig. 2i and Supplementary Fig. 5). Second, non-stimulated animals showed no preference for either chamber (Supplementary Fig. 4) and



there was no effect of the optogenetic manipulations on time spent in the central chamber (Supplementary Fig. 6). Third, stimulation of LDT and LHB neurons projecting to the VTA had no effects on open-field assays of anxiety or locomotor activity (Supplementary Figs 6 and 7). Fourth, the placement of an optical fibre in the LDT and LHB was confirmed in all animals (Supplementary Fig. 7). Fifth, VTA dopamine neuron activation after LDT and LHB stimulation was quantified by assaying the proportion of TH-immunopositive and TH-immunonegative neurons that expressed the activity-dependent immediate early gene *Fos* (Supplementary Fig. 8). After LDT stimulation, ~40% of dopamine neurons in the lateral VTA expressed FOS, whereas in the medial VTA threefold less dopamine neurons expressed this gene. Activation of LHB inputs to the VTA caused an opposite pattern of FOS expression: ~12% of dopamine neurons in the medial VTA were FOS positive, whereas <2% of dopamine neurons in the lateral VTA expressed FOS. Importantly, ~80% of non-dopamine neurons in the RMTg were FOS positive after LHB stimulation (Supplementary Fig. 8).

On the basis of these results we proposed that LHB inputs drive dopamine neurons in the medial posterior VTA that project to the mPFC<sup>4–6</sup>. To test this prediction, we activated LHB inputs to the VTA in animals in which medial VTA neuron subpopulations that project to different targets were identified by the presence of fluorescent retrobeads (Supplementary Fig. 8). In the medial VTA, ~80% of neurons projecting to the mPFC were FOS positive after LHB stimulation. By contrast, <10% of neurons projecting to the NAc medial shell that are located in the medial VTA<sup>4–6</sup> expressed FOS after LHB stimulation.

Although the FOS results confirm that stimulation of LDT and LHB neurons activated neurons in the VTA, axon collaterals of LDT and LHB neurons may project to other brain regions, activation of which mediated the observed CPP and CPA. To address this possibility, we injected adeno-associated viruses expressing ChR2-eYFP (AAV-ChR2) into the LDT or LHB and stimulated axons of infected neurons using light application directly in the caudal VTA and RMTg (Supplementary Fig. 9). This produced a robust CPP after intra-VTA LDT axonal stimulation and a robust CPA after intra-VTA LHB axonal stimulation (Supplementary Figs 9 and 10). A limitation of these experiments is that intra-VTA activation of LDT and LHB axons may cause antidromic activation of axon collaterals projecting to other brain regions. To address this possibility, we injected RV-eGFP or RV-tdTomato into the VTA and the other virus into brain regions that receive inputs from LDT or LHB<sup>27,28</sup>. If single LDT or LHB neurons projecting to the VTA send collaterals to these other brain regions, the neurons will express both fluorophores. An extremely small number of LDT and LHB neurons projecting to other structures (that is, the ventral pallidum, lateral septum, lateral hypothalamus, mPFC, medio-dorsal thalamic nucleus and supraoculomotor central grey) expressed both fluorophores (Supplementary Fig. 11), indicating that almost all of these neurons project solely to the VTA/RMTg. As a positive control we injected one rabies virus into the VTA and the other into the ventral pallidum, and found that dorsal raphe neurons (~20%), which are known to project to these two structures<sup>29</sup>, expressed both eGFP and tdTomato (Supplementary Fig. 11). We also injected rabies viruses into the VTA and either the LDT or LHB and examined labelling of cells in the other structure. Our results confirm that LDT and LHB have reciprocal anatomical connections<sup>28</sup> but the cells providing these projections do not project to the VTA (Supplementary Fig. 11).

### Synaptic connectivity of LDT and LHB inputs

The results thus far indicate that LDT and LHB inputs activate distinct populations of VTA and RMTg neurons and that this leads to reward and aversion, respectively. To address the specific synaptic connectivity of these inputs, we injected AAV-ChR2 into the LDT and fluorescent retrobeads into target structures of VTA dopamine neurons (Fig. 3a and Supplementary Fig. 12). 8–12 weeks after these injections,

ChR2-eYFP was expressed adjacent to VTA dopamine neurons projecting to the NAc lateral shell (Fig. 3b) and its levels were significantly higher in the lateral VTA (Supplementary Fig. 13). To determine the dopamine neuron populations on which LDT inputs directly synapse, we made whole-cell recordings from retrogradely labelled dopamine neurons projecting to the NAc lateral and NAc medial shell as well as non-labelled dopamine substantia nigra neurons (Fig. 3c, d, f). On average, optical stimulation of LDT fibres generated larger excitatory postsynaptic currents (EPSCs) in dopamine neurons projecting to the NAc lateral shell than in dopamine neurons projecting to the medial shell or dopamine neurons in the substantia nigra (Fig. 3g), all recorded in the same sets of slices. The EPSCs in dopamine neurons projecting to the NAc lateral shell were blocked by an AMPA ( $\alpha$ -amino-3-hydroxy-5-methyl-4-isoxazole propionic acid) receptor antagonist (CNQX, 10  $\mu$ M; Fig. 3c), indicating that LDT fibres released glutamate. Importantly, stimulation of LDT inputs generated EPSCs (>10 pA) in 100% of dopamine neurons projecting to the NAc lateral shell but only in ~30–40% projecting to the NAc medial shell or in the substantia nigra (Fig. 3h). Furthermore, only ~10% of dopamine neurons projecting to the mPFC yielded EPSCs (Fig. 3e, g, h).

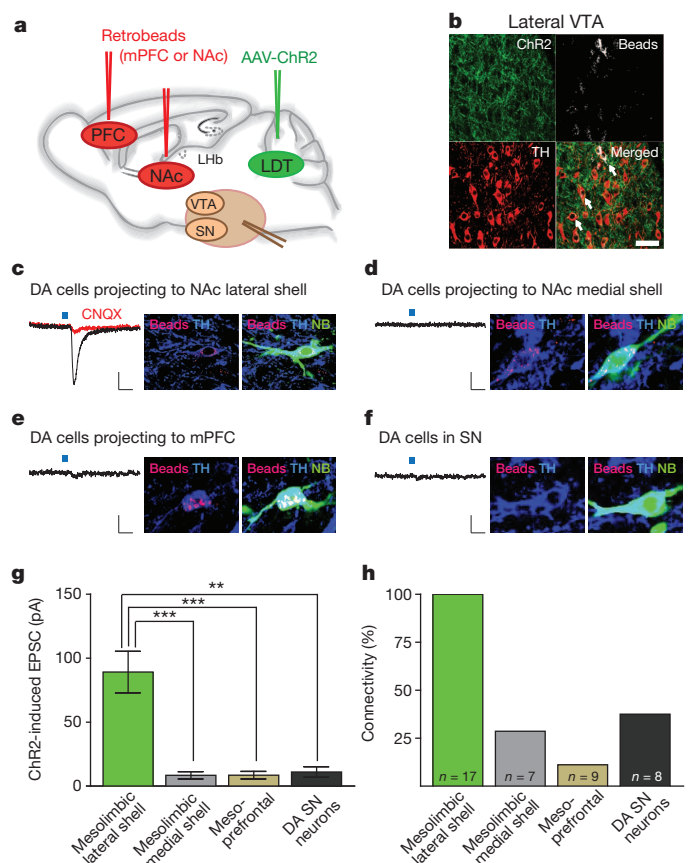


**Figure 3 | LDT neurons preferentially synapse on dopamine neurons projecting to the NAc lateral shell.** **a**, AAV-ChR2 was injected into the LDT and retrobeads were injected into the NAc lateral shell and medial shell, or in the mPFC. **b**, ChR2 expression was in close proximity to retrogradely labelled (beads) TH-immunopositive neurons in the lateral VTA. Scale bar, 50  $\mu$ m. **c–f**, Traces from whole-cell recordings at  $-70$  mV showing EPSCs generated by the stimulation of LDT inputs in retrogradely labelled VTA neurons (beads) projecting to the NAc lateral shell (**c**), NAc medial shell (**d**), mPFC (**e**) or substantia nigra (**f**) neurons. All cells were filled with neurobiotin (NB, green) and are TH-immunopositive (blue). Scale bars, 20 pA 20 ms<sup>-1</sup>. **g**, Summary of average EPSCs generated by optical stimulation of LDT inputs in the four cell populations  $**P < 0.01$ ,  $***P < 0.001$ , one-way analysis of variance (ANOVA) with Bonferroni post-hoc test. Error bars denote  $\pm$  s.e.m. **h**, Percentage of cells in which optical stimulation generated EPSCs >10 pA.  $n$  values shown in each bar are also applicable to **g**.

The same methodology (Fig. 4a and Supplementary Fig. 12) showed that LHB inputs synapse on a different subpopulation of VTA dopamine neurons as well as on GABAergic cells in the RMTg. ChR2-eYFP-expressing fibres from the LHB were found in the medial posterior VTA in close proximity to dopamine neurons projecting to the mPFC as well as in the RMTg (Supplementary Figs 12 and 13). Importantly, light-evoked EPSCs were generated in 100% of dopamine neurons projecting to the mPFC as well as GABAergic RMTg neurons, whereas detectable EPSCs were not generated in dopamine neurons projecting to the NAc medial shell or lateral shell, nor in substantia nigra neurons (Fig. 4b–g). As LHB inputs preferentially synapse on dopamine neurons projecting to the mPFC and RMTg GABAergic cells, we predicted that LHB inputs may inhibit dopamine neurons projecting to the NAc lateral shell through feed-forward inhibition. Indeed, in ~60% of dopamine neurons projecting to the NAc lateral shell, stimulation of LHB inputs evoked inhibitory postsynaptic currents (IPSCs; Fig. 4h, i). By contrast, stimulation of LHB axons did not generate detectable IPSCs in dopamine neurons projecting to the NAc medial shell (Fig. 4h).

These results suggest that LDT and LHB inputs to VTA preferentially activate distinct populations of dopamine neurons that project to different target structures and that, in addition, LHB inputs activate GABAergic cells in the RMTg and perhaps within the VTA itself. Such differences in connectivity can explain the different behavioural consequences of LDT and LHB stimulation (Fig. 2). To further test these conclusions, we generated AAVs expressing a double-floxed rabies virus glycoprotein (AAV-double-floxed inverted open-reading frame (DIO)-RVG) and infected the VTA in TH-Cre mice so that the glycoprotein was only expressed in dopamine neurons (Fig. 5a). Two weeks later, RV-eGFP and RV-tdTomato were injected into the mPFC and NAc lateral shell, respectively (Fig. 5a, b). Because RV-eGFP and RV-tdTomato lack the RVG, expression of eGFP and tdTomato is restricted to initially infected cells<sup>16</sup>. However, in VTA dopamine neurons projecting to these targets (Fig. 5c), transcomplementation with

RVGs occurs and allows RV-eGFP and RV-tdTomato to spread retrogradely, thus labelling cells that synaptically contact the dopamine neurons. After rabies virus injections, cells in the LDT were clearly labelled with tdTomato with almost no cells expressing eGFP (tdTomato,  $n = 18.75 \pm 7.12$  cells per animal; eGFP,  $n = 1.25 \pm 0.75$ ;  $n = 4$  mice; Fig. 5d), whereas LHB cells were clearly labelled with eGFP with almost no cells expressing tdTomato (eGFP,  $8.25 \pm 3.44$  cells; tdTomato,  $0.5 \pm 0.22$ ;  $n = 4$  mice; Fig. 5e). When AAV-DIO-RVG was not injected into the VTA before rabies virus injections, no tdTomato-positive or eGFP-positive cells in the LDT or LHB, respectively, were observed ( $n = 3$  mice) (Fig. 5f, g). These results confirm that LDT neurons preferentially synapse on VTA dopamine neurons projecting to the NAc lateral shell and LHB neurons preferentially synapse on VTA dopamine cells projecting to the mPFC.

### D1/D2R antagonists in mPFC and NAc lateral shell

Activation of VTA GABAergic cells alone can elicit CPA<sup>13</sup> and disrupt reward consummatory behaviour<sup>15</sup>. These results raise the question of whether activation of dopamine neurons projecting to the mPFC is necessary for the CPA elicited by activation of LHB inputs to the VTA and RMTg. To address this question, we infused the D1 dopamine receptor antagonist SCH23390 into the mPFC immediately before stimulating LHB neurons projecting to the VTA and RMTg (Fig. 5h). This manipulation, which does not impair cocaine CPP<sup>30</sup>, prevented the occurrence of CPA, which was elicited in control animals that received vehicle injections into the mPFC (Fig. 5i, j and Supplementary Fig. 14). Similarly, infusion of D1 and D2 receptor antagonists into the NAc lateral shell, but not infusion of vehicle, prevented the CPP elicited by activation of LDT neurons projecting to the VTA (Fig. 5k–m and Supplementary Fig. 14). Control experiments showed that infusion of dopamine receptor antagonists alone into either the mPFC or NAc lateral shell did not elicit CPP or CPA compared to animals that received vehicle infusions ( $n = 4$  mice in each group;  $P > 0.05$ , Mann–Whitney U-test). These results provide further evidence that activation

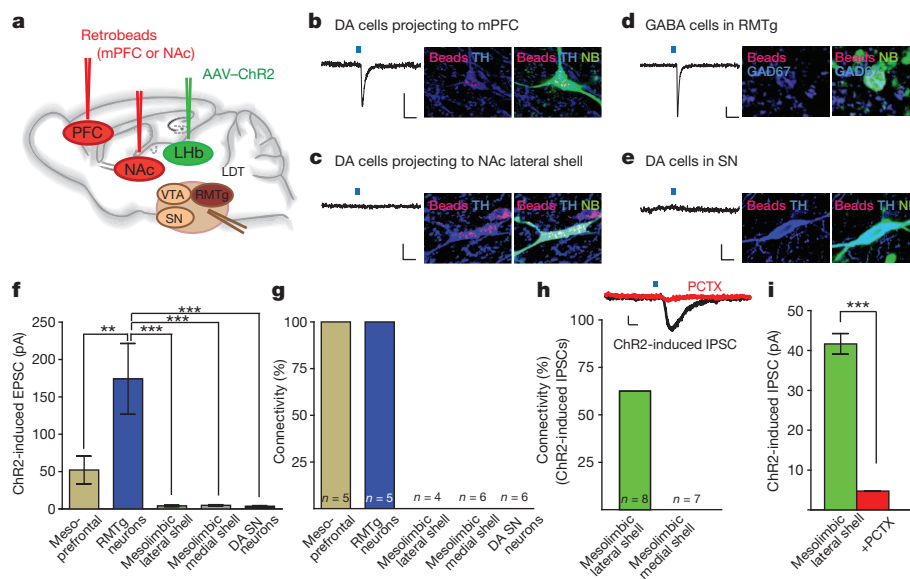


**Figure 4 | LHB neurons preferentially synapse on dopamine neurons projecting to the mPFC and RMTg GABAergic neurons.** **a**, AAV-ChR2 was injected into the LHB and retrobeads were injected into either the NAc lateral shell and medial shell or in the mPFC. **b–e**, Traces from whole-cell recordings at  $-70$  mV showing EPSCs generated by optical stimulation of LHB inputs in retrogradely labelled VTA neurons (beads, red) projecting to the mPFC (**b**), NAc lateral shell (**c**) an RMTg cell (**d**) and substantia nigra cell (**e**). All cells were filled with neurobiotin (green) and are either TH-immunopositive (blue) (**b**, **c**, **e**) or GAD67-immunopositive (blue, **d**). Scale bars, 20 pA 20 ms<sup>-1</sup>. **f**, Summary of average EPSCs generated by optical stimulation of LHB inputs in

five cell populations.  $**P < 0.01$ ,  $***P < 0.001$ , one-way ANOVA with Bonferroni post-hoc test. Error bars denote  $\pm$  s.e.m. **g**, Percentage of cells in which optical stimulation generated EPSCs  $>10$  pA.  $n$  values shown in each bar are also applicable to **f**. **h**, Optical stimulation of LHB inputs generates an IPSC in dopamine cells projecting to the NAc lateral shell. Scale bars, 20 pA 20 ms<sup>-1</sup>. Graph shows the percentage of dopamine cells projecting to the NAc lateral shell or medial shell in which IPSCs were generated by LHB input stimulation. **i**, Average IPSC size from dopamine cells projecting to the NAc lateral shell. IPSCs were blocked by picrotoxin.  $n = 3$ ;  $***P < 0.0001$ , unpaired Student's  $t$ -test. PCTX, picrotoxin.



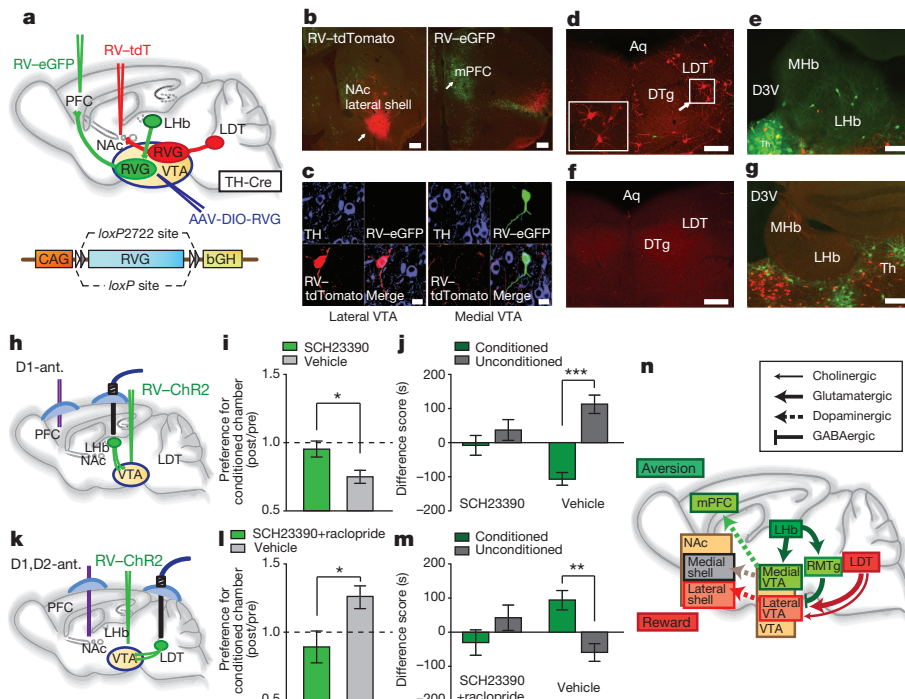


**Figure 5 | Rabies virus reveals distinct VTA circuits and effects of dopamine receptor antagonists on CPP and CPA.** **a**, AAV expressing RVG in a Cre-dependent manner was injected into the VTA of TH-Cre mice. RV-eGFP and RV-tdTomato, injected subsequently into the mPFC and NAc, respectively, were retrogradely transported to subpopulations of dopamine neurons in which transcomplementation occurs, allowing the rabies virus to spread retrogradely and label cells that synaptically contact infected dopamine neurons. **b**, Injection sites in the NAc lateral shell (RV-tdTomato; left) and mPFC (RV-eGFP; right). **c**, TH-immunoreactive neurons in the lateral VTA (left) and medial VTA (right) retrogradely labelled by RV-tdTomato or RV-eGFP. **d**, **e**, tdTomato and eGFP labelling in LDT (**d**) and LHb (**e**) neurons, respectively, when injection of AAV-DIO-RVG into the VTA of TH-Cre mice was performed before rabies virus injections. **f**, **g**, Lack of tdTomato expression in LDT (**f**) and lack of eGFP expression in LHb (**g**) after virus injections in TH-Cre mice that were not injected with AAV-DIO-RVG. **h**, Placements of drug-infusion cannula into the mPFC and optic fibre into the LHb, as well as injection of RV-ChR2 into the VTA. **i**, Ratio of post-test/pre-test time spent in the conditioned chamber when either SCH23390 or vehicle was infused into the mPFC before LHb optical stimulation (SCH23390,  $0.95 \pm 0.05$ ,  $n = 9$ ; vehicle,  $0.75 \pm 0.04$ ,  $n = 7$ ). **j**, Difference between post-test and pre-test in the time mice

spent in the conditioned or unconditioned chambers after LHb stimulation (SCH23390, conditioned chamber,  $-7.24 \pm 28.79$ , unconditioned chamber,  $36.83 \pm 30.74$ ,  $n = 9$ ; vehicle, conditioned chamber,  $-106.88 \pm 18.82$ , unconditioned chamber,  $112.61 \pm 26.48$ ,  $n = 7$ ). **k**, Placements of drug-infusion cannula into the NAc lateral shell and optic fibre into the LDT, as well as injection of RV-ChR2 into the VTA. **l**, Ratio of post-test/pre-test time spent in the conditioned chamber when SCH23390 and raclopride or vehicle were infused into the NAc lateral shell before LDT optical stimulation (SCH23390/raclopride,  $0.89 \pm 0.1$ ,  $n = 7$ ; vehicle,  $1.26 \pm 0.08$ ,  $n = 6$ ). **m**, Difference between post-test and pre-test in time mice spent in conditioned or unconditioned chamber after LDT stimulation (SCH23390/raclopride, conditioned chamber,  $-30.17 \pm 37.38$ , unconditioned chamber,  $42.22 \pm 34.68$ ,  $n = 7$ ; vehicle, conditioned chamber,  $94.58 \pm 27.77$ , unconditioned chamber,  $-59.38 \pm 26.44$ ,  $n = 6$ ).  $*P < 0.05$ ,  $**P < 0.01$ ,  $***P < 0.001$ , Mann-Whitney U-test. Error bars denote  $\pm$  s.e.m. **n**, Proposed circuits driven by LDT and LHb inputs into the VTA. Green shading indicates circuit involved in aversion and red/pink shading indicates circuit involved in reward and salience. ant., antagonist; Aq, aqueduct; DTg, dorsal tegmental nucleus; Th, thalamus. Scale bars, 200  $\mu$ m (**b**), 20  $\mu$ m (**c**), 100  $\mu$ m (**d**–**g**).

of different subpopulations of VTA dopamine neurons and the consequent release of dopamine in different target structures are necessary for mediating the reward and aversion generated by activation of LDT and LHb inputs, respectively.

### Concluding remarks

A fundamental task of the mammalian brain is to assign emotional/motivational valence to environmental stimuli by determining whether they are rewarding and should be approached or are aversive and should be avoided. Internal stimuli also are assigned emotional/motivational valence and prevalent brain disorders, such as addiction and depression, involve pathological dysfunction in the performance of these tasks. Although VTA dopamine neurons have a role in reward-dependent behaviours<sup>1–3,7,10,12,14,31,32</sup> and inhibition of VTA dopamine neurons by GABAergic neurons contributes to reward prediction error calculations and promotes behaviours associated with aversion<sup>10,12,13,15</sup>, the detailed circuits within the VTA that mediate reward and aversion and their control by upstream brain areas have not been defined. By combining virus-mediated tracing, synaptic electrophysiology and *in vitro* and *in vivo* optogenetic manipulations, we have presented evidence that two main inputs to the VTA from the

LDT and LHb trigger reward- and aversion-associated behaviours, respectively, through activation and di-synaptic inhibition of distinct subpopulations of VTA dopamine neurons that project to different target structures. These findings indicate that there are several subpopulations of VTA dopamine neurons embedded in distinct circuits that contribute to different behavioural functions (Fig. 5n). Dopamine neurons projecting to the mPFC may be the primary subpopulation of dopamine neurons that are preferentially activated by aversive stimuli, although these neurons likely subserve other important functions<sup>33</sup>. On the other hand, dopamine neurons projecting to the NAc lateral shell may primarily signal reward and perhaps salience<sup>2,5</sup>. This hypothesis is consistent with studies measuring the release of dopamine in target structures after stimulation of LDT and LHb, as well as recent optogenetic manipulations of VTA dopamine neuron activity<sup>10,19,31,32,34</sup>.

Although LDT and LHb inputs activate different cell populations in the VTA and RMTg, it is probable that these distinct 'circuits' do not routinely function in isolation. They interact with one another anatomically<sup>28</sup> (Supplementary Fig. 11) and functionally (Fig. 4). Indeed, stimuli can have both rewarding and aversive qualities simultaneously and these qualities can change depending on the context.

Thus, LDT and LHB inputs to the VTA and RMTg can be conceptualized as belonging to a more complex global brain system that assigns motivational valence or value to external and internal stimuli. Further elucidation of the detailed synaptic connectivity of LHB inputs to the VTA may be particularly interesting in the context of the potential role of LHB in psychiatric disorders such as depression and schizophrenia<sup>18,35–37</sup>. Overactivity of LHB neurons would be expected to drive depressive symptoms such as anhedonia, whereas LHB pathology in schizophrenia may contribute to the cognitive symptoms that are associated with PFC dysfunction<sup>37</sup>.

**Note added in proof:** A recent paper also finds that optogenetic activation of LHB efferents to the midbrain is aversive<sup>38</sup>.

## METHODS SUMMARY

Male adult (10–12 weeks of age) C57BL/6 (Charles River) or TH-Cre (B6.Cg-Tg(Th-cre)1Tmd/J; Jackson Laboratory) mice were used for all experiments. All procedures complied with the animal care standards set forth by the National Institutes of Health and were approved by Stanford University's Administrative Panel on Laboratory Animal Care.

**Full Methods** and any associated references are available in the online version of the paper.

**Received 23 April; accepted 20 August 2012.**

**Published online 14 October 2012.**

- Björklund, A. & Dunnett, S. B. Dopamine neuron systems in the brain: an update. *Trends Neurosci.* **30**, 194–202 (2007).
- Bromberg-Martin, E. S., Matsumoto, M. & Hikosaka, O. Dopamine in motivational control: rewarding, aversive, and alerting. *Neuron* **68**, 815–834 (2010).
- Schultz, W. Multiple dopamine functions at different time courses. *Annu. Rev. Neurosci.* **30**, 259–288 (2007).
- Lammel, S. *et al.* Unique properties of mesoprefrontal neurons within a dual mesocorticolimbic dopamine system. *Neuron* **57**, 760–773 (2008).
- Lammel, S., Ito, D. I., Roeper, J. & Malenka, R. C. Projection-specific modulation of dopamine neuron synapses by aversive and rewarding stimuli. *Neuron* **70**, 855–862 (2011).
- Margolis, E. B., Mitchell, J. M., Ishikawa, J., Hjelmstad, G. O. & Fields, H. L. Midbrain dopamine neurons: projection target determines action potential duration and dopamine D(2) receptor inhibition. *J. Neurosci.* **28**, 8908–8913 (2008).
- Sesack, S. R. & Grace, A. A. Cortico-basal ganglia reward network: microcircuitry. *Neuropsychopharmacology* **35**, 27–47 (2010).
- Geisler, S., Derst, C., Veh, R. W. & Zahm, D. S. Glutamatergic afferents of the ventral tegmental area in the rat. *J. Neurosci.* **27**, 5730–5743 (2007).
- Berridge, K. C., Robinson, T. E. & Aldridge, J. W. Dissecting components of reward: 'liking', 'wanting', and learning. *Curr. Opin. Pharmacol.* **9**, 65–73 (2009).
- Cohen, J. Y., Haesler, S., Vogt, L., Lowell, B. B. & Uchida, N. Neuron-type-specific signals for reward and punishment in the ventral tegmental area. *Nature* **482**, 85–88 (2012).
- Guarraci, F. A. & Kapp, B. S. An electrophysiological characterization of ventral tegmental area dopaminergic neurons during differential pavlovian fear conditioning in the awake rabbit. *Behav. Brain Res.* **99**, 169–179 (1999).
- Kim, Y., Wood, J. & Moghaddam, B. Coordinated activity of ventral tegmental neurons adapts to appetitive and aversive learning. *PLoS ONE* **7**, e29766 (2012).
- Tan, K. R. *et al.* GABA neurons of the VTA drive conditioned place aversion. *Neuron* **73**, 1173–1183 (2012).
- Matsumoto, M. & Hikosaka, O. Two types of dopamine neuron distinctly convey positive and negative motivational signals. *Nature* **459**, 837–841 (2009).
- van Zessen, R., Phillips, J. L., Budygin, E. A. & Stuber, G. D. Activation of VTA GABA neurons disrupts reward consumption. *Neuron* **73**, 1184–1194 (2012).
- Wickersham, I. R., Finke, S., Conzelmann, K. K. & Callaway, E. M. Retrograde neuronal tracing with a deletion-mutant rabies virus. *Nature Methods* **4**, 47–49 (2007).
- Watabe-Uchida, M., Zhu, L., Ogawa, S. K., Vamanrao, A. & Uchida, N. Whole-brain mapping of direct inputs to midbrain dopamine neurons. *Neuron* **74**, 858–873 (2012).
- Hikosaka, O. The habenula: from stress evasion to value-based decision-making. *Nature Rev. Neurosci.* **11**, 503–513 (2010).
- Forster, G. L. & Blaha, C. D. Laterodorsal tegmental stimulation elicits dopamine efflux in the rat nucleus accumbens by activation of acetylcholine and glutamate receptors in the ventral tegmental area. *Eur. J. Neurosci.* **12**, 3596–3604 (2000).
- Lodge, D. J. & Grace, A. A. The laterodorsal tegmentum is essential for burst firing of ventral tegmental area dopamine neurons. *Proc. Natl Acad. Sci. USA* **103**, 5167–5172 (2006).
- Hou, T. C., Geisler, S., Marinelli, M., Degarmo, B. A. & Zahm, D. S. The mesopontine rostromedial tegmental nucleus: a structure targeted by the lateral habenula that projects to the ventral tegmental area of Tsai and substantia nigra compacta. *J. Comp. Neurol.* **513**, 566–596 (2009).
- Kaufling, J., Veinante, P., Pawlowski, S. A., Freund-Mercier, M. J. & Barrot, M. Afferents to the GABAergic tail of the ventral tegmental area in the rat. *J. Comp. Neurol.* **513**, 597–621 (2009).
- Christoph, G. R., Leonzio, R. J. & Wilcox, K. S. Stimulation of the lateral habenula inhibits dopamine-containing neurons in the substantia nigra and ventral tegmental area of the rat. *J. Neurosci.* **6**, 613–619 (1986).
- Hou, T. C., Fields, H. L., Baxter, M. G., Saper, C. B. & Holland, P. C. The rostromedial tegmental nucleus (RMTg), a GABAergic afferent to midbrain dopamine neurons, encodes aversive stimuli and inhibits motor responses. *Neuron* **61**, 786–800 (2009).
- Ji, H. & Shepard, P. D. Lateral habenula stimulation inhibits rat midbrain dopamine neurons through a GABA(A) receptor-mediated mechanism. *J. Neurosci.* **27**, 6923–6930 (2007).
- Omelenko, N., Bell, R. & Sesack, S. R. Lateral habenula projections to dopamine and GABA neurons in the rat ventral tegmental area. *Eur. J. Neurosci.* **30**, 1239–1250 (2009).
- Araki, M., McGeer, P. L. & Kimura, H. The efferent projections of the rat lateral habenular nucleus revealed by the PHA-L anterograde tracing method. *Brain Res.* **441**, 319–330 (1988).
- Cornwall, J., Cooper, J. D. & Phillipson, O. T. Afferent and efferent connections of the laterodorsal tegmental nucleus in the rat. *Brain Res. Bull.* **25**, 271–284 (1990).
- Vertes, R. P., Fortin, W. J. & Crane, A. M. Projections of the median raphe nucleus in the rat. *J. Comp. Neurol.* **407**, 555–582 (1999).
- Sanchez, C. J., Bailie, T. M., Wu, W. R., Li, N. & Sorg, B. A. Manipulation of dopamine d1-like receptor activation in the rat medial prefrontal cortex alters stress- and cocaine-induced reinstatement of conditioned place preference behavior. *Neuroscience* **119**, 497–505 (2003).
- Tsai, H. C. *et al.* Phasic firing in dopaminergic neurons is sufficient for behavioral conditioning. *Science* **324**, 1080–1084 (2009).
- Witten, I. B. *et al.* Recombinase-driver rat lines: tools, techniques, and optogenetic application to dopamine-mediated reinforcement. *Neuron* **72**, 721–733 (2011).
- Robbins, T. W. & Arnsten, A. F. The neuropsychopharmacology of fronto-executive function: monoaminergic modulation. *Annu. Rev. Neurosci.* **32**, 267–287 (2009).
- Lecourtier, L., DeFrancesco, A. & Moghaddam, B. Differential tonic influence of lateral habenula on prefrontal cortex and nucleus accumbens dopamine release. *Eur. J. Neurosci.* **27**, 1755–1762 (2008).
- Li, B. *et al.* Synaptic potentiation onto habenula neurons in the learned helplessness model of depression. *Nature* **470**, 535–539 (2011).
- Lecourtier, L. & Kelly, P. H. Bilateral lesions of the habenula induce attentional disturbances in rats. *Neuropsychopharmacology* **30**, 484–496 (2005).
- Shepard, P. D., Holcomb, H. H. & Gold, J. M. Schizophrenia in translation: the presence of absence: habenular regulation of dopamine neurons and the encoding of negative outcomes. *Schizophr. Bull.* **32**, 417–421 (2006).
- Stamatakis, A. M. & Stuber, G. D. Activation of lateral habenula inputs to the ventral midbrain promotes behavioural avoidance. *Nature Neurosci.* **15**, 1105–1107 (2012).

**Supplementary Information** is available in the online version of the paper.

**Acknowledgements** We thank the Stanford Neuroscience Imaging Core, the Stanford Neuroscience Behavior Phenotyping and Pharmacology Core and the Stanford Neuroscience Gene Vector and Virus Core (all supported by National Institutes of Health grant NIH NS069375). This work was supported by grants from the Simons Foundation and NIH (to R.C.M.). K.D. is supported by the NIH, the DARPA REPAIR program, and the Wieggers Family Fund. S.L. is supported by a fellowship from the German Academy of Sciences Leopoldina. B.K.L. is supported by a Davis Foundation Postdoctoral Fellowship in Eating Disorders Research. K.M.T. is supported by the JPB Foundation and NIMH.

**Author Contributions** S.L., B.K.L. and R.C.M. designed the study, interpreted results and wrote the paper. S.L. and B.K.L. performed stereotaxic injections, optogenetic experiments and electrophysiology. S.L., C.R., M.J.B. and K.W.H. performed immunohistochemistry. B.K.L. and K.W.H. generated viruses. K.T. and K.D. provided optogenetics training and resources. All authors edited the paper.

**Author Information** Reprints and permissions information is available at [www.nature.com/reprints](http://www.nature.com/reprints). The authors declare no competing financial interests. Readers are welcome to comment on the online version of the paper. Correspondence and requests for materials should be addressed to R.C.M. ([malenka@stanford.edu](mailto:malenka@stanford.edu)).



## METHODS

**Animals.** Male adult (10–12 weeks of age) C57BL/6 (Charles River) or TH-Cre (B6.Cg-Tg(Th-cre)1Tmd/J; Jackson Laboratory) mice were used for all experiments. All procedures complied with the animal care standards set forth by the National Institutes of Health and were approved by Stanford University's Administrative Panel on Laboratory Animal Care.

**Virus generation.** The AAVs used in this study were generated as previously described<sup>39</sup> either by the Deisseroth laboratory (AAV-ChR2) or the Stanford Neuroscience Gene Vector and Virus Core (AAV-DIO-RVG). Rabies virus was generated from a full-length complementary DNA plasmid containing all components of the virus (SAD L16; a gift from K.-K. Conzelmann<sup>40</sup>). We replaced the RVG with eGFP, tdTomato or ChR2(H134R) fused to eYFP to generate virus expressing eGFP (RV-eGFP), tdTomato (RV-tdTomato) or ChR2(H134R) (RV-ChR2). To collect the virus from this cDNA we used a modified version of published protocols<sup>40,41</sup>. In brief, HEK293T cells were transfected with a total of six plasmids; four expressing the viral components pTIT-N, pTIT-P, pTIT-G and pTIT-L; one plasmid expressing T7 RNA polymerase (pCAGGS-T7), and the aforementioned glycoprotein-deleted viral cDNA plasmid expressing eGFP, tdTomato or ChR2. For the amplification of the virus, the media bathing these HEK293T cells was collected 3–4 days after transfection and moved to baby hamster kidney cells stably expressing viral glycoprotein (BHK-B19G)<sup>41</sup>. After 3 days, the media from BHK-B19G cells was collected, centrifuged for 5 min at 3,000g to remove cell debris, and concentrated by ultracentrifugation (55,000g for 2 h). Pellets were suspended in DPBS, aliquoted and stored at  $-80^{\circ}\text{C}$ . The titre of concentrated virus was measured by infecting HEK293 cells and monitoring fluorescence. Plasmids expressing the viral components were gifts from K.-K. Conzelmann and I. Wickersham. BHK cells stably expressing B19G were a gift from E. Callaway.

**Stereotaxic injections and optic fibre/cannula implantations.** As previously described<sup>4,5</sup>, all stereotaxic injections were performed under general ketamine-medetomidine anaesthesia and using a stereotaxic instrument (Kopf Instruments). Adult (10–12 weeks; 25–30 g) male C57BL/6 and TH-Cre mice were group-housed until surgery. Mice were maintained on a 12:12 light cycle (lights on at 07:00). For retrobead labelling (100 nl; LumaFluor Inc.) mice were injected unilaterally with fluorescent retrobeads in the NAc lateral shell (bregma, 1.45 mm; lateral, 1.75 mm; ventral, 4.0 mm), NAc medial shell (bregma, 1.78 mm; lateral, 0.5 mm; ventral, 4.1 mm), or mPFC (two injections at four different sites: bregma, 1.95 mm, 2.05 mm, 2.15 mm and 2.25 mm; lateral, 0.27 mm; ventral, 2.1 mm and 1.6 mm; injected total volume in mPFC, 400 nl; the target area was the prelimbic and infralimbic cortex) using a 1  $\mu\text{l}$  Hamilton syringe (Hamilton). Note that these empirically derived stereotaxic coordinates do not precisely match those given in the mouse brain atlas<sup>42</sup>, which we used as references for the injection-site images. On average, the caudo-rostral axis appeared to be approximately shifted caudally by 400  $\mu\text{m}$ . Little labelling was observed in the pipette tract (that is, cingulate and motor cortices for mPFC injections or in the dorsal striatum for NAc lateral shell injections). To allow adequate time for retrograde transport of the retrobeads into the somas of midbrain dopamine neurons, minimal survival periods before sacrifice depended on the respective injection areas: NAc lateral shell, 3 days; NAc medial shell, 14 days; mPFC, 21 days. For viral infections a small amount of concentrated virus solution (0.5–1  $\mu\text{l}$  RV-eGFP, RV-tdTomato or RV-ChR2) or AAV-DIO-RVG or AAV-ChR2 was injected unilaterally in the LDT (bregma,  $-5.0$  mm; lateral, 0.5 mm; ventral, 3.0 mm) or LHb (bregma,  $-1.58$  mm; lateral, 0.4 mm; ventral, 2.65 mm) or into the VTA (bregma,  $-3.4$  mm; lateral, 0.35 mm; ventral, 4.0 mm) or mPFC or NAc lateral shell (same coordinates as for retrobead injections) using a syringe pump (Harvard Apparatus) at a slow rate (100–150 nl  $\text{min}^{-1}$ ). The injection needle was withdrawn 5 min after the end of the infusion.

For the dual virus injections (Supplementary Fig. 11), one virus (RV-eGFP or RV-tdTomato) was injected into the VTA and the other was injected into either the ventral pallidum (bregma, 0.62 mm; lateral, 1.10 mm; ventral, 4.75 mm), lateral septum (bregma, 0.62 mm; lateral, 0.35 mm; ventral, 3.0 mm), lateral hypothalamus (bregma,  $-0.94$  mm; lateral, 1.00 mm; ventral, 4.75 mm), mPFC (two injections at four different sites: bregma, 1.95 mm, 2.05 mm, 2.15 mm and 2.25 mm; lateral, 0.27 mm; ventral, 2.1 mm and 1.6 mm), mediodorsal thalamic nucleus (bregma,  $-1.22$  mm; lateral, 0.25 mm; ventral, 3.25 mm) or supraoculomotor central grey (bregma,  $-4.04$  mm; lateral, 0.3 mm; ventral, 2.7 mm). For anterograde labelling of LDT and LHb terminals in the VTA the anterograde tracer PHA-L (50 nl; 2.5% in 0.01 M phosphate buffer; Vector) was injected into the LDT or LHb (same coordinates as for virus injections). The survival period for the PHA-L-injected animals was 3 weeks and for the AAV-ChR2 injected animals 8–12 weeks.

For behavioural experiments, mice that were injected with RV-eGFP or RV-ChR2 in the VTA received unilateral implantation of a doric patch-cord chronically implantable fibre (NA = 0.22; Doric lenses) over the LDT (bregma,  $-5.0$  mm, lateral, 0.5 mm, ventral, 2.0 mm) or LHb (bregma,  $-1.58$  mm, lateral, 0.4 mm, ventral, 2.0 mm). One layer of adhesive cement (C&B metabond; Parkell) followed

by cranioplastic cement (Dental cement) was used to secure the fibre guide system to the skull. The incision was closed with a suture and tissue adhesive (Vetbond; Fisher). The animal was kept on a heating pad until it recovered from anaesthesia. For intra-VTA stimulation of LHb or LDT axon terminals, AAV-ChR2 was injected into LHb or LDT, respectively. Ten weeks after the virus injection a doric optic fibre was implanted unilaterally over the caudal medial VTA for stimulation of LHb axon terminals (bregma,  $-3.4$  mm; lateral, 0.35 mm; ventral, 3.6 mm) and over the lateral VTA for stimulation of LDT axon terminals (bregma,  $-3.4$  mm; lateral, 0.5 mm; ventral, 3.6 mm). Behavioural experiments were performed 2 weeks after the implantation. For microinjection of dopamine receptor antagonists into the mPFC or NAc lateral shell a guide cannula (PlasticOne) was implanted directly over the ipsilateral mPFC (bregma, 2.2 mm; lateral, 0.3 mm; ventral,  $-2.0$  mm) or NAc lateral shell (bregma, 1.45 mm; lateral, 1.75 mm; ventral, 4.0 mm) of the mice in which RV ChR2 injection into the VTA and the implantation of doric optic fibres were made. Optical fibre and cannula placements were confirmed in all animals. Although placements varied slightly from mouse to mouse, behavioural data from all mice were included in the study.

**Electrophysiology.** Mice were deeply anaesthetized with pentobarbital (200 mg  $\text{kg}^{-1}$  intraperitoneally; Ovation Pharmaceuticals). Coronal midbrain slices (250  $\mu\text{m}$ ) were prepared after intracardial perfusion with ice-cold artificial cerebrospinal fluid (ACSF) containing elevated (in mM): 50 sucrose, 125 NaCl, 25  $\text{NaHCO}_3$ , 2.5 KCl, 1.25  $\text{NaH}_2\text{PO}_4$ , 0.1  $\text{CaCl}_2$ , 4.9  $\text{MgCl}_2$  and 2.5 glucose (oxygenated with 95%  $\text{O}_2$  and 5%  $\text{CO}_2$ ). After 90 min of recovery, slices were transferred to a recording chamber and perfused continuously at 2–4 ml  $\text{min}^{-1}$  with oxygenated ACSF (125 NaCl, 25  $\text{NaHCO}_3$ , 2.5 KCl, 1.25  $\text{NaH}_2\text{PO}_4$ , 11 glucose, 1.3  $\text{MgCl}_2$  and 2.5  $\text{CaCl}_2$ ) at  $\sim 30^{\circ}\text{C}$ . For the recording of EPSCs, picrotoxin (50  $\mu\text{M}$ ; Sigma) was added to block inhibitory currents mediated by GABA<sub>A</sub> receptors. The internal solution contained (in mM): 117 CsCH<sub>3</sub>SO<sub>3</sub>, 20 HEPES, 0.4 EGTA, 2.8 NaCl, 5 TEA, 4 MgATP, 0.3 NaGTP, 5 QX314, 0.1 spermine, and 0.1% neurobiotin. For recording of IPSCs the internal solution contained (in mM): 130 CsCl, 1 EGTA, 10 HEPES, 2 MgATP, 0.2 NaGTP and 0.1% neurobiotin (for both internal solutions pH 7.35, 270–285 mOsm). Patch pipettes (3.8–4.4 M $\Omega$ ) were pulled from borosilicate glass (G150TF-4; Warner Instruments).

Labelled dopamine neurons were visualized with a 40X water-immersion objective on an upright fluorescent microscope (BX51WI; Olympus) equipped with infrared-differential interference contrast video microscopy and epifluorescence (Olympus) for detection of retrobeads. ChR2 was stimulated by flashing 473 nm light (5-ms pulses; 0.1 Hz; 1–2 mW) through the light path of the microscope using a ultrahigh-powered light-emitting diode (LED) powered by an LED driver (Prizmatix, Modiin Ilite) under computer control. The light intensity of the LED was not changed during the experiments and the whole slice was illuminated. A dual lamp house adaptor (Olympus) was used to switch between fluorescence lamp and LED light source. EPSCs were recorded in whole-cell voltage clamp (Multiclamp 700B, Molecular Devices), filtered at 2 kHz, digitized at 10 kHz (ITC-18 interface, HEKA) and collected online using custom IgorPro software (Wavemetrics). Series resistance (15–25 M $\Omega$ ) and input resistance were monitored online with a 4-mV hyperpolarizing step (50 ms) given with each afferent stimulus. VTA/substantia nigra and RMTg neurons were voltage-clamped at  $-70$  mV and EPSC or IPSC amplitudes were calculated by measuring the peak current from the average EPSC or IPSC response from 10–15 consecutive sweeps.

For pharmacological characterization light-evoked EPSCs or IPSCs were recorded for 5 min followed by bath perfusion of 10  $\mu\text{M}$  CNQX (Tocris Bioscience) or 50  $\mu\text{M}$  picrotoxin (Sigma) for an additional 10 min, respectively. 10–15 consecutive sweeps pre- and post-drug were averaged and peak EPSCs or IPSCs amplitudes were then measured. For detection of IPSCs, labelled cells were recorded from the caudal VTA in slices that contained the RMTg. For determination of dopamine or GABAergic phenotype, neurons were filled with neurobiotin (Vector) during the patch clamp experiment, then fixed in 4% paraformaldehyde (PFA) and 24 h later immunostained for TH or GAD67. Approximately 80% of all whole-cell patch clamped neurons could be successfully recovered. The dopamine phenotype or GABAergic phenotype (in the RMTg) was confirmed in all of these neurons.

**Immunohistochemistry.** Immunohistochemistry and confocal microscopy were performed as described previously in refs 4 and 5. In brief, after intracardial perfusion with 4% paraformaldehyde in PBS, pH 7.4, the brains were post-fixed overnight and coronal midbrain slices (50 or 100  $\mu\text{m}$ ) were prepared. The primary antibodies used were mouse anti-TH (1:1,000; Millipore), rabbit anti-TH (1:1,000; Calbiochem), rabbit anti-PHA-L (1:1,000; Vector), goat anti-EAAC1 (1:1,000; Millipore), rabbit anti-Chat (1:200; Millipore), mouse anti-GAD67 (clone 1G10.2; 1:500; Millipore), rabbit anti-FOS (1:500, Calbiochem) and rabbit anti-NeuN (neuronal nuclei; 1:1,000; Millipore). The secondary antibodies used were Alexa Fluor 488 anti-rabbit, Alexa Fluor 546 anti-goat, Alexa Fluor 546 anti-rabbit, Alexa Fluor 546 anti-mouse, Alexa Fluor 647 anti-rabbit, Alexa Fluor 647 anti-mouse (all 1:750), Alexa Fluor 488 streptavidin (1:1,000) (all Molecular

Probes). Image acquisition was performed with a confocal system (Zeiss LSM510) using 10X, 40X or 63X objectives and on a Zeiss AxioImager M1 upright wide-field fluorescence/differential interference contrast microscope with charged-coupled device camera using 2.5X and 10X objectives. Images were analysed using the Zeiss LSM Image Browser<sup>39</sup> software and ImageJ software.

For quantification of ChR2-eYFP fluorescence intensity and quantification of FOS-positive cells, confocal images were acquired using identical pinhole, gain and laser settings. Images in the medial and lateral VTA as well as the substantia nigra from the same tissue sections were acquired at the same focus level. The medial and lateral VTA was defined as the area that corresponds to the anatomical location of distinct dopamine subpopulations<sup>4,5</sup>. The medial VTA was defined as the region comprising the medial paraventricular nucleus and medial parabrachial pigmented nucleus, whereas the lateral VTA was defined as the lateral parabrachial pigmented nucleus (Supplementary Fig. 8c). No additional post-processing was performed on any of the collected images. ChR2 fluorescence intensity was then quantified using a scale from 0 to 255 in ImageJ to determine the mean intensity across the entire image. For retrobeads, AAV and PHA-L injections and viral injections in the mPFC and NAc lateral shell, the injection sites were confirmed in all animals by preparing coronal sections (100 µm). Counterstaining of injection sites was performed with green or red Nissl (NeuroTrace 500/525 or 530/615, Molecular Probes).

We routinely carried out complete serial analyses of the injection sites. Animals with notable contaminations outside target areas were discarded (see ref. 4 for serial analysis of retrobead injection sites and definition of dopamine target areas). For viral injections into the VTA we confirmed that all animals had the centre of the viral injection located in the caudal VTA (Bregma, -3.4 mm). However, quantification of the 'spread' of the RV-ChR2 injected into the VTA is difficult because for expression of the transgene, the rabies virus must be taken up by terminals and the transgene must be synthesized in the cytosol and then transported within the axons. Any eYFP within the VTA and adjacent structures will represent axons/terminals of cells that project to the VTA and adjacent structures as well as the cell bodies of neurons (that is, RMTg) that have local connectivity within the VTA and adjacent structures. Thus transgene expression in structures adjacent to the VTA does not indicate that Lhb or LDT neurons project to these structures. Nevertheless, in Supplementary Fig. 15 we present a serial reconstruction for the caudo-rostral extent of the midbrain showing the expression of ChR2-eYFP 1 week after injection of RV-ChR2 into the VTA ( $n = 5$  mice). TH-stained coronal mid-brain sections (100 µm) were prepared from the injected mice and reconstructed using NeuroLucida software (MicroBrightField). Sections were labelled relative to bregma using landmarks and neuroanatomical nomenclature as described in ref. 42. We report all brain areas in which detectable eYFP was observed. The strongest transgene expression was observed in the caudal VTA and several of its distinct subnuclei, most commonly in the IPN. We also always detected high transgene expression in the RMTg. Thus when referred to in the text, the VTA includes the RMTg, which was originally termed the 'tail of the VTA'<sup>22</sup>.

Because the IPN expressed ChR2-eYFP after intra-VTA injections, we conducted additional double retrograde tracing experiments in which we injected small amounts of green retrobeads (20 nl; LumaFluor Inc.) into the IPN (bregma, -3.9 mm; lateral, 0 mm; ventral, 4.55 mm) and red Retrobeads (60 nl; LumaFluor Inc.) into the VTA (bregma, -3.4 mm; lateral, 0.35 mm; ventral, 4.0 mm). Fluorescently labelled latex retrobeads were used in these experiments ( $n = 2$  mice) because they show very limited diffusion from the injection site even after several weeks *in vivo*, and thus can be highly localized. Although a large number of cells in the Lhb contained red beads (~84%, 79 out of 94 cells), confirming a projection from this structure to the VTA, only a small proportion of these cells (~12%, 11 out of 94 cells) also contained green beads (Supplementary Fig. 16). By contrast, a large number of medial habenula cells contained green beads (~98%, 214 out of 218 cells) and less than 2% (3 out of 218 cells) of these also contained red beads (Supplementary Fig. 16), demonstrating that the medial habenula preferentially projects to the IPN. In the LDT, many cells (>100) contained red beads and none of these cells contained green beads (Supplementary Fig. 16). These results indicate that LDT cells likely only project to VTA and not the IPN, whereas the proportion of Lhb neurons that project to the IPN in addition to the VTA is small.

For quantification of the expression of RV-ChR2 in the LDT and Lhb 50 µm coronal sections from mice which had been injected with RV-ChR2 in the VTA were stained for NeuN. In total, 66 confocal images from the LDT and 55 confocal images from the Lhb were obtained using a 40X objective ( $n = 3$  mice). The percentage of ChR2-eYFP-positive cells relative to the number of NeuN-positive cells in a 125 µm × 125 µm area was analysed using the ImageJ software. Approximately 20% of all NeuN-positive LDT and Lhb neurons expressed ChR2-eYFP after RV-ChR2 injection into the VTA (Supplementary Fig. 15).

**Behavioural assays.** All behavioural tests were conducted during the same circadian period (13:00–19:00). The CPP and CPA protocols were performed in a rectangular cage with a left chamber measuring 28 cm × 24 cm with black and

white stripes on the walls and a metal grill floor, a centre chamber measuring 11.5 cm × 24 cm with white walls and a smooth plastic floor and a right chamber measuring 28 cm × 24 cm with black and white squares on the walls and a punched metal floor. The apparatus was designed so that mice did not have any consistent bias for a particular chamber (Supplementary Fig. 4b). The CPP and CPA tests consisted of 3 sessions over 3 days. On day 1 (1 week after infusion of RV-eGFP or RV-ChR2 into the VTA), individual mice were placed in the centre chamber and allowed to freely explore the entire apparatus for 15 min (pre-test). On day 2 mice were confined to one of the side chambers for 30 min during optical stimulation. Stimulation in left or right chambers was counterbalanced across mice. For stimulation the optical fibre was connected to a 473-nm laser diode (OEM Laser Systems) through an FC/PC adaptor. Laser output was controlled using a Master-8 pulse stimulator (A.M.P.I.), which delivered 8 pulses of 5-ms light flashes at 30 Hz every 5 s (phasic stimulation) or 5-ms light flashes delivered at 1 Hz (low-frequency stimulation). For stimulation of LDT and Lhb axon terminals in the VTA, 15 pulses of 5-ms light flashes at 30 Hz every 2 s were delivered. Light output through the optical fibres was adjusted to 20 mW using a digital power meter console (Thorlabs) and was checked before and after stimulation of each mouse. On day 3, similar to day 1, mice were placed in the centre chamber and allowed to freely explore the entire apparatus for 15 min (post-test 1). After post-test 1 the blue-light laser was switched on and the mouse received phasic or low-frequency stimulation for whenever it was in the chamber in which it had been conditioned on day 2 for a total duration of 15 min (post-test 2). There was no interruption between post-test 1 and post-test 2. A video tracking system (BIOBSERVE) recorded all animal movements. To calculate preference or aversion during post-test 1, we divided the relative time (in %) the mouse spent during post-test 1 in the conditioned chamber (that is, the chamber in which it received either phasic or low-frequency light stimulation of LDT or Lhb inputs to the VTA) by the relative time (in %) the mouse spent in this chamber during the pre-test (post-test 1/pre-test ratio). During post-test 2, preference or aversion was calculated by dividing the relative time (in %) the mouse spent during post-test 2 in the conditioned chamber by the relative time (in %) the mouse spent in this chamber during the pre-test (post-test 2/pre-test ratio).

For the microinjection of the D1 dopamine receptor antagonist SCH23390 into the mPFC and the microinjection of the D1 and D2 dopamine receptor antagonists SCH23390 and raclopride into the NAc lateral shell, a 33-gauge injector cannula connected to a syringe pump (Harvard Apparatus) was inserted into the guide cannula which had been implanted in the mPFC or NAc lateral shell. All micro-injections were delivered at a rate of 100 nl min<sup>-1</sup>. Injector cannulas remained in place for an additional minute before being removed. Drugs were infused 5 min before the beginning of the light stimulation on day 2. For the pharmacological control experiments, the animals were treated identically except no optical stimulation was provided. Doses of drugs used for microinjections were: 50 ng SCH23390 in 0.2 µl saline (mPFC); 300 ng SCH23390 and 3 µg raclopride in 0.3 µl saline/DMSO (NAc lateral shell).

The open-field test was conducted on different cohorts of mice to measure the effect of optogenetic stimulation on anxiety-like responses and general locomotor ability. The mice were placed in the chamber (50 × 50 cm) and their movement was recorded and analysed for 18 min using the same video-tracking software that was used in the CPP and CPA tests (BIOBSERVE). After 3 minutes without optical stimulation, phasic stimulation was turned on for three 3-min epochs interspersed with 3-min epochs of no stimulation. For all analyses and graphs where total 'off' and 'on' conditions are displayed, the three 'off' epochs were pooled and the three 'on' epochs were pooled. The inner zone of the open-field chamber was defined as the 23 × 23 cm central square area.

For quantification of FOS immunoreactivity, LDT and Lhb inputs to the VTA were stimulated for 30 min using the phasic light-stimulation protocol. During this time the mice remained in their home cage. The mice were perfused with 4% PFA 60 min after the *in vivo* light stimulation and 24 h later immunohistochemistry was performed.

**Statistics.** Student's *t*-tests, Mann-Whitney U-tests or one-way ANOVA tests were used to determine statistical differences using GraphPad prism 5 (Graphpad Software). Bonferroni post hoc analysis was applied, when necessary, to compare means. Statistical significance was set at \* $P < 0.05$ , \*\* $P < 0.01$ , \*\*\* $P < 0.001$ . All data values are presented as mean ± s.e.m.

39. Zhang, F. *et al.* Optogenetic interrogation of neural circuits: technology for probing mammalian brain structures. *Nature Protocols* **5**, 439–456 (2010).
40. Mebatsion, T., Konig, M. & Conzelmann, K. K. Budding of rabies virus particles in the absence of the spike glycoprotein. *Cell* **84**, 941–951 (1996).
41. Wickersham, I. R., Sullivan, H. A. & Seung, H. S. Production of glycoprotein-deleted rabies viruses for monosynaptic tracing and high-level gene expression in neurons. *Nature Protocols* **5**, 595–606 (2010).
42. Franklin, K. & Paxinos, G. *The Mouse Brain in Stereotaxic Coordinates* (Elsevier, 2001).



# Filamentous bacteria transport electrons over centimetre distances

Christian Pfeffer<sup>1</sup>, Steffen Larsen<sup>2</sup>, Jie Song<sup>3</sup>, Mingdong Dong<sup>3</sup>, Flemming Besenbacher<sup>3</sup>, Rikke Louise Meyer<sup>2,3</sup>, Kasper Urup Kjeldsen<sup>1</sup>, Lars Schreiber<sup>1</sup>, Yuri A. Gorby<sup>4</sup>, Mohamed Y. El-Naggar<sup>5</sup>, Kar Man Leung<sup>4,5</sup>, Andreas Schramm<sup>1,2</sup>, Nils Risgaard-Petersen<sup>1</sup> & Lars Peter Nielsen<sup>1,2</sup>

Oxygen consumption in marine sediments is often coupled to the oxidation of sulphide generated by degradation of organic matter in deeper, oxygen-free layers. Geochemical observations have shown that this coupling can be mediated by electric currents carried by unidentified electron transporters across centimetre-wide zones. Here we present evidence that the native conductors are long, filamentous bacteria. They abounded in sediment zones with electric currents and along their length they contained strings with distinct properties in accordance with a function as electron transporters. Living, electrical cables add a new dimension to the understanding of interactions in nature and may find use in technology development.

Marine sediments become anoxic because oxygen is consumed by microbial processes at the surface. Without available oxygen the microorganisms living below the surface are supposed to depend on energetically less favourable, anaerobic processes<sup>1</sup>. Recently, however, electric currents have been found to directly connect oxygen reduction at the surface with sulphide oxidation in the subsurface<sup>2</sup>, even when oxygen and sulphide are separated by more than 1 cm. Half of the sediment oxygen consumption can be driven by electrons transported from below<sup>2,3</sup>. The spatial separation of oxidation and reduction processes invokes steep pH gradients leading to distinct dissolutions and precipitations of minerals<sup>3</sup>. Microbial activity apparently drives the electrochemical half-reactions and the establishment of electron-conducting structures through the sediment<sup>2</sup>. Bacterial nanowires, humus particles and semi-conductive mineral grains are known to conduct electrons over nanometre to micrometre distances, and alone or in combination they have been proposed to facilitate electron transport over centimetre distances in marine sediment<sup>2,4,5</sup>. Experimental tests and observations have failed to confirm these proposals so far, and instead we have unexpectedly found long, filamentous bacteria structured like electric cables as reported below.

## Filamentous *Desulfobulbaceae* in electric sediment

When sulphidic defaunated marine sediment was incubated in the dark with overlying oxic sea water, the porewater chemistry gradually developed in accordance with the establishment of an electron transport mechanism that coupled oxygen reduction at the sediment surface to sulphide oxidation in deeper anoxic layers (Fig. 1a). As described previously<sup>2,3</sup>, the electric coupling of spatially segregated processes was evident from (1) the presence of a distinct pH peak demonstrating aerobic proton consumption—an indicator of electrochemical oxygen reduction<sup>2,3</sup>—and (2) the formation of a 12–15-mm deep suboxic zone separating sulphide oxidation from the associated oxygen reduction<sup>2,3</sup>. When sediment from the top 20 mm was gently washed, tufts of entangled filamentous bacteria appeared (Fig. 1b). Reverse transcription, cloning and sequencing of 16S ribosomal RNA from dissected filaments identified them as novel members of the deltaproteobacterial family *Desulfobulbaceae* with < 92% sequence

identity to any cultured member of this family (Fig. 1d). Almost identical (> 99%) 16S rRNA sequences were detected in the suboxic zones of three replicate cores (Fig. 1d), whereas they were absent in the subjacent sulphidic zones. The filaments were identified and quantified in the sediments by fluorescence *in situ* hybridization (FISH) with specific 16S rRNA-targeting probes (Fig. 1c). The length density of filaments was at least  $117 \text{ m cm}^{-3}$  in the oxic and suboxic sediment zone and no filaments were detected in the deeper sulphidic zone. With an average cell length of 3  $\mu\text{m}$ , this length density corresponded to  $4 \times 10^7 \text{ cells cm}^{-3}$ . Individual filaments were difficult to dissect out without breaking them, however, fragments up to 1.5 cm long were recorded, supporting that the bacteria had the length to span the entire suboxic zone.

## *Desulfobulbaceae* filaments qualify as conductors

We demonstrated experimentally that electron transport through the suboxic zone was mediated by a coherent structure like a bacterial filament and not by diffusive electron shuttles or casual contact between conductive elements. Evidence for solid conductors was found by passing a very thin tungsten wire (50  $\mu\text{m}$  diameter) horizontally through sediment 1–2 mm below the oxic–anoxic interface, thus transiently interrupting the sediment continuum (see Supplementary Information for details). The cut resulted in an immediate and lasting halt of the electron transport, as indicated by a significant drop in oxygen consumption (Tukey's test under analysis of variance (ANOVA);  $P < 0.001$ ;  $\alpha = 0.05$ ;  $n = 27$ ), attenuation of the pH peak in the oxic zone and contraction of the suboxic zone (Fig. 2), the latter being similar to the response to momentary oxygen removal observed in a previous study<sup>2</sup>. The role of bacteria in establishing a centimetre-long electron transport mechanism was further investigated in incubations, where filters with defined pore sizes were inserted into sediment cores to selectively exclude or permit vertical growth or migration of bacteria. Manifestations of long-distance electron transport appeared in cores containing filter barriers with pore sizes of 2.0  $\mu\text{m}$  (Fig. 3), but did not appear in cores containing filter barriers with pore sizes  $\leq 0.8 \mu\text{m}$  as indicated from significantly lower

<sup>1</sup>Center for Geomicrobiology, Department of Bioscience, Aarhus University, 8000 Aarhus C, Denmark. <sup>2</sup>Section for Microbiology, Department of Bioscience, Aarhus University, 8000 Aarhus C, Denmark. <sup>3</sup>Centre for DNA Nanotechnology (CDNA), Interdisciplinary Nanoscience Center (iNANO), Aarhus University, 8000 Aarhus C, Denmark. <sup>4</sup>Department of Biological Sciences, University of Southern California, Los Angeles, California 90089, USA. <sup>5</sup>Department of Physics and Astronomy, University of Southern California, Los Angeles, California 90089, USA.

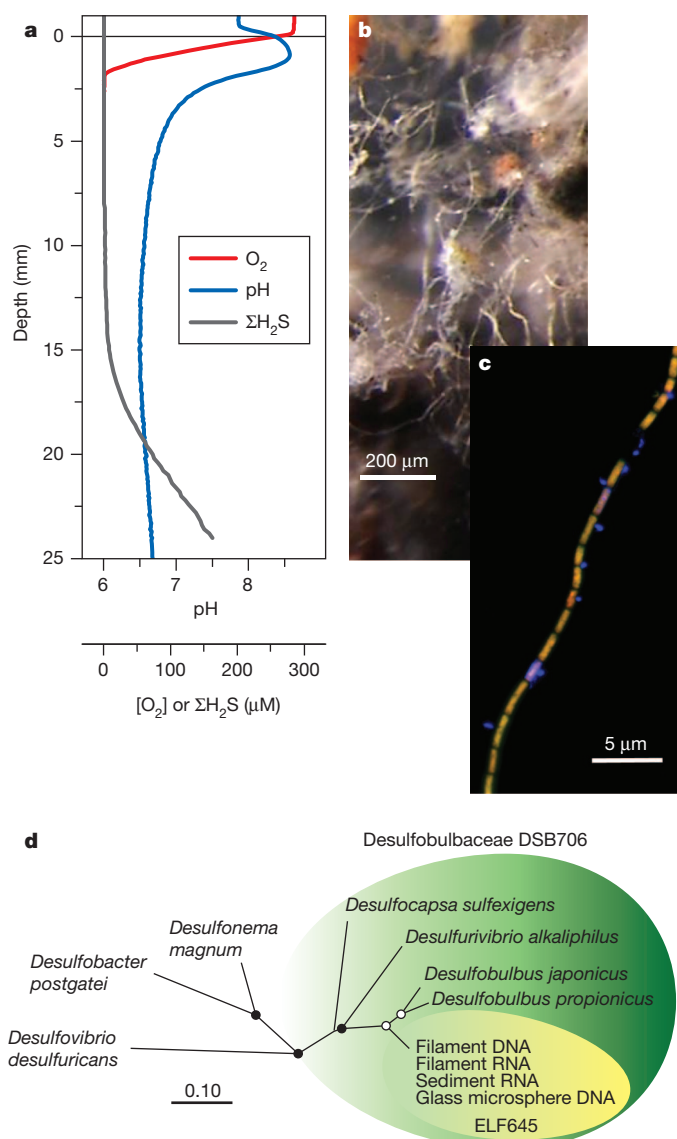


**Figure 1 | Filamentous *Desulfobulbaceae* in current-producing sediments.** **a**, Microprofiles of  $O_2$ , pH and  $\Sigma H_2S$  ( $\Sigma H_2S = ([H_2S] + [HS^-] + [S^{2-}])$ ). **b**, Tuft of filamentous *Desulfobulbaceae* collected from the sulphide-free zone. **c**, Filamentous *Desulfobulbaceae* identified by fluorescence *in situ* hybridization targeting 16S rRNA. Filament cells appear yellow from overlay of images obtained with probe DSB706 (labelled green) and probe ELF654 (labelled red); other cells appear blue from DNA-staining with 4',6-diamidino-2-phenylindole (DAPI). **d**, Phylogenetic affiliation (by maximum likelihood) of the filaments based on 16S rRNA sequences. Scale bar, 10% estimated sequence divergence; filled and open circles show bootstrap support >80% and >60%, respectively (by maximum parsimony; 1,000 iterations); the specificity of the probes used for FISH is indicated by the green and yellow shading. Accession numbers are given in Supplementary Table 1.

oxygen consumption rates (Tukey's test under ANOVA;  $P < 0.001$ ;  $\alpha = 0.05$ ;  $n = 18$ ) and absence of pH peaks in the oxic zone of these cores. This observation confirms that passage of bacteria-sized objects and not only dissolved or colloidal compounds were required. Sediment particles were not essential as mediators for the electron transport either, because manifestations of long-distance electron transport also developed in incubations where a 5-mm sediment layer had been replaced by non-conductive glass microspheres (Fig. 4). The filamentous *Desulfobulbaceae* were abundant in the glass microsphere layer as confirmed by FISH and 16S rRNA gene sequencing (Figs 1c and 4b), and no other connecting structures were observed by light and scanning electron microscopy (SEM) inspection.

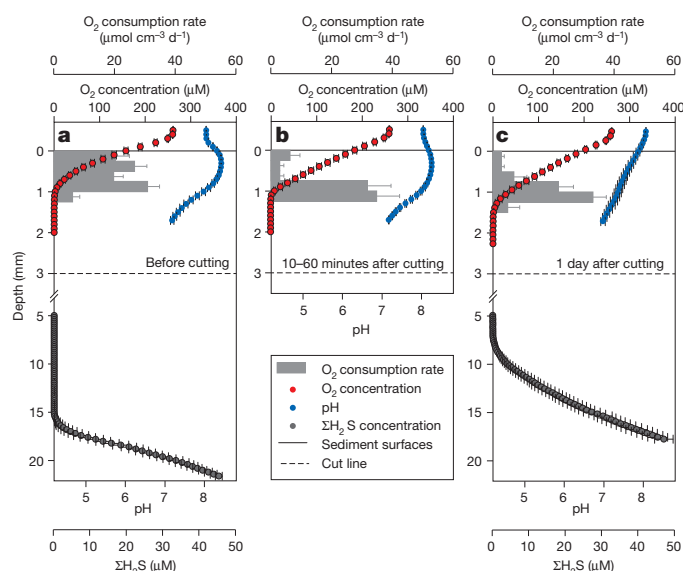


**Figure 2 | Biogeochemical impacts of filament cutting.** **a–c**, Microprofiles of oxygen, sulphide and pH measured in undisturbed sediment cores (**a**), 10–60 min (**b**) and 1 day (**c**) after passing a thin tungsten wire (50  $\mu m$  diameter) horizontally through the sediment near the oxic–anoxic interface. Data are presented as mean values  $\pm$  s.e.m. (oxygen and pH,  $n = 9$ ; sulphide,  $n = 6$ ). Volume-specific rates of oxygen consumption rates (grey areas) are calculated from numerical modelling of the measured oxygen concentration profiles.

### Structure of *Desulfobulbaceae* filaments

The multicellular *Desulfobulbaceae* filaments showed a unique structure with uniform ridges running along their entire length (Fig. 5a). Transmission electron microscopy of thin sections showed two types of filaments that either had 15 ridges and were about 400 nm wide or had 17 ridges and were about 700 nm wide (Fig. 5b, c). Each ridge contained a filled, 70–100 nm wide channel between the cytoplasmic and the outer membrane. The adjacent cells within the filaments were separated by 200 nm wide gaps bridged by the ridge filling and tightly wrapped up by the outer membrane, which seemed to encase the entire filament (Fig. 5d, e). A similar collective outer membrane of the filamentous multicellular cyanobacterium *Anabaena* sp. has been suggested to ease exchange of nutrients between cells without leakage to the surroundings<sup>6</sup>. It is possible that the outer membrane of the *Desulfobulbaceae* filaments has a similar function with respect to electrons. On the basis of all the morphological data, we propose that

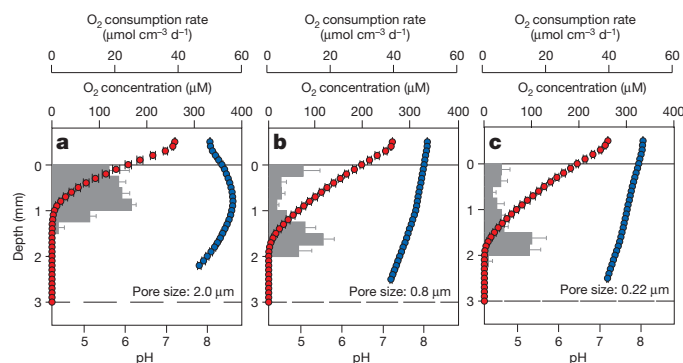


**Figure 3 | Biogeochemical effects of filter pore size.** **a–c**, Depth distributions of oxygen concentrations (red circles) and pH (blue circles) measured after 20 days of incubation in sediment cores containing polycarbonate filters with different pore sizes: 2.0  $\mu m$  (**a**), 0.8  $\mu m$  (**b**) and 0.22  $\mu m$  (**c**). The filter position is indicated by the dashed line. Volume-specific rates of oxygen consumption (grey bars) were estimated from numerical modelling of the oxygen concentration profiles. Data are presented as mean values  $\pm$  s.e.m. ( $n = 6$ ).



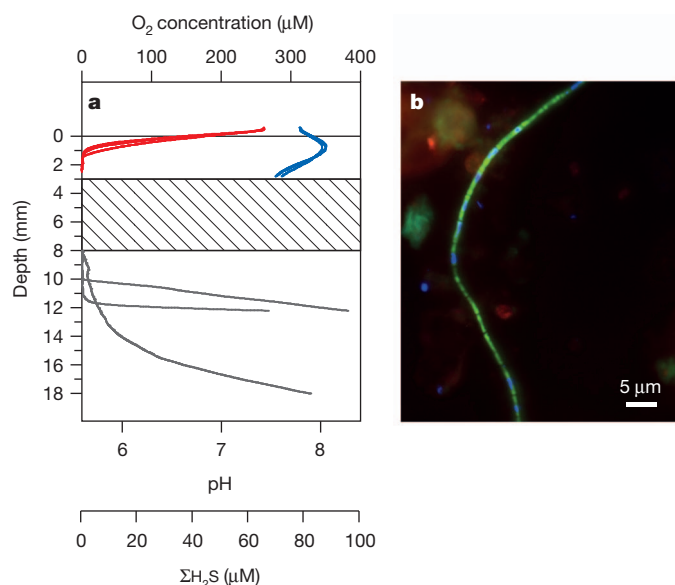


**Figure 4 | Effect of layer of glass beads intercalated in the sediment.** **a**, Oxygen concentrations (red lines), pH (blue lines) and sulphide concentrations (black lines) in three sediment cores with an intercalated layer of electrically inert glass microspheres reaching from 3 mm down to 8 mm sediment depth (hatched area). **b**, Micrograph showing filamentous *Desulfobulbaceae* extracted from a glass bead section and hybridized with the specific ELF654 FISH probe. DAPI-stained chromosomes are visible in some cells of the filament.

the ridges are strings transporting electrons along the filament inside a continuous periplasmic space, with the collective outer membrane serving as electrical insulation from the external medium. To explore the conductive properties of the strings, electrostatic force microscopy (EFM)<sup>7</sup> was applied, as this technique does not require direct contact and may therefore trace electric properties of insulated materials. A distinct elevation of electrostatic force on the ridges as compared to the intermittent areas (Fig. 5g) indicates that the underlying strings possess significant polarizability or charge storage capacity along their length as well as across cell–cell junctions. The highly organized contrast pattern excludes significant contribution from random leakage of polymers like extracellular DNA. These results are consistent with the proposed charge distribution role. Furthermore, we tested the hypothesis using a nanofabrication approach, similar to that previously used to demonstrate charge transfer along the length of a bacterial nanowire<sup>8</sup>. Current–voltage measurements were performed on individual filaments that were bridging two gold electrodes and fixed with platinum leads. In contrast to what should be observed if the conductive structures were exposed to the surface, sweeping the voltage from  $-10$  V to  $10$  V was not accompanied by any measurable electrical currents. This observation supports the hypothesis that conductive structures present in the periplasmic continuum are electrically insulated by the collective outer membrane.

## Discussion

Taken together, the data presented here strongly indicate that long-distance electron transport from sulphide to oxygen in the sediment is mediated by living micro-cables in the form of long filamentous bacteria of the *Desulfobulbaceae* family. As the simplest metabolic model consistent with our data, we propose that the micro-cables are multicellular, aerobic, sulphide oxidizers where electrons generated by sulphide oxidation in cells at one end can be passed through internal, insulated wires to cells at the other end and here are consumed by oxygen reduction. Charge transport by ions in the surrounding environment balances the internal electron transport, thereby completing the electric circuit and retaining charge balance<sup>2,3</sup>.

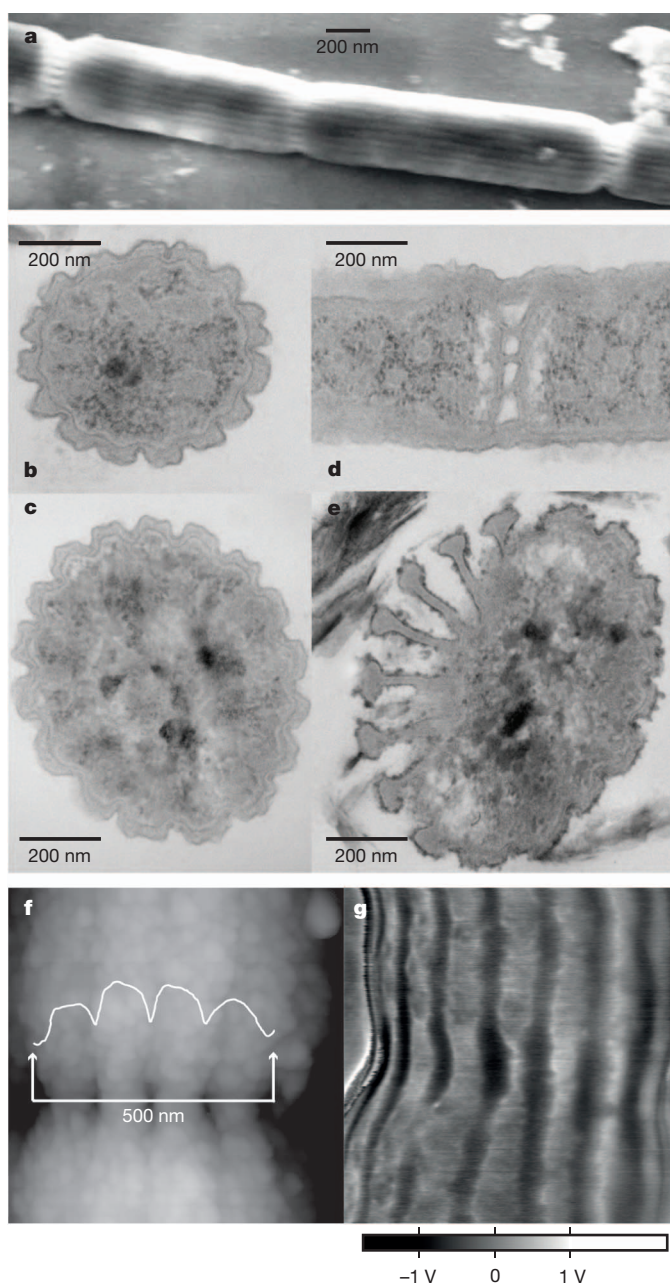


**Figure 5 | AFM, SEM, TEM and EFM micrographs of the filamentous *Desulfobulbaceae*.** **a**, SEM image of four cells. **b**, **c**, Thin-section TEM images of filament cross sections. **d**, **e**, Longitudinal section including a cell–cell junction (**d**) and oblique section of cell–cell junction (**e**). **f**, Height AFM image of cell–cell junction with inserted topographic curve along 500 nm line with the same scaling of  $x$ ,  $y$  and  $z$  axes. **g**,  $1 \times 1 \mu\text{m}$  EFM image above cell–cell junction with lighter contrast following the ridge topography mapped in the preceding AFM scan (not shown).

Many prokaryotes are known to perform extracellular electron exchange as a method to control metabolic interactions with external solids or cells. Electrons are exchanged with insoluble electron acceptors and donors like iron and manganese minerals<sup>9</sup> or electrodes<sup>10</sup>. Furthermore, syntrophic interspecies electron exchange via nanowires and magnetite grains has recently been confirmed<sup>4,11</sup>. External deposition of electrons preventing internal accumulation of insoluble and potentially harmful metabolites has also been found<sup>12</sup>. However, different from these prokaryotes using external electron transport, the competitive advantage of micro-cables seems to be their ability to separate soluble electron acceptors and donors in space, thereby enabling them to monopolise major energy sources. This is done by transport of

electrons from donors to acceptors over long distances via insulated internal wires with no need for electron transfer across the outer membrane. Oxidation of sulphide is a major driver of oxygen consumption in marine sediments, and the question arises how successful the filamentous bacteria are in competing with other sulphide oxidizing bacteria and in controlling the process. Separation of oxygen and sulphide is common in marine sediment and conventionally explained by iron and manganese biogeochemistry driven by particle mixing or by bacterial nitrate transport<sup>13–16</sup>. Few studies have however directly quantified these pathways.

Bacterial micro-cables represent a hitherto unknown lifestyle, which immediately raises many intriguing questions for further research: How are energy conservation and growth allocated among the cells? What is their genetic and metabolic diversity? How are filament division and dispersal controlled? What is the molecular and electronic basis of the electron transport? How widespread are they in nature? Transmission improvement and control of electric currents have been major drivers for electronic innovation. It appears that biological evolution has worked successfully in the same direction.

## METHODS SUMMARY

Microbiological and geochemical data were obtained from sulphidic sediment sampled in Aarhus Bay, Denmark. The sediment was sieved, transferred to glass core liners and incubated for three to four weeks in aquaria with circulating air-saturated sea water as described previously<sup>2</sup>. Oxygen, sulphide and pH micro-profiles were measured as described previously<sup>17–19</sup>.

Nucleic acids were extracted from sediment, glass microspheres and from single filaments collected by micromanipulation. RNA was reverse-transcribed, and 16S rRNA complementary DNA fragments were PCR-amplified, cloned and sequenced. Oligonucleotide probes for FISH were designed specific for the retrieved sequences and used for microscopic identification and quantification of the filamentous *Desulfobulbaceae* by FISH in fixed sediment samples.

AFM images of rinsed air-dried cells were obtained on a Nanowizard II (JPK Instruments) in intermittent contact mode under ambient conditions with an OMCL-AC160TN cantilever (Olympus).

EFM images of rinsed air-dried cells were performed on a Bruker Dimension 3100 (Bruker Corporation) equipped with a Pt/Ir-coated tip (SCMPIC, Veeco Metrology) using the two-pass scan technique<sup>20</sup>. On the second pass, the probe was lifted at 5 nm with respect to the sample topography, while an oscillating bias potential  $V = V_{dc} + V_{ac}\sin(\omega t)$  was applied between the tip and the substrate ( $V_{dc}$ , direct current voltage;  $V_{ac}$ , alternate current voltage;  $\omega$ , modulation frequency (500 Hz)). The electrostatic force can be represented by volts.

SEM of air dried cells were obtained on a NanoSEM (FEI, Nova 600 NanoSEM) operated in low-vacuum (60 Pa) and low-voltage (3 kV) mode to apply the charge contrast imaging data.

TEM of 40–60 nm cell sections were obtained on an FEI CM100 (FEI CM100). Electric conductivity of the cell surface was addressed with nano-fabricated electrodes.

A full description of the methodology applied in the present study is given in the Supplementary Information.

Received 6 July; accepted 17 September 2012.

Published online 24 October 2012.

1. Jørgensen, B. B. in *Marine Geochemistry* (eds Schulz, H. D. & Zabel, M.) 173–207 (Springer, 2000).

2. Nielsen, L. P., Risgaard-Petersen, N., Fossing, H., Christensen, P. B. & Sayama, M. Electric currents couple spatially separated biogeochemical processes in marine sediment. *Nature* **463**, 1071–1074 (2010).
3. Risgaard-Petersen, N., Revil, A., Meister, P. & Nielsen, L. P. Sulfur, iron-, and calcium cycling associated with natural electric currents running through marine sediment. *Geochim. Cosmochim. Acta* **92**, 1–13 (2012).
4. Kato, S., Hashimoto, K. & Watanabe, K. Microbial interspecies electron transfer via electric currents through conductive minerals. *Proc. Natl Acad. Sci. USA* **109**, 10042–10046 (2012).
5. Roden, E. E. *et al.* Extracellular electron transfer through microbial reduction of solid-phase humic substances. *Nature Geosci.* **3**, 417–421 (2010).
6. Mariscal, V., Herrero, A. & Flores, E. Continuous periplasm in a filamentous, heterocyst-forming cyanobacterium. *Mol. Microbiol.* **65**, 1139–1145 (2007).
7. Lu, W., Wang, D. & Chen, L. W. Near-static dielectric polarization of individual carbon nanotubes. *Nano Lett.* **7**, 2729–2733 (2007).
8. El-Naggar, M. Y. *et al.* Electrical transport along bacterial nanowires from *Shewanella oneidensis* MR-1. *Proc. Natl Acad. Sci. USA* **107**, 18127–18131 (2010).
9. Reguera, G. *et al.* Extracellular electron transfer via microbial nanowires. *Nature* **435**, 1098–1101 (2005).
10. Holmes, D. E., Bond, D. R. & Lovley, D. R. Electron transfer by *Desulfobulbus propionicus* to Fe(III) and graphite electrodes. *Appl. Environ. Microbiol.* **70**, 1234–1237 (2004).
11. Summers, Z. M. *et al.* Direct exchange of electrons within aggregates of an evolved syntrophic coculture of anaerobic bacteria. *Science* **330**, 1413–1415 (2010).
12. Cologgi, D. L., Lampa-Pastirk, S., Speers, A. M., Kelly, S. D. & Reguera, G. Extracellular reduction of uranium via *Geobacter* conductive pili as a protective cellular mechanism. *Proc. Natl Acad. Sci. USA* **108**, 15248–15252 (2011).
13. Canfield, D. E. Reactive iron in marine-sediments. *Geochim. Cosmochim. Acta* **53**, 619–632 (1989).
14. Fossing, H. *et al.* Concentration and transport of nitrate by the mat-forming sulphur bacterium *Thioploca*. *Nature* **374**, 713–715 (1994).
15. Preisler, A. *et al.* Biological and chemical sulfide oxidation in a *Beggiatoa* inhabited marine sediment. *ISME J.* **1**, 341–353 (2007).
16. Sayama, M., Risgaard-Petersen, N., Nielsen, L. P., Fossing, H. & Christensen, P. B. Impact of bacterial  $\text{NO}_3^-$  transport on sediment biogeochemistry. *Appl. Environ. Microbiol.* **71**, 7575–7577 (2005).
17. Jeroschewski, P., Steuckart, C. & Kuhl, M. An amperometric microsensor for the determination of  $\text{H}_2\text{S}$  in aquatic environments. *Anal. Chem.* **68**, 4351–4357 (1996).
18. Revsbech, N. P. An oxygen microsensor with a guard cathode. *Limnol. Oceanogr.* **34**, 474–478 (1989).
19. Revsbech, N. P. & Jørgensen, B. B. Microelectrodes: their use in microbial ecology. *Adv. Microb. Ecol.* **9**, 293–352 (1986).
20. Cherniavskaya, O., Chen, L. W., Weng, V., Yuditsky, L. & Brus, L. E. Quantitative noncontact electrostatic force imaging of nanocrystal polarizability. *J. Phys. Chem. B* **107**, 1525–1531 (2003).

Supplementary Information is available in the online version of the paper.

**Acknowledgements** The authors thank P. G. Sørensen and L. B. Pedersen for construction of microsensors. Thanks to K. E. Thomsen for operating the TEM. B. B. Jørgensen is thanked for his general support. This research was financially supported by the European Research Council (L.P.N.), the Danish National Research Foundation (N.R.-P., C.P., K.U.K., L.S., M.D.), the Danish Council for Independent Research | Natural Sciences (FNU) (L.P.N.), the German Max Planck Society (N.R.-P., C.P., K.U.K., L.S.) and the Villum Foundation (M.D.).

**Author Contributions** This study was conceived by L.P.N., N.R.-P. and A.S. Experimental work: C.P. FISH and molecular phylogeny: S.L. Single-cell identification: K.U.K. and L.S. AFM: R.L.M., J.S. and M.D. SEM and EFM: J.S., M.D. and F.B. TEM: L.P.N. and J.S. Conductivity measurements using nanofabricated electro discs: J.S., Y.A.G., M.Y.E.-N., K.M.L. and C.P. All authors contributed to discussions of the data and preparation of the manuscript.

**Author Information** All sequences are deposited in GenBank/EMBL/DBJ under accession numbers JX091023–JX091073. Reprints and permissions information is available at [www.nature.com/reprints](http://www.nature.com/reprints). The authors declare no competing financial interests. Readers are welcome to comment on the online version of the paper. Correspondence and requests for materials should be addressed to N.R.-P. (nils.risgaard-petersen@biology.au.dk) or L.P.N. (biolpn@biology.au.dk).



# Principles for designing ideal protein structures

Nobuyasu Koga<sup>1\*</sup>, Rie Tatsumi-Koga<sup>1\*</sup>, Gaohua Liu<sup>2,3\*</sup>, Rong Xiao<sup>2,3</sup>, Thomas B. Acton<sup>2,3</sup>, Gaetano T. Montelione<sup>2,3</sup> & David Baker<sup>1</sup>

Unlike random heteropolymers, natural proteins fold into unique ordered structures. Understanding how these are encoded in amino-acid sequences is complicated by energetically unfavourable non-ideal features—for example kinked  $\alpha$ -helices, bulged  $\beta$ -strands, strained loops and buried polar groups—that arise in proteins from evolutionary selection for biological function or from neutral drift. Here we describe an approach to designing ideal protein structures stabilized by completely consistent local and non-local interactions. The approach is based on a set of rules relating secondary structure patterns to protein tertiary motifs, which make possible the design of funnel-shaped protein folding energy landscapes leading into the target folded state. Guided by these rules, we designed sequences predicted to fold into ideal protein structures consisting of  $\alpha$ -helices,  $\beta$ -strands and minimal loops. Designs for five different topologies were found to be monomeric and very stable and to adopt structures in solution nearly identical to the computational models. These results illuminate how the folding funnels of natural proteins arise and provide the foundation for engineering a new generation of functional proteins free from natural evolution.

For proteins to fold, the interactions favouring the native state must collectively outweigh the non-native interactions, resulting in funnel-shaped energy landscapes<sup>1–3</sup>. However, it is not obvious how the ubiquitous non-covalent interactions that stabilize proteins—van der Waals interactions, hydrogen bonding and hydrophobic packing—can selectively favour the biologically relevant unique native structure over the vastly larger number of non-native conformations. Protein design provides an opportunity to investigate this problem: hypotheses about how unique folded structures are encoded in amino-acid sequences can be evaluated by designing proteins *de novo* and experimentally assessing how well they fold<sup>4–6</sup>.

Previous work on protein fold design has focused on stabilizing the desired folded state<sup>7–13</sup>. However, robustly designing protein structures with funnel-shaped energy landscapes may require not only the stabilization of a unique folded state<sup>7–13</sup> (positive design), but also the destabilization of non-native states<sup>14–16</sup> (negative design). Protein design methodology has been developed to find sequences that stabilize a desired folded state and destabilize specific non-native states<sup>14–20</sup>. However, the challenge of disfavoring the vast number of non-native states quite generally remains an unsolved problem.

We hypothesized that funnel-shaped energy landscapes can be robustly generated by requiring that the local interactions between residues close along the linear sequence, which determine protein secondary structure, and the non-local interactions between residues distant along the chain, which stabilize protein tertiary structure, consistently favour the same folded conformation<sup>21</sup>. We sought principles for designing ‘ideal’ proteins that have this property. To disfavor non-native states systematically by negative design, we focused on the local interactions because non-local interactions vary strongly with even small changes in tertiary structure. We began by investigating the mapping between local interactions favouring specific secondary structure patterns and protein tertiary structure motifs, seeking local structure patterns that strongly favour single tertiary motifs over all others.

We focused on a basis set of tertiary structure motifs consisting of two or three secondary structure elements adjacent in the linear sequence, which make extensive intramotif interactions. We investigated the mapping from secondary structure patterns to these tertiary structure features using a combination of *de novo* folding calculations with the Rosetta program<sup>22</sup> and analyses of naturally occurring protein structures in the Protein Data Bank. Multiple protein folding simulations were carried out for each motif for a range of different lengths of the strands, helices and loops, using a sequence-independent backbone model. For each choice of lengths, we computed the fraction of trajectories that arrived at the desired motif topology. These calculations revealed that the extent of folding to a particular motif is very strongly dependent on the lengths of the secondary structures. Detailed study of these dependencies identified three fundamental rules, which are described in the following section.

## Rules relating local structures to tertiary motifs

The fundamental rules describe the junctions between adjacent secondary structure elements (Fig. 1). There are three distinct junction classes in the  $\alpha\beta$ -folds we sought to design— $\beta\beta$ ,  $\beta\alpha$  and  $\alpha\beta$ —and three corresponding rules.

Statement of the rules requires the definition of the chirality (L versus R) of a  $\beta\beta$ -unit and the orientation (P versus A) of  $\beta\alpha$ - and  $\alpha\beta$ -units (Fig. 1). The chirality of a  $\beta\beta$ -unit is defined on the basis of the orientation of the  $C\alpha$ -to- $C\beta$  vector,  $\overrightarrow{C\alpha C\beta}$ , of the strand residue preceding or following the connecting loop: letting  $u$  be a vector along the first secondary structure element and  $v$  be a vector from the centre of the first secondary structure element to the centre of the second secondary structure element, if  $(u \times v) \cdot \overrightarrow{C\alpha C\beta}$  (where a cross denotes vector product and a dot denotes scalar product) is positive the unit is right handed (R), and if it is negative the unit is left handed (L) (Fig. 1d). For  $\beta\alpha$ - and  $\alpha\beta$ -units in which the  $\beta$ -strand is in a  $\beta$ -sheet that the helix packs against, the  $\overrightarrow{C\alpha C\beta}$  vectors in the strand are roughly

<sup>1</sup>University of Washington, Department of Biochemistry and Howard Hughes Medical Institute, Seattle, Washington 98195, USA. <sup>2</sup>Rutgers, The State University of New Jersey, Center for Advanced Biotechnology and Medicine, Department of Molecular Biology and Biochemistry, Northeast Structural Genomics Consortium, Piscataway, New Jersey 08854, USA. <sup>3</sup>Department of Biochemistry and Molecular Biology, Robert Wood Johnson Medical School, University of Medicine and Dentistry of New Jersey, Piscataway, New Jersey 08854, USA.

\*These authors contributed equally to this work.

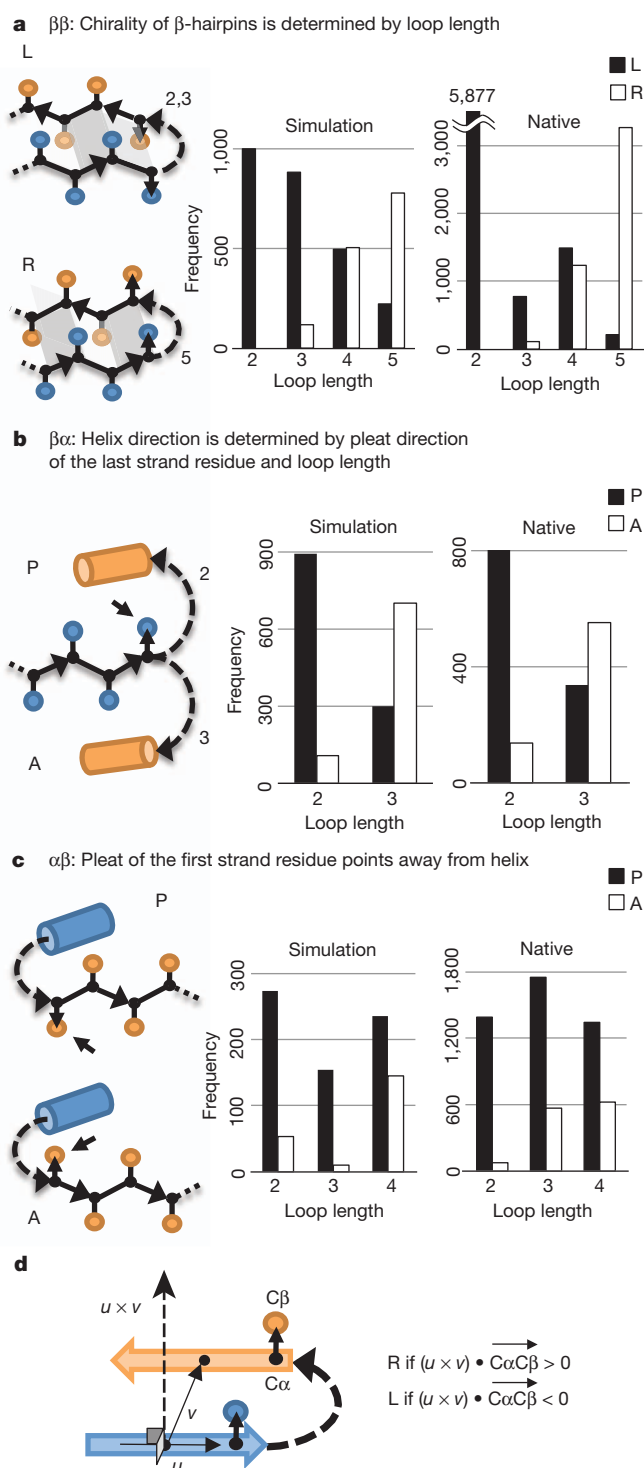


**Figure 1 | Fundamental rules.** **a**,  $\beta\beta$ -rule. L (left-handed) and R (right-handed)  $\beta\beta$ -units are illustrated (see Fig. 1d for chirality definition). The dependence of chirality on loop length is shown in the histograms. **b**,  $\beta\alpha$ -rule. P (parallel) and A (antiparallel)  $\beta\alpha$ -units are illustrated. The dependence of orientation (P versus A) on loop length is shown in the histograms. **c**,  $\alpha\beta$ -rule. **d**, Chirality (L versus R) of a  $\beta\beta$ -unit. The chirality is defined on the basis of the orientation of the  $C\alpha$ -to- $C\beta$  vector,  $C\alpha C\beta$ , of the strand residue preceding or following the connecting loop.  $u$  is a vector along the first strand and  $v$  is a vector from the centre of the first strand to the centre of the second strand.

collinear with the vector between the centres of the strand and the helix. We define the orientation of a  $\beta\alpha$ -unit to be parallel (P) if the vector from strand to helix is parallel to the  $C\alpha C\beta$  vector of the last residue in the strand, and to be antiparallel (A) if the two are

antiparallel (Fig. 1b). The orientation of an  $\alpha\beta$ -unit is P if the  $C\alpha C\beta$  vector of the first residue in the strand is parallel to the vector from helix to strand, and is A if the two are antiparallel (Fig. 1c) (see Supplementary Methods 4 and 5 for details).

### $\beta\beta$ -rule

The chirality of  $\beta$ -hairpins is determined by the length of the loop between the two strands. Rosetta folding simulations of a peptide with two equal-length  $\beta$ -strands connected by a variable-length loop were carried out on a sequence-independent backbone model (Methods Summary, Methods and Supplementary Methods 1). The chirality (Fig. 1d) of the end points of multiple independent Monte Carlo trajectories was computed. The results (Fig. 1a, left) are quite striking: two- and three-residue loops almost always give rise to L-hairpins, whereas five-residue loops give rise primarily to R-hairpins. These results suggest that the chirality of  $\beta$ -hairpins is determined by the chirality (L-amino acids versus D-amino acids) and local structural preferences of the polypeptide chain; indeed, only a restricted set of loop types have been found to be compatible with  $\beta\beta$ -junctions<sup>23</sup>. Analysis of  $\beta\beta$ -units in known protein structures (Supplementary Methods 3) shows that the chirality of  $\beta\beta$ -units in native structures is correlated with loop length in a manner very similar to the simulations (Fig. 1a, right). Consistent with the idea that torsional strain is responsible for the trends, the calculated torsion energies of loops in native structures for two- and three-residue loops are lower for L-hairpins, and those for five-residue loops are lower for R-hairpins (Supplementary Fig. 2). This rule allows control over the pleating of  $\beta$ -hairpins.

### $\beta\alpha$ -rule

The preferred orientation of  $\beta\alpha$ -units is P for two-residue loops and A for three-residue loops. Secondary-structure-constrained folding simulations similar to those described in the previous paragraph strongly show this trend, and it is also observed in native protein structures (Fig. 1b). The rule arises in part from the bendability of the protein backbone (Supplementary Fig. 3). This rule is very useful for both positive and negative design, as it allows control of the side of a  $\beta$ -sheet that a helix will pack onto.

### $\alpha\beta$ -rule

The preferred orientation of  $\alpha\beta$ -units is P. In secondary-structure-constrained folding simulations, this trend is observed strongly for loops two residues in length and for longer lengths when the loop provides a hydrogen-bonded capping interaction to stabilize the helix and does not extend the strand (Fig. 1c, left, and Supplementary Fig. 4). A very similar trend is again observed in native protein structures (Fig. 1c, right).

It must be emphasized that the three rules are largely independent of the amino-acid sequence of the secondary structures or connecting loops. As such, they must arise from the intrinsic chirality and local structural preferences of the polypeptide chain rather than from sequence-specific contributions. Whereas local sequence-structure relationships have been extensively studied<sup>24–27</sup>, there has been much less work on sequence-independent properties (the cataloguing of the discrete sets of loops compatible with junctions between secondary structure elements is a notable exception<sup>23</sup>). These rules provide a powerful way to perform negative design at the backbone level.

### Emergent rules

The next level of complexity in  $\alpha\beta$ -proteins beyond two secondary structure elements is segments of three consecutive secondary structure elements. Secondary-structure-constrained Rosetta folding simulations revealed strong dependencies of the chirality (Supplementary Fig. 1d) of  $\beta\beta\alpha$ - and  $\alpha\beta\beta$ -units and the foldability of  $\beta\alpha\beta$ -units on the lengths of the connecting loops and the secondary structure elements. These dependencies are formulated in emergent rules (Supplementary Fig. 1 and Supplementary Discussion 1), which follow from the fundamental rules described in the previous section. The rules specify how to choose the lengths of secondary structure



elements and the connecting loops to favour a desired conformation of a  $\beta\beta\alpha$ -,  $\alpha\beta\beta$ - or  $\beta\alpha\beta$ -unit.

## Rule-based design of funnelled folding landscapes

The fundamental and emergent rules make possible the encoding of funnel-shaped energy landscapes. We can sculpt energy landscapes to be strongly funnelled by designing secondary structure patterns that favour the tertiary motifs present in the desired topology and disfavour non-native motifs. The desired structure is then further stabilized by using RosettaDesign<sup>8</sup> to obtain sequences with favourable non-local interactions such as complementary hydrophobic core packing. The latter step involves purely positive design because the energy of the desired structure is optimized without regard to competing states, whereas the design of sequences that favour specific secondary structure patterns also has elements of negative design because non-native conformations are disfavoured by the local structural preferences of the protein backbone captured by the rules.

We tested this approach by attempting to design strongly funnelled landscapes for five different folds (Fig. 2 and Supplementary Discussion 2). The first step is to choose secondary structure lengths that favour the desired fold and disfavour alternatives. We illustrate how to choose the secondary structure lengths that favour a desired topology with Fold-I, the classic ferredoxin-like fold (Fig. 2, leftmost fold). The secondary structure elements are, in order,  $\beta_1\alpha_1\beta_2\beta_3\alpha_2\beta_4$ . To assign the lengths of the loops and strands, we apply the emergent rules to the  $\alpha\beta\beta$ - and  $\beta\beta\alpha$ -triples and the  $\beta\alpha$ - and  $\alpha\beta$ -rules to the two  $\beta\alpha\beta$ -units:  $(\beta_1\alpha_1)_A(\alpha_1\beta_2)_P(\alpha_1\beta_2\beta_3)_L(\beta_2\beta_3\alpha_2)_R(\beta_3\alpha_2)_A(\alpha_2\beta_4)_P$ . Reading directly from Fig. 1 and Supplementary Fig. 1, we find that for strand length 7 the ideal loop lengths between successive secondary structure elements are 3, 2, 2, 3 and 2 (from the amino to the carboxy terminus). To assign the lengths of the helices, we find from Supplementary Fig. 10 that for strand length 7 the optimal helix length is 18. We can apply the same procedure to each of the other folds to obtain the corresponding ideal secondary structure lengths (Fig. 2): for Folds-II, -IV and -V, we treat  $(\alpha\beta\alpha)$  as  $(\alpha\beta)_P(\beta\alpha)_{P/A}$  and apply the corresponding two fundamental rules.

To build tertiary backbone structures from the two-dimensional representations of protein folds depicted in Fig. 2, we carry out multiple independent Rosetta folding simulations using the secondary structure strings obtained from the rules. For Folds-I, -III and -V, a significant fraction of trajectories produced the desired topology because the secondary structure lengths were chosen specifically to encode it. Folds-II and -IV are not distinguished by the rules, and to resolve this ambiguity we varied the secondary structure lengths and used folding simulations to select lengths strongly favouring one or the other fold. For larger proteins, such degeneracies are likely to increase and additional rules may need to be identified to resolve them. Within the population of structures with the desired topology, there is still considerable variety in the distances and angles between

the secondary structure elements, the loop conformations and the twist of the  $\beta$ -sheet. This variation is important because it provides a range of starting points for designing sequence-structure pairs with very low energy as described in the next paragraph.

Up to this point, specific sequence information has not been introduced; the representations are of the protein backbone alone. For each backbone in the ensemble, we then use Monte Carlo simulated annealing to identify amino acids and side-chain conformations that give rise to very low-energy structures. This is carried out using fixed-backbone RosettaDesign<sup>8</sup> calculations followed by relaxation of the structure of the backbone and the side chains in the Rosetta all-atom energy function<sup>28</sup>. These sequence design and structure refinement calculations are then iterated<sup>8</sup> to generate a tightly packed hydrophobic core with a packing density approaching that of close-packed crystals. Larger hydrophobic amino acids (Ile, Leu and Phe) are favoured in the core to create a strong driving force for folding<sup>29</sup>. Negative design is applied to the edge  $\beta$ -strands and the protein surface to destabilize non-native conformations and disfavour oligomerization: inward-pointing polar residues are introduced in the strands and hydrophobic patches are removed from the surface. The designed structures are then filtered according to energy, packing (as assessed by RosettaHoles<sup>30</sup>) and the local sequence-structure compatibility (Methods) to disfavour other structures (this last criterion is effectively a negative design step). Finally, for each sequence passing these filters, 200,000–400,000 independent Rosetta *ab initio* structure prediction simulations starting from an extended chain<sup>22</sup> are performed to map out the folding energy landscapes. Roughly 10% of the designs have funnel-shaped energy landscapes leading into the designed structures (Fig. 3a; compare with Supplementary Fig. 11) and these are selected for experimental characterization. Proteins designed with this protocol (summarized in Supplementary Fig. 12) by construction have consistent local and non-local interactions. Notably, the only globular protein designed *de novo* before this work, Top7 (ref. 8), also satisfies our rules and has consistent local and non-local interactions.

## Experimental characterization of designed proteins

We obtained synthetic genes encoding 11 designs for Fold-I, 12 for Fold-II, 14 for Fold-III, 5 for Fold-IV and 12 for Fold-V (Supplementary Table 8). None of these proteins is homologous to any known protein (BLAST E-value < 0.02 against the NCBI nr database of non-redundant protein sequences). The proteins were expressed, purified and characterized by circular dichroism spectroscopy, size-exclusion chromatography combined with multi-angle light scattering (SEC-MALS), and NMR spectroscopy. For all five folds, most of the designs are expressed and soluble and many are extremely stable (Table 1 and Supplementary Tables 1–5). Data for the most stable monomeric design for each fold that had a well-resolved NMR spectrum (Di-I\_5, Di-II\_10, Di-III\_14, Di-IV\_5 and Di-V\_7; 'Di' indicates designed ideal protein, the Roman numeral is the fold type and the number

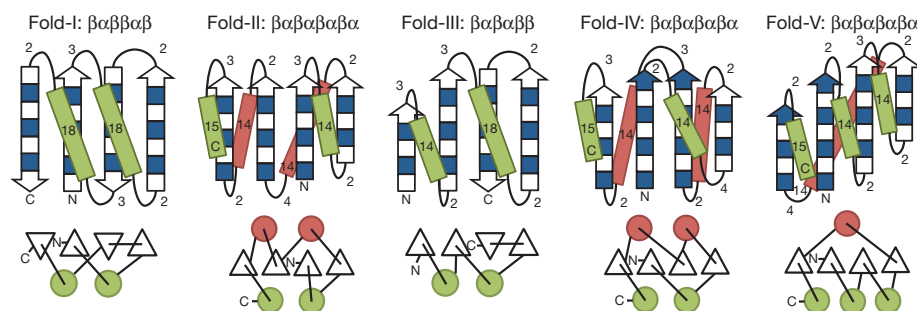


**Figure 2 | Derivation of secondary structure lengths from the rules for five protein topologies.** Fold-I: Ferredoxin-like fold. Fold-II: Rossmann2×2 fold. Fold-III: IF3-like fold. Fold-IV: P-loop2×2 fold. Fold-V: Rossmann3×1 fold. In the upper illustrations, numbers represent the secondary structure lengths following from the rules described in Fig. 1 and Supplementary Fig. 1. Strand

lengths are represented by filled and open boxes. The filled boxes represent pleats coming out of the page, and the open boxes represent pleats going into the page. In the lower illustrations, the design topologies are represented with circles (helices) and triangles (strands) connected by solid lines (loops).

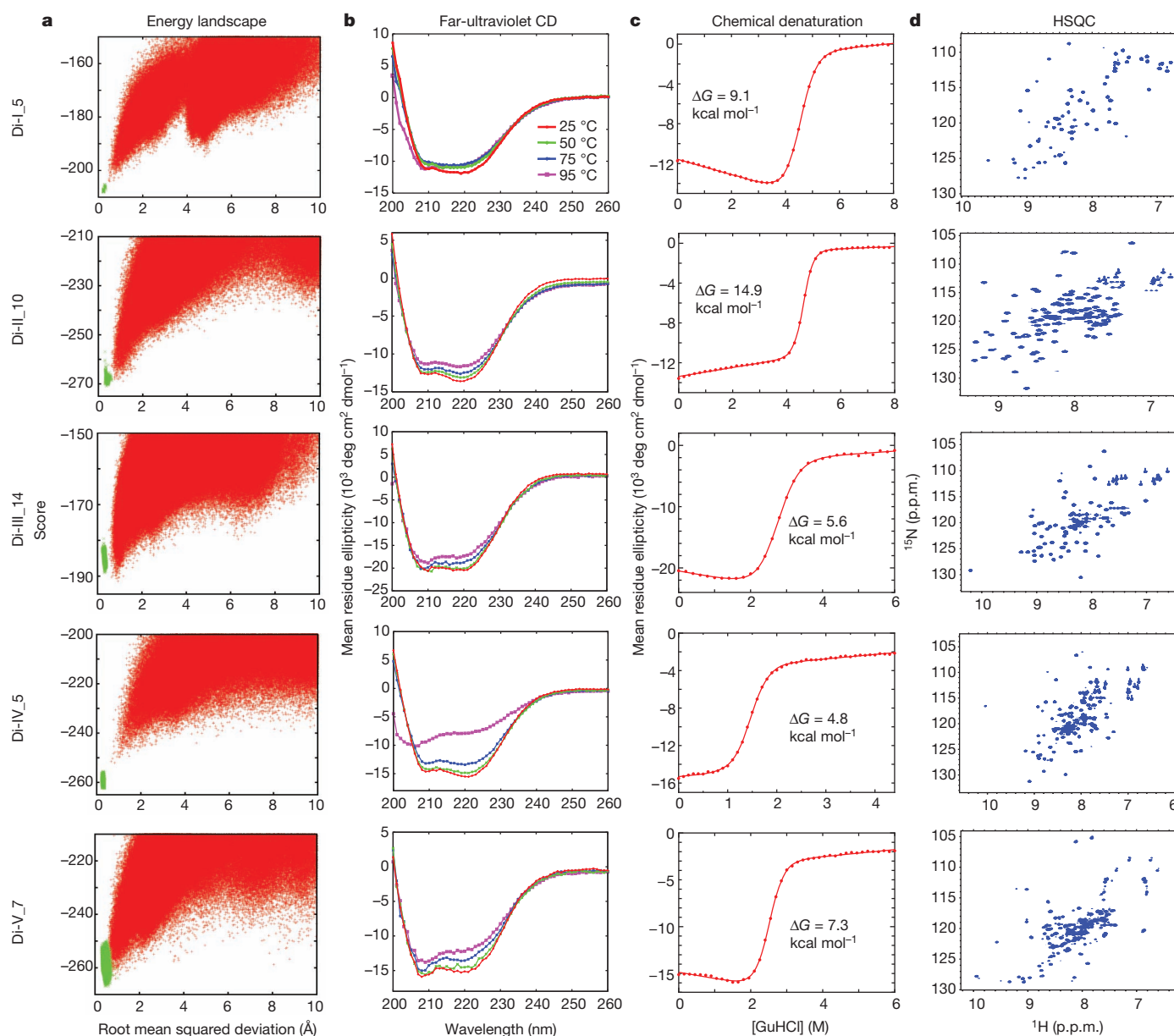


**Figure 3 | Characterization of design for each of the five folds.** **a**, Energy landscapes obtained from Rosetta *ab initio* structure prediction simulations on Rosetta@home. Red points represent the lowest-energy structures obtained in independent Monte Carlo structure prediction trajectories starting from an extended chain for each sequence; the y axis shows the Rosetta all-atom energy and the x axis shows the C $\alpha$  root mean squared deviation from the design model. Green points represent the lowest-energy structures obtained in

trajectories starting from the design model. Less sampling around the designed minima is observed for the higher-contact-order topology, Fold-IV<sup>44</sup>. **b**, The far-ultraviolet circular dichroism (CD) spectra at various temperatures. **c**, Chemical denaturations with GuHCl (square brackets denote concentration) at 220 nm and 25 °C. The data were fitted to a two-state model (red solid line) to obtain the free energy of unfolding  $\Delta G$ . **d**, Two-dimensional  $^1\text{H}$ - $^{15}\text{N}$  HSQC spectra at 25 °C and 600 MHz. p.p.m., parts per million.

**Table 1 | Summary of experimental results for designed proteins**

	Designs tested	Expressed*	Soluble*	$\alpha\beta$ -protein circular dichroism spectrum	Stable† ( $T_m \geq 95$ °C)	Monomeric‡	Well-resolved NMR§	Success
Fold-I	11	9	8	6	3	2	3	1 (9%)
Fold-II	12	12	12	10	10	4	4	4 (33%)
Fold-III	14	13	11	9	7	6	5	3 (21%)
Fold-IV	5	4	4	4	2	4	3	2 (40%)
Fold-V	12	11	10	3	3	1	1	1 (8%)

The second column shows the number of designs experimentally tested for the fold in the leftmost column. The subsequent columns give the number of designs that satisfy each criterion. The successful designs are defined as those that satisfy all criteria. The details of the results are shown in Supplementary Tables 1–5.

\*Expression and solubility were assessed by SDS–polyacrylamide gel electrophoresis and mass spectrometry.

†Stability was measured by thermal denaturation;  $T_m$  is the melting temperature.

‡SEC-MALS was used to determine oligomerization state. We counted the number of designs in which the main peak of the absorbance at 280 nm corresponds to the monomeric state.

§For Folds-I and -II, one-dimensional NMR spectra were collected, and for Folds-III, -IV and -V, two-dimensional  $^1\text{H}$ - $^{15}\text{N}$  HSQC spectra were collected.



is the identifier of the design) are shown in Fig. 3, Supplementary Fig. 13 and Supplementary Table 6. These five proteins are soluble at concentrations of 0.9–1.6 mM, have far-ultraviolet circular dichroism spectra characteristic of  $\alpha\beta$ -proteins and have cooperative unfolding transitions with a free energy of unfolding of  $>5$  kcal mol $^{-1}$  (Fig. 3b, c and Supplementary Table 6). The designed proteins were found to be monomeric by SEC-MALS (Supplementary Fig. 13). The two-dimensional  $^1\text{H}$ - $^{15}\text{N}$  heteronuclear single quantum coherence (HSQC) spectra show the expected number of well-dispersed sharp peaks (Fig. 3d), indicating that the designed proteins are well packed. The solution structures of all five designs were determined by solution-state NMR spectroscopy (Fig. 4). Extensive validation analyses, including excellent agreement between back-calculated and measured NMR data (Supplementary Table 7), suggest that the NMR structures are quite high quality. The structures are remarkably consistent with the computational design models for both the protein backbone and the core side chains (Fig. 4, Supplementary Fig. 14 and Supplementary Table 6).

## Concluding remarks

We have demonstrated that strongly funnelled landscapes can be designed by encoding consistency between the local and non-local interactions using rules that relate secondary structure lengths to tertiary structure patterns. The rules, which arise from the chirality and local structural preferences of the polypeptide chain, make possible the simultaneous positive design of interactions favouring the desired structure and negative design against competing alternatives. It is plausible that the same principles shape the folding landscapes of naturally occurring proteins, which are more frustrated but still exhibit the remarkable property of having unique native states considerably lower in energy than the vast number of alternative topologies. This idea is supported by the fact that the relationships between secondary structure patterns and tertiary structure motifs we identified in simulations are also observed in native structures (Fig. 1 and Supplementary Figs 1, 5, 7, 9 and 10); as in our design strategy, the disfavouring of the myriad alternative states may be achieved by

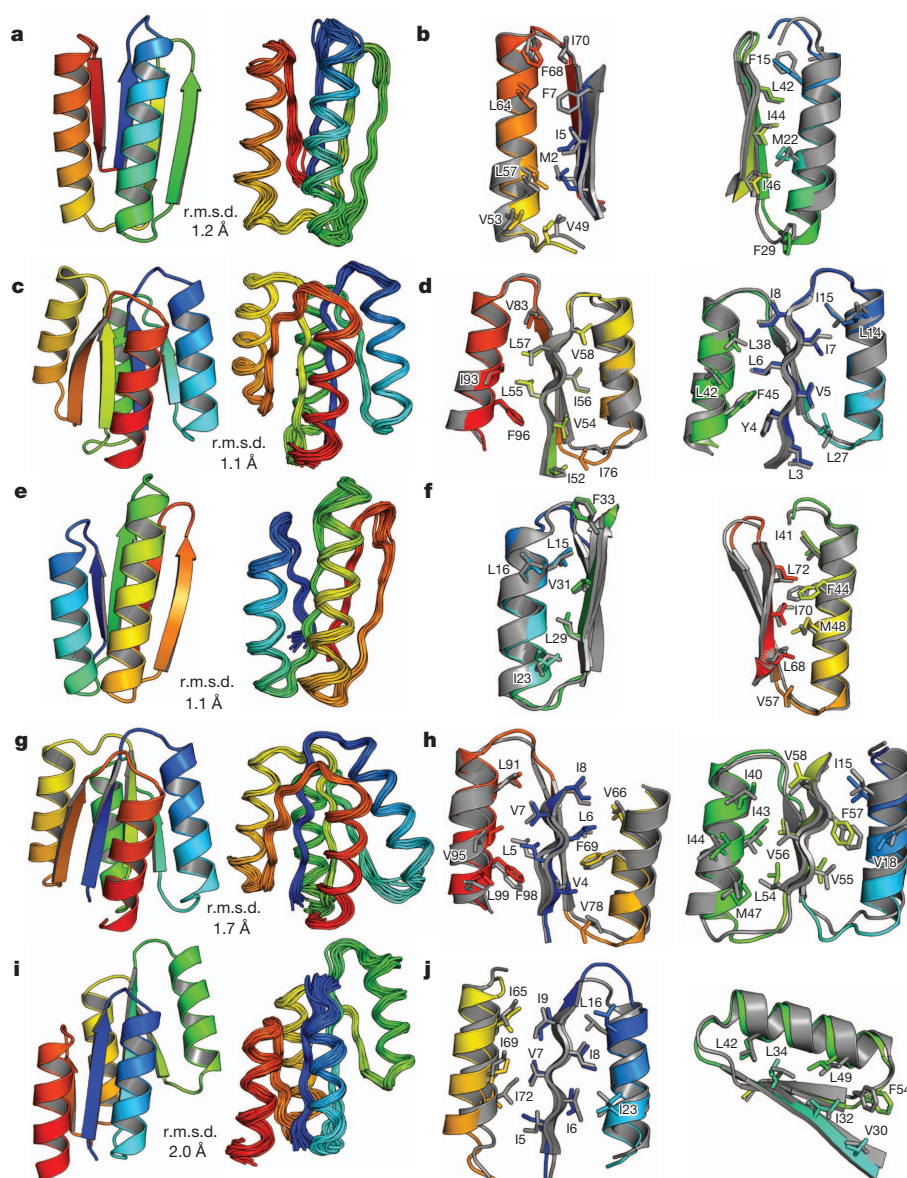


**Figure 4 | Comparison of computational models with experimentally determined structures.** **a, c, e, g, i,** Comparison of overall topology. Design models (left) and NMR structures (right); the C $\alpha$  root mean squared deviation (r.m.s.d.) between them is indicated. **b, d, f, h, j,** Comparison of core side-chain packing in superpositions of design models (rainbow) and NMR structures

(grey). The left and right panels show close-up views of the core packing and correspond to the left and right portions of the structures shown in **a, c, e, g** and **i, a, b,** Di-I\_5 (Protein Data Bank code, 2KL8); **c, d,** Di-II\_10 (2LV8); **e, f,** Di-III\_14 (2LN3); **g, h,** Di-IV\_5 (2LVB); **i, j,** Di-V\_7 (2LTA). The design models and NMR structures are available from [http://psvs-1\\_4-dev.nesg.org/ideal\\_proteins/](http://psvs-1_4-dev.nesg.org/ideal_proteins/).

naturally occurring sequences through the stabilization of local structures that disfavour non-native topologies<sup>31,32</sup>.

The design principles and methodology we have described should allow the ready design of a wide range of robust and stable protein building blocks for the next generation of engineered functional proteins<sup>33–41</sup>. Almost all protein design and engineering efforts so far have repurposed naturally occurring proteins that evolved for some other, often unrelated, function<sup>35–41</sup>. It should now become possible to custom-design protein scaffolds ideal for the desired function, and to build larger assemblies<sup>42,43</sup> and materials from robust ideal building blocks.

## METHODS SUMMARY

Rosetta folding simulations were performed on a sequence-independent backbone model consisting of the N, NH, C $\alpha$ , C, CO and C $\beta$  atoms, with a pseudo-atom representing a generic side chain, using a potential function in which the amide hydrogen and carbonyl oxygen can form energetically favourable hydrogen bonds, repulsive interactions disfavour the overly close approach of atom pairs and an overall compaction term favours compact structures. Each attempted move in the Monte Carlo simulations consists of the replacement of the phi and psi angles of a randomly selected residue with phi and psi angles randomly selected from the region of the Ramachandran plot compatible with the assigned secondary structure.

**Full Methods** and any associated references are available in the online version of the paper.

**Received 17 May; accepted 19 September 2012.**

- Leopold, P. E., Montal, M. & Onuchic, J. N. Protein folding funnels: a kinetic approach to the sequence-structure relationship. *Proc. Natl Acad. Sci. USA* **89**, 8721–8725 (1992).
- Onuchic, J. N., Wolynes, P. G., Luthey-Schulten, Z. & Socci, N. D. Toward an outline of the topography of a realistic protein-folding funnel. *Proc. Natl Acad. Sci. USA* **92**, 3626–3630 (1995).
- Dill, K. A. & Chan, H. S. From Levinthal to pathways to funnels. *Nature Struct. Biol.* **4**, 10–19 (1997).
- Hill, R. B., Raleigh, D. P., Lombardi, A. & DeGrado, W. F. De novo design of helical bundles as models for understanding protein folding and function. *Acc. Chem. Res.* **33**, 745–754 (2000).
- Butterfoss, G. L. & Kuhlman, B. Computer-based design of novel protein structures. *Annu. Rev. Biophys. Biomol. Struct.* **35**, 49–65 (2006).
- Samish, I., MacDermid, C. M., Perez-Aguilar, J. M. & Saven, J. G. Theoretical and computational protein design. *Annu. Rev. Phys. Chem.* **62**, 129–149 (2011).
- Dahiyat, B. I. & Mayo, S. L. De novo protein design: fully automated sequence selection. *Science* **278**, 82–87 (1997).
- Kuhlman, B. *et al.* Design of a novel globular protein fold with atomic-level accuracy. *Science* **302**, 1364–1368 (2003).
- Dantas, G., Kuhlman, B., Callender, D., Wong, M. & Baker, D. A large scale test of computational protein design: folding and stability of nine completely redesigned globular proteins. *J. Mol. Biol.* **332**, 449–460 (2003).
- Calhoun, J. R. *et al.* Computational design and characterization of a monomeric helical dinuclear metalloprotein. *J. Mol. Biol.* **334**, 1101–1115 (2003).
- Isogai, Y., Ito, Y., Ikeya, T., Shiro, Y. & Ota, M. Design of lambda Cro fold: solution structure of a monomeric variant of the de novo protein. *J. Mol. Biol.* **354**, 801–814 (2005).
- Shah, P. S. *et al.* Full-sequence computational design and solution structure of a thermostable protein variant. *J. Mol. Biol.* **372**, 1–6 (2007).
- Hu, X., Wang, H., Ke, H. & Kuhlman, B. Computer-based redesign of a beta sandwich protein suggests that extensive negative design is not required for de novo beta sheet design. *Structure* **16**, 1799–1805 (2008).
- Hecht, M. H., Richardson, J. S., Richardson, D. C. & Ogden, R. C. De novo design, expression, and characterization of Felix: a four-helix bundle protein of native-like sequence. *Science* **249**, 884–891 (1990).
- Richardson, J. S. & Richardson, D. C. Natural beta-sheet proteins use negative design to avoid edge-to-edge aggregation. *Proc. Natl Acad. Sci. USA* **99**, 2754–2759 (2002).
- Jin, W., Kambara, O., Sasakawa, H., Tamura, A. & Takada, S. De novo design of foldable proteins with smooth folding funnel: automated negative design and experimental verification. *Structure* **11**, 581–590 (2003).
- Harbury, P. B., Plecs, J. J., Tidor, B., Alber, T. & Kim, P. S. High-resolution protein design with backbone freedom. *Science* **282**, 1462–1467 (1998).
- Summa, C. M., Rosenblatt, M. M., Hong, J. K., Lear, J. D. & DeGrado, W. F. Computational de novo design, and characterization of an A(2)B(2) diiron protein. *J. Mol. Biol.* **321**, 923–938 (2002).
- Havranek, J. J. & Harbury, P. B. Automated design of specificity in molecular recognition. *Nature Struct. Biol.* **10**, 45–52 (2003).
- Kortemme, T. *et al.* Computational redesign of protein-protein interaction specificity. *Nature Struct. Mol. Biol.* **11**, 371–379 (2004).
- Go, N. Theoretical studies of protein folding. *Annu. Rev. Biophys. Bioeng.* **12**, 183–210 (1983).
- Rohl, C. A., Strauss, C. E., Misura, K. M. & Baker, D. Protein structure prediction using Rosetta. *Methods Enzymol.* **383**, 66–93 (2004).
- Street, T. O., Fitzkee, N. C., Perskie, L. L. & Rose, G. D. Physical-chemical determinants of turn conformations in globular proteins. *Protein Sci.* **16**, 1720–1727 (2007).
- Bystroff, C. & Baker, D. Prediction of local structure in proteins using a library of sequence-structure motifs. *J. Mol. Biol.* **281**, 565–577 (1998).
- Hunter, C. G. & Subramaniam, S. Protein local structure prediction from sequence. *Proteins* **50**, 572–579 (2003).
- Etchebest, C., Benros, C., Hazout, S. & de Brevern, A. G. A structural alphabet for local protein structures: improved prediction methods. *Proteins* **59**, 810–827 (2005).
- Voelz, V. A., Shell, M. S. & Dill, K. A. Predicting peptide structures in native proteins from physical simulations of fragments. *PLoS Comput. Biol.* **5**, e1000281 (2009).
- Tyka, M. D. *et al.* Alternate states of proteins revealed by detailed energy landscape mapping. *J. Mol. Biol.* **405**, 607–618 (2011).
- Dill, K. A. Dominant forces in protein folding. *Biochemistry* **29**, 7133–7155 (1990).
- Sheffler, W. & Baker, D. RosettaHoles: rapid assessment of protein core packing for structure prediction, refinement, design, and validation. *Protein Sci.* **18**, 229–239 (2009).
- Fleming, P. J., Gong, H. & Rose, G. D. Secondary structure determines protein topology. *Protein Sci.* **15**, 1829–1834 (2006).
- Chikenji, G., Fujitsuka, Y. & Takada, S. Shaping up the protein folding funnel by local interaction: lesson from a structure prediction study. *Proc. Natl Acad. Sci. USA* **103**, 3141–3146 (2006).
- Kaplan, J. & DeGrado, W. F. De novo design of catalytic proteins. *Proc. Natl Acad. Sci. USA* **101**, 11566–11570 (2004).
- Correia, B. E. *et al.* Computational design of epitope-scaffolds allows induction of antibodies specific for a poorly immunogenic HIV vaccine epitope. *Structure* **18**, 1116–1126 (2010).
- Bolon, D. N. & Mayo, S. L. Enzyme-like proteins by computational design. *Proc. Natl Acad. Sci. USA* **98**, 14274–14279 (2001).
- Jiang, L. *et al.* De novo computational design of retro-aldol enzymes. *Science* **319**, 1387–1391 (2008).
- Röthlisberger, D. *et al.* Kemp elimination catalysts by computational enzyme design. *Nature* **453**, 190–195 (2008).
- Siegel, J. B. *et al.* Computational design of an enzyme catalyst for a stereoselective bimolecular Diels-Alder reaction. *Science* **329**, 309–313 (2010).
- Fleishman, S. J. *et al.* Computational design of proteins targeting the conserved stem region of influenza hemagglutinin. *Science* **332**, 816–821 (2011).
- Azoitei, M. L. *et al.* Computation-guided backbone grafting of a discontinuous motif onto a protein scaffold. *Science* **334**, 373–376 (2011).
- Khare, S. D. *et al.* Computational redesign of a mononuclear zinc metalloenzyme for organophosphate hydrolysis. *Nature Chem. Biol.* **8**, 294–300 (2012).
- King, N. P. *et al.* Computational design of self-assembling protein nanomaterials with atomic level accuracy. *Science* **336**, 1171–1174 (2012).
- Eisenbeis, S. *et al.* Potential of fragment recombination for rational design of proteins. *J. Am. Chem. Soc.* **134**, 4019–4022 (2012).
- Bonneau, R., Ruczinski, I., Tsai, J. & Baker, D. Contact order and ab initio protein structure prediction. *Protein Sci.* **11**, 1937–1944 (2002).

**Supplementary Information** is available in the online version of the paper.

**Acknowledgements** We thank N. Grishin for suggesting target folds for design, P. Rajagopal for one-dimensional NMR measurements of Folds-I and -II, and J. Siegel for measurements by mass spectrometer. We also thank P.-S. Huang and Y.-E. A. Ban for computational tools; J. L. Gallaher for experimental assistance; J. Castellanos for the help with designing Fold-IV; H.-W. Lee, K. Pederson and J. Prestegard for measurements of residual dipolar couplings; and S. Khare, F. DiMaio, I. Andre, S. Fleishman, J. Mills, S. Takada, S. Fuchigami and G. Chikenji for comments on the manuscript. This work was supported by HHMI, DOE, DARPA, DTRA and the National Institutes of General Medical Science Protein Structure Initiative (PSI:Biolog) programme, grant U54 GM094597. N.K. was also supported by Japan Society for the Promotion of Science (JSPS) Postdoctoral Fellowships for Research Abroad.

**Author Contributions** N.K., R.T.-K., G.L., G.T.M. and D.B. designed the research. N.K. performed folding simulations and analysed natural proteins. N.K. wrote program code. N.K. and R.T.-K. performed computational design work: Di-I\_5 and Di-IV\_5 were designed by N.K., and Di-II\_10, Di-III\_14 and Di-V\_7 were designed by R.T.-K. R.T.-K. expressed, purified and characterized the designed proteins by biochemical assay. R.X. and T.B.A. prepared isotope-enriched protein samples for NMR structure determination. G.L. collected NMR data and determined the solution NMR structures. N.K., R.T.-K., G.L., G.T.M. and D.B. wrote the manuscript.

**Author Information** The NMR structures of the five designs have been deposited in the RCSB Protein Data Bank under the accession numbers 2KL8 (Di-I\_5), 2LV8 (Di-II\_10), 2LN3 (Di-III\_14), 2LVB (Di-IV\_5) and 2LTA (Di-V\_7). NMR data have been deposited in the Biological Magnetic Resonance Data Bank under the accession numbers 16387 (Di-I\_5), 18558 (Di-II\_10), 18145 (Di-III\_14), 18561 (Di-IV\_5) and 18465 (Di-V\_7). Reprints and permissions information is available at [www.nature.com/reprints](http://www.nature.com/reprints). The authors declare no competing financial interests. Readers are welcome to comment on the online version of the paper. Correspondence and requests for materials should be addressed to D.B. ([dabaker@u.washington.edu](mailto:dabaker@u.washington.edu)) or G.T.M. ([guy@cabm.rutgers.edu](mailto:guy@cabm.rutgers.edu)).



## METHODS

**Rosetta folding simulations.** Rosetta folding simulations using a sequence-independent backbone model were carried out in the studies of the fundamental rules (Fig. 1), the emergent rules (Supplementary Fig. 1) and the building of tertiary backbone structures in the rule-based designs. These simulations are referred to as secondary-structure-constrained folding simulations in the main text because the phi and psi angles of each residue are limited to the region of the Ramachandran plot compatible with the assigned secondary structure. We first introduce the backbone model and then describe the fragment assembly method<sup>45</sup> used for simulating the backbone model.

The backbone model consists of main-chain atoms (N, NH, C $\alpha$ , C and CO) and C $\beta$  atoms with a pseudo-atom representing a generic side chain (the centroid model of Rosetta<sup>22</sup>). The Rosetta potential function terms and weights are as follows: steric repulsion ( $v_{dw} = 1.0$ ), overall compaction ( $rg = 1.0$ ), secondary structure pairings ( $ss\_pair = 1.0$ ,  $rsigma = 1.0$  and  $hs\_pair = 1.0$ ) and hydrogen bonds ( $hbond\_sr\_bb = 1.0$ ,  $hbond\_lr\_bb = 1.0$ ). For the steric radius of the side-chain pseudo-atom, the radius of Val was used.

Fragment assembly<sup>45</sup> was used for sampling conformations of the backbone model. Backbone fragment sets consisting of 1, 3 or 9 consecutive residue fragments were prepared in advance from a non-redundant set of X-ray structures<sup>46</sup>; the fragments have information only on the phi, psi and omega torsion angles. We performed Monte Carlo simulations in which in each attempted Monte Carlo trial, a new conformation is generated by replacing the torsion angles (phi, psi and omega) of a randomly selected frame consisting of 1, 3 or 9 consecutive residues with the torsion angles of a randomly selected fragment compatible with the assigned secondary structure. Importantly, in the calculations for the fundamental rules, we used only one-residue fragments to avoid the possibility that the evolutionary history of natural protein structures would bias the simulation results. Because we found that the fundamental rules are observed both in the simulations and in the natural proteins (Fig. 1), we used all fragment lengths in the simulations relating to the emergent rules and the rule-based designs. In the calculations for the fundamental rules, the total number of Monte Carlo steps in one trajectory was  $500 \times$  (length of a simulated chain), and the temperature was 1.0. In the emergent rules and rule-based designs, the total number of Monte Carlo steps in one trajectory was  $300 \times$  (length of a simulated chain), and the temperature was 1.5.

**Sequence design protocol.** Sequence design was performed using the RosettaDesign approach<sup>8</sup> with several extensions.

(1) The environment for each residue position was classified into one of three layers, core, boundary or surface, on the basis of the solvent-accessible surface area (SASA) of main-chain and C $\beta$  atoms and the secondary structure type, and only designated amino-acids for each layer were allowed for design. The core was defined with  $SASA \leq 15 \text{ \AA}^2$  for helices and strands and  $SASA \leq 25 \text{ \AA}^2$  for loops; the boundary was defined with  $15 \text{ \AA}^2 < SASA < 60 \text{ \AA}^2$  for helices and strands and  $25 \text{ \AA}^2 < SASA < 40 \text{ \AA}^2$  for loops; and the surface was defined with  $SASA \geq 60 \text{ \AA}^2$  for helices and strands and  $SASA \geq 40 \text{ \AA}^2$  for loops. The amino acids V, I, L, M, F, Y and W were used in the core; V, I, L, Y, W, D, E, N, Q, K, R, S and T were used at the boundary; and D, E, N, Q, K, R, S, T and H were used on the surface. To favour larger hydrophobic amino acids in the interior of protein structures, Ala was allowed only for helices and loops in the core and at the boundary, and Gly was allowed only for loops in all layers. Pro was allowed in loops and at the beginning of helices and strands. The loop residue immediately before a helix is one of D, N, S and T to provide the helix capping. This method was applied to the design of Folds-II to -V.

(2) To favour larger hydrophobic amino acids (I, L and F) in the core, we modified the reference energy<sup>8</sup> of each amino acid.

(3) To introduce inward-pointing polar residues in the edge strands (in most cases charged residues in the middle of the edge strands), we used a resfile, by which designated amino acids can be assigned at a specified residue position.

(4) For aromatic residues of F, Y and H, we limited the  $\chi^2$  angle to range from  $70^\circ$  to  $110^\circ$ , the range frequently observed in nature. This restriction was applied to the design of Folds-III to -V.

After designing sequences, we relaxed the backbone and side chains of the designed structures<sup>28</sup>. These sequence design and structure refinement calculations were iterated. The designed structures were then filtered on the basis of their Rosetta all-atom energy<sup>22</sup>, packing as assessed by RosettaHoles<sup>30</sup>, and the local sequence and structure compatibility. Finally, we visually inspected the designed structures and mutated buried polar and exposed hydrophobic residues using Foldit<sup>47</sup>.

Rosetta command lines are provided in Supplementary Data to perform the design protocol.

**Local sequence–structure compatibility.** To evaluate the compatibility between the local sequence and the local structure, we collected 200 fragments for each

nine-residue frame in the designed sequence from a non-redundant set of X-ray structures based on the sequence similarity and secondary structure prediction<sup>22</sup> (the standard Rosetta fragment generation protocol for *ab initio* structure prediction). Then, for each frame, we calculated the root mean squared deviation between the designed local structure and each of the 200 fragments. Designs were ranked on the basis of the total number of fragments for which the root mean squared deviation was less than 1.0 Å, and those with high values were selected.

**Protein expression and purification.** For all designed sequences, a Gly–Ser was added at the C terminus to give a spacer between the designed region and the C-terminal 6 $\times$ His tag. The genes encoding the designed sequences, which were cloned into plasmid pET29b, were obtained from GenScript. The designed proteins were expressed in *Escherichia coli* BL21 Star (DE3) cells as non-labelled proteins for all designs for Folds-I and -II, and as uniformly  $U\text{-}^{15}\text{N}$ -labelled proteins for all designs for Folds-III to -V. The non-labelled proteins were expressed using auto-induction media<sup>48</sup>, and the  $U\text{-}^{15}\text{N}$ -labelled proteins were expressed using MJ9 minimal media<sup>49</sup>, which contain  $^{15}\text{N}$  ammonium sulphate as the sole nitrogen source and  $^{12}\text{C}$  glucose as the sole carbon source. The expressed proteins with a 6 $\times$ His tag at the C terminus were purified through a nickel affinity column. The purified proteins were then dialysed against typical PBS buffer, 137 mM NaCl, 2.7 mM KCl, 10 mM  $\text{Na}_2\text{HPO}_4$  and 1.8 mM  $\text{KH}_2\text{PO}_4$ , at pH 7.4; this buffer was used for all the experiments except NMR structure determination. The expression, solubility and purity of the designed proteins were assessed by SDS–polyacrylamide gel electrophoresis and mass spectrometry (TSQ LC/MS, Thermo Scientific).

**Circular dichroism.** All circular dichroism data were collected on an Aviv 62A DS spectrometer. Far-ultraviolet circular dichroism spectra of designed proteins were measured from 260 to 200 nm for 14–25  $\mu\text{M}$  protein samples in PBS buffer (pH 7.4) at various temperatures of 25, 50, 75 and  $95^\circ\text{C}$  in a 1-mm-path-length cuvette. The protein concentrations were determined from the absorbance at 280 nm (ref. 50) using an ultraviolet spectrophotometer (NanoDrop, Thermo Scientific).  $T_m$  is the melting temperature where the number of folded proteins is equal to the number of unfolded proteins during temperature denaturation. Chemical denaturations with GuHCl were monitored at 220 nm for 3–4  $\mu\text{M}$  protein samples in PBS buffer (pH 7.4) at  $25^\circ\text{C}$  in a 1-cm-path-length cuvette. The GuHCl concentration was automatically controlled by a MicroLab titrator (Hamilton). The chemical denaturation curves were fitted by nonlinear least-squares analysis using a two-state unfolding and linear extrapolation model<sup>51</sup>. The free-energy change for the unfolding transition,  $\Delta G$ , and the value representing its dependency on the denaturant, the  $m$ -value (of which a higher value indicates higher cooperativity), were obtained from the fitting.

**Size-exclusion chromatography combined with multi-angle light scattering.** SEC-MALS experiments were performed using a miniDAWN TREOS static light-scattering detector (Wyatt Technology) combined with a HPLC system (LC 1200 Series, Agilent Technologies). One hundred microlitres of 400–700  $\mu\text{M}$  protein samples in PBS buffer (pH 7.4) was injected into a Superdex 75 10/300 GL column (GE Healthcare) equilibrated with PBS buffer at a flow rate of 0.5 ml min<sup>-1</sup>. The protein concentrations were calculated from the absorbance at 280 nm detected by the HPLC system. Static light-scattering data were collected at three different angles,  $41.4^\circ$ ,  $90.0^\circ$  and  $138.6^\circ$ , at 658 nm. These data were analysed using ASTRA software (version 5.3.4, Wyatt Technology) with a change in the refractive index with concentration ( $dn/dc$  value) of 0.185 ml g<sup>-1</sup>.

**Nuclear magnetic resonance.** To assess the core packing of designed proteins, one-dimensional  $^1\text{H}$  NMR spectra were measured for the designs for Folds-I and -II, and two-dimensional  $^1\text{H}$ - $^{15}\text{N}$  HSQC spectra were measured for the designs for Folds-III to -V. The spectra were collected for 0.5–1.5 mM protein samples in 90%  $^1\text{H}_2\text{O}$ /10%  $^2\text{H}_2\text{O}$  PBS buffer (pH 7.4) at  $25^\circ\text{C}$  on a Varian INOVA 600 MHz spectrometer. The most stable monomeric design with a well-resolved NMR spectrum for each fold (Di-I\_5, Di-II\_10, Di-III\_14, Di-IV\_5 and Di-V\_7) was selected for NMR structure determination.

The five designs were expressed and purified following the standard, largely automated NESG protocol<sup>52</sup>. The designs were expressed in *E. coli* BL21 (DE3) pMGK cells as  $U\text{-}^{15}\text{N}$ , 5%  $^{13}\text{C}$ -enriched proteins, and  $U\text{-}^{15}\text{N}$ ,  $U\text{-}^{13}\text{C}$ -enriched proteins using MJ9 minimal media<sup>49</sup>. The  $U\text{-}^{15}\text{N}$ , 5%  $^{13}\text{C}$ -labelled proteins were generated for stereospecific assignments of methyl groups of Val and Leu<sup>33</sup> and for measurements of residual dipolar couplings<sup>54</sup>. The expressed proteins were purified using an ÄKTApur (GE Healthcare) two-step protocol consisting of IMAC (HisTrap HP column, GE Healthcare) and gel filtration chromatography (HiLoad 26/60 Superdex 75 column, GE Healthcare). The purified proteins were dissolved in 90%  $^1\text{H}_2\text{O}$ /10%  $^2\text{H}_2\text{O}$  buffer containing 20 mM MES, 200 mM NaCl, 10 mM DTT, 5 mM  $\text{CaCl}_2$  and 0.02%  $\text{NaN}_3$  at pH 6.5 for Di-I\_5 and Di-II\_10; 100 mM NaCl, 5.6 mM  $\text{Na}_2\text{HPO}_4$ , 1.1 mM  $\text{KH}_2\text{PO}_4$  and 3 mM DTT at pH 7.5 for Di-III\_14; and 100 mM NaCl, 5 mM DTT, 0.02%  $\text{NaN}_3$ , 10 mM Tris-HCl at pH 7.5 for Di-IV\_5 and Di-V\_7. The expression, solubility and purity of the five

proteins were assessed by SDS–polyacrylamide gel electrophoresis and matrix-assisted laser desorption/ionization–time of flight mass spectrometry.

Experimental NMR structure determination was carried out without any knowledge of the design model. For NMR structure determination, all NMR spectra were recorded at 25 °C using cryogenic NMR probes. Triple-resonance NMR data were collected on Varian INOVA 600 MHz or Bruker AVANCE 800 MHz spectrometers, and simultaneous three-dimensional  $^{15}\text{N}/^{13}\text{C}_{\text{aliphatic}}/^{13}\text{C}_{\text{aromatic}}$ -edited nuclear Overhauser enhancement spectroscopy (NOESY<sup>55</sup>; mixing time, 100 ms) and three-dimensional  $^{13}\text{C}$ -edited aromatic NOESY (mixing time, 100 ms) spectra were acquired on the Bruker AVANCE 800 MHz spectrometer. Two-dimensional constant-time  $^1\text{H}$ - $^{13}\text{C}$  HSQC spectra, with 28-ms and 42-ms constant-time delays, were recorded for the  $U$ - $^{15}\text{N}$ , 5%  $^{13}\text{C}$ -enriched samples on the Varian INOVA 600 MHz spectrometer to obtain stereospecific assignments of methyl groups of Val and Leu<sup>53</sup>. Backbone  $^{15}\text{N}$ - $^1\text{H}$  residual dipolar couplings in two alignment media, PEG and phage, were determined from J-modulated spectra<sup>54</sup> for Di-II\_10, Di-III\_14 and Di-V\_7. All NMR data were processed using the program NMRPIPE<sup>56</sup> and analysed using the program XEASY<sup>57</sup>. Spectra were referenced to external DSS. Sequence-specific resonance assignments were determined as described previously<sup>58</sup>. Chemical shift data were deposited in the Biological Magnetic Resonance Data Bank with BMRB IDs 16387, 18558, 18145, 18561 and 18465 for Di-I\_5, Di-II\_10, Di-III\_14, Di-IV\_5 and Di-V\_7, respectively. Initial NOESY peak lists containing expected intraresidue, sequential and  $\alpha$ -helical medium-range NOE peaks were generated from the obtained assignments and then manually edited by visual inspection of the NOESY spectra. Subsequent manual peak picking was then used to identify remaining, primarily long-range NOEs<sup>58</sup>. Backbone dihedral angle constraints were derived from the chemical shifts using the program TALOS+<sup>59</sup> for residues located in well-defined secondary structure elements, and were used for structure determination. Residual dipolar couplings were used as orientational constraints for well-defined residues during structure determination for Di-II\_10, Di-III\_14 and Di-V\_7. The program CYANA<sup>60,61</sup> was used to assign NOEs automatically and to calculate the structure. The 20 conformers with the lowest target function values were refined in explicit water solvent<sup>62</sup> using the program CNS<sup>63</sup>. RPF analysis of AUTOSTRUCTURE<sup>64,65</sup> was used in parallel to guide the iterative cycles of noise/artefact peak removal, peak picking and NOE assignments. The finally obtained structure coordinates were deposited in the Protein Data Bank. The structural statistics and global structure quality factors including VERIFY3D<sup>66</sup>, PROSAII<sup>67</sup>, PROCHECK<sup>68</sup>, and MOLPROBITY<sup>69</sup> raw and statistical Z-scores were computed using PDBSTAT and PSVS 1.4<sup>70</sup>. The global goodness-of-fit of the final structure ensembles with the NOESY peak list data was determined using the RPF analysis program<sup>71</sup>. The NMR data are available from [http://psvs-1\\_4-dev.nesg.org/ideal\\_proteins/](http://psvs-1_4-dev.nesg.org/ideal_proteins/).

45. Simons, K. T., Kooperberg, C., Huang, E. & Baker, D. Assembly of protein tertiary structures from fragments with similar local sequences using simulated annealing and Bayesian scoring functions. *J. Mol. Biol.* **268**, 209–225 (1997).
46. Huang, P. S. *et al.* RosettaRemodel: a generalized framework for flexible backbone protein design. *PLoS ONE* **6**, e24109 (2011).
47. Cooper, S. *et al.* Predicting protein structures with a multiplayer online game. *Nature* **466**, 756–760 (2010).
48. Studier, F. W. Protein production by auto-induction in high density shaking cultures. *Protein Expr. Purif.* **41**, 207–234 (2005).
49. Jansson, M. *et al.* High-level production of uniformly N-15- and C-13-enriched fusion proteins in *Escherichia coli*. *J. Biomol. NMR* **7**, 131–141 (1996).
50. Pace, C. N., Vajdos, F., Fee, L., Grimsley, G. & Gray, T. How to measure and predict the molar absorption coefficient of a protein. *Protein Sci.* **4**, 2411–2423 (1995).
51. Santoro, M. M. & Bolen, D. W. Unfolding free energy changes determined by the linear extrapolation method. 1. Unfolding of phenylmethanesulfonyl alpha-chymotrypsin using different denaturants. *Biochemistry* **27**, 8063–8068 (1988).
52. Acton, T. B. *et al.* Preparation of protein samples for NMR structure, function, and small-molecule screening studies. *Methods Enzymol.* **493**, 21–60 (2011).
53. Neri, D., Szyperski, T., Otting, G., Senn, H. & Wuthrich, K. Stereospecific nuclear magnetic resonance assignments of the methyl groups of valine and leucine in the DNA-binding domain of the 434 repressor by biosynthetically directed fractional  $^{13}\text{C}$  labeling. *Biochemistry* **28**, 7510–7516 (1989).
54. Tjandra, N., Grzesiek, S. & Bax, A. Magnetic field dependence of nitrogen-proton J splittings in N-15-enriched human ubiquitin resulting from relaxation interference and residual dipolar coupling. *J. Am. Chem. Soc.* **118**, 6264–6272 (1996).
55. Shen, Y., Atreya, H. S., Liu, G. H. & Szyperski, T. G-matrix Fourier transform NOESY-based protocol for high-quality protein structure determination. *J. Am. Chem. Soc.* **127**, 9085–9099 (2005).
56. Delaglio, F. *et al.* Nmrpipe - a multidimensional spectral processing system based on unix pipes. *J. Biomol. NMR* **6**, 277–293 (1995).
57. Bartels, C., Xia, T. H., Billeter, M., Guntert, P. & Wuthrich, K. The program Xeasy for computer-supported NMR spectral-analysis of biological macromolecules. *J. Biomol. NMR* **6**, 1–10 (1995).
58. Liu, G. H. *et al.* NMR data collection and analysis protocol for high-throughput protein structure determination. *Proc. Natl Acad. Sci. USA* **102**, 10487–10492 (2005).
59. Shen, Y., Delaglio, F., Cornilescu, G. & Bax, A. TALOS+: a hybrid method for predicting protein backbone torsion angles from NMR chemical shifts. *J. Biomol. NMR* **44**, 213–223 (2009).
60. Güntert, P., Mumenthaler, C. & Wuthrich, K. Torsion angle dynamics for NMR structure calculation with the new program DYANA. *J. Mol. Biol.* **273**, 283–298 (1997).
61. Herrmann, T., Güntert, P. & Wuthrich, K. Protein NMR structure determination with automated NOE assignment using the new software CANDID and the torsion angle dynamics algorithm DYANA. *J. Mol. Biol.* **319**, 209–227 (2002).
62. Linge, J. P., Williams, M. A., Spronk, C. A., Bonvin, A. M. & Nilges, M. Refinement of protein structures in explicit solvent. *Proteins* **50**, 496–506 (2003).
63. Brünger, A. T. *et al.* Crystallography & NMR system: a new software suite for macromolecular structure determination. *Acta Crystallogr. D* **54**, 905–921 (1998).
64. Huang, Y. J., Tejero, R., Powers, R. & Montelione, G. T. A topology-constrained distance network algorithm for protein structure determination from NOESY data. *Proteins* **62**, 587–603 (2006).
65. Huang, Y. J. *et al.* An integrated platform for automated analysis of protein NMR structures. *Methods Enzymol.* **394**, 111–141 (2005).
66. Lüthy, R., Bowie, J. U. & Eisenberg, D. Assessment of protein models with three-dimensional profiles. *Nature* **356**, 83–85 (1992).
67. Sippl, M. J. Recognition of errors in three-dimensional structures of proteins. *Proteins* **17**, 355–362 (1993).
68. Laskowski, R. A., MacArthur, M. W., Moss, D. S. & Thornton, J. M. Procheck - a program to check the stereochemical quality of protein structures. *J. Appl. Crystallogr.* **26**, 283–291 (1993).
69. Word, J. M., Bateman, R. C., Presley, B. K., Lovell, S. C. & Richardson, D. C. Exploring steric constraints on protein mutations using MAGE/PROBE. *Protein Sci.* **9**, 2251–2259 (2000).
70. Bhattacharya, A., Tejero, R. & Montelione, G. T. Evaluating protein structures determined by structural genomics consortia. *Proteins* **66**, 778–795 (2007).
71. Huang, Y. J., Powers, R. & Montelione, G. T. Protein NMR recall, precision, and F-measure scores (RPF scores): structure quality assessment measures based on information retrieval statistics. *J. Am. Chem. Soc.* **127**, 1665–1674 (2005).



# Superluminous supernovae at redshifts of 2.05 and 3.90

Jeff Cooke<sup>1</sup>, Mark Sullivan<sup>2</sup>, Avishay Gal-Yam<sup>3</sup>, Elizabeth J. Barton<sup>4</sup>, Raymond G. Carlberg<sup>5</sup>, Emma V. Ryan-Weber<sup>1</sup>, Chuck Horst<sup>6</sup>, Yuuki Omori<sup>7</sup> & C. Gonzalo Díaz<sup>1</sup>

A rare class of ‘superluminous’ supernovae that are about ten or more times more luminous at their peaks than other types of luminous supernova has recently been found at low to intermediate redshifts<sup>1,2</sup>. A small subset of these events have luminosities that evolve slowly and result in radiated energies of up to about  $10^{51}$  ergs. Therefore, they are probably examples of ‘pair-instability’ or ‘pulsational pair-instability’ supernovae with estimated progenitor masses of 100 to 250 times that of the Sun<sup>3–5</sup>. These events are exceedingly rare at low redshift, but are expected to be more common at high redshift because the mass distribution of the earliest stars was probably skewed to high values<sup>6,7</sup>. Here we report the detection of two superluminous supernovae, at redshifts of 2.05 and 3.90, that have slowly evolving light curves. We estimate the rate of events at redshifts of 2 and 4 to be approximately ten times higher than the rate at low redshift. The extreme luminosities of superluminous supernovae extend the redshift limit for supernova detection using present technology, previously 2.36 (ref. 8), and provide a way of investigating the deaths of the first generation of stars to form after the Big Bang.

We search for high-redshift superluminous supernovae (SLSNe) by modifying our image stacking and analysis technique<sup>9</sup> to their expected light-curve evolution and high luminosities as recently determined from theory and low-redshift observations. Supernovae SN 2213-1745 and SN 1000+0216 were discovered when applying our modified technique to the Canada-France-Hawaii Telescope Legacy Survey Deep Fields. These archival survey data provide deep, consistent photometry of the host galaxies over ~6-month seasons from 2003 to 2008 and allow accurate extraction of the supernova-rest-frame far-ultraviolet light. Follow-up late-time spectroscopy of the supernovae and their host galaxies was obtained using the 10-m Keck I telescope 5.2 and 3.8 yr (~626 and ~286 d, rest frame) after first detection for SN 2213-1745 and SN 1000+0216, respectively. The deep Keck data reveal redshifts of  $z = 2.0458$  for SN 2213-1745 and  $z = 3.8993$  for SN 1000+0216. Details of the supernovae and their host galaxies are listed in Table 1.

SN 2213-1745 is detected in the 2005 and 2006 seasonal (June–November) stacked images for the deep field D4, and SN 1000+0216 is detected in the 2006–2007 and 2007–2008 seasonal (November–June)

stacked images for deep field D2 (Fig. 1). Neither supernova is detected in the previous two seasons above the stacked-image detection limit of  $m \approx 26.5$  mag (Supplementary Information, section A). The nightly images that comprise the seasonal stacks first show the supernovae at the onset of the observing seasons. The lack of detection in previous seasons implies that the initial outbursts occurred between November 2004 and June 2005 for SN 2213-1745 and between June and November 2006 for SN 1000+0216. Both supernovae evolve slowly and reach high peak luminosities of  $\sim 0.5 \times 10^{44}$  to  $1 \times 10^{44}$  erg s<sup>-1</sup>, uncorrected for host galaxy extinction. The peak luminosities correspond to far-ultraviolet absolute AB magnitudes<sup>10,11</sup> of  $M_{\text{peak}} \approx -21$  mag and thereby rule out all normal supernova subtypes. SLSNe are the only supernova type that can generate similar peak magnitudes and light-curve evolution (Fig. 2).

Although active galactic nuclei (AGNs), powered by the erratic accretion of material onto supermassive black holes at the centres of galaxies, can produce similar energies, both host galaxies exhibit a single supernova-like outburst, present no activity during the previous two years and have colours that are inconsistent with high-redshift AGNs, including the eight spectroscopic AGNs in our sample. Moreover, the SN 2213-1745 host spectrum does not show signs of AGN activity (Fig. 3), and although the SN 1000+0216 host spectrum shows narrow Ly $\alpha$  emission, common to high-redshift galaxies, no other AGN-associated features are seen. In contrast, the images reveal zero, or very small, separations (projected in the plane of the sky) from their host galaxy centroids (Supplementary Information, section A). We note that our technique is limited to detecting supernovae within the small extent of the high-redshift host galaxies that produces far-ultraviolet flux, and that far-ultraviolet light directly traces regions of high star formation and does not necessarily provide accurate galaxy centroids. Finally, although the ultraviolet–optical afterglows of long-duration  $\gamma$ -ray bursts can achieve luminosities equivalent to, or greater than, the observed events, the bursts typically reach their peak luminosities within a day and quickly decay<sup>12</sup>, usually in inverse proportion to time. This behaviour is inconsistent with the observed slow rise and slow decay of the events discussed here.

Recently, SLSNe have been classified into groups on the basis of their photometric and spectroscopic properties<sup>2</sup>. Those in group SLSN-I show no evidence of hydrogen in their spectra, whereas those

**Table 1 | Supernova and host galaxy details**

Supernova	Right ascension (J2000)	Declination (J2000)	Host $M_{\text{FUV}}$ (mag)	Supernova peak $M_{\text{FUV}}$ (mag)	Detection dates	Redshift
SN 2213-1745	22 h 13 min 39.970 s	-17° 45' 24.486''	-21.38 $\pm$ 0.03	-21.2 $\pm$ 0.2	June 2005– November 2006	2.0458 $\pm$ 0.0005
SN 1000+0216	10 h 00 min 05.872 s	+02° 16' 23.621''	-21.20 $\pm$ 0.04	-21.5 $\pm$ 0.2	November 2006– June 2008	3.8993 $\pm$ 0.0074

The far-ultraviolet absolute magnitudes,  $M_{\text{FUV}}$ , are derived using the conventional relationship  $M_{\text{FUV}} = m_{\text{AB}} - 5 \log_{10}(D_L(z)/10 \text{ pc}) + 2.5 \log_{10}(1+z)$ , where  $m_{\text{AB}}$  is the observed redshifted far-ultraviolet AB magnitude<sup>10,11</sup> and  $D_L$  is the luminosity distance, adopting a standard cosmology with Hubble parameter  $H_0 = 71$ , mass density  $\Omega_M = 0.73$  and vacuum energy density  $\Omega_\Lambda = 0.27$ . The supernova absolute magnitudes are corrected for extinction by the Milky Way<sup>29</sup> (0.04–0.11 mag) but not corrected for supernova host galaxy extinction.

<sup>1</sup>Centre for Astrophysics and Supercomputing, Swinburne University of Technology, PO Box 218, H30, Hawthorn, Victoria 3122, Australia. <sup>2</sup>Department of Physics, University of Oxford, Denys Wilkinson Building, Keble Road, Oxford OX1 3RH, UK. <sup>3</sup>Ben-Zvi Center for Astrophysics, Weizmann Institute of Science, 76100 Rehovot, Israel. <sup>4</sup>Center for Cosmology, Department of Physics and Astronomy, University of California, Irvine, California 92697, USA. <sup>5</sup>Department of Astronomy & Astrophysics, University of Toronto, Toronto, Ontario M5S 3H4, Canada. <sup>6</sup>Department of Astronomy, San Diego State University, San Diego, California 92182, USA. <sup>7</sup>Department of Physics, McGill University, 3600 rue University, Montreal, Quebec H2A 2T8, Canada.

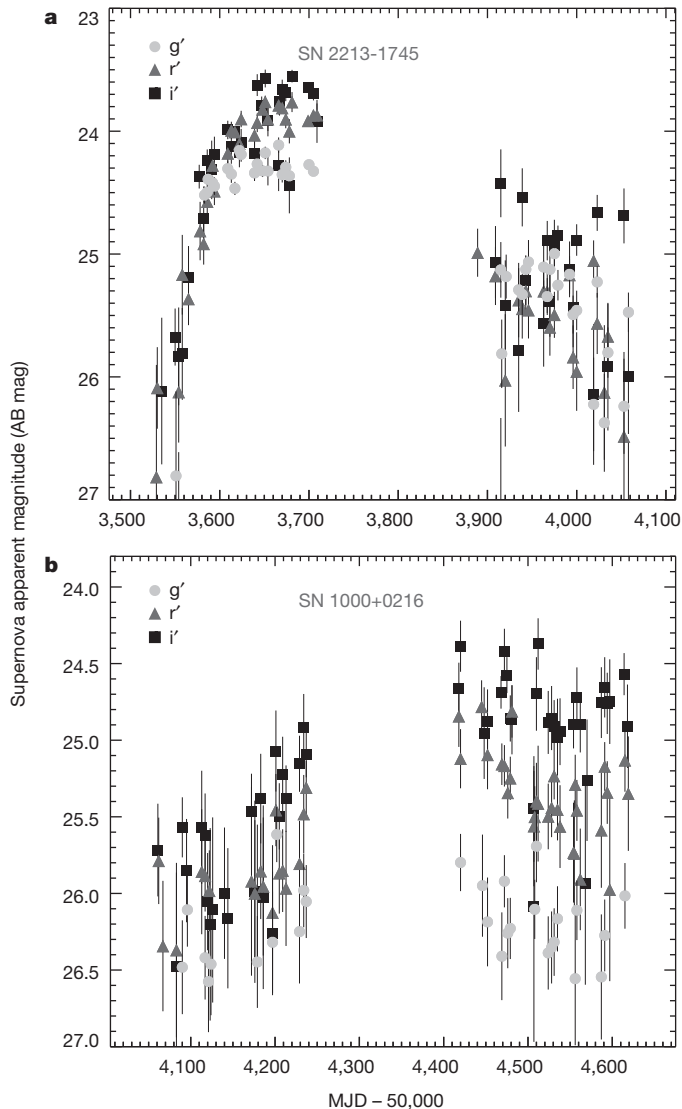


**Figure 1 | Light curves of high-redshift supernovae.** Plotted as functions of time (MJD, modified Julian date) are the observed supernova  $g'$ -,  $r'$ - and  $i'$ -band magnitudes and  $1\sigma$  errors detected in nightly stacked images after host galaxy flux subtraction. The high-quality images used in our study provide consistent and accurate photometry of the supernova host galaxies for  $\sim 6$  months per year for four years (Supplementary Information, section A). **a**, Magnitudes for SN 2213-1745 ( $z = 2.05$ ) detected in deep field D4 during the observing seasons June–November 2005 and June–November 2006. The optical  $g'$ -,  $r'$ - and  $i'$ -band data correspond to rest-frame far-ultraviolet continuum wavelengths of  $\sim 1,600$ ,  $\sim 2,050$  and  $\sim 2,530$  Å, respectively. **b**, Magnitudes for SN 1000+0216 ( $z = 3.90$ ) detected in deep field D2 during the observing seasons November 2006–June 2007 and November 2007–June 2008. Here, the  $g'$ -,  $r'$ - and  $i'$ -filters correspond to rest-frame wavelengths of  $\sim 1,000$ ,  $\sim 1,300$  and  $\sim 1,600$  Å, respectively. As a result, only the  $i'$  filter samples the far-ultraviolet continuum exclusively. The  $r'$  filter probes the continuum and the Lyman  $\alpha$  ( $\text{Ly}\alpha$ ) feature and samples the decrement in flux on the short-wavelength side of the  $\text{Ly}\alpha$  feature caused by optically thick systems at lower redshift in the line of sight (the  $\text{Ly}\alpha$  forest). The  $g'$  filter completely samples the spectral region of the  $\text{Ly}\alpha$  forest to just below the Lyman limit.

in group SLSN-II are rich in hydrogen and include a subset showing signs of interaction with circumstellar material. Finally, those in group SLSN-R have light curves that evolve slowly, powered by the radiative decay of  $^{56}\text{Ni}$ . SLSN-R events are suspected to be pair-instability supernovae: the deaths of stars with initial masses between 140 and 260 solar masses<sup>3–5</sup>. The physics of the pair-instability process has been understood for many years, but the extreme rarity of SLSNe-R ( $\sim 10$  times less frequent than SLSNe-I or SLSNe-II) has resulted in only one believable

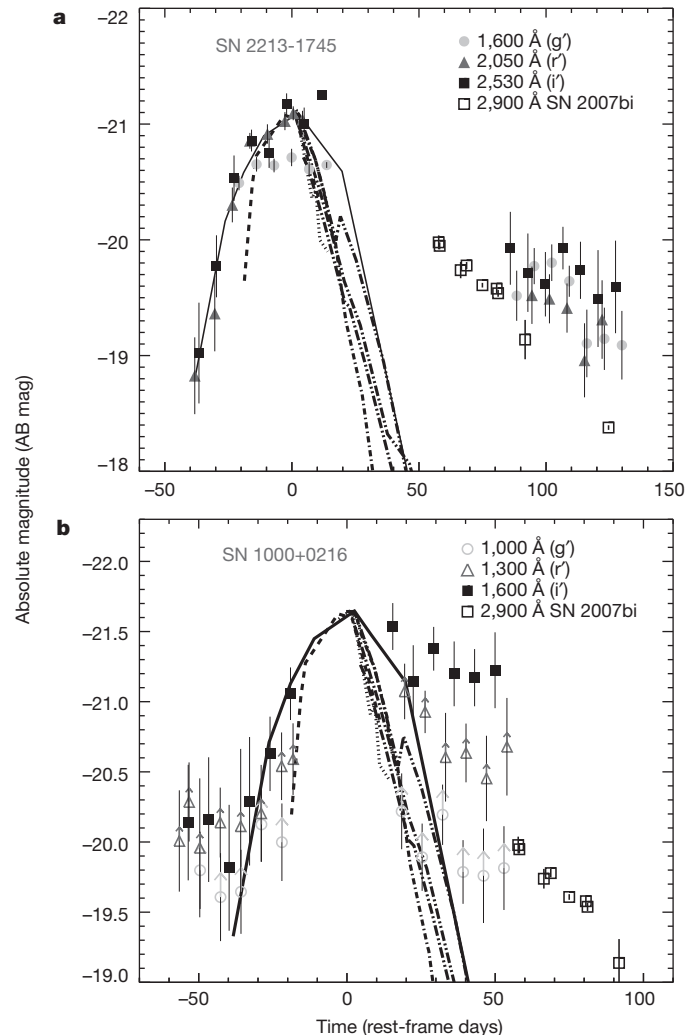


**Figure 2 | Absolute magnitude light curves of SLSNe.** **a**, The rise and decay of the luminosity of SN 2213-1745 in the supernova rest frame, binned in 7-day intervals. At  $z = 2.05$ , the  $g'$ -,  $r'$ - and  $i'$ -filters probe effective wavelengths of 1,600, 2,050 and 2,530 Å, respectively. For comparison of light-curve evolution, the photometry of six lower-redshift SLSNe observed at similar, but typically longer, wavelengths is overlaid and scaled by 0–1.2 mag to match the estimated peak light of the data: SCP 06F6<sup>15</sup> (SLSN-I, 3,500 Å, solid curve), SN 2010gx<sup>16</sup> (SLSN-I, 2,900 Å, dotted curve), PS1-10awh<sup>18</sup> (SLSN-I, 2,500 Å, dashed curve), PS1-10ky<sup>18</sup> (SLSN-I, 2,500 Å, dot-dash curve), and SN 2008es<sup>14</sup> (SLSN-II, 1,700–2,200 Å, dot-dot-dash curves). Also shown is SLSN-R SN 2007bi<sup>17</sup>, with zero magnitude offset. We note that the SN 2007bi data are based on the known peak magnitude from  $r$ -band photometry acquired from just before peak to  $>300$  d after peak<sup>13</sup>. Error bars on all points represent  $1\sigma$ . **b**, Same as **a** but for SN 1000+0216 at  $z = 3.90$ . Here the lower-redshift SLSNe are matched to an estimated peak in the  $i'$  filter (1,600 Å), which is the only filter that samples the far-ultraviolet continuum of the supernova exclusively. This arbitrary peak for SN 1000+0216 results in an offset of  $-0.1$  to  $-0.6$  mag for the lower-redshift SLSNe-I and SLSN-II (as in **a**, SN 2007bi is not offset). As described in Fig. 1, the  $g'$  (1,000 Å) and  $r'$  (1,300 Å) filters partly or completely probe the spectral region of the  $\text{Ly}\alpha$  forest. The upward arrows indicate that the true flux in these filters is higher than indicated.

recorded event, SN 2007bi<sup>13</sup>, which is well studied up to late times, with a few candidates being followed by ongoing low-redshift surveys.

In Fig. 2, we compare the photometric evolution of the high-redshift supernovae with lower-redshift SLSN data at similar wavelengths<sup>14–18</sup>. All SLSNe, except for SLSN-R SN 2007bi, which is estimated to be powered by about four to seven solar masses of  $^{56}\text{Ni}$ , fade significantly quicker than the two high-redshift events. As far as can be determined from the photometry, the evolution of SN 2213-1745 is consistent with SN 2007bi and, as a result, provides the first far-ultraviolet data for an



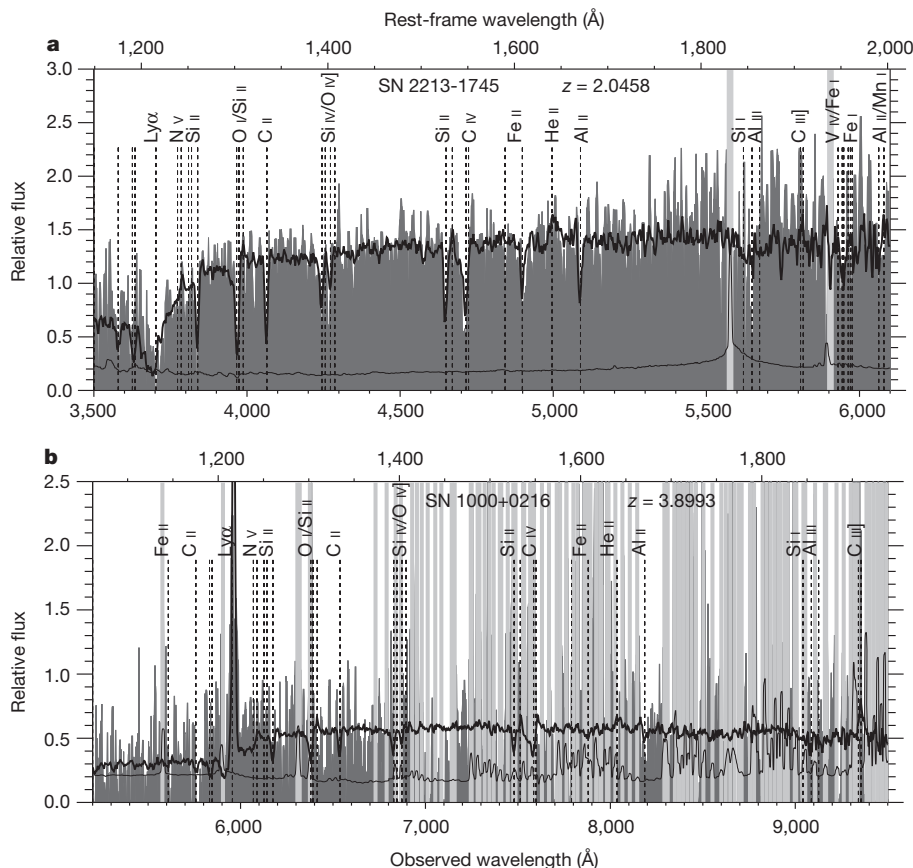


**Figure 3 | Late-time spectra of the supernovae and host galaxies.** The spectra are shown as the dark-grey filled regions. Although Lyman-break galaxies are extremely distant, they have strong absorption features and a prominent Ly $\alpha$  feature at 1,216 Å, seen in absorption and/or emission, which enable reliable identification. Labelled vertical dashed lines indicate typical atomic transitions seen in absorption. Additional absorption features may be present as a result of lower-redshift systems in the line of sight. Thick vertical light-grey lines mark the positions of bright night-sky emission lines that are difficult to remove cleanly from faint spectra. **a**, Spectrum of SN 2213-1745 obtained 626 days (rest frame) after first detection. The 1 $\sigma$ -per-pixel error array is shown by the thin black curve. A composite template of  $\sim 200$  similar spectra from Lyman-break galaxies (thick black curve) is overlaid and confirms galaxy identification and redshift. The spectrum shows no evidence of AGN activity such as strong Ly $\alpha$

1,216 Å, N V 1,240 Å or C IV 1,550 Å emission. **b**, Spectrum of SN 1000+0216 obtained 286 days (rest frame) after first detection, plotted as in **a**. The poorer observing conditions and fainter nature of this object resulted in a spectrum with a lower signal-to-noise ratio and in more difficulty subtracting bright night-sky lines. However, a confident host galaxy identification and redshift determination is achieved in part on the basis of the significant narrow Ly $\alpha$  emission and the decrement in continuum flux at short wavelengths relative to Ly $\alpha$  as a result of the Ly $\alpha$  forest. Although the host galaxy exhibits narrow Ly $\alpha$  emission (observed in  $>50\%$  of Lyman-break galaxies), associated AGN features, such as N V 1,240 Å and C IV 1,550 Å, are not seen at any significance. Flux correction between  $\sim 6,300$  and  $6,800$  Å is underrepresented and less reliable (Supplementary Information, section A).

SLSN-R. The close agreement suggests that SN 2213-1745 may be powered by the radiative decay of a similar amount of synthesized  $^{56}\text{Ni}$ , and, along with an integrated radiated luminosity of  $\sim 10^{51}$  erg, implies a progenitor with an estimated initial mass of about 250 solar masses. We note that although SN 2213-1745 is shown to follow closely the luminosity evolution of a radiation-hydrodynamics SLSN-R simulation<sup>19</sup> for a progenitor star of similar mass, the observed flux is higher and bluer than the model expectations (Supplementary Information, section C).

SN 1000+0216 was observed over a shorter time period than was SN 2213-1745, as a result of time dilation. The range of the light curve sampled suggests a longer rise time than SN 2213-1745 but seems to follow a similar fade rate from peak luminosity to  $\sim 50$  d later (rest frame), if we assume that the peak occurred during the gap in coverage between the two detection seasons. The peak far-ultraviolet magnitude of SN 1000+0216 may exceed that possible for a pair-instability supernova. As a result, SN 1000+0216 may be an example of a pulsational pair-instability supernova<sup>5</sup> or a SLSN-II similar to the low-redshift SN 2006gy<sup>20,21</sup>, which experience enhanced luminosity as a result of interaction with previously expelled circumstellar material (Supplementary Information, sections D and F). The high luminosity of SN 1000+0216 classifies it as an SLSN but, because of its limited photometric coverage

and low signal-to-noise host spectrum, its subclassification remains uncertain.

Our programme searches for  $z \gtrsim 2$  supernovae by monitoring the well-studied population of Lyman-break galaxies<sup>22–24</sup> over several well-defined volumes. Because Lyman-break galaxies comprise the bulk of galaxies at high redshift, where star formation rates are higher, normal populations of short-lived, massive stars are more common at  $z \gtrsim 2$  than locally. From the specifics of our survey, the two SLSN detections imply a rough volumetric high-redshift rate of  $\sim 4 \times 10^{-7} h_{71}^3 \text{ Mpc}^{-3} \text{ yr}^{-1}$  (where  $h_{71}$  is the dimensionless Hubble parameter) at  $z = 2.2 \pm 0.3$  and  $z = 4.1 \pm 0.3$  (mean  $\pm 1\sigma$ ) (Supplementary Information, section B). After correcting for the increase in the cosmic star formation rate from low to high redshift, the SLSN rate remains  $\sim 10$  times higher than that estimated at low redshift<sup>1</sup>, but we caution that our rate estimate is poorly constrained because it is derived from only two events. The far-ultraviolet photometry confirms that the two supernovae are strong sources of escaping high-energy photons. However, far-ultraviolet light is highly susceptible to metal-line absorption and local and global dust extinction that may have a greater effect on other high-redshift SLSNe and cause them to fall below our detection threshold. As a result, our estimated rate is a lower limit and implies that the discrepancy between low and high redshift may be even greater.

The detection of SLSNe at  $z > 2$  presents the possibility of finding the explosions of population III stars, the first stars to form after the Big Bang. Population III stars are predicted to exist at redshifts as low as  $z \approx 2$  (refs 25–28) and have mass distributions skewed towards high masses<sup>6,7</sup>. On the basis of our late-time spectroscopy, the supernovae presented here are unlikely to be from the first generation of stars (Supplementary Information, section E). Deep spectroscopy of future supernovae obtained near maximum brightness, and their use as sight-line probes, offers a means to help distinguish which events formed in regions with essentially no enrichment in elements heavier than helium, and thus probably had population III progenitors.

Received 11 April; accepted 21 August 2012.

Published online 31 October 2012.

1. Quimby, R. M. *et al.* Hydrogen-poor superluminous stellar explosions. *Nature* **474**, 487–489 (2011).
2. Gal-Yam, A. *et al.* Super-luminous supernovae. *Science* **337**, 927–932 (2012).
3. Rakavy, G. & Shaviv, G. Instabilities in highly evolved stellar models. *Astrophys. J.* **148**, 803–816 (1967).
4. Barkat, Z., Rakavy, G. & Sack, N. Dynamics of supernova explosion resulting from pair formation. *Phys. Rev. Lett.* **18**, 379–381 (1967).
5. Heger, A. & Woosley, S. E. The nucleosynthetic signature of population III. *Astrophys. J.* **567**, 532–543 (2002).
6. Larson, R. B. Early star formation and the evolution of the stellar initial mass function in galaxies. *Mon. Not. R. Astron. Soc.* **301**, 569–581 (1998).
7. Bromm, V., Coppi, P. S. & Larson, R. B. Forming the first stars in the Universe: the fragmentation of primordial gas. *Astrophys. J.* **527**, L5–L8 (1999).
8. Cooke, J. *et al.* Type II supernovae at redshift  $z \approx 2$  from archival data. *Nature* **460**, 237–239 (2009).
9. Cooke, J. Detecting  $z > 2$  type II supernovae. *Astrophys. J.* **677**, 137–145 (2008).
10. Oke, J. B. Absolute spectral energy distributions for white dwarfs. *Astrophys. J. Suppl. Ser.* **27**, 21–35 (1974).
11. Fukugita, M. *et al.* The Sloan Digital Sky Survey photometric system. *Astron. J.* **111**, 1748–1756 (1996).
12. Kann, D. A. *et al.* The afterglows of Swift-era gamma-ray bursts. II. Type I GRB versus type II GRB optical afterglows. *Astrophys. J.* **734**, 96–150 (2011).
13. Gal-Yam, A. *et al.* Supernova 2007bi as a pair-instability explosion. *Nature* **462**, 624–627 (2009).
14. Gezari, S. *et al.* Discovery of the ultra-bright type II-L supernova 2008es. *Astrophys. J.* **690**, 1313–1321 (2009).
15. Barbary, K. *et al.* Discovery of an unusual optical transient with the Hubble Space Telescope. *Astrophys. J.* **690**, 1358–1362 (2009).
16. Pastorello, A. *et al.* Ultra-bright optical transients are linked with type Ic supernovae. *Astrophys. J.* **724**, L16–L21 (2010).
17. Young, D. R. *et al.* Two type Ic supernovae in low-metallicity, dwarf galaxies: diversity of explosions. *Astron. Astrophys.* **512**, A70 (2010).
18. Chomiuk, L. *et al.* PAN-STARRS1 discovery of two ultra-luminous supernovae at  $z \sim 0.9$ . *Astrophys. J.* **743**, 114 (2011).
19. Kasen, D., Woosley, S. E. & Heger, A. Pair instability supernovae: light curves, spectra, and shock breakout. *Astrophys. J.* **734**, 102 (2011).
20. Smith, N. *et al.* SN 2006gy: discovery of the most luminous supernova ever recorded, powered by the death of an extremely massive star like  $\eta$  Carinae. *Astrophys. J.* **666**, 1116–1128 (2007).
21. Smith, N. *et al.* Spectral evolution of the extraordinary type II supernova 2006gy. *Astrophys. J.* **709**, 856–883 (2010).
22. Steidel, C. C. *et al.* Lyman-break galaxies at  $z \geq 4$  and the evolution of the ultraviolet luminosity density at high redshift. *Astrophys. J.* **519**, 1–17 (1999).
23. Steidel, C. C. *et al.* Lyman break galaxies at redshift  $z \sim 3$ : survey description and full data set. *Astrophys. J.* **592**, 728–754 (2003).
24. Steidel, C. C. *et al.* A survey of star-forming galaxies in the  $1.4 < z < 2.5$  redshift desert: overview. *Astrophys. J.* **604**, 534–550 (2004).
25. Scannapieco, E. *et al.* The detectability of pair-production supernovae at  $z \approx 6$ . *Astrophys. J.* **633**, 1031–1041 (2005).
26. Tornatore, L., Ferrara, A. & Schneider, R. Population III stars: hidden or disappeared? *Mon. Not. R. Astron. Soc.* **382**, 945–950 (2007).
27. Trenti, M., Stiavelli, M. & Michael Shull, J. Metal-free gas supply at the edge of reionization: late-epoch population III star formation. *Astrophys. J.* **700**, 1672–1679 (2009).
28. Fumagalli, M., O’Meara, J. M. & Prochaska, J. X. Detection of pristine gas two billion years after the big bang. *Science* **334**, 1245–1249 (2011).
29. Schlegel, D. J., Finkbeiner, D. P. & Davis, M. Maps of dust infrared emission for use in estimation of reddening and cosmic microwave background radiation foregrounds. *Astrophys. J.* **500**, 525–553 (1998).

Supplementary Information is available in the online version of the paper.

**Acknowledgements** We acknowledge support from ARC, NSERC and the Royal Society. A.G.-Y. acknowledges support from ISF, GIF, Minerva grants, an ARCHEs award and the Lord Seiff of Brimpton Fund. This work was supported in part by a grant from the ANSTO AMRFP. The Access to Major Research Facilities Program is supported by the Commonwealth of Australia under the International Science Linkages program. The results presented here are based on observations obtained with MegaPrime/MegaCam, a joint project of the Canada-France-Hawaii Telescope (CFHT) and CEA-Irfu, at the CFHT, which is operated by the National Research Council (NRC) of Canada, the Institut National des Sciences de l’Univers of the Centre National de la Recherche Scientifique (CNRS) of France, and the University of Hawaii. This work is based in part on data products produced at TERAPIX and the Canadian Astronomy Data Centre as part of the CFHT Legacy Survey, a collaborative project of the NRC and CNRS. We used data products from the Canadian Astronomy Data Centre as part of the CFHT Legacy Survey. The spectroscopic data presented here were obtained at the W. M. Keck Observatory, which is operated as a scientific partnership among the California Institute of Technology, the University of California and the National Aeronautics and Space Administration. The observatory was made possible by the generous financial support of the W. M. Keck Foundation. The CFHT and the W. M. Keck Observatory are located near the summit of Mauna Kea, Hawaii.

**Author Contributions** J.C. developed the detection technique and the modification for SLSNe; analysed the imaging data and performed the supernova selection; and obtained, reduced and analysed the spectroscopic observations. M.S. was responsible for the reduction and analysis of the seasonal image stacks, supernova flux extraction and supernova candidate light curves. A.G.-Y. provided supernova analysis and manuscript contributions and advice. E.J.B. performed observations and provided observing time and scientific discussions. R.G.C. provided manuscript advice, was one of the proponents of the CFHT Legacy Survey and, as the Canadian Principal Investigator, assembled the team responsible for much of the operation and analysis of the legacy survey. E.V.R.-W. enabled spectroscopic observations and provided discussions and student support. C.H. performed Keck spectroscopic observations and data reduction. Y.O. and C.G.D. performed Keck spectroscopic observations.

**Author Information** Reprints and permissions information is available at [www.nature.com/reprints](http://www.nature.com/reprints). The authors declare no competing financial interests. Readers are welcome to comment on the online version of the paper. Correspondence and requests for materials should be addressed to J.C. ([jcooke@astro.swin.edu.au](mailto:jcooke@astro.swin.edu.au)).



# Non-invasive imaging through opaque scattering layers

Jacopo Bertolotti<sup>1,2\*</sup>, Elbert G. van Putten<sup>1†\*</sup>, Christian Blum<sup>3</sup>, Ad Lagendijk<sup>1,4</sup>, Willem L. Vos<sup>1</sup> & Allard P. Mosk<sup>1</sup>

**Non-invasive optical imaging techniques, such as optical coherence tomography<sup>1–3</sup>, are essential diagnostic tools in many disciplines, from the life sciences to nanotechnology. However, present methods are not able to image through opaque layers that scatter all the incident light<sup>4,5</sup>. Even a very thin layer of a scattering material can appear opaque and hide any objects behind it<sup>6</sup>. Although great progress has been made recently with methods such as ghost imaging<sup>7,8</sup> and wavefront shaping<sup>9–11</sup>, present procedures are still invasive because they require either a detector<sup>12</sup> or a nonlinear material<sup>13</sup> to be placed behind the scattering layer. Here we report an optical method that allows non-invasive imaging of a fluorescent object that is completely hidden behind an opaque scattering layer. We illuminate the object with laser light that has passed through the scattering layer. We scan the angle of incidence of the laser beam and detect the total fluorescence of the object from the front. From the detected signal, we obtain the image of the hidden object using an iterative algorithm<sup>14,15</sup>. As a proof of concept, we retrieve a detailed image of a fluorescent object, comparable in size (50 micrometres) to a typical human cell, hidden 6 millimetres behind an opaque optical diffuser, and an image of a complex biological sample enclosed between two opaque screens. This approach to non-invasive imaging through strongly scattering media can be generalized to other contrast mechanisms and geometries.**

As experienced on a foggy day, scattering of light severely impairs our ability to see. A strongly scattering medium allows light to pass in the form of a diffuse halo, but completely scrambles all the spatial information<sup>6</sup>. A strategy that has proved very successful in imaging through scattering materials is to separate the small amount of light that did not change direction owing to random scattering (ballistic light) from the scattered background using a gated technique such as optical coherence tomography<sup>1–3</sup>. In this way it is possible to obtain sharp images through semi-transparent media, but for stronger scattering the medium appears opaque to the eye and prevents present non-invasive optical imaging techniques from obtaining detailed images<sup>5</sup>. Absorptive objects deep inside a scattering medium can be located using diffuse wave tomography, which does not allow one to resolve details much smaller than the depth<sup>16,17</sup>.

Speckle correlations can be used to transmit highly detailed image information through scattering media<sup>9,18–21</sup>. To demonstrate non-invasive imaging with speckle correlations, we constructed the setup illustrated in Fig. 1a. A 50- $\mu\text{m}$ -wide fluorescent object made of dye-doped polymer (Supplementary Information) is placed a distance  $d = 6\text{ mm}$  behind a scattering layer (an Edmund Optics 120-grit ground-glass diffuser) that completely hides it. As shown in Fig. 1b, the scattering layer makes it impossible to resolve even millimetre-sized details at this distance. We shine a laser (wavelength, 532 nm) on the scattering layer where, owing to the scattering, the transmitted light produces a speckle pattern that illuminates the object. The fluorescent

light is scrambled by scattering and through the diffuser we cannot measure any spatial information about the shape of the object (Fig. 1c). However, the total amount of transmitted fluorescence can be measured and retains the information on the overlap between the object's fluorescent response,  $O(r)$ , and the speckle intensity,  $S(r)$ , where  $r$  is the vector of spatial coordinates.

In our measurement procedure, we scan the angle of incidence,  $\theta = (\theta_x, \theta_y)$ , of the laser beam using a pair of scanning galvanic mirrors (Supplementary Information). Although the speckle illuminating the object might appear random, it contains correlations that can be exploited. In particular, the angular correlation known as the memory effect<sup>22,23</sup> means that rotating the incident beam over small angles  $\theta$  does not change the resulting speckle pattern but only translates it over a distance  $\Delta r \approx \theta d$ . Therefore, up to a proportionality constant that we will set to 1, the total measured fluorescence as a function of the incident angle is given by

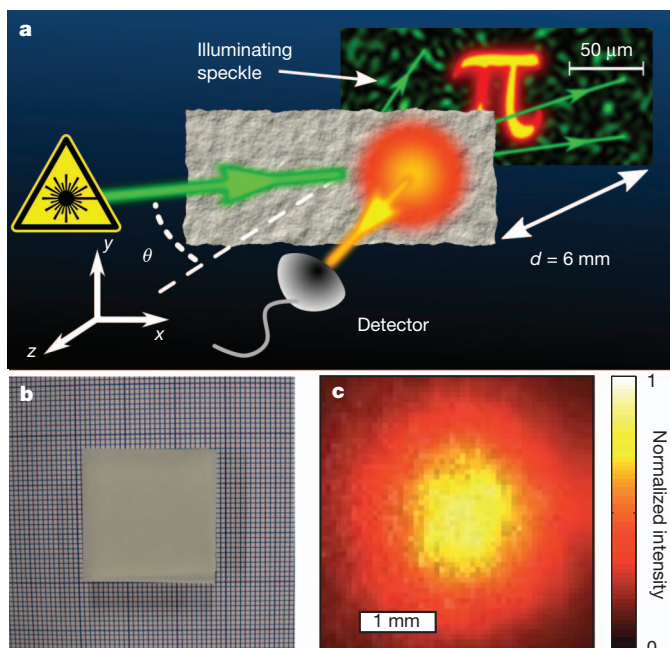


**Figure 1 | Schematic of the apparatus for non-invasive imaging through strongly scattering layers.** **a**, A monochromatic laser beam illuminates an opaque layer of thickness  $L$  at an angle  $\theta$ . A fluorescent object is hidden a distance  $d = 6\text{ mm}$  behind the layer. The fluorescent light is detected from the front of the scattering layer by a charge-coupled device camera. **b**, Photograph of the scattering layer a distance  $d = 6\text{ mm}$  from a millimetre-grid background. The grid behind the layer is completely hidden. **c**, Intensity of fluorescence emitted by the hidden object, as measured in front of the scattering layer. A single fluorescent image contains no information on the shape of the object.

<sup>1</sup>Complex Photonic Systems (COPS), MESA+ Institute for Nanotechnology, University of Twente, PO Box 217, 7500 AE Enschede, The Netherlands. <sup>2</sup>University of Florence, Dipartimento di Fisica, 50019 Sesto Fiorentino, Italy. <sup>3</sup>Nanobiophysics (NBP), MESA+ Institute for Nanotechnology, University of Twente, PO Box 217, 7500 AE Enschede, The Netherlands. <sup>4</sup>FOM Institute for Atomic and Molecular Physics, Science Park 104, 1098 XG Amsterdam, The Netherlands. <sup>†</sup>Present address: Philips Research Laboratories, 5656 AE Eindhoven, The Netherlands.

\*These authors contributed equally to this work.

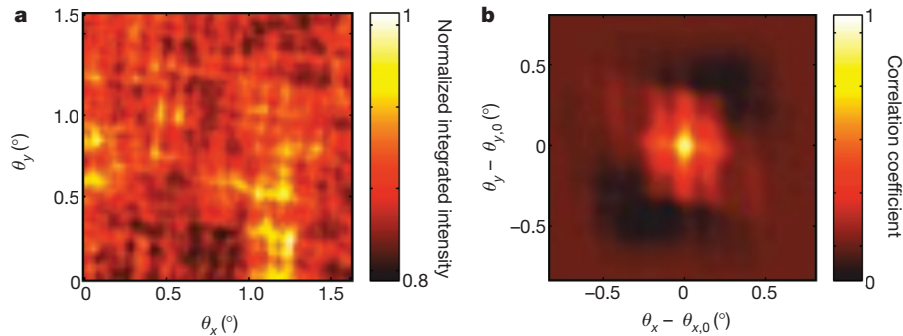


**Figure 2 | Experimental retrieval of the hidden object's autocorrelation.** **a**, Integrated fluorescent intensity,  $I$ , as a function of the incident angle,  $\theta = (\theta_x, \theta_y)$ . **b**, Autocorrelation  $I * I$  averaged over nine scans taken at different

$$I(\theta) = \int_{-\infty}^{\infty} O(r) S(r - \theta d) \, d^2 r = [O * S](\theta)$$

where  $*$  denotes the convolution product. Owing to the random nature of the speckle pattern, the measured intensity,  $I(\theta)$  (Fig. 2a), does not directly resemble that of the original hidden object. Instead, the image information is encoded in the correlations of the measured signal.

To separate the shape of the object from the random speckle, we calculate the autocorrelation product of the measured intensity and obtain

$$\begin{aligned} \langle I * I \rangle(\Delta\theta) &= \langle O * S \rangle * \langle O * S \rangle \\ &= \langle O * O \rangle * \langle S * S \rangle = [O * O] * \langle S * S \rangle \end{aligned}$$

where  $*$  is the cross-correlation product and angle brackets denote the average over speckle realizations (that is, the average over different scans). Because the average autocorrelation of a speckle pattern,  $\langle S * S \rangle$ , is a sharply peaked function<sup>24</sup>, we are effectively measuring the autocorrelation of the object  $O * O$  with a resolution given by the average speckle size. For a circular illumination beam of width  $W$ , we find that

$$\begin{aligned} \langle I * I \rangle(\Delta\theta) &= \left[ [O * O] * \left( \frac{2J_1(k|\theta|W)}{k|\theta|W} \right)^2 \right](\Delta\theta) \\ &\times \left( \frac{k|\Delta\theta|L}{\sinh(k|\Delta\theta|L)} \right)^2 \end{aligned} \quad (1)$$

where  $J_1$  is a first-order Bessel function of the first kind,  $L$  is the layer thickness and  $k$  is the wavenumber<sup>24</sup>. The second term in the convolution represents the average speckle size and can be made arbitrarily close to the diffraction limit by increasing  $W$ . The final (multiplicative) factor accounts for the fact that when the change in the angle of incidence of the laser is not small enough the speckle pattern is not only rotated but also decorrelates, effectively limiting the memory range<sup>22–25</sup> and, thus, the available field of view. We note that ground-glass diffusers are effectively single scattering layers and thus have a very large memory range while being completely opaque<sup>25</sup> (Supplementary Information). Equation (1) does not depend on the detailed scattering properties of the scattering layer, allowing us to measure  $O * O$  for objects hidden behind any completely opaque layer.

The average autocorrelation of nine subsequent scans is shown in Fig. 2b. We obtained the independent measurements of  $I(\theta)$  needed to average  $S * S$  by starting each scan at a different incidence angle. In fact, if the difference between the starting angles is larger than the angular size of the object, the speckle realizations are independent. Comparing the measured autocorrelation with a microscope image of the object (Fig. 3a), we recognize some features such as the presence of two vertical legs. Yet an autocorrelation contains only information on the relative distance between the various parts of an object, and not directly on the object itself. Furthermore, the autocorrelation of a real

values of the starting incidence angle,  $\theta_0$ , to average over the different realizations of the speckle,  $S$ .

object is always centred and centrosymmetric. To obtain an image of the object we need to invert the autocorrelation.

In two and three dimensions, autocorrelations can be numerically inverted using a Gerchberg–Saxton-type iterative algorithm by exploiting some manifest properties of the measured signal as constraints<sup>14,26</sup>. In our case, we used the fact that a fluorescent image is always real and positive. Other common choices are the fact that  $O$  is a real function, as in stellar speckle interferometry<sup>27</sup>, and the positiveness of both the real and the imaginary part of  $O$ , as in X-ray scattering<sup>15,28</sup>. We used a standard version of this algorithm, which can perform the inversion in a few seconds on a normal desktop computer (Supplementary Information). The results of the inversion are shown in Fig. 3. In Fig. 3a we show a fluorescence microscope image of the object before it is placed behind the scattering layer, and in Fig. 3b we show the object retrieved from the measured autocorrelation presented in Fig. 2b. The two images of the symbol  $\pi$  show an excellent resemblance to each other. Small features such as the flattening of the left ‘foot’ of the symbol or the inhomogeneities in the intensity are faithfully recovered, demonstrating successful imaging of the object through an opaque layer.

To test our method on a complex biological sample, we placed a slice of the stem of *Convallaria majalis* between two diffusers (4.5 cm behind the front one and 6 mm in front of the back one), effectively enclosing the sample. The structure presents intracellular autofluorescence and did not require staining. The light emitted when the sample was illuminated with the speckled light was collected from behind the back diffuser (Fig. 4a), and after averaging over five scans we obtained the autocorrelation shown in Fig. 4b. Figures 4c and 4d respectively show an image of the sample taken with the back diffuser removed (thus allowing free optical access) and the reconstructed image obtained starting from the measured autocorrelation. The blue lines in Fig. 4c are contours of the reconstructed image at 20% of the maximum intensity, showing that all the high-intensity features of the

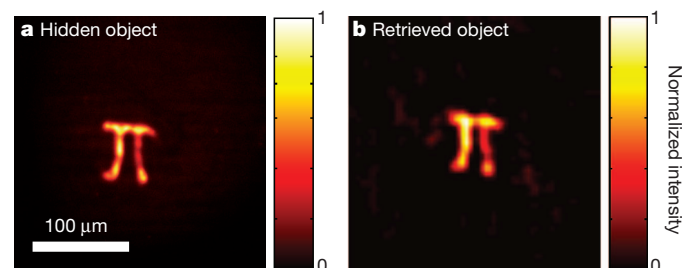


**Figure 3 | Comparison of the retrieved image with the hidden object.** **a**, Fluorescence microscope image of the object taken without the scattering layer in place. **b**, The retrieved object that we found from the measured autocorrelation in Fig. 2b. Even small details such as the intensity inhomogeneities of the original object are recovered in the retrieved image.



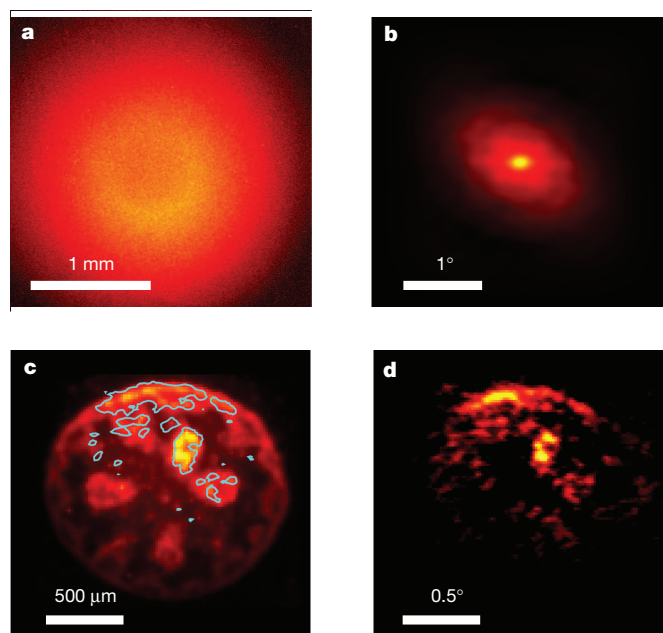


**Figure 4 | Retrieval of a complex, biological structure.** **a**, Autofluorescence from the sample of *C. majalis* as seen through the back diffuser. **b**, Measured autocorrelation averaged over five scans. **c**, Fluorescence image of the structure taken after removing the back diffuser and averaging over many ( $\sim 200$ ) speckle illuminations. The blue line is a contour (at 20% of the maximum intensity) of the reconstructed object. **d**, The reconstructed object. All high-intensity features in the original object are recovered. The colour scale is the same as in Fig. 3.

object were faithfully recovered. To reduce the complexity of the reconstruction, we lowered the resolution by increasing the speckle size. Higher resolution (up to the diffraction limit) can be obtained by decreasing the size of the speckle spots. The main limitation on the reconstruction fidelity is given by the background signal, which can distort the measured autocorrelation<sup>29</sup>.

We have experimentally demonstrated non-invasive imaging of a two-dimensional fluorescent object through a completely opaque layer. Other optical signals that depend on speckle intensity, such as chemically selective Raman scattering, photoacoustic absorption contrast<sup>30</sup> and second-harmonic generation, can also be used. Three-dimensional imaging, for example to study cell morphology<sup>4</sup>, is possible by also scanning the speckle pattern in the third direction, which can be done by adding a parabolic phase pattern to the beam.

## METHODS SUMMARY

A collimated laser beam was shone on the scattering layer with a controllable angle of incidence. The total amount of fluorescent light coming from the hidden object was detected through the scattering layer as a function of the angle of incidence, using a charge-coupled device. After subtracting the background, the measured signal was autocorrelated and the autocorrelations obtained from several independent scans were averaged. The resulting average autocorrelation was multiplied with a Hamming window and used as the input for a Gerchberg–Saxton-type iterative algorithm that can be used to determine the shape of the hidden object.

Received 27 July; accepted 12 September 2012.

1. Abramson, N. Light-in-flight recording by holography. *Opt. Lett.* **3**, 121–123 (1978).
2. Huang, D. *et al.* Optical coherence tomography. *Science* **254**, 1178–1181 (1991).

3. Nasr, M. B., Saleh, B. E. A., Sergienko, A. V. & Teich, M. C. Demonstration of dispersion-canceled quantum-optical coherence tomography. *Phys. Rev. Lett.* **91**, 083601 (2003).
4. Ntziachristos, V. Going deeper than microscopy: the optical imaging frontier in biology. *Nature Methods* **7**, 603–614 (2010).
5. Ishimaru, A., Sermsak, J. & Kuga, Y. Imaging through random multiple scattering media using integration of propagation and array signal processing. *Waves Rand. Compl. Media* **22**, 24–39 (2012).
6. Sheng, P. *Introduction to Wave Scattering, Localization and Mesoscopic Phenomena* (Academic, 1995).
7. Strekalov, D. V., Sergienko, A. V., Klyshko, D. N. & Shih, Y. H. Observation of two-photon “ghost” interference and diffraction. *Phys. Rev. Lett.* **74**, 3600–3603 (1995).
8. Bennink, R. S., Bentley, S. J. & Boyd, R. W. “Two-photon” coincidence imaging with a classical source. *Phys. Rev. Lett.* **89**, 113601 (2002).
9. Freund, I. Looking through walls and around corners. *Physica A* **168**, 49–65 (1990).
10. Mosk, A. P., Lagendijk, A., Lerosey, G. & Fink, M. Controlling waves in space and time for imaging and focusing in complex media. *Nature Photon.* **6**, 283–292 (2012).
11. Katz, O., Small, E. & Silberberg, Y. Focusing and compression of ultrashort pulses through scattering media. *Nature Photon.* **5**, 372–377 (2011).
12. van Putten, E. G. *et al.* Scattering lens resolves sub-100 nm structures with visible light. *Phys. Rev. Lett.* **106**, 193905 (2011).
13. Hsieh, C.-L., Pu, Y., Grange, R., Laporte, G. & Psaltis, D. Imaging through turbid layers by scanning the phase conjugated second harmonic radiation from a nanoparticle. *Opt. Express* **18**, 20723–20731 (2010).
14. Fienup, J. R. Phase retrieval algorithms: a comparison. *Appl. Opt.* **21**, 2758–2769 (1982).
15. Miao, J., Charalambous, P., Kirz, J. & Sayre, D. Extending the methodology of X-ray crystallography to allow imaging of micrometre-sized non-crystalline specimens. *Nature* **400**, 342–344 (1999).
16. Gibson, A., Hebden, J. & Arridge, S. Recent advances in diffuse optical imaging. *Phys. Med. Biol.* **50**, R1–R43 (2005).
17. Culver, J. P., Ntziachristos, V., Holboke, M. J. & Yodh, A. G. Optimization of optode arrangements for diffuse optical tomography: a singular-value analysis. *Opt. Lett.* **26**, 701–703 (2001).
18. Fink, M. Time reversed acoustics. *Phys. Today* **50**, 34–40 (1997).
19. Yaqoob, Z., Psaltis, D., Feld, M. S. & Yang, C. Optical phase conjugation for turbidity suppression in biological samples. *Nature Photon.* **2**, 110–115 (2008).
20. Popoff, S. M. *et al.* Measuring the transmission matrix in optics: an approach to the study and control of light propagation in disordered media. *Phys. Rev. Lett.* **104**, 100601 (2010).
21. Vellekoop, I. M. & Aegerter, C. Scattered light fluorescence microscopy: imaging through turbid layers. *Opt. Lett.* **35**, 1245–1247 (2010).
22. Feng, S., Kane, C., Lee, P. A. & Stone, A. D. Correlations and fluctuations of coherent wave transmission through disordered media. *Phys. Rev. Lett.* **61**, 834–837 (1988).
23. Freund, I., Rosenbluh, M. & Feng, S. Memory effects in propagation of optical waves through disordered media. *Phys. Rev. Lett.* **61**, 2328–2331 (1988).
24. Akkermans, E. & Montambaux, G. *Mesoscopic Physics of Electrons and Photons* 427–439 (Cambridge Univ. Press, 2007).
25. Katz, T., Small, E. & Silberberg, Y. Looking around corners and through thin turbid layers in real time with scattered incoherent light. *Nature Photon.* **6**, 549–553 (2012).
26. Fienup, J. R. Reconstruction of an object from the modulus of its Fourier transform. *Opt. Lett.* **3**, 27–29 (1978).
27. Dainty, J. C. (ed.) *Laser Speckle and Related Phenomena* (Springer, 1984).
28. Abbey, B. *et al.* Lensless imaging using broadband X-ray sources. *Nature Photon.* **5**, 420–424 (2011).
29. Thurman, S. T. & Fienup, J. R. Phase retrieval with signal bias. *J. Opt. Soc. Am. A* **26**, 1008–1014 (2009).
30. Wang, L. V. & Hu, S. Photoacoustic tomography: *in vivo* imaging from organelles to organs. *Science* **335**, 1458–1462 (2012).

**Supplementary Information** is available in the online version of the paper.

**Acknowledgements** We thank W. L. Barnes for discussions and for reading the manuscript, and M. Claessens, V. Subramaniam and J. Schleipen for discussions and for help with samples and equipment. This work is supported by the Stichting Technische Wetenschappen and the Stichting voor Fundamenteel Onderzoek der Materie, which are financially supported by the Nederlandse Organisatie voor Wetenschappelijk Onderzoek (NWO). J.B. acknowledges a grant by FIRB-MIUR ‘Futuro in Ricerca’ (project RBFR08UH60). A.P.M. acknowledges a ‘Vidi’ grant from NWO and European Research Council grant no. 279248.

**Author Contributions** All authors take full responsibility for the content of the paper.

**Author Information** Reprints and permissions information is available at [www.nature.com/reprints](http://www.nature.com/reprints). The authors declare no competing financial interests. Readers are welcome to comment on the online version of the paper. Correspondence and requests for materials should be addressed to J.B. ([j.bertolotti@utwente.nl](mailto:j.bertolotti@utwente.nl)).

# Integration of chemical catalysis with extractive fermentation to produce fuels

Pazhamalai Anbarasan<sup>1,2\*</sup>, Zachary C. Baer<sup>2,3\*</sup>, Sanil Sreekumar<sup>1,2</sup>, Elad Gross<sup>1,4</sup>, Joseph B. Binder<sup>2</sup>, Harvey W. Blanch<sup>2,3</sup>, Douglas S. Clark<sup>2,3</sup> & F. Dean Toste<sup>1,2,4</sup>

Nearly one hundred years ago, the fermentative production of acetone by *Clostridium acetobutylicum* provided a crucial alternative source of this solvent for manufacture of the explosive cordite. Today there is a resurgence of interest in solventogenic *Clostridium* species to produce n-butanol and ethanol for use as renewable alternative transportation fuels<sup>1–3</sup>. Acetone, a product of acetone–n-butanol–ethanol (ABE) fermentation, harbours a nucleophilic  $\alpha$ -carbon, which is amenable to C–C bond formation with the electrophilic alcohols produced in ABE fermentation. This functionality can be used to form higher-molecular-mass hydrocarbons similar to those found in current jet and diesel fuels. Here we describe the integration of biological and chemocatalytic routes to convert ABE fermentation products efficiently into ketones by a palladium-catalysed alkylation. Tuning of the reaction conditions permits the production of either petrol or jet and diesel precursors. Glyceryl tributyrate was used for the *in situ* selective extraction of both acetone and alcohols to enable the simple integration of ABE fermentation and chemical catalysis, while reducing the energy demand of the overall process. This process provides a means to selectively produce petrol, jet and diesel blend stocks from lignocellulosic and cane sugars at yields near their theoretical maxima.

Natural biological routes to produce alcohols (ethanol and n-butanol) from carbohydrates have been known for more than 100 years, and these compounds have been produced in fermentations at high titres ( $\sim 100$  and  $15\text{ g l}^{-1}$ , respectively) and at yields near their theoretical maxima. These low-molecular-mass compounds are primarily suitable as additives or in certain situations (for example, E100 flex fuel vehicles) as alternatives to petrol. Advances in metabolic engineering have enabled the biological production of several higher-molecular-mass jet and diesel fuel compounds from carbohydrates, but until now these processes have suffered from low titres and yields<sup>4–6</sup>.

Here we propose a chemical route to convert fermentation products from a variety of renewable carbohydrate sources into hydrocarbons that can be used for petrol, jet fuel and diesel. Because solventogenic fermentation products have lower carbon numbers than are appropriate for these fuels, coupling chemistry can be used to produce molecules that are larger than these natural fermentation products, ideally achieved by exploiting the functionalities inherent in the starting materials<sup>7–9</sup>. The acetone, n-butanol and ethanol (ABE) mixture produced by *Clostridium acetobutylicum* in a 2.3:3.7:1 molar ratio (3:6:1 mass ratio) provides such a system. *C. acetobutylicum* is able to produce ABE from a variety of sugars and carboxylic acids<sup>10</sup>, providing the flexibility needed to accommodate regionally specific feedstocks. The ABE products harbour both the nucleophilic  $\alpha$ -carbons of the acetone and the electrophilic  $\alpha$ -carbon of the alcohols. These paired functionalities enable us to construct higher alkanes from two-carbon, three-carbon and four-carbon precursors by the alkylation of acetone with the electrophilic alcohols. As shown in Fig. 1, alkylation under suitable conditions results in  $\text{C}_5$ – $\text{C}_{11}$  or longer-chain ketones, which may be

deoxygenated to paraffins. These paraffins, from pentane to undecane, are components of petrol, diesel and jet fuel.

Using a synthetic ABE mixture of pure acetone, n-butanol and ethanol, we investigated the double alkylation of acetone to obtain heptan-4-one (B in Fig. 1) (alkylation with ethanol), nonan-4-one (D) (alkylation with one molecule each of ethanol and butanol) and undecan-6-one (F) (alkylation with butanol) under transition-metal-catalysed conditions (Fig. 1)<sup>11,12</sup>. Two possible side reactions in the transition-metal-catalysed alkylation of acetone with primary alcohols are self-condensation of the alcohol through the corresponding aldehyde (Guerbet reaction)<sup>13</sup> and oligomerization of acetone into diacetone alcohol, mesityl oxide, cyclohexenones and other products<sup>14</sup>. In particular, self-condensation of acetone affects the overall efficiency of the desired process by lowering the ratio of ketone to alcohol in the reaction mixture. Similarly, if too much butanol reacts through the Guerbet pathway then not all of the acetone will be consumed; however, the Guerbet reaction does form higher branched alcohols that could themselves be valuable fuel precursors or be combined with acetone to form up to  $\text{C}_{19}$  ketones (Supplementary Fig. 1). The transition metal and base catalysts should therefore be chosen to minimize these competing processes. As previously observed<sup>15</sup>, we found that solid potassium phosphate tribasic ( $\text{K}_3\text{PO}_4$ ) was the optimal base for the transition-metal-catalysed alkylation of acetone (Supplementary Table 1). Using solid  $\text{K}_3\text{PO}_4$  as a heterogeneous base, we observed only minor amounts of products from acetone condensation (E) and no Guerbet products.

Our tests of different transition-metal catalysts (Ir, Ru, Rh, Pt, Pd and Ni) with  $\text{K}_3\text{PO}_4$  in toluene for the alkylation reaction revealed that palladium was superior to the other metals (Supplementary Table 2)<sup>15</sup>. Further, trials of various palladium precursors showed a marked effect of the precursor on the outcome of the reaction (Supplementary Table 3). Although most of the palladium precursors examined catalysed the alkylation of acetone, Pd/C was significantly more active than the other palladium precursors at  $110^\circ\text{C}$  in toluene.

Increasing the reaction temperature to  $145^\circ\text{C}$  resulted in a minor improvement in the selectivity for doubly alkylated products, but the overall efficiency of the reaction declined with increasing temperature (Fig. 2a). Increasing the amount of base led to a marked improvement in both the selectivity for double alkylation and the overall yield. With 1.28 molar equivalents of  $\text{K}_3\text{PO}_4$  with respect to total alcohols (ethanol and butanol) at  $145^\circ\text{C}$ , an overall 86% molar yield, based on acetone as the limiting reagent, of identified ketone products was obtained (Fig. 2b). We envisaged that tuning the reaction conditions would afford selective monoalkylation of acetone to obtain petrol-range hydrocarbon chains. Consequently, alkylation was examined at various temperatures with only 0.32 molar equivalents of  $\text{K}_3\text{PO}_4$ . Under these conditions, pentan-2-one and heptan-2-one became the major products, with  $\text{C}_5$ – $\text{C}_7$  species accounting for nearly 50% of the overall yield, with respect to acetone as the limiting reagent. The best result

<sup>1</sup>Department of Chemistry, University of California, Berkeley, California 94720, USA. <sup>2</sup>Energy Biosciences Institute, University of California, Berkeley, California 94720, USA. <sup>3</sup>Department of Chemical and Biomolecular Engineering, University of California, Berkeley, California 94720, USA. <sup>4</sup>Chemical Sciences Division, Lawrence Berkeley National Laboratory, 1 Cyclotron Road, Berkeley, California 94720, USA.

\*These authors contributed equally to this work.



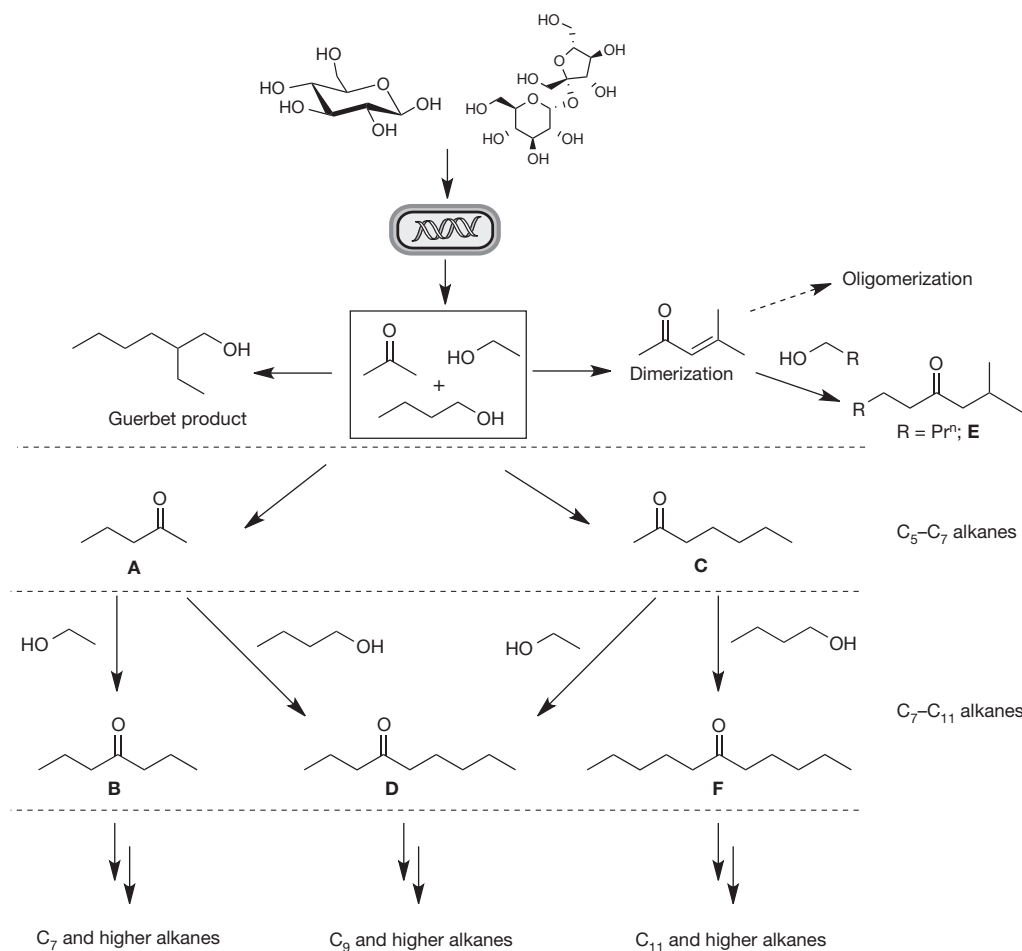


**Figure 1** | A general approach to the transition-metal-catalysed production of biofuels from the ABE fermentation mixture.

was obtained at 145 °C with the production of pentan-2-one and heptan-2-one in 11% and 38% yield, respectively, along with 17% of double-alkylated products.

We explored the mechanism of the reaction by following the reaction progress. As shown in Fig. 2c, monoalkylation of acetone with butanol and ethanol occurred quickly within the first 1.0–1.5 h of the reaction to produce pentan-2-one and heptan-2-one. These species underwent further reaction to form double-alkylated products. No aldehydes were observed during the reaction, suggesting that the aldehyde intermediates were present in very low concentrations and reacted rapidly with acetone and other ketones. Hence, the formation of Guerbet products was minimized, and acetone alkylation predominated.

On the basis of our experiments and previous studies of the alkylation of N-nucleophiles and C-nucleophiles<sup>11,16,17</sup>, we propose a mechanism for the double alkylation of acetone with ethanol and butanol (Fig. 3). The alcohols (butanol and ethanol) are dehydrogenated by the palladium catalyst, generating the reactive aldehydes and hydrogen. At this stage the aldehydes undergo either a self-aldol reaction to form the Guerbet product precursor, or an aldol reaction with acetone. Under the conditions employed here, condensation with acetone seems to be favoured, because acetone is present at much higher concentrations than the transient aldehydes. Subsequent dehydration of the aldol product under the reaction conditions furnishes  $\alpha,\beta$ -unsaturated ketones that undergo palladium-catalysed hydrogenation with the hydrogen generated in the first step. Completing the same cycle with monoalkylated products affords the expected double alkylation products. The relative ease of attack by the unsubstituted versus the substituted  $\alpha$ -carbon of the monoalkylated products leads primarily to

unbranched products. This combination of kinetic controls on the alkylation reaction therefore enables the conversion of a mixture of renewable metabolites into a well-defined range of ketone products.

One important aspect of any catalytic process is the lifetime of the catalyst, which we investigated by adding additional starting material after the reaction had been allowed to proceed to near completion. In a typical experiment using Pd/C and 0.96 molar equivalents of K<sub>3</sub>PO<sub>4</sub> at 145 °C, we added an additional ABE mixture equivalent to the initial charge at 10 and 20 h after the beginning of the reaction and measured the overall yield at 10, 20 and 30 h. In this case, the overall yield based on the total acetone feed for each time point was only slightly decreased: 80% at 10 h, 72% at 20 h, and 61% at 30 h, demonstrating that the catalysts remained active and continued to convert each new amount of starting material. Furthermore, catalytic activity was maintained for 25 h under flow reaction conditions (Supplementary Fig. 4). The catalyst also retained activity in the absence of added solvent, achieving catalytic turnover numbers of more than 3,000 (moles of product per mole of palladium; Supplementary Tables 4 and 6). Although wet organic solvents could be used for the alkylation reaction, no reaction was observed in water. The addition of water was found to slow the overall reaction, resulting in lower double alkylation and overall yields (Supplementary Fig. 2).

To overcome the sensitivity of the catalysts to water, it was of interest to investigate highly selective water-immiscible extractants to remove acetone, n-butanol and ethanol *in situ*. *In situ* removal of the inhibitory product n-butanol during fermentation has been shown to increase solvent titres and yields, decrease distillation costs significantly, and decrease water use and reactor sizes<sup>18–21</sup>. However, the extractants typically employed are only capable of efficiently removing

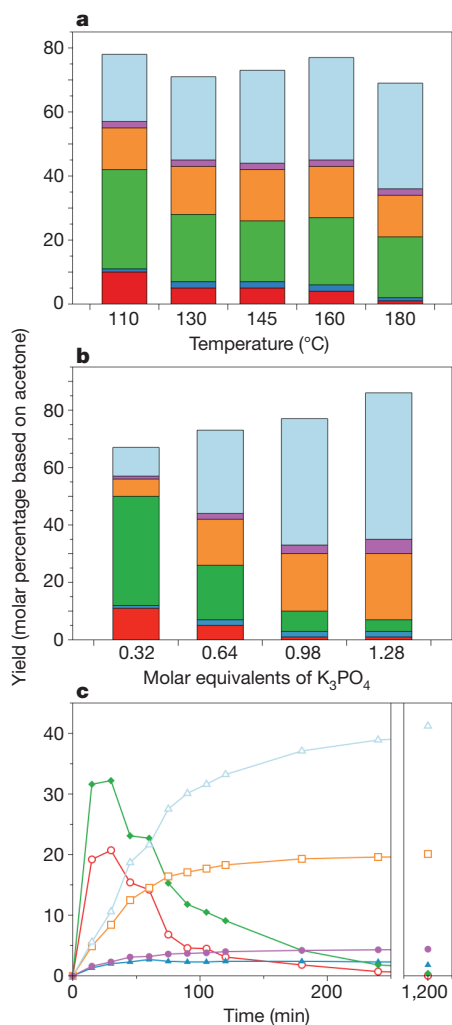


**Figure 2 | Product distribution in Pd-catalysed alkylation as a function of reaction parameters and time course.** **a**, Effects of temperature on product yields and distribution. Red, pentan-2-one; dark blue, heptan-4-one; green, heptan-2-one; orange, nonan-4-one; purple, 2-methylnonan-4-one; light blue, undecan-6-one. Yields based on acetone. Reaction conditions: acetone (2.3 mmol), ethanol (1 mmol), butanol (3.7 mmol), 5% Pd/C (0.01 mmol),  $K_3PO_4$  (3 mmol), toluene (1.5 ml), temperature (x axis), 20 h. **b**, Effect of  $K_3PO_4$  loading on product yields.  $K_3PO_4$  loading is represented as molar equivalents with respect to total alcohol loading (ethanol + butanol). Reaction conditions were identical to the temperature studies with the exception of  $K_3PO_4$  loading (x equivalents) and  $T = 145^\circ C$ . **c**, Time course of product distributions during the palladium-catalysed alkylation reaction. Colours as in **b**. Reaction conditions: acetone (4.6 mmol), ethanol (2 mmol), butanol (7.4 mmol), 5% Pd/C (0.02 mmol),  $K_3PO_4$  (9 mmol), toluene (3 ml),  $145^\circ C$ .

acetone ( $K_d = 1.1$ ) and n-butanol ( $K_d = 2.6$ ) from aqueous solution<sup>22</sup>. Ethanol, however, remains preferentially in the aqueous phase ( $K_d = 0.2$ ). In addition, glyceryl tributyrate efficiently removed several of the inhibitors of biofuel fermentation (for example furfural, *p*-coumaric acid and ferulic acid) found in acid-pretreated lignocellulosic biomass (Supplementary Table 5). This affords the simultaneous removal of residual inhibitors and the desired product during biofuel fermentation, a key advantage over other recovery technologies<sup>23</sup>. Studies of growth inhibition and cell viability with the use of up to 1:1 volume ratios of extractant to media showed glyceryl tributyrate to be non-toxic to *C. acetobutylicum* (data not shown). A 60-h 2-l fermentation of *C. acetobutylicum* on glucose with a 1:1 volume ratio of medium and glyceryl tributyrate produced 40.8 g of solvents with 16.4 g of n-butanol, 3.7 g of acetone and 0.8 g of ethanol, partitioning into the extractant phase (Fig. 4). These solvents were produced from 105 g of glucose and 1.6 g of acetate, achieving an overall ABE weight yield of 90% of the theoretical maximum. Similar results were observed with sucrose, the main carbohydrate of sugar cane, as the primary carbon source (Supplementary Fig. 5).

The *in situ* removal of ABE from the aqueous phase by a high-boiling-point extractant such as glyceryl tributyrate decreases energy requirements for product distillation<sup>24</sup> and allows integration of the biological and catalytic processes. Furthermore, any high-boiling impurities present in the extractant (for example furfural, *p*-coumaric acid or ferulic acid) would remain in the distilled extractant upstream of the catalyst, thus having no effect on catalyst performance. Solvents distilled from the extractant phase of the 2-l fermentation were as reactive as the pure chemicals, achieving an overall molar yield of

n-butanol from the aqueous phase, leaving most of the acetone produced in the aqueous phase. Glyceryl tributyrate was identified as a water-immiscible solvent capable of efficiently recovering both

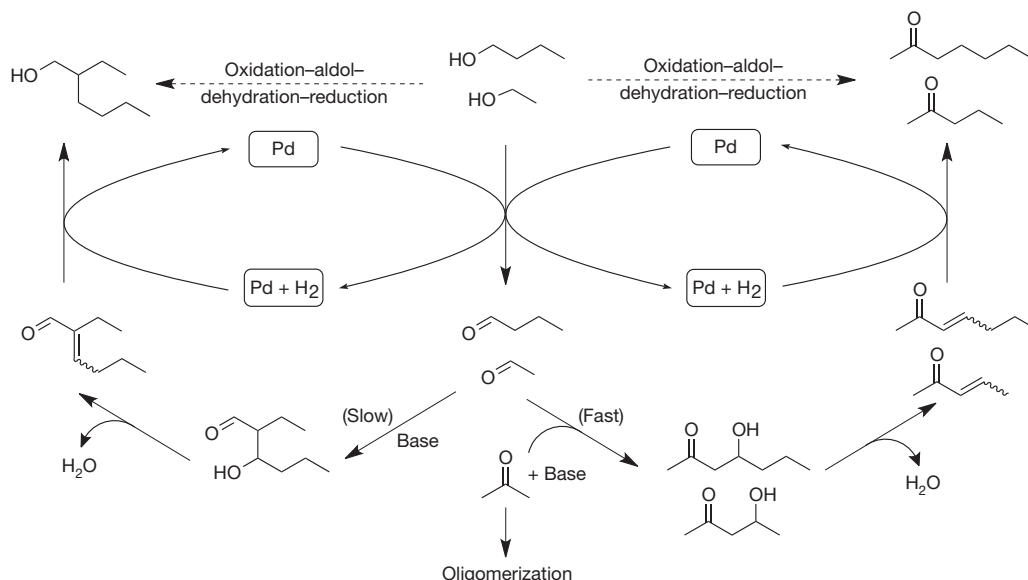


**Figure 3 | Possible mechanism for the palladium-catalysed alkylation of acetone.**



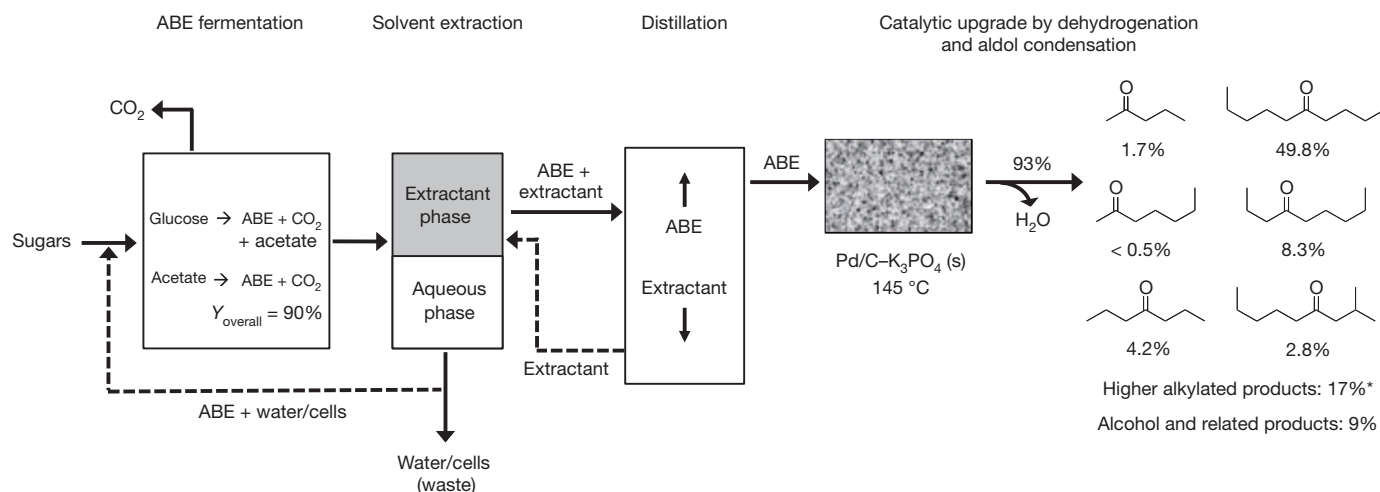


**Figure 4 | Block flow diagram for integration of ABE fermentation with chemical catalysis.** Dashed lines represent proposed recycle streams for continuous operation. The results correspond to a 2-l 60-h fed-batch extractive fermentation with glyceryl tributyrates to produce ABE from glucose. Alkylation reactions were performed on distilled solvents from the extractant phase after

93% and 97% conversion of acetone (Fig. 4). Assuming complete recovery of ABE products from both the extractant and aqueous phases, ~20 g of C<sub>7</sub>–C<sub>15</sub> products would be formed, which represents ~38% of the carbon contained in the glucose feed (Supplementary Table 6). The combined selectivity of the fermentation and the alkylation results in this particularly high-yielding transformation of carbohydrates into fuel ketones. In comparison, a previous study<sup>25</sup> used similar aldol reactions to convert the alcohols and ketones in an aqueous-phase reformat into C<sub>7</sub> and higher species with a carbon yield of 42% from the intermediate oil feed and an overall carbon yield of 21% from the initial sorbitol feed. The lower yield of higher ketones resulted from the non-selective production of oxygenates that could not be upgraded in the aldol reaction. The 38% carbon yield in the present work does not account for the 15.1 g of lower-molecular-mass (C<sub>4</sub>–C<sub>6</sub>) petrol precursors also produced, which would then raise the overall carbon yield to ~58%. Further deoxygenation (Supplementary Fig. 6) of the products obtained from alkylation of the ABE mixture by using standard hydrotreating chemistry<sup>25–27</sup> would yield alkanes compatible with refinery infrastructure and suitable for blending with petrol, diesel and jet fuels.

Using this controlled alkylation of acetone, n-butanol and ethanol, we developed a high-yield method for transforming readily accessible fermentation products from a variety of carbohydrates into precursors for petrol, diesel and jet fuels. By catalytically upgrading low-carbon-number fermentation products we are able to exploit highly efficient metabolic pathways and achieve near theoretical yields<sup>28</sup>. Combined with the near theoretical yields attained during the alkylation reaction these higher-molecular-mass fuel precursors can be produced at relatively high titre. The tunability of this reaction to produce predominantly petrol or jet and diesel blend stocks is a significant advantage over other methods, and aligns well with current refining processes. Although further improvements will be required for commercial implementation, the results demonstrate that *in situ* extraction of the products from the ABE fermentation coupled with catalytic conversion of these products can provide hydrocarbon fuel blend stocks at high yields from biomass. The integration of extractive fermentation with chemical catalysis is thus a novel and potentially enabling route for the economical conversion of biomass into liquid transportation fuels.

## METHODS SUMMARY

**Transition-metal catalysis.** All reactions were performed in closed systems using 12-ml Q-Tubes (pressure tubes) in a parallel optimizer and were analysed by

drying over molecular sieves; they were performed for 20 h in toluene at 145 °C with 1.28 molar equivalents of K<sub>3</sub>PO<sub>4</sub>. Yields are based on acetone. Asterisk, higher alkylated products and alcohol and related product yields were approximated by FID response factor and were assumed to have incorporated a single equivalent of acetone.

gas chromatography–flame ionization detection, with dodecane as an internal standard. Reaction conditions (including temperature, catalyst and base loading) for individual alkylation reactions are described in Supplementary Methods.

**Inhibitor extraction.** Simulated clostridia fermentation medium as described in Supplementary Methods was used to calculate glyceryl tributyrates distribution coefficients. Acid-pretreated lignocellulosic inhibitors were produced from *Miscanthus × giganteus* as described in Supplementary Methods. The liquid hydrolysate was pH adjusted and inhibitor concentrations were analysed by gas chromatography–mass spectrometry.

**Fermentation conditions.** *Clostridium acetobutylicum* ATCC824 was routinely grown in clostridial growth medium (CGM) as described previously<sup>1</sup>. Fed-batch fermentations were conducted in 3-l bioreactors (Bioengineering AG) with a 2-l working volume. Additional glucose and yeast extract were added intermittently to the culture using a concentrated solution of 450 and 50 g l<sup>-1</sup>, respectively. Cultures were grown anaerobically at 37 °C under pH control as described in Supplementary Methods. Sugars and major metabolites were measured in the aqueous phase by high-pressure liquid chromatography as described previously (Supplementary Fig. 5). Acetone, n-butanol and ethanol concentrations in the extractant phase were measured by gas chromatography–flame ionization detection (Supplementary Fig. 5).

Received 9 February; accepted 14 September 2012.

- Alsaker, K. V., Paredes, C. & Papoutsakis, E. T. Metabolite stress and tolerance in the production of biofuels and chemicals: gene-expression-based systems analysis of butanol, butyrate, and acetate stresses in the anaerobe *Clostridium acetobutylicum*. *Biotechnol. Bioeng.* **105**, 1131–1147 (2010).
- Tracy, B. P., Jones, S. W., Fast, A. G., Indurthy, D. C. & Papoutsakis, E. T. Clostridia: the importance of their exceptional substrate and metabolite diversity for biofuel and biorefinery applications. *Curr. Opin. Biotechnol.* **23**, 364–381 (2012).
- Green, E. M. Fermentative production of butanol—the industrial perspective. *Curr. Opin. Biotechnol.* **22**, 337–343 (2011).
- Steen, E. J. *et al.* Microbial production of fatty-acid-derived fuels and chemicals from plant biomass. *Nature* **463**, 559–562 (2010).
- Wang, C. *et al.* Metabolic engineering of *Escherichia coli* for  $\alpha$ -farnesene production. *Metab. Eng.* **13**, 648–655 (2011).
- Peralta-Yahya, P. P. *et al.* Identification and microbial production of a terpene-based advanced biofuel. *Nature Commun.* **2**, 483 (2011).
- Blommel, P. G., Keenan, G. R., Rozmiarek, R. T. & Cortright, R. D. Catalytic conversion of sugar into conventional gasoline, diesel, jet fuel, and other hydrocarbons. *Int. Sugar J.* **110**, 672–679 (2008).
- Corma, A., de la Torre, O., Renz, M. & Vollandier, N. Production of high-quality diesel from biomass waste products. *Angew. Chem. Int. Ed.* **50**, 2375–2378 (2011).
- Huber, G. W., Chheda, J. N., Barrett, C. J. & Dumesic, J. A. Production of liquid alkanes by aqueous-phase processing of biomass-derived carbohydrates. *Science* **308**, 1446–1450 (2005).
- Ren, C. *et al.* Identification and inactivation of pleiotropic regulator CcpA to eliminate glucose repression of xylose utilization in *Clostridium acetobutylicum*. *Metab. Eng.* **12**, 446–454 (2010).

11. Guillena, G., Ramón, D. J. & Yus, M. Alcohols as electrophiles in C–C bond-forming reactions: the hydrogen autotransfer process. *Angew. Chem. Int. Ed.* **46**, 2358–2364 (2007).
12. Hamid, M. H. S. A., Slatford, P. & Williams, J. M. J. Borrowing hydrogen in the activation of alcohols. *Adv. Synth. Catal.* **349**, 1555–1575 (2007).
13. Carlini, C., Macinai, A., Raspolli Galletti, A. M. & Sbrana, G. Selective synthesis of 2-ethyl-1-hexanol from n-butanol through the Guerbet reaction by using bifunctional catalysts based on copper or palladium precursors and sodium butoxide. *J. Mol. Catal. Chem.* **212**, 65–70 (2004).
14. Salvapati, G. S., Ramanamurty, K. V. & Janardana Rao, M. Selective catalytic self-condensation of acetone. *J. Mol. Catal.* **54**, 9–30 (1989).
15. Kwon, M. S. *et al.* Recyclable palladium catalyst for highly selective  $\alpha$  alkylation of ketones with alcohols. *Angew. Chem. Int. Ed.* **44**, 6913–6915 (2005).
16. Guillena, G., Ramón, J. D. & Yus, M. Hydrogen autotransfer in the N-alkylation of amines and related compounds using alcohols and amines as electrophiles. *Chem. Rev.* **110**, 1611–1641 (2010).
17. Dobereiner, G. E. & Crabtree, R. H. Dehydrogenation as a substrate-activating strategy in homogeneous transition-metal catalysis. *Chem. Rev.* **110**, 681–703 (2010).
18. Wayman, M. & Parekh, R. Production of acetone-butanol by extractive fermentation using dibutylphthalate as extractant. *J. Ferment. Technol.* **65**, 295–300 (1987).
19. Roffler, S. R., Blanch, H. W. & Wilke, C. R. In-situ recovery of butanol during fermentation. Part 2: fed-batch extractive fermentation. *Bioprocess Engng* **2**, 181–190 (1987).
20. Roffler, S. R., Blanch, H. W. & Wilke, C. R. In-situ recovery of butanol during fermentation. Part 1: batch extractive fermentation. *Bioprocess Engng* **2**, 1–12 (1987).
21. Roffler, S. R., Blanch, H. W. & Wilke, C. R. In situ extractive fermentation of acetone and butanol. *Biotechnol. Bioeng.* **31**, 135–143 (1988).
22. Jeon, Y. J. & Lee, Y. Y. Membrane-assisted extractive butanol fermentation. *Ann. NY Acad. Sci.* **506**, 536–542 (1987).
23. Vane, L. M. Separation technologies for the recovery and dehydration of alcohols from fermentation broths. *Biofuels Bioprod. Biorefining* **2**, 553–588 (2008).
24. Kraemer, K., Harwardt, A., Bronneberg, R. & Marquardt, W. Separation of butanol from acetone–butanol–ethanol fermentation by a hybrid extraction–distillation process. *Comput. Chem. Eng.* **35**, 949–963 (2011).
25. Gürbüz, E. I., Kunkes, E. L. & Dumesic, J. A. Dual-bed catalyst system for C–C coupling of biomass-derived oxygenated hydrocarbons to fuel-grade compounds. *Green Chem.* **12**, 223–227 (2010).
26. Kunkes, E. L. *et al.* Catalytic conversion of biomass to monofunctional hydrocarbons and targeted liquid-fuel classes. *Science* **322**, 417–421 (2008).
27. Xing, R. *et al.* Production of jet and diesel fuel range alkanes from waste hemicellulose-derived aqueous solutions. *Green Chem.* **12**, 1933–1946 (2010).
28. Dugar, D. & Stephanopoulos, G. Relative potential of biosynthetic pathways for biofuels and bio-based products. *Nature Biotechnol.* **29**, 1074–1078 (2011).

**Supplementary Information** is available in the online version of the paper.

**Acknowledgements** We are grateful to H.-J. Song for performing initial experiments on the catalytic alkylation of acetone, and V. Mitchell for analysing acid pretreatment hydrolysate inhibitors present in *Miscanthus giganteus*. F.D.T. and E.G. acknowledge funding from the Director, Office of Science of the US Department of Energy, under contract no. DE-AC02-05CH11231. This work was funded by the Energy Biosciences Institute.

**Author Contributions** Z.C.B. and P.A. contributed equally to this work. P.A. and S.S. performed experiments on the chemical catalysts, and E.G. performed experiments in the flow reactor. Z.C.B. optimized the fermentation and extractive processes. All authors contributed to the conception of the experiments, discussion of the results and preparation of manuscript.

**Author Information** Reprints and permissions information is available at [www.nature.com/reprints](http://www.nature.com/reprints). The authors declare no competing financial interests. Readers are welcome to comment on the online version of the paper. Correspondence and requests for materials should be addressed to F.D.T. ([fdtoste@berkeley.edu](mailto:fdtoste@berkeley.edu)).

# Greenland ice-sheet contribution to sea-level rise buffered by meltwater storage in firn

J. Harper<sup>1</sup>, N. Humphrey<sup>2</sup>, W. T. Pfeffer<sup>3</sup>, J. Brown<sup>1</sup> & X. Fettweis<sup>4</sup>

Surface melt on the Greenland ice sheet has shown increasing trends in areal extent and duration since the beginning of the satellite era<sup>1–3</sup>. Records for melt were broken in 2005<sup>4</sup>, 2007<sup>5</sup>, 2010<sup>6</sup> and 2012<sup>7</sup>. Much of the increased surface melt is occurring in the percolation zone, a region of the accumulation area that is perennially covered by snow and firn (partly compacted snow). The fate of melt water in the percolation zone is poorly constrained: some may travel away from its point of origin and eventually influence the ice sheet's flow dynamics and mass balance and the global sea level, whereas some may simply infiltrate into cold snow or firn and refreeze with none of these effects. Here we quantify the existing water storage capacity of the percolation zone of the Greenland ice sheet and show the potential for hundreds of gigatonnes of meltwater storage. We collected *in situ* observations of firn structure and meltwater retention along a roughly 85-kilometre-long transect of the melting accumulation area. Our data show that repeated infiltration events in which melt water penetrates deeply (more than 10 metres) eventually fill all pore space with water. As future surface melt intensifies under Arctic warming, a fraction of melt water that would otherwise contribute to sea-level rise will fill existing pore space of the percolation zone. We estimate the lower and upper bounds of this storage sink to be  $322 \pm 44$  gigatonnes and  $1,289^{+388}_{-252}$  gigatonnes, respectively. Furthermore, we find that decades are required to fill this pore space under a range of plausible future climate conditions. Hence, routing of surface melt water into filling the pore space of the firn column will delay expansion of the area contributing to sea-level rise, although once the pore space is filled it cannot quickly be regenerated.

The annual mass loss of the Greenland ice sheet (GIS) is estimated to be due evenly to tidewater calving and surface ablation processes<sup>8</sup>. Future changes in calving are highly uncertain, but confidence is high that ongoing Arctic warming will promote increases in the GIS's surface melt<sup>9,10</sup>. The consequences of higher melt on the ice sheet's mass budget and global sea level, however, depend on the fraction of melt water that actually escapes to the ocean<sup>4,11,12</sup>. Melt water has been observed to infiltrate vertically and heterogeneously through multiyear accumulations of snow and firn<sup>13–15</sup>, although it remains unclear how structural changes brought about by refreezing influence large-scale downslope transport of water and run-off. On the gently sloping flanks of the GIS, near-surface ice layers formed by refrozen melt water that has infiltrated could form an impermeable barrier that would conduct subsequent melt water laterally downslope. A warming climate could thus lead to rapid inland migration of hydrologic conditions allowing run-off, expanding the area of the ice sheet contributing to mass loss, with a simultaneous increase in melt<sup>4,11,12</sup>. Alternatively, if future melt water infiltrates deeply into firn on a widespread basis, the largely unknown storage capacity of the existing ice-laden firn structure at depth may absorb a considerable amount of water before hydrologic structures permitting run-off develop. Because observations are lacking and models for simulating surface mass balance do not include heterogeneous vertical infiltration and development of complex firn

structure<sup>16</sup>, infiltration processes represent a large uncertainty in current projections of mass balance and sea level.

To address this problem, we performed an intensive field study along the EGIG line<sup>17</sup> on the western flank of the GIS. We collected data during the 2007–2009 melt seasons along a ~85-km transect that is located above the equilibrium line and spans most of the accumulation zone experiencing substantial summer melt (Fig. 1). At fifteen study sites spaced 5–10 km apart, we collected firn temperatures, ice cores and data from ground-penetrating radar. Along this transect, the mean number of melt days observed by satellite ranges from 70 at an elevation of 1,180 m to 13 at 2,000 m (ref. 18). Winter snow accumulation is roughly 0.5 m water equivalent<sup>19–21</sup>, and the annual mass budget varies over the transect primarily as a result of the strong melt gradient.

Field measurements along this transect reveal deep infiltration events over a 2-yr interval<sup>22</sup>. Thermistor strings installed in boreholes show numerous transient heating events occurring to >10-m depth, caused by freezing of liquid water. Three-dimensional radar surveys document discontinuities in ice layers >0.5 m thick<sup>23</sup>, implying that thick ice layers merely divert water short horizontal distances before it resumes downward motion. Hence, refreezing events occur deep in the firn column, below many years of accumulation and even beneath decimetre-thick ice layers. In this Letter, additional field observations reveal the effect of the infiltration events on the structure of the firn column. We quantify the elevation gradient of firn density and stratigraphy with 34 ice cores<sup>24</sup> and geophysical inversions of radar velocities collected at each of the study sites<sup>25</sup>. The core data provide high-resolution (1 cm in the vertical direction) observations of the upper 10 m of firn, and lower-resolution (1–10 m vertical) radar observations extend to ~80-m depth.

The ice content of the firn column shows strong elevation dependency (Fig. 2). Infiltration and refreezing events fill available pore space in the firn column with ice, thereby reducing remaining pore space and intrinsic permeability. At an elevation of 2,000 m, ice layers are ~1 cm thick and are relatively rare. As firn density increases with depth, it reaches pore close-off density ( $830 \text{ kg m}^{-3}$ ) at a depth of 58 m. Mid way across the transect, at an elevation of 1,680 m, well-developed ice layers exceed 1 m in thickness and pore close-off density occurs at a depth of 25 m. Near the bottom of the transect, solid ice occurs immediately below the recent winter snowfall, creating an impermeable substrate. These observations of the physical structure of the percolation zone are supported by detailed measurements of the thermal structure<sup>22</sup> of this area. Our field measurements indicate that although deep heterogeneous infiltration occurs as isolated local events, numerous events repeated over time fill underlying pore space with ice. With decreasing elevation, infiltration events are greater in magnitude and are more frequent, and the firn has a longer history of events as it moves downslope by ice motion.

Our ice-core and radar data enable us to quantify the mass of water per unit area needed to fill open pore space, which we term firn 'capacity' (Methods Summary). At an elevation of 2,000 m, accumulated capacity increases with depth until the firn reaches close-off density

<sup>1</sup>Geosciences, University of Montana, Missoula, Montana 59812, USA. <sup>2</sup>Geology and Geophysics, University of Wyoming, Laramie, Wyoming 82071, USA. <sup>3</sup>Institute of Arctic and Alpine Research, University of Colorado, Boulder, Colorado 80309, USA. <sup>4</sup>Géographie, Université de Liège, Liège B11-4000, Belgium.



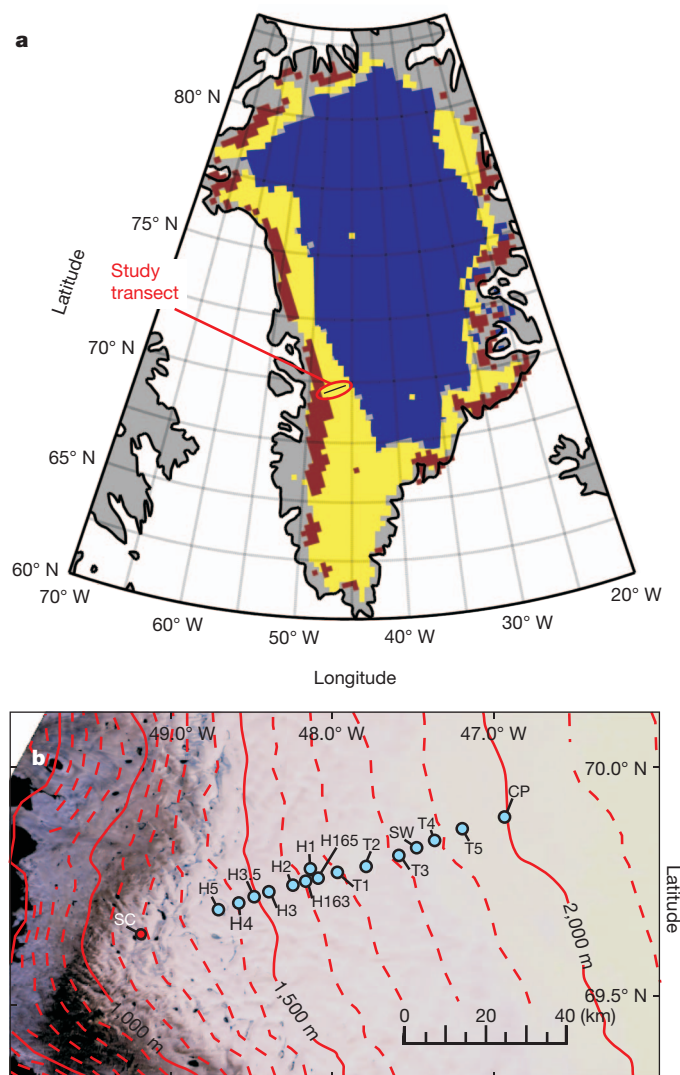


**Figure 1 | Greenland melt and study location.** **a**, Map of Greenland showing satellite backscatter measurements of melt in 2007<sup>18</sup> delineating dry snow (blue), areas receiving at least one day of surface melt (yellow) and areas that have modelled negative surface mass<sup>29</sup> balance in 2007 and are therefore below the equilibrium line (red). **b**, Study transect and intensive study sites plotted on an image from NASA's Advanced Spaceborne Thermal Emission and Reflection Radiometer. The contours show elevation.

(Fig. 3). Here the observed capacity profile resembles a modelled profile (Supplementary Fig. 5) assuming dry-firm compaction<sup>26</sup> despite there being up to 30 melt days<sup>18</sup> in some years. Hence, 2,000 m is the lowest elevation along our transect at which the firm capacity profile is effectively unreduced by prior meltwater infiltration and refreezing. At lower (warmer) elevations, the firm capacity is lower than the dry-firm value because some fraction of the pore space has already been filled by water or infiltration ice. At the lowest elevations, the capacity at the start of a melt season is limited to only the prior winter's snowfall because all underlying pore space has already been filled. Our transect therefore spans the portion of Greenland's firm altered by melt water, that is, the percolation zone. Because the percolation zone is already in transition to conditions permitting run-off, near-future sea-level rise associated with increased melt in the accumulation zone hinges on the structure and processes in this zone.

To estimate how much water the firm column can actually absorb, we consider upper and lower bounds on retention. Our use of 'retention' does not distinguish between water stored in liquid or frozen form. The minimum bound is set by our core data, and is based on

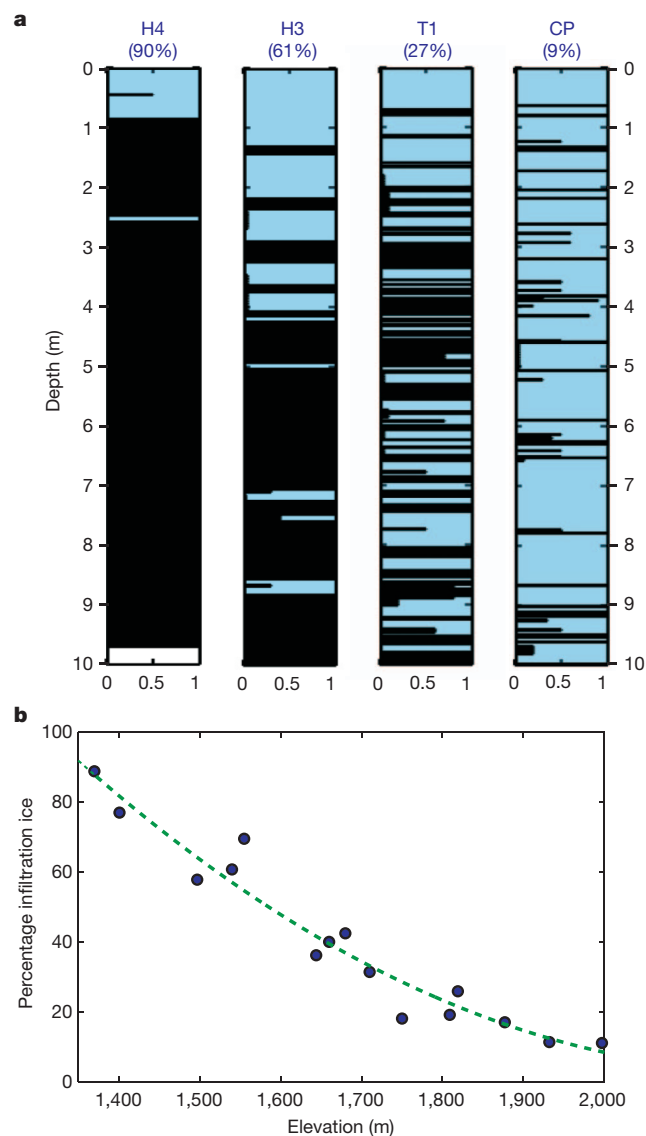


**Figure 2 | Firn-ice content.** **a**, Simplified stratigraphic columns from ice cores showing infiltration ice layers (black) and firn with open pore space (blue). The bottom axis indicates proportion of core occupied by ice. Core locations increase in elevation from left to right (1,401, 1,540, 1,710 and 1,997 m) and are shown in Fig. 1. **b**, Percentage of 10-m cores occupied by infiltration ice at each site along study transect (blue circles). The green line is a second-order polynomial fit to the data with a coefficient of determination of 0.94 and root mean square error of 6.5.

the assumption that all firn capacity in the upper 10 m is filled with infiltration ice. The high resolution of our ice-core measurements give confidence that at least this condition is satisfied (Fig. 2a); however, it is clear from our data that a substantial fraction of melt water is actually retained at depths of >10 m, and so this estimate produces a certain lower bound. The maximum-retention bound is set by our radar data, and is based on the assumption that all existing firn capacity is filled down to the pore close-off depth. Our radar measurements support this assumption, but confidence is lower owing to the poorer resolution of those data. Nevertheless, because we have observed substantial refreezing events at depths of >10 m, we see no reason why water should not penetrate through all open and connected pore space.

The quantity of water required to fill pore space, expressed as an equivalent layer thickness, increases with elevation to a maximum of ~4–10 m, depending on the scenario (Fig. 3c). Integration of a power-law fit to these data yields an estimate of the total fill capacity of the percolation zone. The capacity is primarily a function of the ratio of

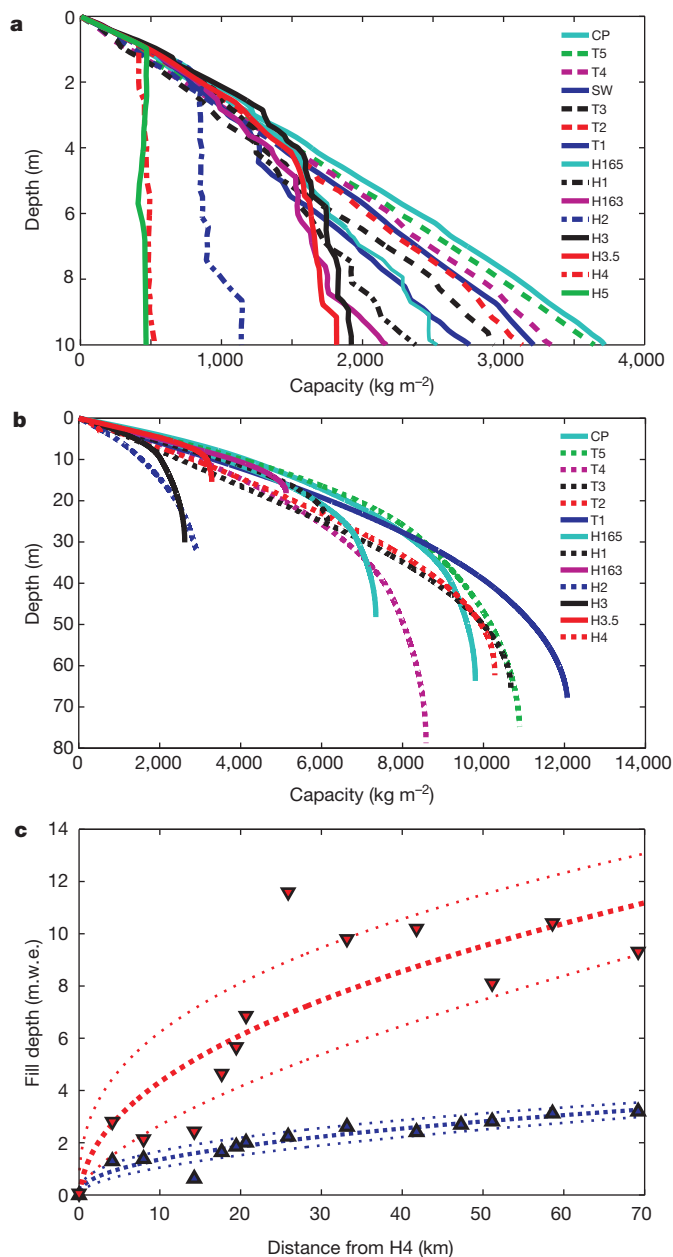


**Figure 3 | Capacity and fill depth at sites along study transect.** **a**, Measured capacity versus depth from ice cores at 15 locations shown in Fig. 1. **b**, Measured capacity versus depth from 13 radar inversions. **c**, Total fill depth for the minimum (blue triangles) and maximum (red triangles) retention bounds. The dashed lines are fits to the data (thick) and the associated uncertainties (curve fits to 1 s.d. of the residuals, thin). m.w.e., metres water equivalent.

accumulation and melt rates over time, with greater pore space generated by higher accumulation for a given melt rate. Our transect is probably representative of much of the ice sheet where the percolation zone undergoes transition from the equilibrium line to the dry-snow zone following topography, but it remains unclear how representative it is of portions of southern Greenland where both accumulation and melt rates are higher. Extending our results to the area of Greenland located between bare ice and the upper extent of melt (Supplementary Information) yields estimates of the storable water mass of the entire percolation zone:  $322 \pm 44$  Gt as a lower bound and  $1,289^{+388}_{-252}$  Gt as an upper bound. Our error bounds are curve fits to one standard deviation of the residuals. This is a first estimate of initial conditions of the percolation zone, which dictate the rate at which ablation-zone conditions can propagate upward in elevation.

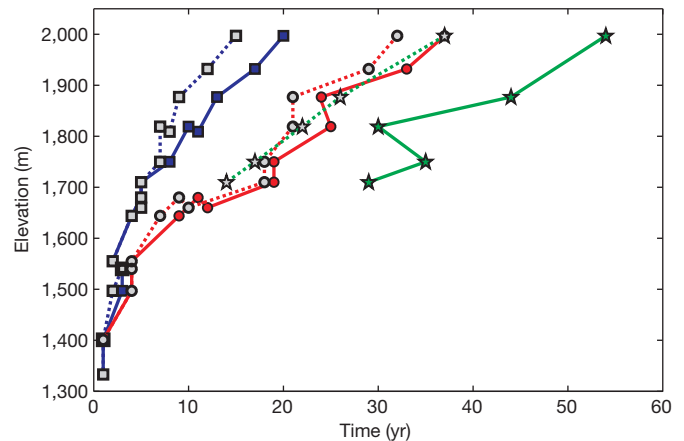


**Figure 4 | Pore space fill time under various future climate scenarios.** Both the minimum retention bound (grey markers and dashed lines) and the maximum retention bound (coloured markers and solid lines) are shown. A surface mass-balance model driven by a regional climate model is used to calculate fill times, under climate scenarios RCP4.5 (squares) and RCP8.5 (circles). Also shown is a scenario based on forward projection of *in situ* observations of refreezing in 2007 (stars).

Future filling in of percolation-zone pore space depends upon rates of melt, rainfall and firn compaction and on pore space additions from snowfall. A high degree of uncertainty surrounds the details of future climate and the feedbacks with the heat and mass balances of the GIS. We therefore explore potential fill-in times using a range of different climate forcing scenarios, including a regional climate model and a projection of *in situ* observations (Supplementary Information). The most high-magnitude climate-change case, normally considered extreme, results in the entire transect filling in in 15 yr (minimum bound) or 20 yr (maximum bound) (Fig. 4). Fill-in times in all other cases exceed three decades, meaning that this much time is required to develop full ablation-zone runoff conditions. These results demonstrate how important heterogeneous infiltration processes and the initial conditions of the percolation zone are to sea-level rise in upcoming decades. Melt is spreading into the dry-snow zone and the percolation zone is spreading upwards, but the present conditions of the percolation zone have an important role in capturing melt water and, therefore, in the response of the GIS to increased melt in upcoming decades.

Our results quantify the infiltration hurdle that will delay the sea-level response of the GIS to increasing surface melt in the accumulation zone. Climate warming and concomitant surface melt can migrate up the ice sheet faster than run-off; there will probably be a lag of decades before run-off conditions extend through the present percolation zone. The propagation of wet basal conditions towards the interior of the ice sheet as a result of surface melt is also delayed, because the firn slows the formation of catchments feeding moulins. This is relevant to projections of the acceleration of ice dynamics and sea-level rise<sup>27</sup>. Importantly, increased run-off from the ablation area can offset increased meltwater storage in firn; how much the melt can increase from the relatively small bare-ice areas (Fig. 1) in the upcoming decades is therefore an important question. Although our results demonstrate that the deep pore space of the percolation zone acts as a buffer between climate warming and sea-level response, other mechanisms may continue to accelerate mass loss from Greenland. Furthermore, once the present-day firn column is filled with melt water, regenerating it requires many decades (at least) because this can only be done in relatively small annual increments.

## METHODS SUMMARY

We used ice cores to determine that the average density of discrete layers of ice formed by infiltration and refreezing is  $843 \text{ kg m}^{-3}$ , with a relatively small standard

deviation of  $36 \text{ kg m}^{-3}$ . To calculate firn capacity, we first computed the 'load' profile of the firn column<sup>13</sup> by integrating firn density (from ice cores and radar data) with respect to depth (Supplementary Fig. 3). We then calculated the integral of the difference between the observed load profile and a hypothetical load profile representing complete conversion to infiltration ice. This is the 'ice capacity', or the maximum amount of melt water that could possibly be accommodated as infiltration ice by the firn. The firn capacity,  $C(z)$ , is thus defined by

$$C(z) = \int_0^z (\rho(\xi) - \rho_{ii}(\xi)) d\xi$$

where  $\rho$  is the firn density and  $\rho_{ii}$  is the infiltration ice density.

To calculate future filling in of pore space, we reduced pore space at yearly time steps to account for refreezing of surface melt and rain (if present). The compaction over time of new pore space added from snowfall and existing firn was calculated using a firn densification model. We calculated the time until the minimum and maximum retention bounds were satisfied, on the basis of two future scenarios for pore filling, one based on climate modelling and one based on projection of *in situ* observations. The first scenario includes two cases from the regional climate/mass-balance model MAR<sup>28</sup>, one in which there is a mid-range change in climate conditions (RCP4.5) and one in which there is a large change in climate (RCP8.5). These model runs are forced by the CMIP5 global circulation model CanESM2. The second scenario is based on forward projection of *in situ* observations of refreezing made at five sites during the record melt year of 2007.

Received 23 April; accepted 31 August 2012.

- Mote, T. L. Greenland surface melt trends 1973–2007: evidence of a large increase in 2007. *Geophys. Res. Lett.* **34**, L22507 (2007).
- Tedesco, M. Snowmelt detection over the Greenland ice sheet from SSM/I brightness temperature daily variations. *Geophys. Res. Lett.* **34**, L02504 (2007).
- Fettweis, X., Tedesco, M., van den Broeke, M. & Ettema, J. Melting trends over the Greenland ice sheet (1958–2009) from spaceborne microwave data and regional climate models. *Cryosphere* **5**, 359–375 (2011).
- Hanna, E. *et al.* Increased runoff from melt from the Greenland Ice Sheet: a response to global warming. *J. Clim.* **21**, 331–341 (2008).
- Tedesco, M. A new record in 2007 for melting in Greenland. *Eos Trans. AGU* **88**, 383 (2007).
- Box, J. E. *et al.* in *State of the Climate in 2010* (eds Blunden, J., Arndt, D. S. & Baringer, M. O.) 156–160 (AMS, 2011).
- Cole, S. *Satellites See Unprecedented Greenland Ice Sheet Surface Melt*. NASA News Release 12–249 (2012).
- van Den Broeke, M. *et al.* Partitioning recent Greenland mass loss. *Science* **326**, 984–986 (2009).
- Huybrechts, P. *et al.* Response of the Greenland and Antarctic Ice Sheets to multi-millennial greenhouse warming in the earth system model of intermediate complexity LOVECLIM. *Surv. Geophys.* **32**, 397–416 (2011).
- Vizcaino, M., Mikolajewicz, U., Jungclaus, J. & Schurgers, G. Climate modification by future ice sheet changes and consequences for ice sheet mass balance. *Clim. Dyn.* **34**, 301–324 (2010).
- Pfeffer, W. T., Meier, M. F. & Illangasekare, T. H. Retention of Greenland runoff by refreezing: implications for projected future sea level change. *J. Geophys. Res.* **96**, 22117–22124 (1991).
- Janssens, I. & Huybrechts, P. The treatment of meltwater retention in mass-balance parameterizations of the Greenland ice sheet. *Ann. Glaciol.* **31**, 133–140 (2000).
- Braithwaite, R. J., Laternser, M. & Pfeffer, W. T. Variations of near-surface firn density in the lower accumulation area of the Greenland ice sheet, Pákitsoq, West Greenland. *J. Glaciol.* **40**, 477–485 (1994).
- Müller, F. Zonation in the accumulation area of the glaciers of Axel Heiberg Island, NWT, Canada. *J. Glaciol.* **4**, 302–313 (1962).
- Marsh, P. & Woo, M. K. Wetting front advance and freezing of meltwater within a snow cover: 1. Observations in the Canadian Arctic. *Wat. Resour. Res.* **20**, 1853–1864 (1984).
- Reijmer, C., van den Broeke, M., Fettweis, X., Ettema, J. & Stap, L. Refreezing on the Greenland ice sheet: a comparison of parameterizations. *Cryosphere* **6**, 743–762 (2012).
- Fischer, H., Wagenbach, D., Laternser, M. & Haeberli, W. Glacio-meteorological and isotopic studies along the EGIS line, central Greenland. *J. Glaciol.* **41**, 515–527 (1995).
- Abdalati, W. & Steffen, K. Greenland ice sheet melt extent: 1979–1999. *J. Geophys. Res.* **106**, 33983–33988 (2001).
- Bales, R. C., McConnell, J. R., Mosley-Thompson, E. & Csatho, B. Accumulation over the Greenland ice sheet from historical and recent records. *J. Geophys. Res.* **106**, 33813–33825 (2001).
- Burgess, E. W. *et al.* A spatially calibrated model of annual accumulation rate on the Greenland Ice Sheet (1958–2007). *J. Geophys. Res.* **115**, F02004 (2010).
- McConnell, J. R., Mosley-Thompson, E., Bromwich, D. H., Bales, R. C. & Kyne, J. D. Interannual variations of snow accumulation on the Greenland Ice Sheet (1985–1996): new observations versus model predictions. *J. Geophys. Res.* **105**, 4039–4046 (2000).
- Humphrey, N. F., Harper, J. T. & Pfeffer, W. T. Thermal tracking of meltwater retention in Greenland's accumulation area. *J. Geophys. Res.* **117**, F01010 (2012).
- Brown, J., Harper, J., Pfeffer, W. T., Humphrey, N. & Bradford, J. High-resolution study of layering within the percolation and soaked facies of the Greenland ice sheet. *Ann. Glaciol.* **52**, 35–42 (2011).
- Harper, J. T., Humphrey, N. F., Pfeffer, W. T. & Brown, J. Firn stratigraphy and temperature to 10 m depth in the percolation zone of Western Greenland, 2007–2009. *INSTAAR Occas. Pap.* 60 (2011).
- Brown, J. *et al.* Georadar-derived estimates of firn density in the percolation zone, western Greenland ice sheet. *J. Geophys. Res.* **117**, F01011 (2012).
- Herron, M. M. & Langway, C. C. Jr. Firn densification: an empirical model. *J. Glaciol.* **25**, 373–385 (1980).
- Alley, R. B., Clark, P. U., Huybrechts, P. & Joughin, I. Ice-sheet and sea-level changes. *Science* **310**, 456–460 (2005).
- Fettweis, X., Belleflamme, A., Erpicum, M., Franco, B. & Nicolay, S. in *Climate Change – Geophysical Foundations and Ecological Effects* (eds Blanco, J. & Kheradmand, H.) 503–520 (Intech, 2011).
- Box, J. E., Bromwich, D. H. & Bai, L. S. Greenland ice sheet surface mass balance 1991–2000: application of Polar MM5 mesoscale model and *in situ* data. *J. Geophys. Res.* **109**, D16105 (2004).

Supplementary Information is available in the online version of the paper.

**Acknowledgements** This work was funded by the US National Science Foundation Office of Polar Programs, Arctic Natural Sciences with grants to J.H. (0612506), N.H. (0612374) and W.T.P. (0612351).

**Author Contributions** J.H. led the analysis, N.H. led the thermal measurements, W.T.P. led the ice-core measurements, J.B. led the radar measurements and X.F. downscaled MAR model output to the study transect. J.H., W.T.P., N.H. and J.B. contributed to the preparation of the manuscript.

**Author Information** Reprints and permissions information is available at [www.nature.com/reprints](http://www.nature.com/reprints). The authors declare no competing financial interests. Readers are welcome to comment on the online version of the paper. Correspondence and requests for materials should be addressed to J.H. (joel@mso.umt.edu).



# Mechanisms for oscillatory true polar wander

J. R. Creveling<sup>1</sup>, J. X. Mitrovica<sup>1</sup>, N.-H. Chan<sup>1</sup>, K. Latychev<sup>2</sup> & I. Matsuyama<sup>3</sup>

Palaeomagnetic studies<sup>1–5</sup> of Palaeoproterozoic to Cretaceous rocks propose a suite of large and relatively rapid (tens of degrees over 10 to 100 million years) excursions of the rotation pole relative to the surface geography, or true polar wander (TPW). These excursions may be linked in an oscillatory, approximately coaxial succession about the centre of the contemporaneous supercontinent<sup>5–7</sup>. Within the framework of a standard rotational theory<sup>8,9</sup>, in which a delayed viscous adjustment of the rotational bulge acts to stabilize the rotation axis<sup>10</sup>, geodynamic models for oscillatory TPW generally appeal to consecutive, opposite loading phases of comparable magnitude<sup>6,11,12</sup>. Here we extend a nonlinear rotational stability theory<sup>10</sup> to incorporate the stabilizing effect of TPW-induced elastic stresses in the lithosphere<sup>13,14</sup>. We demonstrate that convectively driven inertia perturbations acting on a nearly prolate, non-hydrostatic Earth<sup>6,7</sup> with an effective elastic lithospheric thickness of about 10 kilometres yield oscillatory TPW paths consistent with palaeomagnetic inferences. This estimate of elastic thickness can be reduced, even to zero, if the rotation axis is stabilized by long-term excess ellipticity in the plane of the TPW. We speculate that these sources of stabilization, acting on TPW driven

by a time-varying mantle flow field<sup>11,12,15–18</sup>, provide a mechanism for linking the distinct, oscillatory TPW events of the past few billion years.

Palaeomagnetic inferences of TPW are complicated by the difficulty of disentangling polar motion and continental drift. However, independent inferences of five distinct episodes of large-amplitude TPW spanning the Palaeoproterozoic to the Cretaceous<sup>1–5</sup> (Fig. 1a; see Supplementary Information) suggest a marked tendency for pseudo-oscillatory reorientation of the rotation axis<sup>6,7</sup>. Rotational stability is established, in part, by the non-hydrostatic figure of the Earth, that is, the figure after correction for the equilibrium hydrostatic form. The Earth's present-day triaxial figure<sup>9</sup> (Fig. 1b) is driven by mantle convection associated with large thermochemical anomalies or 'super-swells' beneath southern Africa and the Pacific Ocean and the circum-Pacific ring of subduction<sup>19,20</sup>. The minimum axis of inertia aligns with the superswells and the difference between the maximum and intermediate moments of inertia is about half the difference between the maximum and minimum moments:  $I_{\max} - I_{\text{int}} \approx \frac{1}{2}(I_{\max} - I_{\min})$ . Thus, mantle convection currently drives significant excess ellipticity along both equatorial axes, stabilizing the rotation

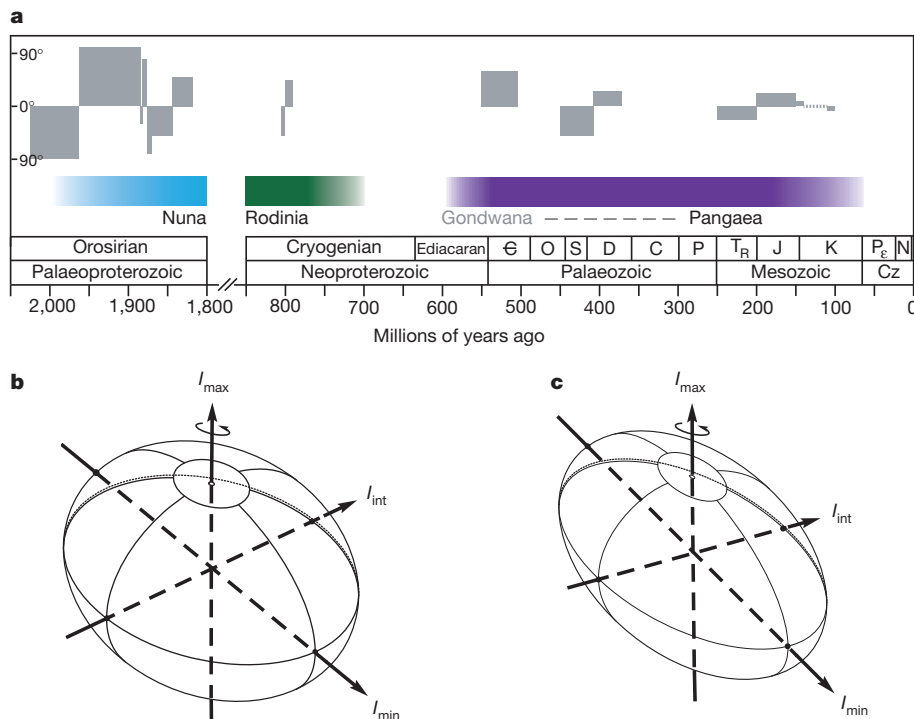


**Figure 1 | TPW, supercontinent phases and the Earth's figure.** **a**, Time line (in millions of years ago) for palaeomagnetically inferred TPW events<sup>1–5,26</sup> (shaded grey boxes) through the Proterozoic and Phanerozoic eons, together with the associated history of supercontinent aggregation, stability, and disaggregation. The Gondwanan superterrane is shown as a precursor to Pangaea. If the grey box is plotted rising above (below) 0°, the pole moved

clockwise (counterclockwise) relative to an observer on the contemporaneous supercontinent or superterrane. The abbreviations listing Phanerozoic periods represent, from left to right, the Cambrian, Ordovician, Silurian, Devonian, Carboniferous, Permian, Triassic, Jurassic, Cretaceous, Palaeogene, and Neogene. Cz, Cenozoic. **b**, **c**, Schematic illustration of Earth models with a triaxial (**b**) or nearly prolate (**c**) non-hydrostatic figure.

<sup>1</sup>Department of Earth and Planetary Sciences, Harvard University, 20 Oxford Street, Cambridge, Massachusetts 02138, USA. <sup>2</sup>Department of Physics, University of Toronto, Toronto M5S 1A7, Canada. <sup>3</sup>Department of Planetary Sciences, Lunar and Planetary Laboratory, University of Arizona, Tucson, Arizona 85721, USA.

pole<sup>9</sup>. This stabilization may explain the more muted TPW in the last hundred million years (100 Myr)<sup>5,6,9,12,20,21</sup> (Fig. 1a). However, superswells are dynamic structures<sup>18,22,23</sup> subject to long-timescale doming<sup>18</sup>. Likewise, the geometry of subduction evolves<sup>12,15–17</sup>. It is thus probable that there were times in Earth history when large-scale convective flow was more symmetric about the axis of minimum inertia, leading to a prolate figure<sup>10</sup> (Fig. 1c). This prolate form would have a strong propensity for TPW in the plane defined by  $I_{\max}$  and  $I_{\min}$ , and it has been identified as a favourable pre-condition for episodes of rapid, large-magnitude ‘coaxial’ TPW in deep time<sup>6,7</sup> (Fig. 1a). However, although a prolate figure strongly favours TPW coaxial to the axis  $I_{\min}$ , the mechanism(s) responsible for the oscillatory nature of the reorientations remain enigmatic.

One route to resolving this enigma may be provided by studies of planetary rotation<sup>13,14</sup> that revise the standard equilibrium rotational theory<sup>8,9</sup> to argue that a rotating system can retain long-term memory of previous pole orientations (Supplementary Fig. 1). Consider a rotating Earth in hydrostatic equilibrium. The rotational bulge stabilizes the rotation axis<sup>10,24,25</sup>. However, according to refs 8 and 9, this stabilization is transient because the bulge will ultimately readjust perfectly (that is, hydrostatically) to any reorientation of the rotation axis (Supplementary Fig. 1a). In a revised stability theory<sup>13,14</sup>, TPW-induced elastic stresses in the lithosphere preclude a perfect adjustment of the rotational bulge (Supplementary Fig. 1b). This residual memory is termed the ‘remnant bulge’. Thus, the rotation axis is stabilized by both the delayed viscous adjustment of the rotational bulge<sup>10</sup> and, over timescales less than the visco-elastic relaxation time of the lithosphere, the remnant bulge<sup>13,14</sup>. The remnant bulge stabilization introduces a tendency for the axis to return to the original orientation if the load is removed.

The rotation axis may be subject to a third stabilization mechanism linked to the convective forcing itself (Supplementary Fig. 1c). In particular, the relatively rapid convective forcing responsible for driving excursions of the pole in Fig. 1a may have been superimposed on a convective geometry with long-term stability. If such a geometry supported an excess ellipticity in the plane of the TPW, then this stable background excess ellipticity would also provide a memory of the original orientation of the rotation axis and it would also act to drive the pole back to this orientation once the convective pulse weakened.

We adopted the nonlinear rotational stability theory of ref. 10 to investigate TPW driven by mantle convection. We used a form of the theory that incorporates a stable background excess ellipticity, and we introduced a new term that adds stabilization by the remnant bulge (see Supplementary Information). The formulation was applied to model the Mesozoic<sup>5,26</sup> (Fig. 2a–d) and Neoproterozoic<sup>2</sup> (Fig. 3a) oscillatory TPW events included in Fig. 1a. The Mesozoic event involves two oscillations of amplitude 22.5° and 8° and duration around 100 Myr and 50 Myr, respectively<sup>26</sup>, coaxial about an axis near the centre of Pangaea. The Neoproterozoic event is characterized by a >50° oscillation with duration around 11–30 Myr (ref. 2), coaxial about Rodinia.

Mantle convection simulations indicate that supercontinents reorganize flow into two antipodal superswells, one of which rises below the supercontinent and serves as the driving force for disaggregation<sup>23</sup>. Accordingly, our numerical simulations aligned the minimum axis of inertia (and maximum excess ellipticity) with the centre of the supercontinent (for example, Fig. 3b). The axis of maximum non-hydrostatic inertia is coincident with the rotation pole. We introduced a simple convective pulse symmetric about the plane of  $I_{\max}$  and  $I_{\min}$ , and this guarantees, given the symmetry of the background Earth model, that

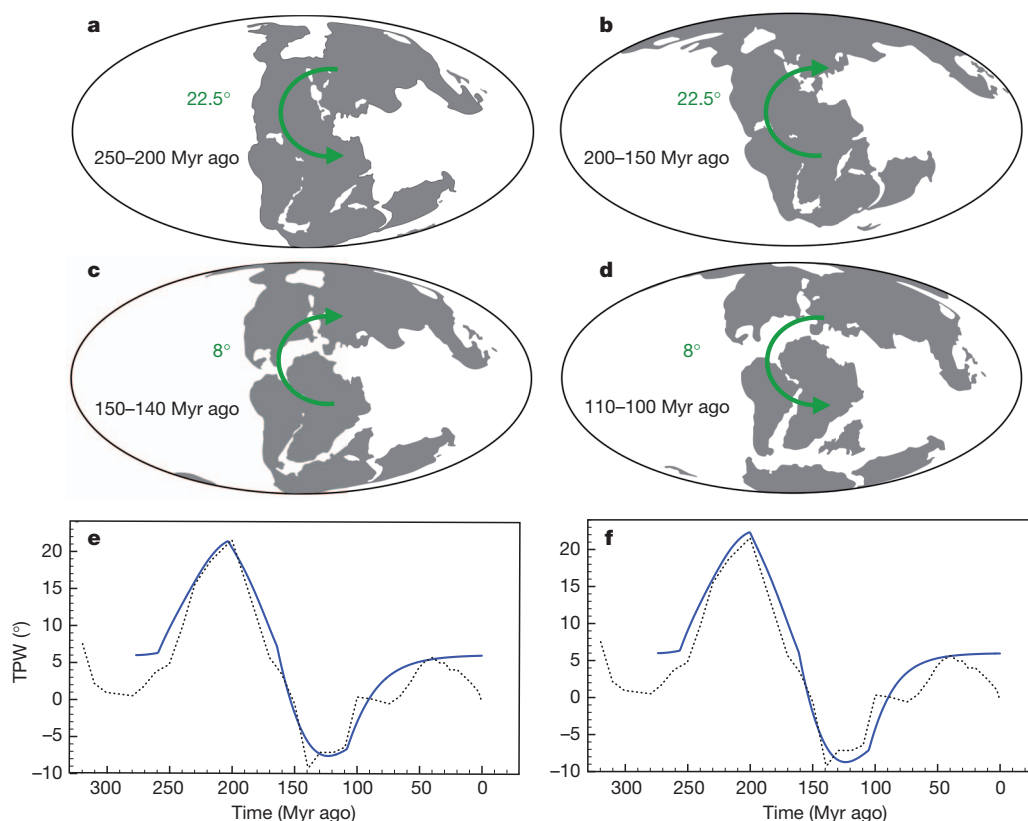


**Figure 2 | Modelling palaeomagnetically inferred TPW during the Mesozoic.** a–d, Inferred sense and amplitude (green) of coherent continental motion (interpreted as TPW) superimposed on the palaeogeography at the start of each (labelled) time interval<sup>26</sup>. e, f, Dotted lines show the inferred, cumulative TPW around an equatorial axis coinciding with the centre of mass of the continents<sup>26</sup>. The solid blue lines are numerical predictions of TPW based

on the following parameters. For e, EET = 15 km,  $\Delta^n I_{\text{MD}} = 0.0$ , and two convective pulses (both with  $\Delta^n I_{\max, \text{int}} = 0.035$ ) initiated at 277 Myr ago and 221 Myr ago. For f,  $\Delta^n I_{\text{MD}} = 0.12$ , EET = 0 km, and convective forcings (both with  $\Delta^n I_{\max, \text{int}} = 0.035$ ) initiated at 274 Myr ago and 218 Myr ago. The simulations adopt  $\nu = 3 \times 10^{22}$  Pa s.

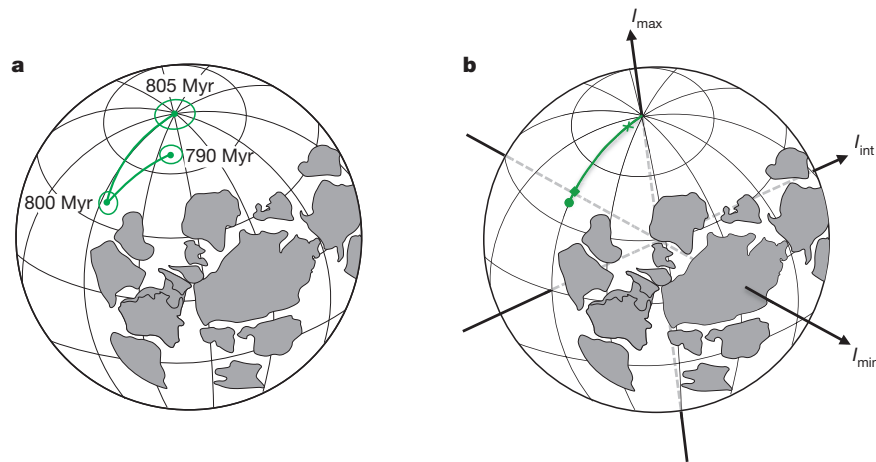


**Figure 3 | Modelling palaeomagnetically inferred TPW during the Neoproterozoic.** **a**, Rodinian palaeogeographic configuration before the pair of large-amplitude TPW events (green line with  $1\sigma$  error ellipses) with total duration of about 15 Myr (see ref. 2). **b**, Schematic showing the results of two numerical simulations of TPW (green line) that both adopt a convective forcing of  $\Delta^i I_{\max, \text{int}} = 0.3$  and  $\nu = 10^{22}$  Pa s. These simulations introduce either a

TPW is confined to this plane (see Methods). The numerical model has four free parameters: the moment difference (stable background excess ellipticity) of the Earth's figure,  $\Delta I_{\text{MD}} = I_{\max} - I_{\text{int}}$ ; the effective elastic thickness of the broken lithosphere (EET; see Supplementary Information); the lower mantle viscosity,  $\nu$ ; and the peak perturbation in the product of inertia,  $\Delta I_{\max, \text{int}}$ , driven by the convective flow. We normalized both  $\Delta I_{\max, \text{int}}$  and  $\Delta I_{\text{MD}}$  using the present-day moment difference<sup>27</sup>,  $\Delta I_{\text{PD}} = I_{\text{PD}}^{\text{max}} - I_{\text{PD}}^{\text{int}}$ , so that  $\Delta^i I_{\max, \text{int}} = \Delta I_{\max, \text{int}} / \Delta I_{\text{PD}}$  and  $\Delta^i I_{\text{MD}} = \Delta I_{\text{MD}} / \Delta I_{\text{PD}}$ .

For our 'standard' simulation, we adopted values of  $\Delta^i I_{\max, \text{int}} = 0.1$  and  $\nu = 10^{22}$  Pa s, with the latter being at the lower bound of a joint inversion of ice-age and mantle convection data<sup>28</sup>. The upper mantle viscosity was set to  $5 \times 10^{20}$  Pa s. We defined two test cases based on the standard simulation. In the first, we adopt  $\Delta^i I_{\text{MD}} = 0$  (that is, a prolate spheroid) and an EET of 15 km. In the second,  $\Delta^i I_{\text{MD}} = 0.1$  and EET = 0. These cases invoke stabilization by the remnant bulge or stable background excess ellipticity, respectively.

The black lines in Fig. 4a and e are predictions of TPW based on test cases 1 and 2, respectively. The perturbation to the inertia tensor driven by convective flow progressively increases in the first 15 Myr or so of these simulations (see Supplementary Fig. 5a). The motion of the rotation pole lags behind this forcing, and reaches a maximum displacement of about  $34^\circ$  (case 1) or  $41^\circ$  (case 2) in approximately 21 Myr. As the forcing diminishes, elastic stress in the lithosphere or the stable background excess ellipticity begins to dominate the rotational force balance. Once this resistance overcomes the driving force, the pole reverses direction and returns relatively rapidly towards its initial position. The net displacement of the pole drops to half the peak amplitude in about 9 Myr.

To investigate the sensitivity of the TPW predictions to the parameter choices listed above, we performed analyses in which one of four parameters is varied over the following ranges:  $\Delta^i I_{\max, \text{int}} = 0.025\text{--}0.20$ , EET = 0–50 km,  $\Delta^i I_{\text{MD}} = 0.0\text{--}1.0$  and  $\nu = (3\text{--}30) \times 10^{21}$  Pa s (see Fig. 4a–d, e–h). (An analysis in which these parameters are varied simultaneously is described in the Supplementary Information). We refer to three specific measures of the polar motion: the maximum displacement of the pole ( $\text{TPW}_{\max}$ ), the time required to reach this maximum displacement ( $t_{\max}$ ), and, subsequently, the time for the pole to return to a displacement of half of  $\text{TPW}_{\max}$  ( $t_{1/2}$ ). These values are  $\text{TPW}_{\max} = 33.6^\circ$ ,  $t_{\max} = 21.0$  Myr and  $t_{1/2} = 9.5$  Myr for test case 1 and  $\text{TPW}_{\max} = 40.5^\circ$ ,  $t_{\max} = 20.7$  Myr and  $t_{1/2} = 8.8$  Myr for test case 2.

We first explored the impact of varying the magnitude of the forcing,  $\Delta^i I_{\max, \text{int}}$  (Fig. 4a, e). The velocity of the convective flow

remnant bulge (EET = 15 km;  $\Delta^i I_{\text{MD}} = 0$ ) or a stable background excess ( $\Delta^i I_{\text{MD}} = 0.1$ ; EET = 0) to drive a return of the rotation axis. In these two cases, the pole moves about  $44^\circ$  (diamond) and  $51^\circ$  (circle), respectively, in the first 6 Myr or so and then returns to a position around  $8^\circ$  (cross) from the initial location in the next 20 Myr.

is proportional to the imposed density (buoyancy) perturbation. Accordingly, increasing the inertia tensor perturbation from 5% to 20% of  $\Delta I_{\text{PD}}$  reduces  $t_{\max}$  by a factor of about 4.  $\text{TPW}_{\max}$  increases with the size of the forcing, and it reaches  $40^\circ$  when the convection-induced inertia tensor perturbation  $\Delta^i I_{\max, \text{int}} = 0.2$  (case 1) or 0.1 (case 2). In contrast to both these sensitivities, the timescale of recovery  $t_{1/2}$  varies by only a few million years for  $\Delta^i I_{\max, \text{int}} \geq 0.05$ .

Next, we considered the two parameters that stabilize the rotation axis,  $\Delta^i I_{\text{MD}}$  and EET. Varying EET in test case 1 (Fig. 4b) or  $\Delta^i I_{\text{MD}}$  in case 2 (Fig. 4g) has a profound effect on  $\text{TPW}_{\max}$  and  $t_{1/2}$ , but little effect on  $t_{\max}$ . Moreover, introducing a stable background excess ellipticity in test case 1 (Fig. 4c) or a remnant bulge in case 2 (Fig. 4f) enhances the already existing stabilizations in these test cases, further decreasing the peak TPW and the recovery time. When EET = 0 and  $\Delta^i I_{\text{MD}} = 0$  (Fig. 4b,g) (that is, a prolate Earth with no remnant bulge), only the delayed viscous adjustment of the rotational bulge acts to resist polar motion<sup>10</sup> and the TPW has no return phase.

Finally, we considered simulations in which  $\nu$  is varied from  $3 \times 10^{21}$  Pa s to  $3 \times 10^{22}$  Pa s (Fig. 4d, h). The latter is a reasonable upper bound from modern inferences<sup>28</sup>, and the former is consistent with thermal history modelling<sup>29</sup>, suggesting that mantle viscosity was about 3–10 times smaller than the present value about a billion years ago. Flow velocity is inversely proportional to mantle viscosity, so  $t_{\max}$  increases by a factor of about 10 across this range. However, although the timescale across which the flow-induced perturbation is active increases by this factor, the TPW rate is decreased, and the net effect is a relatively small variation in  $\text{TPW}_{\max}$ ; the sensitivity would be higher in models forced by continuous convective motion<sup>21,25</sup>.

We conclude that a relatively rapid pulse of mantle convection acting on an Earth with elastic lithospheric strength and/or an excess ellipticity that is stable over the timescale of the pulse leads to an inherent tendency for oscillatory TPW events. Whether variability in downwelling<sup>12,15–17</sup> or upwelling<sup>11,18</sup> mantle flow is the dominant driver of TPW, these stabilization mechanisms remove the necessity of invoking load symmetry to explain a rapid return of the rotation pole to a position near its original location<sup>6,11,12</sup>. (For mantle-viscosity profiles characterized by a large increase in viscosity with depth, a reversal in the sign of the associated geoid kernel may also contribute to the reversal in the direction of polar motion<sup>10</sup>.)

The sensitivity studies reveal a trade-off such that one can reduce the stabilization associated with the remnant bulge (that is, lower EET) by increasing the stable background excess ellipticity ( $\Delta I_{\text{MD}}$ ). Consider, as



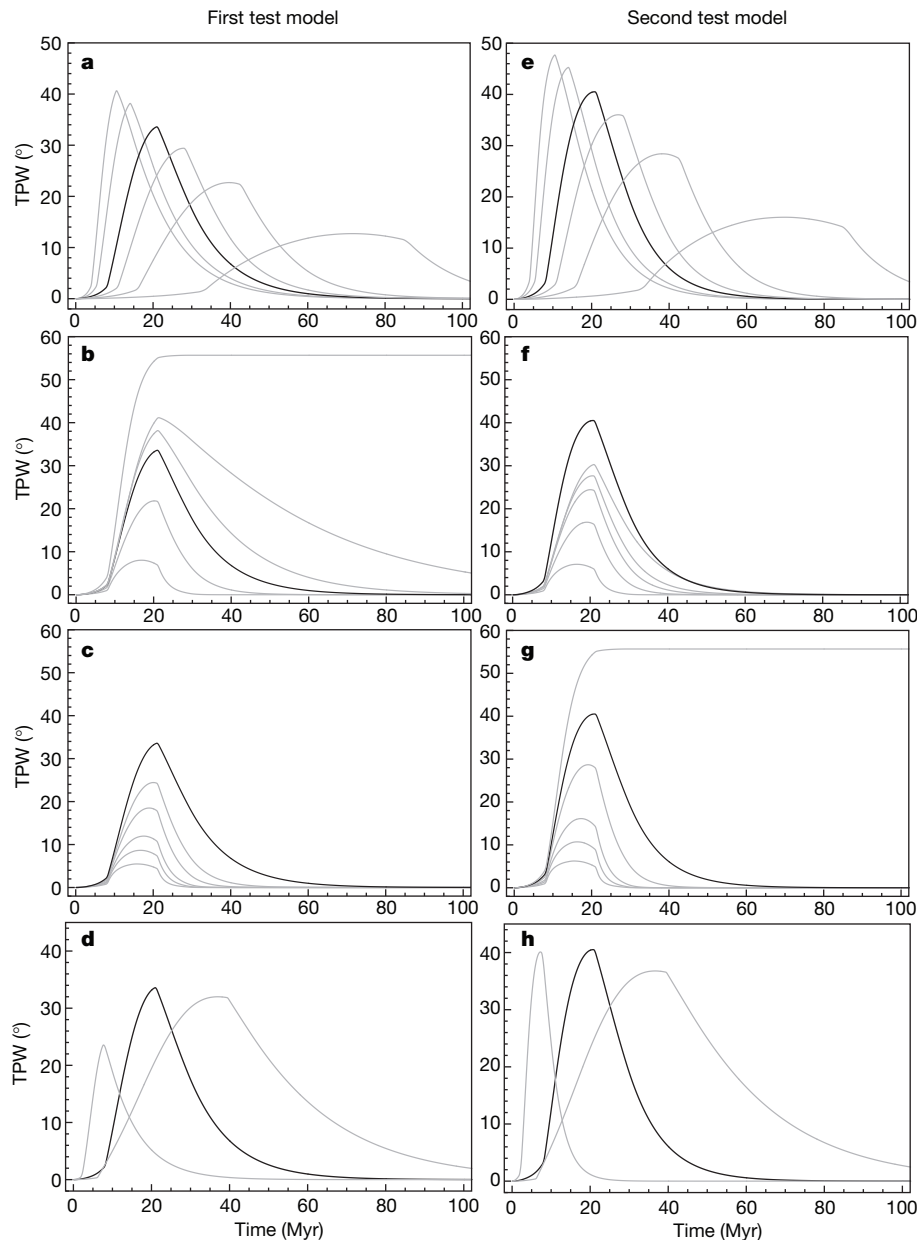


**Figure 4 | Sensitivity of numerical predictions of convectively driven TPW to variations in model parameters.** **a–d**, The black line in each panel shows the TPW prediction based on the first test model ( $\Delta^n I_{\text{max,int}} = 0.1$ ,  $\nu = 10^{22}$  Pa s,  $\Delta^n I_{\text{MD}} = 0$ , EET = 15 km). Each panel shows predictions in which one of these parameters is varied: **a**,  $\Delta^n I_{\text{max,int}}$  of (from left to right) 0.2, 0.15, 0.1, 0.075, 0.05 and 0.025; **b**, EET of (from top to bottom) 0 km, 5 km, 10 km, 15 km, 25 km and

50 km; **c**,  $\Delta^n I_{\text{MD}}$  of (from top to bottom) 0, 0.1, 0.2, 0.4, 0.6 and 1.0; **d**,  $\nu$  of (from left to right)  $3 \times 10^{21}$  Pa s,  $10^{22}$  Pa s and  $3 \times 10^{22}$  Pa s (in each case, plume density contrasts are chosen so that  $\Delta^n I_{\text{max,int}} = 0.1$ ). **e–h**, The black line in each panel shows the prediction based on the second test model ( $\Delta^n I_{\text{max,int}} = 0.1$ ,  $\nu = 10^{22}$  Pa s,  $\Delta^n I_{\text{MD}} = 0.1$ , EET = 0 km). Each panel shows predictions of TPW in which one of these parameters is varied (as listed for **a–d**).

an example, the palaeomagnetically inferred oscillation in pole position during the Neoproterozoic era<sup>2</sup> (Fig. 3a). The large amplitude of the event can only be reconciled with an Earth model of nearly prolate form and relatively small EET. Figure 3b summarizes the results of two simulations, both driven by a convective perturbation of  $\Delta^n I_{\text{max,int}} = 0.3$ . The first adopts a prolate Earth model ( $\Delta^n I_{\text{MD}} = 0$ ) with EET = 15 km, and the second adopts  $\Delta^n I_{\text{MD}} = 0.1$  and EET = 0. The simulations predict approximately 44° or 51°, respectively, of TPW in about 6 Myr, followed by a return of the pole to within about 8° of the initial location in the next 20 Myr or so, yielding good fits to the palaeomagnetically inferred TPW path<sup>2</sup>. One could reduce the total duration of the modelled event by increasing EET or  $\Delta^n I_{\text{MD}}$ . However, these changes would significantly reduce the predicted TPW amplitude. Thus, if large, rapid, oscillatory TPW events occurred in the Palaeoproterozoic through to the Palaeozoic era (Fig. 1a), then

their rarity in the geological record may reflect these restrictive constraints on the Earth's shape and rheology.

We next turned to the inference of two back-to-back episodes of oscillatory TPW during the Mesozoic era<sup>26</sup> (Fig. 2a–d). These events are more muted than those inferred for the Proterozoic and Palaeozoic, and they are of longer duration than the Neoproterozoic TPW event (Fig. 1a). To reduce the level of non-uniqueness, we considered only simulations in which the EET of the lithosphere and  $\Delta^n I_{\text{MD}}$  are the same for both oscillations. Excellent fits to the inferred TPW path can be found for scenarios in which either: (1) remnant bulge stabilization (EET = 15 km) acts on a prolate ( $\Delta^n I_{\text{MD}} = 0$ ) Earth model (Fig. 2e); or (2) a background excess ellipticity ( $\Delta^n I_{\text{MD}} = 0.12$ ) stabilizes an Earth model with an EET = 0 (Fig. 2f).

Estimates of the EET for various palaeocontinental configurations are uncertain (see Supplementary Information). However, flexure

observed at seamounts, long-lived passive margins and intracratonic basins suggests that the Earth's broken lithosphere retains non-zero elastic strength over the timescales considered here<sup>30</sup>. Thus, a stable background excess ellipticity augmented, but probably did not entirely replace, remnant bulge stabilization as a mechanism for oscillatory TPW in deep time. The memory of previous rotational states provided by a lithosphere will be partially lost if the timescale of the convective forcing approaches the relaxation time of the crust–lithosphere system (or if the supercontinent disaggregates; see Supplementary Information). Similarly, memory associated with excess ellipticity will be lost as the Earth's figure evolves. For these reasons, predictions of oscillatory TPW events need not fully return to the original pole location. Moreover, the remnant bulge stabilization will be reset if the timescale of the convective forcing significantly exceeds the longest relaxation time of the lithosphere.

There have been suggestions that the longevity of the present-day superswells beneath Africa and the Pacific may extend uninterrupted to the Neoproterozoic. Numerical experiments suggest that the African superswells have persisted for the past 200 Myr or so and the Pacific superswell much longer<sup>23</sup>, while a suite of observations suggest a lifespan extending 500 Myr (ref. 31) or more<sup>32</sup>. Indeed, the current equatorial location of the superswells<sup>33</sup> implies that any remnant bulge stabilization of TPW driven by these features has since relaxed. However, laboratory experiments on thermochemical convection suggest that long-lived superswells experience pseudo-periodic doming with timescales of 100–1,000 Myr (ref. 18), and such events may drive a relatively rapid pulse of subduction in the plane perpendicular to  $I_{\min}$  (Fig. 1c). This, or other classes of rapid, repetitive convective forcing, acting on an Earth with a small EET and/or a relatively stable background excess ellipticity, may provide an overarching physical framework linking the suite of palaeomagnetically inferred, oscillatory TPW events spanning the past few billion years of Earth history.

## METHODS SUMMARY

Our numerical predictions of oscillatory TPW are based on the nonlinear rotational stability theory described in the Supplementary Information. This theory requires that the following be specified: (1) the Earth's background figure; (2) the EET of the lithosphere (see Supplementary Information); (3) the mantle viscosity; and (4) the inertia tensor perturbation due to the convective load,  $I^c(t)$ . For (1), we assume that the axis of minimum inertia (that is, maximum excess ellipticity) intersects the centre of the supercontinent (for example, Fig. 3b). Moreover, we adopt a Stokes flow treatment of mantle convection, with buoyancy comprised of upwelling and downwelling plumes symmetric about the plane defined by  $I_{\max}$  and  $I_{\min}$ . This geometry, together with symmetry in the Earth model, confines the predicted pole path to a great circle within this plane (that is, coaxial to the axis of minimum inertia). The background moment difference,  $\Delta I_{MD} = I_{\max} - I_{\min}$ , thus controls the level of stabilization associated with long-term excess ellipticity in the plane of TPW, and it is a free parameter in the modelling. The EET, which governs the strength of the remnant bulge stabilization, is a second free parameter. We set the upper mantle viscosity to  $5 \times 10^{20}$  Pa s, and treat the lower mantle viscosity,  $\nu$ , as a third free parameter. The viscosity governs the decay time of stabilization associated with delayed adjustment of the rotational bulge, and the timescale of the convective loading. Finally, we compute the time-dependent inertia tensor perturbation,  $I^c(t)$ , by first mapping the mantle buoyancy field into a geoid anomaly time series using depth-dependent kernels. The geoid time series is then mapped into an evolving inertia tensor perturbation using analytic relationships. The peak perturbation to the product of inertia,  $\Delta I_{\max, \text{int}}$ , serves as the fourth free parameter of the modelling.

**Full Methods** and any associated references are available in the online version of the paper.

**Received 13 August 2011; accepted 10 September 2012.**

1. Mitchell, R. N., Hoffman, P. F. & Evans, D. A. D. Coronation loop resurrected: oscillatory apparent polar wander of Orosirian (2.05–1.8 Ga) paleomagnetic poles from Slave craton. *Precamb. Res.* **179**, 121–134 (2010).
2. Maloof, A. C. et al. Combined paleomagnetic, isotopic, and stratigraphic evidence for true polar wander from the Neoproterozoic Akademikerbreen Group, Svalbard, Norway. *Geol. Soc. Am. Bull.* **118**, 1099–1124 (2006).

3. Mitchell, R. N., Evans, D. A. D. & Kilian, T. M. Rapid Early Cambrian rotation of Gondwana. *Geology* **38**, 755–758 (2010).
4. Van der Voo, R. True polar wander during the middle Paleozoic? *Earth Planet. Sci. Lett.* **122**, 239–243 (1994).
5. Steinberger, B. & Torsvik, T. H. Absolute plate motions and true polar wander in the absence of hotspot tracks. *Nature* **452**, 620–623 (2008).
6. Evans, D. A. D. True polar wander, a supercontinental legacy. *Earth Planet. Sci. Lett.* **157**, 1–8 (1998).
7. Evans, D. A. D. True polar wander and supercontinents. *Tectonophysics* **362**, 303–320 (2003).
8. Gold, T. Instability of the Earth's axis of rotation. *Nature* **175**, 526–529 (1955).
9. Goldreich, P. & Toomre, A. Some remarks on polar wandering. *J. Geophys. Res.* **74**, 2555–2567 (1969).
10. Ricard, Y., Spada, G. & Sabadini, R. Polar wandering of a dynamic Earth. *Geophys. J. Int.* **113**, 284–298 (1993).
11. Greff-Lefftz, M. Upwelling plumes, superswells and true polar wander. *Geophys. J. Int.* **159**, 1125–1137 (2004).
12. Steinberger, B. & Torsvik, T. H. Toward an explanation for the present and past locations of the poles. *Geochem. Geophys. Geosyst.* **11**, Q06W06 (2010).
13. Willemann, R. Reorientation of planets with elastic lithospheres. *Icarus* **60**, 701–709 (1984).
14. Matsuyama, I., Mitrova, J. X., Perron, J. T., Manga, M. & Richards, M. A. Rotational stability of dynamic planets with elastic lithospheres. *J. Geophys. Res.* **111**, E02003 (2006).
15. Spada, G., Ricard, Y. & Sabadini, R. Excitation of true polar wander by subduction. *Nature* **360**, 452–454 (1992).
16. Rouby, H., Greff-Lefftz, M. & Besse, J. Mantle dynamics, geoid, inertia and TPW since 120 Myr. *Earth Planet. Sci. Lett.* **292**, 301–311 (2010).
17. Richards, M. A., Bunge, H.-P., Ricard, Y. & Baumgardner, J. R. Polar wandering in mantle convection models. *Geophys. Res. Lett.* **26**, 1777–1780 (1999).
18. Davaille, A. Simultaneous generation of hotspots and superswells by convection in a heterogeneous planetary mantle. *Nature* **402**, 756–760 (1999).
19. Ritsema, J. & Van Heijst, H. J. Seismic imaging of structural heterogeneity in Earth's mantle: evidence for large-scale mantle flow. *Sci. Prog.* **83**, 243–259 (2000).
20. Zhang, N., Zhong, S., Leng, W. & Li, Z.-X. A model for the evolution of the Earth's mantle structure since the Early Paleozoic. *J. Geophys. Res.* **115**, B06401 (2010).
21. Chan, N.-H., Mitrova, J. X., Matsuyama, I., Creveling, J. R. & Stanley, S. The rotational stability of a convecting Earth: assessing inferences of rapid TPW in the Late Cretaceous. *Geophys. J. Int.* **187**, 1319–1333 (2011).
22. Oldham, D. & Davies, J. H. Numerical investigation of layered convection in a three-dimensional shell with application to planetary mantles. *Geochem. Geophys. Geosyst.* **5**, Q12C04 (2004).
23. Zhong, S., Zhang, N., Li, Z.-X. & Roberts, J. H. Supercontinent cycles, true polar wander, and very long-wavelength mantle convection. *Earth Planet. Sci. Lett.* **261**, 551–564 (2007).
24. Steinberger, B. & O'Connell, R. J. In *Ice Sheets, Sea Level and the Dynamic Earth* (eds Mitrova, J. X. & Vermeersen, L. L. A.) 233–256 (AGU, Geodynamics Series 29, 2002).
25. Tsai, V. C. & Stevenson, D. J. Theoretical constraints on true polar wander. *J. Geophys. Res.* **112**, B05415 (2007).
26. Torsvik, T. H. et al. Phanerozoic polar wander, palaeogeography. *Earth Sci. Rev.* **114**, 325–368 (2012).
27. Chambat, F., Ricard, Y. & Valette, B. Flattening of the Earth: further from hydrostaticity than previously estimated. *Geophys. J. Int.* **183**, 727–732 (2010).
28. Mitrova, J. X. & Forte, A. M. A new inference of mantle viscosity based upon a joint inversion of convection and glacial isostatic adjustment data. *Earth Planet. Sci. Lett.* **225**, 177–189 (2004).
29. Crowley, J., Gerault, M. & O'Connell, R. J. On the relative influence of thermal and water cycles on planetary dynamics. *Earth Planet. Sci. Lett.* **310**, 380–388 (2011).
30. Watts, A. B. *Isostasy and Flexure of the Lithosphere* (Cambridge Univ. Press, 2001).
31. Torsvik, T. H., Burke, K., Steinberger, B., Webb, S. J. & Ashwal, L. D. Diamonds sampled by plumes from the core-mantle boundary. *Nature* **466**, 352–355 (2010).
32. Dziewonski, A., Lekic, V. & Romanowicz, B. A. Mantle anchor structure: an argument for bottom-up tectonics. *Earth Planet. Sci. Lett.* **299**, 69–79 (2010).
33. Spada, G., Sabadini, R. & Boschi, E. True polar wander affects the Earth dynamic topography and implies a highly viscous lower mantle. *Geophys. Res. Lett.* **21**, 137–140 (1994).

**Supplementary Information** is available in the online version of the paper.

**Acknowledgements** We thank D. Evans, T. Torsvik and B. Steinberger for comprehensive and constructive reviews; A. Forte for providing us with geoid kernels; and C. Hay, N. Gomez, E. Morrow and A. Wickert for assistance with figures. We also thank A. Maloof, R. van der Voo, A. Watts, P. Hoffman, G. Spada, R. Mitchell, S. Stanley, S. Zhong, V. Tsai, D. Rowley and N. Swanson-Hysell for critical discussions; and D. Johnston and A. Knoll for reading of the manuscript. We acknowledge support from the Canadian Institute for Advanced Research and Harvard University.

**Author Contributions** J.R.C. developed the conceptual idea for the study. All authors contributed to the technical analysis and the writing of the paper.

**Author Information** Reprints and permissions information is available at [www.nature.com/reprints](http://www.nature.com/reprints). The authors declare no competing financial interests. Readers are welcome to comment on the online version of the paper. Correspondence and requests for materials should be addressed to J.R.C. ([jrc@caltech.edu](mailto:jrc@caltech.edu)).

## METHODS

To investigate the link between mantle flow and TPW, we apply the nonlinear rotational stability theory described in Supplementary Information to inertia perturbations computed using a simple Stokes flow<sup>34</sup> treatment of mantle convection.

In computing TPW, the background figure of the Earth—that is, the figure before the application of the convective pulse—has a geometry that is motivated by the supercontinent configurations shown in Figs 2a–d and 3a. As in Fig. 3b, we assume that the axis of minimum inertia passes through the centre of the supercontinent. The convective pulse is comprised of upwelling and downwelling plumes (see below) symmetric about the plane defined by  $I_{\max}$  and  $I_{\min}$ . This placement, together with the symmetry in the Earth model, ensures that the predicted pole path will be confined to a great circle within this plane. Three free parameters of the modelling relate to the Earth model. These are (1) the difference in the background values of the maximum and intermediate moments of inertia,  $I_{\max} - I_{\min}$ , denoted as  $\Delta I_{\text{MD}}$  in the main text (that is, the stable excess ellipticity in the plane of the TPW); (2) the effective elastic thickness of the lithosphere, EET (see Supplementary Information); and (3) the viscosity of the lower mantle,  $\nu$ . The upper mantle viscosity is fixed to  $5 \times 10^{20}$  Pa s in all simulations.

The free parameters EET,  $\Delta I_{\text{MD}}$  and  $\nu$  are linked to the three mechanisms that act to stabilize the rotation axis in the presence of a convective forcing: the remnant bulge, stable background excess ellipticity in the plane of TPW, and the delayed viscous adjustment of the rotational bulge, respectively. Moreover, EET and  $\Delta I_{\text{MD}}$  introduce a memory of the original (pre-loading) orientation of the rotation axis and a tendency for the pole to return towards this initial position once the forcing ends.

Convective forcing within our model involves a pair of plumes upwelling from the core–mantle boundary at  $55^\circ$  N and a second antipodal pair at  $55^\circ$  S. The plumes that comprise each pair are displaced by  $60^\circ$  in longitude, at locations symmetric about the plane defined by  $I_{\max}$  and  $I_{\min}$ . An equal number of downwelling plumes are also included in the model. These are located at positions defined by a  $90^\circ$  rotation about  $I_{\min}$  from each of the upwellings. This configuration permits a maximum TPW of around  $60^\circ$ . We also performed several test calculations where the plumes were placed at higher latitudes ( $75^\circ$  N and  $75^\circ$  S) and found that the predicted peak TPW varied by about  $5^\circ$ . Each plume has a radius of  $6^\circ$ . The speed of the plumes is given by Stokes flow equations, and we use the method of images<sup>34</sup> to account for the slowing of the plumes near boundaries. The fourth and final free parameter of the modelling is related to the strength of the convective forcing on TPW, which was varied from one simulation to another via the adopted density contrast (see below) between the plumes and surrounding mantle. As discussed in the main text, we quantify the strength of the convective forcing in terms of the peak perturbation in the product of inertia  $\Delta I_{\max, \text{int}}$ . The time series of  $\Delta I_{\max, \text{int}}$  for three simulations, including the standard model run defined in the text, are provided in Supplementary Fig. 5a.

The evolving mantle flow field was converted to a time-dependent geoid anomaly (at spherical harmonic degree two) using depth-dependent kernels valid for a compressible, viscous Earth<sup>35</sup>. We adopt kernels computed using free-slip boundary conditions at the core–mantle boundary and no-slip conditions at the surface; the latter is appropriate for plume-driven flow away from plate boundaries<sup>36</sup>. The geoid kernels were calculated using the PREM density profile and  $g(r)$  is fully consistent with this profile. Moreover, the calculation is based on a gravitationally self-consistent treatment in which the self-gravity term (the product of the depth-dependent density and perturbed gravity) is included. These kernels account for the geoid signal associated with both internal density heterogeneities and the dynamic topography of all density interfaces. Finally, the geoid perturbation at each time step is converted to an inertia tensor perturbation using a well-established mapping<sup>14</sup>, and the latter time series serves as the input to the nonlinear rotational stability theory.

Our plume-model of mantle convective flow is highly simplified; however, it allows us to quantitatively test the central hypothesis of this study, namely that stabilization associated with a remnant bulge and/or stable excess ellipticity would have been sufficient to return the rotation axis to its initial location after large-amplitude, convectively driven excursions. In designing the simulations, we were guided by several checks of the plausibility of the convective forcing. First, we distributed mantle buoyancy across a suite of plumes, rather than placing it in a single plume, so that the associated density contrast between the plume and surrounding mantle is reasonable. As an example, the density contrast adopted in the standard simulation described in the text ( $\Delta I_{\max, \text{int}}^{\text{r}} = 0.1$ ; black lines in Fig. 4) was  $42.5 \text{ kg m}^{-3}$ . This value is less than 1% of the density of lower-mantle material and it is consistent with inferences based on seismic tomography<sup>32</sup>. Second, given that the present-day, non-hydrostatic (excess) ellipticity of the Earth is presumably a consequence of mantle convection, our normalization of the plume-induced perturbation to the product of inertia,  $\Delta I_{\max, \text{int}}$  in terms of the observed excess ellipticity in the same plane ( $\Delta I_{\text{PD}} = I_{\text{PD}}^{\text{max}} - I_{\text{PD}}^{\text{int}}$ ), provides a direct check of the size of the forcing. We note, in this regard, that TPW excursions of order  $40^\circ$  are predicted for peak (product of) inertia perturbations of only 10%–20% of  $\Delta I_{\text{PD}}$ .

In modelling the palaeomagnetically inferred TPW events shown in Figs 2a–d and 3a, we consider Earth models with prolate, or nearly prolate forms. For this class of Earth models, the TPW path would be coaxial to  $I_{\min}$ , or very nearly so, regardless of the orientation of the pulse of convective forcing. Thus, our placement of the plumes symmetric about the plane defined by  $I_{\max}$  and  $I_{\min}$  is made out of numerical convenience, and it does not imply that a nearly coaxial TPW path requires a convective forcing of specific geometry.

34. Milne-Thomson, L. M. *Theoretical Hydrodynamics* 743 (Courier Dover, 1996).

35. Forte, A. M. & Peltier, W. R. Viscous flow models of global geophysical

observables: 1. Forward problems. *J. Geophys. Res.* **96**, 20131–20159 (1991).

36. Forte, A. M. Constraints on seismic models from other disciplines—implications for mantle dynamics and composition. *Treat. Geophys.* **1**, 805–858 (2007).



# Genetic programs constructed from layered logic gates in single cells

Tae Seok Moon<sup>1†</sup>, Chunbo Lou<sup>1</sup>, Alvin Tamsir<sup>2</sup>, Brynne C. Stanton<sup>1</sup> & Christopher A. Voigt<sup>1</sup>

Genetic programs function to integrate environmental sensors, implement signal processing algorithms and control expression dynamics<sup>1</sup>. These programs consist of integrated genetic circuits that individually implement operations ranging from digital logic to dynamic circuits<sup>2–6</sup>, and they have been used in various cellular engineering applications, including the implementation of process control in metabolic networks and the coordination of spatial differentiation in artificial tissues. A key limitation is that the circuits are based on biochemical interactions occurring in the confined volume of the cell, so the size of programs has been limited to a few circuits<sup>1,7</sup>. Here we apply part mining and directed evolution to build a set of transcriptional AND gates in *Escherichia coli*. Each AND gate integrates two promoter inputs and controls one promoter output. This allows the gates to be layered by having the output promoter of an upstream circuit serve as the input promoter for a downstream circuit. Each gate consists of a transcription factor that requires a second chaperone protein to activate the output promoter. Multiple activator–chaperone pairs are identified from type III secretion pathways in different strains of bacteria. Directed evolution is applied to increase the dynamic range and orthogonality of the circuits. These gates are connected in different permutations to form programs, the largest of which is a 4-input AND gate that consists of 3 circuits that integrate 4 inducible systems, thus requiring 11 regulatory proteins. Measuring the performance of individual gates is sufficient to capture the behaviour of the complete program. Errors in the output due to delays (faults), a common problem for layered circuits, are not observed. This work demonstrates the successful layering of orthogonal logic gates, a design strategy that could enable the construction of large, integrated circuits in single cells.

We designed the architecture of an AND gate according to two constraints (Fig. 1a). First, the gate needs to consist of parts that can be diversified to build multiple orthogonal gates. Second, the inputs and outputs of the gate should have a common signal carrier that enables them to be layered (the output of one serves as the input to the next)<sup>8</sup>. For transcriptional circuits, the inputs and the outputs are promoters. We have designed a transcriptional 2-input AND gate, in which one input promoter drives the expression of an activator and the second input promoter drives the expression of a chaperone protein. The chaperone is required by the activator to turn on the output promoter (Fig. 1b). Both proteins need to be expressed for the transcription factor to be active. The output promoter is therefore active only when both input promoters are active.

The transcription factors and chaperones were gleaned from gene clusters encoding type III secretion systems, which are found in many pathogenic bacteria<sup>9</sup>. One of the best characterized is encoded within *Salmonella* Pathogenicity Island 1 (SPI-1)<sup>10</sup>. Within this island, a genetic circuit has been identified that regulates the expression of proteins that are exported by the system through a feedback mechanism mediated by protein–protein interactions between effectors, a chaperone (SicA) and a transcription factor (InvF) (Fig. 1c)<sup>11</sup>. The SicA–InvF complex activates

transcription from the *sicA* promoter. Thus, SPI-1 provides three parts that can form the core of an AND gate: the activator, the chaperone and the inducible promoter.

The genes associated with the T3SS are encoded together within a genomic cluster. This simplifies the identification of sets of three of the parts that are likely to function together. Of more than 1,000 prokaryotic genomes in NCBI, 64 species have InvF homologues. We selected three genomes from which to glean parts: *Shigella flexneri*, *Yersinia enterocolitica* and *Pseudomonas aeruginosa*. The homologues share 27% (MxiE)<sup>12</sup>, 15% (YsaE)<sup>13</sup> and 10% (ExsA)<sup>14</sup> identity with InvF. The SicA homologues are 54% (IpgC), 50% (SycB) and 13% (ExsC) identical. The *Pseudomonas* system has a different mechanism, involving three proteins and a partner-swapping mechanism<sup>14</sup>. The InvF and SicA homologues from each organism were codon-optimized for *E. coli* and synthesized. The *Salmonella*, *Shigella* and *Pseudomonas* parts had to be modified before their performance characteristics (orthogonality and dynamic range) were sufficient for incorporation into gates (Fig. 2a). The *Yersinia* parts were non-functional and were not pursued further.

The first *invF* gene we synthesized was based on the amino acid sequence from the annotated *Salmonella typhimurium* genome (AE006468). However, when co-expressed with *sicA*, it failed to activate the *psicA* promoter (Fig. 2b, ‘Annotated InvF’). This was corrected by determining that the gene was misannotated and is translated from an upstream ATG that adds 33 amino acids (Fig. 2b, ‘Correct InvF’).

Other changes had to be made to improve the dynamic ranges of the gates. Wild-type *pipaH* has a high basal background and is only induced threefold (Fig. 2c). A saturation mutagenesis library was designed to change the –10 region and screened to identify a mutant with a decreased background and higher dynamic range (Fig. 2a). A mutant was identified (*pipaH\**) that decreased the background and increased the dynamic range to 13-fold (Fig. 2c).

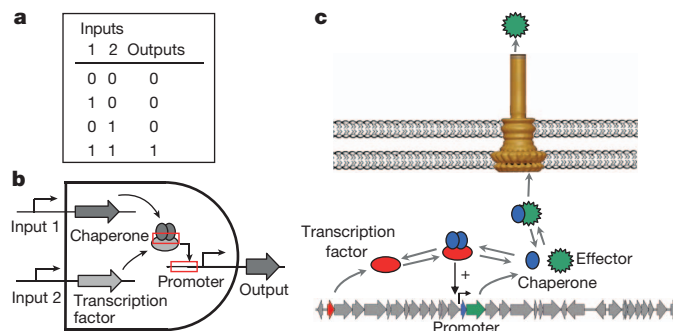


**Figure 1 | Mining circuits from genomic islands.** **a**, The truth table for an AND gate. **b**, The architecture of an AND gate. The protein–protein and protein–DNA interactions that can lead to crosstalk between gates are shown as red rectangles. **c**, The gene cluster from SPI-1 and the needle structure<sup>27,28</sup>. The transcription factor InvF is shown in red, the chaperone SicA in blue, and the SipC effector in green.

<sup>1</sup>Synthetic Biology Center, Department of Biological Engineering, Massachusetts Institute of Technology, Cambridge, Massachusetts 02139, USA. <sup>2</sup>Tetrad Graduate Program, University of California San Francisco, San Francisco, California 94158, USA. <sup>†</sup>Present address: Department of Energy, Environmental & Chemical Engineering, Washington University in St Louis, St Louis, Missouri 63130, USA.

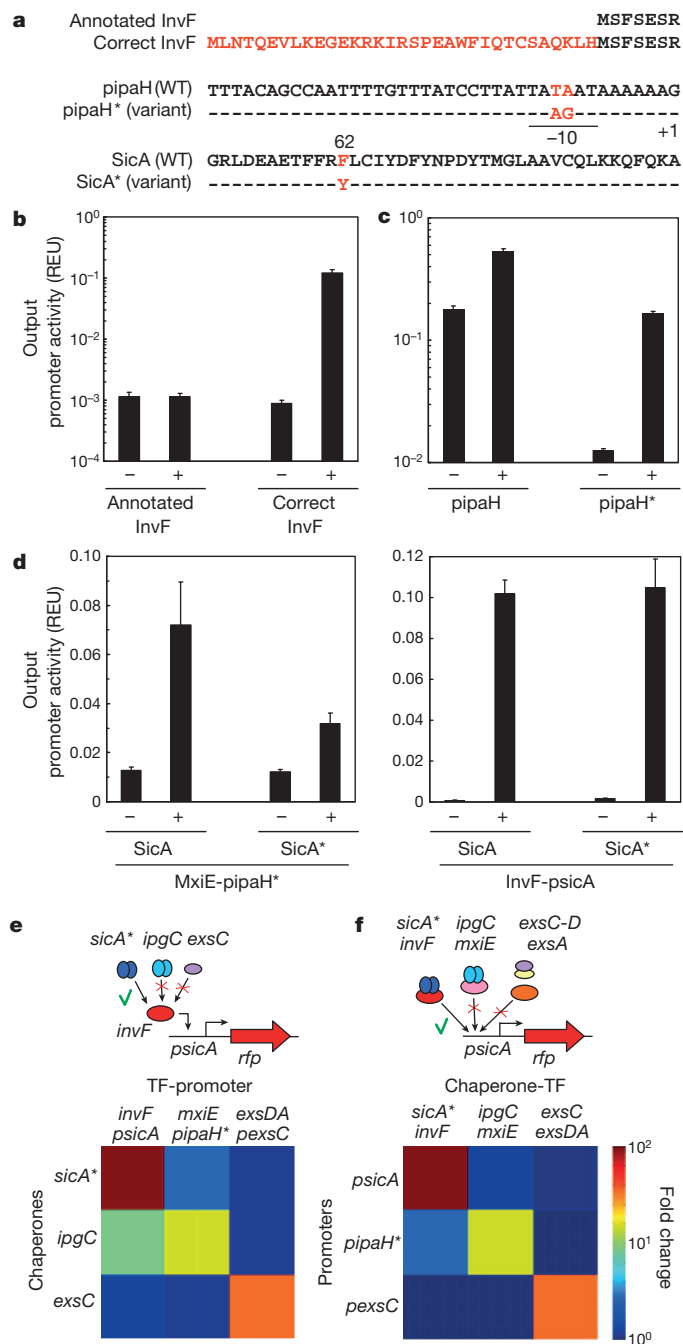


**Figure 2 | Part engineering to improve dynamic range and orthogonality.**

**a**, Sequences for the InvF activator (top), the pipaH promoter variant (middle) and the SicA mutant (bottom). **b**, A comparison in the induction of the *psicA* promoter by the short (annotated) and long (correct) InvF sequences. **c**, A comparison of the wild-type and mutant (pipaH\*) promoters. **d**, A comparison of the wild-type and mutant (SicA\*) chaperones. Activation of either the pipaH\* promoter by MxiE (left) or the *psicA* promoter by InvF (right) is shown. In **b–d** the chaperone (SicA and IpgC) and activator (InvF and MxiE) are expressed from the pBAD and pTet promoters, respectively: –, no inducer; +, 5 mM Ara and 50 ng ml<sup>-1</sup> aTc. **e**, The orthogonality of protein–protein interactions. This figure shows the fold change, calculated by dividing the fluorescence values (with both inputs on) by the minimum fluorescence from each promoter (with both inputs off). The inducers were 5 mM Ara for *sicA\** and *ipgC*, 1 μM 3OC6 for *exsC*, and 50 ng ml<sup>-1</sup> aTc for *invF*, *mxIE* and *exsDA*. **f**, The orthogonality of protein–DNA interactions. All of the error bars in these figures were calculated as the s.d. of three replicates performed on different days. The error bars for **e** and **f** are shown in Supplementary Fig. 4.

Of the six possible non-cognate protein–protein interactions that could exhibit crosstalk, only one was found to be significant. The SicA chaperone induced the MxiE transcription factor (Fig. 2d). Error-prone PCR was applied to *sicA*, and the library was screened for mutants that decreased crosstalk with MxiE but maintained the ability to induce InvF (Supplementary Information). A SicA mutant (SicA\*) containing a single F62Y mutation was identified that decreased the activation of MxiE to 2.6-fold, while retaining wild-type 70-fold activation of InvF (Fig. 2d).

The engineered parts from each system were then tested for orthogonality. The first potential for crosstalk is at the level of interaction between activators and chaperones (Fig. 2e). The SicA, IpgC and ExsC chaperones were able to activate their cognate systems 87-fold, 14-fold and 34-fold, respectively, and the off-target effects were minimal (Supplementary Fig. 4). The second possibility for crosstalk was on the level of the interaction between the transcription factor and the promoter (Fig. 2f). To test this, we co-expressed each cognate activator–chaperone pair and measured the ability of the complex to activate the three promoters (Supplementary Fig. 4). As with the protein–protein interactions, strong induction was observed only between cognate parts.

The sets of parts from each organism were assembled to form three 2-input AND gates (Fig. 3). To characterize each gate, two input promoters were chosen that were induced by small molecules: arabinose (pBAD) and aTc (pTet) for *Salmonella/Shigella* and AI-1 (pLux\*) and aTc (pTet\*) for *Pseudomonas* (Fig. 3a). The output promoter of each gate was transcriptionally fused to red fluorescent protein (RFP). The AND gates based on InvF–SicA\*, MxiE–IpgC and ExsDA–ExsC showed 73-fold, 14-fold and 33-fold induction, respectively (Fig. 3b). These AND gates can be converted to NAND gates (providing a Boolean complete function) through the addition of a NOT gate<sup>4</sup>. We demonstrated this by connecting the *Salmonella* AND gate to a new NOT gate based on the PhlF repressor, which yields a 13-fold inverted response (Supplementary Fig. 6).

A problem with the gate characterization is that the data are presented where the input is an inducer concentration and the output is fluorescence. To guide the connection of circuits, the data need to be in a form in which the inputs and the outputs have the same units. This was achieved by using a mathematical model combined with additional experiments (Supplementary Information). The activity of the promoter of each inducible system was characterized independently and was fitted to a simple thermodynamic model (Supplementary Figs 7 and 8). This formed the basis on which to parameterize a model of each AND gate such that the inputs and outputs were the activities of the respective promoters (Fig. 3c). To report the data in relative expression units (REUs)<sup>15</sup>, the activities were normalized by the activity of a constitutive promoter, as measured with the same fluorescent reporter (Supplementary Fig. 15)<sup>16</sup>.

The 2-input AND gates were designed to be layered to create more complex programs. We constructed 3-input and 4-input AND gates through different permutations of the 2-input gates (Fig. 4). There are alternative logic combinations, some much simpler, that would produce the same functions; these particular designs were chosen with the purpose of studying gate layering. The inputs into these programs were promoters that were activated by small-molecule inducers. In both cases, the output of the program was on only when all of the inducers were present in the medium. For the 3-input gate, the output when all inducers were present [111] was 4.5-fold above the highest off state [011] (Fig. 4b). For the 4-input gate, the output when all the inducers are present [1111] was 5.1-fold above the highest off state [1011] (Fig. 4e). The dynamic behaviour was characterized for the induction and relaxation of the 4-input program by switching between the [0000] and [1111] states (Fig. 5a). The 4-input AND gate represents a large genetic program that requires connecting 7 genetic devices (3 gates and 4 inducible systems) and includes 11 regulatory proteins, making it the largest and most complex program constructed so far<sup>7</sup>.

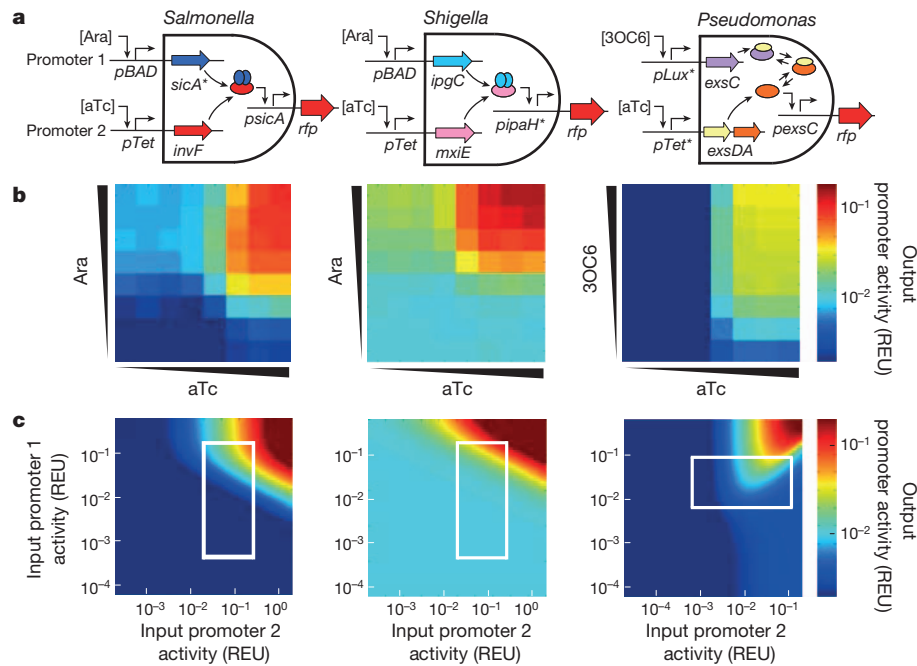


**Figure 3 | Three 2-input AND gates constructed using *Salmonella* (left), *Shigella* (middle) and *Pseudomonas* (right) parts. a**, The architecture of three AND gates. **b**, The transfer functions obtained by measuring fluorescence. The inducers used were Ara (0, 0.0016, 0.008, 0.04, 0.2, 1, 5 and 25 mM) and 3OC6 (0, 0.32, 1.6, 8, 40, 200, 1,000 and 5,000 nM) from left to right; and aTc (0, 0.0032, 0.016, 0.08, 0.4, 2, 10 and 50 ng ml<sup>-1</sup>) from left to right. Data are

averages of three replicates performed on different days. **c**, The transfer functions as fitted to mathematical models. The white boxes show the experiment ranges obtained by the inducible promoters. Note that **b** and **c** cannot be visually compared to determine the goodness of the fit because the axes are rescaled. Supplementary Fig. 10 shows a quantitative comparison, which yields an  $R^2$  of 0.9.

A key question is whether characterization data for individual circuits is sufficient to predict the performance of a program. This assumption could be false as a result of differences in the genetic context, interference

between circuits, or a combined impact on cellular resources<sup>17,18</sup>. To test this, we used the data obtained for the individual gates (Fig. 3c) and the inducible systems (Supplementary Fig. 8) to calculate the expected

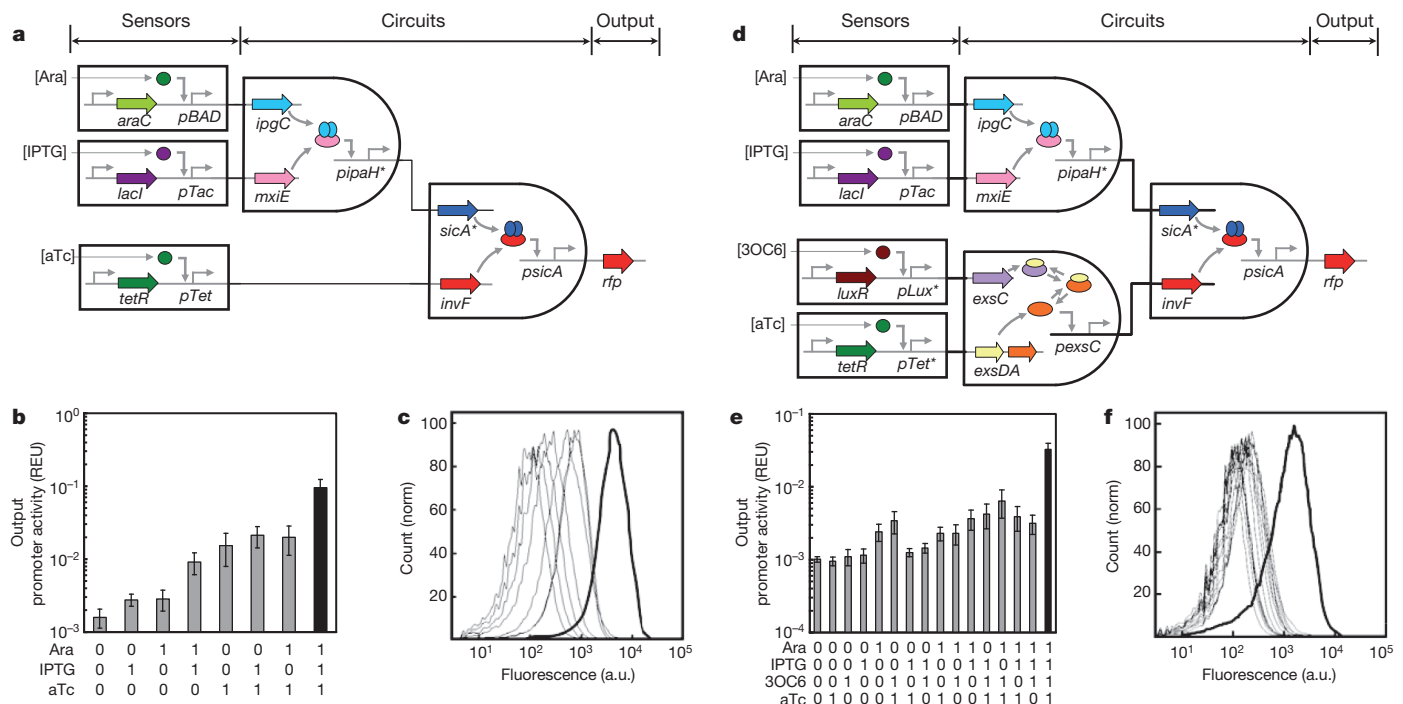


**Figure 4 | Genetic programs formed by layering AND gates. a**, 3-input AND gate. This system consists of three sensors, an integrated circuit and a reporter gene. **b**, The fluorescence measured from cells containing the 3-input AND gate. The three inducers used for the on (1) input are Ara (5 mM), IPTG (0.1 mM) and aTc (10 ng ml<sup>-1</sup>). Data are means and s.d. for three replicates performed on different days. **c**, Raw cytometry data for all sets of input states.

The thick line is for the [111] set of inducers. **d**, 4-input AND gate. **e**, The output fluorescence for different combinations of inputs. The four inducers used for the on input were Ara (5 mM), IPTG (0.1 mM), 3OC6 (5  $\mu$ M) and aTc (10 ng ml<sup>-1</sup>). **f**, Raw cytometry data for all input states. The thick line is for [111].



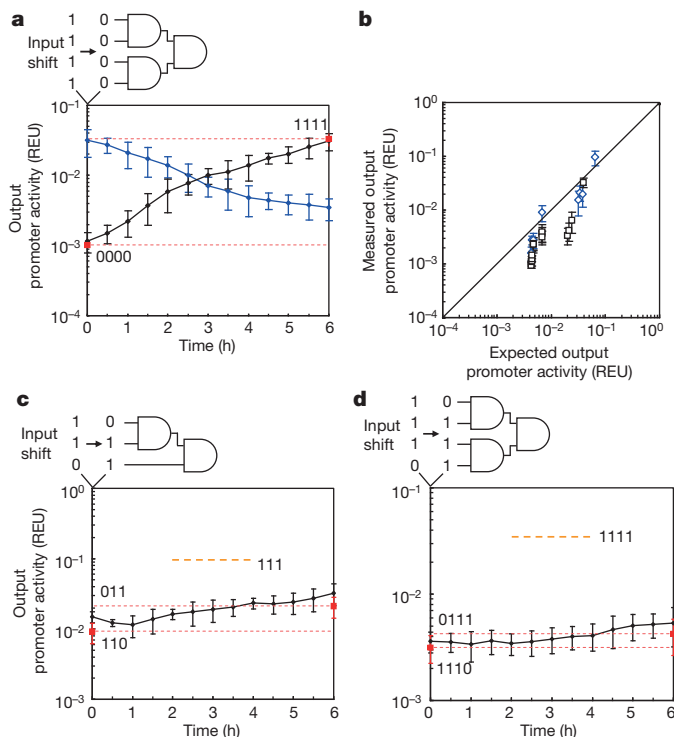


**Figure 5 | Performance of genetic programs.** **a**, The dynamic behaviour for the induction and relaxation of the 4-input program. The input states were switched either [0000] to [1111] (at  $D_{600} = 0.25$ ; black diamonds) or [1111] to [0000] (at  $D_{600} = 0.05$ ; blue diamonds). The off and on states are shown as a reference (red dashed lines, values from Fig. 4). **b**, A comparison for the output 'expected' from combining the independently measured transfer functions of each gate with that 'measured' in the final context. Each data point is from a different combination of inducers for the 3-input (blue diamonds) and 4-input (black squares) programs. The line shown is  $y = x$ . **c**, The dynamic behaviour for the 3-input gate switching from [110] to [011] (at  $D_{600} = 0.25$ ). The input states are listed as [Ara IPTG aTc]. **d**, The dynamic behaviour for the 4-input gate switching from [1110] to [0111]. The input states are listed as [Ara IPTG 3OC6 aTc]. The four inducer concentrations used for the on input for the 3- and 4-input AND gate were Ara (5 mM), IPTG (0.1 mM), 3OC6 (5  $\mu$ M) and aTc (10 ng ml $^{-1}$ ). The on state is shown as a reference (orange dashed lines). The red dashed lines indicate the steady-state outputs for the corresponding inputs (Fig. 4). The error bars show s.d. calculated on the basis of three replicates performed on different days.

response of the programs. This was then compared with the measured values (Fig. 4b, e). Both programs behaved as expected for all of the input states (Fig. 5b).

A potential problem in layering genetic logic gates is that the resulting programs are asynchronous<sup>19</sup>. In other words, there is no clock that synchronizes the progression of the signal between gates. Because there are delays at each layer, this can lead to transient errors in the output, known as faults<sup>20</sup>. This is a well-studied phenomenon in electronic systems. A fault can occur when a signal is divided and then one branch skips a layer (for example, in Fig. 4a the pTet input signal skips the first layer). Because the on signal reaches the next layer faster than the other, the gate at the second layer will transiently respond to the wrong state of input signals. This phenomenon is related to pulses that can occur in incoherent feedforward loops in signalling networks<sup>21</sup>.

Genetic programs composed of layered transcriptional circuits could be susceptible to faults because there can be delays between layers (about 20–40 min)<sup>22</sup> and the dynamics of each circuit consists of mixed timescales<sup>21</sup>. A simple kinetic model was used to determine the condition for faults to occur (Supplementary Information). Considering an AND gate consisting of two proteins  $x$  and  $y$ , large faults occur when the delay time

$$t_d > \frac{\gamma_x \gamma_y}{K \alpha_x \alpha_y \gamma_g},$$

where  $K$  is the association constant of  $x$  and  $y$  to each other and DNA,  $\alpha$  is the expression rate,  $\gamma$  is the degradation rate and  $\gamma_g$  is the degradation rate of the reporter protein. For typical values ( $K = 0.001$  nM $^{-2}$ ,  $\alpha = 10$  nM min $^{-1}$  and  $\gamma_g = 0.01$  min $^{-1}$ ), avoiding a fault due to a 30-min delay (about one layer) requires degradation half-times to be faster than about 20 min. When binding cooperativity is included, this further decreases the magnitude of the fault.

We designed experiments to measure faults that could occur in the 3-input and 4-input AND gates. In particular, the 3-input gate (Fig. 4a) has the potential for a fault when shifting from a +Ara/+IPTG/−aTc [110] to a [011] state (removal of Ara and addition of aTc). Both of these states should correspond to an off output, so when the inputs are changed, the output should stay off. However, there is the potential for a fault because the pTet inducible system could turn on faster than the first AND gate (MxiE-IpgC) turns off. There is also the potential for the SicA\* protein to persist if it were to degrade slowly, even after the gate has been turned off. Thus, a fault would occur and the output (RFP) would be expressed until the first gate is inactivated and SicA\* degrades. No such fault is observed when cells are shifted between these input states (Fig. 5c). This implies that the chaperones degrade more quickly than the transcription factors are expressed. Similar experiments with the 4-input gate (Fig. 5d) also failed to show any faults. This may become a larger issue as the size of the program and the number of circuits increases, which could yield higher-order effects on the cell<sup>23</sup>.

This work represents the design of genetic circuits with the intent to be scalable; in other words, an underlying architecture chosen to use part classes can easily be diversified to build orthogonal gates. Part mining proved valuable to expand the number of gates, but it was also necessary to apply directed evolution to tune their properties functionally. Once characterized, the circuits were combined in different permutations to build programs. The largest program required 11 regulatory proteins and 38 additional genetic parts, all of which were encoded in 21 kilobases on three plasmids. Building larger integrated circuits will require new tools, including computer-aided design<sup>24</sup>, a better understanding of how circuits interact with each other and affect the host<sup>17,25</sup>, and methods to minimize the impact of environment, evolution and genetic context on circuit performance.

## METHODS SUMMARY

**Strains, plasmids and growth media.** *E. coli* DH10B was used for all the experiments and grown in Luria–Bertani (LB) medium (Miller, BD Biosciences). Kanamycin (20  $\mu$ g ml $^{-1}$ ), ampicillin (100  $\mu$ g ml $^{-1}$ ) and chloramphenicol (34  $\mu$ g ml $^{-1}$ ) were added as appropriate. Four inducers were obtained from Sigma Aldrich: Ara (Arabinose), IPTG (isopropyl  $\beta$ -D-1-thiogalactopyranoside), 3OC6 (*N*-( $\beta$ -ketocaproyl)-L-homoserine lactone) and aTc (anhydrotetracycline). All the newly constructed plasmids were made by the one-step isothermal DNA assembly method as described previously<sup>26</sup>.

**Part mutagenesis.** Promoter regions were modified by saturation mutagenesis. To construct the promoter libraries, the bases were randomized by using oligonucleotides (Integrated DNA Technologies) as shown in Supplementary Fig. 3. After PCR reactions, the blunt ends were ligated with T4 DNA ligase (New England BioLabs) to give the mixture of the modified plasmids. To obtain *sicA* variants, error-prone PCR was performed. Random mutations were introduced by PCR reactions with 1  $\times$  PCR buffer supplemented with 7 mM MgCl<sub>2</sub>, 0.3 mM MnCl<sub>2</sub>, 0.2 mM dATP, 0.2 mM dGTP, 1 mM dCTP, 1 mM dTTP and 0.05 U *Taq* DNA polymerase (Invitrogen). The detailed methods including library screening are described in Supplementary Methods.

**Flow cytometry.** *E. coli* was grown overnight in LB medium at 37 °C and then transferred to fresh LB medium in 96-well plates (USA Scientific). Each culture (0.6 ml) was induced at a  $D_{600}$  of 0.5 (unless otherwise specified) with inducers of different concentrations as indicated, and flow cytometer data were obtained using an LSRII flow cytometer (BD Biosciences). All the data were gated by forward and side scatter, and each data consists of at least 10,000 cells. The arithmetic mean fluorescence was calculated with FlowJo (TreeStar Inc.), and the averages of means were obtained from three replicates performed on different days.

Received 2 February; accepted 15 August 2012.

Published online 7 October 2012.

1. Khalil, A. S. & Collins, J. J. Synthetic biology: applications come of age. *Nature Rev. Genet.* **11**, 367–379 (2010).
2. Lucks, J. B., Qi, L., Mutalik, V. K., Wang, D. & Arkin, A. P. Versatile RNA-sensing transcriptional regulators for engineering genetic networks. *Proc. Natl Acad. Sci. USA* **108**, 8617–8622 (2011).
3. Anderson, J. C., Voigt, C. A. & Arkin, A. P. Environmental signal integration by a modular AND gate. *Mol. Syst. Biol.* **3**, 133 (2007).
4. Wang, B., Kitney, R. I., Joly, N. & Buck, M. Engineering modular and orthogonal genetic logic gates for robust digital-like synthetic biology. *Nature Commun.* **2**, 508, <http://dx.doi.org/10.1038/ncomms1516> (2011).
5. Danino, T., Mondragon-Palomino, O., Tsimring, L. & Hasty, J. A synchronized quorum of genetic clocks. *Nature* **463**, 326–330 (2010).
6. Basu, S., Mehreja, R., Thiberge, S., Chen, M. T. & Weiss, R. Spatiotemporal control of gene expression with pulse-generating networks. *Proc. Natl Acad. Sci. USA* **101**, 6355–6360 (2004).
7. Purnick, P. E. & Weiss, R. The second wave of synthetic biology: from modules to systems. *Nature Rev. Mol. Cell Biol.* **10**, 410–422 (2009).
8. Canton, B., Labno, A. & Endy, D. Refinement and standardization of synthetic biological parts and devices. *Nature Biotechnol.* **26**, 787–793 (2008).
9. Galan, J. E. & Collmer, A. Type III secretion machines: bacterial devices for protein delivery into host cells. *Science* **284**, 1322–1328 (1999).
10. Galan, J. E. & Curtiss, R. Cloning and molecular characterization of genes whose products allow *Salmonella typhimurium* to penetrate tissue culture cells. *Proc. Natl Acad. Sci. USA* **86**, 6383–6387 (1989).
11. Darwin, K. H. & Miller, V. L. Type III secretion chaperone-dependent regulation: activation of virulence genes by SicA and InvF in *Salmonella typhimurium*. *EMBO J.* **20**, 1850–1862 (2001).
12. Mavris, M., Sansonetti, P. J. & Parsot, C. Identification of the *cis*-acting site involved in activation of promoters regulated by activity of the type III secretion apparatus in *Shigella flexneri*. *J. Bacteriol.* **184**, 6751–6759 (2002).
13. Walker, K. A. & Miller, V. L. Regulation of the Ysa type III secretion system of *Yersinia enterocolitica* by YsaE/SycB and YsrS/YsrR. *J. Bacteriol.* **186**, 4056–4066 (2004).
14. Thibault, J., Faudry, E., Ebel, C., Attree, I. & Elsen, S. Anti-activator ExsD forms a 1:1 complex with ExsA to inhibit transcription of type III secretion operons. *J. Biol. Chem.* **284**, 15762–15770 (2009).
15. Temme, K., Zhao, D. & Voigt, C. A. Refactoring the nitrogen fixation gene cluster from *Klebsiella oxytoca*. *Proc. Natl Acad. Sci. USA* **109**, 7085–7090 (2012).
16. Kelly, J. R. *et al.* Measuring the activity of BioBrick promoters using an *in vivo* reference standard. *J. Biol. Eng.* **3**, 4 (2009).
17. Tan, C., Marguet, P. & You, L. Emergent bistability by a growth-modulating positive feedback circuit. *Nature Chem. Biol.* **5**, 842–848 (2009).
18. Arkin, A. Setting the standard in synthetic biology. *Nature Biotechnol.* **26**, 771–774 (2008).
19. Harold, A. *et al.* Amorphous computing. *Commun. ACM* **43**, 74–82 (2000).
20. Katz, R. H. & Borriello, G. *Contemporary Logic Design* (Prentice Hall, 1994).
21. Mangan, S. & Alon, U. Structure and function of the feed-forward loop network motif. *Proc. Natl Acad. Sci. USA* **100**, 11980–11985 (2003).
22. Hooshangi, S., Thiberge, S. & Weiss, R. Ultrasensitivity and noise propagation in a synthetic transcriptional cascade. *Proc. Natl Acad. Sci. USA* **102**, 3581–3586 (2005).
23. Cookson, N. A. *et al.* Queueing up for enzymatic processing: correlated signaling through coupled degradation. *Mol. Syst. Biol.* **7**, 561 (2011).
24. Clancy, K. & Voigt, C. A. Programming cells: towards an automated ‘Genetic Compiler’. *Curr. Opin. Biotechnol.* **21**, 572–581 (2010).
25. Del Vecchio, D., Ninfa, A. J. & Sontag, E. D. Modular cell biology: retroactivity and insulation. *Mol. Syst. Biol.* **4**, 161 (2008).
26. Gibson, D. G. *et al.* Enzymatic assembly of DNA molecules up to several hundred kilobases. *Nature Methods* **6**, 343–345 (2009).
27. Marlovits, T. C. *et al.* Structural insights into the assembly of the type III secretion needle complex. *Science* **306**, 1040–1042 (2004).
28. Temme, K. *et al.* Induction and relaxation dynamics of the regulatory network controlling the type III secretion system encoded within *Salmonella* pathogenicity island 1. *J. Mol. Biol.* **377**, 47–61 (2008).

**Supplementary Information** is available in the online version of the paper.

**Acknowledgements** C.A.V. is supported by Life Technologies, Defense Advanced Research Projects Agency Chronicle of Lineage Indicative of Origins (DARPA; CLIO N66001-12-C-4018), the Office of Naval Research (N00014-10-1-0245), the National Science Foundation (NSF; CCF-0943385), the National Institutes of Health (AI067699) and the NSF Synthetic Biology Engineering Research Center (SynBERC; SA5284-11210). The content of the information does not necessarily reflect the position or the policy of the Government, and no official endorsement should be inferred.

**Author Contributions** T.S.M. designed and performed the experiments, analysed the data, developed the computational models and wrote the manuscript. C.L. developed the computational models. A.T. analysed the data. B.C.S. performed experiments. C.A.V. designed experiments, analysed the data, developed the computational models and wrote the manuscript.

**Author Information** Reprints and permissions information is available at [www.nature.com/reprints](http://www.nature.com/reprints). The authors declare no competing financial interests. Readers are welcome to comment on the online version of the paper. Correspondence and requests for materials should be addressed to C.A.V. ([cavoigt@gmail.com](mailto:cavoigt@gmail.com)).

# Adenoma-linked barrier defects and microbial products drive IL-23/IL-17-mediated tumour growth

Sergei I. Grivennikov<sup>1\*</sup>, Kepeng Wang<sup>1,2\*</sup>, Daniel Mucida<sup>3,4</sup>, C. Andrew Stewart<sup>5</sup>, Bernd Schnabl<sup>6</sup>, Dominik Jauch<sup>1</sup>, Koji Taniguchi<sup>1,7</sup>, Guann-Yi Yu<sup>1</sup>, Christoph H. Österreicher<sup>6,8</sup>, Kenneth E. Hung<sup>9</sup>, Christian Datz<sup>10</sup>, Ying Feng<sup>11</sup>, Eric R. Fearon<sup>11</sup>, Mohamed Oukka<sup>12</sup>, Lino Tessarollo<sup>13</sup>, Vincenzo Coppola<sup>14</sup>, Felix Yarovinsky<sup>15</sup>, Hilde Cheroutre<sup>3</sup>, Lars Eckmann<sup>6</sup>, Giorgio Trinchieri<sup>5</sup> & Michael Karin<sup>1</sup>

Approximately 2% of colorectal cancer is linked to pre-existing inflammation known as colitis-associated cancer, but most develops in patients without underlying inflammatory bowel disease. Colorectal cancer often follows a genetic pathway whereby loss of the adenomatous polyposis coli (*APC*) tumour suppressor and activation of  $\beta$ -catenin are followed by mutations in *K-Ras*, *PIK3CA* and *TP53*, as the tumour emerges and progresses<sup>1,2</sup>. Curiously, however, 'inflammatory signature' genes characteristic of colitis-associated cancer are also upregulated in colorectal cancer<sup>3,4</sup>. Further, like most solid tumours, colorectal cancer exhibits immune/inflammatory infiltrates<sup>5</sup>, referred to as 'tumour-elicited inflammation'<sup>6</sup>. Although infiltrating CD4<sup>+</sup> T<sub>H</sub>1 cells and CD8<sup>+</sup> cytotoxic T cells constitute a positive prognostic sign in colorectal cancer<sup>7,8</sup>, myeloid cells and T-helper interleukin (IL)-17-producing (T<sub>H</sub>17) cells promote tumorigenesis<sup>5,6</sup>, and a 'T<sub>H</sub>17 expression signature' in stage I/II colorectal cancer is associated with a drastic decrease in disease-free survival<sup>9</sup>. Despite its pathogenic importance, the mechanisms responsible for the appearance of tumour-elicited inflammation are poorly understood. Many epithelial cancers develop proximally to microbial communities, which are physically separated from immune cells by an epithelial barrier<sup>10</sup>. We investigated mechanisms responsible for tumour-elicited inflammation in a mouse model of colorectal tumorigenesis, which, like human colorectal cancer, exhibits upregulation of IL-23 and IL-17. Here we show that IL-23 signalling promotes tumour growth and progression, and development of a tumoural IL-17 response. IL-23 is mainly produced by tumour-associated myeloid cells that are likely to be activated by microbial products, which penetrate the tumours but not adjacent tissue. Both early and late colorectal neoplasms exhibit defective expression of several barrier proteins. We propose that barrier deterioration induced by colorectal-cancer-initiating genetic lesions results in adenoma invasion by microbial products that trigger tumour-elicited inflammation, which in turn drives tumour growth.

Specimens of human colorectal cancer (CRC) show increased expression of IL-23p19 and IL-17A messenger RNA (mRNAs) (Fig. 1a). IL-23p19 is the specific subunit of IL-23, a positive regulator of T<sub>H</sub>17 and other IL-17-producing cells<sup>11</sup>, previously found to promote skin carcinogenesis<sup>12</sup>. To address the role of these cytokines in CRC-related tumour-elicited inflammation and tumour growth, we

used *Apc*<sup>F/wt</sup> mice that harboured a *Cdx2-Cre* transgene (CPC-APC mice) in which colorectal tumorigenesis was driven by *Apc* allelic loss<sup>13</sup>. Unlike *Apc*<sup>Min</sup> mice, CPC-APC mice develop tumours primarily in the distal colon, providing a relevant model of human CRC<sup>13</sup>. Mouse colon tumours also exhibited marked upregulation of IL-23 and IL-17A mRNA and IL-23 protein relative to matched non-tumour colon (Fig. 1b, c). IL-23 induction was specific, as tumoural expression of other IL-12/23 family members was not substantially elevated and IL-23 itself was already seen in early tumours (Supplementary Fig. 1a, b). IL-23 expression did not further increase in more advanced mouse CRC caused by *Apc* loss and forced *K-Ras* or *B-Raf* activation (Supplementary Fig. 1c). Analysis of *Il23*<sup>-/-</sup> mice harbouring green fluorescent protein (GFP) gene in the *Il23p19* locus, staining with IL-23p19 antibody and flow cytometry showed that IL-23p19 is particularly expressed in tumour-infiltrating cells such as CD11b<sup>+</sup> and F4/80<sup>+</sup> myeloid cells (Supplementary Fig. 1d–f). Both IL-23 subunits, p19 and p40, need to be simultaneously expressed to generate a functional cytokine. Analysis by quantitative PCR with reverse transcription (RT-qPCR) and fluorescence-activated cell sorting (FACS) of tumoural cell populations showed that CD11b<sup>+</sup> cells expressed substantial amounts of both p19 and p40 (Fig. 1d). T<sub>H</sub>17- and other IL-17-producing cells were detected in mesenteric lymph nodes and tumours of CPC-APC mice and demonstrated dependence on IL-23 signalling (Fig. 1e). Thus, expression of IL-23 and its downstream target IL-17A is increased during spontaneous colorectal tumorigenesis.

Colorectal tumour multiplicity and growth were diminished upon ablation of IL-23 or IL-23R in CPC-APC mice (Fig. 1f, g and Supplementary Fig. 2a). Although intra-tumoural apoptosis was unaffected, cancer cell proliferation was reduced in *Il23*<sup>-/-</sup>/CPC-APC mice (Supplementary Fig. 2b, c). Epithelial STAT3 phosphorylation was decreased without IL-23, but genetically driven nuclear  $\beta$ -catenin accumulation was unaffected (Fig. 1g and Supplementary Fig. 2d). IL-23 signalling was important for intra-tumoural production of downstream cytokines, which are either direct (IL-6, IL-22) or indirect (IL-17A) STAT3 activators (Fig. 1h). Pro-tumorigenic IL-23 signalling was particularly confined to the haematopoietic compartment, as CPC-APC chimaeras harbouring *Il23*<sup>-/-</sup> or *Il23*<sup>tg/tg</sup> bone marrow also exhibited reduced tumour load (Supplementary Fig. 3a–d) and diminished expression of IL-23-dependent cytokines (Supplementary Fig. 3e). To examine the role of IL-17 signalling in CRC tumorigenesis,

<sup>1</sup>Laboratory of Gene Regulation and Signal Transduction, Departments of Pharmacology and Pathology, School of Medicine, University of California, San Diego, 9500 Gilman Drive, La Jolla, California 92093-0723, USA. <sup>2</sup>Biomedical Research Institute, Shenzhen-PKU-HKUST Medical Center, No. 1120, Lianhua Road, Shenzhen, Guangdong Province, China. <sup>3</sup>La Jolla Institute for Allergy and Immunology, La Jolla, California 92093, USA. <sup>4</sup>Laboratory of Mucosal Immunology, The Rockefeller University, New York, New York 10065, USA. <sup>5</sup>Cancer and Inflammation Program, Laboratory of Experimental Immunology, Center for Cancer Research, National Cancer Institute, National Institutes of Health, Frederick, Maryland 21702-1201, USA. <sup>6</sup>Department of Medicine, School of Medicine, University of California, San Diego, 9500 Gilman Drive, La Jolla, California 92093-0723, USA. <sup>7</sup>Department of Microbiology and Immunology, Keio University School of Medicine, Tokyo 160-8582, Japan. <sup>8</sup>Institute of Pharmacology, Center for Physiology and Pharmacology Medical University of Vienna, Vienna, Austria. <sup>9</sup>Department of Medicine, Tufts Medical Center, Boston, Massachusetts 02111, USA. <sup>10</sup>Department of Internal Medicine, Oberndorf Hospital, Paracelsus Medical University, Salzburg, Austria. <sup>11</sup>Departments of Internal Medicine, Human Genetics and Pathology, University of Michigan Medical School, Ann Arbor, Michigan 48109, USA. <sup>12</sup>Seattle Children's Research Institute, Seattle, Washington 98105, USA. <sup>13</sup>Mouse Cancer Genetics Program, National Cancer Institute, National Institutes of Health, Frederick, Maryland 21702-1201, USA. <sup>14</sup>Department of Molecular Virology, Immunology & Medical Genetics, Ohio State University Comprehensive Cancer Center, Wexner Medical Center, Columbus, Ohio 43210, USA. <sup>15</sup>Department of Immunology, University of Texas Southwestern Medical Center at Dallas, Dallas, Texas 75390, USA.

\*These authors contributed equally to this work.



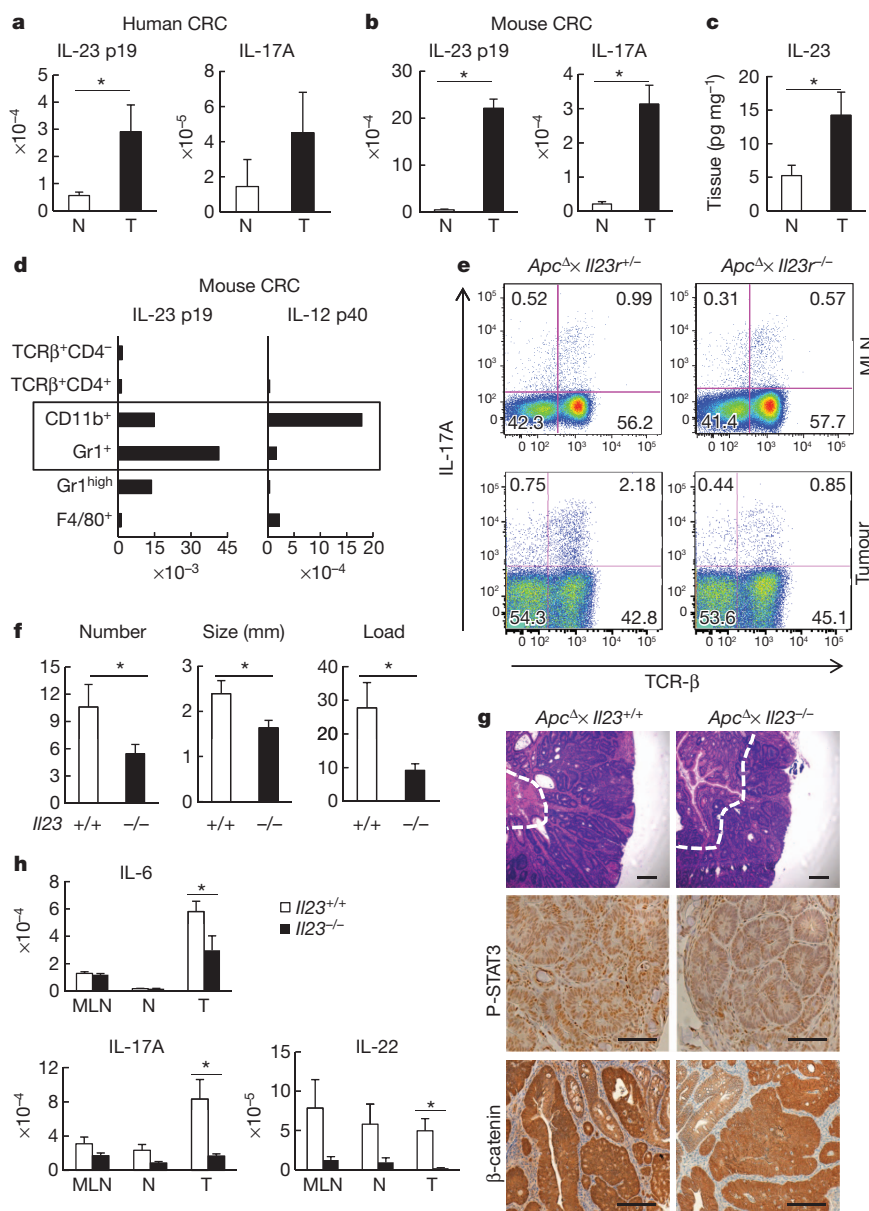


**Figure 1 | IL-23 controls CRC inflammation and tumorigenesis.** **a, b**, RT-qPCR for IL-23p19 and IL-17A mRNAs from colorectal tumours (T) and matching normal (N) colons of **(a)** human CRC patients ( $n = 7$ ,  $P = 0.037$  for IL-23p19) or **(b)** CPC-APC mice ( $n = 8$ ,  $P = 5 \times 10^{-5}$ ,  $3.6 \times 10^{-4}$ , respectively). **c**, IL-23 protein was measured by ELISA in supernatants of cultured tumours and normal tissues of CPC-APC mice ( $n = 5$ ,  $P = 0.04$ ). **d**, RT-qPCR analysis of sorted haematopoietic myeloid cells ( $\text{CD45}^{+}\text{TCR}\beta^{-}\text{CD11b}^{+}$ ) from tumours of CPC-APC mice ( $n = 4$ ; pooled); populations:  $\text{CD11b}^{+} = \text{Gr1}^{-}\text{F4/80}^{\text{low}}$ ;  $\text{Gr1}^{+} = \text{Gr1}^{+}\text{F4/80}^{-}$ ;  $\text{Gr1}^{\text{high}} = \text{Gr1}^{\text{high}}\text{F4/80}^{-}$ ;  $\text{F4/80}^{+} = \text{Gr1}^{-}\text{F4/80}^{+}$  and T cells

( $\text{CD45}^{+}\text{TCR}\beta^{+}$ ). **e**, Intracellular cytokine staining of phorbol myristate acetate and ionomycin re-stimulated cells (Live/Dead<sup>+</sup>  $\text{CD45}^{+}$  gate). **f**, Five-month-old  $\text{Il23}^{-/-}$  and control CPC-APC mice were killed and tumour numbers, size and load were determined ( $n = 7$ ,  $P = 0.04$ ,  $0.03$ ,  $0.01$ , respectively). **g**, Tumour sections were stained with haematoxylin and eosin or phospho-STAT3 and  $\beta$ -catenin antibodies. **h**, Cytokine mRNA analysis by RT-qPCR in mesenteric lymph nodes (MLN), normal (N) and tumour (T) tissue of 5-month-old  $\text{Il23}^{-/-}$  and control CPC-APC mice ( $n = 6$ ,  $P = 0.044$ ,  $0.007$ ,  $0.045$ , respectively). Data represent averages  $\pm$  s.e.m.  $*P < 0.05$ . Scale bars,  $100 \mu\text{m}$ .

we crossed CPC-APC mice with  $\text{Il17ra}^{-/-}$  mice, which do not respond to either IL-17A or IL-17F. Both tumour multiplicity and growth were reduced in the absence of IL-17A (Supplementary Fig. 4a–c).

We examined the cause of IL-23 upregulation in CRC. The commensal microflora regulates basal colonic IL-23 expression in naive mice<sup>14</sup>. Microbial products are sensed by Toll-like receptors (TLRs), which rely on the adaptors MyD88 and TRIF<sup>15</sup>. Similar to its effect on small intestinal polyps in  $\text{Apc}^{\text{Min}}$  mice<sup>16</sup>, whole body MyD88 ablation reduced tumour multiplicity and growth in CPC-APC mice (data not shown). We transplanted  $\text{Myd88}^{-/-}$ ,  $\text{Tr2,4,9}^{-/-}$  triple knockout or control bone marrow into lethally irradiated CPC-APC mice. Expression of IL-23p19 mRNA by sorted tumoural myeloid cells

was decreased upon TLR/MyD88 inactivation in the haematopoietic compartment (Fig. 2a). Intratumoural expression of IL-6 and IL-17A was also dependent on MyD88 in bone-marrow-derived cells (Fig. 2b). Transplantation with  $\text{Myd88}^{-/-}$  or  $\text{Tr2,4,9}^{-/-}$  bone marrow reduced colorectal tumour growth (Fig. 2c and Supplementary Fig. 5). By contrast, deletion of IL-18R in bone marrow had no effect on tumorigenesis or IL-23 production by TAM (Supplementary Fig. 6a, b). Short-term depletion of intestinal microflora with a combination of broad-spectrum antibiotics, which reduced microbial counts by over 99.9%, also inhibited IL-23 expression by TAM, resulting in reduced tumoural IL-17A and decreased STAT3 activation in cancer cells (Fig. 2d–f). Prolonged depletion of commensal microflora by antibiotic treatment

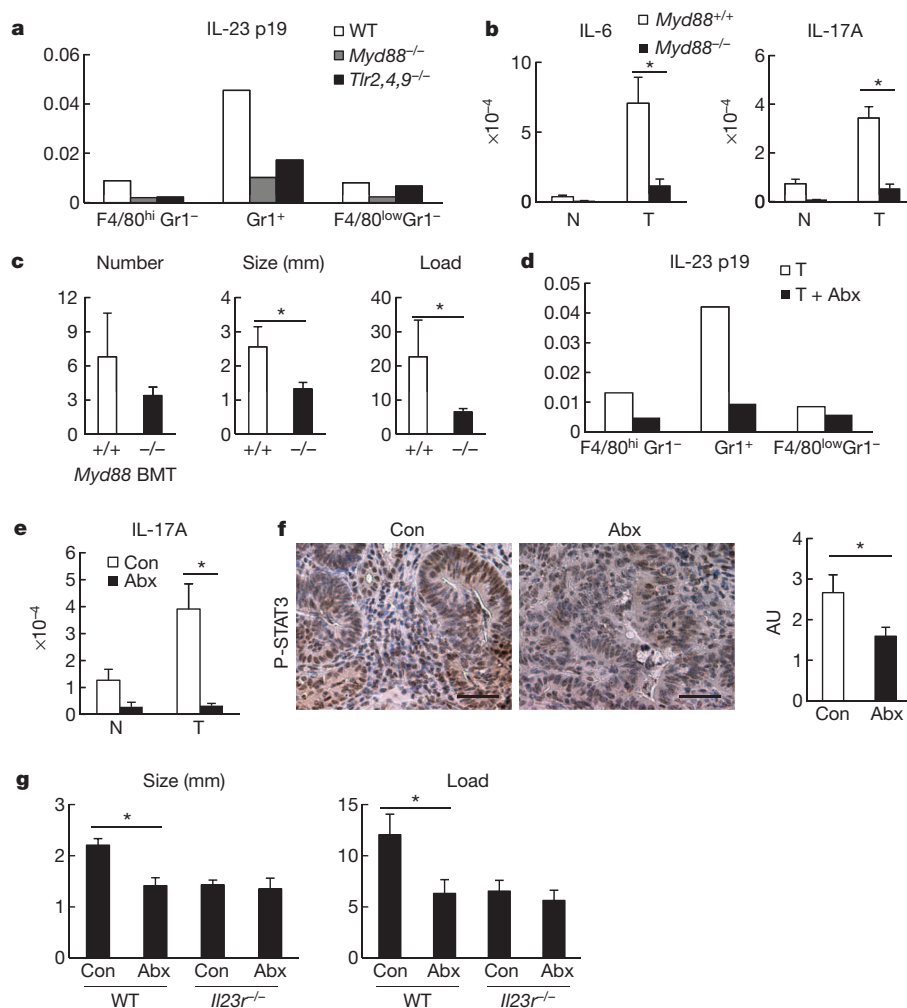


**Figure 2 | TLR-MyD88 signalling and commensal microflora promote cytokine expression and tumorigenesis.** **a–c**, CPC-APC mice were transplanted with *Myd88*<sup>-/-</sup>, *Tlr2,4,9*<sup>-/-</sup> or control bone marrow (BM) and analysed 4 months later by RT-qPCR for cytokine mRNAs in sorted tumour myeloid cells (Live/Dead<sup>-</sup> TCRβ<sup>-</sup> CD11b<sup>+</sup>), representative of two independent experiments, each including four pooled mice (**a**) or in tumours and normal tissues ( $n = 5$ ,  $P = 0.004$ ,  $0.032$ ) (**b**). **c**, Tumour number, size and load in mice transplanted with indicated bone marrow ( $n = 5$ ,  $P = 0.14$ ,  $0.048$ ,  $0.046$ , respectively). BMT, bone marrow transfer. **d–f**, CPC-APC mice were treated with

a cocktail of antibiotics (Abx) for 3 weeks. **d**, Myeloid cells were sorted from tumours and analysed by RT-qPCR, representative of two independent experiments, each including four pooled mice. **e**, IL-17A mRNA expression in normal and tumour tissues from the control and Abx-treated CPC-APC mice ( $n = 9$ ,  $P = 0.003$ ). **f**, Colon sections from mice were stained with phospho-STAT3 antibody, and intensity of staining was quantified ( $n = 8$ ,  $P = 0.049$ ). **g**, WT (*Il23r*<sup>+/+</sup>) or *Il23r*<sup>-/-</sup> CPC-APC mice were treated with antibiotics for 3.5 months and tumour size and load were determined ( $n = 5$ ,  $P = 0.027$  and  $0.043$ ). Data represent averages  $\pm$  s.e.m. \* $P < 0.05$ . Scale bars, 50  $\mu$ m.

for 3.5 months starting at weaning reduced tumour size and load in control CPC-APC mice but not in *Il23r*<sup>-/-</sup>/CPC-APC counterparts (Fig. 2g), emphasizing the importance of microbial product-driven IL-23 signalling.

By injecting fluorescein isothiocyanate (FITC)-labelled dextran into clamped colonic loops, we found that tumour development in CPC-APC mice was associated with translocation of FITC-dextran into the circulation (Fig. 3a). This suggested that CRC development may result in increased penetration of microbial products or microbes into tumours. Indeed, Alexa488-labelled lipopolysaccharide (LPS) injected into colonic loops of CPC-APC mice translocated into tumours where it particularly co-localized with F4/80<sup>+</sup> TAMs, but did not penetrate adjacent normal tissue (Fig. 3b). Tumour development also coincided with elevated endotoxin in portal blood (Fig. 3c). Occasional bacteria were detected by *in situ* hybridization with a eubacterial 16S ribosomal RNA (rRNA) probe within colorectal tumours (Fig. 3d) and proximal to tumour epithelial cells in mouse early lesions that resembled aberrant crypt foci and early human adenomas (Fig. 3e, f).

Mucus from goblet cells prevents bacterial penetration through the colonic epithelial barrier. Correspondingly, *Muc2*<sup>-/-</sup> mice develop

spontaneous colitis followed by colitis-associated cancer<sup>17,18</sup>. Periodic acid-Schiff staining indicated absence of mucus-producing cells and mucins in tumours but not in adjacent normal tissue (Fig. 4a). Staining with wheat germ agglutinin (WGA) for glycosylated mucus proteins and mucin 2 (Muc2)-specific antibody demonstrated markedly reduced Muc2 production and coating of tumour tissue (Fig. 4a). Muc2 was barely detected in human CRC, but was prominent in adjacent normal tissues (Fig. 4b). Muc2 mRNA was downregulated in human and mouse colorectal tumours relative to healthy tissues (Supplementary Fig. 7a, b). Epithelial barriers also depend on tight and adherent junctions<sup>10</sup>. Human CRC demonstrated notable loss of polarized expression of junctional proteins JAM-A and JAM-B (Fig. 4c). JAM-A/B mRNAs were also reduced in human CRC and JAM-C mRNA was downregulated in mouse tumours (Supplementary Fig. 7a, b). Although claudin 4 mRNA was not downregulated in human or mouse tumours (Supplementary Fig. 7a, b), the protein was no longer distinctly localized to tight junctions in human or mouse tumours, similar to claudins 3, 5 and 7 (Supplementary Fig. 8a, b). Early human adenomas also showed defective mucin expression and organization of tight junctions (Fig. 4d), coinciding with elevated IL-23

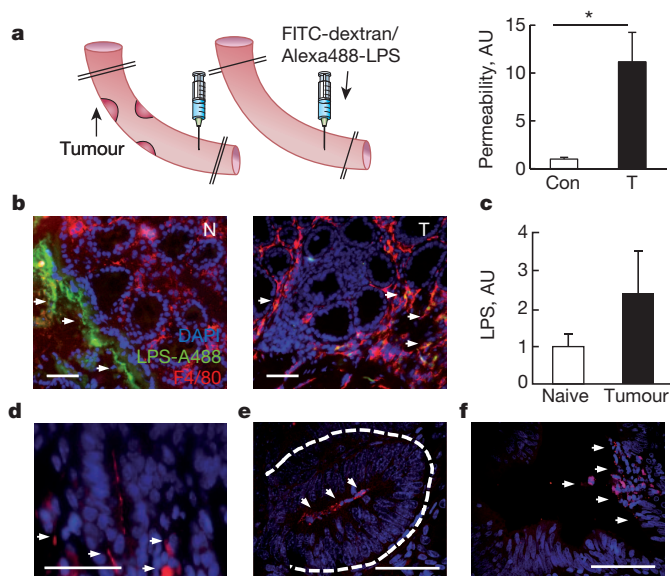


**Figure 3 | Colorectal tumours exhibit increased permeability to bacteria and their products.** **a**, Colon segments of CPC-APC and control mice were clipped as indicated and their lumens injected with FITC-dextran or Alexa488-LPS. FITC fluorescence was measured in plasma 1 h later ( $n = 7$ ,  $P = 0.017$ ). **b**, Frozen colon sections prepared 30 min after Alexa488-LPS injection were stained with F4/80 antibody and DAPI and examined by fluorescent microscopy. **c**, Endotoxin was measured in portal blood of naive or tumour-bearing CPC-APC mice by *Limulus* bioassay ( $n = 9$ ,  $P = 0.066$ ). **d–f**, Colon sections from CPC-APC mice containing tumours (**d**) and early lesions (aberrant crypt foci) (**e**), and early human adenomas (**f**) were subjected to fluorescent *in situ* hybridization with eubacterial 16S-rRNA-specific Alexa594-labelled probe and stained with DAPI. Signals are indicated by the arrows. Data represent averages  $\pm$  s.e.m. \* $P < 0.05$ . Scale bars, 50  $\mu$ m.

and IL-17A in adenoma tissue (Supplementary Fig. 9a). Early CRC lesions, such as aberrant crypt foci, are marked by enhanced expression and nuclear translocation of  $\beta$ -catenin, and such areas were devoid of WGA and JAM-A staining (Fig. 4e). To demonstrate further that barrier loss is an early and direct consequence of tumour emergence, we studied rapid colonic transformation in *Cdx2*<sup>ERT-Cre</sup>  $\times$  *Apc*<sup>F/F</sup> mice using tamoxifen to induce bi-allelic APC inactivation. APC loss resulted in patches of proliferating transformed cells with enlarged nuclei, which coincided with loss of mucin and induction of IL-23 (Fig. 4f and Supplementary Fig. 9b).

Nearly all solid malignancies contain inflammatory infiltrates, influencing tumour promotion, progression and metastasis<sup>5,6</sup>. The contribution of inflammation to CRC pathogenesis is emphasized by the protective effect of non-steroidal anti-inflammatory drugs, such as aspirin<sup>19</sup>, but sources of tumour-elicited inflammation in CRC were heretofore unknown. We now suggest that early CRC-inducing genetic events may cause local loss of barrier function and entry of microbial products into the tumour microenvironment. This results in activation of IL-23-producing myeloid cells, which regulate expression of downstream tumour-promoting cytokines, including IL-17 and IL-6. A similar mechanism may apply to other cancers that develop in epithelia that are exposed to commensal and pathogenic bacteria. Deregulation of tight junctions and cell–cell contacts was described in advanced human adenocarcinomas, but suggested to cause detachment of carcinoma cells from their neighbours, increased motility and metastasis<sup>20</sup>. The importance of the mucus layer is emphasized by whole body Muc2 deficiency, which causes colonic inflammation<sup>17,18</sup>. Prolonged treatment with dextran sulphate sodium, which promotes development of colitis-associated cancer in wild type (WT) or *Apc*<sup>Min</sup> mice, also causes erosion of the intestinal epithelial barrier and microbial-dependent inflammation<sup>21,22</sup>, and so do the barrier-disrupting pathogens *Citrobacter rodentium*<sup>23</sup> and enterotoxigenic *Bacteroides fragilis*<sup>24</sup>. The

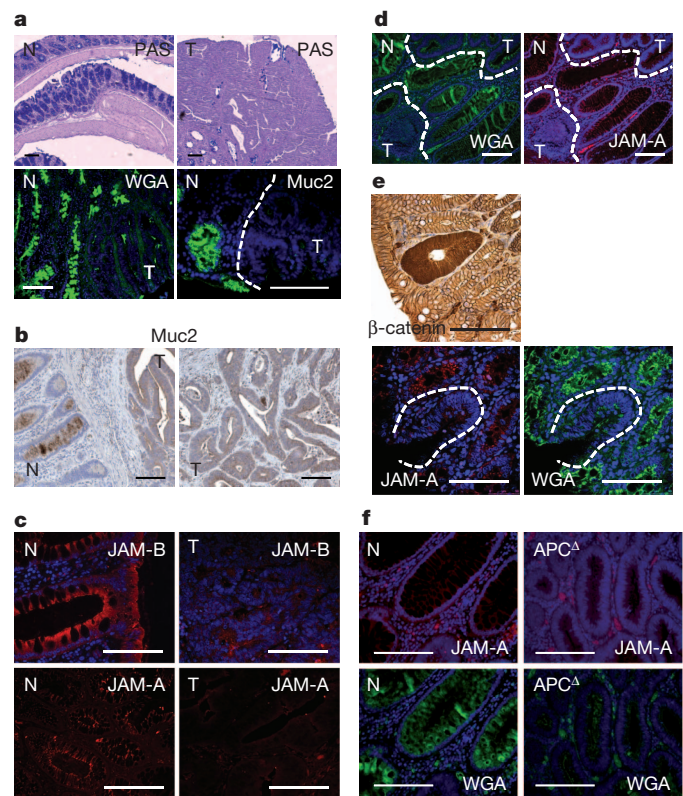


**Figure 4 | Colorectal tumours show defective mucin production and aberrant expression of junctional proteins.** **a**, Colon sections from CPC-APC mice were stained with periodic acid-Schiff reagent, Oregon488-WGA or mucin 2 antibody. Normal (N) and tumour (T) areas are depicted. **b, c**, Sections of normal human colon and adjacent CRC specimens were stained with mucin-2-specific antibody (**b**) or JAM-A or JAM-B antibodies (**c**). **d**, Human adenomas were stained with WGA or JAM-A antibodies. Normal and tumour areas are marked. **e**, Sections of CPC-APC colons were stained with  $\beta$ -catenin antibody and analysed by light microscopy or WGA and JAM-A antibodies and analysed by confocal microscopy. **f**, Colon sections of tamoxifen-injected control or *Cdx2*<sup>ERT-Cre</sup>  $\times$  *Apc*<sup>F/F</sup> mice were stained with JAM-A antibody or WGA. Normal (N) and APC-deleted areas are shown. Scale bars, 100  $\mu$ m.

commensal microflora was suggested to promote adenoma development, as germ-free *Apc*<sup>Min</sup> mice exhibit a twofold reduction in small intestinal adenomas<sup>25</sup> and *Tbx21*<sup>−/−</sup>; *Rag2*<sup>−/−</sup> ulcerative colitis (TRUC), and *Il10*<sup>−/−</sup> mice fail to develop colitis-associated cancer when rendered germ-free<sup>26,27</sup>. Our work demonstrates that defective expression of barrier proteins is an early event in CRC tumorigenesis, coupled to upregulation of IL-23 and its downstream cytokines. We also found that IL-23 does not act directly on adenoma cells and that its receptor is expressed and signals within the haematopoietic compartment. Probably, IL-23 acts through IL-17 family members, as ablation of IL-17R attenuated colorectal tumorigenesis. IL-23 is instrumental for stabilizing the ‘T<sub>H</sub>17 signature’, which includes IL-17A, ROR $\gamma$ t and IL-23R, and was linked to extremely poor prognosis in human stage I/II CRC, which otherwise show 75–90% survival<sup>9</sup>. IL-23 itself is not a part of the ‘T<sub>H</sub>17 signature’, arguably because its expression is already elevated in early colorectal tumours. The ‘IL-23/T<sub>H</sub>17’ and ‘T<sub>H</sub>17-cytotoxic’ signatures are not mutually exclusive in human CRC<sup>9</sup>. Although in genetically uniform mice in barrier facilities IL-23 invariably leads to IL-17 induction, the genetic heterogeneity of human populations and their exposure to a broader spectrum of microbes may explain why certain individuals mount a stronger T<sub>H</sub>17 response than others. T<sub>H</sub>17 development is promoted by several cytokines, including IL-21, IL-6 and IL-1, all of which can be induced by microbial components<sup>28</sup>. It remains to be investigated which of these cytokines contributes to the tumoural T<sub>H</sub>17 response and how it is



affected by distinct microflora components. Segmented filamentous bacteria persisting in proximity to epithelial cells initiate T<sub>H</sub>17 responses in the small intestine<sup>29</sup>. In tumours lacking protective barrier, other microbial species and products may invade the tumour and influence the 'IL-23/T<sub>H</sub>17' signature.

Loss of APC and activation of  $\beta$ -catenin induces a proliferative state and blocks the differentiation of certain IEC lineages, including mucin-producing goblet cells<sup>30</sup>. Epithelial barrier loss may therefore be a consequence of  $\beta$ -catenin activation and/or of APC loss, which apart from  $\beta$ -catenin can also control cytoskeleton dynamics. Hence, early barrier loss and activation of IL-23/IL-17-driven tumour-elicited inflammation act additively and sequentially to genetically controlled events that govern CRC development and progression (Supplementary Fig. 10). We propose that screening of early tumours for IL-17 expression and adjuvant treatment of patients showing a 'T<sub>H</sub>17 signature' with IL-23 or IL-17 antagonists should reduce mortality due to CRC.

## METHODS SUMMARY

Mice were backcrossed to the C57BL/6 background for at least seven (CPC-APC) or ten (others) generations and maintained and studied in filter-topped cages on autoclaved food and water in a barrier facility at the University of California, San Diego, according to institutional and National Institutes of Health (NIH) guidelines. Male and female mice were used in this study, including littermate and cage mate controls. *Il23r<sup>F/F</sup>* mice were generated by C.A.S., L.T., V.C. and G.T. (Supplementary Fig. 11). *Cdx2<sup>ERT-Cre</sup>* mice were generated and maintained by Y.F. and E.R.F. and will be reported elsewhere. Mice were allowed to develop spontaneous CRC for 4–5 months. At the end of each study, mice were killed and colonic tumours and non-tumour tissue, along with mesenteric lymph nodes, were analysed using flow cytometry, enzyme-linked immunosorbent assay (ELISA), RT-qPCR, immunohistochemistry and fluorescent microscopy. Lethally irradiated (2 × 600 rad) littermate CPC-APC recipient mice were intravenously injected with 10<sup>7</sup> nucleated bone marrow cells from various donors to generate radiation chimaeras. Endotoxin was measured in portal vein blood/plasma by a *Limulus* assay. For intestinal permeability analysis, tumour-bearing and control mice were surgically clipped and FITC-dextran or Alexa488-LPS were injected into the colonic lumen, followed by fluorescent detection of FITC in serum or Alexa488-LPS in frozen colon sections.

**Full Methods** and any associated references are available in the online version of the paper.

Received 8 February; accepted 31 July 2012.

Published online 3 October; corrected online 7 November 2012 (see full-text HTML version for details).

- Vogelstein, B. & Kinzler, K. W. Cancer genes and the pathways they control. *Nature Med.* **10**, 789–799 (2004).
- Fearon, E. R. & Vogelstein, B. A genetic model for colorectal tumorigenesis. *Cell* **61**, 759–767 (1990).
- Wood, L. D. *et al.* The genomic landscapes of human breast and colorectal cancers. *Science* **318**, 1108–1113 (2007).
- Reichling, T. *et al.* Transcriptional profiles of intestinal tumors in Apc(Min) mice are unique from those of embryonic intestine and identify novel gene targets dysregulated in human colorectal tumors. *Cancer Res.* **65**, 166–176 (2005).
- Mantovani, A., Allavena, P., Sica, A. & Balkwill, F. Cancer-related inflammation. *Nature* **454**, 436–444 (2008).
- Grivennikov, S. I., Greten, F. R. & Karin, M. Immunity, inflammation, and cancer. *Cell* **140**, 883–899 (2010).
- Schreiber, R. D., Old, L. J. & Smyth, M. J. Cancer immunoediting: integrating immunity's roles in cancer suppression and promotion. *Science* **331**, 1565–1570 (2011).
- Galon, J. *et al.* Type, density, and location of immune cells within human colorectal tumors predict clinical outcome. *Science* **313**, 1960–1964 (2006).
- Tosolini, M. *et al.* Clinical impact of different classes of infiltrating T cytotoxic and helper cells (Th1, Th2, Treg, Th17) in patients with colorectal cancer. *Cancer Res.* **71**, 1263–1271 (2011).
- Brenchley, J. M. & Douek, D. C. Microbial translocation across the GI tract. *Annu. Rev. Immunol.* **30**, 149–173 (2012).

- McKenzie, B. S., Kastelein, R. A. & Cua, D. J. Understanding the IL-23-IL-17 immune pathway. *Trends Immunol.* **27**, 17–23 (2006).
- Langowski, J. L. *et al.* IL-23 promotes tumour incidence and growth. *Nature* **442**, 461–465 (2006).
- Hinoi, T. *et al.* Mouse model of colonic adenoma-carcinoma progression based on somatic Apc inactivation. *Cancer Res.* **67**, 9721–9730 (2007).
- Sawa, S. *et al.* ROR $\gamma$ <sup>+</sup> innate lymphoid cells regulate intestinal homeostasis by integrating negative signals from the symbiotic microbiota. *Nature Immunol.* **12**, 320–326 (2011).
- Medzhitov, R. Recognition of microorganisms and activation of the immune response. *Nature* **449**, 819–826 (2007).
- Rakoff-Nahoum, S. & Medzhitov, R. Regulation of spontaneous intestinal tumorigenesis through the adaptor protein MyD88. *Science* **317**, 124–127 (2007).
- Van der Sluis, M. *et al.* Muc2-deficient mice spontaneously develop colitis, indicating that MUC2 is critical for colonic protection. *Gastroenterology* **131**, 117–129 (2006).
- Velcich, A. *et al.* Colorectal cancer in mice genetically deficient in the mucin Muc2. *Science* **295**, 1726–1729 (2002).
- Rothwell, P. M. *et al.* Effect of daily aspirin on long-term risk of death due to cancer: analysis of individual patient data from randomised trials. *Lancet* **377**, 31–41 (2011).
- Wang, X., Tully, O., Ngo, B., Zitin, M. & Mullin, J. M. Epithelial tight junctional changes in colorectal cancer tissues. *Sci. World J.* **11**, 826–841 (2011).
- Tanaka, T. *et al.* Dextran sodium sulfate strongly promotes colorectal carcinogenesis in Apc(Min/+) mice: inflammatory stimuli by dextran sodium sulfate results in development of multiple colonic neoplasms. *Int. J. Cancer* **118**, 25–34 (2006).
- Meira, L. B. *et al.* DNA damage induced by chronic inflammation contributes to colon carcinogenesis in mice. *J. Clin. Invest.* **118**, 2516–2525 (2008).
- Newman, J. V., Kosaka, T., Sheppard, B. J., Fox, J. G. & Schauer, D. B. Bacterial infection promotes colon tumorigenesis in Apc(Min/+) mice. *J. Infect. Dis.* **184**, 227–230 (2001).
- Wu, S. *et al.* A human colonic commensal promotes colon tumorigenesis via activation of T helper type 17 T cell responses. *Nature Med.* **15**, 1016–1022 (2009).
- Dove, W. F. *et al.* Intestinal neoplasia in the ApcMin mouse: independence from the microbial and natural killer (beige locus) status. *Cancer Res.* **57**, 812–814 (1997).
- Yang, L. & Pei, Z. Bacteria, inflammation, and colon cancer. *World J. Gastroenterol.* **12**, 6741–6746 (2006).
- Garrett, W. S. *et al.* Colitis-associated colorectal cancer driven by T-bet deficiency in dendritic cells. *Cancer Cell* **16**, 208–219 (2009).
- Zhou, L. *et al.* IL-6 programs T(H)-17 cell differentiation by promoting sequential engagement of the IL-21 and IL-23 pathways. *Nature Immunol.* **8**, 967–974 (2007).
- Ivanov, I. I. *et al.* Specific microbiota direct the differentiation of IL-17-producing T-helper cells in the mucosa of the small intestine. *Cell Host Microbe* **4**, 337–349 (2008).
- Barker, N. *et al.* Crypt stem cells as the cells-of-origin of intestinal cancer. *Nature* **457**, 608–611 (2009).

**Supplementary Information** is available in the online version of the paper.

**Acknowledgements** We thank eBioscience, GeneTex, Santa Cruz, BioLegend and Cell Signaling for antibodies; Genentech and Amgen for *Il23<sup>-/-</sup>* and *Il17a<sup>-/-</sup>* mice, respectively, and S. Reid and E. Southon for the help in generating *Il23r<sup>F/F</sup>* mice. This work was supported by Crohn's and Colitis Foundation of America (Career Development Award number 2693), NIH/National Institute of Diabetes and Digestive and Kidney Diseases (K99-DK088589) and a University of California, San Diego, Digestive Disease Research Development Center Pilot Grant (DK080506) to S.I.G.; Croucher Foundation and China Postdoctoral Science Foundation (20110490919) to K.W.; Strategic Young Researcher Overseas Visits Program for Accelerating Brain Circulation to K.T.; SPAR Austria to C.D.; NIH (R01CA082223) to E.R.F.; and NIH (AIO43477; DK035108) and American Association for Cancer Research (07-60-21-KARI) grants to M.K., who is an American Cancer Society Research Professor. The content is solely the responsibility of the authors and does not necessarily represent the official views of the NIH.

**Author Contributions** S.G. and M.K. conceived the project. S.I.G., K.W., D.M., B.S., D.J., K.T., G.Y.Y., C.O., Y.F. and K.E.H. performed the experiments. S.I.G., K.W., D.M., D.J., H.C., L.E. and M.K. analysed data. C.A.S., V.C., L.T. and G.T. generated *Il23r<sup>F/F</sup>* mice. M.O. and F.Y. provided *Il23<sup>gfp/gfp</sup>* and *Tlr2,4,9<sup>-/-</sup>* bone marrow, respectively, and Y.F. and E.R.F. provided CPC-APC mice and tissues from *Cdx2<sup>ERT-Cre</sup>*-APC mice. C.A.S., E.R.F., H.C. and G.T. provided conceptual advice. C.D. collected and provided human specimens. S.I.G., K.W. and M.K. wrote the manuscript, with all authors contributing to the writing and providing advice.

**Author Information** Reprints and permissions information is available at [www.nature.com/reprints](http://www.nature.com/reprints). The authors declare no competing financial interests. Readers are welcome to comment on the online version of the paper. Correspondence and requests for materials should be addressed to M.K. ([karinoffice@ucsd.edu](mailto:karinoffice@ucsd.edu)).

## METHODS

**Human samples.** Paraffin-embedded human ulcerative colitis and CRC specimens were provided by Oberndorf Hospital, Paracelsus Medical University Salzburg, Austria. Patients with ulcerative colitis or sporadic CRC underwent colonoscopy as a part of the diagnostic workup at the Department of Internal Medicine, Oberndorf Hospital (Salzburg, Austria). Diagnosis of ulcerative colitis was based on appropriate clinical, endoscopic, histopathological and radiological findings that satisfied the internationally accepted Lennard-Jones criteria<sup>31</sup>. Additionally, colonoscopic findings were classified as tubular adenoma, size less than 6 mm (early lesion), advanced adenoma (that is, villous or tubulovillous features), size at least 1 cm or high-grade dysplasia or carcinoma after a combined analysis of macroscopic and histological results<sup>32,33</sup>. Biopsies from colonic tissue with macroscopically normal appearance were taken in patients who underwent colonoscopy for CRC screening. For histological examination, specimens were fixed in 4% buffered formalin and embedded into paraffin. When available, a small tissue portion of the biopsy specimen was separated and preserved for RNA and protein extraction in RNAlater (Ambion's RNAlater solution, Applied Biosystems, Vienna, Austria). Biopsies from colonic tissue with macroscopically normal appearance were taken in patients who underwent colonoscopy for CRC screening. Written informed consent was obtained from all study participants to use one biopsy specimen for scientific purposes. The study was approved by the local ethics committee (Ethikkommission des Landes Salzburg, approval number 415-E/1262/2-2010). Frozen human CRC and normal colon tissues were obtained from Cooperative Human Tissue Network of Vanderbilt University Medical Center.

**Generation of *Il23r*<sup>F/F</sup> and *Il23r*<sup>-/-</sup> mice.** The targeted region includes exons 2 (3,708–3,810) and 3 (8,085–8,381) of *Il23r* that encode a portion of the signal peptide and the amino (N)-terminal Ig-like domain (Supplementary Fig. 11a). The targeting vector was generated by recombineering using  $\lambda$  phage *Red* as described by Liu *et al.*<sup>34</sup>. Homology arms for the retrieval vector were amplified by PCR on C57BL/6 genomic DNA. Homology arms were cloned into pLMJ235 (pBSKS+ containing a 2.8kb SalI TK fragment of pGKTK) by triple ligation to form the retrieval plasmid. Retrieval of the targeting region (covering 753–12,812; numbering relative to indicated BamHI site) was performed according to Liu *et al.*<sup>34</sup> using C57BL/6 bacterial artificial chromosome RP23-283M8 (BACPAC Resources) as template in DY380 cells. Recombineering was performed to insert cassettes containing *LoxP*-flanked Neo cassettes from pGKEM7Neo-pA into the targeting vector. First, *LoxP*-Neo-*LoxP* was inserted at position 3,524, followed by induced expression of *Cre* in EL350 cells to excise the Neo selection cassette but leaving the upstream *LoxP* site. A second cassette (*LoxP*-*Frt*-*Intron-Eng2SA-Neo-LoxP*-*Frt*) was inserted into position 8,503. After NotI-linearization, the targeting construct was electroporated into Bruce 4 C57BL/6 ES cells, and G418-selected clones were screened for integration by Southern analysis using sequences outside the targeting vector (Supplementary Fig. 11b). Selected clones were injected into C57BL/6-albino blastocysts and transferred to pseudopregnant females. Chimeric offspring were bred with C57BL/6-Albino partners to generate F<sub>1</sub> mice that were screened for integration by Southern blotting (Supplementary Fig. 11c). Resulting mice with the *Il23r*<sup>SA-F-neo</sup> allele were crossed with C57BL/6-FLPe mice to facilitate recombination between *Frt* sequences and generate the *Il23r*<sup>F</sup> allele. The null allele (*Il23r*<sup>-/-</sup>) was generated by crossing *Il23r*<sup>F/F</sup> mice with *CPC-Cre* transgenic mice. The F<sub>2</sub> generation exhibits germline deletion of floxed alleles owing to early *CPC-Cre* expression in caudal regions of the body and gonads<sup>13</sup>. Complete ablation of IL-23R was confirmed by RT-qPCR of spleen and tumour-derived cells.

**Animal models.** C57BL/6 control mice obtained from Charles River Laboratories were bred locally at University of California, San Diego. *Il23*<sup>-/-</sup> and *Il17ra*<sup>-/-</sup> mice were from Genentech<sup>35</sup> and Amgen<sup>36</sup>, respectively. Bone marrow from *Il23*<sup>gfp/gfp</sup> and *Thr2,4,9*<sup>-/-</sup> mice was provided by M. Oukka<sup>37</sup> and F. Yarovinsky<sup>38</sup>, respectively. *Apc*<sup>F/F</sup> and *Cdx2-Cre* (*CPC-Cre*) mice<sup>13</sup> were provided by E. Fearon, who also generated the *Cdx2-Cre*<sup>ERT</sup> mice, which will be described elsewhere. *Myd88*<sup>-/-</sup> mice<sup>39</sup> were obtained from the Jackson Laboratory, and *Il18r*<sup>-/-</sup> mice<sup>40</sup> were from H. Hoffman. All mice were maintained in filter-topped cages on autoclaved food and water at University of California, San Diego, according to NIH guidelines, and all experiments were performed in accordance with University of California, San Diego, and NIH guidelines and regulations. Most experiments used littermate controls housed in the same cage; in addition, dirty beddings were switched between cages of the same experiment to make sure that the microflora was balanced.

For spontaneous CRC tumorigenesis, male and female *CPC-APC* mice were allowed to develop colorectal tumours spontaneously for 4–5 months and then killed. Macroscopic tumours were counted and their diameter measured with a calliper. Average tumour size per individual mouse was determined by averaging diameters of all tumours present. Tumour load was determined as the sum of the diameters of all tumours presented in a given mouse, as previously described<sup>41</sup>. Typically, one-half of the distal colon was taken as a tissue sample, tumours and

normal tissue dissected and snap-frozen in liquid nitrogen or used for *ex vivo* cultures or fluorescence-activated cell sorting. The other half was fixed in 10% neutral buffered formalin for 24 h and transferred to 70% ethanol for subsequent paraffin embedding, or alternatively frozen in optimal cutting temperature (OCT) compound for further sectioning and histological analysis.

To induce colorectal tumours with inactivated *Apc* and activated *K-Ras* or *B-Raf*, open laparotomies were performed in mice bearing floxed *Apc* (*Apc*<sup>F/F</sup>) in combination with either latent *Kras*<sup>G12D</sup> (*Apc-Kras*) or *Braf*<sup>V600E</sup> (*Apc-Braf*) alleles under isoflurane anaesthesia. A dosage of adenovirus-*Cre* was administered to the distal colon, which resulted in solitary colonic tumours, as described<sup>42,43</sup>. Subsequent tumour formation was monitored by serial optical colonoscopy. Tumours were collected after more than 75% occlusion of the colonic lumen was observed and banked in RNA later for subsequent analysis.

**Colonic loops and injections of FITC-dextran and Alexa488-LPS.** After anaesthesia, a midline laparotomy incision was made. A 2–3 cm long segment of the colon with or without tumours inside was created with two vascular haemoclips without disrupting the mesenteric vascular arcades. The length of intestine between the two clips was injected with 50  $\mu$ l of 100 mg ml<sup>-1</sup> FITC-dextran solution or 50  $\mu$ l of Alexa488-LPS at 70  $\mu$ g per mouse. At the indicated time points, mice were killed and fluorescence was measured in the plasma with a fluorimeter, or colon fragments were embedded into OCT compound, and frozen sections prepared and analysed for Alexa488-LPS tissue distribution by fluorescent microscopy.

**Antibiotic treatment.** Mice were given the following antibiotics in their drinking water: 100  $\mu$ g ml<sup>-1</sup> neomycin, 50  $\mu$ g ml<sup>-1</sup> vancomycin, 50  $\mu$ g ml<sup>-1</sup> imipenem, 100  $\mu$ g ml<sup>-1</sup> metronidazole, 50  $\mu$ g ml<sup>-1</sup> streptomycin and 100 U ml<sup>-1</sup> penicillin. Fresh antibiotics were supplied every week. For long-term antibiotic treatment after 2 months of initial treatment, drinking water was further supplemented with streptomycin (1 mg ml<sup>-1</sup>), gentamycin (170  $\mu$ g ml<sup>-1</sup>), ciprofloxacin (125  $\mu$ g ml<sup>-1</sup>) and bacitracin 1 mg ml<sup>-1</sup> as previously described<sup>44</sup>. Control mice were placed on bottled water. Faeces were collected and cultured on 5% sheep blood agar plates (Fisher Scientific) under aerobic or anaerobic conditions at 37 °C to determine the extent of colon sterilization, which exceeded 99.9%. Alternatively, DNA was isolated from stools of mice using QIAamp DNA Stool mini kit (Qiagen) and content of 16S bacterial rRNA was analysed by RT-qPCR. Mice were kept on antibiotics for the indicated time and killed for tumour and tissue analysis.

**Portal blood vein drainage and endotoxin measurement.** Mice were anaesthetized with isoflurane and their portal vein exposed to insert a 28-gauge needle and draw 100–200  $\mu$ l of blood, which was collected into EDTA coated tubes (BD Biosciences). Plasma was isolated by centrifugation and endotoxin amounts were determined by microplate Limulus Amebocyte Lysate (LAL) colorimetric bioassay (Lonza) according to the manufacturer's recommendations.

**Bone marrow transplantation.** Six- to eight-week-old littermate recipient mice were irradiated twice during one day to achieve a lethal dose (2  $\times$  600 rad) and intravenously injected with single-cell suspension containing 10<sup>7</sup> donor bone marrow cells. Every cage of recipient mice contained mice receiving both gene-deficient and wild-type bone marrow to compare mice living in the same cage. For 2 weeks after irradiation, mice were placed on sulphamethoxazole and trimethoprim antibiotics in drinking water followed by transfer to the cages from the same room/rack with dirty bedding to restore microflora. Mice were killed and analysed for tumour development 4–5 months after transplantation.

**Antibodies and stains.** Fluorescent-labelled antibodies for flow cytometry were from eBioscience. Immunoblot analysis and immunohistochemistry were performed with antibodies to Ki-67, claudin7, claudin 5, claudin 4, claudin 3, JAM-B, mucin2, GFP, IL-23p19 (Genetex), JAM-A (Santa Cruz), active caspase 3, phospho-STAT3 (Cell Signaling), F4/80 and E-cadherin (BD Biosciences). Secondary antibodies (host: donkey) for fluorescent microscopy labelled with Alexa 488 or 594 were from Invitrogen. For TdT-mediated dUTP nick end labelling (TUNEL) assay the *In situ* Cell Death Kit (Roche) was used according to the manufacturer's recommendations. Alexa488-LPS and Oregon488-WGA were from Invitrogen.

**Immunohistology.** Paraffin-embedded slides were de-paraffinized. Antigen unmasking was performed by incubation in 94 °C water bath in 10 mM sodium citrate buffer with 0.1% Tween 20 for 1 h. Slides were incubated with primary antibodies in PBS containing 1% BSA and 10% normal goat or donkey serum, depending on the host of secondary antibodies used. Biotinylated secondary anti-rat or anti-rabbit antibodies (Pharmingen) were added and incubated at room temperature for 1 h. Streptavidin-HRP (Pharmingen) was added and after 40 min the sections were developed with DAB substrate and counterstained with haematoxylin. Alternatively, paraffin-embedded or acetone fixed frozen slides were stained with antibodies followed by secondary donkey antibodies labelled with Alexa488 or Alexa594, counterstained with DAPI and analysed by immunofluorescence. Images were acquired on an upright light/fluorescent Imager A2 microscope (Zeiss) equipped with an AxioCam camera or on a confocal microscope (Leica SPE).

**Bacteria fluorescent *in situ* hybridization.** Paraffin embedded slides were deparaffinized and hybridized to universal eubacterial or control probes labelled with Alexa594. Hybridization was performed in 48 °C oven for 2 h followed by washing and counter-stained by DAPI. The sequences of the probes are listed below: Eubacteria: GCTGCCTCCCGTAGGAGT; control: CGACGGAGGGCATCCTCA.

**Flow cytometry and cell sorting.** Isolated cells were stained with labelled antibodies in PBS with 2% FCS and analysed on a BD LSRII or on an Accuri C6 flow cytometer. Dead cells were excluded on the basis of staining with Live/Dead fixable Aqua dye (Invitrogen). For intracellular cytokine staining cell were restimulated in the presence of Brefeldin A as indicated, fixed and permeabilized with Cytofix/Cytoperm reagent (BD Biosciences) according to the manufacturer's recommendations and stained with labelled antibody for the cytokine of interest. For cell sorting, a BD FACSAria II cell sorter was used. Data were analysed using FlowJo software (Treestar).

**ELISA.** Pieces (20–40 mg) of normal or tumour tissue were cultured in 0.5 ml RPMI medium supplemented with antibiotics and 2% FCS at 37 °C for 24 h. Supernatants were collected, centrifuged and concentration of IL-23 protein was determined using ELISA Quantikine kit (R&D Systems) according to the manufacturer's recommendations.

**RT-qPCR analysis.** Total RNA was extracted using RNeasy Plus kit to eliminate genomic DNA contamination (Qiagen). RNA was reverse transcribed using a IScript kit (Biorad). RT-qPCR was performed using EvaGreen PCR mix (Biorad) on a Biorad CFX96 machine. Expression data were normalized to L32 mRNA expression. The data are presented in arbitrary units and were calculated as  $2^{-(Ct(\text{rpl32} - \text{gene of interest}))}$ . Primer sequences are listed in Supplementary Table 1 and generally were obtained from the NIH qPrimerDepot for mouse (<http://mouseprimerdepot.nci.nih.gov>) and human (<http://primerdepot.nci.nih.gov>). Whenever possible, primers were intron-spanning, such that amplification was only feasible on complementary DNA.

**Statistical analysis.** Data are presented as averages  $\pm$  s.e.m. and were analysed by built-in *t*-test using Microsoft Excel software. *P* values less than 0.05 were considered significant.

31. Lennard-Jones, J. E. Classification of inflammatory bowel disease. *Scand. J. Gastroenterol.*, Suppl. 170, 2–6 (1989).
32. Bond, J. H. Polyp guideline: diagnosis, treatment, and surveillance for patients with colorectal polyps. Practice Parameters Committee of the American College of Gastroenterology. *Am. J. Gastroenterol.* **95**, 3053–3063 (2000).
33. Winawer, S. J. & Zauber, A. G. The advanced adenoma as the primary target of screening. *Gastrointest. Endosc. Clin. N. Am.* **12**, 1–9 (2002).
34. Liu, P., Jenkins, N. A. & Copeland, N. G. A highly efficient recombineering-based method for generating conditional knockout mutations. *Genome Res.* **13**, 476–484 (2003).
35. Ghilardi, N. *et al.* Compromised humoral and delayed-type hypersensitivity responses in IL-23-deficient mice. *J. Immunol.* **172**, 2827–2833 (2004).
36. Ye, P. *et al.* Requirement of interleukin 17 receptor signaling for lung CXCL chemokine and granulocyte colony-stimulating factor expression, neutrophil recruitment, and host defense. *J. Exp. Med.* **194**, 519–527 (2001).
37. Awasthi, A. *et al.* Cutting edge: IL-23 receptor gfp reporter mice reveal distinct populations of IL-17-producing cells. *J. Immunol.* **182**, 5904–5908 (2009).
38. Kirkland, D. *et al.* B cell-intrinsic MyD88 signaling prevents the lethal dissemination of commensal bacteria during colonic damage. *Immunity* **36**, 228–238 (2012).
39. Kawai, T., Adachi, O., Ogawa, T., Takeda, K. & Akira, S. Unresponsiveness of MyD88-deficient mice to endotoxin. *Immunity* **11**, 115–122 (1999).
40. Hoshino, K. *et al.* Cutting edge: generation of IL-18 receptor-deficient mice: evidence for IL-1 receptor-related protein as an essential IL-18 binding receptor. *J. Immunol.* **162**, 5041–5044 (1999).
41. Grivennikov, S. *et al.* IL-6 and Stat3 are required for survival of intestinal epithelial cells and development of colitis-associated cancer. *Cancer Cell* **15**, 103–113 (2009).
42. Kim, P. *et al.* In vivo wide-area cellular imaging by side-view endomicroscopy. *Nature Methods* **7**, 303–305 (2010).
43. Hung, K. E. *et al.* Development of a mouse model for sporadic and metastatic colon tumors and its use in assessing drug treatment. *Proc. Natl Acad. Sci. USA* **107**, 1565–1570 (2010).
44. Chen, G. Y., Shaw, M. H., Redondo, G. & Nunez, G. The innate immune receptor Nod1 protects the intestine from inflammation-induced tumorigenesis. *Cancer Res.* **68**, 10060–10067 (2008).



# IL-22BP is regulated by the inflammasome and modulates tumorigenesis in the intestine

Samuel Huber<sup>1,2\*</sup>, Nicola Gagliani<sup>1\*</sup>, Lauren A. Zenewicz<sup>1</sup>, Francis J. Huber<sup>2</sup>, Lidia Bosurgi<sup>1</sup>, Bo Hu<sup>1</sup>, Matija Hedl<sup>3</sup>, Wei Zhang<sup>4</sup>, William O'Connor Jr<sup>1</sup>, Andrew J. Murphy<sup>5</sup>, David M. Valenzuela<sup>5</sup>, George D. Yancopoulos<sup>5</sup>, Carmen J. Booth<sup>6</sup>, Judy H. Cho<sup>4</sup>, Wenjun Ouyang<sup>7</sup>, Clara Abraham<sup>3</sup> & Richard A. Flavell<sup>1,8</sup>

Chronic mucosal inflammation and tissue damage predisposes patients to the development of colorectal cancer<sup>1</sup>. This association could be explained by the hypothesis that the same factors and pathways important for wound healing also promote tumorigenesis. A sensor of tissue damage should induce these factors to promote tissue repair and regulate their action to prevent development of cancer. Interleukin 22 (IL-22), a cytokine of the IL-10 superfamily, has an important role in colonic epithelial cell repair, and its levels are increased in the blood and intestine of inflammatory bowel disease patients<sup>2,3</sup>. This cytokine can be neutralized by the soluble IL-22 receptor, known as the IL-22 binding protein (IL-22BP, also known as IL22RA2); however, the significance of endogenous IL-22BP *in vivo* and the pathways that regulate this receptor are unknown<sup>4,5</sup>. Here we describe that IL-22BP has a crucial role in controlling tumorigenesis and epithelial cell proliferation in the colon. IL-22BP is highly expressed by dendritic cells in the colon in steady-state conditions. Sensing of intestinal tissue damage via the NLRP3 or NLRP6 inflammasomes led to an IL-18-dependent downregulation of IL-22BP, thereby increasing the ratio of IL-22/IL-22BP. IL-22, which is induced during intestinal tissue damage, exerted protective properties during the peak of damage, but promoted tumour development if uncontrolled during the recovery phase. Thus, the IL-22–IL-22BP axis critically regulates intestinal tissue repair and tumorigenesis in the colon.

IL-22 is produced by innate lymphoid cells, T<sub>H</sub>17 cells, and T<sub>H</sub>22 cells, particularly at mucosal surfaces<sup>6–7</sup>. The membrane-bound IL-22 receptor 1 (IL-22R1, also known as IL22RA1) is absent on immune cells, but expressed within tissues, such as the epithelial cells of the gastrointestinal tract and skin<sup>4</sup>. IL-22 has an important function in the promotion of antimicrobial immunity via induction of antimicrobial peptides, and in tissue repair via induction of epithelial cell proliferation and survival<sup>5,8,9</sup>. However, IL-22 can also promote pathological inflammatory responses in the skin<sup>10</sup> or intestine<sup>11</sup> in mouse models, and its concentration is increased in a variety of human diseases including psoriasis, rheumatoid arthritis, infections and inflammatory bowel disease<sup>5</sup>. In line with the pleiotropic role(s) of IL-22, it is known that this cytokine signals via STAT3, which is important for wound healing, but also for tumour development<sup>1</sup>. However, the role of IL-22 during tumour development needs to be clarified, because both inhibitory and promoting effects have been reported (for review see ref. 4).

IL-22BP is a soluble IL-22 receptor, which lacks a transmembrane and intracellular domain. IL-22BP specifically binds to IL-22 but not to other IL-10 family members, and prevents the binding of IL-22 to membrane-bound IL-22R1<sup>12–15</sup>. The binding of IL-22 to IL-22BP is of 20- to 1,000-fold higher affinity compared to its binding to the membrane-bound IL-22R1<sup>3,16</sup>. It is also known that IL-22BP expression

is downregulated in the intestine during tissue damage. However, the cellular source of IL-22BP is unclear. Moreover, the mechanism regulating IL-22BP expression and the significance of endogenous IL-22BP *in vivo* are unknown<sup>4,5</sup>.

IL-22BP is highly expressed in the colon (Supplementary Fig. 1) and IL-22 has been suggested to have a role in tumour development. We therefore generated *Il22bp*<sup>−/−</sup> mice (*Il22bp* is also known as *Il22ra2*) (Supplementary Fig. 2) and used a colitis-associated colon cancer model, which resembles the pathology of human colitis-associated neoplasia<sup>17,18</sup> (Supplementary Fig. 3), to analyse the role of IL-22BP during tumorigenesis in the colon. Interestingly, tumour development was strongly accelerated and the number and size of the tumours were increased in *Il22bp*<sup>−/−</sup> compared to wild-type control mice (Fig. 1a–c). Tumour morphology was similar between *Il22bp*<sup>−/−</sup> and wild-type control mice (Fig. 1c). Thus, IL-22BP deficiency leads to accelerated and increased tumorigenesis in a colitis-associated colon cancer model.

Inflammation is one of the major drivers of tumour development in the colitis-associated colon cancer model<sup>1,18</sup>. IL-22 has been reported to have both protective and pathogenic properties during colitis<sup>9,11</sup>. However, wild-type and *Il22bp*<sup>−/−</sup> mice showed no difference in colitis disease severity in the acute dextran sodium sulphate (DSS)-induced colitis model (Supplementary Fig. 4a–g). In line with a previous report<sup>3</sup>, we found that *Il22bp* was downregulated during acute DSS-colitis, and was not detectable on day 10 of the experiment (Supplementary Fig. 4g), which could explain the lack of phenotype in *Il22bp*<sup>−/−</sup> mice. We then examined a model of chronic DSS-induced colitis in which DSS is administered for 5 days followed by 16 days of a water regimen for four separate cycles, similar to the colitis-associated colon cancer model. No difference in disease severity was observed between wild type and *Il22bp*<sup>−/−</sup> in this chronic colitis model (Supplementary Fig. 5).

IL-22 is well known to promote epithelial cell proliferation<sup>4,8</sup>. Therefore another hypothesis for the increased experimental colon tumorigenesis in *Il22bp*<sup>−/−</sup> mice is that the effect of IL-22BP is to inhibit IL-22-induced epithelial cell proliferation. However, the significance of endogenous IL-22BP for the control of IL-22 is currently unclear<sup>4,5</sup>. Furthermore, both IL-22 and IL-22BP expression are modulated during intestinal tissue damage<sup>3,19</sup>. We examined the expression of IL-22 and IL-22BP during one cycle of DSS administration for 5 days followed by 16 days of water. Mice treated with DSS lost weight and developed histological signs of colitis (Fig. 2a). The peak of disease occurred between day 7 and day 8 (Fig. 2a). *Il22bp* messenger RNA was expressed under steady-state conditions. The lowest expression of *Il22bp* correlated with the peak of disease. However, *Il22bp* was expressed once again during the recovery phase (Fig. 2a, b). Consistent with previous studies<sup>3,9</sup>, we found increased *Il22* mRNA levels in the colon with maximal expression between day 7 and day 8 (Fig. 2b). Accordingly

<sup>1</sup>Department of Immunobiology, Yale University School of Medicine, New Haven, Connecticut 06520, USA. <sup>2</sup>I. Medizinische Klinik, Universitätsklinikum Hamburg-Eppendorf, Hamburg 20246, Germany.

<sup>3</sup>Department of Internal Medicine, Section of Digestive Diseases, Yale University, New Haven, Connecticut 06520, USA. <sup>4</sup>Departments of Medicine and Genetics, Section of Digestive Diseases, Yale University School of Medicine, New Haven, Connecticut 06520, USA. <sup>5</sup>Regeneron Pharmaceuticals, Inc., Tarrytown, New York 10591, USA. <sup>6</sup>Section of Comparative Medicine, Yale University School of Medicine, New Haven, Connecticut 06520, USA. <sup>7</sup>Department of Immunology, Genentech, Inc., South San Francisco, California 94080, USA. <sup>8</sup>Howard Hughes Medical Institute, New Haven, Connecticut 06520, USA.

\*These authors contributed equally to this work.

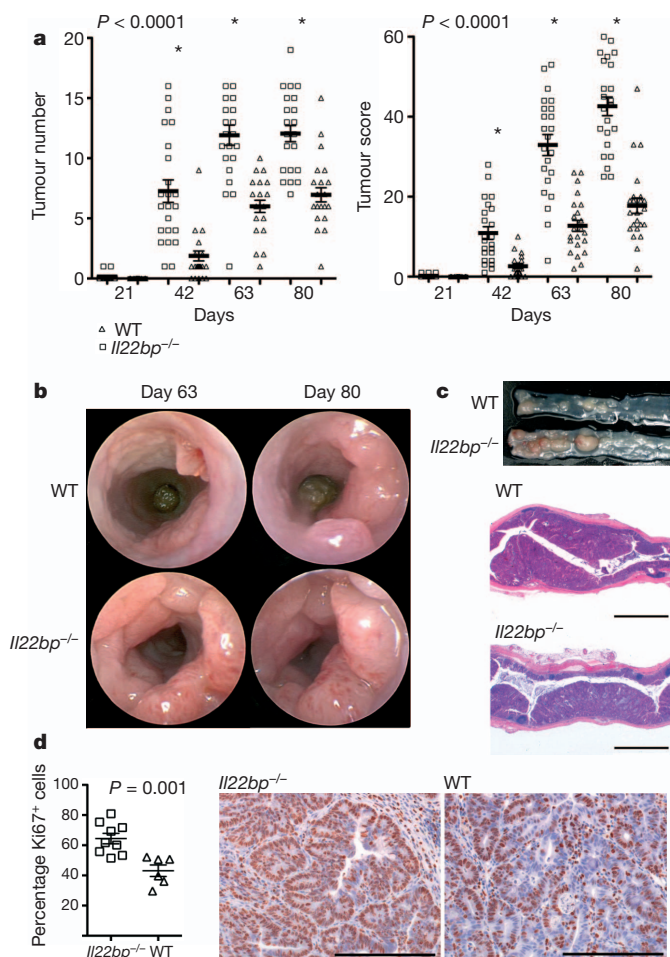


**Figure 1 | Increased tumorigenesis in *Il22bp*<sup>-/-</sup> mice in a colitis-associated colon cancer model.** **a**, Time course of the tumour number and tumour score. WT, wild type. **b, c**, Representative endoscopic view of the mouse colon at the indicated time points (**b**); macroscopic view and histology on day 80 (bars, 2,000  $\mu$ m) (**c**). Results are cumulative from two independent experiments. **d**, Frequency of Ki67<sup>+</sup> cells in tumours from wild-type and *Il22bp*<sup>-/-</sup> mice and representative histology are shown (bars, 200  $\mu$ m). Ki67 expression was analysed in a total number of 48 KO and 28 WT tumours. Each dot represents one mouse; bars, mean  $\pm$  s.e.m.

IL-22 serum levels were increased with the same pattern (data not shown). We next validated the inverse expression pattern of IL-22 and IL-22BP in another model of intestinal damage. Following wounding of the colon using an endoscopic biopsy forceps<sup>8</sup> (Fig. 2c), *Il22bp* was expressed in the initial biopsy (Fig. 2d). However, 2 days later *Il22bp* expression was reduced in a re-biopsy close to the wound, but not in a control biopsy taken at a distance of 0.5 cm from the initial biopsy (Fig. 2d). Thus IL-22BP is downregulated upon damage of the epithelial barrier in the colon, but induced once again during the recovery, and IL-22 shows an inverse expression pattern to IL-22BP.

On the basis of these results we tested if IL-22BP has a significant effect on epithelial cell proliferation during DSS-induced intestinal tissue damage. There was no difference in epithelial cell proliferation between wild-type and *Il22bp*<sup>-/-</sup> mice on day 0 or 7 of the experiment. However, whereas in wild-type mice epithelial cell proliferation on day 14 was comparable to steady-state conditions, *Il22bp*<sup>-/-</sup> mice continued to demonstrate elevated epithelial cell proliferation (Fig. 2e and Supplementary Fig. 6). At this time point both *Il22* and *Il22bp* were expressed in the colon (Fig. 2b). In line with these data, tumour cells of *Il22bp*<sup>-/-</sup> mice proliferated more compared to wild type (Fig. 1d). Thus endogenous IL-22BP is required to terminate the IL-22-induced regenerative program.

We generated *Il22bp*<sup>-/-</sup>*Il22*<sup>-/-</sup> double KO (dKO) mice to establish that the effect of IL-22BP is dependent on the presence of IL-22. *Il22bp*<sup>-/-</sup>*Il22*<sup>-/-</sup> mice showed a similar tumour number and score compared to *Il22*<sup>-/-</sup> mice, which was lower than the score observed in *Il22bp*<sup>-/-</sup> mice. These data confirm that the effect of IL-22BP is dependent on the presence of IL-22 (Supplementary Fig. 7). Unexpectedly *Il22*<sup>-/-</sup> mice developed a higher tumour load compared to wild-type mice (Supplementary Fig. 7), which seems to be in contrast to the increased tumour load in *Il22bp*<sup>-/-</sup> mice. It is known, however, that *Il22*<sup>-/-</sup> mice exhibit an increased disease severity in the DSS-colitis model<sup>9</sup>. We therefore proposed the hypothesis that IL-22 has a dual function during colitis-associated colon cancer: Deficiency of IL-22 might lead to delayed colonic repair and increased intestinal inflammation, thereby promoting tumour development. However, the increased availability of IL-22 in *Il22bp*<sup>-/-</sup> mice during the recovery phase caused prolonged epithelial proliferation, thereby also promoting the development of intestinal tumours. In support of this hypothesis, we confirmed that *Il22*<sup>-/-</sup> mice have increased disease and inflammation with marked IL-6 production after DSS administration (Supplementary Fig. 8). To further validate our hypothesis we performed two sets of experiments. First we showed, by the administration of neutralizing IL-22 antibody, that IL-22 is protective during the peak of disease, but detrimental during the recovery phase (Supplementary Fig. 9). Second we used a model of spontaneous tumorigenesis, in which a genetic mutation and not inflammation induces tumour development in the colon. We crossed *Il22*<sup>-/-</sup> and *Il22bp*<sup>-/-</sup> with *Apc*<sup>min/+</sup> mice. Min (multiple intestinal neoplasia) mice carry a dominant mutation in the adenomatous polyposis coli (*Apc*) gene and develop multiple adenomas throughout their intestinal tract, mainly in the small intestine<sup>20</sup>. This mouse model resembles the human disease known as familial adenomatous polyposis, which is also caused by mutations in the *APC* gene. Humans carrying this mutation develop polyps, mainly in the colon, and malignant transformation into colon cancer occurs, if untreated, in almost 100% of the cases.

*Il22bp*<sup>-/-</sup>*Apc*<sup>min/+</sup> mice developed an increased number and size of tumours, whereas *Il22*<sup>-/-</sup>*Apc*<sup>min/+</sup> developed fewer tumours in the colon compared to *Apc*<sup>min/+</sup>. In contrast to the human disease, in the mouse model most tumours are seen in the small intestine. The tumour number and load was also significantly lower in the small intestine of *Il22*<sup>-/-</sup>*Apc*<sup>min/+</sup> compared to wild-type mice, although *Il22bp*<sup>-/-</sup>*Apc*<sup>min/+</sup> showed similar tumour development in the small intestine compared to wild-type mice (Fig. 3). This lack of effect of the *Il22bp* genotype in the small intestine is in line with the expression of *Il22bp*, which is high in the colon and low in the small intestine (Supplementary Fig. 1). Taken together, these data support our hypothesis that the increased tumour burden in *Il22*<sup>-/-</sup> mice in the colitis-associated colon cancer model is due to the increased susceptibility to DSS-induced colitis. In summary, IL-22 and IL-22BP are regulated during intestinal tissue damage. IL-22 has both protective and detrimental effects during intestinal tissue damage and therefore needs to be controlled via IL-22BP.

The cellular source of IL-22 and the mechanism regulating IL-22 expression have been studied<sup>5,21</sup>. In contrast, the mechanism regulating IL-22BP expression is unknown<sup>4,5</sup>. IL-22BP expression has been reported in different haematopoietic cells and also in intestinal epithelial cells<sup>4,14</sup>. However, these studies contradict each other. Interestingly, we observed *Il22bp* expression in haematopoietic cells and preparations of epithelial cells isolated from the colon (Fig. 4a). One caveat, however, was that the purity of the epithelial cells was about 98% and the *Il22bp* expression was about 50 times lower than in the haematopoietic cells. We used bone marrow chimaeras to show that the vast majority of IL-22BP expression in the colon was due to the haematopoietic compartment both in steady-state condition (Fig. 4b) and in the colitis-associated colon cancer model (Supplementary Fig. 10). We next used a stepwise approach to identify the haematopoietic source of IL-22BP in the colon. *Il22bp* was expressed in TCR- $\beta$ <sup>-</sup> cells, but

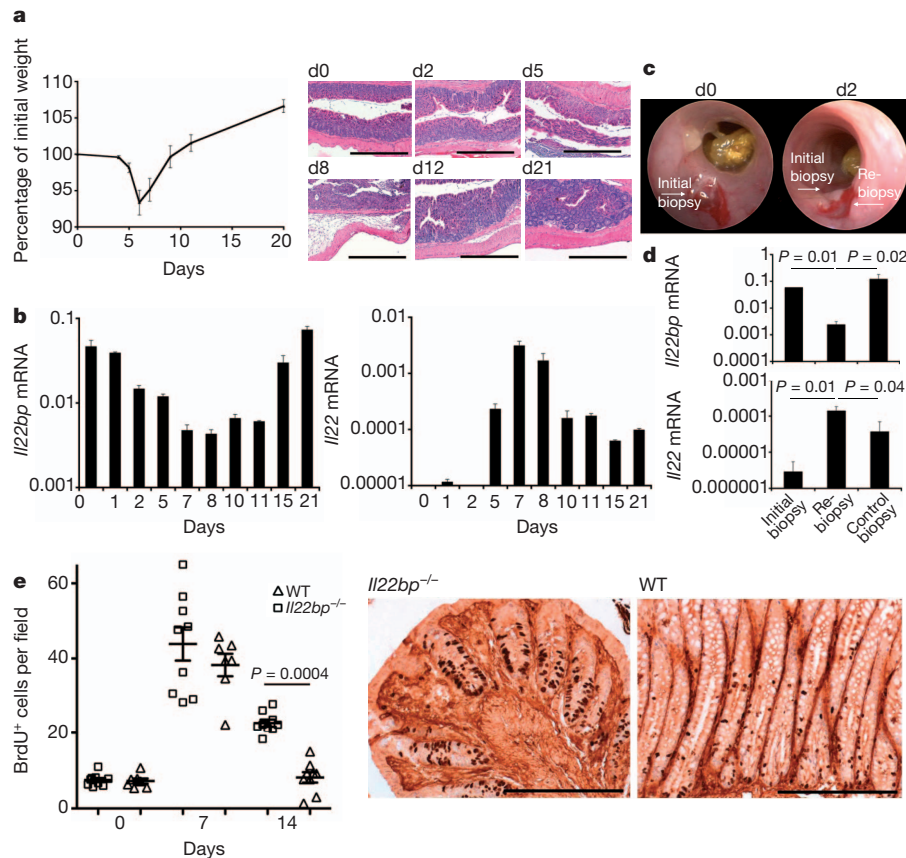


**Figure 2 | Inverse expression of *Il22bp* and *Il22* during chemical and mechanical intestinal tissue damage.** **a**, Weight loss during DSS-colitis (2.5% for 5 days; mean  $\pm$  s.e.m.;  $n = 11$ ), and histology (bars, 500  $\mu$ m). **b**, *Il22* and *Il22bp* mRNA (normalized to *Hprt*) in total colon (mean  $\pm$  s.e.m. of triplicates). **c**, **d**, *Il22bp* and *Il22* mRNA after mechanical wounding (mean  $\pm$  s.e.m.;  $n = 4$ ).

not in TCR- $\beta$ <sup>+</sup> cells (data not shown). Within the TCR- $\beta$ <sup>-</sup> cells MHCII<sup>+</sup>CD11c<sup>+</sup> cells were the main source of *Il22bp* (Fig. 4c and Supplementary Fig. 10).

Next we aimed to identify the trigger and the pathway regulating IL-22BP expression. As shown in Fig. 2 we found that *Il22bp* is

downregulated at day two after DSS administration before the development of histological signs of disease. However, it is known that DSS induces the loss of tight junctions within 2 days, and that the epithelial barrier is therefore permeable, allowing penetrance of bacteria and bacterial products<sup>22</sup>. Interestingly, depletion of the bacterial flora by administration of antibiotics in the DSS-colitis model impaired the downregulation of IL-22BP (data not shown, Fig. 4e). We therefore tested whether the downregulation of IL-22BP is dependent on MYD88 and/or TRIF signalling. To that end we used the endoscopic wounding model as described in Fig. 2. Remarkably, *Il22bp* was not downregulated in *Myd88*<sup>-/-</sup>*Trif*<sup>-/-</sup> dKO mice after wounding of the colon. Moreover, expression appeared to be elevated in the wounded dKO mice compared to the unwounded tissue of these mice. As expected, *Cd11c* (also known as *Itgax*) was also upregulated in the wounded compared to the unwounded tissue. We therefore normalized *Il22bp* expression to *Cd11c*, which showed that the *Il22bp* expression remained stable in *Myd88*<sup>-/-</sup>*Trif*<sup>-/-</sup> dKO mice, but was drastically reduced in wild-type mice after wounding (Fig. 4d). Finally, we could demonstrate that the downregulation of *Il22bp* was independent of the TLR2, TLR4, TLR5 or IL-1 pathways, but dependent on IL-18 (Fig. 4e).

Inflammasomes are cytoplasmic multiprotein complexes that function as sensors of endogenous or exogenous stress. Inflammasomes typically assemble with the adaptor protein ASC (apoptosis-associated speck-like protein) into a multiprotein complex that leads to caspase 1 activation and subsequent cleavage of pro-IL-18 (or pro-IL-1)<sup>23</sup>. Accordingly, the downregulation of *Il22bp* was blocked in *Caspase1*<sup>-/-</sup> and *Asc*<sup>-/-</sup> mice, and we found furthermore that the NLRP3 and NLRP6 inflammasomes, but not NLRC4, were important for this process (Fig. 4e, data not shown). Inflammasomes can be

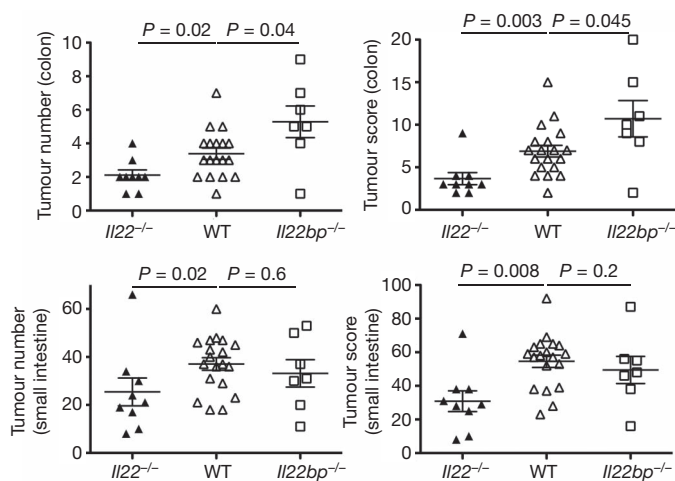


**Figure 3 | IL-22BP controls tumorigenesis in *APC*<sup>min/+</sup> mice.** *Il22bp*<sup>-/-</sup> and *Il22*<sup>-/-</sup> mice were crossed with *APC*<sup>min/+</sup> mice. Six-months-old mice were analysed. Tumour number and size were measured using a dissecting microscope (size 1, < 2 mm; size 2, 2–5 mm; size 3, > 5 mm). Each dot represents one mouse, lines indicate mean  $\pm$  s.e.m. All mice displayed are *APC*<sup>min/+</sup>. No tumours were observed in *APC*<sup>+/+</sup> mice regardless of the *Il22* and *Il22bp* genotype.



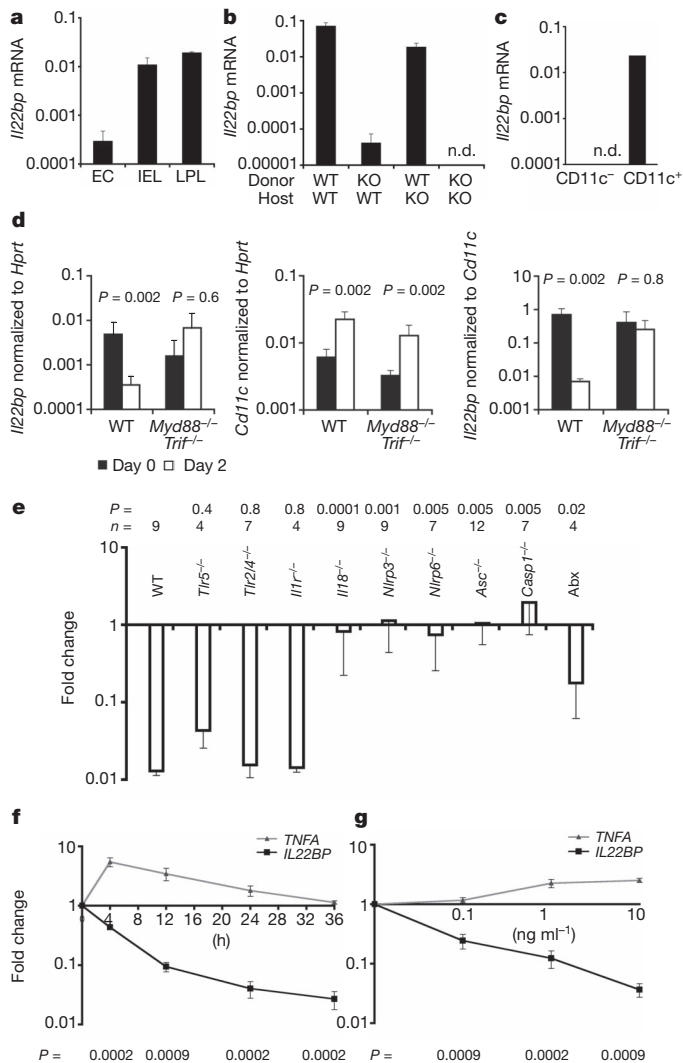


**Figure 4 | IL-18 regulates *Il22bp* expression by CD11c<sup>+</sup> cells.** **a–d**, *Il22bp* expression in the colon. **a**, EC, epithelial cells; IEL, intraepithelial lymphocytes, LPL; lamina propria lymphocytes; mean of triplicates. **b**, Analysis of bone marrow chimaeras ( $n = 8$ ). **c**, Isolation of CD11c<sup>+</sup> cells; mean of duplicates. **d**, Expression of *Il22bp* and *Cd11c* during wounding of WT and *Myd88*<sup>-/-</sup> *Trif*<sup>-/-</sup> mice ( $n = 3$ ). **e**, *Il22bp* expression (re-biopsy relative to initial biopsy; Abx, antibiotic-treated WT mice). **f**, *Il22bp* expression in cultured human-monocyte-derived dendritic cells ( $n = 8$ ). **g**, 10 ng ml<sup>-1</sup> IL-18, variable time; **f**, 24 h, variable IL-18 concentration. Results are representative of two independent experiments (**a–d**, **f**, **g**), cumulative from seven experiments (**e**). Mean  $\pm$  s.e.m.

activated by host-derived factors which are released upon tissue damage, such as ATP, uric acid and hyaluronan, and also by microbial ligands<sup>23</sup>. Using the antibiotic treatment that we validated previously<sup>24</sup>, we found that the downregulation of *Il22bp* was partially dependent on the intestinal microbiota (Fig. 4e). We recently reported that *Nlrp6*<sup>-/-</sup> mice have an altered microflora<sup>24</sup>. We therefore co-housed wild-type mice with *Nlrp6*<sup>-/-</sup> mice, conditions under which the dysbiotic flora are transferred to co-housed recipients. But the downregulation of *Il22bp* upon wounding of the wild-type intestine was not impaired (fold reduction of *Il22bp*: wild type  $0.0123 \pm 0.002$ , wild type (co-housed)  $0.0118 \pm 0.0003$ , *Nlrp6*<sup>-/-</sup> (co-housed)  $0.405 \pm 0.152$ ). These data show that, although the downregulation of *Il22bp* is partially dependent on the microflora (Fig. 4e), it is not affected by the transmissible flora of inflammasome-deficient mice.

It is known that IL-18 is upregulated very early after DSS-induced intestinal tissue damage<sup>25,26</sup>. We therefore tested the role of IL-18 in the

modulation of IL-22BP in this model. We observed that IL-18 is crucial for the complete downregulation of *Il22bp* also upon DSS-induced tissue damage (Supplementary Fig. 11). Whereas loss of IL-18 strongly reduced the level of downregulation of *Il22bp*, there was some residual downregulation of *Il22bp* even in the absence of IL-18, indicating that other factors may also contribute to the regulation of *Il22bp*.

We next aimed to further support and extend our murine *in vivo* data to human biology. We first validated that human dendritic cells express IL-22BP, and then we established, *in vitro*, that IL-18 is able to downregulate IL-22BP (also known as IL22RA2) in human (Fig. 4f, g) and mouse dendritic cells (data not shown) in a time- and dose-dependent manner. Taken together, these data show that IL-18 downregulates *Il22bp* expression by CD11c<sup>+</sup> cells upon intestinal wounding.

Recent publications have shown that *Il18*<sup>-/-</sup> mice have increased inflammation and tumour development in the colitis-associated colon cancer model<sup>26,27</sup>. This is in line with our finding that IL-18 downregulates IL-22BP, and that *Il22*<sup>-/-</sup> mice have increased inflammation and tumorigenesis in the colitis-associated colon cancer model. However, our data do not exclude other important functions of IL-18 besides the regulation of IL-22BP.

Chronic mucosal inflammation and tissue damage as seen in inflammatory bowel disease predisposes patients to the development of colorectal cancer, one of the most frequent fatal cancers in the world. This association could be explained by the hypothesis that the same factors and pathways that are important for wound healing, also promote tumorigenesis. Our data indicate that IL-22 is such a factor. Several studies have linked the microbial status with colon tumorigenesis<sup>28–30</sup>. These data are in line with our results that sensing of microbial ligands and intestinal tissue damage by the NLRP3 and NLRP6 inflammasomes regulates IL-22BP expression by CD11c<sup>+</sup> cells via caspase-1-mediated IL-18 activation. This regulation of IL-22BP is crucial to control the effects of IL-22 during intestinal tissue damage and tumorigenesis (Supplementary Fig. 12). Therefore we propose a link between the microflora, the epithelium and the immune system regulating the balance between tissue regeneration and tumour development in the intestine. The regulation of IL-22BP via the inflammasome provides an unanticipated mechanism, controlling IL-22 and thereby the development of colon cancer.

## METHODS SUMMARY

**Tumour induction.** Co-housed mice were injected intraperitoneally with AOM (azoxymethane) (Sigma) at a dose of 7.5 mg kg<sup>-1</sup> body weight. After 5 days, mice were fed 2–2.5% DSS (MP Biomedicals, molecular mass 36,000–50,000 Da) in the drinking water for 5 days, followed by 16 days of regular water. This cycle was repeated twice.

**Endoscopic procedures.** Colonoscopy was performed in a blinded fashion for colitis and tumour monitoring using the Coloview system (Karl Storz). Colitis scoring was based on granularity of mucosal surface, stool consistence, vascular pattern, translucency of the colon and fibrin visible (0–3 points for each). Tumour sizes were graded from 1 to 5. The total tumour score per mouse was calculated as sum of all tumour sizes. In some experiments the colon was wounded using the endoscopy and a biopsy forceps. A re-biopsy was taken 2 days after the wounding close to the initial biopsy. A control biopsy was taken at a distance of about 0.5 cm.

**Statistical analysis.** For comparison of groups, the non-parametric two-sided Mann–Whitney test or analysis of variance (ANOVA) and post-hoc analysis was applied. The significance level  $\alpha$  was set to 0.05.

**Full Methods** and any associated references are available in the online version of the paper.

Received 14 March; accepted 21 August 2012.

Published online 17 October 2012.

- Grivennikov, S. I., Greten, F. R. & Karin, M. Immunity, inflammation, and cancer. *Cell* **140**, 883–899 (2010).
- Brand, S. *et al.* IL-22 is increased in active Crohn's disease and promotes proinflammatory gene expression and intestinal epithelial cell migration. *Am. J. Physiol. Gastrointest. Liver Physiol.* **290**, G827–G838 (2006).
- Wolk, K. *et al.* IL-22 induces lipopolysaccharide-binding protein in hepatocytes: a potential systemic role of IL-22 in Crohn's disease. *J. Immunol.* **178**, 5973–5981 (2007).

4. Witte, E., Witte, K., Warszawska, K., Sabat, R. & Wolk, K. Interleukin-22: a cytokine produced by T, NK and NKT cell subsets, with importance in the innate immune defense and tissue protection. *Cytokine Growth Factor Rev.* **21**, 365–379 (2010).
5. Sonnenberg, G. F., Fouser, L. A. & Artis, D. Border patrol: regulation of immunity, inflammation and tissue homeostasis at barrier surfaces by IL-22. *Nature Immunol.* **12**, 383–390 (2011).
6. Duhen, T., Geiger, R., Jarrossay, D., Lanzavecchia, A. & Sallusto, F. Production of interleukin 22 but not interleukin 17 by a subset of human skin-homing memory T cells. *Nature Immunol.* **10**, 857–863 (2009).
7. Trifari, S., Kaplan, C. D., Tran, E. H., Crellin, N. K. & Spits, H. Identification of a human helper T cell population that has abundant production of interleukin 22 and is distinct from T<sub>H</sub>-17, T<sub>H</sub>-1 and T<sub>H</sub>-2 cells. *Nature Immunol.* **10**, 864–871 (2009).
8. Pickert, G. *et al.* STAT3 links IL-22 signaling in intestinal epithelial cells to mucosal wound healing. *J. Exp. Med.* **206**, 1465–1472 (2009).
9. Zenewicz, L. A. *et al.* Innate and adaptive interleukin-22 protects mice from inflammatory bowel disease. *Immunity* **29**, 947–957 (2008).
10. Zheng, Y. *et al.* Interleukin-22, a T<sub>H</sub>17 cytokine, mediates IL-23-induced dermal inflammation and acanthosis. *Nature* **445**, 648–651 (2007).
11. Kamanaka, M. *et al.* Memory/effector (CD45RB<sup>lo</sup>) CD4 T cells are controlled directly by IL-10 and cause IL-22-dependent intestinal pathology. *J. Exp. Med.* **208**, 1027–1040 (2011).
12. Wei, C. C., Ho, T. W., Liang, W. G., Chen, G. Y. & Chang, M. S. Cloning and characterization of mouse IL-22 binding protein. *Genes Immun.* **4**, 204–211 (2003).
13. Kosenko, S. V. *et al.* Identification, cloning, and characterization of a novel soluble receptor that binds IL-22 and neutralizes its activity. *J. Immunol.* **166**, 7096–7103 (2001).
14. Xu, W. *et al.* A soluble class II cytokine receptor, IL-22RA2, is a naturally occurring IL-22 antagonist. *Proc. Natl Acad. Sci. USA* **98**, 9511–9516 (2001).
15. Dumoutier, L., Lejeune, D., Colau, D. & Renauld, J. C. Cloning and characterization of IL-22 binding protein, a natural antagonist of IL-10-related T cell-derived inducible factor/IL-22. *J. Immunol.* **166**, 7090–7095 (2001).
16. Jones, B. C., Logsdon, N. J. & Walter, M. R. Structure of IL-22 bound to its high-affinity IL-22R1 chain. *Structure* **16**, 1333–1344 (2008).
17. Tanaka, T. *et al.* A novel inflammation-related mouse colon carcinogenesis model induced by azoxymethane and dextran sodium sulfate. *Cancer Sci.* **94**, 965–973 (2003).
18. Becker, C. *et al.* TGF- $\beta$  suppresses tumor progression in colon cancer by inhibition of IL-6 trans-signaling. *Immunity* **21**, 491–501 (2004).
19. Sugimoto, K. *et al.* IL-22 ameliorates intestinal inflammation in a mouse model of ulcerative colitis. *J. Clin. Invest.* **118**, 534–544 (2008).
20. Su, L. K. *et al.* Multiple intestinal neoplasia caused by a mutation in the murine homolog of the APC gene. *Science* **256**, 668–670 (1992).
21. Kinnebrew, M. A. *et al.* Interleukin 23 production by intestinal CD103<sup>+</sup>CD11b<sup>+</sup> dendritic cells in response to bacterial flagellin enhances mucosal innate immune defense. *Immunity* **36**, 276–287 (2012).
22. Poritz, L. S. *et al.* Loss of the tight junction protein ZO-1 in dextran sulfate sodium induced colitis. *J. Surg. Res.* **140**, 12–19 (2007).
23. Schroder, K. & Tschopp, J. The inflammasomes. *Cell* **140**, 821–832 (2010).
24. Elinav, E. *et al.* NLRP6 inflammasome regulates colonic microbial ecology and risk for colitis. *Cell* **145**, 745–757 (2011).
25. Sivakumar, P. V. *et al.* Interleukin 18 is a primary mediator of the inflammation associated with dextran sulphate sodium induced colitis: blocking interleukin 18 attenuates intestinal damage. *Gut* **50**, 812–820 (2002).
26. Siegmund, B. Interleukin-18 in intestinal inflammation: friend and foe? *Immunity* **32**, 300–302 (2010).
27. Salcedo, R. *et al.* MyD88-mediated signaling prevents development of adenocarcinomas of the colon: role of interleukin 18. *J. Exp. Med.* **207**, 1625–1636 (2010).
28. Li, Y. *et al.* Gut microbiota accelerate tumor growth via c-jun and STAT3 phosphorylation in APCmin/+ mice. *Carcinogenesis* **33**, 1231–1238 (2012).
29. Uronis, J. M. *et al.* Modulation of the intestinal microbiota alters colitis-associated colorectal cancer susceptibility. *PLoS one* **4**, e6026 (2009).
30. Wu, S. *et al.* A human colonic commensal promotes colon tumorigenesis via activation of T helper type 17 T cell responses. *Nature Med.* **15**, 1016–1022 (2009).

**Supplementary Information** is available in the online version of the paper.

**Acknowledgements** The authors would like to thank F. Manzo for expert administrative assistance, E. Eynon and J. Alderman for managing the mouse program. We also thank T. Taylor and G. Tokmoulina for expert help with the FACS sorting. R.A.F. is an Investigator of the Howard Hughes Medical Institute. S.H. was supported by a post-doctoral fellowship from the Crohn's and Colitis Foundation of America, the 'Stiftung experimentelle Biomedizin' and the Ernst Jung Foundation. N.G. was supported by an EMBO post-doctoral fellowship. L.A.Z. was supported by a post-doctoral fellowship from the American Cancer Society. A.J.M., D.M.V. and G.D.Y. were employees of Regeneron Pharmaceuticals at the time this work was performed. W.O. is an employee of Genentech Inc. This work was supported by R01DK077905, DK-P30-34989 and U19-AI082713 (to C.A. and R.A.F.) and by the DFG, SFB841 (to S.H.).

**Author Contributions** R.A.F., S.H. and N.G. designed the experiments, analysed the data and wrote the manuscript. L.A.Z. performed colitis-associated colon cancer experiments with *Il22*<sup>-/-</sup> single-KO mice, and provided *Il22*<sup>-/-</sup> mice. F.J.H. assisted during the mouse endoscopy. L.B. performed immuno histochemistry. B.H. provided mice for colitis-associated cancer experiment. W.O.C. made key suggestions for experiments and edited the manuscript. A.J.M., D.M.V. and G.D.Y. generated *Il22bp*<sup>-/-</sup> mice and are employees of Regeneron Pharmaceuticals Inc. C.J.B. performed the histopathological analyses. W.O. provided IL-22 antibody and is an employee of Genentech. W.Z., J.H.C., C.A. and M.H. did the experiments using human material. S.H. and N.G. performed all other experiments.

**Author Information** Reprints and permissions information is available at [www.nature.com/reprints](http://www.nature.com/reprints). The authors declare competing financial interests: details accompany the full-text HTML version of the paper at [www.nature.com/nature](http://www.nature.com/nature). Readers are welcome to comment on the online version of the paper. Correspondence and requests for materials should be addressed to R.A.F. ([richard.flavell@yale.edu](mailto:richard.flavell@yale.edu)) or S.H. ([shuber@uke.de](mailto:shuber@uke.de)).

## METHODS

**Animals.** Generation of *Il22bp*<sup>-/-</sup> mice: the gene encoding *Il22bp* (*Il22ra2*) was ablated in embryonic stem cells using the Velocigene method<sup>31</sup>. Briefly, a bacterial artificial chromosome (BAC) containing the *Il22ra2* gene (clone 305f24 from Incyte Genomics mouse “BAC embryonic stem cell release 2” library) was isolated and bacterial homologous recombination (BHR) was performed to replace 9.4 kb of the *Il22ra2* gene with a cassette containing a transmembrane (TM)-*lacZ* reporter gene and a floxed neomycin resistance selectable marker gene. The resulting mutant allele (designated VG437) encodes a fusion protein containing 7 amino acids of the mature form of IL-22BP, fused to a transmembrane segment, fused to *Escherichia coli* beta-galactosidase under transcriptional control of the *Il22ra2* gene. BHR resulted in a large targeting vector (BACvec) in which the reporter/selection cassette was flanked with homology arms of 155 and 45 kb. The BACvec was electroporated into VGF1 (ref. 31) embryonic stem cells and G418-resistant colonies were screened for targeting using a loss of native allele (LONA) assay with two quantitative PCR probe/primer sets within the deleted region: 437TU (primers 437TUF: GGGACCTTCAGCTTCTCTGC and 437TUR: CTAAGCAAGTGGCTGCCAGC and probe 437TUP: TGCACAAGGGCTCCTCAGTATGTCAAATG) and 437TD (primers 437TDF: CCAGCCCATGTTTGACAGAAG and 437TDR: TAGCGCCTCAGACCAGTTCAT and probe 437TDP: TGCACACATCTCTCCTTGCTTCTGGG) and appropriate reference probes as described<sup>31</sup>. Correctly targeted embryonic stem cells were microinjected into C57/BL6 blastocysts to produce chimaeras that were subsequently bred to generate knockout mice. *Il22bp*<sup>-/-</sup> mice were backcrossed for 12 generations on C57/BL6 background. For all experiments age- and sex-matched KO mice and co-housed in house breed C57/BL6 wild-type animals between 8 and 14 weeks of age were used. *Casp1*<sup>-/-</sup> were generated in our laboratory<sup>32</sup>. *Apc*<sup>min/+</sup>, *Il18*<sup>-/-</sup>, *Il1r*<sup>-/-</sup>, *Myd88*<sup>-/-</sup>, *Trif*<sup>-/-</sup>, *Tlr4*<sup>-/-</sup> and *Tlr5*<sup>-/-</sup> mice were obtained from The Jackson Laboratory. *Nlrp3*<sup>-/-</sup>, *Nlrp6*<sup>-/-</sup>, *Asc*<sup>-/-24</sup> and *Il22*<sup>-/-9</sup> mice are described elsewhere. For antibiotic treatment, mice were given either a combination of ciprofloxacin (0.2 g l<sup>-1</sup>) and metronidazole (1 g l<sup>-1</sup>) or a combination of vancomycin (1 g l<sup>-1</sup>), ampicillin (1 g l<sup>-1</sup>), kanamycin (1 g l<sup>-1</sup>), and metronidazole (1 g l<sup>-1</sup>) for 4 weeks in the drinking water<sup>24</sup>.

Mice were cared for in accordance with institutional animal care and use committee-approved protocols at the Yale University School of Medicine animal facility.

**Tumour induction.** Mice were injected intraperitoneally with AOM (Sigma) at a dose of 7.5 mg kg<sup>-1</sup> body weight. After 5 days, mice were fed 2.5% DSS (MP biomedical, molecular mass 36,000–50,000 Da) in the drinking water for 5 days, followed by 16 days of regular water. This cycle was repeated twice<sup>33</sup>. Mice were killed on day 80 of the experiment.

**DSS colitis.** For acute DSS colitis induction mice were administered 2–2.5% DSS in the drinking water for 7 days, followed by 3 days of regular water. For chronic DSS colitis induction mice were fed 2.5% DSS for 5 days followed by 16 days of regular water. This cycle was repeated three times. According to the animal protocol, mice were killed if they lost more than 20% of their initial body mass.

**Endoscopic procedures.** Colonoscopy was performed in a blinded fashion for colitis and tumour monitoring using the Coloview system (Karl Storz) as previously described<sup>6</sup>. Briefly, colitis scoring was based on granularity of mucosal surface, stool consistence, vascular pattern, translucency of the colon and fibrin visible (0–3 points for each). Tumour sizes were graded from 1 to 5. Tumours

observed during endoscopy were counted to obtain the total number of tumours per animal. The total tumour score per mouse was calculated as sum of all tumour sizes. The colon was wounded using the endoscopy and a biopsy forceps as described previously<sup>8,34</sup>. A re-biopsy was taken 2 days after the wounding either close to the initial biopsy or at a distance of about 0.5 cm.

**Histopathology procedures.** Colons were evaluated and were assigned scores by investigators blinded to experimental manipulation. Each section was evaluated by a semiquantitative criterion-based method (score 0–5) essentially as described before<sup>35</sup>. For immunohistochemistry paraffin-embedded sections were stained with anti-BrdU (Sigma) or anti-Ki67 (Thermo (Lab Vision)). DAKO EnVision System was used for detection. All sections were counterstained with haematoxylin. TUNEL (TdT-mediated dUTP nick end labelling) staining was performed using an ApoAlert DNA fragmentation assay kit according to the manufacturer's instruction. BrdU was injected 4 h before the animals were killed.

**Isolation of epithelial cells and haematopoietic cells from the intestine.** and haematopoietic cells were isolated from the freshly obtained colon. After removal of the Payer's patches and the adventitial fat, the colon was cut longitudinally and washed with PBS. For disruption of the epithelial cells the colon was incubated in HBSS/EDTA at 37 °C. The supernatant was collected and further separated in CD45-positive (intraepithelial lymphocytes) and -negative cells using MACS (magnetic-activated cell sorting). The remaining colon was digested using collagenase/DNase incubation at 37 °C. CD45-positive cells (lamina propria lymphocytes) were purified using MACS. In a second step CD45-positive IEL and LPL cells were further purified using a MoFlo. The purity of CD45-positive cells was >95%, epithelial cells were >98% CD45 negative.

**Colon explant culture.** One centimeter of the distal colon was removed, washed with PBS, scaled and cultured for 3 days in X-Vivo medium containing penicillin, streptomycin and tetracycline. IL-6 was measured using CBA (cytometric bead array).

**RNA analysis.** Total RNA was extracted from colon tissue, tumours, colon biopsies or cells using TRIzol reagent, followed by RNA clean up using the RNeasy Kit (Qiagen) or the Dynabeads mRNA Kit (Applied Biosystems). The high capacity cDNA synthesis kit (Applied Biosystems) was used for synthesis of cDNA. Real-time PCR analysis using TaqMan Fast Universal PCR Mater Mix and TaqMan Gene Expression Assays (Applied Biosystems) was performed on 7500 Fast Real-time PCR system machine (Applied Biosystems).

**Human subjects.** Informed consent was obtained from healthy participants per protocol approved by the institutional review board at Yale University.

- Valenzuela, D. M. *et al.* High-throughput engineering of the mouse genome coupled with high-resolution expression analysis. *Nature Biotechnol.* **21**, 652–659 (2003).
- Sutterwala, F. S. *et al.* Critical role for NALP3/CIA1/cryopyrin in innate and adaptive immunity through its regulation of caspase-1. *Immunity* **24**, 317–327 (2006).
- Okayasu, I., Ohkusa, T., Kajiura, K., Kanno, J. & Sakamoto, S. Promotion of colorectal neoplasia in experimental murine ulcerative colitis. *Gut* **39**, 87–92 (1996).
- Becker, C., Fantini, M. C. & Neurath, M. F. High resolution colonoscopy in live mice. *Nature Protocols* **1**, 2900–2904 (2006).
- O'Connor, W. Jr *et al.* A protective function for interleukin 17A in T cell-mediated intestinal inflammation. *Nature Immunol.* **10**, 603–609 (2009).



# Regulatory B cells control T-cell autoimmunity through IL-21-dependent cognate interactions

Ayumi Yoshizaki<sup>1</sup>\*, Tomomitsu Miyagaki<sup>1</sup>\*, David J. DiLillo<sup>1</sup>, Takashi Matsushita<sup>1</sup>, Mayuka Horikawa<sup>1</sup>, Evgueni I. Kountikov<sup>1</sup>, Rosanne Spolski<sup>2</sup>, Jonathan C. Poe<sup>1</sup>, Warren J. Leonard<sup>2</sup> & Thomas F. Tedder<sup>1</sup>\*

B cells regulate immune responses by producing antigen-specific antibodies<sup>1</sup>. However, specific B-cell subsets can also negatively regulate T-cell immune responses, and have been termed regulatory B cells<sup>2–4</sup>. Human and mouse regulatory B cells (B10 cells) with the ability to express the inhibitory cytokine interleukin-10 (IL-10) have been identified<sup>2–5</sup>. Although rare, B10 cells are potent negative regulators of antigen-specific inflammation and T-cell-dependent autoimmune diseases in mice<sup>5–7</sup>. How B10-cell IL-10 production and regulation of antigen-specific immune responses are controlled *in vivo* without inducing systemic immunosuppression is unknown. Using a mouse model for multiple sclerosis, here we show that B10-cell maturation into functional IL-10-secreting effector cells that inhibit *in vivo* autoimmune disease requires IL-21 and CD40-dependent cognate interactions with T cells. Moreover, the *ex vivo* provision of CD40 and IL-21 receptor signals can drive B10-cell development and expansion by four-million-fold, and generate B10 effector cells producing IL-10 that markedly inhibit disease symptoms when transferred into mice with established autoimmune disease. The *ex vivo* expansion and reinfusion of autologous B10 cells may provide a novel and effective *in vivo* treatment for severe autoimmune diseases that are resistant to current therapies.

A subset of regulatory B cells has been functionally defined in humans and mice by their ability to express IL-10 (refs 5–7). B cells that are competent to express IL-10 after 5 h of *ex vivo* phorbol ester and ionomycin stimulation are called B10 cells<sup>6</sup> to distinguish them from other regulatory B cells that modulate immune responses through other mechanisms<sup>2,8</sup>. B10 cells are found at low frequencies (1–5%) in naive mice but expand with autoimmunity<sup>9</sup>. Spleen B10 cells are predominantly found within the minor CD1d<sup>hi</sup>CD5<sup>+</sup> B-cell subpopulation, along with B10 progenitor (B10pro) cells that are induced to become IL-10 competent during *in vitro* culture with agonistic CD40 monoclonal antibody or lipopolysaccharide (LPS)<sup>9,10</sup>. The capacity of human and mouse B10 cells to produce IL-10 is central to their ability to negatively regulate inflammation and autoimmune disease, as well as innate and antigen-specific adaptive immune responses<sup>5–7,9–12</sup>, but the physiological signals controlling IL-10 production *in vivo* are unknown.

B10-cell immunoregulation is antigen specific, and B-cell antigen receptor (BCR) specificity markedly influences B10-cell development<sup>6,9</sup>. Receptors or pathways that positively or negatively regulate BCR signalling can also modulate B10-cell numbers *in vivo*. For example, CD19-deficient (*Cd19*<sup>−/−</sup>) mice are essentially devoid of regulatory B10 cells, which leads to exacerbated inflammation and disease symptoms during contact hypersensitivity, and in the experimental autoimmune encephalomyelitis (EAE) model of multiple sclerosis<sup>6,7</sup>. IL-10 itself is not required for B10-cell development as B cells with the capacity to express IL-10 reporter genes develop normally in *Il10*<sup>−/−</sup> mice<sup>13</sup>. B10-cell numbers are also normal in T-cell-deficient nude mice and in mice deficient in expression of major histocompatibility complex class II

(MHC-II) or CD40 molecules that are both important for cognate B-cell–T-cell interactions<sup>9</sup>. Consequently, appropriate BCR signals are thought to select a subset of B cells to become IL-10-competent B10 cells. Innate pathogen-induced signals also influence regulatory B10-cell IL-10 production *in vivo*<sup>3,13</sup>. Little is otherwise known about how B10-cell IL-10 production is regulated, and it remains unclear how these rare B cells exert such potent *in vivo* effects and selectively inhibit antigen-specific T-cell function during inflammation and autoimmunity.

To identify signals that regulate B10 cells *in vivo*, purified B cells were cultured with cytokines known to influence B-cell function. Stimulation with IL-21, but not IL-4, -6, -10, -12, -23 or -27, induced 2.7- to 3.2-fold higher B10-cell frequencies, and 4.4- to 5.3-fold more IL-10 secretion ( $P < 0.01$ ) at 48 and 72 h, respectively, whereas interferon- $\gamma$  (IFN- $\gamma$ ) or transforming growth factor- $\beta$  (TGF- $\beta$ ) reduced IL-10<sup>+</sup> B-cell frequencies by 56% ( $P < 0.05$ ; Fig. 1a). In fact, IL-21 induced B10 cells to produce IL-10 without the need for *in vitro* stimulation (Fig. 1b and Supplementary Fig. 1a) and induced IL-10 secretion at levels similar to LPS stimulation (Fig. 1a). IL-21 also induced a threefold increase in IL-10<sup>+</sup> B cells within the spleen CD1d<sup>hi</sup>CD5<sup>+</sup> B-cell subset that is enriched for B10pro and B10 cells, but it did not induce IL-10<sup>+</sup> B cells among the CD1d<sup>lo</sup>CD5<sup>−</sup> subset (Fig. 1b). T-cell-derived IL-21 has multiple important roles in B-cell effector function<sup>14–18</sup>, and IL-21 is a potent inducer of T-cell IL-10 production<sup>19,20</sup>. Both B10 and non-B10 cells expressed cell surface IL-21 receptor (IL-21R) at similar levels (Fig. 1c). Despite this, *ex vivo* B10-, B10pro- and CD1d<sup>hi</sup>CD5<sup>+</sup> B-cell numbers were similar in wild-type, IL-21R-deficient (*Il21r*<sup>−/−</sup>), *MHC-II*<sup>−/−</sup> and *Cd40*<sup>−/−</sup> mice (Supplementary Fig. 1b–d, data not shown). However, IL-21R expression was required for B10-cell expansion *in vivo* after myelin oligodendrocyte glycoprotein peptide (MOG<sub>35–55</sub>) immunizations to induce EAE (Fig. 1d). Thus, IL-21R-generated signals induced B10-cell expansion and IL-10 secretion *in vivo*.

Whether B10 cells require IL-21 to induce their regulatory function *in vivo* was determined by the adoptive transfer of *Il21r*<sup>−/−</sup> B cells into *Cd19*<sup>−/−</sup> mice before the induction of EAE. Because *Cd19*<sup>−/−</sup> mice are B10-cell deficient (Fig. 1d), their EAE disease severity is worse (Fig. 2a)<sup>11</sup>. The adoptive transfer of wild-type CD1d<sup>hi</sup>CD5<sup>+</sup> B cells normalized EAE severity in *Cd19*<sup>−/−</sup> mice. By contrast, the transfer of CD1d<sup>hi</sup>CD5<sup>+</sup> B cells from *Il21r*<sup>−/−</sup> or *Il10*<sup>−/−</sup> mice, or wild-type CD1d<sup>lo</sup>CD5<sup>−</sup> non-B10 cells, did not alter disease. Because CD4<sup>+</sup> T cells are a major source of IL-21, we determined whether cognate B10–T-cell interactions also controlled B10-cell-mediated suppression of EAE. The transfer of CD1d<sup>hi</sup>CD5<sup>+</sup> B cells from *MHC-II*<sup>−/−</sup> or *Cd40*<sup>−/−</sup> mice into *Cd19*<sup>−/−</sup> mice before MOG immunizations did not reduce EAE disease severity (Fig. 2a, bottom right). CD1d<sup>lo</sup>CD5<sup>−</sup> B cells from *Il21r*<sup>−/−</sup>, *Cd40*<sup>−/−</sup> or *MHC-II*<sup>−/−</sup> mice were also without effect (data not shown). EAE is also exacerbated in wild-type mice depleted of mature B cells by CD20 monoclonal antibody<sup>7,11</sup>. However, transfer of CD1d<sup>hi</sup>CD5<sup>+</sup> B cells from *Cd20*<sup>−/−</sup> mice, but

<sup>1</sup>Departments of Immunology, Duke University Medical Center, Durham, North Carolina 27710, USA. <sup>2</sup>Laboratory of Molecular Immunology, National Heart, Lung, and Blood Institute, National Institutes of Health, Bethesda, Maryland 20892-1674, USA.

\*These authors contributed equally to this work.

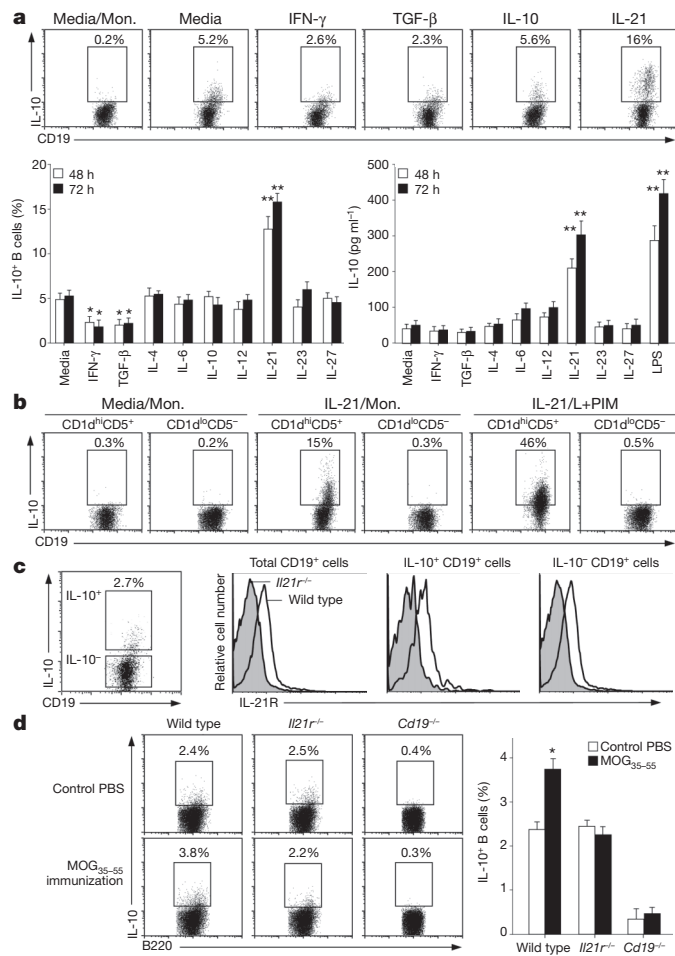
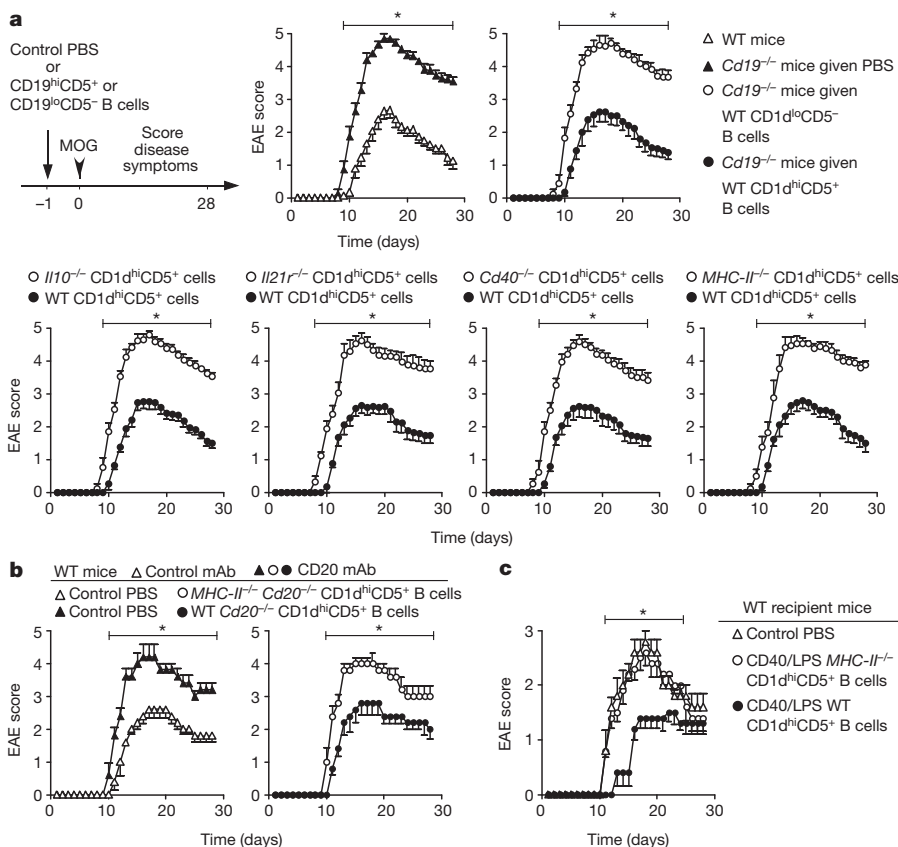


**Figure 1 | IL-21 induces regulatory B10-cell function.** **a**, IL-21 induces B10-cell IL-10 production and secretion. Purified spleen CD19<sup>+</sup> B cells from wild-type mice were cultured in medium alone or containing the indicated cytokines or LPS. To visualize IL-10-competent B cells, LPS, phorbol-12-myristate-13-acetate (PMA), ionomycin and monensin (L+PIM) were added to the cultures 5 h before the cells were stained for cell-surface CD19 and cytoplasmic IL-10 expression and analysed by flow cytometry. Representative histograms show IL-10<sup>+</sup> cell frequencies within the indicated gates, with background staining shown for cells cultured with monensin (Mon.) alone. Bar graphs indicate mean  $\pm$  s.e.m. IL-10<sup>+</sup> B-cell frequencies or culture supernatant fluid IL-10 concentrations at 48 or 72 h from three independent experiments using individual mice. **b**, IL-21 induces CD1d<sup>hi</sup>CD5<sup>+</sup> B-cell IL-10 production. Purified spleen CD1d<sup>hi</sup>CD5<sup>+</sup> or CD1d<sup>lo</sup>CD5<sup>+</sup> B cells from wild-type mice were cultured with media alone or containing IL-21 for 48 h before IL-10<sup>+</sup> B-cell frequencies were assessed as in **a**. **c**, B10 cells express IL-21R. CD19<sup>+</sup> splenocytes purified from wild-type mice were cultured with L+PIM for 5 h before cell-surface CD19 and IL-21R, and cytoplasmic IL-10 staining to identify IL-10-competent B10 cells (dot plot, left panel). Representative IL-21R expression by IL-10<sup>+</sup> and IL-10<sup>-</sup> B cells from wild-type mice is shown in comparison with control B cells from *Il21r*<sup>-/-</sup> mice (grey histograms). Results represent three independent experiments using individual mice. **d**, IL-21R expression is required for B10-cell expansion *in vivo* after MOG immunization. B10-cell numbers were assessed in wild-type, *Il21r*<sup>-/-</sup> or *Cd19*<sup>-/-</sup> mice 7 days after saline (PBS) or MOG<sub>35-55</sub> immunization. Representative flow cytometry histograms are shown. Bar graphs indicate mean  $\pm$  s.e.m. B10-cell frequencies ( $\geq 3$  mice per group). **a**, **d**, Significant differences between sample means are indicated: \* $P < 0.05$ ; \*\* $P < 0.01$ .

not *MHC-II*<sup>-/-</sup> *Cd20*<sup>-/-</sup> mice, normalized disease severity in this model, and CD1d<sup>lo</sup>CD5<sup>-</sup> B cells from *Cd20*<sup>-/-</sup> or *MHC-II*<sup>-/-</sup> *Cd20*<sup>-/-</sup> mice were without effect (Fig. 2b, data not shown). Similarly, the adoptive transfer of *in vitro* activated CD1d<sup>hi</sup>CD5<sup>+</sup> B cells from wild-type mice significantly reduced EAE disease severity in wild-type mice, whereas activated *MHC-II*<sup>-/-</sup> CD1d<sup>hi</sup>CD5<sup>+</sup> or wild-type CD1d<sup>lo</sup>CD5<sup>-</sup> B cells had no effect (Fig. 2c, data not shown). Thus, regulatory B10-cell function required IL-10 expression and IL-21R signalling, as well as CD40 and MHC-II interactions, potentially explaining antigen-specific B10-cell effector function<sup>6</sup>.

**Figure 2 | B10 cells require IL-10, IL-21R, CD40 and MHC-II expression to regulate EAE severity.**

**a**, One day before *Cd19*<sup>-/-</sup> or wild-type (WT) mice were immunized with MOG<sub>35-55</sub> on day 0, the *Cd19*<sup>-/-</sup> mice received PBS or purified spleen CD1d<sup>hi</sup>CD5<sup>+</sup> or CD1d<sup>lo</sup>CD5<sup>-</sup> B cells from either wild-type, *Il10*<sup>-/-</sup>, *Il21r*<sup>-/-</sup>, *Cd40*<sup>-/-</sup> or *MHC-II*<sup>-/-</sup> mice. Mice were scored daily thereafter for disease severity. The top two graphs show data from the same experiment, but were separated to facilitate visualization of the overlapping curves. **b**, B10 cells require MHC-II expression to regulate EAE severity in wild-type mice treated with CD20 or control monoclonal antibody (mAb) 7 days before MOG<sub>35-55</sub> immunization on day 0. The mice also received PBS or purified CD1d<sup>hi</sup>CD5<sup>+</sup> B cells from either *Cd20*<sup>-/-</sup> or *MHC-II*<sup>-/-</sup> *Cd20*<sup>-/-</sup> mice 1 day before MOG<sub>35-55</sub> immunization. The two graphs are from the same experiment, but were separated to facilitate visualization of the overlapping curves. **c**, Activated *MHC-II*<sup>-/-</sup> B10 cells do not reduce disease severity in wild-type mice. Purified CD1d<sup>hi</sup>CD5<sup>+</sup> B cells from wild-type or *MHC-II*<sup>-/-</sup> mice were cultured with agonistic CD40 monoclonal antibody for 48 h to induce B10pro-cell maturation, with LPS added during the final 5 h of culture. Wild-type mice were given either PBS or CD1d<sup>hi</sup>CD5<sup>+</sup> B cells 1 day before MOG<sub>35-55</sub> immunization on day 0. **a–c**, Values represent mean ( $\pm$  s.e.m.) symptom scores from  $\geq 3$  mice in each group, with similar results obtained in three independent experiments. Significant differences between sample means are indicated: \* $P < 0.05$ .



To determine whether cognate B10–T-cell interactions regulate antigen-specific T-cell proliferation *in vivo*, B10-cell function was assessed in MOG<sub>35–55</sub>-immunized *Cd19*<sup>−/−</sup> mice after the adoptive transfer of dye-labelled CD4<sup>+</sup> T cells from transgenic mice expressing antigen receptors specific for the MOG<sub>35–55</sub> (TCR<sup>MOG</sup>) peptide<sup>21</sup>. CD1d<sup>hi</sup>CD5<sup>+</sup> B cells from naive wild-type mice significantly reduced TCR<sup>MOG</sup> CD4<sup>+</sup> T-cell proliferation, as measured by *in vivo* dye dilution (Fig. 3a). CD1d<sup>hi</sup>CD5<sup>+</sup> B cells obtained from mice with EAE were even more potent inhibitors of T-cell proliferation, whereas

CD1d<sup>lo</sup>CD5<sup>−</sup> B cells from wild-type mice, or CD1d<sup>hi</sup>CD5<sup>+</sup> B cells from *Il10*<sup>−/−</sup>, *Il21r*<sup>−/−</sup>, *Cd40*<sup>−/−</sup>, or *MHC-II*<sup>−/−</sup> mice were without effect. CD1d<sup>hi</sup>CD5<sup>+</sup> B cells from naive or antigen-experienced wild-type mice also significantly reduced TCR<sup>MOG</sup> CD4<sup>+</sup> T-cell IFN-γ and IL-17 production in MOG<sub>35–55</sub>-immunized *Cd19*<sup>−/−</sup> mice, whereas CD1d<sup>hi</sup>CD5<sup>+</sup> B cells from *Il10*<sup>−/−</sup>, *Il21r*<sup>−/−</sup>, *Cd40*<sup>−/−</sup> or *MHC-II*<sup>−/−</sup> mice did not (Fig. 3b). The ability of B10 cells to inhibit T-cell IL-17 production is particularly important because pathogenic T<sub>H</sub>17 T cells induce EAE and can produce IL-21 (ref. 22). The majority of

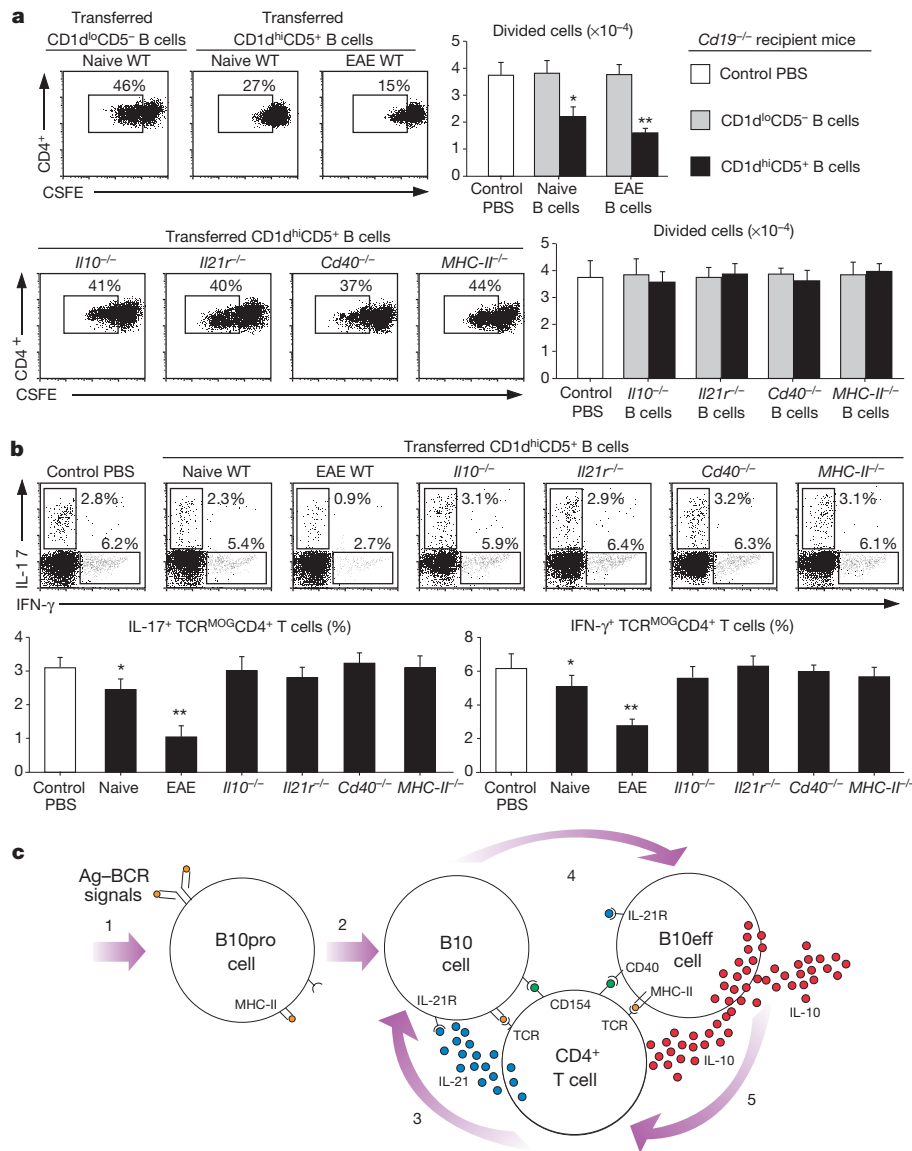


**Figure 3 | B10-cell expansion and regulation of T-cell-mediated autoimmunity.** **a**, B10 cells require IL-10, IL-21R, CD40 and MHC-II expression to regulate antigen-specific T-cell proliferation *in vivo*. *Cd19*<sup>−/−</sup> recipient mice were given PBS as a control, or purified CD1d<sup>hi</sup>CD5<sup>+</sup> or CD1d<sup>lo</sup>CD5<sup>−</sup> B cells from naive wild-type (WT), *Il10*<sup>−/−</sup>, *Il21r*<sup>−/−</sup>, *Cd40*<sup>−/−</sup> or *MHC-II*<sup>−/−</sup> mice, or wild-type mice with EAE (day 28) 1 day before MOG<sub>35–55</sub> immunization on day 0. Four days after immunization, dye (CFSE)-labelled TCR<sup>MOG</sup> CD4<sup>+</sup>Thy1.1<sup>+</sup> T cells were transferred into *Cd19*<sup>−/−</sup> recipient mice. Five days later, peripheral lymph node CD4<sup>+</sup>Thy1.1<sup>+</sup> T cells were analysed for proliferation, with representative flow cytometry analysis of CFSE dilution shown. Bar graphs indicate mean (± s.e.m.) numbers of divided TCR<sup>MOG</sup> T cells. **b**, B10 cells require IL-10, IL-21R, CD40 and MHC-II expression to regulate antigen-specific T-cell cytokine production. Purified CD1d<sup>hi</sup>CD5<sup>+</sup> B cells from the indicated mice were transferred into *Cd19*<sup>−/−</sup> recipient mice 1 day before MOG<sub>35–55</sub> immunization on day 0, with TCR<sup>MOG</sup>

Thy1.1<sup>+</sup>CD4<sup>+</sup> T cells transferred on day 4. Fourteen days later, lymph node Thy1.1<sup>+</sup>CD4<sup>+</sup> T cells were analysed for IL-17 and IFN-γ production by intracellular cytokine staining, with representative flow cytometry results shown. **a**, **b**, Bar graphs indicate mean (± s.e.m.) frequencies of divided or cytokine-expressing cells, with three mice in each group. Significant differences between sample means are indicated: \**P* < 0.05; \*\**P* < 0.01. **c**, Model for autoantigen (Ag)-specific B10-cell function. B cells capture autoantigens that trigger appropriate BCR signals (step 1) and promote IL-10-competent B10pro-cell development. During immune responses (step 2), B10pro cells present peptides to antigen-specific T cells through cognate interactions that induce T-cell activation and CD40/CD154 interactions. Activated T cells may produce IL-21 locally, which binds to proximal B10 cell IL-21R (step 3). IL-21R signals induce B10-cell IL-10 production and effector function (B10eff, step 4), which may negatively regulate antigen-specific T-cell function (step 5).



T follicular helper cells isolated from mice with MOG<sub>35–55</sub>-induced EAE also express IL-21 (ref. 23), and *Cd19*<sup>−/−</sup> mice have T follicular helper cells (Supplementary Fig. 2). Thus, B10 and T cells may require intimate interactions during reciprocal IL-10 and IL-21 production to optimally regulate antigen-specific disease (Fig. 3c).

To verify that T-cell-derived IL-21 and CD40 signals drive B10-cell expansion and IL-10 production, B cells were cultured using optimized conditions that promote mouse B10-cell expansion *in vivo*<sup>24</sup> and B-cell expansion *in vitro*<sup>25</sup>. B cells were cultured on monolayers of NIH-3T3 cells expressing the T-cell ligand for CD40 (CD154) and B-lymphocyte stimulator (BLyS; also known as TNFSF13B) in the presence of IL-4, for 4 days to induce B10pro-cell maturation into IL-10-competent B10 cells. The B cells were then cultured on fresh NIH-3T3–CD154/BLyS cells with exogenous IL-21 for 5 days, which was essential to optimally expand B10 cells and induce IL-10 production (Fig. 4a). After the 9-day culture period, B-cell and B10-cell numbers were increased by 25,000- and 4,000,000-fold, respectively, with 38% of the B cells actively producing IL-10 (Fig. 4b). The vast majority of IL-10<sup>+</sup> B cells in the cultures expressed CD5 (Fig. 4c), facilitating their purification and underscoring the marked effect of IL-21 on B10-cell numbers *in vitro*.

*In vitro* expanded CD5<sup>+</sup> B10 cells retained their regulatory function. The transfer of CD5<sup>+</sup> B10 cells markedly reduced EAE disease severity in wild-type mice, even when given after the appearance of disease symptoms, whereas CD5<sup>−</sup> B cells were without effect (Fig. 4d). Although the *in vitro* expansion of B10 cells required both IL-21R and CD40 signals, MHC-II expression was not required (Fig. 4e). However, *in vitro* expanded *MHC-II*<sup>−/−</sup> CD5<sup>+</sup> B10 cells and *Il10*<sup>−/−</sup> CD5<sup>+</sup> B cells did not regulate EAE disease severity (Fig. 4f), further showing a requirement for IL-10 and cognate interactions in the regulation of T-cell-mediated disease. B10 cells did not expand during *in vitro* cultures of B cells from *Cd19*<sup>−/−</sup> mice or MD4 transgenic mice<sup>26</sup> that have a fixed BCR specific for egg lysozyme (Fig. 4e), highlighting the importance of BCR specificity and signalling in B10-cell generation. Otherwise, *in vitro* expanded B10 effector cells were potent regulators of both disease initiation and progression.

This study demonstrates that CD40 signals induce B10pro-cell acquisition of IL-10 competence, with IL-21 driving B10-cell expansion and effector cell generation. These critical checkpoints in B10-cell development may lead to localized IL-10 production that blunts antigen-specific T-cell responses during cognate interactions (Fig. 3c), without untoward immunosuppression. Transient IL-10 production by B10 cells *in vivo* may further restrict the effects of IL-10 secretion<sup>13</sup>. B10 effector cells may also regulate T-cell responses to autoantigens in addition to MOG once inflammation and tissue destruction are initiated by MOG<sub>35–55</sub> immunization. Because human and mouse B10 cells are also potent regulators of macrophage and dendritic cell function<sup>5,12</sup>, T-cell induction of B10 effector cells may also contribute to EAE resolution by restraining monocyte and dendritic cell activation. Together, these results may explain in part why EAE is exacerbated in the absence of IL-21 signalling<sup>27</sup>. By contrast, TGF- $\beta$  and IFN- $\gamma$  may counterbalance B10-cell expansion *in vivo* based on the current *in vitro* findings (Fig. 1a). Regulatory T cells provide an independent layer of regulation during EAE, as their expansion, accumulation in the central nervous system, and suppressive activity are normal when B10 cells are absent<sup>11,28</sup>. The *in vitro* recapitulation of these collective signals induced a several-million-fold expansion of B10 cells, and their functional maturation into potent B10 effector cells, which then reversed established autoimmune disease (Fig. 4). In addition to BCR specificity, MHC-II expression remained an important checkpoint for B10 effector cell regulatory function during EAE (Fig. 4f), as first described for regulatory type II monocytes<sup>29</sup>. Because autoimmunity has multigenic origins and autoantigens vary between patients and disease, *in vitro* expansion of the rare pool of human B10pro and B10 effector cells<sup>5</sup> may provide a potent future immunotherapy for individuals with severe autoimmune disease.

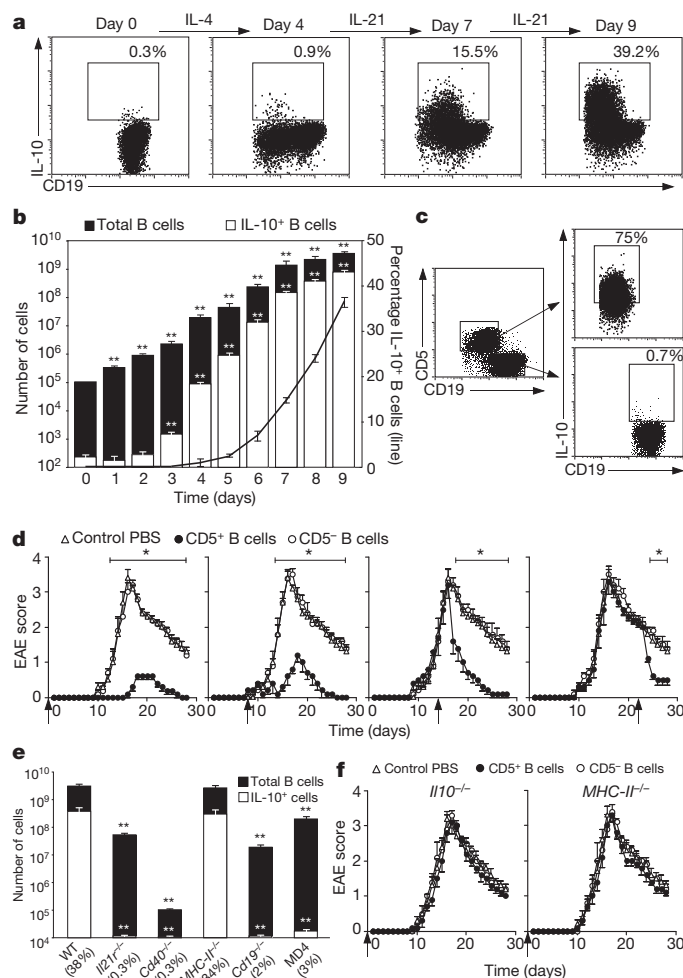


**Figure 4 | IL-21 drives *ex vivo* regulatory B10-cell expansion.** **a**, B10-cell development *in vitro*. Purified spleen B cells were cultured on NIH-3T3–CD154/BLyS-cell monolayers with exogenous IL-4 for 4 days, then cultured on fresh NIH-3T3–CD154/BLyS cells with exogenous IL-21 for 3 or 5 days as indicated, isolated, cultured with monensin for 5 h and stained for cytoplasmic IL-10 expression. Representative IL-10<sup>+</sup> B-cell frequencies within the indicated gates are shown. Similar results were obtained in  $\geq 10$  experiments. **b**, IL-21 drives B10-cell expansion *in vitro*. B cells cultured as in **a** were harvested each day. Bar values represent mean ( $\pm$  s.e.m.) B-cell and B10-cell numbers, or B10-cell frequencies (solid line) from three independent experiments. **c**, IL-21-induced B10 cells express CD5. B cells cultured for 9 days as in **a** were stained for CD5 and CD19 expression. CD5<sup>+</sup> or CD5<sup>−</sup> B cells were then purified and cultured with monensin for 5 h before cytoplasmic IL-10 staining. Results represent three independent experiments. **d**, B10 effector cells inhibit EAE initiation and progression. CD5<sup>+</sup> CD19<sup>+</sup> or CD5<sup>−</sup> CD19<sup>+</sup> cells were isolated as in **c** and adoptively transferred into wild-type mice on days −1, 7, 14 or 21 (arrows) before/after MOG immunization and EAE induction, as in Fig. 2. **e**, B10-cell expansion *in vitro* requires IL-21R and CD40 expression, and *in vivo* BCR signalling. Purified spleen B cells isolated from wild-type, *Il21r*<sup>−/−</sup>, *Cd40*<sup>−/−</sup>, *MHC-II*<sup>−/−</sup>, *Cd19*<sup>−/−</sup> or MD4 mice were cultured as in **a**, with mean ( $\pm$  s.e.m.) cell numbers quantified after culture. Values represent means  $\pm$  s.e.m. of three independent experiments. IL-10<sup>+</sup> B-cell frequencies in the cultures are shown in parentheses. **f**, B10 effector cells require IL-10 and MHC-II expression to inhibit EAE. B cells from *Il10*<sup>−/−</sup> or *MHC-II*<sup>−/−</sup> mice were cultured as in **a**, separated into CD5<sup>+</sup> or CD5<sup>−</sup> cells as in **c**, and adoptively transferred into wild-type mice before MOG<sub>35–55</sub> immunization as in **d**. **d**, **f**, Values represent mean ( $\pm$  s.e.m.) symptom scores from  $\geq 3$  mice in each group, with similar results obtained in three independent experiments. **b**, **d**, **e**, Significant differences between sample means are indicated: \* $P < 0.05$ ; \*\* $P < 0.01$ .

## METHODS SUMMARY

**Mice.** Mice were used at 6–12 weeks of age. The Duke University and National Heart, Lung, and Blood Institute Animal Care and Use Committee approved all studies.

**Immunofluorescence analysis.** For two- to six-colour immunofluorescence analysis, single-cell spleen suspensions were purified, stained and analysed as described<sup>6,7,11,30</sup>.

**In vitro B-cell cultures.** Purified splenic B cells (95–98%) were cultured with either recombinant IFN- $\gamma$  (10 ng ml<sup>-1</sup>), IL-4 (2 ng ml<sup>-1</sup>), IL-6 (10 ng ml<sup>-1</sup>), IL-21 (100 ng ml<sup>-1</sup>), TGF- $\beta$  (10 ng ml<sup>-1</sup>), IL-10 (10 ng ml<sup>-1</sup>), IL-12 (10 ng ml<sup>-1</sup>), IL-23 (20 ng ml<sup>-1</sup>), IL-27 (100 ng ml<sup>-1</sup>), LPS (10  $\mu$ g ml<sup>-1</sup>), or CD40 monoclonal antibody (1  $\mu$ g ml<sup>-1</sup>) before B10-cell numbers were determined. In separate experiments, purified spleen B cells were cultured with NIH-3T3 cells expressing CD154 and BLyS, with exogenous recombinant IL-4 (2 ng ml<sup>-1</sup>) or IL-21 (10 ng ml<sup>-1</sup>)<sup>25</sup>. IL-10 concentrations were determined by ELISA.

**EAE and adoptive transfer experiments.** Purified B-cell and TCR<sup>MOG</sup> T-cell subsets (95–98% pure) were transferred into recipient mice as described<sup>6,7,11,30</sup>. Of the CD1d<sup>hi</sup>CD5<sup>+</sup> or CD1d<sup>lo</sup>CD5<sup>-</sup> B cells (1  $\times$  10<sup>6</sup>) transferred, 13–20% and <0.1% were B10 cells, respectively<sup>6,30</sup>. Active EAE was induced and scored as described<sup>7,11</sup>.

**Statistical analysis.** All data are shown as means  $\pm$  s.e.m. Significant differences between sample means were determined using the Student's *t*-test.

**Full Methods** and any associated references are available in the online version of the paper.

Received 5 May; accepted 10 August 2012.

Published online 14 October 2012.

- LeBien, T. W. & Tedder, T. F. B-lymphocytes: how they develop and function. *Blood* **112**, 1570–1580 (2008).
- DiLillo, D. J., Matsushita, T. & Tedder, T. F. B10 cells and regulatory B cells balance immune responses during inflammation, autoimmunity, and cancer. *Ann. NY Acad. Sci.* **1183**, 38–57 (2010).
- Fillatreau, S. Novel regulatory functions for Toll-like receptor-activated B cells during intracellular bacterial infection. *Immunol. Rev.* **240**, 52–71 (2011).
- Mauri, C. Regulation of immunity and autoimmunity by B cells. *Curr. Opin. Immunol.* **22**, 761–767 (2010).
- Iwata, Y. *et al.* Characterization of a rare IL-10-competent B cell subset in humans that parallels mouse regulatory B10 cells. *Blood* **117**, 530–541 (2011).
- Yanaba, K. *et al.* A regulatory B cell subset with a unique CD1d<sup>hi</sup>CD5<sup>+</sup> phenotype controls T cell-dependent inflammatory responses. *Immunity* **28**, 639–650 (2008).
- Matsushita, T., Yanaba, K., Bouaziz, J.-D., Fujimoto, M. & Tedder, T. F. Regulatory B cells inhibit EAE initiation in mice while other B cells promote disease progression. *J. Clin. Invest.* **118**, 3420–3430 (2008).
- Ray, A., Basu, S., Williams, C. B., Salzman, N. H. & Dittel, B. N. A novel IL-10-independent regulatory role for B cells in suppressing autoimmunity by maintenance of regulatory T cells via GITR ligand. *J. Immunol.* **188**, 3188–3198 (2012).
- Yanaba, K., Bouaziz, J.-D., Matsushita, T., Tsubata, T. & Tedder, T. F. The development and function of regulatory B cells expressing IL-10 (B10 cells) requires antigen receptor diversity and TLR signals. *J. Immunol.* **182**, 7459–7472 (2009).
- Haas, K. M. *et al.* Protective and pathogenic roles for B cells during systemic autoimmunity in NZB/W F<sub>1</sub> mice. *J. Immunol.* **184**, 4789–4800 (2010).
- Matsushita, T., Horikawa, M., Iwata, Y. & Tedder, T. F. Regulatory B cells (B10 cells) and regulatory T cells have independent roles in controlling EAE initiation and late-phase immunopathogenesis. *J. Immunol.* **185**, 2240–2252 (2010).
- Horikawa, M., Minard-Colin, V., Matsushita, T. & Tedder, T. F. Regulatory B cell production of IL-10 inhibits lymphoma depletion during CD20 immunotherapy in mice. *J. Clin. Invest.* **121**, 4268–4280 (2011).
- Maseda, D. *et al.* Regulatory B10 cells differentiate into antibody-secreting cells after transient IL-10 production *in vivo*. *J. Immunol.* **188**, 1036–1048 (2012).
- Spolski, R. & Leonard, W. J. IL-21 and T follicular helper cells. *Int. Immunol.* **22**, 7–12 (2009).
- Linterman, M. A. & Vinuesa, C. G. T follicular helper cells during immunity and tolerance. *Prog. Mol. Biol. Transl. Sci.* **92**, 207–248 (2010).
- Ettinger, R. *et al.* IL-21 induces differentiation of human naive and memory B cells into antibody-secreting plasma cells. *J. Immunol.* **175**, 7867–7879 (2005).
- Ozaki, K. *et al.* Regulation of B cell differentiation and plasma cell generation by IL-21, a novel inducer of Blimp-1 and Bcl-6. *J. Immunol.* **173**, 5361–5371 (2004).
- Ozaki, K. *et al.* A critical role for IL-21 in regulating immunoglobulin production. *Science* **298**, 1630–1634 (2002).
- Spolski, R., Kim, H. P., Zhu, W., Levy, D. E. & Leonard, W. J. IL-21 mediates suppressive effects via its induction of IL-10. *J. Immunol.* **182**, 2859–2867 (2009).
- Pot, C. *et al.* Cutting edge: IL-27 induces the transcription factor c-Maf, cytokine IL-21, and the costimulatory receptor ICOS that coordinately act together to promote differentiation of IL-10-producing Tr1 cells. *J. Immunol.* **183**, 797–801 (2009).
- Bettelli, E. *et al.* Myelin oligodendrocyte glycoprotein-specific T cell receptor transgenic mice develop spontaneous autoimmune optic neuritis. *J. Exp. Med.* **197**, 1073–1081 (2003).
- Bettelli, E. *et al.* Reciprocal developmental pathways for the generation of pathogenic effector T<sub>H</sub>17 and regulatory T cells. *Nature* **441**, 235–238 (2006).
- Chen, G. *et al.* Regulation of the IL-21 gene by the NF- $\kappa$ B transcription factor c-Rel. *J. Immunol.* **185**, 2350–2359 (2010).
- Poe, J. C. *et al.* Amplified B lymphocyte CD40 signaling drives regulatory B10 cell expansion in mice. *PLoS ONE* **6**, e22464 (2011).
- Nojima, T. *et al.* In-vitro derived germinal centre B cells differentially generate memory B or plasma cells *in vivo*. *Nature Comm.* **2**, 465 (2011).
- Goodnow, C. C. *et al.* Altered immunoglobulin expression and functional silencing of self-reactive B lymphocytes in transgenic mice. *Nature* **334**, 676–682 (1988).
- Coquet, J. M., Chakravarti, S., Smyth, M. J. & Godfrey, D. I. Cutting edge: IL-21 is not essential for Th17 differentiation or experimental autoimmune encephalomyelitis. *J. Immunol.* **180**, 7097–7101 (2008).
- Hoehlig, K. *et al.* Activation of CD4<sup>+</sup> Foxp3<sup>+</sup> regulatory T cells proceeds normally in the absence of B cells during EAE. *Eur. J. Immunol.* **42**, 1164–1173 (2012).
- Weber, M. S. *et al.* Type II monocytes modulate T cell-mediated central nervous system autoimmune disease. *Nature Med.* **13**, 935–943 (2007).
- Matsushita, T. & Tedder, T. F. Identifying regulatory B cells (B10 cells) that produce IL-10. *Methods Mol. Biol.* **677**, 99–111 (2011).

**Supplementary Information** is available in the online version of the paper.

**Acknowledgements** We thank D. Maseda, E. Weimer, J. Bryant, K. Candando and G. Venturi for help and comments. These studies were supported by grants from the National Institutes of Health (NIH; AI56363 and AI057157), the Lymphoma Research Foundation, and the Division of Intramural Research, National Heart, Lung, and Blood Institute, NIH.

**Author Contributions** A.Y., T.Mi., D.J.D., T.Ma., M.H., J.C.P., W.J.L. and T.F.T. conceived and designed the studies. A.Y., T.Mi., D.J.D., T.Ma., M.H., E.I.K., R.S., J.C.P. and W.J.L. carried out or contributed essential reagents and materials for the experiments. All authors contributed to data analysis and manuscript preparation.

**Author Information** Reprints and permissions information is available at [www.nature.com/reprints](http://www.nature.com/reprints). The authors declare competing financial interests: details are available in the online version of the paper. Readers are welcome to comment on the online version of the paper. Correspondence and requests for materials should be addressed to T.F.T. ([thomas.tedder@duke.edu](mailto:thomas.tedder@duke.edu)).

## METHODS

**Mice.** C57BL/6, *Il10*<sup>-/-</sup> (B6.129P2-*Il10*<sup>tm1Cgn/J</sup>)<sup>31</sup>, *Cd40*<sup>-/-</sup> (B6.129P2-*Cd40*<sup>tm1Kik/J</sup>), and MD4 (C57BL/6-Tg(IghelMD4)4Ccg/J) mice were from the Jackson Laboratory. *MHC-II*<sup>-/-</sup> (B6.129-H2-*Ab1*<sup>tm1Jae</sup>*B2m*<sup>tm1Ghm</sup>N17) mice (Taconic Farms) were as described<sup>32</sup>. *Cd19*<sup>-/-</sup> mice were backcrossed onto the C57BL/6 background for 14 generations<sup>33,34</sup>. *Il21r*<sup>-/-</sup> mice were as described<sup>18</sup>. TCR<sup>MOG</sup> transgenic mice<sup>21</sup> (Thy1.2<sup>+</sup>, provided by V. K. Kuchroo) were crossed to C57BL/6.Thy1.1 mice to generate Thy1.1-expressing T cells. All mice were bred in a specific pathogen-free barrier facility and used at 6–12 weeks of age. The Duke University and National Heart, Lung, and Blood Institute Animal Care and Use Committee approved all studies.

**Cell preparation.** Single-cell suspensions from spleens and peripheral lymph nodes (paired axillary and inguinal) were generated by gentle dissection, with the cells passed through 70-mm cell strainers (BD Biosciences) followed by percoll gradient (70/37%) centrifugation. Lymphocytes were collected from the 37:70% interface and washed. MACS (Miltenyi Biotech) was used to purify lymphocyte populations according to the manufacturer's instructions. CD19 monoclonal-antibody-coated microbeads and CD4<sup>+</sup> T-cell isolation kits (Miltenyi Biotech) were used to purify B cells and CD4<sup>+</sup> T cells, respectively. When necessary, the cells were enriched a second time using a fresh MACS column to obtain >95% cell purities.

**Immunofluorescence analysis.** FITC-, PE-, PE-Cy5-, PE-Cy7-, or APC-conjugated CD1d (1B1), CD4 (H129.19), CD5 (53-7.3), CD19 (1D3), B220 (RA3-6B2) and Thy1.1 (OX-7) monoclonal antibodies were from BD Biosciences. PE-conjugated IL-21R (4A9) monoclonal antibody was from BioLegend. Intracellular staining used monoclonal antibodies reactive with IL-10 (JES5-16E3), IL-17 (17B7) and IFN- $\gamma$  (XMG1.2) (all from eBioscience) and Cytofix/Cytoperm kits (BD Biosciences). Background staining was assessed using non-reactive, isotype-matched control monoclonal antibodies (Caltag Laboratories). For two- to six-colour immunofluorescence analysis, single-cell suspensions (10<sup>6</sup> cells) were stained at 4 °C using predetermined optimal monoclonal antibody concentrations for 20 min as described<sup>35</sup>. Blood erythrocytes were lysed after staining using FACS<sup>TM</sup> Lysing Solution (Becton Dickinson).

B-cell intracellular IL-10 expression was visualized by immunofluorescence staining and analysed by flow cytometry as described<sup>6,30</sup>. Briefly, isolated leukocytes or purified cells were resuspended (2  $\times$  10<sup>6</sup> cells ml<sup>-1</sup>) in complete medium (RPMI 1640 media containing 10% FCS, 200  $\mu$ g ml<sup>-1</sup> penicillin, 200 U ml<sup>-1</sup> streptomycin, 4 mM L-glutamine and 5  $\times$  10<sup>-5</sup> M 2-mercaptoethanol, all from Gibco) with LPS (10  $\mu$ g ml<sup>-1</sup>, *Escherichia coli* serotype 0111:B4, Sigma), PMA (50 ng ml<sup>-1</sup>; Sigma), ionomycin (500 ng ml<sup>-1</sup>; Sigma) and monensin (2  $\mu$ M; eBioscience) for 5 h in 48-well flat-bottom plates. In some experiments, the cells were incubated for 48 h with an agonistic anti-mouse CD40 monoclonal antibody (1  $\mu$ g ml<sup>-1</sup>; HM40-3 monoclonal antibody; BD Pharmingen) as described<sup>9</sup>. For IL-10 detection, Fc receptors were blocked with mouse Fc receptor monoclonal antibody (2.4G2; BD Pharmingen), and dead cells were detected using a LIVE/DEAD Fixable Violet Dead Cell Stain Kit (Invitrogen-Molecular Probes) before cell surface staining. Stained cells were fixed and permeabilized using a Cytofix/Cytoperm kit (BD Pharmingen) according to the manufacturer's instructions and stained with PE-conjugated mouse anti-IL-10 monoclonal antibody. Splenocytes from *Il10*<sup>-/-</sup> mice served as negative controls to demonstrate specificity and to establish background IL-10 staining levels. For T-cell intracellular cytokine staining, lymphocytes were stimulated *in vitro* with PMA (50 ng ml<sup>-1</sup>; Sigma) and ionomycin (1  $\mu$ g ml<sup>-1</sup>; Sigma) in the presence of brefeldin A (BFA; 1  $\mu$ l ml<sup>-1</sup>; eBioscience) for 5 h before staining. Viable cells with the forward and side light-scatter properties of lymphocytes were analysed using a FACScan flow cytometer (Becton Dickinson) or BD FACSCanto II (BD Biosciences).

**In vitro B-cell cultures.** Purified splenic B cells (1  $\times$  10<sup>6</sup> ml<sup>-1</sup>) were cultured in RPMI 1640 medium containing 10% FBS, 2 mM glutamine, penicillin (100 I.U. ml<sup>-1</sup>), streptomycin (100  $\mu$ g ml<sup>-1</sup>), and 50  $\mu$ M 2-mercaptoethanol, and either recombinant IFN- $\gamma$  (10 ng ml<sup>-1</sup>), IL-4 (2 ng ml<sup>-1</sup>), IL-6 (10 ng ml<sup>-1</sup>) or IL-21 (100 ng ml<sup>-1</sup>) (from eBioscience); TGF- $\beta$  (10 ng ml<sup>-1</sup>), IL-10 (10 ng ml<sup>-1</sup>) or IL-12 (10 ng ml<sup>-1</sup>) (from R&D systems); or IL-23 (20 ng ml<sup>-1</sup>) and IL-27 (100 ng ml<sup>-1</sup>) (Biolegend), or LPS (10  $\mu$ g ml<sup>-1</sup>) before B10-cell numbers and culture supernatant fluid IL-10 concentrations were determined. In separate experiments, purified spleen B cells were cultured with NIH-3T3 cells expressing CD154 and BLyS as described<sup>25,36</sup> with exogenous recombinant IL-4 (2 ng ml<sup>-1</sup>) or IL-21 (10 ng ml<sup>-1</sup>) added to the cultures. For adoptive transfer experiments, cultured CD5<sup>+</sup> and CD5<sup>-</sup> B cells were purified by cell sorting (FACS Vantage SE, Becton Dickinson), with purities of 95–98%. After purification, 1  $\times$  10<sup>6</sup> cells were immediately transferred intravenously into each recipient mouse. In some experiments, CD40 monoclonal antibody (clone HM40-3; hamster, no azide/endotoxin-free, BD Pharmingen) was added to cultures where indicated.

**EAE induction.** EAE was induced in 6- to 8-week-old female mice by subcutaneous immunization with 100  $\mu$ g of MOG<sub>35–55</sub> peptide (MEVGWYRSPFSRVVHLYRNGK; NeoMPS) emulsified in CFA containing 200  $\mu$ g of heat-killed *Mycobacterium tuberculosis* H37RA (Difco) on day 0. Additionally, mice received 200 ng of pertussis toxin (List Biological Laboratories) intraperitoneally in 0.5 ml of PBS on days 0 and 2. Clinical signs of disease were assessed daily with a 0 to 6 point scoring system: 0, normal; 1, flaccid tail; 2, impaired righting reflex and/or gait; 3, partial hind limb paralysis; 4, total hind limb paralysis; 5, hind limb paralysis with partial forelimb paralysis; 6, moribund state, as described<sup>37</sup>. Moribund mice were given disease severity scores of 6 and euthanized.

**Adoptive transfer experiments.** B cells from naive mice or mice with EAE (day 28) were first enriched using CD19 monoclonal-antibody-coated microbeads, stained for cell surface CD19, CD1d and CD5 expression, with CD1d<sup>hi</sup>CD5<sup>+</sup> and CD1d<sup>lo</sup>CD5<sup>-</sup> B cells purified by cell sorting as described<sup>6,30</sup> with purities of 95–98%. After purification, the CD1d<sup>hi</sup>CD5<sup>+</sup> or CD1d<sup>lo</sup>CD5<sup>-</sup> B cells (1  $\times$  10<sup>6</sup>) were immediately transferred intravenously into recipient mice, with B10 cells representing 13–20% and <0.1% of the transferred cells<sup>6,30</sup>. In some experiments, donor Thy1.1 CD4<sup>+</sup> T cells were isolated from pooled spleens and lymph nodes of TCR<sup>MOG</sup> transgenic mice, then labelled with CFSE Vybrant CFDA SE fluorescent dye (5  $\mu$ M; CFSE; Invitrogen) and transferred intravenously (5  $\times$  10<sup>6</sup> per mouse) into Thy1.2 congenic recipients. Five days after adoptive transfer, the TCR<sup>MOG</sup> CD4<sup>+</sup> T cells were assessed by flow cytometry.

**Statistical analysis.** All data are shown as means  $\pm$  s.e.m. The significance of differences between sample means was determined using the Student's *t*-test.

31. Kühn, R., Lohler, J., Rennick, D., Rajewsky, K. & Muller, W. Interleukin-10-deficient mice develop chronic enterocolitis. *Cell* **75**, 263–274 (1993).
32. Grusby, M. J. *et al.* Mice lacking major histocompatibility complex class I and class II molecules. *Proc. Natl Acad. Sci. USA* **90**, 3913–3917 (1993).
33. Sato, S., Ono, N., Steeber, D. A., Pisetsky, D. S. & Tedder, T. F. CD19 regulates B lymphocyte signaling thresholds critical for the development of B-1 lineage cells and autoimmunity. *J. Immunol.* **157**, 4371–4378 (1996).
34. Sato, S., Steeber, D. A., Jansen, P. J. & Tedder, T. F. CD19 expression levels regulate B lymphocyte development: human CD19 restores normal function in mice lacking endogenous CD19. *J. Immunol.* **158**, 4662–4669 (1997).
35. Zhou, L.-J. *et al.* Tissue-specific expression of the human CD19 gene in transgenic mice inhibits antigen-independent B lymphocyte development. *Mol. Cell. Biol.* **14**, 3884–3894 (1994).
36. Tedder, T. F., Wagner, N. & Engel, P. in *Leukocyte Typing V: White Cell Differentiation Antigens* Vol. 1 (eds Schlossman, S. F. *et al.*) 483–504 (Oxford Univ. Press, 1995).
37. Fillatreau, S., Sweeney, C. H., McGeachy, M. J., Gray, D. & Anderton, S. M. B cells regulate autoimmunity by provision of IL-10. *Nature Immunol.* **3**, 944–950 (2002).



# CaMKII determines mitochondrial stress responses in heart

Mei-ling A. Joiner<sup>1</sup>, Olha M. Koval<sup>1</sup>, Jingdong Li<sup>1†</sup>, B. Julie He<sup>1,2</sup>, Chantal Allamargot<sup>3</sup>, Zhan Gao<sup>1</sup>, Elizabeth D. Luczak<sup>1</sup>, Duane D. Hall<sup>1</sup>, Brian D. Fink<sup>4</sup>, Biyi Chen<sup>1</sup>, Jinying Yang<sup>1</sup>, Steven A. Moore<sup>2,5</sup>, Thomas D. Scholz<sup>6</sup>, Stefan Strack<sup>7</sup>, Peter J. Mohler<sup>1†</sup>, William I. Sivitz<sup>1,4</sup>, Long-Sheng Song<sup>1</sup> & Mark E. Anderson<sup>1,2</sup>

Myocardial cell death is initiated by excessive mitochondrial  $\text{Ca}^{2+}$  entry causing  $\text{Ca}^{2+}$  overload, mitochondrial permeability transition pore (mPTP) opening and dissipation of the mitochondrial inner membrane potential ( $\Delta\Psi\text{m}$ )<sup>1,2</sup>. However, the signalling pathways that control mitochondrial  $\text{Ca}^{2+}$  entry through the inner membrane mitochondrial  $\text{Ca}^{2+}$  uniporter (MCU)<sup>3–5</sup> are not known. The multifunctional  $\text{Ca}^{2+}$ /calmodulin-dependent protein kinase II (CaMKII) is activated in ischaemia reperfusion, myocardial infarction and neurohumoral injury, common causes of myocardial death and heart failure; these findings suggest that CaMKII could couple disease stress to mitochondrial injury. Here we show that CaMKII promotes mPTP opening and myocardial death by increasing MCU current ( $I_{\text{MCU}}$ ). Mitochondrial-targeted CaMKII inhibitory protein or cyclosporin A, an mPTP antagonist with clinical efficacy in ischaemia reperfusion injury<sup>6</sup>, equivalently prevent mPTP opening,  $\Delta\Psi\text{m}$  deterioration and diminish mitochondrial disruption and programmed cell death in response to ischaemia reperfusion injury. Mice with myocardial and mitochondrial-targeted CaMKII inhibition have reduced  $I_{\text{MCU}}$  and are resistant to ischaemia reperfusion injury, myocardial infarction and neurohumoral injury, suggesting that pathological actions of CaMKII are substantially mediated by increasing  $I_{\text{MCU}}$ . Our findings identify CaMKII activity as a central mechanism for mitochondrial  $\text{Ca}^{2+}$  entry in myocardial cell death, and indicate that mitochondrial-targeted CaMKII inhibition could prevent or reduce myocardial death and heart failure in response to common experimental forms of pathophysiological stress.

Excessive activation of the multifunctional CaMKII by  $\text{Ca}^{2+}$  triggers myocardial death and heart failure<sup>7,8</sup>. Excessive CaMKII activity promotes multiple defects in myocardial  $\text{Ca}^{2+}$  homeostasis including increased mitochondrial  $\text{Ca}^{2+}$  (refs 9, 10). CaMKII inhibition is protective against ischaemia reperfusion, myocardial infarction and neurohumoral toxicity, clinically relevant forms of myocardial injury marked by disturbed intracellular  $\text{Ca}^{2+}$  homeostasis<sup>7,8,11</sup>, but the mechanisms for myocardial protection by CaMKII inhibition are unknown. Excessive increases in mitochondrial  $\text{Ca}^{2+}$  lead to mPTP opening and dissipation of the  $\Delta\Psi\text{m}$  (refs 1, 2). We first asked if excessive activation of CaMKII localized in mitochondria could be a mechanism for myocardial dysfunction or death during ischaemia reperfusion injury, because ischaemia reperfusion injury occurs in the setting of increased mitochondrial  $\text{Ca}^{2+}$  and ischaemia reperfusion injury is alleviated in rats by Ru360 (ref. 12), a selective inhibitor of  $I_{\text{MCU}}$  (ref. 12), and in patients by cyclosporin A (CsA), an inhibitor of mPTP<sup>6</sup>. Here we show that mitochondrial-targeted CaMKII inhibition or treatment with CsA, an mPTP antagonist with clinical efficacy in ischaemia reperfusion injury<sup>6</sup>, are both protective against mPTP opening, loss of  $\Delta\Psi\text{m}$ , mitochondrial disruption and programmed

cell death in response to ischaemia reperfusion, myocardial infarction or isoprenaline. The myocardial protective effects of mitochondrial CaMKII inhibition are multivalent and involve increasing mPTP  $\text{Ca}^{2+}$  tolerance and reduction in  $I_{\text{MCU}}$ .

To test if CaMKII catalytic activity is the mechanism for  $\text{Ca}^{2+}$  to affect downstream responses to ischaemia reperfusion injury, we developed mice with myocardial-delimited CaMKII inhibition by transgenic expression of CaMKIIN, the most potent and specific CaMKII inhibitory protein<sup>13</sup>. We engineered CaMKIIN with a palmitoylation sequence to enhance partitioning into intracellular membranes. We identified CaMKIIN expression in isolated mitochondria of transgenic mice (Supplementary Fig. 1a, b). To determine if CaMKIIN transgenic mice were resistant to ischaemia reperfusion injury by a  $\text{Ca}^{2+}$ -regulated pathway, we used isolated, perfused, working mouse hearts to measure directly myocardial mechanical responses to ischaemia reperfusion injury under conditions designed to restrict glycolytic metabolism. Wild-type hearts or hearts with transgenic CaMKIIN expression were perfused with a pyruvate-containing solution (at non-physiological levels) without glucose (so that ATP production relied on oxidative metabolism), and CsA (to prevent mPTP opening), or vehicle (Supplementary Fig. 2a–c). Left ventricular developed pressure (LVDP) (Supplementary Fig. 2b) and the first derivative of left ventricular developed pressure (Supplementary Fig. 3a) were reduced in wild-type vehicle-treated hearts after ischaemia reperfusion injury, but were preserved at normal levels after ischaemia reperfusion injury in hearts with CaMKII inhibition or in wild-type hearts treated with CsA. Baseline recordings were similar between CaMKIIN-expressing, wild type and wild type with CsA (Supplementary Fig. 3b). The area of infarcted myocardium after ischaemia reperfusion injury (Supplementary Fig. 2d, e) was  $66 \pm 3.3\%$  of the area at risk for wild-type littermate control hearts, and was reduced by half with CsA or CaMKIIN expression. The relative area of infarcted myocardium (Supplementary Fig. 2e) was inversely related to the extent of mechanical recovery (Supplementary Fig. 2c), suggesting that the beneficial effects of CsA and CaMKII inhibition ultimately derived from prevention of myocardial death in response to ischaemia reperfusion injury. We measured caspase 9 activity, a marker of mitochondrial-triggered apoptosis<sup>14</sup>. Caspase 9 was significantly reduced in the CaMKIIN transgenic hearts after ischaemia reperfusion injury and in wild-type hearts treated with CsA (Supplementary Fig. 2f).

We tested if transgenic expression of CaMKIIN protected mitochondria from ischaemia reperfusion injury. Mitochondria are structurally dynamic organelles and loss of the highly ordered internal membrane cristae is an ultrastructural correlate of mPTP opening, loss of  $\Delta\Psi\text{m}$  and apoptosis initiation<sup>15</sup>. We used transmission electron microscopy (TEM) to examine mitochondrial ultrastructure and to quantify mitochondrial disruption (Supplementary Fig. 2g, h) after

<sup>1</sup>Department of Internal Medicine and Cardiovascular Center, Carver College of Medicine, University of Iowa, Iowa City, Iowa 52242, USA. <sup>2</sup>Department of Molecular Physiology and Biophysics, Carver College of Medicine, University of Iowa, Iowa City, Iowa 52242, USA. <sup>3</sup>University of Iowa Central Microscopy Research Facility, Carver College of Medicine, University of Iowa, Iowa City, Iowa 52242, USA. <sup>4</sup>Iowa City Veterans Affairs Medical Center, Iowa City, Iowa 52246, USA. <sup>5</sup>Department of Pathology, Carver College of Medicine, University of Iowa, Iowa City, Iowa 52242, USA. <sup>6</sup>Department of Pediatrics, Carver College of Medicine, University of Iowa, Iowa City, Iowa 52242, USA. <sup>7</sup>Department of Pharmacology, Carver College of Medicine, University of Iowa, Iowa City, Iowa 52242, USA. <sup>†</sup>Present address: The Dorothy M. Davis Heart and Lung Research Institute, The Ohio State University, Columbus, Ohio 43210, USA.

ischaemia reperfusion injury. Mitochondria suffered extensive disruption after ischaemia reperfusion injury in vehicle-treated wild-type hearts; however, mitochondria were significantly protected in CsA-treated wild-type hearts. In contrast, mitochondria from CaMKIIN transgenic hearts were resistant to ischaemia reperfusion injury, with or without CsA treatment (Supplementary Fig. 2h). These data show that infarct size, mitochondrial structural integrity and mitochondrial-triggered cell death and dysfunction are similarly improved by CsA or CaMKII inhibition, consistent with a model in which CsA and CaMKII both engage a mitochondrial pathway leading to mPTP opening during pathological stress.

To better elucidate the protective effects of mitochondrial CaMKIIN expression, we measured  $\text{Ca}^{2+}$ -induced injury in isolated mitochondria. Loss of mitochondria function by mPTP opening can be measured in isolated mitochondria in response to supraphysiological mitochondrial  $\text{Ca}^{2+}$  increases<sup>16</sup>. Decreases in light scattering are a correlate of mPTP opening<sup>17</sup>. We found that mitochondria with CaMKIIN expression were resistant to  $\text{Ca}^{2+}$ -triggered decreases in light scattering compared to wild-type controls (Fig. 1a). We corroborated this finding using another mitochondrial integrity assay in which a fluorescence decrease corresponds to a loss of  $\Delta\Psi\text{m}$ . We loaded mitochondria isolated from wild-type and CaMKIIN transgenic mice with a voltage-sensitive fluorescent indicator, JC-1 (ref. 15), to compare their  $\Delta\Psi\text{m}$  responses to  $\text{Ca}^{2+}$ . Mitochondria isolated from wild-type hearts were significantly more sensitive to  $\Delta\Psi\text{m}$  loss in response to a lethal  $\text{Ca}^{2+}$  challenge compared to mitochondria with CaMKIIN expression (Fig. 1b). Treatment with CsA, an mPTP opening inhibitor, preserved the  $\Delta\Psi\text{m}$  during exogenous  $\text{Ca}^{2+}$  challenge in mitochondria isolated from wild-type hearts, whereas mitochondria derived from CaMKIIN transgenic hearts were protected without requiring CsA treatment (Fig. 1c).

We detected CaMKII associated with mitochondria and mitoplasts, inner mitochondrial membrane vesicles from osmotically shocked isolated cardiac mitochondria (Supplementary Fig. 4a–d), similar to previous studies<sup>18,19</sup>. However, CaMKII may contribute to  $\text{Ca}^{2+}$  overload and myocardial death by actions at extra-mitochondrial  $\text{Ca}^{2+}$  homeostatic proteins<sup>20</sup>. Therefore, we developed transgenic mice with CaMKIIN expression limited to myocardial mitochondria (mtCaMKIIN) to test if CaMKII inhibition targeted to mitochondria affected mitochondria susceptibility to excess  $\text{Ca}^{2+}$ . Unlike CaMKIIN transgenic mice, hearts expressing mtCaMKIIN have expression restricted to mitoplasts (Supplementary Fig. 1b). Mitochondria isolated from mtCaMKIIN hearts showed no difference in baseline metabolic function compared with wild-type littermates (Supplementary Fig. 5). We measured mitochondrial  $\text{Ca}^{2+}$  uptake with a membrane-impermeable indicator, Calcium green-5N (ref. 4). We found that cardiomyocytes from mtCaMKIIN transgenic mice had significantly slower mitochondrial  $\text{Ca}^{2+}$  uptake (measured as a rate of decrease in Calcium green-5N fluorescence), than mitochondria of wild-type cardiomyocytes (Fig. 1d, e). We tested the overall  $\text{Ca}^{2+}$  capacity of myocardial mitochondria with serial additions of  $\text{Ca}^{2+}$ , and found that mtCaMKIIN expression increased the mitochondrial  $\text{Ca}^{2+}$  capacity reached before mPTP opening (Supplementary Fig. 6a, b). We monitored mitochondrial  $\text{Ca}^{2+}$  concentration changes within the mitochondria using Cameleon, a mitochondrial-targeted GFP-based  $\text{Ca}^{2+}$  indicator<sup>21</sup>. HeLa cells co-transfected with Cameleon and mtCaMKIIN show reduced ATP-triggered  $\text{Ca}^{2+}$  entry into mitochondria compared with control cells without mtCaMKIIN expression (Fig. 1f and Supplementary Fig. 7a, b). These data indicate that the protective benefits of CaMKII inhibition against mitochondrial stress derive from reducing mitochondria  $\text{Ca}^{2+}$  entry and enhancing mPTP  $\text{Ca}^{2+}$  tolerance.

The MCU is a major  $\text{Ca}^{2+}$  entry pathway through the mitochondrial inner membrane<sup>3–5</sup>. In the presence of  $I_{\text{MCU}}$  inhibitor drugs, isolated cardiomyocytes<sup>22</sup> and perfused hearts<sup>12</sup> are resistant to opening and cell death after  $\text{Ca}^{2+}$  challenge. To examine potential effects of CaMKII on the MCU, we performed mitoplast patch clamp studies.

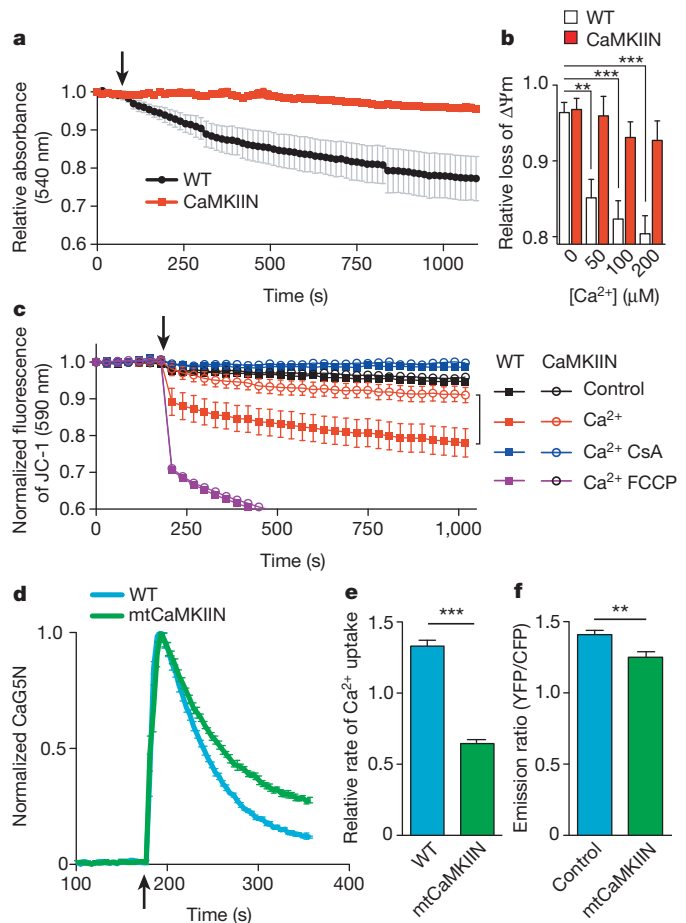


**Figure 1 | Isolated heart mitochondria with transgenic, membrane-targeted CaMKII inhibition (CaMKIIN) are resistant to  $\text{Ca}^{2+}$  challenge.**

**a**, Mitochondria mPTP  $\text{Ca}^{2+}$ -dependent opening (arrow, 200  $\mu\text{M}$  free- $\text{Ca}^{2+}$ ) reflected by a decrease in light scattering corresponding to an increase in mitochondrial volume;  $n = 3$  per genotype. **b**, Increasing  $[\text{Ca}^{2+}]$  promotes a greater relative loss of  $\Delta\Psi\text{m}$  in wild type compared to CaMKIIN mitochondria isolated from mouse hearts. Relative loss of  $\Delta\Psi\text{m}$  calculated as final relative absorbance (540 nm) divided by initial relative absorbance. ( $P$  values compare bars as indicated using Bonferroni post (ANOVA) test,  $^{**}P < 0.001$ ,  $^{***}P < 0.0001$ ,  $n = 3$  hearts per group with duplicate measurements.) **c**, Inner mitochondrial membrane potential ( $\Delta\Psi\text{m}$ ) measurements in isolated mitochondria using JC-1, a voltage-sensitive fluorescent reporter. Addition of 200  $\mu\text{M}$  free  $\text{Ca}^{2+}$  indicated by arrow. Black bracket indicates loss of  $\Delta\Psi\text{m}$  (reduced signal from baseline) after addition of  $\text{Ca}^{2+}$  alone (when comparing wild type and CaMKIIN, red squares versus open circles ( $P < 0.03$  for all time points after the  $\text{Ca}^{2+}$  challenge). The control sample (black) is DMSO alone and positive and negative controls are shown with CsA (blue) and carbonyl cyanide *p*-[trifluoromethoxy]-phenyl-hydrazone (FCCP) (purple), respectively ( $n = 5$  hearts per group with duplicate measurements.) **d**, Normalized traces showing rate of mitochondrial  $\text{Ca}^{2+}$  uptake in saponin-permeabilized cardiomyocytes after the addition of 100  $\mu\text{M}$  free  $\text{Ca}^{2+}$  (arrow). Mitochondrial  $\text{Ca}^{2+}$  uptake rate was monitored in cells by decline of the external Calcium green-5N (CaG5N) fluorescence. **e**, The rate of mitochondrial  $\text{Ca}^{2+}$  uptake in wild-type and CaMKIIN cardiomyocytes. Nonlinear regression fits for mitochondria  $\text{Ca}^{2+}$  uptake between wild type and CaMKIIN cardiomyocytes ( $^{***}P < 0.0001$ ,  $n = 6$  per genotype). **f**,  $\text{Ca}^{2+}$  uptake in mitochondria, measured using a Cameleon mitochondrial-targeted  $\text{Ca}^{2+}$  indicator, shows reduced  $\text{Ca}^{2+}$  uptake from HeLa cells expressing mtCaMKIIN compared to Myc-expressing controls. ( $^{**}P = 0.003$ ,  $n = 23$  cells per group.) For all data, error bars = means  $\pm$  s.e.m.

We used Ru360, a specific mitochondrial calcium uptake inhibitor, and we measured an Ru360-sensitive mitochondrial  $\text{Ca}^{2+}$  current that was activated by  $\text{Ca}^{2+}$  ( $K_{1/2} = 23 \text{ mM}$ ), consistent with known properties of  $I_{\text{MCU}}$  (ref. 3) (Fig. 2a and inset). Furthermore, CsA had no

effect on this  $I_{MCU}$  (Supplementary Fig. 8a), indicating that the beneficial actions of CaMKII inhibition on mPTP were distinct from the effects of CaMKII on the MCU.  $I_{MCU}$  was increased by addition of a constitutively active, monomeric CaMKII mutant (T287D)<sup>23</sup> to the pipette solution (equivalent to the mitochondrial matrix) in the presence of ATP (Fig. 2b and Supplementary Fig. 8b). Addition of the T287D mutant CaMKII did not increase  $I_{MCU}$  in the presence of a non-hydrolysable ATP analogue, adenosine 5'-( $\beta,\gamma$ -imido) triphosphate tetralithium salt (Fig. 2b), or in the absence of ATP (data not shown). Furthermore, a catalytically incompetent CaMKII mutant (K43M)<sup>24</sup> failed to increase  $I_{MCU}$  in the presence of activating ATP and calmodulin (Fig. 2b and Supplementary Fig. 8b). Therefore the catalytic activity of CaMKII was necessary to increase  $I_{MCU}$ . As a control, inhibiting serine/threonine phosphatases with calyculin A increased  $I_{MCU}$  (Fig. 2c and Supplementary Fig. 8c), showing that endogenous and exogenous CaMKII were both capable of increasing  $I_{MCU}$  under appropriate experimental conditions. To test if mitoplast CaMKIIN expression affected  $\text{Ca}^{2+}$  uptake, we measured  $I_{MCU}$  in CaMKIIN and mtCaMKIIN heart mitoplasts.  $I_{MCU}$  was lower in CaMKIIN-expressing mitoplasts using  $\text{Ca}^{2+}$  as the charge carrier (Fig. 2d and Supplementary Fig. 8d). In contrast, when  $\text{Na}^{+}$  was substituted for  $\text{Ca}^{2+}$ , a condition that does not support CaMKII activation,

differences were not apparent between wild-type and CaMKIIN-expressing mitoplasts, indicating that CaMKIIN was unlikely to affect MCU expression (Supplementary Fig. 8d). Ru360 nearly and equivalently eliminated  $I_{MCU}$  in all genotypes, suggesting that MCU antagonist sensitivity was not affected by CaMKIIN (Fig. 2d and Supplementary Fig. 8a). CaMKII and MCU co-immunoprecipitated from myocardial mitochondria lysate (Fig. 2e), suggesting that CaMKII is associated with MCU in the heart. CaMKII enhances  $\text{Ca}^{2+}$  currents through sarcolemmal voltage-gated  $\text{Ca}^{2+}$  channels ( $\text{Ca}_v1.2$ )<sup>25</sup> and intracellular  $\text{Ca}^{2+}$ -gated ryanodine receptor  $\text{Ca}^{2+}$  release channels<sup>26</sup> by phosphorylation of defined serines/threonines<sup>25,26</sup>. We identified two putative CaMKII target sites on MCU, serines 57 and 92, and mutated them both to alanines, to test for a direct effect of CaMKII on MCU. We overexpressed wild-type and S57A/S92A MCU in HEK cells and measured  $I_{MCU}$  from isolated mitoplasts. Constitutively active, monomeric CaMKII (T287D) added to the pipette solution failed to increase  $I_{MCU}$  in mitochondria from cells transfected with S57A/S92A MCU compared to wild-type MCU transfections (Fig. 2f and Supplementary Fig. 8e). In contrast, CaMKII added to the bath solution failed to affect  $I_{MCU}$  recorded from wild-type or S57A/S92A overexpressing mitoplasts (not shown). These studies, using a CaMKII-resistant S57A/S92A MCU mutant, suggest that the amino terminus of MCU is facing the

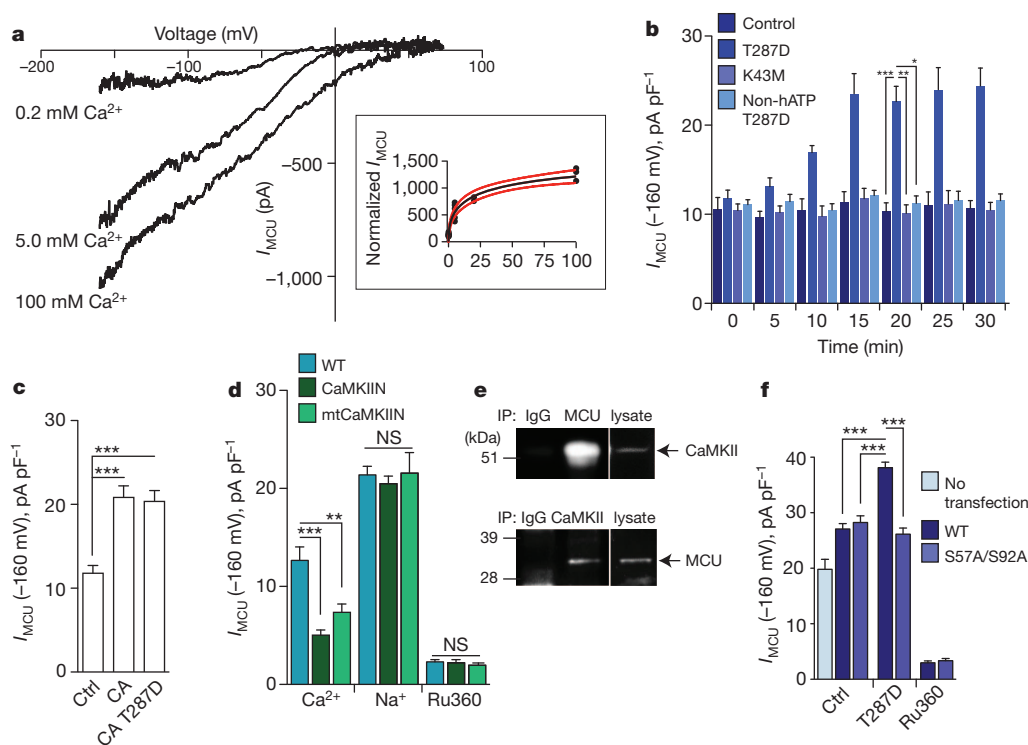


**Figure 2 | CaMKII agonist actions on  $I_{MCU}$  require MCU serines 57 and 92.** **a**,  $I_{MCU}$  is a  $\text{Ca}^{2+}$ -dependent conductance. Inset shows  $I_{MCU}$  in 0.2, 5 and 100 mM  $[\text{Ca}^{2+}]$  bath fit with the Hill equation (standard slope).  $V_{1/2} = 23.8$  mM,  $R^2 = 0.955$  and  $h = 0.057$ . Red lines show the 95% confidence intervals (runs test  $P = 0.743$ ). **b**, Time course for  $I_{MCU}$  recorded with 0.2 mM  $\text{Ca}^{2+}$  after obtaining a high resistance seal and mitoplast membrane rupture (time = 0) allowing dialysis of CaMKII T287D. Replacing ATP with a non-hydrolysable analogue (non-hATP) does not allow a CaMKII-dependent increase in  $I_{MCU}$ . Samples tested were: control (CaM + ATP,  $n = 5$ ); T287D (T287D + ATP,  $n = 7$ ); K43M (K43M + CaM + ATP,  $n = 3$ ); and non-hATP T287D (T287D + non-hATP,  $n = 3$ ), (ATP or non-hATP at 0.1 mM, CaM at 50  $\mu\text{M}$ , all mutant CaMKII at 0.5  $\mu\text{M}$ ,  $^{*}P < 0.01$ ,  $^{**}P < 0.001$ ,  $^{***}P < 0.0001$  at 20 min.). **c**,  $I_{MCU}$  recorded using mitoplasts of wild-type hearts after addition of 0.2 mM  $\text{Ca}^{2+}$  (control,  $n = 7$ ), 0.2 mM  $\text{Ca}^{2+}$  with 100 nM calyculin A (CA,  $n = 9$ ) and 0.2 mM  $\text{Ca}^{2+}$  with 100 nM calyculin A plus 0.5  $\mu\text{M}$  CaMKII T287D (CA T287D,  $n = 7$ ) ( $^{***}P < 0.0001$ ). **d**,  $I_{MCU}$  recorded from wild-type,

CaMKIIN and mtCaMKIIN mitochondria.  $\text{Na}^{+}$  current (150 mM) recorded in the absence of  $\text{Ca}^{2+}$  bath (intermembrane space equivalent) or with Ru360 (10 nM). For  $\text{Ca}^{2+}$ : (WT,  $n = 10$ ; CaMKIIN,  $n = 10$ ; mtCaMKIIN,  $n = 7$ ), for  $\text{Na}^{+}$ : (WT,  $n = 15$ ; CaMKIIN,  $n = 13$ ; mtCaMKIIN,  $n = 12$ ); and for Ru360: (WT,  $n = 8$ ; CaMKIIN,  $n = 8$ ; mtCaMKIIN,  $n = 5$ ). ( $^{**}P < 0.001$ ,  $^{***}P < 0.0001$ ). NS, not significant. **e**, MCU and CaMKII co-immunoprecipitate from heart mitochondrial lysate. **f**,  $I_{MCU}$  recorded from HEK cell mitoplasts without transfection (no transfection) or transfection of wild-type MCU (WT) or S57A/S92A MCU mutant (S57A/S92A). For control samples (Ctrl), without addition of CaMKII T287D: (no transfection,  $n = 7$ ; WT MCU,  $n = 7$ ; S57A/S92A MCU mutant,  $n = 7$ ); for T287D: (WT MCU,  $n = 8$ ; S57A/S92A MCU mutant,  $n = 9$ ); and for Ru360: (WT MCU,  $n = 6$ ; S57A/S92A MCU mutant,  $n = 6$ ). HEK mitoplast  $\text{Ca}^{2+}$  currents were inhibited by Ru360 (10 nM). (All data represent means  $\pm$  s.e.m., except for inset, see **a**.  $P$  value comparisons as indicated using Bonferroni post (ANOVA) test.)



mitochondrial matrix<sup>4</sup>. Altogether, these data show that CaMKII interacts with MCU and promotes mitochondrial  $\text{Ca}^{2+}$  entry, probably by catalysing phosphorylation of serines 57 and 92, consistent with the concept that MCU is an important CaMKII target in mitochondria.

We next used the mtCaMKIIN mice to determine if mitochondrial CaMKII inhibition was sufficient to explain the protective effects of CaMKII inhibition on ischaemic injury in isolated perfused hearts in the absence of glucose (Supplementary Fig. 2)<sup>7,11</sup>. We found that after ischaemia reperfusion injury, hearts from mtCaMKIIN mice had preserved mechanical function (Fig. 3a), reduced myocardial infarction size (Fig. 3b, c), preserved mitochondrial integrity (Fig. 3d, e) and reduced Caspase 9 activity (Fig. 3f) compared to wild-type littermate control hearts. Baseline left ventricular developed pressures were similar between wild-type and mtCaMKIIN hearts (Supplementary Fig. 9). We found no difference in left ventricular mechanical recovery ( $P = 0.976$ ) between wild-type and mtCaMKIIN hearts treated with CsA, and CsA added no further protection for mtCaMKIIN hearts subjected to ischaemia reperfusion injury ( $P = 0.946$ ). Neurohumoral toxicity is a major cause of adverse outcomes after myocardial infarction, including heart failure<sup>27</sup>, and  $\beta$ -adrenergic receptor antagonist drugs are a current favoured therapeutic treatment for reducing myocardial death and dysfunction after ischaemic injury and myocardial infarction<sup>27</sup>. CaMKII is activated by isoprenaline in heart and CaMKII inhibition protects against isoprenaline-mediated myocardial injury<sup>7,8</sup>.

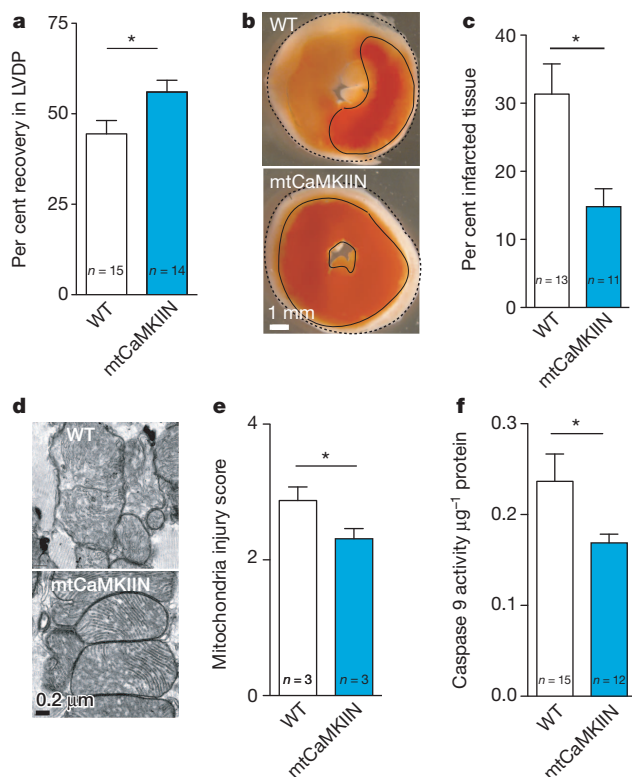


**Figure 3 | mtCaMKIIN hearts are resistant to ischaemia reperfusion injury.** **a**, LVDP recovery after ischaemia reperfusion as a percentage of the baseline value (\* $P = 0.026$ ). **b**, Representative 2,3,5-triphenyltetrazolium chloride (TTC) stained heart sections from **a**. The dark red staining represents living myocardium and the solid black outlines form boundaries demarcating viable from dead tissue. **c**, Relative area of infarct in TTC-stained hearts normalized to wild type, measured as in Supplementary Fig. 2e; \* $P = 0.006$ . **d**, Representative TEM images from hearts undergoing ischaemia reperfusion injury treatment as in **a**. **e**, Mitochondrial injury scores for TEM studies by the criteria used in Supplementary Fig. 2h. A higher score indicates an increased response to injury (\* $P = 0.003$ , more than 500 mitochondria from at least 10 random fields were counted per genotype). **f**, Caspase 9 activity from hearts treated as in panel **a** (\* $P = 0.033$ ,  $n$  = number of hearts per genotype). Data represent means  $\pm$  s.e.m.

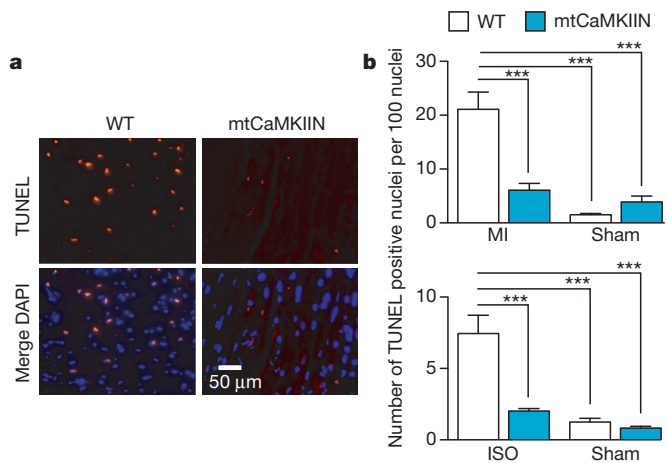


**Figure 4 | mtCaMKIIN hearts are resistant to apoptosis *in vivo*.**

**a**, Representative images of TUNEL-stained nuclei from wild-type and mtCaMKIIN heart transverse sections 5 h after myocardial infarction. DAPI stain (blue) labels nuclei. Scale bar, 50  $\mu\text{m}$ . **b**, Proportion of TUNEL-stained nuclei from wild-type and mtCaMKIIN heart sections 5 h after myocardial infarction (MI) (upper panel, 3 hearts per genotype, 10 images per heart) or 30 min after isoprenaline (ISO) treatment (lower panel, 15 mg  $\text{kg}^{-1}$  body weight, 3 hearts per genotype, 10 images per heart, \*\*\* $P < 0.0001$ ). Data represent means  $\pm$  s.e.m.

The protective effects of mtCaMKIIN expression were also evident *in vivo*, because mtCaMKIIN mice showed fewer TdT-mediated dUTP nick end labelling (TUNEL)-stained nuclei, a measurement of cell death, than wild-type controls 5 h after a myocardial infarction (Fig. 4a, b) or 30 min after isoprenaline treatment (Fig. 4b). Thus, mitochondrial targets seem to be essential for the cardioprotective benefits of CaMKII inhibition in a diverse set of clinically-relevant injury models.

Our findings identify CaMKII as a modulator of mitochondrial  $\text{Ca}^{2+}$  homeostasis and a crucial component of a final  $\text{Ca}^{2+}$ -dependent pathway in heart disease due to ischaemia and neurohumoral toxicity, by showing that CaMKII increases  $I_{\text{MCU}}$  and that CaMKII inhibition reduces  $I_{\text{MCU}}$  and the mPTP opening. Our study suggests that CaMKII inhibition could reduce adverse responses, including death, to common forms of pathological myocardial stress by multivalent actions on mitochondria, including  $I_{\text{MCU}}$  inhibition and blunting  $\text{Ca}^{2+}$  responsiveness of mPTP.

## METHODS SUMMARY

CaMKII inhibition was achieved by expressing CaMKIIN, an endogenous brain-derived inhibitor protein<sup>13</sup>. *In vivo* experiments were done with transgenic mice expressing the inhibitor under  $\alpha$ -MHC control to limit expression to the heart<sup>11</sup>, in addition to cellular localization specified by a palmitoyl amino acid sequence addition to CaMKIIN (CaMKIIN mice) or a *Cox8a* (mitochondrial localization sequence added to CaMKIIN (mtCaMKIIN mice)). Opening of mPTP was measured by both a mitochondria swelling assay and the fluorescent dye indicator, JC-1. Extra-mitochondrial calcium in permeabilized isolated cardiomyocytes<sup>28</sup> was measured using Calcium green-5N. Mitochondrial  $\text{Ca}^{2+}$  uptake was measured in HeLa cells transfected with plasmids expressing the mitochondrial-targeted Cameleon (4mtD3CPV) along with mitochondrial-targeted CaMKIIN or a control plasmid.  $I_{\text{MCU}}$  was measured in mitoplast preparations<sup>3</sup> from cardiomyocytes of wild-type or transgenic mouse hearts or HEK cells expressing wild-type or mutated MCU. *Ex vivo* hearts were prepared to measure left ventricular developed pressure<sup>29</sup> with 2 mM pyruvate as the energy source.

**Full Methods** and any associated references are available in the online version of the paper.

Received 6 April 2010; accepted 26 July 2012.

Published online 10 October 2012.

1. Kroemer, G. & Reed, J. C. Mitochondrial control of cell death. *Nature Med.* **6**, 513–519 (2000).

2. Clapham, D. E. Calcium signaling. *Cell* **131**, 1047–1058 (2007).
3. Kirichok, Y., Krapivinsky, G. & Clapham, D. E. The mitochondrial calcium uniporter is a highly selective ion channel. *Nature* **427**, 360–364 (2004).
4. Baughman, J. M. *et al.* Integrative genomics identifies MCU as an essential component of the mitochondrial calcium uniporter. *Nature* **476**, 341–345 (2011).
5. De Stefani, D., Raffaello, A., Teardo, E., Szabo, I. & Rizzuto, R. A forty-kilodalton protein of the inner membrane is the mitochondrial calcium uniporter. *Nature* **476**, 336–340 (2011).
6. Piot, C. *et al.* Effect of cyclosporine on reperfusion injury in acute myocardial infarction. *N. Engl. J. Med.* **359**, 473–481 (2008).
7. Erickson, J. R. *et al.* A dynamic pathway for calcium-independent activation of CaMKII by methionine oxidation. *Cell* **133**, 462–74 (2008).
8. Yang, Y. *et al.* Calmodulin kinase II inhibition protects against myocardial cell apoptosis *in vivo*. *Am. J. Physiol. Heart Circ. Physiol.* **291**, H3065–H3075 (2006).
9. Zhang, T. *et al.* The  $\delta_c$  isoform of CaMKII is activated in cardiac hypertrophy and induces dilated cardiomyopathy and heart failure. *Circ. Res.* **92**, 912–919 (2003).
10. Odagiri, K. *et al.* Local control of mitochondrial membrane potential, permeability transition pore and reactive oxygen species by calcium and calmodulin in rat ventricular myocytes. *J. Mol. Cell. Cardiol.* **46**, 989–997 (2009).
11. Zhang, R. *et al.* Calmodulin kinase II inhibition protects against structural heart disease. *Nature Med.* **11**, 409–417 (2005).
12. Garcia-Rivas, G. J., Carvajal, K., Correa, F. & Zazueta, C. Ru360, a specific mitochondrial calcium uptake inhibitor, improves cardiac post-ischaemic functional recovery in rats *in vivo*. *Br. J. Pharmacol.* **149**, 829–837 (2006).
13. Singh, M. V. *et al.*  $\text{Ca}^{2+}$ /calmodulin-dependent kinase II triggers cell membrane injury by inducing complement factor B gene expression in the mouse heart. *J. Clin. Invest.* **119**, 986–996 (2009).
14. Hakem, R. *et al.* Differential requirement for Caspase 9 in apoptotic pathways *in vivo*. *Cell* **94**, 339–352 (1998).
15. Olichon, A. *et al.* Loss of OPA1 perturbs the mitochondrial inner membrane structure and integrity, leading to cytochrome c release and apoptosis. *J. Biol. Chem.* **278**, 7743–7746 (2003).
16. Wang, W. *et al.* Superoxide flashes in single mitochondria. *Cell* **134**, 279–290 (2008).
17. Halestrap, A. P. What is the mitochondrial permeability transition pore? *J. Mol. Cell. Cardiol.* **46**, 821–831 (2009).
18. Timmins, J. M. *et al.* Calcium/calmodulin-dependent protein kinase II links ER stress with Fas and mitochondrial apoptosis pathways. *J. Clin. Invest.* **119**, 2925–2941 (2009).
19. Sharma, V., Abraham, T., So, A., Allard, M. & McNeill, J. Functional effects of protein kinases and peroxynitrite on cardiac carnitine palmitoyltransferase-1 in isolated mitochondria. *Mol. Cell. Biochem.* **337**, 223–237 (2010).
20. Anderson, M. E., Brown, J. H. & Bers, D. M. CaMKII in myocardial hypertrophy and heart failure. *J. Mol. Cell. Cardiol.* **51**, 468–473 (2011).
21. Miyawaki, A. *et al.* Fluorescent indicators for  $\text{Ca}^{2+}$  based on green fluorescent proteins and calmodulin. *Nature* **388**, 882–887 (1997).
22. Saotome, M. *et al.* Mitochondrial membrane potential modulates regulation of mitochondrial  $\text{Ca}^{2+}$  in rat ventricular myocytes. *Am. J. Physiol. Heart Circ. Physiol.* **288**, H1820–H1828 (2005).
23. Fong, Y. L., Taylor, W. L., Means, A. R. & Soderling, T. R. Studies of the regulatory mechanism of  $\text{Ca}^{2+}$ /calmodulin-dependent protein kinase II. Mutation of threonine 286 to alanine and aspartate. *J. Biol. Chem.* **264**, 16759–16763 (1989).
24. Hanson, P. I., Meyer, T., Stryer, L. & Schulman, H. Dual role of calmodulin in autophosphorylation of multifunctional cam kinase may underlie decoding of calcium signals. *Neuron* **12**, 943–956 (1994).
25. Koval, O. M. *et al.* CaV1.2 b-subunit coordinates CaMKII-triggered cardiomyocyte death and afterdepolarizations. *Proc. Natl Acad. Sci. USA* **107**, 4996–5000 (2010).
26. Wehrens, X. H. T., Lehnart, S. E., Reiken, S. R. & Marks, A. R.  $\text{Ca}^{2+}$ /calmodulin-dependent protein kinase II phosphorylation regulates the cardiac ryanodine receptor. *Circ. Res.* **94**, e61–e70 (2004).
27. Feldman, D. S., Carnes, C. A., Abraham, W. T. & Bristow, M. R. Mechanisms of disease:  $\beta$ -adrenergic receptors—alterations in signal transduction and pharmacogenomics in heart failure. *Nature Clin. Pract. Cardiovasc. Med.* **2**, 475–483 (2005).
28. Wu, Y., Colbran, R. J. & Anderson, M. E. Calmodulin kinase is a molecular switch for cardiac excitation-contraction coupling. *Proc. Natl Acad. Sci. USA* **98**, 2877–2881 (2001).
29. Li, J. *et al.* Calmodulin kinase II inhibition enhances ischemic preconditioning by augmenting ATP-sensitive  $\text{K}^{+}$  current. *Channels* **1**, 387–394 (2007).

**Supplementary Information** is available in the online version of the paper.

**Acknowledgements** The authors wish to acknowledge discussions with A. Lee, B. Davidson, K. Campbell and C. Sigmund. This work was funded by: AHA 0635357N (M.A.J.); NIH R01 HL090905 (L.-S.S.); NIH R01 HL079031, R01 HL62494, R01 HL70250 and R01 HL113001 and supported by a grant from the Fondation Leducq for the Alliance for CaMKII Signaling (M.E.A.); NIH R01 HL084583, R01 HL083422 and Pew Scholars Trust (P.J.M.).

**Author Contributions** M.A.J. designed the project, carried out experimental work and wrote the manuscript. O.M.K. and L.-S.S. carried out experimental work, analysed data and participated in data interpretation. C.A. Z.G. and E.D.L., carried out experimental work and interpreted data. J.L., B.J.H., D.D.H., B.D.F., B.C. and J.Y. carried out experimental work. S.S. provided critical materials and wrote the manuscript. S.A.M. and T.D.S. interpreted data. P.J.M. supervised the research. W.I.S. supervised the research and wrote the manuscript. M.E.A. conceived the project, supervised the research and wrote the manuscript.

**Author Information** Reprints and permissions information is available at [www.nature.com/reprints](http://www.nature.com/reprints). The authors declare competing financial interests: details are available on the online version of the paper. Readers are welcome to comment on the online version of the paper. Correspondence and requests for materials should be addressed to M.A.J. ([mei-ling-joiner@uiowa.edu](mailto:mei-ling-joiner@uiowa.edu)) or M.E.A. ([mark-e-anderson@uiowa.edu](mailto:mark-e-anderson@uiowa.edu)).

## METHODS

**Transgenic mice.** Animals were maintained in the University of Iowa Animal Facility and treated in accordance with Institutional Animal Care and Use Committee guidelines (PHS Animal Welfare Assurance, A3021-01). CaMKIIN transgenic mice (C57BL/6 background) were generated as described<sup>13</sup>. Targeting of  $\beta$ CaMKIIN (accession NM\_033259.2) to mitochondria in transgenic mice was achieved by fusion of the cox8a N terminus. The N-terminal 28 amino acids of cox8a were added to the 5' of haemagglutinin (HA)- $\beta$ CaMKIIN sequence by PCR using the forward primer: 5'-CGGTGACATGTCCGTCCTGAC-3' and the reverse primer 5'-ATGTCGACTTCTCCGCGGCA-3' (Integrated DNA Technologies) with SalI sites at the extreme ends. The product ~100 base pairs (bp) was purified from an agarose gel (Qiagen gel extraction kit) and digested with SalI restriction enzyme. The resulting DNA product was ligated into the SalI site 5' of the HA sequence of p $\alpha$ -MHC-script-Hgh-HA-tagged CaMKIIN vector. Mouse embryonic stem cells were injected with the linearized DNA (digested with NotI) in the University of Iowa Transgenic Mouse Core Facility and implanted into B6D2 pseudo-pregnant females. Insertion of the transgene into the mouse genome was confirmed by PCR analysis (data not shown) using the forward primer, 5'-CGATAAAGTTATGTCCGAGATCCTA-3' and reverse primer, 5'-GTCATCCTCGATCACCACCTCTCT-3', producing a 196-bp product. Mice were backcrossed to F<sub>4</sub> generation or later into the C57BL/6 background. Transgenic and control mice of either gender were killed at 2–3 months of age.

**Isolated perfused working mouse hearts.** Langendorff-perfused mouse hearts were used to measure left ventricular function and myocardial viability, as described<sup>29</sup>. Mice were anaesthetized with avertin and hearts were quickly excised and rinsed in icy Tyrode's solution containing: 137 mM NaCl, 5.4 mM KCl, 0.5 mM MgCl<sub>2</sub>, 0.16 mM NaH<sub>2</sub>PO<sub>4</sub>, 3 mM NaHCO<sub>3</sub>, 5 mM HEPES-NaOH and heparin 0.1 mg ml<sup>-1</sup>, which was previously adjusted to a pH 7.4 with NaOH at room temperature. All chemicals were from Sigma-Aldrich unless otherwise noted. Excess tissue was dissected away. Hearts were perfused retrogradely through the aorta for 1–2 min at room temperature with Hanks' balanced salt solution (GIBCO) and mounted on a modified Langendorff apparatus (HSE-HA perfusion systems, Harvard Apparatus) for retrograde aortic perfusion at a constant pressure of 80 mm Hg with carbogen (95% O<sub>2</sub>, 5% CO<sub>2</sub>) and Krebs-Henseleit bicarbonate (KHB) solution consisting of: 25 mM NaHCO<sub>3</sub>, 118 mM NaCl, 4.7 mM KCl, 1.2 mM MgSO<sub>4</sub>, 1.2 mM NaH<sub>2</sub>PO<sub>4</sub>, 2.5 mM CaCl<sub>2</sub>, 0.5 mM Na-EDTA, 2 mM pyruvate, with pH equilibrated to 7.4 with 5  $\mu$ M CsA or dimethylsulphoxide (DMSO) for a control. Hearts were perfused for 10 min to ensure metabolic equilibrium, followed by 20 or 30 min of global ischaemia and then 50 min of reperfusion. Measurements were recorded from each heart for the entire duration of perfusion.

**Heart infarct size and caspase 9 activity assay.** Following the ischaemia reperfusion protocol shown in Supplementary Fig. 2, hearts were immediately frozen. Three 0.5-mm sections were cut from frozen hearts, labelled with 5% (wt/vol) 2,3,5-triphenyltetrazolium chloride (TTC) in PBS buffer and fixed in 10% formalin. Caspase 9 activity assays were performed on tissue lysate following manufacturer's protocol (Invitrogen) and normalized to protein concentration ( $\mu$ g ml<sup>-1</sup>).

**Transmission electron microscopy.** Hearts were fixed in 2.5% glutaraldehyde and 0.1 M Na cacodylate buffer overnight at 4 °C, followed by three 20-min washes in 0.1 M pH 7.2 sodium cacodylate buffer, fixed in 4% OsO<sub>4</sub>, washed in 0.1 M sodium cacodylate buffer, then dH<sub>2</sub>O, followed by 2.5% uranyl acetate. A series of ethanol washes was used to dehydrate the sample, which was then exchanged with an ethanol and Spurr's mixture series of increasing Spurr's concentration, culminating in a final solution of 100% Spurr's resin. Hearts were embedded in Spurr's resin at 60 °C for 24–48 h. Ultramicrotomy was carried out at 90 nm and samples collected on 200 mesh for formvar grids for staining with uranyl and lead. Stained sections were examined with a JEOL JEM-1230 transmission electron microscope and digital images were collected with a Gatan UltraScan 1000 2k  $\times$  2k CCD camera.

**Mitochondrial isolation and subcellular fractionation.** Isolation of mitochondria was performed on ice. Freshly collected mouse hearts were injected with 1.0% protease XXIV in MSE buffer (5 mM MOPS, 70 mM sucrose, 2 mM EGTA, 220 mM mannitol, pH 7.2 with KOH) then homogenized. HEK cells were washed then homogenized. Nuclei and unbroken cells were pelleted by centrifugation twice at 600g for 10 min. The crude mitochondrial and cytosolic fraction was obtained from the supernatant by centrifugation at 8,500g for 20 min. The pellet was further purified with a 40% percoll gradient, washed twice in MSE buffer then resuspended in 200  $\mu$ l MSE with protease inhibitors. For mitoplast preparation, mitochondria were resuspended in hypotonic solution (5 mM sucrose, 5 mM HEPES and 1 mM EGTA (pH 7.2 with KOH)) for 5 min to remove outer membrane. After sedimenting for 5 min at 4,000g, mitoplasts were resuspended in 750 mM KCl, 100 mM HEPES and 1 mM EGTA (pH 7.2 with KOH).

**MCU current recording (whole-mitoplast configuration).** Signals were measured with an Axon 200B patch-clamp amplifier controlled by a personal computer

using a Digidata 1320A acquisition board driven by pClamp 8.0 software (Axon Instruments). For formation of gigaohm seals and initial break-in to the whole-cell voltage clamp configuration, mitoplasts were perfused with solution containing: 150 mM Na gluconate, 10 mM HEPES and 0.2 mM CaCl<sub>2</sub> (pH 7.4, adjusted with NaOH). Bath solutions with different Ca<sup>2+</sup> concentrations were made by adding the necessary volume of 1 M CaCl<sub>2</sub>. Pipettes, after filling with a 150 mM Na gluconate, 5 mM NaCl, 135 mM sucrose, 10 mM HEPES and 1.5 mM EGTA (pH 7.2 with NaOH) solution had an access resistance of 25–35 M $\Omega$  (ref. 3). After mitoplast membranes rupture the capacitance ranged from 5 to 9 pF. A ramp voltage command protocol from -160 to 80 mV, for 2 s, was applied from a holding potential of 0 mV to evoke currents. Reagents and enzyme added (as noted in text) were 100  $\mu$ M ATP, 100  $\mu$ M non-hydrolysable ATP, 2  $\mu$ M CaM, 0.5  $\mu$ M CaMKII (wild type and mutants: T287D and K43M), 10 nM Ru360 and 5  $\mu$ M CsA.

**Mitochondrial  $\Delta\Psi$  measurement.** Isolated mitochondria were loaded with JC-1 following manufacturer's instructions (Invitrogen) and placed in a 96-well black-walled plate with 0.2  $\mu$ g ml<sup>-1</sup> JC-1 in buffer with DMSO, or either 0.2  $\mu$ M CsA or 2.5  $\mu$ M carbonyl cyanide *p*-[trifluoromethoxy]-phenyl-hydrazone (FCCP). At the indicated time point 200  $\mu$ M CaCl<sub>2</sub> was added to the suspension. Fluorescent measurements were taken according to the manufacturer's protocol. Light scattering was assessed after adding CaCl<sub>2</sub> (free Ca<sup>2+</sup> was calculated using the Maxchelator at <http://www.stanford.edu/~cpatton>) by decreased absorbance over 30 min at 540 nm using a F200 96-well plate reader (Tecan) in swelling buffer (200 mM sucrose, 0.002 mM EGTA, 5 mM succinate, 0.0002 mM rotenone, 200 mM Tris buffer, 20 mM HEPES, 1 mM KH<sub>2</sub>PO<sub>4</sub> and 1  $\mu$ g ml<sup>-1</sup> oligomycin, pH 7.2), with a use gain of 100. Data were normalized to the initial measurement and plotted using Prism Graph.

**Ca<sup>2+</sup> retention assay.** Calcium green-5N was used to monitor extramitochondrial Ca<sup>2+</sup> in saponin-permeabilized, isolated adult mouse cardiomyocytes. The ventricular cardiomyocytes were isolated from adult mice as described<sup>28</sup>. Recordings of cardiomyocyte mitochondrial Ca<sup>2+</sup> uptake were performed in a 96-well plate with 100  $\mu$ l of respiration buffer (100 mM KAsp, 20 mM KCl, 10 mM HEPES, 5 mM glutamate, 5 mM malate and 5 mM succinate pH 7.3) supplemented with 100  $\mu$ M blebbistatin, 5  $\mu$ M thapsigargin, 0.005% saponin and 1  $\mu$ M Calcium green-5N (Invitrogen) with freshly isolated cardiomyocytes. Calcium green-5N fluorescence was monitored at 485 nm excitation; 535 nm emission, after adding CaCl<sub>2</sub> (100  $\mu$ M free Ca<sup>2+</sup> at 3-min intervals at 30 °C). Cyclosporin A (5  $\mu$ M) and Ru360 (0.1  $\mu$ M) were used to block the mitochondrial permeability transition pore and the mitochondrial Ca<sup>2+</sup> uniporter (MCU), respectively.

**Myocardial infarction and isoprenaline-treated mice.** Assays are described in previous publications<sup>8</sup>.

**Transmission immuno-electron microscopy.** Isolated mitochondria fixed in EM grade 4% paraformaldehyde with 0.05% glutaraldehyde in PBS pH 7.4 for 1 h at 4 °C were processed and labelled with antibodies (CaMKII, CoxIV, rabbit IgG and HA) at 1:250.

**Immunoprecipitation, western blot and activity assays.** Immunoprecipitation was performed over 1 h with mitochondrial lysate (200  $\mu$ g protein) and protein A magnetic beads. SDS-PAGE and western blotting studies used lysate of heart subcellular fractions. Protein content was determined with a Bradford assay. Samples (25  $\mu$ g) were separated on NuPAGE 4–12% Bis-Tris gels (Invitrogen) and transferred to polyvinylidene difluoride (PVDF) membranes. After blocking with Odyssey blocking buffer (LI-COR Biosciences), the membranes were incubated with the following primary antibodies (dilutions): CaMKII (1:500), SERCA2 (1:250), calnexin (1:250), CoxIV (1:500) ATP5a (1:500), MCU (1:500), nucleolin (1:100), mfn1 (1:500) and HA (1:1,000). Appropriate secondary antibodies were used and bands visualized. Activity assays<sup>30</sup> were carried out using mitochondria lysate with biotin capture membrane (Promega).

**Mitochondrial respiration.** State 3 and state 4 respiration were measured by polarography in a 600  $\mu$ l incubation chamber with stir bar and oxygen electrode as in past studies<sup>31</sup>. The ADP/O ratio was calculated as molar ADP added divided by molar oxygen consumed during conversion to ATP as described previously<sup>31</sup>. Respiratory coupling was assessed by simultaneous determination of respiration and membrane potential<sup>31</sup>.

**Statistical analysis.** Statistical analysis was performed using the analysis of variance (ANOVA or Student's *t*-test, as appropriate). Post hoc pairwise comparisons were performed using Bonferroni's multiple-comparison test (Prism graph), as appropriate. Other tests were carried out as noted in the text using Prism graph. Results were given as means  $\pm$  s.e.m. A *P* value <0.05 was considered significant. NS, not significant.

30. He, B. J. *et al.* Oxidation of CaMKII determines the cardiotoxic effects of aldosterone. *Nature Med.* **17**, 1610–1618 (2011).
31. Herlein, J. A., Fink, B. D., O'Malley, Y. & Sivitz, W. I. Superoxide and respiratory coupling in mitochondria of insulin-deficient diabetic rats. *Endocrinology* **150**, 46–55 (2009).



# Direct imaging of RecA nucleation and growth on single molecules of SSB-coated ssDNA

Jason C. Bell<sup>1,2,3</sup>, Jody L. Plank<sup>1,2\*</sup>, Christopher C. Dombrowski<sup>1,2\*</sup> & Stephen C. Kowalczykowski<sup>1,2,3</sup>

*Escherichia coli* RecA is the defining member of a ubiquitous class of DNA strand-exchange proteins that are essential for homologous recombination, a pathway that maintains genomic integrity by repairing broken DNA<sup>1</sup>. To function, filaments of RecA must nucleate and grow on single-stranded DNA (ssDNA) in direct competition with ssDNA-binding protein (SSB), which rapidly binds and continuously sequesters ssDNA, kinetically blocking RecA assembly<sup>2,3</sup>. This dynamic self-assembly on a DNA lattice, in competition with another protein, is unique for the RecA family compared to other filament-forming proteins such as actin and tubulin. The complexity of this process has hindered our understanding of RecA filament assembly because ensemble measurements cannot reliably distinguish between the nucleation and growth phases, despite extensive and diverse attempts<sup>2–5</sup>. Previous single-molecule assays have measured the nucleation and growth of RecA—and its eukaryotic homologue RAD51—on naked double-stranded DNA and ssDNA<sup>6–12</sup>; however, the template for RecA self-assembly *in vivo* is SSB-coated ssDNA<sup>3</sup>. Using single-molecule microscopy, here we directly visualize RecA filament assembly on single molecules of SSB-coated ssDNA, simultaneously measuring nucleation and growth. We establish that a dimer of RecA is required for nucleation, followed by growth of the filament through monomer addition, consistent with the finding that nucleation, but not growth, is modulated by nucleotide and magnesium ion cofactors. Filament growth is bidirectional, albeit faster in the 5'→3' direction. Both nucleation and growth are repressed at physiological conditions, highlighting the essential role of recombination mediators in potentiating assembly *in vivo*. We define a two-step kinetic mechanism in which RecA nucleates on transiently exposed ssDNA during SSB sliding and/or partial dissociation (DNA unwrapping) and then the RecA filament grows. We further demonstrate that the recombination mediator protein pair, RecOR (RecO and RecR), accelerates both RecA nucleation and filament growth, and that the introduction of RecF further stimulates RecA nucleation.

To image the assembly of RecA filaments on SSB-coated ssDNA, we first developed a procedure to generate and visualize single molecules of ssDNA. Bacteriophage  $\lambda$  double-stranded DNA (dsDNA) 48.5 kilobase pairs (kb) long was biotinylated at the 3' ends, alkali denatured, neutralized with buffer and saturated with a fluorescently modified SSB (SSB<sup>AF488</sup>). This complex was then attached to the surface of a streptavidin-coated glass coverslip within a microfluidic chamber, extended by buffer flow, and visualized using total internal reflection fluorescence (TIRF) microscopy (Fig. 1a, b, top panels). Because the binding affinity of SSB<sup>AF488</sup> is attenuated<sup>13,14</sup>, we next replaced it with unlabelled wild-type SSB *in situ* (Fig. 1a, b, second panels, and Supplementary Video 1). The exchange of proteins in the flow cell is fast, with a half-time of approximately 2–3 s, resulting in a non-fluorescent native SSB–ssDNA complex. RecA filament assembly on the wild-type SSB–ssDNA complexes was then imaged using a

fluorescent RecA protein, fluorescein-RecA (RecA<sup>f</sup>), described previously<sup>7</sup>. Assembly was initiated by injecting RecA<sup>f</sup>, free SSB, and either ATP (plus an ATP regenerating system) or the non-hydrolysable ATP analogue, ATP $\gamma$ S. RecA filament formation occurred slowly (Fig. 1a, b, third and subsequent panels), first appearing as a single spot (referred to as a cluster herein). Molecules were imaged intermittently over the course of 1–2 h; when the molecules were not being imaged, both the laser excitation and flow were turned off to minimize photobleaching, reduce sample volumes, and allow filament assembly to proceed on SSB-coated ssDNA in its relaxed state. With time, the nascent clusters elongated and new clusters appeared; these mixed nucleoprotein complexes comprised relatively stiff, rod-like RecA filament clusters interspersed between compacted and flexible SSB-coated ssDNA<sup>15</sup>. The composition of these intermediates was confirmed using atomic force microscopy (Supplementary Fig. 1). At the flow rate used, the SSB–ssDNA complexes are compacted to approximately 15% of the corresponding length

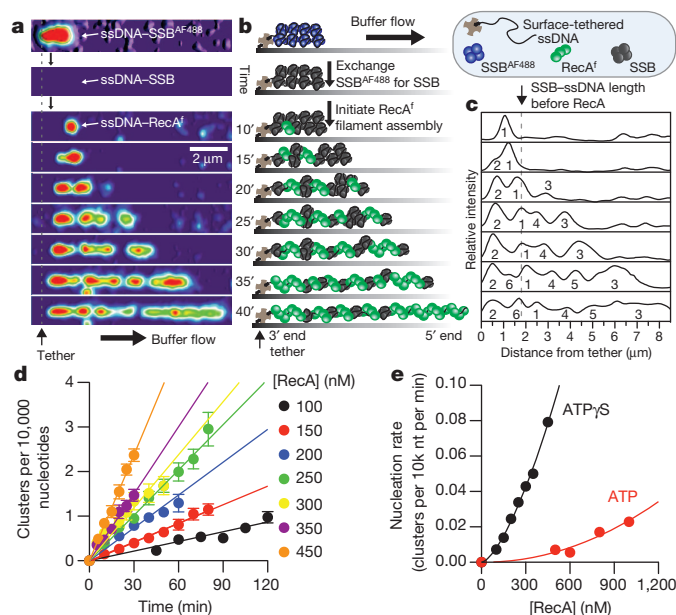


**Figure 1 | Direct visualization of RecA filament assembly on single molecules of SSB-coated ssDNA shows that RecA nucleates as a dimer.** a, RecA<sup>f</sup> filament assembly with ATP $\gamma$ S on a single molecule of SSB-coated ssDNA tethered within a microfluidic flow chamber was visualized using TIRF microscopy; montage is rendered into a topographic fluorescent intensity map b, c, Schematic (b) and fluorescent intensity profile (c) from a, d, The number of RecA clusters increases linearly with time (shown in minutes); slope is the nucleation rate ( $n = 18$ –93 clusters for each concentration;  $\pm$  s.d.). e, Nucleation rate increases with RecA concentration ( $[RecA]$ ) according to the equation  $J = k[RecA]^n$ , in which  $n$  is  $2.2 \pm 0.6$  for ATP $\gamma$ S and  $1.5 \pm 0.1$  for ATP (the error from the linear fits in d is smaller than the symbols). nt, nucleotides.

<sup>1</sup>Department of Microbiology, University of California, Davis, California 95616, USA. <sup>2</sup>Department of Molecular & Cellular Biology, University of California, Davis, California 95616, USA. <sup>3</sup>Biochemistry and Molecular Biology Graduate Group, University of California, Davis, California 95616, USA.

\*These authors contributed equally to this work.

of B-form dsDNA (Fig. 1a, b, top panels); by contrast, RecA–ssDNA filaments are extended to about 160% of dsDNA length<sup>14</sup>.

The number of RecA clusters bound to individual SSB–ssDNA complexes was determined by comparing images of each molecule with its fluorescence intensity profile (Fig. 1a, c and Supplementary Fig. 2). The number of clusters formed increased linearly with time (Fig. 1d), allowing for direct measurement of the RecA nucleation rate, expressed as the number of clusters formed per minute per 10,000 nucleotides. When the concentration of RecA was increased, the rate of nucleation became faster, exhibiting a nonlinear dependence with respect to RecA concentration (Fig. 1e). The data were fit to the relationship  $J = k[\text{RecA}]^n$ , in which  $J$  is the frequency of nucleation,  $k$  is a rate constant, and  $n$  is the number of protomers in a critical nucleus<sup>7,16</sup>. In the presence of ATP or ATPγS, the rate of nucleation of RecA on SSB–ssDNA exhibited a power dependence, in which  $n$  is  $2.2 \pm 0.6$  ( $\pm$  s.e.m.) or  $1.5 \pm 0.1$ , respectively (Fig. 1e). Because the nucleotide-binding site of a RecA nucleoprotein filament lies in a binding pocket between monomers<sup>17</sup>, our conclusion is consistent with the expectation that a dimer would be the minimal oligomeric species that could form a stable nucleus on ssDNA.

The sizes of individual RecA filaments grew with time (Fig. 2a), and the lengths of well-resolved individual clusters were plotted as a function of time and analysed by linear regression to determine their growth rate from the slope (Fig. 2b). Increasing RecA concentration resulted in a net increase in the growth rate as well as the distribution of rates, which varied from 10 to 100 nm min<sup>−1</sup> (Fig. 2c); given that the RecA–ssDNA filament comprises approximately 6 monomers per 10 nm, these rates correspond to about 6 to 60 monomers min<sup>−1</sup>. The net growth rate increased linearly with respect to the RecA concentration, with a slope of  $1.8 (\pm 1.0) \times 10^6 \text{ M}^{-1} \text{ s}^{-1}$  in the presence of ATPγS, and  $0.8 (\pm 0.1) \times 10^6 \text{ M}^{-1} \text{ s}^{-1}$  in the presence of ATP (Fig. 2d). This rate measures the bimolecular rate of association of RecA for the ends of a filament, and is about 10–100 times slower than the theoretical diffusion-controlled limit<sup>18</sup>. This linear concentration dependence indicates that filaments grow primarily through monomer addition, in agreement with previous observations<sup>8</sup>. Although the variation in

growth rates for different filaments was large, as is evident in their broad distribution (Fig. 2c, d), the measurement error for the growth rate of any individual filament was low (Supplementary Table 1). The nature of this broad distribution is discussed later as a salient property of RecA filament growth.

A further measure of filament nucleation is the time at which filaments begin to grow (that is, the lag times), which are evident in the individual growth trajectories<sup>16</sup>. The lag time for each growing cluster is an extrapolation to a real time of nucleation that is not limited by our detection system, and was determined from the  $x$  axis intercept of the linear regression for each filament analysed (Fig. 2b). Analysis of these lag times demonstrates that nucleation is slow and stochastic at low RecA concentrations and becomes markedly shorter at high concentrations (Fig. 2e), following an inverse power dependence in which  $n = 1.9 \pm 0.3$  (Fig. 2f). This independent method of analysis further confirms our conclusion that RecA filaments nucleate as a dimer (Fig. 1d, e). This is in contrast to previous observations that RecA requires a larger critical nucleus of 3–5 monomers to assemble on dsDNA<sup>7,9</sup>, possibly owing to its lower affinity for dsDNA. Nucleation of RecA filaments on dsDNA is strongly inhibited in the presence of salt<sup>2</sup>. Our observation that neither the nucleation nor growth rate of RecA filament assembly is altered over the range of salt concentration tested (50–200 mM NaCl) is also consistent with the interpretation that RecA nucleation on SSB–ssDNA requires a smaller critical nucleus owing to a higher affinity of RecA for ssDNA (Supplementary Fig. 3).

Previous single-molecule experiments monitoring RecA filament growth on dsDNA and ssDNA demonstrated that RecA filaments could grow in both directions<sup>7,8</sup>. We sought to determine whether this would be the case in the presence of SSB, and whether growth was symmetric or asymmetric (that is, whether there was a preferred directionality)<sup>19</sup>. We compared the growth of RecA clusters close to the point of attachment (that is, within  $\sim 0.5$  to  $1 \mu\text{m}$  of the 3' biotinylated end of the ssDNA tethered to the surface) relative to a cluster located on the same ssDNA molecule, but at an internal site. We rationalized that filaments growing from the tethered end could grow only in the 3'→5' direction owing to it being attached to the surface at the 3' end of the ssDNA, whereas filaments forming elsewhere on the molecule would be free to grow in both directions. Therefore, if both ends were available for elongation, clusters growing at internal regions should grow faster than the clusters forming at the tethered end of the molecule. Indeed, the cluster growth rates measured at internal sites ( $k_i$ ) were faster than cluster growth rates measured near the ssDNA end ( $k_e$ ), which are limited to growth in the 3'→5' direction (Fig. 3a). This is evident in the dot plot in Fig. 3a where most of the data points fall above the lowermost dashed line representing hypothetical unidirectional growth in the 3'→5' direction ( $k_i = k_e$ ). The uppermost dashed line represents the hypothetical scenario where filament growth is bidirectional and each end grows at the same rate ( $k_i = 2k_e$ ). The distribution of these relative rates is not affected by the concentration of RecA (Fig. 3a). Although this analysis provides good evidence that RecA filament growth on SSB-coated ssDNA is bidirectional (that is, almost all of the growth rates for internal clusters are greater than for those at an end), alone, it is insufficient to establish whether one direction grows faster than the other.

We therefore sought to measure the growth rates unambiguously at each end of a filament by direct single-molecule visualization. We first formed discrete clusters of Cy3-conjugated RecA (RecA<sup>Cy3</sup>) on SSB–ssDNA. The solution was then exchanged, replacing RecA<sup>Cy3</sup> (red) with RecA<sup>f</sup> (green) (Fig. 3b). Growth of RecA<sup>f</sup> from the pre-formed, internal RecA<sup>Cy3</sup> clusters was directly imaged and measured (Fig. 3c); growth from the left side of the RecA<sup>Cy3</sup> clusters is in the 5'→3' direction, and growth from the right side of the clusters is in the 3'→5' direction. Filament growth from the red RecA<sup>Cy3</sup>, through addition of the green RecA<sup>f</sup>, is seen to start in the leftward direction proceeding with an apparent preference for the 5'→3' direction (that is, towards the tethered end). The mean growth rate in the 5'→3'

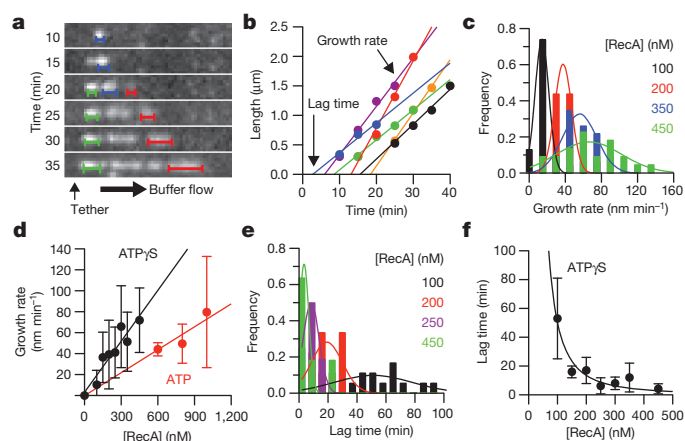


**Figure 2 | RecA filaments grow via rapid addition of monomers.**

**a, b,** Lengths for RecA clusters were measured (**a**) and analysed (**b**, same colours as in **a**, plus additional data) to determine the growth rate (slope) and lag time ( $x$  axis intercept) (100 nM RecA and ATPγS); same molecule and approximate scale as in Fig. 1a. The right-most cluster marked by the red line at 35 min is 2  $\mu\text{m}$ ; see also Supplementary Fig. 2a, b for measured lengths. **c,** Distribution of growth rates at increasing [RecA]. **d,** Mean growth rates increase linearly with [RecA]; slope is  $0.16 (\pm 0.08) \text{ nm min}^{-1} \text{ nM}^{-1}$  (ATPγS, black) (or  $1.1 (\pm 0.6) \times 10^8 \text{ M}^{-1} \text{ min}^{-1}$  at  $1.5 \text{ nm/RecA}^{17}$ ) and  $0.07 (\pm 0.01) \text{ nm min}^{-1} \text{ nM}^{-1}$  (ATP, red) (or  $0.47 (\pm 0.3) \times 10^8 \text{ M}^{-1} \text{ min}^{-1}$ ). **e,** Lag time distribution at increasing [RecA]. **f,** Lag times plotted with respect to [RecA] and fit to an inverse power law,  $J^{-1} = 1/k[\text{RecA}]^n$ , in which  $n$  is  $1.9 \pm 0.3$ . Lines in **c** and **e** are Gaussian fits. See Supplementary Table 1 statistics for more details ( $n = 207$  filaments, total; data are mean  $\pm$  s.d.).

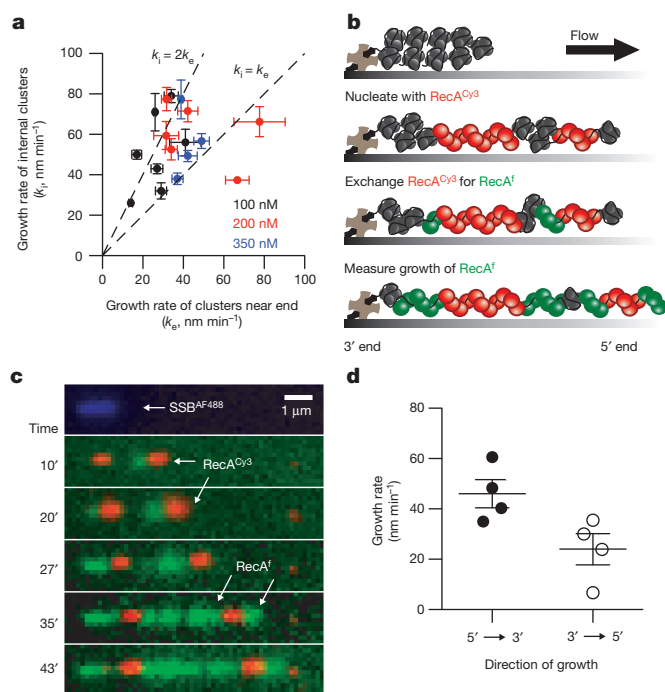


**Figure 3 | RecA filament growth on SSB-coated ssDNA is bidirectional.** **a**, Growth rates of clusters at the tethered 3' end of the ssDNA ( $k_e$ ) were plotted against growth rates of internal clusters on the same molecule ( $k_i$ ) ( $n = 18$ ; data are mean  $\pm$  s.e.m.). **b**, RecA<sup>Cy3</sup> (50 nM, red) clusters were preformed with ATP $\gamma$ S on SSB-coated ssDNA followed by growth with RecA<sup>f</sup> (250 nM, green). **c**, Visualization of RecA<sup>f</sup> (green) growth from preformed RecA<sup>Cy3</sup> (red) clusters, showing faster growth from the left side of the RecA<sup>Cy3</sup> clusters in the 5'  $\rightarrow$  3' direction. **d**, The plotted growth rates were  $44 \pm 11$  nm min<sup>-1</sup> in the 5'  $\rightarrow$  3' direction and  $27 \pm 12$  nm min<sup>-1</sup> in the 3'  $\rightarrow$  5' direction; ( $n = 4$ ; data are mean  $\pm$  s.d.).

direction is  $44 \pm 11$  nm min<sup>-1</sup>, whereas the growth rate in the 3'  $\rightarrow$  5' direction is  $27 \pm 12$  nm min<sup>-1</sup> (Fig. 3d). Although our observations demonstrate that bidirectional growth on SSB-ssDNA is possible, it should not be considered obligatory during RecA filament assembly. The broad distribution of growth rates in our analysis (Fig. 2c, d), the analysis of growth rates of internal clusters relative to end clusters (Fig. 3a), and the direct visualization of bidirectional growth (Fig. 3c) suggest that filament growth proceeds through stochastic phases of unidirectional growth from either end, as well as bidirectional growth from both ends.

Nucleation of the RecA filament on SSB-ssDNA requires formation of a RecA dimer (Figs 1e and 2f), the interface of which is the binding site for the magnesium-bound nucleotide cofactor<sup>17</sup>. Therefore, we tested whether these cofactors might affect nucleation and growth. Increasing the concentration of magnesium acetate (Mg(OAc)<sub>2</sub>) stimulated nucleation, with a plateau occurring at concentrations equal to or greater than the ATP $\gamma$ S concentration (Fig. 4a), consistent with the need for this metal ion as a component of the nucleating species; by contrast, the rate of filament growth was unaffected by divalent ion concentration (Fig. 4b). RecA binds to ssDNA with a higher affinity in the presence of ATP $\gamma$ S or dATP compared with ATP<sup>20,21</sup>. ATP $\gamma$ S is a non-hydrolysable analogue of ATP, whereas dATP is hydrolysed about 30% faster than ATP<sup>20</sup>; thus, a comparison of the assembly kinetics in the presence of these nucleotides experimentally uncouples hydrolysis from binding in these steps. In the presence of ATP $\gamma$ S and dATP, nucleation is approximately tenfold and fivefold faster, respectively, relative to assembly with ATP (Fig. 4c), showing that stabilization is not correlated with the absence of hydrolysis; by contrast, the rate of filament growth is only modestly affected (not a statistically significant difference) by the nucleotide cofactor (Fig. 4d). Therefore, the stabilization of nascent nuclei by ATP $\gamma$ S and dATP can

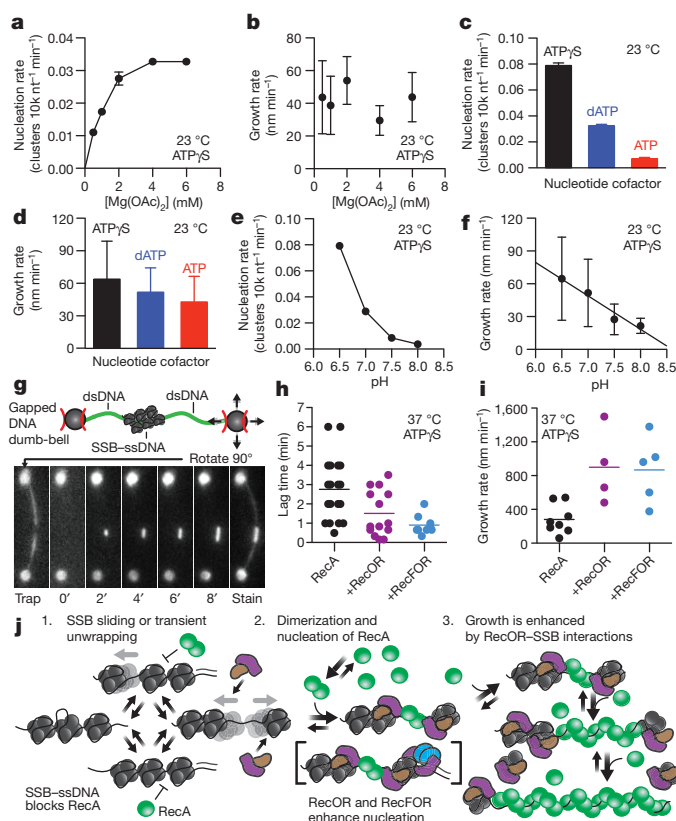


**Figure 4 | Nucleation is modulated by ligand binding, repressed at physiological pH, and enhanced by RecOR and RecFOR; growth is enhanced by RecOR.** **a–f**, RecA nucleation and growth rates plotted as function of [Mg(OAc)<sub>2</sub>] (**a**, **b**), nucleotide cofactors (**c**, **d**), and pH (**e**, **f**; slope =  $-2.0 \pm 0.3$  monomers min<sup>-1</sup> pH<sup>-1</sup>). Data in **a–f** are mean  $\pm$  s.d. **g**, Image montage of RecA<sup>f</sup> filament assembly on gapped DNA; centre to centre bead distance is 15.4  $\mu$ m. **h**, Nucleation is enhanced by RecOR and RecFOR. **i**, Growth accelerated by RecOR, with no additional increase by RecFOR. **j**, Kinetic model for RecA nucleation in which a RecA dimer binds ssDNA transiently released from SSB through either sliding or unwrapping, which is enhanced by RecOR and RecFOR; growth by monomer addition is accelerated by RecOR. [RecA] was 250 nM (**a**, **b**), 500 nM (**c–f**) and 1  $\mu$ M (**h**, **i**).

be attributed to the nucleotide binding-linked induction of a conformation with high affinity for ssDNA, consistent with the interpretation that nucleotide binding is important for filament assembly to the extent that it serves as a conformational modulator of RecA affinity for ssDNA that defines the stability of the critical nucleus<sup>2,21</sup>. Because the Mg<sup>2+</sup>-ATP cofactor binds between adjacent RecA monomers in the filament<sup>17</sup>, our conclusions are consistent with the simplest expectations that nucleation of a filament should require minimally two monomers. Our observation that growth is affected by neither Mg(OAc)<sub>2</sub> nor nucleotide cofactor—but is linearly dependent on RecA concentration—is consistent with the simplest interpretation that RecA monomers add to the ends of a filament, but require a conformational change that is slower than nucleotide binding.

Unexpectedly, we observed that the assembly of RecA on SSB-ssDNA at the approximately physiological pH of 7.5 was very slow; however, it was strongly stimulated by reducing the pH to 6.5, conditions in which RecA is predominantly a dimer<sup>22</sup>. Increasing the pH to 8.0 resulted in a marked monotonic inhibition of both nucleation (Fig. 4e) and growth (Fig. 4f), suggesting that the overall rates, but not the mechanism, are altered in a pH-dependent manner. The intracellular pH of *E. coli* is highly regulated and maintained in the range of 7.5 to 8.0, where the rate of uncatalysed nucleation, seemingly paradoxically, would be very low (Fig. 4e). These findings show that, at physiological conditions, neither nucleation nor growth of RecA



filaments on SSB-coated ssDNA occurs at its observed maximal rate. This finding, in turn, would suggest that *in vivo* cellular mediator proteins could promote RecA filament assembly on SSB-coated ssDNA by accelerating either of these steps. In *E. coli*, RecF, RecO and RecR are genetically and biochemically defined mediator proteins<sup>23,24</sup>. Stimulation of assembly is by means of the RecOR complex, which interacts with SSB to mediate assembly onto SSB-coated ssDNA in a structure-independent manner, and the RecFOR complex (RecOR and RecF), which acts at a junction of ssDNA with dsDNA<sup>23–25</sup>.

The addition of RecO (or RecOR) in our TIRF-based assay invariably resulted in the adsorption of SSB-coated ssDNA to the glass surface. To circumvent this problem and to determine the mechanism by which these mediator proteins act, we switched to epifluorescent detection and optical trapping<sup>7,12,26</sup>, which moves the DNA molecule away from the glass surface. To create a suitable DNA substrate with an ssDNA gap, we designed a derivative of bacteriophage  $\lambda$ gt11 containing a  $\phi$ C31 *attP* recognition site and modified a derivative of bacteriophage M13mp7 ssDNA to contain the *attB* recognition site when annealed to a PCR-based segment of ssDNA. Integration of the ssDNA into the biotinylated  $\lambda$  DNA resulted in a dsDNA substrate containing an ssDNA gap of 8,155 nucleotides that was flanked by dsDNA 'handles' at both ends (Supplementary Fig. 6). Using a microfluidic flow cell coupled to a fluorescence microscope and a split-beam dual optical trap<sup>26</sup>, two streptavidin-coated polystyrene beads were isolated and a single molecule of gapped DNA, biotinylated at each end, was tethered between the beads *in situ* (Fig. 4g and Supplementary Fig. 4). The molecule was rotated perpendicular to the flow and successively dipped in a reaction channel containing RecA<sup>f</sup> and Mg<sup>2+</sup>-ATP $\gamma$ S at 37 °C (ref. 7) (Fig. 4g, bottom). With time, RecA<sup>f</sup> filaments nucleated on the SSB-coated ssDNA segment and grew at rates quantitatively consistent with our TIRF-based measurements, albeit faster owing to the increased temperature and RecA concentration (Fig. 4g and Supplementary Video 2). With RecOR present, nucleation remained stochastic, but the mean rate of nucleation increased (that is, lag times decreased), the distribution shifted to faster rates, and some nucleation events were even faster than those seen for RecA alone; these nucleation characteristics were further enhanced by the addition of RecF (Fig. 4h). RecOR also accelerated RecA filament growth; however, addition of RecF had no further effect on the rate of filament growth (Fig. 4i).

We have demonstrated that RecA filament nucleation on SSB-coated ssDNA is a slow and stochastic kinetic process requiring a RecA dimer. Under physiological conditions, nascent RecA filaments grow at a rate of approximately 50–500 nm min<sup>-1</sup> (~30–300 monomers min<sup>-1</sup> or 0.5 to 5 monomer s<sup>-1</sup>) (Fig. 4i), in good agreement with previous work<sup>2,4</sup>. The bimolecular rate of association is rapid, but it is below the theoretical diffusion-controlled limit, suggesting that filament growth proceeds through monomer addition<sup>8</sup> followed by a required conformational change at the end of the filament. We have further demonstrated that growth of RecA clusters on SSB–ssDNA complexes is bidirectional, with net growth occurring preferentially in the 5'→3' direction. In light of these results, we define a simultaneous two-step kinetic model for nucleation of a RecA filament on SSB-coated ssDNA (Fig. 4j). *In vivo*, SSB binds rapidly to ssDNA, wrapping ~60–70 nucleotides of ssDNA per tetramer. Once bound, ssDNA binding proteins can slide on ssDNA<sup>27</sup>, with SSB sliding at ~260 nucleotides<sup>2</sup> s<sup>-1</sup> in approximately three nucleotide steps<sup>28</sup>. Likewise, ssDNA can locally unwrap from a subunit of the tetramer on a microsecond timescale<sup>29</sup>. This transient, limited unwrapping of ssDNA from an SSB tetramer could create a site available for RecA binding; however, larger ssDNA segments could be rapidly rebound by another SSB tetramer<sup>29</sup>. Given that a RecA monomer requires three nucleotides of ssDNA for binding<sup>28</sup>, nucleation of a RecA dimer would require the sliding of two adjacent tetramers away from each other on a nearly saturated ssDNA lattice, or the partial, transient release of at least six nucleotides of ssDNA. Kinetic trapping of these transient

states by RecA protomers is consistent with the slower kinetics of nucleation (requiring dimers) relative to growth (occurring with monomers). RecO binds to both SSB and RecR; however, RecO and/or RecR do not displace SSB from ssDNA<sup>30</sup>. Instead RecOR interacts with SSB to facilitate RecA filament assembly<sup>23</sup>. We propose that RecOR traps the transient states in which ssDNA is released by SSB during either sliding or unwrapping, effectively weakening the SSB–ssDNA interaction through stoichiometric interactions with SSB. Consequently, RecOR binding to SSB–ssDNA also enhances RecA filament growth. Here we establish that recombination mediators can differentially facilitate the rate-limiting step of nucleation, enhance filament growth, or enhance both nucleation and growth. We anticipate that the conclusions and technical approach presented here will be particularly useful, and in some cases maybe even essential, for future experiments designed to further determine the mechanism by which filament assembly of RecA orthologues, such as mammalian RAD51, is regulated by the analogues, such as the tumour-suppressor, BRCA2, and the RAD51 paralogues, which play important but poorly understood functions in the early steps of recombination-mediated DNA repair.

## METHODS SUMMARY

For TIRF, all protein-containing reagents were diluted into single molecule buffer (SMB) (20 mM MES, pH 6.5, 50 mM dithiothreitol (DTT), 100 mM NaCl and 20% sucrose). Bacteriophage  $\lambda$  genomic DNA (48.5 kb) was biotinylated by incorporating biotin-dGTP at the 3' ends using T4 polymerase (16 °C, New England Biolabs Buffer 2, 10 min). Before each experiment, the DNA (200 fmols, molecules) was denatured in 5–10  $\mu$ l of 0.5 M NaOH at 37 °C for 5–10 min. Addition of 0.4 ml SMB containing 200 nM SSB<sup>AF488</sup> (approximately sixfold excess over stoichiometric binding sites) neutralized the reaction and also coated the ssDNA. The SSB<sup>AF488</sup>–ssDNA complexes were injected into a flow cell and incubated for ~5 min to tether to the surface and then imaged using TIRF microscopy. After recording the length and position of each molecule, SSB<sup>AF488</sup> was replaced with unlabelled, wild-type SSB (500 nM SSB in SMB). RecA filament assembly was initiated by injecting SMB containing 4 mM Mg(OAc)<sub>2</sub>, 2 mM ATP $\gamma$ S (unless ATP or dATP indicated), 200 nM SSB, and the indicated concentration of RecA<sup>f</sup> (Supplementary Fig. 5) or RecA<sup>C33</sup> (Supplementary Fig. 6) at room temperature (~23 °C). For optical trapping experiments, reactions were at 37 °C and contained 20 mM Tris(OAc), pH 7.5, 200 mM NaCl, 4 mM Mg(OAc)<sub>2</sub>, 50 mM DTT, 20% sucrose, 2 mM ATP $\gamma$ S, 200 nM SSB and 1  $\mu$ M RecA, plus (when added) 100 nM RecO, 100 nM RecR and 50 nM RecF. Experiments conducted with ATP or dATP contained 1 mM phosphoenol pyruvate and 20 U ml<sup>-1</sup> pyruvate kinase. Images were obtained by taking 20–30 successive 100-ms exposures at the times indicated. During intervals between imaging in TIRF, flow and laser excitation were turned off to preserve the sample and minimize photobleaching; however, flow was turned on 4–5 s before imaging to allow the flow to stabilize.

**Full Methods** and any associated references are available in the online version of the paper.

Received 9 March; accepted 20 September 2012.

Published online 24 October 2012.

- Kowalczykowski, S. C. & Eggleston, A. K. Homologous pairing and DNA strand-exchange proteins. *Annu. Rev. Biochem.* **63**, 991–1043 (1994).
- Kowalczykowski, S. C. Biochemistry of genetic recombination: energetics and mechanism of DNA strand exchange. *Annu. Rev. Biophys. Chem.* **20**, 539–575 (1991).
- Kowalczykowski, S. C., Clow, J., Somani, R. & Varghese, A. Effects of the *Escherichia coli* SSB protein on the binding of *Escherichia coli* RecA protein to single-stranded DNA: demonstration of competitive binding and the lack of a specific protein-protein interaction. *J. Mol. Biol.* **193**, 81–95 (1987).
- Thresher, R. J., Christiansen, G. & Griffith, J. D. Assembly of presynaptic filaments. Factors affecting the assembly of RecA protein onto single-stranded DNA. *J. Mol. Biol.* **201**, 101–113 (1988).
- Cazenave, C., Toulme, J. J. & Helene, C. Binding of RecA protein to single-stranded nucleic acids: spectroscopic studies using fluorescent polynucleotides. *EMBO J.* **2**, 2247–2251 (1983).
- Shivashankar, G. V., Feingold, M., Krichevsky, O. & Libchaber, A. RecA polymerization on double-stranded DNA by using single-molecule manipulation: the role of ATP hydrolysis. *Proc. Natl Acad. Sci. USA* **96**, 7916–7921 (1999).
- Galletto, R., Amitani, I., Baskin, R. J. & Kowalczykowski, S. C. Direct observation of individual RecA filaments assembling on single DNA molecules. *Nature* **443**, 875–878 (2006).
- Joo, C. *et al.* Real-time observation of RecA filament dynamics with single monomer resolution. *Cell* **126**, 515–527 (2006).

9. Handa, N., Amitani, I., Gumlaw, N., Sandler, S. J. & Kowalczykowski, S. C. Single molecule analysis of a red fluorescent RecA protein reveals a defect in nucleoprotein filament nucleation that relates to its reduced biological functions. *J. Biol. Chem.* **284**, 18664–18673 (2009).
10. Modesti, M. *et al.* Fluorescent human RAD51 reveals multiple nucleation sites and filament segments tightly associated along a single DNA molecule. *Structure* **15**, 599–609 (2007).
11. van der Heijden, T. *et al.* Real-time assembly and disassembly of human RAD51 filaments on individual DNA molecules. *Nucleic Acids Res.* **35**, 5646–5657 (2007).
12. Hilario, J., Amitani, I., Baskin, R. J. & Kowalczykowski, S. C. Direct imaging of human Rad51 nucleoprotein dynamics on individual DNA molecules. *Proc. Natl Acad. Sci. USA* **106**, 361–368 (2009).
13. Dillingham, M. S. *et al.* Fluorescent single-stranded DNA binding protein as a probe for sensitive, real-time assays of helicase activity. *Biophys. J.* **95**, 3330–3339 (2008).
14. Bell, J. C. *Dynamic Assembly of RecA Filaments on Single Molecules of SSB-coated ssDNA*. PhD thesis, Univ. of California, Davis (2011).
15. Griffith, J. D., Harris, L. D. & Register, J. III. Visualization of SSB-ssDNA complexes active in the assembly of stable RecA-DNA filaments. *Cold Spring Harb. Symp. Quant. Biol.* **49**, 553–559 (1984).
16. Kowalczykowski, S. & Steinhardt, J. Kinetics of hemoglobin S gelation followed by continuously sensitive low-shear viscosity. *J. Mol. Biol.* **115**, 201–213 (1977).
17. Chen, Z., Yang, H. & Pavletich, N. P. Mechanism of homologous recombination from the RecA-ssDNA/dsDNA structures. *Nature* **453**, 489–494 (2008).
18. Berg, O. G. & von Hippel, P. H. Diffusion-controlled macromolecular interactions. *Annu. Rev. Biophys. Biophys. Chem.* **14**, 131–158 (1985).
19. Register, J. C. III & Griffith, J. The direction of RecA protein assembly onto single strand DNA is the same as the direction of strand assimilation during strand exchange. *J. Biol. Chem.* **260**, 12308–12312 (1985).
20. Menetski, J. P. & Kowalczykowski, S. C. Enhancement of *Escherichia coli* RecA protein enzymatic function by dATP. *Biochemistry* **28**, 5871–5881 (1989).
21. Menetski, J. P. & Kowalczykowski, S. C. Interaction of recA protein with single-stranded DNA. Quantitative aspects of binding affinity modulation by nucleotide cofactors. *J. Mol. Biol.* **181**, 281–295 (1985).
22. McEntee, K., Weinstock, G. M. & Lehman, I. R. Binding of the recA protein of *Escherichia coli* to single- and double-stranded DNA. *J. Biol. Chem.* **256**, 8835–8844 (1981).
23. Umez, K., Chi, N. W. & Kolodner, R. D. Biochemical interaction of the *Escherichia coli* RecF, RecQ, and RecR proteins with RecA protein and single-stranded DNA binding protein. *Proc. Natl Acad. Sci. USA* **90**, 3875–3879 (1993).
24. Morimatsu, K. & Kowalczykowski, S. C. RecFOR proteins load RecA protein onto gapped DNA to accelerate DNA strand exchange: a universal step of recombinational repair. *Mol. Cell* **11**, 1337–1347 (2003).
25. Handa, N., Morimatsu, K., Lovett, S. T. & Kowalczykowski, S. C. Reconstitution of initial steps of dsDNA break repair by the RecF pathway of *E. coli*. *Genes Dev.* **23**, 1234–1245 (2009).
26. Forget, A. L. & Kowalczykowski, S. C. Single-molecule imaging of DNA pairing by RecA reveals a three-dimensional homology search. *Nature* **482**, 423–427 (2012).
27. Lohman, T. M. & Kowalczykowski, S. C. Kinetics and mechanism of the association of the bacteriophage T4 gene 32 (helix destabilizing) protein with single-stranded nucleic acids: evidence for protein translocation. *J. Mol. Biol.* **152**, 67–109 (1981).
28. Roy, R., Kozlov, A. G., Lohman, T. M. & Ha, T. SSB protein diffusion on single-stranded DNA stimulates RecA filament formation. *Nature* **461**, 1092–1097 (2009).
29. Kuznetsov, S. V., Kozlov, A. G., Lohman, T. M. & Ansari, A. Microsecond dynamics of protein-DNA interactions: direct observation of the wrapping/unwrapping kinetics of single-stranded DNA around the *E. coli* SSB tetramer. *J. Mol. Biol.* **359**, 55–65 (2006).
30. Umez, K. & Kolodner, R. D. Protein interactions in genetic recombination in *Escherichia coli*. Interactions involving RecQ and RecR overcome the inhibition of RecA by single-stranded DNA-binding protein. *J. Biol. Chem.* **269**, 30005–30013 (1994).

**Supplementary Information** is available in the online version of the paper.

**Acknowledgements** We are grateful to members of the laboratory for their comments on this work. J.C.B. was funded by a National Institutes of Health (NIH) Predoctoral Training Program in Molecular & Cellular Biology (T32 GM007377); C.C.D. and J.L.P. were funded by the NIH T32 Training Program in Oncogenic Signals and Chromosome Biology (CA10052159); J.L.P. was also funded by a NIH Postdoctoral Fellowship (CA136103); and S.C.K. was supported by the NIH (GM62653 and GM64745).

**Author Contributions** J.C.B., J.L.P., C.C.D. and S.C.K. conceived the general ideas, designed the experiments and interpreted the data. J.C.B., J.L.P. and C.C.D. performed experiments. J.C.B. and S.C.K. wrote the manuscript.

**Author Information** Reprints and permissions information is available at [www.nature.com/reprints](http://www.nature.com/reprints). The authors declare no competing financial interests. Readers are welcome to comment on the online version of the paper. Correspondence and requests for materials should be addressed to S.C.K. ([sckowalczykowski@ucdavis.edu](mailto:sckowalczykowski@ucdavis.edu)).

## METHODS

**TIRF and single-channel flow cells.** An Eclipse TE2000-U, upright TIRF microscope (Nikon), using a CFI Plan Apo TIRF x100, 1.45 numerical aperture, oil-immersed objective was used as previously described<sup>26</sup>. Single-channel flow cells were constructed by drilling holes into a glass microscope slide and adhering a glass coverslip using 3M Thermo-Bond Film (0.635 mm or 2.5 mils (thousandths of an inch)) with a channel cut out from the tape of approximate dimensions of  $5 \times 35 \times 0.1$  mm. Inlet ports (PEEK tubing, 0.5 mm inner diameter) were attached to the flow cell using epoxy. The surface was functionalized by incubating the flow cell successively with the following solutions for 5 min each: 1 M NaOH, water, single molecule buffer (SMB: 20 mM MES, pH 6.5, 50 mM dithiothreitol (DTT), 100 mM NaCl and 20% sucrose), 0.2 mg ml<sup>-1</sup> biotin-BSA, SMB, 0.2 mg ml<sup>-1</sup> streptavidin (Pierce), and 0.15 mg ml<sup>-1</sup> Roche blocking reagent. Proteins were diluted into SMB. Bacteriophage  $\lambda$  genomic DNA (48.5 kb) was biotinylated by incorporating biotin-dGTP at the 3' ends using T4 polymerase at 16 °C in Buffer 2 (New England Biolabs) for 10 min. The enzyme was inactivated with 20 mM EDTA followed by heat (70 °C for 10 min) and removal of nucleotides with an Illustra Microspin S-400 Column (GE) equilibrated in TE buffer (10 mM TrisOAc, pH 7.5, and 1 mM EDTA). The concentration of DNA was determined by ultraviolet absorbance, with  $A_{260\text{ nm}} = 1$  taken to be equivalent to 50 ng  $\mu\text{l}^{-1}$  for dsDNA. Single-stranded DNA was generated for single-molecule experiments by denaturing the biotinylated bacteriophage  $\lambda$  DNA (200 fmols, molecules) in 5–10  $\mu\text{l}$  of 0.5 M NaOH at 37 °C for 5–10 min. The alkali conditions were rapidly neutralized with the addition of 0.4 ml SMB containing 200 nM SSB<sup>AF488</sup>, yielding a final concentration of  $\sim 480$  nM nucleotides. Assuming a site size of 15 nucleotides per SSB monomer, SSB should be in approximately sixfold excess over possible stoichiometric binding sites. The SSB<sup>AF488</sup>-ssDNA complexes were then injected into a flow cell and allowed to incubate for approximately 5 min to allow for the attachment of the biotinylated molecules to the streptavidin-coated glass surface.

**RecA<sup>f</sup> filament formation on SSB-ssDNA using TIRF microscopy.** SSB<sup>AF488</sup>-ssDNA complexes were attached to the functionalized surface of a flow cell as described above and imaged. The solution containing fluorescent SSB<sup>AF488</sup> was then replaced with unlabelled wild-type SSB (500 nM) in SMB, resulting in the displacement of SSB<sup>AF488</sup> from the ssDNA. When displacement was complete, as monitored by the rapid disappearance of fluorescence, reaction buffer containing 20 mM MES, pH 6.5, 100 mM NaCl (unless otherwise indicated), 50 mM DTT, 4 mM Mg(OAc)<sub>2</sub>, 2 mM ATP $\gamma$ S (unless ATP or dATP as indicated), 200 nM SSB and the indicated concentration of RecA<sup>f</sup> was injected. Experiments in which Mg(OAc)<sub>2</sub> was titrated (Fig. 4a, b) contained 250 nM RecA. Experiments comparing nucleotide cofactors and pH (Fig. 4c–f) contained 500 nM RecA. All experiments were performed at 23 °C. Experiments conducted with ATP and dATP also contained 1 mM phosphoenol pyruvate (PEP) and 20 U ml<sup>-1</sup> of pyruvate kinase. Furthermore, experiments performed using above 500 nM total RecA contained 250 nM RecA<sup>f</sup> plus the amount of unmodified RecA necessary to achieve the final concentration indicated; this was done to reduce the extent of background fluorescence. Bulk-phase analyses of RecA filament formation on SSB-coated ssDNA, using the kinetics of ATP hydrolysis<sup>31</sup>, did not demonstrate any discernible difference for mixtures of unmodified RecA and RecA<sup>f</sup> (Supplementary Fig. 5) (ref. 14). Between the imaging intervals, flow was shut off to preserve the sample and reduce photobleaching; flow was restored approximately 4–5 s before laser excitation and imaging. Experiments designed to directly visualize bidirectional growth used RecA<sup>Cy3</sup>, which retains normal biochemical activity (Supplementary Fig. 6).

**Image processing and analysis.** For each time interval,  $\sim 25$ – $35$  frames ( $\sim 2$ – $4$  s at 100 ms exposure) were averaged using ImageJ v.1.41o. A theoretical point spread function was generated using the ImageJ plugin Deconvolution Lab, and subsequently deconvolved using the Tikhonov–Miller algorithm<sup>32</sup>. Images collected during a time-lapse experiment were then compiled into a stack, aligned to correct for stage drift and the intensity was normalized. Those stacks were then converted to 3D surface plots using the ImageJ 3D surface plot function, which applies a nearest neighbour smoothing function. Plots were directly compared to fluorescent intensity profiles in ImageJ to more accurately visually analyse clusters of RecA<sup>f</sup> forming at longer time intervals. Only molecules in which SSB<sup>AF488</sup>-ssDNA-complexes initially appeared as distinct single molecules were analysed. Nucleation data were normalized by taking the number of clusters per molecule and dividing by the relative length of the SSB<sup>AF488</sup>-ssDNA of that molecule to the longest molecules from that particular experiment. As the length of the SSB<sup>AF488</sup>-ssDNA complexes changes with flow-cell variation (which affects flow rate and extension) as well as buffer conditions<sup>14</sup>, this serves as an internal normalization factor for each experiment.

**Atomic force microscopy imaging of SSB-coated and RecA-coated ssDNA complexes.** SSB-coated ssDNA complexes were formed by incubating 35  $\mu\text{M}$  (nucleotides) M13 ssDNA with 1.75  $\mu\text{M}$  SSB for 5–10 min at 37 °C in 20 mM

TrisOAc, pH 7.5, 20 mM NaCl, 1 mM Mg(OAc)<sub>2</sub>, 0.5 mM ATP $\gamma$ S, 0.1  $\mu\text{M}$  spermidine-HCl and 7  $\mu\text{M}$  RecA. The nucleoprotein complexes were purified away from free protein using a C-1000 spin column washed with binding buffer, adsorbed onto freshly cleaved mica for 1 min, rinsed with water, stained with 0.02% uranyl acetate and visualized using a Nanoscope IV in tapping mode with an Al-T300 tip (Budget Sensors). Uranyl acetate stain facilitates atomic force microscopy imaging of the SSB-ssDNA complex<sup>33</sup>.

**ATPase assays for monitoring the kinetics of RecA binding to SSB-coated ssDNA.** ATPase assays comparing relative amounts of RecA<sup>f</sup> and unmodified RecA were performed in 20 mM MES, pH 6.5, 20% sucrose, 50 mM DTT, 100 mM NaCl, 0.2 mg ml<sup>-1</sup> NADH, 20 U ml<sup>-1</sup> pyruvate kinase and lactate dehydrogenase, 4 mM Mg(OAc)<sub>2</sub>, 2 mM ATP, 1 mM phosphoenolpyruvate (PEP), 3  $\mu\text{M}$  M13 ssDNA, 1.5  $\mu\text{M}$  SSB and 1  $\mu\text{M}$  total RecA at the ratio of RecA<sup>f</sup>:RecA indicated. All assays were performed at 37 °C with a 5-min preincubation of all components except for RecA, which was used to initiate the reaction. The change in absorbance ( $\lambda = 340$  nm) was converted to  $\mu\text{mol}$  ATP using the extinction coefficient for NADH =  $6.22 \times 10^{-3}$   $\mu\text{M cm}^{-1}$ . The data were then fit to a second order polynomial ( $Y = A + Bx + Cx^2$ , in which the intercept,  $A$ , was constrained to the time at mixing, 0 s). The derivative of the fit was taken and the slope determined to be the change in hydrolysis rate as a function of time, expressed as  $\Delta v/\Delta t$  (that is, the instantaneous change in the reaction velocity ( $v$ ) with time ( $t$ ) in  $\mu\text{mol min}^{-2}$ ), which defines the acceleration of the reaction velocity, and is a measure of RecA filament formation on SSB-ssDNA complexes<sup>31</sup>.

**Fluorescent modification and activity of RecA<sup>Cy3</sup>.** RecA<sup>Cy3</sup> was made as described previously for RecA<sup>f</sup> by covalently modifying the amino terminus of the protein with Cy3-succinimidyl ester (GE Healthcare) instead of 5,6-carboxy-fluorescein-succinimidyl ester<sup>7</sup>. The ssDNA binding activity of RecA<sup>Cy3</sup> was determined by monitoring the ATP hydrolysis rate of RecA at increasing concentrations of polydeoxythymidylate ssDNA. The ATP hydrolysis rate was calculated from the linear decrease in the absorbance of NADH at 340 nm. The reaction buffer contained 25 mM TrisOAc, pH 7.5, 8 mM Mg(OAc)<sub>2</sub>, 1 mM ATP, 1.5 mM PEP, 1 mM DTT, 30 U ml<sup>-1</sup> pyruvate kinase, 20 U ml<sup>-1</sup> lactate dehydrogenase and 2 mg ml<sup>-1</sup> NADH at 37 °C.

### Preparation of the gapped ssDNA substrate for the single-molecule studies.

An engineered derivative of bacteriophage  $\lambda$ gt11, containing a  $\phi$ C31 *attP* recognition site, was created as follows. An EcoRI fragment derived from pDHJS AN+ (ref. 34) containing a kanamycin-resistance cassette and the  $\phi$ C31 *attP* recognition site was ligated into EcoRI-digested bacteriophage  $\lambda$ gt11 DNA. The *attP*-containing derivative of bacteriophage  $\lambda$ gt11 is hereafter called bacteriophage  $\lambda$ Kyotos. A modified derivative of bacteriophage M13mp7 ssDNA contained the *attB* recognition site, from which a 500 base pair dsDNA containing the  $\phi$ C31 *attB* at its centre was generated by PCR using Phusion High-Fidelity PCR Master Mix from New England Biolabs. After heat denaturation, it was annealed to the M13mp7 ssDNA derivative. Integration of the ssDNA plasmid into  $\lambda$ Kyotos dsDNA resulted in a gapped DNA substrate (Supplementary Fig. 4c).  $\phi$ C31 integrase was used to recombine  $\lambda$ Kyotos dsDNA and the annealed 13mp7 ssDNA containing the *attB* recognition site. The construct pHS62, containing the full coding sequence of  $\phi$ C31 integrase, was provided by M. Smith<sup>35</sup>. Biotin was incorporated into the *cos* sites of  $\lambda$ Kyotos in a reaction consisting of 10 mM Tris-HCl, pH 7.9, 10 mM MgCl<sub>2</sub>, 50 mM NaCl, 1 mM DTT, 33  $\mu\text{M}$  dATP, 33  $\mu\text{M}$  dTTP, 3  $\mu\text{M}$  dCTP, 33  $\mu\text{M}$  biotin-dGTP, 17 ng  $\mu\text{l}^{-1}$   $\lambda$ Kyotos and 0.17 U  $\mu\text{l}^{-1}$  Klenow exo- DNA polymerase. After 15 min at 22 °C, the polymerase was heat inactivated at 70 °C for 20 min.

### Epifluorescence microscopy, optical trapping and multi-channel flow cells.

Infrared optical trapping capability was achieved on the same TE-2000-U microscope (Nikon) used for the TIRF-based assay with the addition of a polarizer (Newport) to split the beam, generating two traps and a steering mirror (Newport) to control the  $x$ - $y$  position of one of the beams<sup>26</sup>. Excitation of the sample in epifluorescence mode was achieved using a cyan 488 nm laser (Picarro) by adjusting the angle of the laser to pass completely through the sample chamber (not in TIRF mode). The fluorescence emission was directed through a polychroic mirror (515/30 nm and 600/40 nm, Chroma). Images were captured on a DU-897E iXon CCD camera (Andor). Channels were laser etched into glass slides ( $25 \times 75 \times 1$  mm, Fisher Scientific) covered with an adhesive abrasive blasting mask (Rayzist Photomask) using a 30 W mini-24 laser engraver (Epilog Lasers). The slides were sandblasted using 220-grit silicon carbide (Electro Abrasives) to remove residual laser-ablated glass from the channels, resulting in channels  $\sim 100$ – $150$   $\mu\text{m}$  deep. Holes were drilled using a diamond-bit Dremel tool, washed with 2% Hellmanex and rinsed with water and methanol. The cover glass ( $24 \times 60$  mm, Corning no. 1) was cleaned in 1 M potassium hydroxide dissolved in 100% methanol with sonication for 1 h, rinsed with water and methanol and dried. The cleaned cover glass was attached to the etched microscope slide with ultraviolet optical adhesive 74 (Norland Products) applied through capillary action on a 45 °C heat block. The adhesive was cured by placing the flow cell



30 cm from a 100 W HBO lamp (Zeiss) for 60 min followed by curing at 50 °C overnight. PEEK tubing with 0.5 mm inner diameter (Upchurch Scientific) was inserted into each of the etched holes to create inlet and outlet connection ports using epoxy (5 minute epoxy, Devcon). The flow cell was mounted to the microscope and attached to a syringe pump (KD Scientific). The temperature of the objective lens was held at 37 °C by circulating water through a brass and copper collar machined to fit around the objective lens. The flow cell had six laminar flow channels containing the following components in addition to 20% sucrose and 50 mM DTT, channel 1: 100 mM NaHCO<sub>3</sub>, pH 8.3, 100 mM NaCl, 1 mM Mg(OAc)<sub>2</sub>, 5 nM YOYO-1, and 0.2% streptavidin-coated polystyrene beads (1 µm, Bangs); channel 2: 100 mM NaHCO<sub>3</sub>, pH 8.3, 100 mM NaCl, 1 mM Mg(OAc)<sub>2</sub>, 50 nM YOYO-1, 4 pM gapped DNA and 300 nM SSB; channel 3: 100 mM NaHCO<sub>3</sub>, pH 8.3, 100 mM NaCl, 1 mM Mg(OAc)<sub>2</sub>, 50 nM YOYO-1 and 100 nM SSB; channel 4: 100 mM NaHCO<sub>3</sub>, pH 8.3 and 100 nM SSB; channel 5: 20 mM Tris(OAc), pH 7.5, 200 mM NaCl, 4 mM Mg(OAc)<sub>2</sub>, 2 mM ATPγS and 200 nM SSB; and channel 6: 20 mM Tris(OAc), pH 7.5, 200 mM NaCl, 4 mM Mg(OAc)<sub>2</sub>, 2 mM ATPγS, 200 nM SSB and 1 µM RecA. When indicated, RecO and RecR were present at 100 nM each in channel 6, whereas RecF was present at 50 nM. Sterile 0.2-µm filtered sucrose solutions were degassed for at least 1 h in a vacuum chamber before the addition of buffer and DTT, and degassed for an extra 15 min; reactions were then assembled at room temperature and protected from

light. Optically trapped molecules were moved between flow channels by movement of the sample stage, which was automated and synchronized with both laser excitation and camera acquisition during dipping experiments using custom software coded in LabView. RecA<sup>f</sup> filaments were successively transferred from channel 6 to 5, imaged for 1 s, and immediately transferred back to channel 6. The time at which a RecA<sup>f</sup> cluster first appeared was determined to be the apparent lag time. Images were processed in ImageJ by frame averaging and contrast enhancement.

31. Kowalczykowski, S. C. & Krupp, R. A. Effects of *Escherichia coli* SSB protein on the single-stranded DNA-dependent ATPase activity of *Escherichia coli* RecA protein: evidence that SSB protein facilitates the binding of RecA protein to regions of secondary structure within single-stranded DNA. *J. Mol. Biol.* **193**, 97–113 (1987).
32. Napolitano, M. A. *et al.* Brg1 chromatin remodeling factor is involved in cell growth arrest, apoptosis and senescence of rat mesenchymal stem cells. *J. Cell Sci.* **120**, 2904–2911 (2007).
33. Hamon, L. *et al.* High-resolution AFM imaging of single-stranded DNA-binding (SSB) protein–DNA complexes. *Nucleic Acids Res.* **35**, e58 (2007).
34. Plank, J. L. & Hsieh, T. S. A novel, topologically constrained DNA molecule containing a double Holliday junction: design, synthesis, and initial biochemical characterization. *J. Biol. Chem.* **281**, 17510–17516 (2006).
35. Thorpe, H. M. & Smith, M. C. *In vitro* site-specific integration of bacteriophage DNA catalyzed by a recombinase of the resolvase/invertase family. *Proc. Natl Acad. Sci. USA* **95**, 5505–5510 (1998).

# The structural biochemistry of Zucchini implicates it as a nuclease in piRNA biogenesis

Jonathan J. Ipsaro<sup>1,2\*</sup>, Astrid D. Haase<sup>2\*</sup>, Simon R. Knott<sup>2</sup>, Leemor Joshua-Tor<sup>1,2</sup> & Gregory J. Hannon<sup>2</sup>

PIWI-family proteins and their associated small RNAs (piRNAs) act in an evolutionarily conserved innate immune mechanism to provide essential protection for germ-cell genomes against the activity of mobile genetic elements<sup>1</sup>. piRNA populations comprise a molecular definition of transposons, which permits them to distinguish transposons from host genes and selectively silence them. piRNAs can be generated in two distinct ways, forming either primary or secondary piRNAs. Primary piRNAs come from discrete genomic loci, termed piRNA clusters, and seem to be derived from long, single-stranded precursors<sup>2</sup>. The biogenesis of primary piRNAs involves at least two nucleolytic steps. An unknown enzyme cleaves piRNA cluster transcripts to generate monophosphorylated piRNA 5' ends. piRNA 3' ends are probably formed by exonucleolytic trimming, after a piRNA precursor is loaded into its PIWI partner<sup>1,3</sup>. Secondary piRNAs arise during the adaptive 'ping-pong' cycle, with their 5' termini being formed by the activity of PIWIs themselves<sup>2,4</sup>. A number of proteins have been implicated genetically in primary piRNA biogenesis. One of these, *Drosophila melanogaster* Zucchini, is a member of the phospholipase-D family of phosphodiesterases, which includes both phospholipases and nucleases<sup>5–7</sup>. Here we produced a dimeric, soluble fragment of the mouse Zucchini homologue (mZuc; also known as PLD6) and show that it possesses single-strand-specific nuclease activity. A crystal structure of mZuc at 1.75 Å resolution indicates greater architectural similarity to phospholipase-D family nucleases than to phospholipases. Together, our data suggest that the Zucchini proteins act in primary piRNA biogenesis as nucleases, perhaps generating the 5' ends of primary piRNAs.

*zucchini* (*zuc*) was first noted as a gene essential for female fertility in *Drosophila*. Two independent alleles caused fully penetrant sterility and the production of eggs with dorsoventral patterning defects<sup>7</sup>. Subsequent studies have traced the effects of Zucchini on germ-cell development to its function in the piRNA pathway. Animals lacking Zucchini fail to silence transposons and show a general collapse of primary piRNA populations<sup>6,8,9</sup>. Mutant animals also accumulate transcripts from piRNA clusters, indicating a failure to process these precursors into small RNAs<sup>5</sup>. Thus, Zucchini has been strongly implicated as a factor promoting primary piRNA biogenesis.

Zucchini belongs to the phospholipase-D (PLD) family of phosphodiesterases, which share a common biochemical mechanism and a signature H(X)K(X4)D (HKD) motif within their active site (reviewed in ref. 10). Notably, one of the *zuc* alleles that emerged from the original forward genetic screen was a point mutation that changed the catalytic histidine to a tyrosine. This produced a phenocopy of the presumed null allele, including similar effects on piRNA populations, indicating that the catalytic activity of Zucchini was critical for piRNA production or stability<sup>5,6</sup>.

Biochemical and genetic studies of the mouse Zucchini homologue, mZuc, led to the conclusion that it acted as a phospholipase that affected mitochondrial fusion in a manner linked to its processing of

the mitochondrial lipid cardiolipin<sup>11–13</sup>. Thus, it was suggested that the impact of Zucchini on the piRNA pathway was indirect, through alterations in lipid levels or through changes in the structure of mitochondria. However, the proposed model of Zucchini activity required an enzyme that localized to the outer mitochondrial membrane and faced the cytoplasm to hydrolyse a lipid that is almost exclusively found on the inner mitochondrial membrane<sup>14</sup>. We therefore sought to discriminate between the two divergent hypotheses for Zucchini function in piRNA biogenesis; namely that it acts indirectly through its role as a phosphodiesterase, or that it acts directly as a nuclease.

To enable biochemical analysis of mZuc, we expressed an amino-terminally truncated form of the protein in Sf9 cells (Fig. 1a). This produced a soluble enzyme by removal of the transmembrane domain that normally anchors it to the mitochondrial outer membrane. One of the hallmarks of the PLD family is the presence of two HKD motifs that are brought together to create the catalytic centre<sup>10</sup>. This active site can arise from a single polypeptide that contains two copies of the motif, an arrangement typical of PLDs with phospholipid substrates. Alternatively, the catalytic centre can be assembled as an intermolecular dimer, a form most common with PLDs that act as nucleases<sup>10</sup>. mZuc has only one HKD motif, but the protein formed a stable, ~41 kDa dimer in Sf9 cells, as indicated by both gel-filtration chromatography and multi-angle light scattering (Supplementary Fig. 1). For comparison, we also produced a mutant version of the protein, which lacks an intact catalytic motif (H153N).

We used two assays to test whether recombinant mZuc could function as a phospholipase, liberating phosphatidic acid (PA) from cardiolipin as previously reported<sup>11</sup>. Liposomes containing commercial cardiolipin were incubated with recombinant proteins, and PA was measured by thin-layer chromatography (TLC). This did not reveal the production of measurable amounts of PA by mZuc, whereas a commercially available PLD from *Streptomyces chromofuscus* (scPLD) completely hydrolysed the substrate (Supplementary Fig. 2a). We also used a more sensitive assay based on mass spectrometry (MS). Selected reaction monitoring MS (SRM-MS) provides an extremely accurate and sensitive method for measuring reaction components. Using this approach, no substantial changes in cardiolipin or PA were observed when comparing buffer controls to either wild-type or catalytically inactive mZuc proteins (Fig. 1b and Supplementary Fig. 2b, c); whereas scPLD again completely hydrolysed the substrate. These results failed to support mZuc acting as a phospholipase to promote piRNA biogenesis, and prompted us to examine whether it has alternative activities.

PLD-family enzymes have been demonstrated to act as nucleases, cleaving double-stranded DNA (dsDNA) substrates<sup>15–17</sup>. For example, prototypic PLD nucleases Nuc and BfiI cleave dsDNA either non-specifically or at a defined recognition site<sup>10</sup>. We therefore incubated mZuc with a selection of end-labelled DNAs: single-stranded, double-stranded, or partially duplexed (Fig. 1c). The wild-type enzyme hydrolysed single-stranded DNA (ssDNA) or the single-stranded portions of partially duplexed substrates, but did not cleave dsDNA. The mutant

<sup>1</sup>W. M. Keck Structural Biology Laboratory, Cold Spring Harbor Laboratory, Cold Spring Harbor, New York 11724, USA. <sup>2</sup>Howard Hughes Medical Institute, Cold Spring Harbor Laboratory, Cold Spring Harbor, New York 11724, USA.

\*These authors contributed equally to this work.

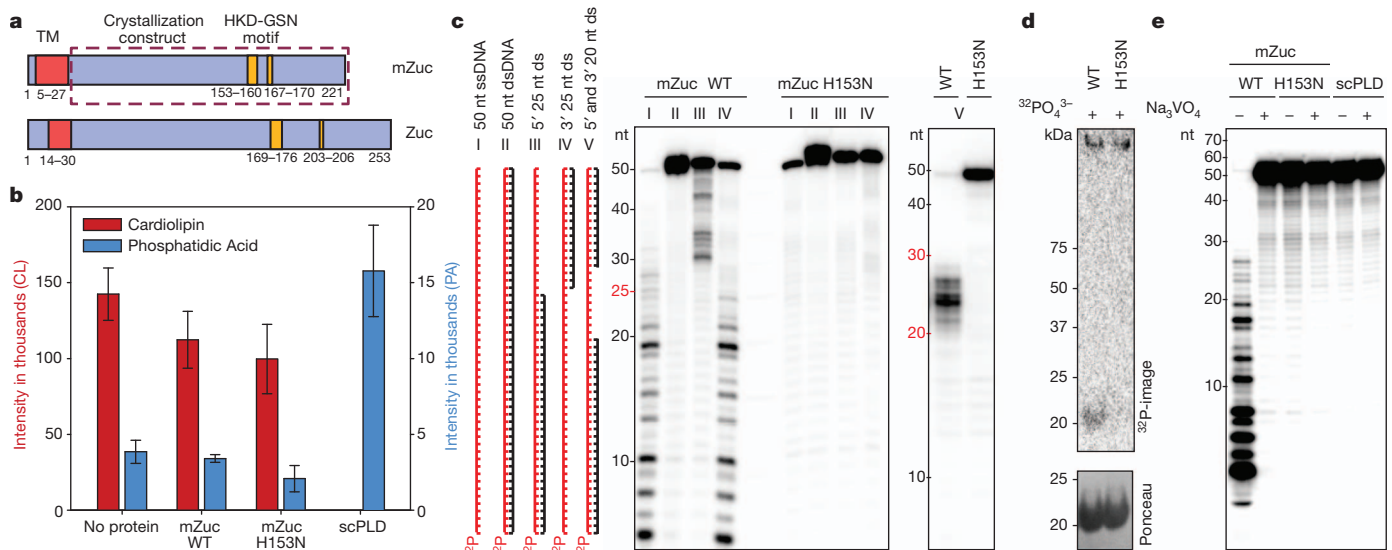


**Figure 1 | mZuc acts as a nuclease but not a phospholipase *in vitro*.** **a**, The domain architecture of mZuc and Zuc are similar, with an N-terminal transmembrane helix (TM, red) and a cytoplasmic domain, which contains the catalytic HKD motif (gold). The construct used for crystallization is indicated as a dashed box. Residue numbers delineating each domain are indicated below each schematic. **b**, Phosphodiesterase activity for mZuc, its catalytic mutant (H153N), and a known phospholipase (scPLD) were monitored by SRM-MS. Levels of the cardiolipin (CL) substrate and the expected PA product are shown for each reaction. Error bars indicate standard deviation ( $n = 3$ ). WT, wild type.

enzyme (H153N) was inactive against all substrates. As expected from studies of related PLD-family nucleases<sup>17</sup>, mZuc activity did not depend on the presence of divalent cations for substrate cleavage, but it could be stimulated by the presence of specific cations, particularly  $\text{Mn}^{2+}$ ,  $\text{Ca}^{2+}$  and  $\text{Zn}^{2+}$  (Supplementary Fig. 3a). The impact of  $\text{Zn}^{2+}$  may be explained by structural effects (see later), but as yet we do not understand how the other cations enhance activity.

The known catalytic mechanisms of PLD-family nucleases, including bacterial Nuc, suggest that cleavage proceeds via a two-step reaction scheme<sup>15</sup>. This includes the formation of a short-lived, covalent enzyme–substrate intermediate, joining a phosphate to the histidine in the HKD motif (Supplementary Fig. 4a). A similar mechanism for mZuc is supported by our ability to label the enzyme by incubation with  $^{32}\text{P}$ -labelled inorganic phosphate in a manner that depends on the presence of the HKD histidine (Fig. 1d). The specificity of this adduct was confirmed by performing a similar incubation of mZuc with  $\text{PO}_4^{3-}$  followed by denaturation, proteolysis and SRM-MS, which detected phosphorylation of a His-153-containing peptide. The fragmentation of this peptide was able to resolve further the location of the phosphorylation to residues 152–155 (Supplementary Fig. 4b). Our phosphate-labelling data combined with the proposed catalytic mechanism for PLD family nucleases suggested that mZuc might be inhibited by phosphate analogues. Indeed, sodium orthovanadate completely abolished the ability of mZuc to cleave ssDNA substrates (Fig. 1e).

If mZuc functions as a nuclease in the piRNA pathway, it would probably act on RNA substrates, and the biochemical mechanism used by PLD-family enzymes is consistent with their potentially cleaving either DNA or RNA. We therefore tested the ability of mZuc to cleave a variety of single-stranded or duplexed RNA substrates. mZuc cleaved only ssRNA, and this reaction was fully inhibited by orthovanadate (Fig. 2a). The mZuc mutant bearing an alteration in its catalytic site was inactive in these assays (Fig. 2b and Supplementary Fig. 3b). These data indicate that mZuc can function as a backbone-non-specific, single-strand-specific nuclease, cleaving either RNA or DNA substrates. The binding affinity of mZuc for ssDNA or ssRNA substrates was nearly

identical, measured at roughly 50 nM in each case (Supplementary Fig. 5). *In vivo*, the physiologically relevant targets of mZuc are probably determined by its subcellular localization and perhaps involve the help of additional proteins, which would focus its activity towards certain substrates.

HKD-family nucleases are predicted to leave 5' phosphate and 3' hydroxyl termini. These termini also correspond to the end polarities

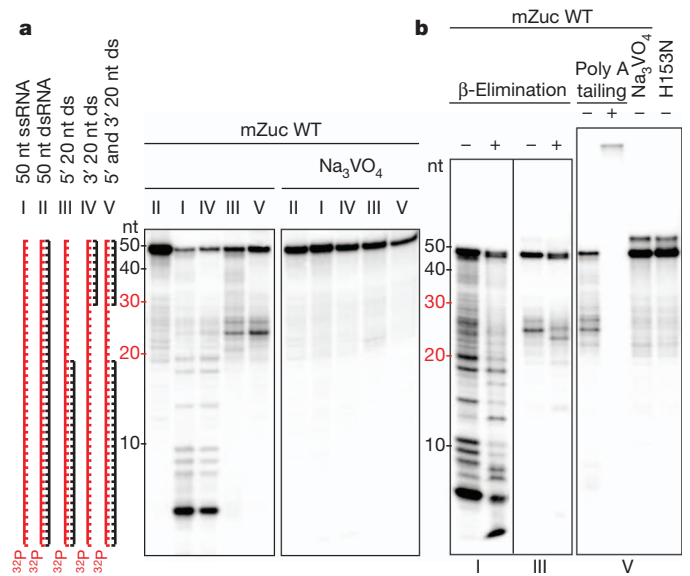


**Figure 2 | mZuc acts as a single-strand-specific endoribonuclease *in vitro*.** **a**, mZuc was incubated with single-stranded, double-stranded, and partially dsRNA substrates in the absence and presence of  $\text{Na}_3\text{VO}_4$ , as indicated. **b**, mZuc RNA cleavage products (from reactions shown in panel a, as indicated below) were tested for sensitivity to  $\beta$ -elimination and accessibility for polyadenylation.



that would be expected of a nuclease that participated in the processing of primary piRNA transcripts. We tested whether the nucleolytic products of mZuc had such termini in several ways.  $\beta$ -Elimination shifted mZuc cleavage products by a single base, a reaction that is diagnostic of the presence of a 3'-OH terminus (Fig. 2b). We also confirmed the presence of a 3'-OH group by extending the cleavage products with poly A polymerase (Fig. 2b). DNA cleavage also produced 5' phosphate and 3' hydroxyl termini (Supplementary Fig. 3c).

To gain further insight into mZuc activity and substrate specificity, we determined its structure to 1.75 Å resolution. Like other members of the HKD family, the structure of mZuc consists of a conserved  $\beta$ -sheet core sandwiched between two  $\alpha$ -helical layers (Fig. 3a). As seen in the crystal structure of the bacterial family member, Nuc<sup>18</sup>, the monomers of the mZuc dimer are related by a crystallographic two-fold axis. The dimer interface is extensive, with a buried surface area of 2,600 Å<sup>2</sup>, as calculated by the Protein Interfaces, Surfaces and Assemblies (PISA) server<sup>19</sup>. The resulting arrangement of the active site residues and the distance between the catalytic histidines (His 153) is consistent among both monomeric and dimeric PLD structures, as evidenced by both the apo structure and the structure of the protein in complex with tungstate, a phosphate mimic that binds to the active site of the enzyme, as observed in Nuc<sup>18</sup> (Fig. 3b and Supplementary Fig. 6).

Although mZuc is clearly an HKD-family enzyme, a number of features unique to this structure support its biological activity as a nuclease and, more specifically, a single-stranded RNase. First, and most strikingly, a long, ordered loop is inserted between  $\beta$ 1 and  $\alpha$ 2 (residues Pro 44–Ser 75). This loop extends away from the active site and contains three cysteines (Cys 49, Cys 66 and Cys 68) as well as a histidine (His 72) that form an unexpected CCCH 'zinc wing' (Fig. 3c and Supplementary Fig. 7). Although zinc finger motifs are widely used for nucleic-acid binding, this particular instance escaped bioinformatic detection due to the atypical primary sequence of the CCCH (CX<sub>16</sub>CPCX<sub>3</sub>H as opposed to the canonical CX<sub>6-14</sub>CX<sub>4-5</sub>CX<sub>3</sub>H; see ref. 20). Interestingly, the CCCH class of zinc fingers, in particular, has been implicated in the binding of ssRNA molecules such as messenger

RNA<sup>21–23</sup> and viral RNAs<sup>24</sup>, in accord with ssRNA being the likely *in vivo* substrate for mZuc.

PLD-family members that are responsible for lipid metabolism typically have their active site in a structural 'pocket'. In contrast, we observed that those with nucleic acid substrates typically provide a larger substrate-binding 'groove' (Fig. 4 and Supplementary Fig. 8). In the mZuc structure, the active site is flanked by a positively charged groove that extends to the zinc wings (Fig. 4a and Supplementary Fig. 9), probably serving as a nucleic-acid-binding interface. When compared to the structure of Nuc, a PLD nuclease that acts on dsDNA (Fig. 4b), the width of the groove in mZuc is considerably narrower, consistent with the biochemically observed single-strand specificity of the enzyme.

We constructed a hypothetical model to examine the potential interaction between the proposed substrate-binding groove of mZuc and a ssRNA. This was subjected to energy minimization using the Groningen Machine for Chemical Simulations (GROMACS)<sup>25</sup>. The resulting model (Fig. 4a and Supplementary Fig. 10) illustrates the shape and charge complementarity that a single-stranded nucleic acid substrate provides, including appropriate placement of the scissile phosphate in the active site. The surface complementarity is particularly notable; however, based on the projections of the bases away from the core of the protein, it seems unlikely that mZuc would show a strong sequence bias for binding or cleavage.

Our results indicate that Zucchini functions as a nuclease to promote primary piRNA biogenesis. Given the results of biochemical analyses performed in silkworm extracts, it is highly probable that the mature 3' ends of piRNAs are formed by exonucleolytic trimming of precursor piRNAs that are already loaded into PIWI proteins<sup>3</sup>. This leaves open the possibility that Zucchini could generate the 5' ends of primary piRNAs. mZuc does produce products with the correct phosphate polarity. Yet, primary piRNAs show an overwhelming bias for a terminal U residue<sup>2,26,27</sup>, which does not seem to be a preference of mZuc, based either upon biochemical or structural studies. Therefore, if Zucchini does generate piRNA 5' ends, the prevalence of their characteristic

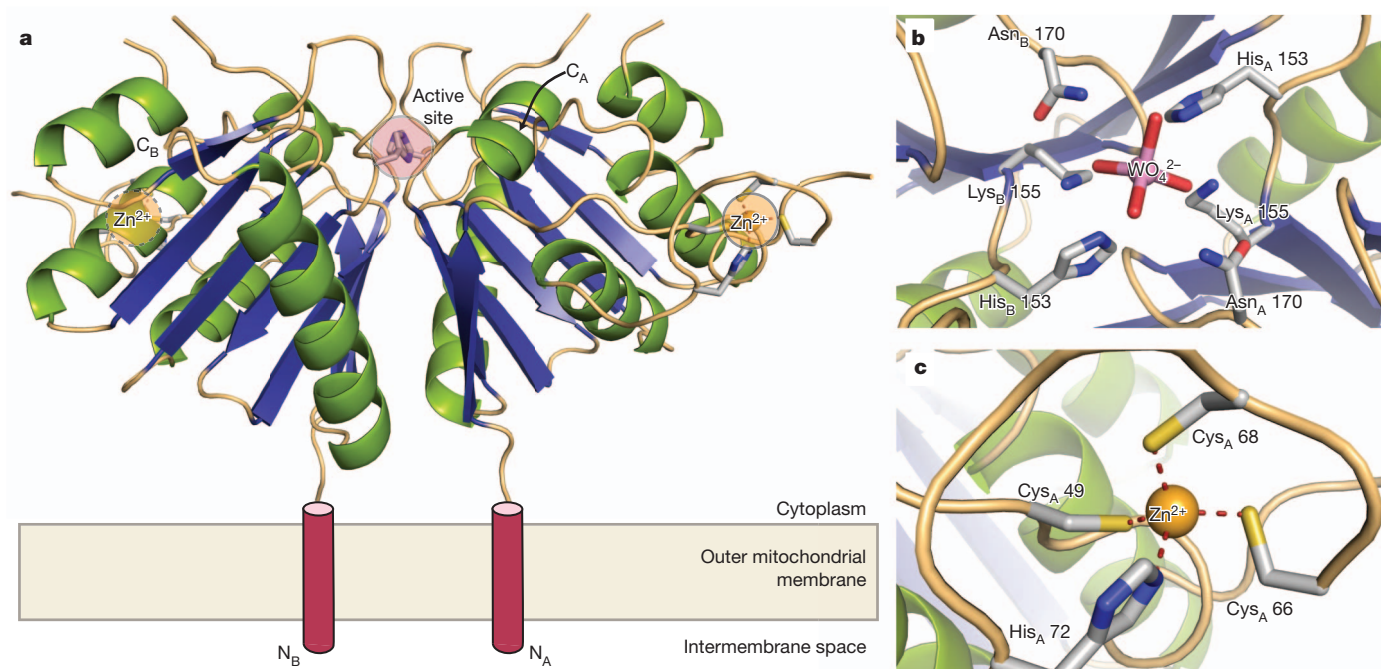


**Figure 3 | Crystal structure of mZuc.** **a**, The overall structure of the mZuc dimer is shown as a ribbon diagram. Helices are in green, strands in blue, and loops in beige. Each monomer binds one Zn<sup>2+</sup> (yellow) in an extended zinc wing. The active site histidine residues (His 153) are highlighted in red. The

N- and C-termini for each protomer are indicated. **b**, A close-up of the zinc wing consisting of residues Cys 49, Cys 66, Cys 68 and His 72 is shown. **c**, A detailed view of mZuc co-crystallized with tungstate bound in the active site is presented.

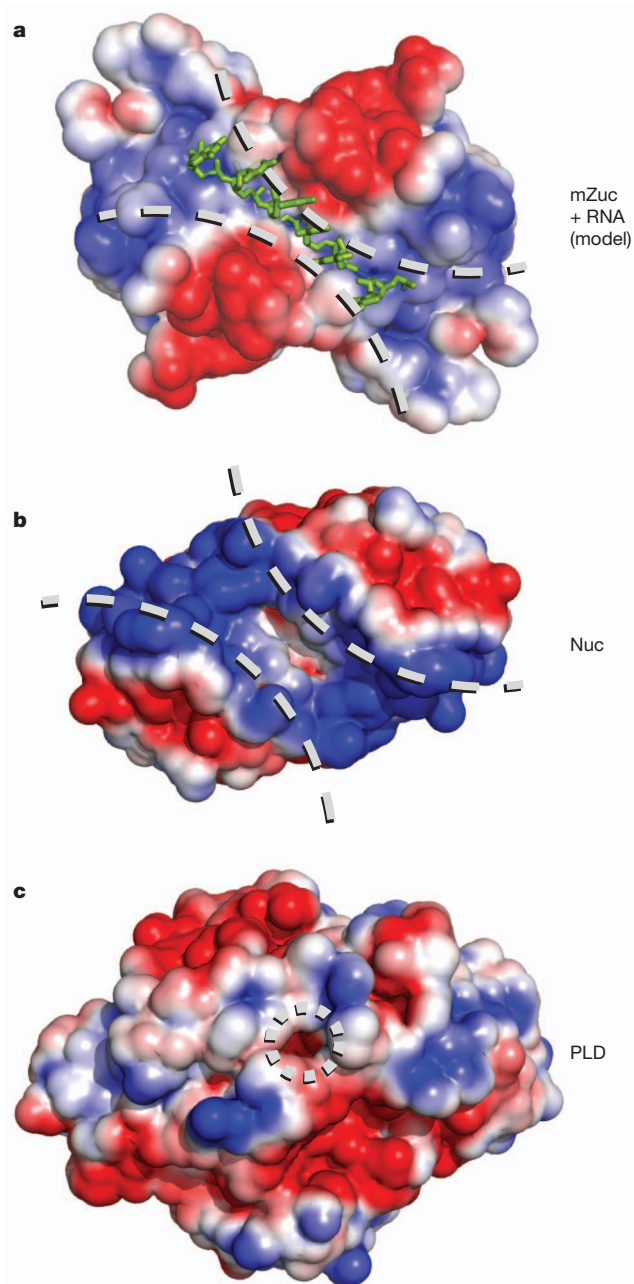


**Figure 4 | Electrostatic surfaces of PLD-family proteins indicate distinct binding surfaces for specific substrates.** **a**, The electrostatic surface for mZuc shows a long, narrow, positively charged groove laying across the zinc wings and active site. A short RNA molecule was manually built into the structure of mZuc, then subjected to energy minimization using GROMACS<sup>25</sup>. The minimized model shows the phosphates of the RNA backbone positioned in the most positively charged areas of the groove with the bases extending away from the dimer core. **b**, In Nuc (PDB accession 1BYR<sup>18</sup>), which acts on dsDNA, the equivalent groove is considerably wider. **c**, A bona fide phospholipase, PLD (PDB accession 2ZE9), uses the same active site architecture in a notably different structural context. PLD has a small pocket for binding phospholipids, rather than an elongated groove. Each surface depicts the solvent-accessible surface contoured at  $\pm 2 \text{ k}_B T e^{-1}$  using the Adaptive Poisson–Boltzmann Solver (ABPS)<sup>30</sup>.

terminal residue must result either from an unknown co-factor or from the selectivity of a 5'-end-binding pocket within PIWI-family proteins. The latter is a reasonable possibility as there is ample biochemical and structural support within the Argonaute sub-family for strong binding preferences for 5'-terminal nucleotides<sup>28,29</sup>. We must also consider the possibility that Zucchini proteins could contribute

an additional, as yet unanticipated activity, perhaps generating intermediate 3' ends of precursor piRNAs that are further resected by trimming to form mature termini. Attributing a definitive role to Zucchini will rest on further studies, perhaps ultimately requiring a full biochemical reconstitution of primary piRNA biogenesis to finally resolve its function.

In addition to their implications for piRNA production, our studies also highlight some general features of the phosphodiesterases, which use HKD motifs as their active sites. A comparison of the available structures of the PLD/nuclease family proteins indicates that these enzymes define their substrate specificity by their binding properties. Whereas phospholipases within this family seem to harbour pocket-like substrate-binding structures, nucleases show extended binding grooves for nucleic acid chains. These structural motifs are nearly diagnostic of the substrate specificity of these proteins. That said, solely on the basis of our biochemical assays and existing literature<sup>11–13</sup> we cannot exclude that mZuc can act in some circumstances as a phospholipase. We can simply argue that its structural features are more consistent with its action as a nuclease. The fact that enzymes in this family can be divided into classes based on their structural and biochemical features may also suggest that the PLD nomenclature for some of these enzymes, particularly for mZuc and Nuc, has become misleading and deserves reconsideration.

## METHODS SUMMARY

**Cloning, expression and purification of recombinant mZuc.** A complementary DNA coding for *Mus musculus* Zucchini (residues 31–221; mZuc) fused to a carboxy-terminal, thrombin-protease-cleavable Strep tag was cloned into the vector pFL for expression in Sf9 cells. The recombinant protein was affinity purified using StrepTactin resin followed by tag cleavage and Superdex75 gel filtration in 0.1 M MES, pH 6.5, 150 mM NaCl, 1 mM dithiothreitol (DTT).

**Protein characterization.** Protein was judged to be >99% pure by SDS-PAGE. The oligomeric state and mass of the protein were measured by multi-angle light scattering and liquid chromatography electrospray ionization-mass spectrometry (LC ESI-MS), respectively.

**Nuclease activity assay.** Recombinant proteins and 5'-<sup>32</sup>P-labelled nucleotide substrates were incubated at 37 °C in 50 mM MES, pH 6.5, 75 mM NaCl, 2 mM CaCl<sub>2</sub>, 1 mM DTT for DNase activity; 5 mM MES, pH 6.5, 7.5 mM NaCl, 2 mM CaCl<sub>2</sub>, 1 mM DTT for RNase activity. After proteinase K treatment, nucleic acids were extracted using phenol/chloroform and analysed by urea-PAGE.

**Lipase activity assay.** Liposomes were prepared using standard methods, then mixed with recombinant protein at 37 °C for 2 h. Lipids were then extracted and analysed by TLC and SRM-MS.

**Crystallization and structure solution.** Crystals of mZuc were grown by hanging-drop vapour diffusion at 4 °C. Immediately before crystallization, the protein was mixed with chymotrypsin (1:100 m/m ratio). Protein solution at 3 mg ml<sup>-1</sup> was mixed with reservoir solution (50 mM Bis-Tris, pH 6.5, 18% PEG-3350 and 2% tascimate, pH 6.0). Crystals were cryoprotected in reservoir solution with 20% ethylene glycol. Diffraction data were collected at the National Synchrotron Light Source. The structure was solved by molecular replacement using Nuc<sup>18</sup> as a search model.

**RNA modelling.** RNA modelling was performed manually, then subjected to energy minimization using GROMACS<sup>25</sup>.

**Full Methods** and any associated references are available in the online version of the paper.

Received 7 June; accepted 10 August 2012.

Published online 14 October 2012.

1. Senti, K. A. & Brennecke, J. The piRNA pathway: a fly's perspective on the guardian of the genome. *Trends Genet.* **26**, 499–509 (2010).
2. Brennecke, J. *et al.* Discrete small RNA-generating loci as master regulators of transposon activity in *Drosophila*. *Cell* **128**, 1089–1103 (2007).
3. Kawaoka, S., Izumi, N., Katsuma, S. & Tomari, Y. 3' end formation of PIWI-interacting RNAs *in vitro*. *Mol. Cell* **43**, 1015–1022 (2011).
4. Gunawardane, L. S. *et al.* A slicer-mediated mechanism for repeat-associated siRNA 5' end formation in *Drosophila*. *Science* **315**, 1587–1590 (2007).
5. Haase, A. D. *et al.* Probing the initiation and effector phases of the somatic piRNA pathway in *Drosophila*. *Genes Dev.* **24**, 2499–2504 (2010).
6. Pane, A., Wehr, K. & Schupbach, T. *zucchini* and *squash* encode two putative nucleases required for rasiRNA production in the *Drosophila* germline. *Dev. Cell* **12**, 851–862 (2007).

7. Schupbach, T. & Wieschaus, E. Female sterile mutations on the second chromosome of *Drosophila melanogaster*. II. Mutations blocking oogenesis or altering egg morphology. *Genetics* **129**, 1119–1136 (1991).
8. Malone, C. D. *et al.* Specialized piRNA pathways act in germline and somatic tissues of the *Drosophila* ovary. *Cell* **137**, 522–535 (2009).
9. Olivieri, D., Sykora, M. M., Sachidanandam, R., Mechtler, K. & Brennecke, J. An *in vivo* RNAi assay identifies major genetic and cellular requirements for primary piRNA biogenesis in *Drosophila*. *EMBO J.* **29**, 3301–3317 (2010).
10. Selvy, P. E., Lavieri, R. R., Lindsley, C. W. & Brown, H. A. Phospholipase D: enzymology, functionality, and chemical modulation. *Chem. Rev.* **111**, 6064–6119 (2011).
11. Choi, S. Y. *et al.* A common lipid links Mfn-mediated mitochondrial fusion and SNARE-regulated exocytosis. *Nature Cell Biol.* **8**, 1255–1262 (2006).
12. Huang, H. *et al.* piRNA-associated germline nuage formation and spermatogenesis require MitoPLD profusogenic mitochondrial-surface lipid signaling. *Dev. Cell* **20**, 376–387 (2011).
13. Watanabe, T. *et al.* MITOPLD is a mitochondrial protein essential for nuage formation and piRNA biogenesis in the mouse germline. *Dev. Cell* **20**, 364–375 (2011).
14. Gonzalez, F. & Gottlieb, E. Cardiolipin: setting the beat of apoptosis. *Apoptosis* **12**, 877–885 (2007).
15. Gottlin, E. B., Rudolph, A. E., Zhao, Y., Matthews, H. R. & Dixon, J. E. Catalytic mechanism of the phospholipase D superfamily proceeds via a covalent phosphohistidine intermediate. *Proc. Natl Acad. Sci. USA* **95**, 9202–9207 (1998).
16. Lackey, D., Walker, G. C., Keng, T. & Linn, S. Characterization of an endonuclease associated with the drug resistance plasmid pKM101. *J. Bacteriol.* **131**, 583–588 (1977).
17. Pohlman, R. F., Liu, F., Wang, L., More, M. I. & Winans, S. C. Genetic and biochemical analysis of an endonuclease encoded by the IncN plasmid pKM101. *Nucleic Acids Res.* **21**, 4867–4872 (1993).
18. Stuckey, J. A. & Dixon, J. E. Crystal structure of a phospholipase D family member. *Nature Struct. Biol.* **6**, 278–284 (1999).
19. Krissinel, E. & Henrick, K. Inference of macromolecular assemblies from crystalline state. *J. Mol. Biol.* **372**, 774–797 (2007).
20. Berg, J. M. & Shi, Y. The galvanization of biology: a growing appreciation for the roles of zinc. *Science* **271**, 1081–1085 (1996).
21. Lai, W. S., Carballo, E., Thorn, J. M., Kennington, E. A. & Blackshear, P. J. Interactions of CCCH zinc finger proteins with mRNA. Binding of tristetraprolin-related zinc finger proteins to Au-rich elements and destabilization of mRNA. *J. Biol. Chem.* **275**, 17827–17837 (2000).
22. Kelly, S. M. *et al.* Recognition of polyadenosine RNA by zinc finger proteins. *Proc. Natl Acad. Sci. USA* **104**, 12306–12311 (2007).
23. Hurt, J. A. *et al.* A conserved CCCH-type zinc finger protein regulates mRNA nuclear adenylation and export. *J. Cell Biol.* **185**, 265–277 (2009).
24. Gao, G., Guo, X. & Goff, S. P. Inhibition of retroviral RNA production by ZAP, a CCCH-type zinc finger protein. *Science* **297**, 1703–1706 (2002).
25. Van Der Spoel, D. *et al.* GROMACS: fast, flexible, and free. *J. Comput. Chem.* **26**, 1701–1718 (2005).
26. Aravin, A. *et al.* A novel class of small RNAs bind to MILI protein in mouse testes. *Nature* **442**, 203–207 (2006).
27. Girard, A., Sachidanandam, R., Hannon, G. J. & Carmell, M. A. A germline-specific class of small RNAs binds mammalian Piwi proteins. *Nature* **442**, 199–202 (2006).
28. Frank, F., Sonenberg, N. & Nagar, B. Structural basis for 5'-nucleotide base-specific recognition of guide RNA by human AGO2. *Nature* **465**, 818–822 (2010).
29. Mi, S. *et al.* Sorting of small RNAs into *Arabidopsis* argonaute complexes is directed by the 5' terminal nucleotide. *Cell* **133**, 116–127 (2008).
30. Esnouf, R. M. Further additions to MolScript version 1.4, including reading and contouring of electron-density maps. *Acta Crystallogr. D* **55**, 938–940 (1999).

**Supplementary Information** is available in the online version of the paper.

**Acknowledgements** We thank W. Filipowicz, R. MacDonald and members of the G.J.H. and L.J. laboratories for discussions; G. Bencze, K. Rivera and D. Pappin of the Cold Spring Harbor Laboratory proteomics facility, which is funded in part by an National Cancer Institute Cancer Center Support Grant (CA045508), for support with mass spectrometry; and H. Robinson for help at the National Synchrotron Light Source, which is supported by the Department of Energy, Office of Basic Energy Sciences. J.J.I. was supported by the Harvey L. Karp award and by a Ruth L. Kirschstein National Research Service Awards National Institutes of Health (NIH) fellowship F32GM97888. This work was supported by NIH grant R01GM062534. G.J.H. and L.J. are Howard Hughes Medical Institute Investigators.

**Author Contributions** L.J., G.J.H., A.D.H. and J.J.I. planned studies and wrote the paper. A.D.H. and J.J.I. performed the experiments, and S.R.K. analysed datasets.

**Author Information** Coordinates were deposited in the Protein Data Bank under accession codes 4GGJ (native) and 4GGK (tungstate derivative). Reprints and permissions information is available at [www.nature.com/reprints](http://www.nature.com/reprints). The authors declare no competing financial interests. Readers are welcome to comment on the online version of the paper. Correspondence and requests for materials should be addressed to G.J.H. ([hannon@cshl.edu](mailto:hannon@cshl.edu)) or L.J. ([leemor@cshl.edu](mailto:leemor@cshl.edu)).



## METHODS

**Cloning, expression and purification of mZuc fragments.** To screen for biochemically well-behaved targets, a panel of mZuc constructs was generated from *M. musculus* complementary DNA by sequence- and ligation-independent cloning (SLIC) cloning. These constructs presented various N- or C-terminal tags for enhanced expression and purification using either *Escherichia coli* or baculoviral-induced insect cell culture systems. The sequence of each construct was verified by the Cold Spring Harbour Laboratory DNA Sequencing Facility.

The data presented here resulted from a 30-residue N-terminal deletion of mZuc to create a protein that spans residues 31–221 fused to a thrombin-cleavable Strep-tag at the C terminus (mZucΔ30–ThStrep<sub>2</sub>). This construct was cloned into the vector pFL for expression in Sf9 cells using the baculovirus expression system<sup>31</sup>. After expression, cells were harvested by centrifugation at 1,000g, resuspended in lysis buffer (0.1 M MES, pH 6.5, 0.15 M NaCl, 1 mM dithiothreitol (DTT)) (~20 ml per litre culture), and lysed by sonication. The cell lysate was then clarified by ultracentrifugation at 125,000g for 1 h and the supernatant was applied to a Strep-Tactin (IBA) column equilibrated with lysis buffer. The bound mZucΔ30–ThStrep<sub>2</sub> was subsequently washed with lysis buffer, further washed with lysis buffer containing 2 mM ATP, and finally eluted in lysis buffer containing 5 mM D-dethiobiotin. To remove the C-terminal affinity purification tag, 15 units of thrombin protease were added per mg of purified protein and incubated overnight at 4 °C. The cleaved mZucΔ30 (referred to as mZuc) was then further purified by gel filtration using a Superdex75 column equilibrated with lysis buffer. Once purified, the protein was concentrated to 5–10 mg ml<sup>-1</sup> and stored at 4 °C for short periods or in 50% (v/v) glycerol at -20 °C for extended periods. Typical yields were 1–2 mg of purified protein (>98% purity as assessed by SDS-PAGE) per litre culture. Active site mutants were constructed using SLIC cloning methods. Purification of mutant proteins was identical to that for the wild type.

For SRM-MS experiments, mZucΔ30–ThStrep<sub>2</sub> and mZucΔ30–ThHis<sub>6</sub> H153N were co-expressed in Sf9 cells. The resulting heterodimer population (WT/H153N) was isolated by Strep-Tactin purification followed by a second round of affinity purification with Ni-NTA resin. The purified protein was immediately concentrated and desalted into 20 mM MES, pH 6.5, 0.15 M NaH<sub>2</sub>PO<sub>4</sub>, 1 mM DTT for subsequent SRM-MS processing.

**Multi-angle light scattering.** Multi-angle light scattering (MALS) was used to determine the oligomeric state of the purified proteins. Roughly 1 mg of purified protein (at 2 mg ml<sup>-1</sup>) was taken for in-line gel filtration on a Superdex75 column followed by light scattering analysis. MALS was measured with a Wyatt Dawn Heleos-II and processed using the included software (ASTRA Version 5.3.4). Bovine serum albumin (BSA) was used as a control to ensure proper calibration.

**Intact mass measurements from MS.** Each purified protein was diluted in water to 1 μM and applied to a Zorbax 300SB-C8 enrichment chip at 600 nl min<sup>-1</sup>. In total, ~20 pmol of material was injected. A mobile phase gradient from 0.1% formic acid and 3% acetonitrile in water to 0.1% formic acid and 90% acetonitrile was used to chromatograph each sample, which was then taken for in-line electrospray ionization mass spectrometry. Mass spectra were obtained on an Agilent 6520 Accurate-Mass Quadrupole time-of-flight mass spectrometer with an accelerating voltage of 1,850 V. Deconvolution was performed with the included software, Agilent MassHunter Qualitative Analysis Version B.04.00. Masses of all proteins were within 1.0 Da of those predicted.

**Liposome preparation.** To assess the phospholipase activity of the mZuc, cardiolipin-containing liposomes were prepared. Defined liposomes (phosphatidylcholine:phosphatidylethanolamine:phosphatidylserine:cardiolipin (PC:PE:PS:CL) at 2.2:1:1) or extract-based liposomes (made with bovine heart lipid extract supplemented with CL) were made using standard methods. Briefly, lipids (Avanti Polar Lipids) in chloroform were mixed and then dried using a stream of nitrogen followed by vacuum evaporation. Lipid films were then resuspended in 10 mM HEPES, pH 7.4, 0.1 M NaCl such that the final concentration of total lipids was 1 mg ml<sup>-1</sup>. The resuspended lipids were vortexed vigorously and sonicated using a bath sonicator for ~15 min, until the suspension clarified. Absorbance measurements of the pre- and post-sonication liposomes were used to estimate the effective diameters<sup>32</sup> of the resulting small unilamellar vesicles (SUVs) at less than 200 nm. Lipids and liposomes were stored under nitrogen at -20 °C and 4 °C, respectively, to limit oxidation when not in use.

**Cardiolipase activity assay using TLC.** Cardiolipin cleavage assays were performed in a similar manner to those previously reported<sup>11</sup>. For each reaction, 20 μl of liposome solution (20 μg of total lipids) were mixed with 5 μg purified protein in a reaction buffer of either 50 mM MES, pH 6.5, 75 mM NaCl, 1 mM DTT (nuclease buffer conditions) or 50 mM HEPES, pH 7.4, 80 mM KCl, 3 mM MgCl<sub>2</sub>, 2 mM CaCl<sub>2</sub>, 1 mM DTT (previously reported lipase conditions<sup>11</sup>). Commercially available PLD from *S. chromofuscus* (MP Biomedicals) was used as a positive control. Each 200 μl reaction was incubated at 37 °C for 2 h, then quenched by the addition of 750 μl of methanol:chloroform (2:1).

Lipids were extracted by sequentially adding 250 μl chloroform and 250 μl 0.5 M NaCl in 0.1 M HCl (in water) with vigorous vortexing after each addition. The lower (organic) phase was removed, dried by vacuum evaporation, and resuspended in a small volume of methanol:chloroform for TLC analysis.

Each of the extracts was spotted onto 2.5 × 7.5 cm, glass-backed silica 60 F<sub>254</sub> TLC plates (EMD). The extracts were chromatographed using a running solvent of chloroform:methanol:water:ammonium hydroxide (120:75:6:2), stained using permanganate (0.75% KMnO<sub>4</sub>, 5% KH<sub>2</sub>PO<sub>4</sub>, 0.06% NaOH), and developed by heating. Extract components appeared as yellow spots on a magenta background. Lipid identification was based on standards run in parallel.

**Cardiolipase activity assay using SRM-MS.** To confirm the findings of the TLC-based phospholipase activity assay and to obtain higher sensitivity for detecting the presumed phosphatidic acid product, an SRM-MS assay was used. After performing the lipase reaction described above, 5 μl of each (non-extracted) defined liposome lipase reaction were infused into a Thermo Scientific Triple-Stage Quadrupole (TSQ) Vantage mass spectrometer. Mass-to-charge ratio (*m/z*) peaks corresponding to cardiolipin ((18:2)<sub>4</sub> species with a +1 charge state at 1448 Da; (18:2)<sub>4</sub> species with a +2 charge state at 723 Da) and phosphatidic acid ((18:2)<sub>2</sub> species with +1 charge state at 695 Da) were monitored. Injections were performed in triplicate.

**Nuclease activity assays.** DNA and RNA oligonucleotides were ordered from Integrated DNA Technologies (IDT) or Dharmacon. TGGCACTGTACCTCA TCGACATTGAGAAGTGGCTCTCTGACTGGCGAATA (50 nucleotides DNA), TATTCGCCAGTCAGAGGCCACTTCTCAATGTTCGATGAGGTACAGTGC CA (50 nucleotides DNA), TATTCGCCAGTCAGAGAGCCACTTC (25 nucleotides DNA), TCAATGTTCGATGAGGTACAGTGCCA (25 nucleotides DNA), TATTCGCCAGTCAGAGAGCC (20 nucleotides DNA), GTCGATGAGGTAC AGTGCCA (20 nucleotides DNA), UGGCACUGUACCUCACUGACA AUU GAGAAGUGGUCUCUGACUGGCGAAUA (50 nucleotides RNA), UAUU GCCAGUCAGAGAGCCACUUCUCAUUGUCGAUGAGGUACAGUGCCA (50 nucleotides RNA), UAUUCGCCAGUCAGAGAGCC (20 nucleotides RNA), GUCGAUGAGGUACAGUGCCA (20 nucleotides RNA), UGGCACUGUAC CUCACUGAC (20 nucleotides RNA), GGCUCUCUGACUGGCGAAUA (20 nucleotides RNA).

Oligonucleotides were 5' labelled with <sup>32</sup>P γ-ATP (PerkinElmer) or ATP (Sigma-Aldrich) using T4 polynucleotide kinase (NEB) according to the manufacturer's instructions. Free ATP was removed and the buffer was exchanged using illustra MicroSpin G-25 Columns (GE Healthcare). Double-stranded substrates were annealed by mixing equimolar amounts of the complementary strands in water, denaturing at 95 °C for 1 min, then cooling slowly from 65 °C to 25 °C in the presence of 30 mM NaCl, 10 mM MES, pH 6.5.

For enzymatic assays, mZuc was stored in 50% (v/v) glycerol at -20 °C. scPLD (EMD) was freshly prepared from the lyophilized stock according to the manufacturer's protocol. To assess nuclease activity, substrates were incubated with recombinant protein in 50 mM MES, pH 6.5, 75 mM NaCl, 2 mM CaCl<sub>2</sub>, 1 mM DTT for DNase activity, or 5 mM MES, pH 6.5, 7.5 mM NaCl, 2 mM CaCl<sub>2</sub>, 1 mM DTT for RNase activity at 37 °C for 3 h (Fig. 1c and Supplementary Fig. 3c) or 6 h (Figs 1e, 2 and Supplementary Fig. 2b). DNA and RNA substrates were used at a final concentration of 5 μM (Fig. 1 and Supplementary Fig. 3), or 50 nM (Fig. 2). Recombinant mZuc dimer was used at a final concentration of 5 μM (Fig. 1) or 50 μM (Fig. 2 and Supplementary Fig. 2b). When RNA was used as a substrate, RNasin Plus RNase Inhibitor (Promega) was added. Protein was removed from the cleavage reactions by proteinase K treatment (Roche) at a final concentration of 2 mg ml<sup>-1</sup> (in 50 mM Tris-HCl, pH 7.5, 75 mM NaCl, 6 mM EDTA, 1% (w/v) SDS) at 50 °C for 30 min. Nucleic acids were extracted using phenol:chloroform (Ambion), precipitated with sodium acetate/ethanol and separated by 15% urea-PAGE. Low molecular weight marker 10–100 nucleotides (Affimetrix) was labelled with <sup>32</sup>P γ-ATP and used as a size ladder. Visualization was accomplished using a Storm PhosphorImager.

To assess the chemical properties of mZuc cleavage products, nucleic acids were recovered from the cleavage reactions using proteinase K and phenol:chloroform extraction followed by an additional chloroform extraction and sodium acetate/ethanol precipitation. For DNA products, terminal deoxynucleotidyl transferase (TdT) (NEB) was incubated with the extracted oligonucleotides in the presence of ddATP or dATP according to the manufacturer's protocol. For RNA products, β-elimination was performed as previously described<sup>33</sup>. Poly-A tailing was performed using Poly(A) tailing kit (Ambion) at 37 °C for 15 min.

**Detection of the phosphohistidine intermediate using <sup>32</sup>P-disodium phosphate.** mZuc wild-type and H135N (at a dimer concentration of 50 μM) were incubated with 0.4 mM <sup>32</sup>P-disodium phosphate (PerkinElmer) in 50 mM MES, pH 6.5, 75 mM NaCl, 1 mM DTT at 37 °C for 3 h. Proteins were separated by SDS-PAGE on a 10% NuPAGE gel (Invitrogen) and transferred to a nitrocellulose

membrane. Proteins bound to the membrane were visualized by Ponceau S staining (0.1% Ponceau S, 5% acetic acid), and  $^{32}\text{P}$  was detected by phosphorimaging. **Detection of the phosphohistidine intermediate using SRM-MS.** To confirm the findings of the  $^{32}\text{PO}_4^{3-}$  labelling assay and further resolve the phosphorylation site, SRM-MS was used. mZuc wild-type/H153N heterodimer was incubated in 50 mM MES, pH 6.5, 0.15 M  $\text{NaH}_2\text{PO}_4$ , 1 mM DTT for 1 h at 4 °C. The protein (20 µg) was then denatured and reduced by adding 0.1% Protease-Max surfactant (Promega) and 5 mM TCEP in 200 mM triethylammonium bicarbonate, pH 10, and incubated at 55 °C for 20 min. The sample was then treated with 5 mM methyl methanethiosulphonate and proteolysed with 2 µg Lys-C overnight at 37 °C. After digestion, 1 µg of the proteolytic fragments were applied to a home-packed C18 column. Peptides were chromatographed with a mobile phase gradient from 0.1% formic acid and 3% acetonitrile in water to 0.1% formic acid and 90% acetonitrile followed by in-line electrospray ionization mass spectrometry.

Mass spectra were collected on a Thermo Scientific TSQ Vantage mass spectrometer. In the first round of MS,  $m/z$  peaks corresponding to a Lys-C generated, His-153-containing peptide (AGIQVRHDDQLGYMHKK) were selected (+4 charge state masses of 522.0 Da and 502.0 Da for the phosphorylated and non-phosphorylated precursors, respectively). These precursors were then fragmented while monitoring for several y and b ion transitions.

**Fluorescence polarization.** The affinity of mZuc for ssDNA and ssRNA was assessed using fluorescence polarization. Fluorescein-labelled 20-oligonucleotide probes (5'-ACAGAGTGCCACTTCTCAAC-Fluorescein-3' DNA, Sigma; 5'-ACAGAGUGCCACUUCUCAAC-Fluorescein-3' RNA, Dharmacon) at 10 nM were mixed with mZuc at various concentrations in a binding buffer of 0.1 M MES, pH 6.5, 75 mM NaCl, 1 mM DTT and incubated at room temperature (27 °C) for 10 min. Fluorescence polarization was then measured at room temperature (27 °C) on a BioTek Synergy4 microplate reader using excitation and emission wavelengths of 485 and 528 nm, respectively. Readings were performed in duplicate.

**Crystallization.** Crystals of mZuc were grown by hanging-drop vapour diffusion on siliconized glass coverslips (Hampton Research). Immediately before crystallization, the purified protein was mixed in a 1:100 (m/m) ratio with chymotrypsin. Two microlitres of the protein solution at 3 mg ml<sup>-1</sup> were then mixed with an equal volume of reservoir solution containing 50 mM Bis-Tris, pH 6.5, 18% PEG-3350, and 2% tascimate, pH 6.0, and suspended over 0.5 ml of reservoir solution. Rectangular prismatic crystals (~150 µm × 50 µm × 50 µm) grew at 4 °C within 24 h. Crystals were harvested and frozen in liquid nitrogen after serial transfer to 50 mM Bis-Tris, pH 6.5, 18% PEG-3350, and 2% tascimate, pH 6.0, and 20% ethylene glycol in increasing steps of 5% ethylene glycol. Tungstate-derivatized crystals were obtained by co-crystallization with 10 mM  $\text{Na}_2\text{WO}_4$  added to the crystallization drop.

**Crystallographic data collection and structure determination.** Data were collected at 100 K using synchrotron radiation at the X29 beamline at the National Synchrotron Light Source at Brookhaven National Laboratory. Data were processed with XDS<sup>34</sup> and scaled with SCALA<sup>35</sup>. Additional processing was performed with programs from the CCP4 suite<sup>35</sup>.

The crystals belong to the space group  $P4_32_12$  with  $a = b = 38.7$  Å,  $c = 213.1$  Å,  $\alpha = \beta = \gamma = 90^\circ$  with one molecule per asymmetric unit and a solvent content of ~35%. The structure was solved by molecular replacement with the program Phaser<sup>36</sup> using the structure of Nuc, a bacterial PLD-family nuclease (PDB accession 1BYR) as a search model<sup>18</sup>. Automatic model building was performed using ARP/wARP<sup>37</sup>, which correctly built approximately 140 residues of the 158 in the final structure. Subsequent model building and inspection were carried out using the program Coot<sup>38</sup>. Model refinement was performed using REFMAC5<sup>39</sup>. TLS refinement was carried out using one TLS group. The final native model consists of residues 35–58, 66–126 and 130–209 in addition to one coordinated  $\text{Zn}^{2+}$  and 106 water molecules. The final models were validated by MolProbity<sup>40</sup>. All residues in

the final structures were in the allowed regions of the Ramachandran plot with 152/158 residues being in favoured regions. Data collection and refinement statistics are listed in Supplementary Table 1.

In addition to native crystals, tungstate-derivatized crystals were also produced. These diffracted to similar resolution and had nearly identical unit cell parameters. Initial processing was performed as described earlier. The native structure was used as an isomorphous replacement search model and then refined accordingly. To avoid over-fitting, refinement of the tungstate derivative used the same  $R_{\text{free}}$  set as the native. To confirm the identity of the  $\text{Zn}^{2+}$ , two data sets were collected from a single tungstate-derivatized crystal at  $\pm 100$  eV from the Zinc K edge. Anomalous maps for each data set confirmed the identity of the metal. The root mean squared deviation for all protein atoms in the native and tungstate derivative was 0.49 Å. Crystallographic statistics for the tungstate-derivatized crystals are also presented in Supplementary Table 1.

**Figures.** Figures of molecular models were generated using PyMOL<sup>41</sup>. Electrostatic surface calculations were performed with APBS<sup>30</sup> with a solvent ion concentration of 0.15 M using the PARSE force field. Superpositioning of structural homologues was performed by the DALI server<sup>42</sup>.

**RNA modelling and energy minimization.** The refined mZuc structure was used as a template for manual model building of a short ssRNA using Coot<sup>38</sup>. The initial ssRNA model placed the phosphate backbone along the observed positively charged active site groove (with the scissile phosphate positioned at the tungstate position in the derivative structure) while maintaining approximate two-fold symmetry of phosphates with respect to the homodimer (the RNA breaks the strict two-fold symmetry due to its polarity). Energy minimization was performed using GROMACS v.4.5.5<sup>25</sup> with the AMBER-99SB-ILDN force field<sup>43</sup> and particle-mesh Ewald (PME) long-range electrostatic modelling<sup>44</sup> with a conjugate gradient energy minimization algorithm, keeping the protein model (including  $\text{Zn}^{2+}$ ) fixed while allowing minimization of the RNA molecule and solvent model. A nearly indistinguishable model was also generated using the steepest descent algorithm.

- Bieniossek, C., Richmond, T. J. & Berger, I. MultiBac: multigene baculovirus-based eukaryotic protein complex production. *Curr. Protoc. Protein Sci.* Chapter 5, Unit 5.20 (2008).
- Pozharski, E. V., McWilliams, L. & MacDonald, R. C. Relationship between turbidity of lipid vesicle suspensions and particle size. *Anal. Biochem.* **291**, 158–162 (2001).
- Vagin, V. V. *et al.* A distinct small RNA pathway silences selfish genetic elements in the germline. *Science* **313**, 320–324 (2006).
- Kabsch, W. Automatic processing of rotation diffraction data from crystals of initially unknown symmetry and cell constants. *J. Appl. Crystallogr.* **26**, 795–800 (1993).
- Collaborative Computation Project, Number 4. The CCP4 suite: programs for protein crystallography. *Acta Crystallogr. D* **50**, 760–763 (1994).
- McCoy, A. J. *et al.* Phaser crystallographic software. *J. Appl. Crystallogr.* **40**, 658–674 (2007).
- Perrakis, A., Harkiolaki, M., Wilson, K. S. & Lamzin, V. S. ARP/wARP and molecular replacement. *Acta Crystallogr. D* **57**, 1445–1450 (2001).
- Emsley, P. & Cowtan, K. Coot: model-building tools for molecular graphics. *Acta Crystallogr. D* **60**, 2126–2132 (2004).
- Murshudov, G. N., Vagin, A. A. & Dodson, E. J. Refinement of macromolecular structures by the maximum-likelihood method. *Acta Crystallogr. D* **53**, 240–255 (1997).
- Chen, V. B. *et al.* MolProbity: all-atom structure validation for macromolecular crystallography. *Acta Crystallogr. D* **66**, 12–21 (2010).
- DeLano, W. L. The PyMOL Molecular Graphics System. (Schrödinger, LLC, 2002).
- Holm, L. & Rosenstrom, P. Dali server: conservation mapping in 3D. *Nucleic Acids Res.* **38**, W545–W549 (2010).
- Lindorff-Larsen, K. *et al.* Improved side-chain torsion potentials for the Amber ff99SB protein force field. *Proteins* **78**, 1950–1958 (2010).
- Essmann, U. *et al.* A smooth particle mesh Ewald method. *J. Chem. Phys.* **103**, 8577–8593 (1995).

# Structure and function of Zucchini endoribonuclease in piRNA biogenesis

Hiroshi Nishimasu<sup>1\*</sup>, Hirotsugu Ishizu<sup>1,2\*</sup>, Kuniaki Saito<sup>2</sup>, Satoshi Fukuhara<sup>1</sup>, Mihar K. Kamatani<sup>2</sup>, Luc Bonnefond<sup>1†</sup>, Naoki Matsumoto<sup>1</sup>, Tomohiro Nishizawa<sup>1</sup>, Keita Nakanaga<sup>3</sup>, Junken Aoki<sup>3</sup>, Ryuichiro Ishitani<sup>1</sup>, Haruhiko Siomi<sup>2</sup>, Mikiko C. Siomi<sup>1,2,4</sup> & Osamu Nureki<sup>1,4</sup>

PIWI-interacting RNAs (piRNAs) silence transposons to maintain genome integrity in animal germ lines<sup>1–4</sup>. piRNAs are classified as primary and secondary piRNAs, depending on their biogenesis machinery<sup>5–10</sup>. Primary piRNAs are processed from long non-coding RNA precursors transcribed from piRNA clusters in the genome through the primary processing pathway<sup>5,8–10</sup>. Although the existence of a ribonuclease participating in this pathway has been predicted, its molecular identity remained unknown. Here we show that Zucchini (Zuc), a mitochondrial phospholipase D (PLD) superfamily member<sup>11</sup>, is an endoribonuclease essential for primary piRNA biogenesis. We solved the crystal structure of *Drosophila melanogaster* Zuc (DmZuc) at 1.75 Å resolution. The structure revealed that DmZuc has a positively charged, narrow catalytic groove at the dimer interface, which could accommodate a single-stranded, but not a double-stranded, RNA. DmZuc and the mouse homologue MmZuc (also known as Pld6 and MitoPLD)<sup>12–14</sup> showed endoribonuclease activity for single-stranded RNAs *in vitro*. The RNA cleavage products bear a 5'-monophosphate group, a hallmark of mature piRNAs. Mutational analyses revealed that the conserved active-site residues of DmZuc are critical for the ribonuclease activity *in vitro*, and for piRNA maturation and transposon silencing *in vivo*. We propose a model for piRNA biogenesis in animal germ lines, in which the Zuc endoribonuclease has a key role in primary piRNA maturation.

Zuc is conserved among animals, and loss-of-function mutations in *zuc* in flies and mice cause a severe defect in piRNA accumulation in the germ lines, implying a role for Zuc in piRNA biogenesis<sup>8,10,11,13,15,16</sup>. Zuc contains a mitochondrial localization sequence (MLS) at the amino terminus and an HKD (His-Lys-Asp) motif, a hallmark of PLD superfamily members, in the central region (Supplementary Fig. 1a)<sup>12</sup>. The PLD superfamily members have diverse cellular functions<sup>17</sup>, and Zuc shares the highest sequence similarity with the bacterial nuclease Nuc<sup>18,19</sup> among the superfamily members (Supplementary Fig. 1b). Zuc has therefore been considered to be a candidate for the RNase required for piRNA biogenesis<sup>11</sup>. However, previous attempts to detect the nuclease activity in Zuc were unsuccessful<sup>12,13</sup>.

To obtain structural clues to Zuc's function, we solved the 1.75-Å resolution crystal structure of the cytoplasmic region (residues 41–253) of DmZuc, which lacks the N-terminal MLS and a predicted transmembrane helix (Fig. 1a and Supplementary Fig. 2a–c). The structure consists of a catalytic domain (residues 49–62 and 89–245) and a zinc-binding domain (residues 63–88), with the two protomers in the asymmetric unit forming a dimer. Co-immunoprecipitation experiments suggested this oligomeric state *in vivo* (Supplementary Fig. 2d). The catalytic domain consists of an eight-stranded mixed  $\beta$ -sheet flanked by  $\alpha$ -helices on both sides, and shares structural similarity with the catalytic domains of other PLD superfamily members, such as Nuc<sup>19,20</sup> (PDB 1BYR; 26% sequence identity, root mean

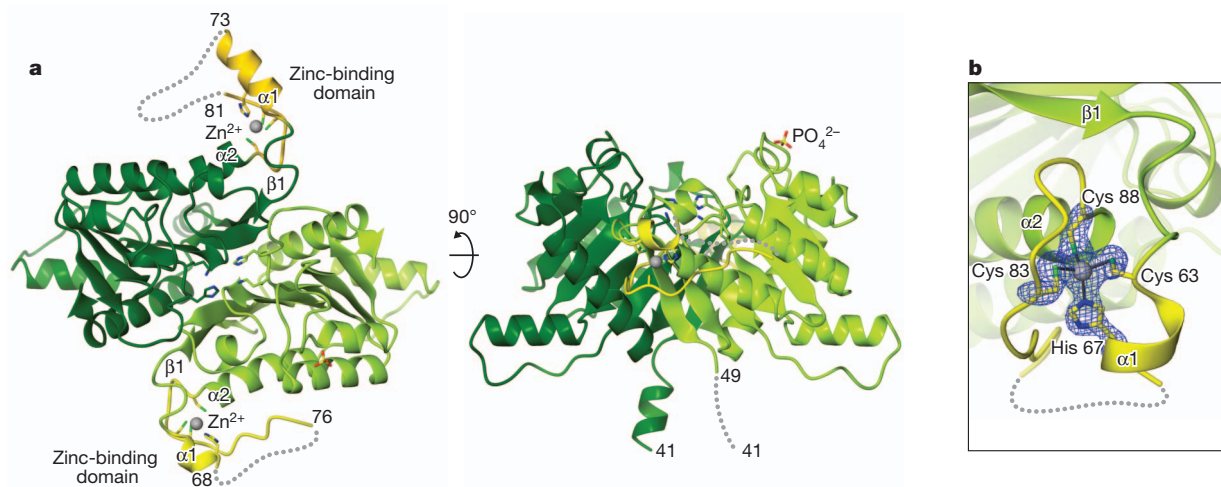


**Figure 1 | Crystal structure of DmZuc.** **a**, Overall structure. The two protomers are coloured green and yellow-green, and the zinc-binding domains are coloured gold and yellow. The bound zinc ions are shown as grey spheres. Cys 63, His 67, Cys 83, Cys 88, His 169, Lys 171 and the bound phosphate ion

are shown as sticks. Disordered regions are shown as dashed lines. **b**, The zinc-binding domain. The bound zinc ion is shown as a grey sphere, and a simulated annealing  $F_o - F_c$  omit electron density map (contoured at  $4\sigma$ ) is shown as a blue mesh.

<sup>1</sup>Department of Biophysics and Biochemistry, Graduate School of Science, The University of Tokyo, Tokyo 113-0032, Japan. <sup>2</sup>Department of Molecular Biology, Keio University School of Medicine, Tokyo 160-8582, Japan. <sup>3</sup>Graduate School of Pharmaceutical Sciences, Tohoku University, Miyagi 980-8578, Japan. <sup>4</sup>Japan Science and Technology Agency (JST), Core Research for Evolutional Science and Technology (CREST), Saitama 332-0012, Japan. <sup>†</sup>Present address: Institut de Génétique et de Biologie Moléculaire et Cellulaire, UMR7104 CNRS-UDS, INSERM U964, 1 rue Laurent Fries, BP 10142, 67404 Illkirch Cedex, France.

\*These authors contributed equally to this work.



squared deviation 1.8 Å for 145 C $\alpha$  atoms) (Supplementary Fig. 3a, b). His 169 and Lys 171 in the HKD motif in the two protomers form an active site at the dimer interface, and Asp 176 in the motif helps to maintain the structural integrity of each protomer (Supplementary Fig. 2e). The crystal structure revealed that a zinc ion is tetrahedrally coordinated by Cys 63, His 67, Cys 83 and Cys 88 in the zinc-binding domain, which is mostly disordered, and is absent from the other PLD superfamily members (Fig. 1b and Supplementary Fig. 4a, b). In the CHCC motif, only Cys 83 is conserved in animals (Supplementary Fig. 1a). In the corresponding region of MmZuc, the residues Cys 49, Glu 51, Cys 66 and Cys 68 are highly conserved among animals except for flies (Supplementary Fig. 1a), suggesting that these residues may coordinate a zinc ion in these species.

The active-site groove is composed of conserved residues from the two protomers, including Tyr 112, His 169, Lys 171, Ser 204, Asn 206, Trp 207, Thr 208, Asn 215 and Glu 217, which correspond to Tyr 35, His 94, Lys 96, Ser 109, Asn 111, Phe 112, Thr 113, Asn 120 and Glu 122, respectively, in Nuc (Fig. 2). Nuc cleaves substrates through a two-step catalytic mechanism, in which His 94 in one protomer forms a phosphoenzyme intermediate with a substrate phosphorus atom, followed by the hydrolysis of this intermediate by a water molecule, activated by His 94 in the other protomer<sup>19,21</sup>. Lys 96, Ser 109, Asn 111 and Glu 122 in Nuc form a hydrogen-bonding network and participate in catalysis<sup>19</sup>. The active-site residues are similarly arranged in DmZuc and Nuc (Fig. 2b, c and Supplementary Fig. 3c), suggesting that Zuc cleaves a substrate phosphodiester linkage through a similar catalytic mechanism. However, a structural comparison revealed a notable difference in their active-site architectures (Fig. 2a and Supplementary Fig. 5a, b). Nuc cleaves single-stranded and double-stranded nucleic acids *in vitro*<sup>18,22</sup> (Supplementary Fig. 6), and has a wide, positively charged groove that can readily accommodate double-stranded nucleic acids<sup>19</sup> (Supplementary Fig. 5a). In contrast, the active-site groove of DmZuc is narrower than that of Nuc, and can apparently accommodate single-stranded, but not double-stranded, nucleic acids (Fig. 2a and Supplementary Fig. 5b). This structural difference is partly due to the replacements of Gly 64 and Ala 115 in Nuc with the bulkier Met 141 and Leu 210 residues in DmZuc, respectively (Fig. 2a, b and Supplementary Fig. 3c). A phosphate ion derived from

the crystallization buffer binds to a positively charged patch near the active-site groove (Supplementary Fig. 5c), suggesting that this patch could interact with the phosphate group of nucleic acid substrates. The molecular surface on the side opposite the active-site groove is positively charged (Supplementary Fig. 5d). The N termini of the two protomers are located on the same face, and the N-terminal residues 41–48 of one protomer form a positively charged helix, which would follow the transmembrane helix (residues 41–48 are disordered in the other protomer). This structural feature supports a previous model in which Zuc localizes on the outer mitochondrial membrane<sup>12–15</sup>. Taken together, the structural features of DmZuc suggested that Zuc is a single-stranded nuclease that functions on the mitochondrial surface.

To determine whether DmZuc is a nuclease, purified DmZuc (residues 41–253; hereafter referred to as wild-type (WT) DmZuc) was incubated with a 42-nucleotide (nt) single-stranded RNA (ssRNA) labelled with <sup>32</sup>P at the 5' end. DmZuc cleaved the ssRNA substrate (Fig. 3a). In contrast, the DmZuc mutants H169A, K171A, N206A and N215A failed to cleave the substrate (Fig. 3a), highlighting the importance of the conserved residues for the ssRNase activity. These results also confirmed that the observed cleavage was not due to contaminants. A DmZuc  $\Delta$ 63–88 mutant, lacking the zinc-binding domain, showed decreased ssRNase activity (Fig. 3a), indicating the importance of this domain for the nuclease activity. The crystal structure of a shorter DmZuc construct (residues 89–250), lacking the  $\beta$ 1 strand that contributes to dimerization, was solved as a monomer (Supplementary Fig. 2b). This shorter construct failed to cleave the ssRNA substrate (Fig. 3a), indicating the requirement of dimerization for the ssRNase activity. Purified MmZuc (residues 35–221) also showed a ssRNase activity comparable to that of DmZuc (Fig. 3a). Thus, Zuc is an evolutionarily conserved RNase. Unlike Nuc (Supplementary Fig. 6), DmZuc cleaved poly(U) and circular ssRNA, and also ssDNA (Supplementary Fig. 7a), but not double-stranded RNA (dsRNA) (Fig. 3b). Thus, DmZuc is a single-strand-specific endonuclease. Although the poly(U) cleavage products showed an even distribution, DmZuc did not always cleave the ssRNA substrates at specific nucleotides (Fig. 3b), suggesting that DmZuc does not have strict sequence specificity. DmZuc showed similar activity in the presence of magnesium ions or EDTA (Fig. 3c), indicating that, like Nuc<sup>19,22</sup>, DmZuc is a metal-independent nuclease. The DmZuc ssRNase activity was inhibited by NaCl at concentrations of 50 mM or higher (Fig. 3c). Sodium ions may inhibit substrate binding, as observed for T4 DNA ligase<sup>23</sup> and the dsRNA-specific RNase Pac1 (ref. 24). We characterized the 5' end structure of the cleavage products, using the 42-nt ssRNA labelled with <sup>32</sup>P at the 3' end. The cleavage products showed resistance to treatment with 5'-phosphate ssRNA-specific exonuclease (Terminator Exonuclease) after treatment with calf intestinal phosphatase (Fig. 3d), suggesting that the cleavage products contain a 5' monophosphate. The endonuclease activity of DmZuc is modest *in vitro*, although it showed dose dependence (Supplementary Fig. 7b). The DmZuc activity may be stimulated *in vivo* by unknown cofactors. Although MmZuc reportedly hydrolysed the mitochondrial lipid cardiolipin to phosphatidic acid<sup>12</sup>, the active-site groove of DmZuc seems too narrow to accommodate such a bulky lipid molecule as a substrate (Fig. 2a and Supplementary Fig. 5b). Indeed, neither DmZuc nor MmZuc hydrolysed cardiolipin *in vitro* (Supplementary Fig. 8). The reason for this discrepancy is currently unclear. Together, these results indicated that Zuc is an endonuclease specific for single-stranded nucleic acids.

To explore the biological relevance of the DmZuc ssRNase activity in transposon silencing, we expressed RNA-mediated interference (RNAi)-resistant WT and mutants of full-length DmZuc (residues 1–253) in DmZuc-depleted ovarian somatic cells (OSCs), and then monitored the expression levels of the *mdg1* transposon by quantitative PCR with reverse transcription (RT-PCR). Western blotting confirmed the similar expression levels of DmZuc WT and mutants (Fig. 4a). WT DmZuc rescued *mdg1* derepression, whereas the H169A and K171A mutants failed to rescue it (Fig. 4a). The *mdg1*

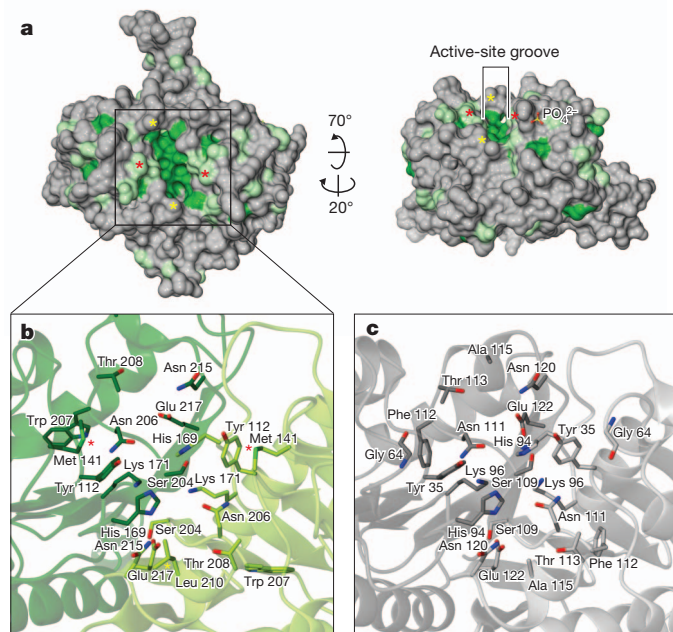


**Figure 2 | Active site of DmZuc.** **a**, Molecular surface of DmZuc. Conserved residues are coloured green, and Met 141 and Leu 210 are indicated by red and yellow asterisks, respectively. **b**, Active site of DmZuc. **c**, Active site of Nuc (PDB 1BYR).

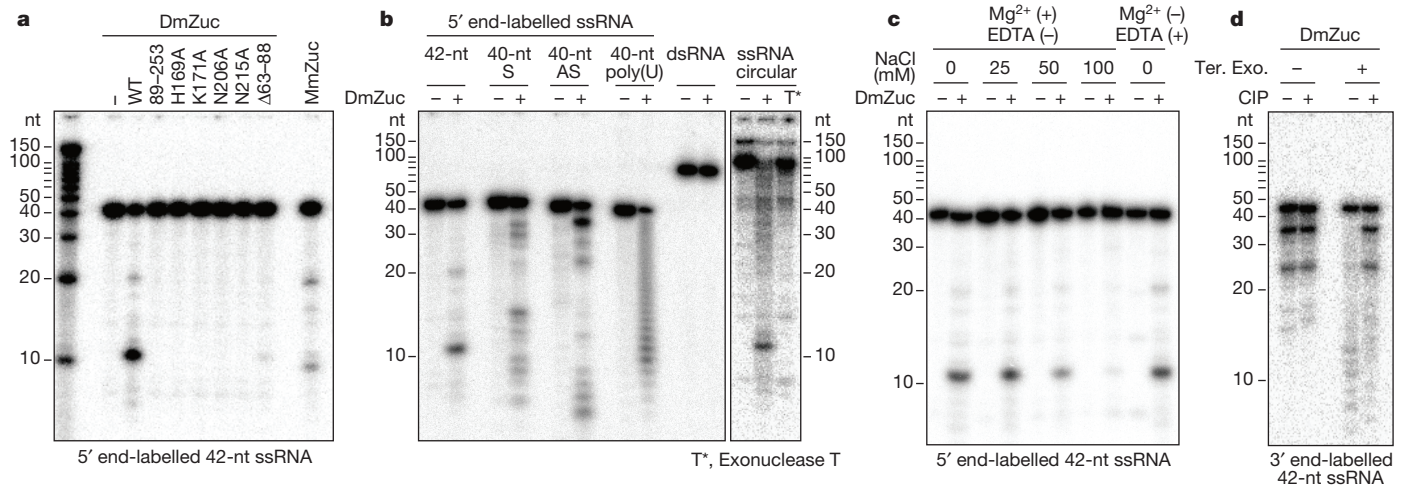


**Figure 3 | Zuc is an endonuclease for single-stranded nucleic acids.**

**a**, DmZuc and MmZuc, but not monomeric DmZuc or the DmZuc mutants, cleave a 42-nt ssRNA substrate. **b**, DmZuc cleaves ssRNAs of various sequences and circular ssRNA, but not dsRNA. Exonuclease T failed to cleave the circular ssRNA. S and AS correspond to the sense and antisense strands of dsRNA, respectively. **c**, DmZuc endonuclease activity requires no magnesium ions, and is inhibited by NaCl. **d**, The ssRNA products cleaved by DmZuc have a 5' monophosphate. The cleavage products were resistant to treatment with Terminator Exonuclease (Ter. Exo.) after treatment with calf intestinal phosphatase (CIP).

expression was higher in OSCs expressing the H169A or K171A mutant than in control OSCs. The mutants may have dominant-negative effects, although the underlying mechanism is unknown. The C63A, H67A and  $\Delta 63$ -88 mutants rescued *mdg1* derepression. The  $\Delta 63$ -88 mutant had a lower ssRNase activity (about 5% of the WT activity) (Fig. 3a), which may suffice for transposon silencing. None of the mutants Y112A, S204A, N206A, W207A, T208A, N215A or E217A rescued *mdg1* derepression (Fig. 4a). These residues are conserved (Supplementary Fig. 1a) and form the active-site groove (Fig. 2b). The N218A mutant rescued *mdg1* derepression (Fig. 4a). Asn 218 is buried within the protein, and thus would not contribute to substrate binding. The H169A, K171A, N206A and N215A mutants lacked ssRNase activity *in vitro* (Fig. 3a) and the ability to repress transposons *in vivo* (Fig. 4a), indicating that the DmZuc ssRNase activity is critical for transposon silencing. The expression of WT DmZuc, but not that of the H169A and K171A mutants, rescued the defects in *Idefix*-piRNA maturation in DmZuc-depleted OSCs (Fig. 4b), suggesting that the DmZuc ssRNase activity is required for

primary piRNA maturation. RT-PCR after immunoprecipitation of DmZuc from OSCs revealed that DmZuc interacts with the piRNA precursors in OSCs (Supplementary Fig. 9). Together, these results indicate that Zuc is an endoribonuclease essential for primary piRNA processing.

We propose a model for primary piRNA biogenesis in *Drosophila* OSCs (Supplementary Fig. 10). Mature piRNAs show a strong bias for 5' uridine (1-U)<sup>5,25</sup>. DmZuc cleaved ssRNAs with little sequence specificity, to produce ssRNA fragments bearing a 5' monophosphate (Fig. 3b, d), a hallmark of mature piRNAs associated with Piwi, suggesting that DmZuc generates the 5' end of mature piRNAs. These observations suggested that DmZuc cleaves piRNA intermediates to generate the 5' end of mature piRNAs during the processing step, and that Piwi then preferentially binds 1-U piRNAs during the loading step. Our findings provide a starting point for explaining the molecular mechanism by which Zuc recognizes genuine piRNA intermediates to produce mature piRNAs, which in turn should shed light on the mechanism of primary piRNA biogenesis in animal germ lines.

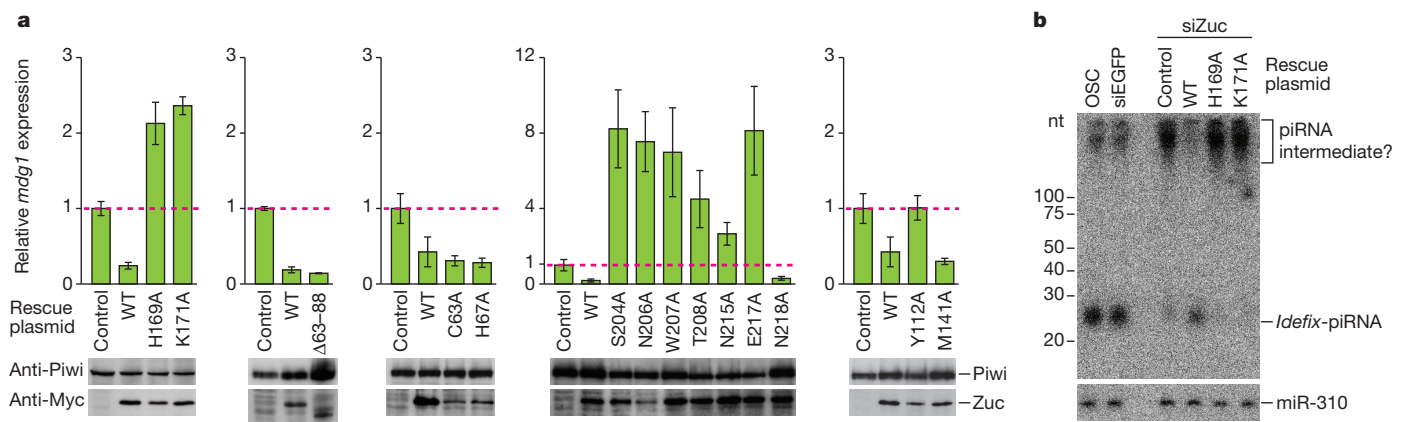


**Figure 4 | DmZuc endoribonuclease activity is required for transposon silencing.** **a**, Myc-tagged full-length WT and mutant DmZuc, mutated at a short interfering RNA (siRNA) recognition site and thus resistant to RNAi, were expressed in DmZuc-depleted OSCs. The expression levels of Piwi and DmZuc were examined by western blotting, and the expression levels of the *mdg1* transposon were monitored by quantitative RT-PCR. Results are shown as means  $\pm$  s.e.m. ( $n = 3$ ). As a control, OSCs were transfected with an empty

vector. **b**, Northern blotting with a piRNA probe, *Idefix*-piR1-R, showed that WT DmZuc, but not H169A or K171A, rescued the defects in piRNA maturation in DmZuc-depleted OSCs. The expression of WT DmZuc increased mature piRNAs with a concomitant decrease in piRNA intermediate-like molecules. miR-310, one of the microRNAs in OSCs, was used as an internal loading control. 'piRNA intermediate?' corresponds to 'piRNA-intermediate-like molecules'.



## METHODS SUMMARY

DmZuc and MmZuc were overexpressed in *Escherichia coli* as glutathione S-transferase (GST)-tagged proteins, and purified by glutathione-Sepharose, Resource S and Superdex 200 chromatography, as described<sup>26</sup>. Crystals were obtained at 20 °C by the hanging-drop vapour diffusion method. X-ray diffraction data were collected on beamline BL32XU at SPring-8 (Hyogo, Japan). The crystal structure of DmZuc (residues 41–253) was determined by molecular replacement using the structure of monomeric DmZuc (residues 89–250), which was solved by the multiwavelength anomalous dispersion (MAD) method using a selenomethionine (SeMet)-labelled protein. Nuclease assays were performed in buffer containing 25 mM HEPES-KOH pH 7.4, 2.5 mM EDTA and 5 mM dithiothreitol. Rescue experiments were performed essentially as described previously<sup>15</sup>.

**Full Methods** and any associated references are available in the online version of the paper.

**Received 29 May; accepted 14 August 2012.**

**Published online 14 October 2012.**

- Malone, C. D. & Hannon, G. J. Small RNAs as guardians of the genome. *Cell* **136**, 656–668 (2009).
- Siomi, M. C., Sato, K., Pezic, C. & Aravin, A. A. PIWI-interacting small RNAs: the vanguard of genome defence. *Nature Rev. Mol. Cell Biol.* **12**, 246–258 (2011).
- Pillai, R. S. & Chuma, S. piRNAs and their involvement in male germline development in mice. *Dev. Growth Differ.* **54**, 78–92 (2012).
- Senti, K. A. & Brennecke, J. The piRNA pathway: a fly's perspective on the guardian of the genome. *Trends Genet.* **26**, 499–509 (2010).
- Brennecke, J. et al. Discrete small RNA-generating loci as master regulators of transposon activity in *Drosophila*. *Cell* **128**, 1089–1103 (2007).
- Vagin, V. V. et al. A distinct small RNA pathway silences selfish genetic elements in the germline. *Science* **313**, 320–324 (2006).
- Gunawardane, L. S. et al. A slicer-mediated mechanism for repeat-associated siRNA 5' end formation in *Drosophila*. *Science* **315**, 1587–1590 (2007).
- Malone, C. D. et al. Specialized piRNA pathways act in germline and somatic tissues of the *Drosophila* ovary. *Cell* **137**, 522–535 (2009).
- Li, C. et al. Collapse of germline piRNAs in the absence of Argonaute3 reveals somatic piRNAs in flies. *Cell* **137**, 509–521 (2009).
- Saito, K. et al. A regulatory circuit for piwi by the large Maf gene *traffic jam* in *Drosophila*. *Nature* **461**, 1296–1299 (2009).
- Pane, A., Wehr, K. & Schüpbach, T. *zucchini* and *squash* encode two putative nucleases required for rasiRNA production in the *Drosophila* germline. *Dev. Cell* **12**, 851–862 (2007).
- Choi, S. Y. et al. A common lipid links Mfn-mediated mitochondrial fusion and SNARE-regulated exocytosis. *Nature Cell Biol.* **8**, 1255–1262 (2006).
- Watanabe, T. et al. MITOPLD is a mitochondrial protein essential for nuage formation and piRNA biogenesis in the mouse germline. *Dev. Cell* **20**, 364–375 (2011).
- Huang, H. et al. piRNA-associated germline nuage formation and spermatogenesis require MitoPLD profusogenic mitochondrial-surface lipid signaling. *Dev. Cell* **20**, 376–387 (2011).
- Saito, K. et al. Roles for the Yb body components Armitage and Yb in primary piRNA biogenesis in *Drosophila*. *Genes Dev.* **24**, 2493–2498 (2010).
- Olivieri, D., Sykora, M. M., Sachidanandam, R., Mechtler, K. & Brennecke, J. An *in vivo* RNAi assay identifies major genetic and cellular requirements for primary piRNA biogenesis in *Drosophila*. *EMBO J.* **29**, 3301–3317 (2010).
- Ponting, C. P. & Kerr, I. D. A novel family of phospholipase D homologues that includes phospholipid synthases and putative endonucleases: Identification of duplicated repeats and potential active site residues. *Protein Sci.* **5**, 914–922 (1996).
- Pohlman, R. F. et al. Genetic and biochemical analysis of an endonuclease encoded by the IncN plasmid pKM101. *Nucleic Acids Res.* **21**, 4867–4872 (1993).
- Stuckey, J. A. & Dixon, J. E. Crystal structure of a phospholipase D family member. *Nature Struct. Biol.* **6**, 278–284 (1999).
- Leiros, I., Secundo, F., Zambonelli, C., Servi, S. & Hough, E. The first crystal structure of a phospholipase D. *Structure* **8**, 655–667 (2000).
- Gottlin, E. B., Rudolph, A. E., Zhao, Y., Matthews, H. R. & Dixon, J. E. Catalytic mechanism of the phospholipase D superfamily proceeds via a covalent phosphohistidine intermediate. *Proc. Natl Acad. Sci. USA* **95**, 9202–9207 (1998).
- Zhao, Y., Studkey, J. A., Lohse, D. L. & Dixon, J. E. Expression, characterization, and crystallization of a member of the novel phospholipase D family of phosphodiesterases. *Protein Sci.* **6**, 2655–2658 (1997).
- Raae, A. J., Kleppe, R. K. & Kleppe, K. Kinetics and effect of salts and polyamines on T4 polynucleotide ligase. *Eur. J. Biochem.* **60**, 437–443 (1975).
- Rotondo, G. & Frensdewey, D. Purification and characterization of the Pac1 ribonuclease of *Schizosaccharomyces pombe*. *Nucleic Acids Res.* **24**, 2377–2386 (1996).
- Saito, K. et al. Specific association of Piwi with rasiRNAs derived from retrotransposon and heterochromatic regions in the *Drosophila* genome. *Genes Dev.* **20**, 2214–2222 (2006).
- Fukuhara, S. et al. Expression, purification, crystallization and preliminary X-ray crystallographic analysis of Zucchini from *Drosophila melanogaster*. *Acta Crystallogr. F.* (in the press).

**Supplementary Information** is available in the online version of the paper.

**Acknowledgements** We thank A. Kurabayashi, H. Kotani and Y. Tamaki for technical assistance; other members of the Siomi laboratory for discussions and comments on the manuscript; the beamline staff at BL32XU of SPring-8 for assistance in data collection; and T. Suzuki and H. Suga for technical suggestions and comments. This work was supported by a grant from the Japan Society for the Promotion of Science (JSPS) through its 'Funding Program for World-Leading Innovative R&D on Science and Technology (FIRST) program' to O.N., by the Core Research for Evolutional Science and Technology (CREST) program 'The Creation of Basic Medical Technologies to Clarify and Control the Mechanisms Underlying Chronic Inflammation' of the Japan Science and Technology Agency (JST) to O.N. and M.C.S., and by a Grant-in-Aid for Scientific Research from the Ministry of Education, Culture, Sports, Science and Technology (MEXT) of Japan to H.N., H.I., H.S., M.C.S. and O.N. K.S. is supported by the JSPS.

**Author Contributions** H.N., H.I., K.S., H.S., M.C.S. and O.N. conceived and designed the experiments and wrote the manuscript. H.N., S.F., L.B., N.M., T.N. and R.I. performed the structural analyses. H.I., K.S. and M.K.K. performed biochemical and biological analyses. K.N. and J.A. performed PLD activity assays. All authors discussed the data and the manuscript. M.C.S. and O.N. supervised all the work.

**Author Information** The atomic coordinates and structure factors are deposited in the Protein Data Bank under accession numbers 4GEL (DmZuc WT dimer), 4GEM (DmZuc K171A dimer) and 4GEN (DmZuc WT monomer). The authors declare no competing financial interests. Reprints and permissions information is available at [www.nature.com/reprints](http://www.nature.com/reprints). Readers are welcome to comment on the online version of the paper. Correspondence and requests for materials should be addressed to O.N. ([nureki@biochem.s.u-tokyo.ac.jp](mailto:nureki@biochem.s.u-tokyo.ac.jp)) or M.C.S. ([siomim@biochem.s.u-tokyo.ac.jp](mailto:siomim@biochem.s.u-tokyo.ac.jp)).



## METHODS

**Protein preparation.** Protein samples were prepared as described<sup>26</sup>. In brief, the gene encoding DmZuc (residues 41–253) was cloned between the *SacI* and *XhoI* sites of the pCold-GST vector<sup>27</sup>. The protein was expressed at 20 °C in *E. coli* Rosetta 2 (DE3) (Novagen) and purified using glutathione-Sepharose (GE Healthcare). The protein was treated with Turbo3C protease (Nacalai Tesque) to remove the His<sub>6</sub>-GST tag, and was further purified by NiNTA (Qiagen), Resource S (GE Healthcare) and Superdex 200 gel filtration (GE Healthcare). The DmZuc mutants were prepared using a PCR-based method, and the sequences were verified by DNA sequencing. The DmZuc mutants and MmZuc (residues 35–221) were prepared using a protocol similar to that used for WT DmZuc. DmZuc (residues 89–253) was expressed at 20 °C in *E. coli* Rosetta 2 (DE3) and purified using glutathione-Sepharose. The protein was treated with Turbo3C protease and was further purified by Superdex 75 gel filtration (GE Healthcare). SeMet-labelled DmZuc (residues 89–250) was expressed in *E. coli* B834 (DE3) (Novagen) and purified using a protocol similar to that used for the native protein.

**Crystallization.** During our expression trials, we found that DmZuc (residues 89–250) and the K171A mutant of DmZuc (residues 41–253) were more highly expressed than WT DmZuc (residues 41–253) in *E. coli*. Thus, we first solved the crystal structure of DmZuc (residues 89–250) by the MAD method, using a SeMet-labelled crystal. We next screened and optimized the crystallization conditions using the K171A mutant of DmZuc (residues 41–253). We then crystallized WT and K171A DmZuc under similar crystallization conditions, and solved the crystal structures by molecular replacement, using the structure of DmZuc (residues 89–250) as a search model.

Crystallization was performed at 20 °C by the vapour diffusion methods. Crystals of SeMet-labelled DmZuc (residues 89–250) were obtained by mixing 0.4 µl of protein solution (3 mg ml<sup>-1</sup> DmZuc, 10 mM Tris-HCl pH 8.0, 150 mM NaCl, 1 mM dithiothreitol (DTT)) and 0.4 µl of reservoir solution (50 mM MES pH 6.0, 8% polyethylene glycol 400, 100 mM KCl, 10 mM MgCl<sub>2</sub>, 3% trehalose). Crystals of WT and K171A DmZuc (residues 41–253) were obtained by mixing 1 µl of protein solution (3–5 mg ml<sup>-1</sup> DmZuc, 10 mM Tris-HCl pH 8.0, 150 mM NaCl, 1 mM DTT) and 1 µl of reservoir solution (16% polyethylene glycol 3350, 200 mM KH<sub>2</sub>PO<sub>4</sub>).

**Crystallography.** X-ray diffraction data were collected at 100 K on beamline BL32XU at SPring-8 (Hyogo, Japan). The crystals were cryoprotected in reservoir solution supplemented with 30% ethylene glycol. Diffraction data were processed using HKL2000 (HKL Research Inc.). The structure of DmZuc (residues 89–250) was determined by the MAD method, using the 2.2-Å resolution data from the SeMet-labelled crystal. Four Se atoms were located using SHELXD<sup>28</sup>, and the initial phases were calculated using SHARP<sup>29</sup>, followed by automated model building using RESOLVE<sup>30</sup>. The model was further built manually using COOT<sup>31</sup> and refined using PHENIX<sup>32</sup>. The structures of WT and K171A DmZuc (residues 41–253) were solved by molecular replacement with MOLREP<sup>33</sup>, using the structure of DmZuc (residues 89–250) as a search model. Data collection and refinement statistics are provided in Supplementary Table 1. Structural figures were prepared using CUEMOL (<http://www.cuemol.org>).

**Nuclease assay.** The RNA substrates used for nuclease assays were: 5'-AUU UAAUCAAGCUAUCGAUACCGUCGACCUCGAGGGGGGGC-3' (42-nt), 5'-GGUCUGAUUUCGAUCUGGUUCCUGGAACAAAGUGGCAG-3' (40-nt sense strand), 5'-CUGCCACUUUUGUCCAGGGAACCAAGAUCAUGAAAUCA GACC-3' (40-nt antisense strand), and poly(U) (40-nt). ssRNAs were synthesized (Sigma) and labelled at their 5' ends using [ $\gamma$ -<sup>32</sup>P]ATP and T4 polynucleotide kinase (New England Biolabs). For 3' end labelling, RNAs were labelled at their 3' ends using 5'-[<sup>32</sup>P]pCp and T4 RNA ligase 1 (New England Biolabs). To make circular ssRNA, 5' end-labelled 42-nt RNAs were circularized by intramolecular ligation using T4 RNA ligase 1. The labelled RNAs were purified by electrophoresis on 12% denaturing polyacrylamide gels. To make dsRNA, 5' end-labelled 40-nt sense strand RNA and non-labelled 40-nt antisense strand RNA were mixed at a molar ratio of 1:2 (sense:antisense) in annealing buffer (10 mM Tris-HCl pH 7.5, 50 mM NaCl, 1 mM EDTA), heated at 95 °C for 15 min, and then cooled slowly to 30 °C.

<sup>32</sup>P-end-labelled RNA substrate (10<sup>4</sup> c.p.m.) was incubated with purified recombinant DmZuc (1.62 µM) in buffer A (25 mM HEPES-KOH pH 7.4, 2.5 mM EDTA, 5 mM DTT) for 1 h at 26 °C (37 °C for MmZuc). The reaction was terminated by treatment with proteinase K, followed by extraction with phenol-chloroform and precipitation with ethanol. The products were resolved on 20% denaturing polyacrylamide gels. The effects of NaCl on the nuclease activity were tested using the 42-nt ssRNA substrate in buffer B (25 mM HEPES-KOH pH 7.4, 5 mM magnesium acetate, 5 mM DTT, 0–100 mM NaCl). Terminator 5'-phosphate-dependent exonuclease was used in accordance with the manufacturer's instructions (Epicentre). The DNA substrate used for ssDNase

assays was 5'-AATTGGTACGTAGCGCTTGATCTAGAGGGGTTTGCCAAAT AGCAATCCGACGCTTCCTCGTCTCGACAAT-3'.

**PLD assay.** PLD from *Actinomadura* sp. no. 362 was purchased from Meito Sangyo Inc. (Tokyo Japan). Tetraoleoyl cardiolipin (CL) (0.1 µmol; Avanti Polar Lipids) and dipalmitoyl phosphatidylcholine (PC) (0.5 µmol; Avanti Polar Lipids) were dried under nitrogen gas and resuspended in 10 mM HEPES pH 7.5 (0.6 ml) by sonication. The enzyme reaction was performed at 26 °C (DmZuc) or 37 °C (MmZuc and *Actinomadura* PLD) for 2 h with 10 µl of lipid solution, 38 µl of assay buffer (50 mM HEPES pH 7.5, 80 mM KCl, 3 mM MgCl<sub>2</sub>, 2 mM CaCl<sub>2</sub>, 1 mM DTT) and purified recombinant DmZuc (0.4 µg), MmZuc (0.4 µg) or *Actinomadura* PLD (0.3 U). The reaction was stopped by adding 450 µl of methanol containing an internal standard (1 µM diheptadecanoyl PC) and centrifuged at 21,500g. The sample solution (5 µl) was injected into liquid chromatography (LC) and analysed by tandem mass spectrometry (MS/MS). In brief, lipids were separated by Nanospace LC (Shiseido) with a silica column (5 µm, 2.0 mm × 150 mm; Shiseido), using a gradient of solvent A (5 mM ammonium formate in water) and solvent B (acetonitrile), and then analysed by MS/MS using a Quantum Ultra triple quadrupole mass spectrometer (Thermo Fisher Scientific). Lipids were monitored in negative-ion mode and quantified by multiple reaction monitoring (MRM). Tetraoleoyl CL, dioleoyl phosphatidic acid (PA), dipalmitoyl PA and dipalmitoyl PC were monitored with the MRM transition of *m/z* 1,456.1 > 281.2, *m/z* 699.4 > 281.2, *m/z* 759.5 > 255.2 and *m/z* 778.6 > 255.2, respectively. The ratio between analyte and internal standard peak area was used for quantification. Calibration curves (0.5–5,000 ng) and LC retention times for each compound were established using synthetic standards.

**Rescue and dimerization assays in OSCs.** The RNAi-resistant WT and mutants of DmZuc were prepared by a PCR-based method, using a pAc-Zuc-Myc vector<sup>15</sup> as the template. Transfection was performed essentially as described previously<sup>10</sup>. In brief, trypsinized OSCs (5 × 10<sup>6</sup> cells) were transfected with siRNA duplex (200 pmol), transferred to fresh OSC medium and incubated at 26 °C. Two days after transfection, OSCs (3 × 10<sup>6</sup> cells) were again transfected with siRNA duplex (200 pmol) and plasmid vector (5 µg). The cells were again incubated at 26 °C for 2 days, and then total RNAs were purified using ISOGEN reagent (Nippon Gene). Total RNA (0.5 µg) was used to reverse transcribe target sequences using oligo(dT) primers. The resulting cDNAs were analysed by quantitative RT-PCR using a LightCycler real-time PCR system (Roche Diagnostics) and SYBR Premix Ex Taq (Takara). Relative steady-state mRNA levels were determined from the threshold cycle for amplification. Ribosomal protein 49 was used as an internal control. The expression levels of Piwi and DmZuc were analysed by western blotting using culture supernatants of anti-Piwi hybridoma cells (P4D2; 1:1 dilution)<sup>25</sup> and a mouse monoclonal antibody 9E10 against the Myc tag (1:1,000 dilution; Sigma), respectively.

Carboxy-terminal Flag-tagged DmZuc (pAc-Zuc-Flag) was prepared, by inserting oligonucleotides encoding a 3 × Flag tag between the *XhoI* and *BamHI* sites of pAc-Zuc-Myc (ref. 15). OSCs (5 × 10<sup>6</sup> cells) were co-transfected with pAc-Zuc-Flag and either pAc-Zuc-Myc or pAcM-EGFP. Two days after transfection, the OSCs were homogenized in lysis buffer (30 mM HEPES pH 7.3, 150 mM potassium acetate, 2 mM magnesium acetate, 5 mM DTT, 0.1% Nonidet P40) to prepare OSC lysate. Zuc-Flag was immunoprecipitated using an anti-Flag M2 antibody (Sigma) immobilized on GammaBind beads (GE Healthcare). The mixtures were rocked at 4 °C for 2 h and the beads were washed five times with lysis buffer. After immunoprecipitation, proteins were resolved by SDS-PAGE and then detected by western blotting using anti-Flag M2 and anti-Myc antibodies.

**RNA immunoprecipitation.** C-terminal Myc-tagged, full-length DmZuc was expressed in OSCs by transfection. Two days after transfection, the OSCs were homogenized in lysis buffer (50 mM HEPES pH 7.5, 140 mM NaCl, 1 mM EDTA, 1 mM DTT, 2 µg ml<sup>-1</sup> pepstatin, 2 µg ml<sup>-1</sup> leupeptin, 0.5% aprotinin, 20 µl ml<sup>-1</sup> RNasin Plus (Promega), 1% Triton X-100) to prepare OSC lysate. Zuc-Myc was immunoprecipitated using a monoclonal anti-Myc antibody (9E10) immobilized on Dynabeads Protein G (Invitrogen). The mixtures were rocked at 4 °C for 2 h and the beads were washed five times with lysis buffer. Total RNAs were isolated from the immunoprecipitates with phenol-chloroform and were precipitated with ethanol. Total RNA was reverse transcribed using SuperScript III reverse transcriptase (Invitrogen) and a strand-specific RT primer for a fragment of the *flamenco* transcript. PCR was performed using Ex Taq DNA polymerase (Takara) and primers for a fragment of the *flamenco* transcript. The primer sequences were as follows: *flamenco* forward, 5'-AACGATGCTCAGTCCAG TGAA-3'; *flamenco* RT and reverse, 5'-AAAACCTTCTAGCTTGCCCTCT-3'.

27. Hayashi, K. & Kojima, C. pCold-GST vector: a novel cold-shock vector containing GST tag for soluble protein production. *Protein Expr. Purif.* **62**, 120–127 (2008).
28. Sheldrick, G. M. A short history of SHELX. *Acta Crystallogr. A* **64**, 112–122 (2008).
29. de La Fortelle, E. & Bricogne, G. SHARP: a maximum likelihood heavy-atom parameter refinement program for the MIR and MAD methods. *Methods Enzymol.* **276**, 472–494 (1997).

30. Terwilliger, T. C. & Berendzen, J. Automated MAD and MIR structure solution. *Acta Crystallogr. D* **55**, 849–861 (1999).
31. Emsley, P. & Cowtan, K. Coot: model-building tools for molecular graphics. *Acta Crystallogr. D* **60**, 2126–2132 (2004).
32. Adams, P. D. *et al.* PHENIX: building new software for automated crystallographic structure determination. *Acta Crystallogr. D* **58**, 1948–1954 (2002).
33. Vagin, A. & Teplyakov, A. Molecular replacement with MOLREP. *Acta Crystallogr. D* **66**, 22–25 (2010).

# CORRECTIONS & AMENDMENTS

---

## CORRIGENDUM

doi:10.1038/nature11666

### **Corrigendum: Comprehensive genomic characterization of squamous cell lung cancers**

The Cancer Genome Atlas Research Network

*Nature* **489**, 519–525 (2012); doi:10.1038/nature11404

In this Article, author Kristen Rodgers was spelt incorrectly. This error has been corrected in the HTML and PDF of the original paper.



## CORRIGENDUM

doi:10.1038/nature11667

### Corrigendum: Reconstructing Native American population history

David Reich, Nick Patterson, Desmond Campbell, Arti Tandon, Stéphane Mazieres, Nicolas Ray, Maria V. Parra, Winston Rojas, Constanza Duque, Natalia Mesa, Luis F. García, Omar Triana, Silvia Blair, Amanda Maestre, Juan C. Dib, Claudio M. Bravi, Graciela Bailliet, Daniel Corach, Tábita Hünemeier, Maria Cátira Bortolini, Francisco M. Salzano, María Luiza Petzl-Erler, Victor Acuña-Alonzo, Carlos Aguilar-Salinas, Samuel Canizales-Quinteros, Teresa Tusié-Luna, Laura Riba, Maricela Rodríguez-Cruz, Mardia Lopez-Alarcón, Ramón Coral-Vazquez, Thelma Canto-Cetina, Irma Silva-Zolezzi, Juan Carlos Fernandez-Lopez, Alejandra V. Contreras, Gerardo Jimenez-Sanchez, Maria José Gómez-Vázquez, Julio Molina, Ángel Carracedo, Antonio Salas, Carla Gallo, Giovanni Poletti, David B. Witonsky, Gorka Alkorta-Aranburu, Rem I. Sukernik, Ludmila Osipova, Sardana A. Fedorova, René Vasquez, Mercedes Villena, Claudia Moreau, Ramiro Barrantes, David Pauls, Laurent Excoffier, Gabriel Bedoya, Francisco Rothhammer, Jean-Michel Dugoujon, Georges Larrouy, William Klitz, Damian Labuda, Judith Kidd, Kenneth Kidd, Anna Di Rienzo, Nelson B. Freimer, Alkes L. Price & Andrés Ruiz-Linares

*Nature* **488**, 370–374 (2012); doi:10.1038/nature11258

At the time of publication of this Letter, the authors were unaware of a manuscript arriving at broadly similar conclusions based on allotype analysis by Williams *et al.*<sup>1</sup>, which appeared in the *American Journal of Physical Anthropology*.

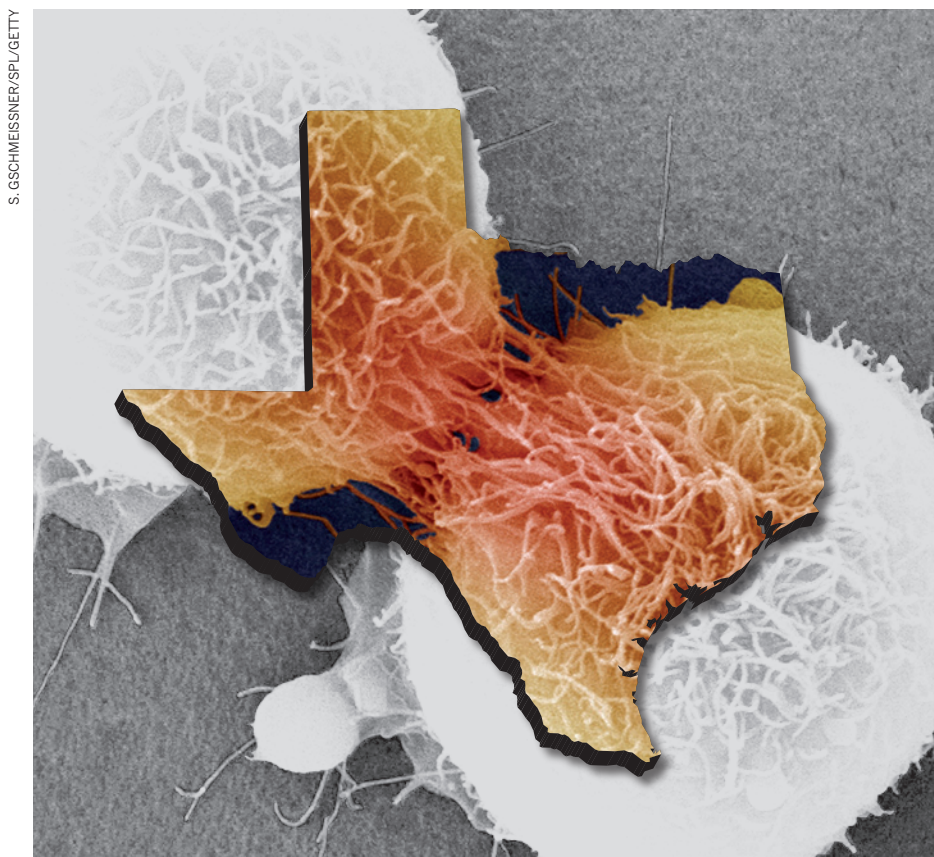
1. Williams, R. C. *et al.* GM allotypes in Native Americans: evidence for three distinct migrations across the Bering land bridge. *Am. J. Phys. Anthropol.* **66**, 1–19 (1985).

# CAREERS

**TURNING POINT** Astronomer aims to promote search for exoplanets **p.291**

**PROSPECTS** Red tape hinders recruitment at US defence agency **p.291**

**NATUREJOBS** For the latest career listings and advice [www.naturejobs.com](http://www.naturejobs.com)



S. GSCHMEISSNER/SPL/GETTY

## BIOMEDICAL RESEARCH

# Texas potential

*If it can weather some controversy, a US\$3-billion cancer-research initiative stands to offer ample opportunities.*

BY LAURA BEIL

Until last spring, the Cancer Prevention and Research Institute of Texas (CPRIT), based in Austin, was operating smoothly, awarding more than US\$650 million in grants to scientists such as Daniel Siegwart. In 2011, Siegwart was a postdoc at the Massachusetts Institute of Technology in Cambridge, studying polymer architecture and planning to stay in the northeast, close to his hometown of Pittsburgh. Then he spotted an advert for “exceptional scientists”, placed by the University of Texas Southwestern (UT

Southwestern) Medical Center in Dallas. The campus sought to recruit innovative thinkers as part of the CPRIT’s Scholar in Cancer Research programme. Using CPRIT money, UT Southwestern was seeking an entry-level scientist to investigate the barriers that keep drugs from getting into tumours. Texas seemed a world away, but Siegwart jumped at the opportunity. He has no regrets.

Until then, Siegwart had never heard of the CPRIT, or given any serious thought to the idea of moving south. Texas voters established and funded the CPRIT in 2007 by constitutional amendment, following overwhelming support

and lobbying from patient advocates. The legislation created a cancer-research funding pool second only to that of the National Cancer Institute (NCI) in Bethesda, Maryland: \$3 billion over 10 years. Financed through bonds, the money began to flow in 2009, and since then, the organization has awarded 427 grants that now total about \$755 million.

All has not gone entirely according to plan, however. Earlier this year, the CPRIT’s chief scientific officer, Nobel laureate Alfred Gilman, tendered his resignation, in large part over frustration at the sequence of events that led to the awarding of a \$20-million grant, mostly to the MD Anderson Cancer Center in Houston. The grant was awarded without going through scientific review. That grant has now been withdrawn and will be re-reviewed. CPRIT executive director William Gimson says that the institute’s leadership has “put in place checks and balances” to ensure proper review. “We’re moving forward,” he adds. “Our mission is defeating cancer in the state of Texas.”

But the CPRIT took another hit in October when at least seven reviewers resigned, accusing the initiative of “dishonouring” the system of peer review (see *Nature* **490**, 459–460; 2012). Gilman, now retired, believes an oversight commission should be appointed to determine whether members of the oversight committee violated public trust; if so, they should be removed, he says. And he has called for the board to bring on more cancer expertise. But given these corrections, he remains sanguine about the many opportunities that the CPRIT can offer cancer researchers. It can have “an enormously positive impact”, he says.

## POTENTIAL IMPACT

If the CPRIT can weather these peer-review setbacks, those opportunities abound. Since the funding began, more than 200 science positions have been created by these grants, and that number is expected to grow as laboratories and biotech start-ups fill their benches. The sheer size of the fund gives the CPRIT the potential to turn the state into a major centre of cancer research. Anyone wanting to tap into the funding must have an innovative idea and a solid track record. Grants are open to both junior and senior faculty members, but CPRIT officials say that junior faculty members must have sufficient publication history and experience to show that they have the ability to lead a major project.

The one non-negotiable requirement for funding is Texas residence, although the ►

► funding kicks in immediately and can be used to pay for the expense of moving. This geographical stipulation has allowed research institutions and businesses in Texas to attract talent that might have otherwise gone — or stayed — elsewhere. For young scientists, the best opportunity might be the scholars programme that drew Siegwart. Some grants even bear the formal name “Recruitment of Rising Stars”. Institutions can identify investigators with particular skills, and then apply to the CPRIT to sweeten an offer with more money. Jim Willson, head of the UT Southwestern’s Simmons Cancer Center in Dallas, calls the scholars programme “one of the jewels of the CPRIT”.

### AMPLE OPPORTUNITY

But the CPRIT provides other opportunities for emerging investigators, as new laboratories and programmes staff their labs. Some grants follow traditional lines of research. The largest single award, for \$25 million, established the Clinical Trials Network of Texas, which will link the state’s clinical institutions and oncology practices into a cooperative network to make trials more efficient and accessible. The grant will also establish an annotated library of tissue samples for further research, and is expected to create a total of 10–12 clinical and scientific positions.

About 10% of the money has gone to cancer prevention, including grants for programmes aimed at stopping smoking in high-risk populations. And the University of Texas Medical Branch in Galveston has received \$1.2 million to provide the human papilloma virus vaccine against cervical cancer to hundreds of low-income women who receive care at university clinics.

One thread running through the CPRIT grants has been an emphasis on cross-disciplinary work. As a case in point, Rice University in Houston pulled off a recruitment triple last year, in part using CPRIT money to entice two physicists and a chemist to transfer to Texas from the University of California, San Diego. None of them had been involved in cancer research before, working instead on protein folding and other basic cellular processes. Under the CPRIT rules, cancer-research experience isn’t necessary. “I was interested in working on cancer problems, but I’ve never done that,” says physicist Herbert Levine, who arrived at Rice University this summer. His laboratory plans to investigate the cellular cross-talk within and around malignancies and how gene expression determines whether a tumour lives, dies, retreats or seeds secondary tumours in distant tissues.

He’ll be looking for assistance from young

thinkers willing to venture outside familiar lines of thought. Levine plans to hire up to ten students and postdocs trained in physics and biophysics. “The goal is to find people trained in some of the basic techniques and redirect them based on their interests,” he says. Even if their background has been completely outside medical science, “this might give them new perspectives about cancer”.

New talent is also nurtured by grants



The Simmons Cancer Center in Dallas has benefited from CPRIT funding.

that provide training for pre- and postdocs. Universities can design plans to fit their needs, and then apply to the CPRIT for finance. At the University of Texas Health Science Center in San Antonio, molecular biologist Susan Naylor has received more than \$2 million to bring in five doctoral candidates and eight postdocs each year to work in labs on her campus. Naylor had

***“The goal is to find people trained in some of the basic techniques and redirect them based on their interests.”***

already formulated a basic training programme. “It just so happens the CPRIT call came when I was trying to fund this,” she says. CPRIT funding then provided the substrate for the NCI to kick in additional

support. She doubts whether the programme would have launched so successfully without CPRIT backing. Naylor encourages these researchers to secure their own funding, separate from that of their mentors, from whatever source they can find. At the end of the two-year programme, she says, “those are the ones who will get hired”.

In the wake of recent criticisms, Gimson

concedes that the CPRIT’s granting system has had problems as a result of tensions between commercial and basic-science priorities.

But there are plenty of initiatives on the commercial side. Whereas the bulk of CPRIT grants support scientific research, 17% of the funding has been used to encourage the commercialization of drugs and technology. These awards can be impressive — five of the six largest single grants have gone to commercialization-focused projects. Another is to Craig Tooman, a former senior executive at Enzon Pharmaceuticals in Piscataway, New Jersey, who is the first person to be funded under the CPRIT’s Entrepreneur in Residence programme. He is charged with setting up an oncology-based company in Texas. Tooman is now searching for ideas to commercialize. He doesn’t care, he says, whether they come from academic scientists or existing companies.

He cites two companies with whom he has had discussions; both are developing cancer drugs but need additional funding and scientists to take these drugs into clinical trials. Tooman hopes that, eventually, CPRIT-aided companies will attract others to the state because of the density of qualified employees.

The CPRIT is also bolstering companies directly. Apollo Endosurgery in Austin has received \$5 million in seed money from the CPRIT to develop surgical tools that can remove flat and hard-to-snare polyps using an endoscope. In February, the company announced an influx of \$47.6 million in venture capital from other sources. “It would have been extremely challenging to raise that money without the CPRIT funding to really validate our concepts,” says chief executive Dennis McWilliams. With the additional money, the company has expanded to around 25 engineers and clinical specialists, and hopes to hire more.

As the CPRIT tries to get past the mass exodus of key reviewers and appoint a new chief scientific officer, the organization’s leaders do not expect an interruption in funding, with the next round of grants still set for review in early 2013. In a statement, Gimson said that the top priorities for a new chief scientific officer will be to “bring in new peer reviewers and to protect the integrity of CPRIT’s peer review process”. Despite the problems, Gilman still sees an upside for talented researchers seeking funds. “Everyone has been very pleased with the recruitment so far,” he says. “I think everyone is committed to that being given priority.” ■

*Laura Beil is a freelance writer based in Dallas, Texas.*

B. COATS, UT SOUTHWESTERN MEDICAL CENTER



# TURNING POINT

## Olivier Guyon

M. GARCIA/GETTY/MACARTHUR FOUNDATION

Optical physicist and astronomer Olivier Guyon splits his time between the University of Arizona in Tucson and the Subaru Telescope at the National Observatory of Japan in Hawaii. In October he won a John D. and Catherine T. MacArthur Foundation 'genius grant' of US\$500,000.

### What launched your interest in telescopes?

I grew up in the French countryside, where there was no light pollution, and became interested in astronomy at an early age. I got a small telescope as a teenager but ran out of things to look at in the sky because of the instrument's limitations. So I joined astronomy clubs and began building my own telescopes because I wanted one that was larger than what I could afford. That gave me a strong taste for instrumentation and fuelled my interests in optics.

### How did you first make a name for yourself?

I started graduate school soon after two radio astronomers discovered the first Earth-like planets outside the Solar System in 1992. Funding was starting to flow and the environment was ripe for suggesting ideas and developing new techniques. My PhD was very heavy on instrumentation and focused on adaptive optics — combining sensors and mirrors to remove the effects of atmospheric distortion that prevent the detection of planets around stars. Astronomers needed a way to overcome this distortion, and adoptive optics help to recover a sharp image. My success was really due to having the right skills at the time the topic was becoming high profile.

### What was your most important turning point before winning the MacArthur award?

When I came up with what I consider my biggest contribution to the field — designing a better method to block out the direct light from a star in order to detect very faint objects, like exoplanets, next to them. I created a way to alter the telescope beam to physically remove the starlight. The technique halves the costs of deploying a planet-locating telescope in space. That led to other work and projects on the ground as well as to my involvement in future space missions.

### Is that how you came to split your time between two institutions?

Yes. My first position after my PhD was at the Subaru Telescope, where I developed ground-based techniques. When things ramped up on the space side, I took another position at the University of Arizona, where I



was working on NASA future missions. Both institutions agreed to my schedule. I tend to spend more time in Arizona in the spring, when I'm teaching an annual course, and more time in the autumn at Subaru.

### What's it like to get a MacArthur prize?

It's a very strange phone call. They ask two questions when you answer the phone: 'Are you alone?' and 'Are you sitting down?' I knew this was not the type of call I usually receive. My first reactions were a mix of being thrilled and extremely grateful — in part to the unnamed colleagues who told the committee I was worthy of this prize.

### What will the funding allow you to do?

It is well suited to a project my colleague and I started two years ago. We want to prove that you don't have to be at a research institution to discover exoplanets. All that the public, schools or amateurs need is an understanding of how to detect when exoplanets are passing in front of a star, and commercial hardware to build an instrument.

We've built a prototype — a low-cost, lightweight telescope for amateurs that has now demonstrated that it can measure stars' brightness accurately enough to hunt for exoplanets. The funding will help to refine and perfect the prototype. I would like to see it take off and prompt more people to participate in the search for exoplanets. The ultimate goal is to encourage schools and amateurs to build robotic small units that will help them to join our process of discovery. Hopefully, the MacArthur prize and the visibility it generates will build interest and prompt the formation of partnerships to push this further. ■

INTERVIEW BY VIRGINIA GEWIN

## RECRUITMENT

### Federal talent drive

The US Department of Defense needs an overhaul if it is to successfully recruit and retain leading global talent in science, technology, engineering and maths, according to the report *Assuring the U.S. Department of Defense a Strong Science, Technology, Engineering, and Mathematics (STEM) Workforce*. Released on 25 October by the US National Academies in Washington DC, the report finds that STEM professionals view the federal agency as an undesirable workplace because of red tape, a lack of civilian training opportunities, burdensome security-clearance requirements and below-average facilities and equipment. In the near- to mid-term, the agency will probably need to recruit researchers and engineers with expertise in cybersecurity, intelligence, biosecurity and nanotechnology, among other areas, the report notes. To maximize recruitment potential, the agency should relax or expedite some of its security-clearance requirements, the report recommends. It also proposes that the US federal government modify its work-visa and green-card systems to help non-US researchers work and stay in the country.

## TRANSLATIONAL RESEARCH

### Entrepreneurial boost

Universities should provide scientists with mentorship, business-support services and private-sector connections to help them exploit the commercial potential of their research discoveries, says a study published on 24 October (K. D. Harrison *et al. Sci. Transl. Med.* **4**, 157fs37; 2012). The study cites the 'Garage Network' at the California Institute for Quantitative Biosciences (QB3) as an example of success. The QB3 network is a business incubator that supports entrepreneurs at the University of California's San Francisco, Berkeley and Santa Cruz campuses. By providing inexpensive space on campus and easing access to financing, it has helped to launch some 60 businesses, mainly in therapeutics and medical devices, and has generated around 280 jobs since 2006. "Universities have an obligation to ensure that their basic research leads to treatments for diseases and supports a growing economy," says study co-author and QB3 associate director Douglas Crawford. He says that universities should offer space for working on business plans and investor pitches, and should help with company launches and small-business grants.